

PS92-147131

Geostationary Operational Environmental Satellite (GOES-N Report)
Technical Appendix. Volume 2

(U.S.) National Aeronautics and Space Administration, Greenbelt, MD

Feb 92

U.S. Department of Commerce
National Technical Information Service

NTIS

GEOSTATIONARY OPERATIONAL ENVIRONMENTAL SATELLITE

GOES-N

REPORT

TECHNICAL APPENDIX

VOLUME II

PREPARED BY

ADVANCED MISSIONS ANALYSIS OFFICE

GODDARD SPACE FLIGHT CENTER

FEBRUARY 1992

REPRODUCED BY
U S DEPARTMENT OF COMMERCE
NATIONAL TECHNICAL
INFORMATION SERVICE
SPRINGFIELD, VA 22161

GEOSTATIONARY OPERATIONAL ENVIRONMENTAL SATELLITE

GOES-N

REPORT

TECHNICAL APPENDIX

VOLUME II

STUDY PROJECT MANAGER: DR. HARRY E. MONTGOMERY

STUDY PROJECT SCIENTIST: DR. ROBERT F. ADLER

PREPARED BY

ADVANCED MISSIONS ANALYSIS OFFICE

GODDARD SPACE FLIGHT CENTER

FEBRUARY 1992

A.2.1.2.1	Approach	18
A.2.1.2.2	Brief description of the GOES Type II Earth Sensor	19
A.2.1.3	Results of studies/analyses	19
A.2.1.3.1	Modification to reduce the Earth Sensor noise – Use 4 Bolometers	19
A.2.1.3.2	Modification to reduce the effective noise of the Earth Sensor – Run two Earth Sensors and combine their data	22
A.2.1.3.3	Modifications to reduce the low frequency noise content by improving the filtering of threshold control voltage	23
A.2.1.3.4	Modifications to improve stability and reduce noise by using all digital processing of amplified bolometer signals	24
A.2.1.3.5	Modification to the GOES-II Earth Sensor to reduce the low frequency noise content – Combine Type I and Type II signal processing	25
A.2.1.3.6	Modifications to minimize disturbances due To entering/exiting single chord operation	26
A.2.1.4	Comments on Earth Sensors from other vendors	27
A.2.1.4.1	EDO Corp/ Barnes Engineering Div., Shelton, CT	27
A.2.1.4.2	Officina Galileo, Florence, Italy	28
A.2.1.5	Conclusions and recommendations	29
A.2.2	MOMENTUM WHEEL IMPROVEMENTS	30
A.2.2.1	Wheel noise improvements	30
A.2.2.1.1	Introduction	30
A.2.2.1.2	Study methods	33
A.2.2.1.3	Hardware tradeoffs	35
A.2.2.1.4	Conclusions	43
A.2.2.2	Dynamic interaction improvements	49
A.2.2.2.1	Introduction	49
A.2.2.2.2	Study results and system tradeoffs	50
A.2.2.2.3	Conclusions	52
ADDENDUM A.2.2-1:	CALCULATION OF QUANTIZATION & NOISE LEVELS	54
ADDENDUM A.2.2-2:	VARIANCE ANALYSIS OF TACHOMETER/EUROPEAN SPACE AGENCY (ESA) NOISE	55
ADDENDUM A.2.2-3:	MULTIRATE SAMPLING	59
ADDENDUM A.2.2-4:	VARIANCE ANALYSIS OF REALISTIC TACHOMETER NOISE	63
ADDENDUM A.2.2-5:	RATIO OF NOISE IMPROVEMENT FROM INCREASED SAMPLE	64
A.3.1	SENSOR CONFIGURATIONS STUDIED	65
A.3.1.1	Alternative configurations	65
A.3.1.1.1	Inertial reference units	65

A.3.1.1.2	Star trackers	65
A.3.1.1.3	Earth beacon trackers	70
A.3.1.1.4	Polaris tracker with Earth beacon tracker	71
A.3.1.1.5	Landmarks	72
A.3.1.2	Attitude determination (navigation) performance	72
A.3.1.3	Orbit ephemeris performance implications for inertial reference sensing systems	76
A.3.1.3.1	Importance of orbit determination	76
A.3.1.3.2	Orbit errors due to thruster activity	77
A.3.1.3.3	Orbit determination options	82
A.3.1.3.3.1	Landmark and range orbit determination	82
A.3.1.3.3.2	DSN orbit determination	82
A.3.1.3.3.3	GPS orbit determination	83
A.3.1.3.3.4	ATDRSS/TONS orbit determination	83
A.3.1.3.3.5	Multistation ranging orbit determination	83
A.3.1.3.4	Multistation ranging system implementation	87
A.3.1.3.4.1	Multistation ranging options	87
A.3.1.3.4.2	Hybrid ranging system	88
A.3.1.3.5	Summary of orbit determination requirements and options	95
A.3.1.4	Sensor configuration recommendations	96
A.3.1.5	Power, volume, weight, and cost impacts	97
A.3.1.6	Risks	97
A.3.2	MOMENTUM MANAGEMENT SYSTEM DESIGN	98
A.3.2.1	Introduction	98
A.3.2.1.1	Requirements overview	98
A.3.2.1.2	Spacecraft configurations studied	98
A.3.2.1.3	Geostationary disturbance torque overview	98
A.3.2.1.4	Momentum management hardware configurations studied	101
A.3.2.2	Design description and analysis results	101
A.3.2.2.1	Wheel design criteria	101
A.3.2.2.1.1	Torque requirements	103
A.3.2.2.1.2	Momentum storage requirements	103
A.3.2.2.1.3	Weight, cost, power	103
A.3.2.2.2	Momentum management characterization	103
A.3.2.2.2.1	Solar torque estimation	103
A.3.2.2.2.2	Momentum management computer program description	106
A.3.2.2.2.3	Analysis results	106
A.3.2.2.3	Configuration tradeoffs	109
A.3.2.2.3.1	Solar sail trades	110
A.3.2.2.3.2	Thruster firing to dump momentum	110
A.3.2.2.3.3	Magnetic torquer sizing	111
A.3.2.2.3.4	Configuration selection	111
A.3.2.3	Conclusions	111
A.3.3	REACTION WHEEL INDUCED DYNAMIC INTERACTION	113
A.3.3.1	Introduction	113
A.3.3.2	Study results	114

A.3.3.3	Magnetic bearing merits	115
A.3.3.4	Conclusions	115
A.3.4	CONTROLLER DESIGN	116
A.3.4.1	Stability analysis	116
A.3.5	SPACECRAFT MOTION COMPENSATION	121
A.3.5.1	Introduction	121
A.3.5.2	Disturbance environment	121
A.3.5.3	SMC configuration	127
A.3.5.4	Software algorithm description	127
A.3.5.5	Interface definition	127
A.3.5.6	Command and telemetry requirements	127
A.3.5.7	Performance expectations	127
A.3.5.8	Spacecraft impacts	132
A.3.5.9	Conclusions	132
A.3.6	OPTION II & III CONTROLLER PERFORMANCE	132
A.3.6.1	Baseline controller overview	132
A.3.6.2	Simulation description, limitations, etc.	132
A.3.6.2.1	Dynamic models	132
A.3.6.2.2	Star measurements, attitude estimator and error sources	133
A.3.6.2.3	Controller	134
A.3.6.3	Quiescent registration performance	135
A.3.6.4	Spacecraft disturbance accommodation	149
A.3.6.5	SMC disturbance accommodation	157
A.3.6.6	References	157
B.1	ANALOG FILTERING	158
B.1.1	Introduction	158
B.1.1.1	Purpose	158
B.1.1.2	Design requirements	158
B.1.2	Analysis approach	158
B.1.2.1	Finite element model correlation	158
B.1.2.2	Mode sorting procedure	160
B.1.2.3	Compensation design considerations	163
B.1.2.4	Filter design study	167
B.1.3	Analysis results	175
B.1.3.1	Baseline case	175
B.1.3.1.1	Structure transfer function	175
B.1.3.1.2	Block diagram	175
B.1.3.1.3	System frequency response	179
B.1.3.1.4	Time response simulation	179
B.1.3.2	Co-located motor/encoder design	186
B.1.3.3	Two point mirror mount design	186
B.1.3.3.1	Structure transfer function	188
B.1.3.3.2	Block diagram	188
B.1.3.3.3	System frequency response	188

B.1.3.3.4	Time response simulation	193
B.1.3.4	GFRP design	193
B.1.3.4.1	Structure transfer function	197
B.1.3.4.2	Block diagram	197
B.1.3.4.3	System frequency response	197
B.1.3.4.4	Time response simulation	203
B.1.3.5	Prefilter concept	203
B.1.3.5.1	Baseline case with prefilter	207
B.1.3.5.2	Two point mirror mount with prefilter	207
B.1.3.5.3	GFRP design with prefilter	207
B.1.4	Discussion	220
B.1.4.1	Conclusions	220
B.1.4.2	Areas for additional study	220
B.1.5	References	221
B.2	GFRP SERVO DESIGN – MODERN CONTROL APPROACH	222
B.2.1	Introduction	222
B.2.2	Pole placement design procedure	226
B.2.2.1	State equations	226
B.2.2.2	Time scaling	227
B.2.2.3	State feedback	227
B.2.2.4	The Luenberger Observer	229
B.2.2.5	Input gain calculation	230
B.2.2.6	Model order reduction	231
B.2.3	Controller design and analysis	232
B.2.3.1	Controller design	235
B.2.3.2	Simulation results	236
B.2.4	Conclusion	262
B.2.4.1	Further study	262
B.2.5	References	262
B.3	TIME DOMAIN TWO AXIS SIMULATION OF IMAGER EAST/WEST AND NORTH/SOUTH SERVO "BASELINE" DESIGN	265
B.3.1	Introduction	265
B.3.1.1	Purpose	265
B.3.1.2	Background	265
B.3.2	Approach	265
B.3.2.1	ITT Imager East/West and North/South servo block diagrams	265
B.3.2.2	Modal selection	265
B.3.2.3	Modeling the modal equations	276
B.3.2.4	Dahl friction	278
B.3.2.5	IMC (Image Motion Compensation) signal	288
B.3.3	Results	288
B.3.4	Conclusions	293
B.4	FEEDFORWARD COMPENSATION AS APPLIED TO GOES-I SOUNDER	294
B.4.1	Background	294
B.4.2	System concept	297

B.4.3	Servo bandwidth considerations	303
B.4.4	Performance expectations	303
B.4.5	Robustness analysis	304
B.4.6	Hardware requirements	310
B.4.7	Conclusions	311
B.5	INDUCTOSYN VS. OPTICAL ENCODER TRADE STUDY	312
B.5.1	Background	312
B.5.1.2	Summary	312
B.5.1.2	Functional overview	312
B.5.1.3	GOES-I inductosyn	313
B.5.2	Inductosyn limitations	313
B.5.3	Proposed optical encoder baseline	314
B.5.4	Trade study details	314
B.5.4.1	Assumptions	314
B.5.4.2	Resolution	315
B.5.4.3	Accuracy	315
B.5.4.4	Complexity	317
B.5.4.5	Reliability	318
B.5.4.6	Power, weight, size	318
B.5.4.7	Cost	318
B.5.5	Volume, weight, power, and cost impacts	319
B.5.6	Recommendations and conclusions	319
B.6	Digital Image and Spacecraft Motion Compensation (IMC/SMC) Interface for Imager and Sounder	320
B.6.1	Introduction to the GOES I-M IMC system	320
B.6.1.1	Description of the GOES-I IMC interface approach	320
B.6.2	Digital IMC and SMC approaches	320
B.6.2.1	Approach 1	322
B.6.2.2	Approach 2	322
B.6.2.3	Approach 3	322
B.7	EAST/WEST FLEX PIVOT DESIGN STUDY	324
B.7.1	Introduction	324
B.7.1.1	Task objective	324
B.7.1.2	Rationale	324
B.7.2	Design considerations	324
B.7.2.1	Known flex-pivot characteristics	324
B.7.2.2	Drive assembly	325
B.7.2.3	Outstanding questions	325
B.7.3	Conclusions	330
C.1	DISCUSSION OF ALLOCATION OF NAVIGATION, INFRAME REGISTRATION, AND IMAGE-TO-IMAGE ERROR BUDGET OVERVIEW	331
C.1.1	Purpose	331
C.1.2	Background	331
C.1.3	Organization of material	331

C.2	DESCRIPTION OF SYSTEM PERFORMANCE ALLOCATION ERROR SOURCES	331
C.2.1	Option I and GOES I-M	331
C.2.1.1	General	332
C.2.1.2	Short term errors	332
C.2.1.2.1	Attitude stability	332
C.2.1.2.2	Mirror Motion Compensation (MMC) errors	332
C.2.1.2.3	Image Motion Compensation (IMC) errors	336
C.2.1.2.4	Instrument pointing errors	336
C.2.1.2.5	Attitude/Orbit Control Electronics (AOCE) interface errors	336
C.2.1.3	Long Term Errors	336
C.2.1.3.1	Orbit/Attitude Determination with Perfect Attitude Model	336
C.2.1.3.2	Non-repeatable and O/A modeling errors with short span attitude adjustment (SSAA)	337
C.2.1.3.3	Modeling errors	337
C.2.1.3.4	Non-repeatable errors	337
C.2.1.4	Combining error sources for navigation, within frame registration and image-image registration (Option I)	337
C.2.1.4.1	Navigation allocation budget	337
C.2.1.4.2	Within frame registration	338
C.2.1.4.3	Image-Image registration	338
C.2.2	Options II and III (GOES-N)	339
C.2.2.1	General	339
C.2.2.2	Satellite attitude stability errors	339
C.2.2.2.1	Attitude control	339
C.2.2.2.2	Dynamic interaction – rigid body	339
C.2.2.2.3	Dynamic interaction – non-rigid body	346
C.2.2.3	Motion compensation – instrument pointing	346
C.2.2.3.1	Image Motion Compensation (IMC)	346
C.2.2.3.2	Spacecraft Motion Compensation (SMC)	347
C.2.2.3.3	Instrument pointing	347
C.2.2.4	Combining error sources for navigation, within frame registration and image-image registration (Options II & III)	348
C.3	DESCRIPTION OF PROPOSED GOES-N SYSTEMS	348
C.3.1	GOES I-M/Option I system description	348
C.3.2	Option II system description	348
C.3.3	Option III system description	349
C.4	SYSTEM PERFORMANCE ASSESSMENTS	349
D.1	SPATIAL RESPONSE AND CLOUD SMEARING STUDY	357
D.1.1	Overview	357
D.1.2	Theory	357
D.1.3	Implementation	359
D.1.4	Results	361
D.1.5	Conclusions	364

D.2	NOTES ON THE IMPACT OF IMC ON LARGE FOCAL PLANE ARRAYS FOR THE GOES-N IMAGER	382
D.3	SUN SHADE GEOMETRY	386
D.3.1	Overview	386
D.3.1.1	Theory	386
D.3.1.2	Implementation	392
D.3.2.3	Results	392
Conclusions	395
D.4	LONG-TERM STABILITY CALIBRATION OF GOES-N VISIBLE CHANNEL ..	396
D.4.1	Requirements	396
D.4.2	Lunar Calibration	396
D.4.3	Full aperture calibration with indirect sunlight	397
D.4.4	Perforated plate requirement	398
D.4.5	Preliminary perforated plate parameters	399
D.4.6	Ordered array vs random array trade-off	400
D.4.7	Implementation of the perforated plate	402
D.4.8	Earthshine	403
D.4.9	Strawman radiometric error budget	404
D.4.10	Conclusions	405
D.4.11	References	406
D.5	ABERRATIONS OF REFLECTING TELESCOPES	417
D.5.1	Cassegrain and Ritchey-Chretien (RC) aberrations	417
D.5.2	Aberration vs. aperture and field size	420
D.5.3	Conclusions	427
D.5.4	References	427
D.6	SOUNDER PERFORMANCE PREDICTION	428
D.6.1	Overview	428
D.6.2	Assumptions	428
D.6.3	Noise Sources	430
D.6.3.1	Detector noise	430
D.6.3.2	Shot noise	431
D.6.3.3	Quantizer noise	431
D.6.3.4	Omitted noise sources	431
D.6.4	Results	432
D.6.5	Conclusions	432
D.6.6	Bibliography	433
	ATTACHMENT A – SPREADSHEET CHANGES	442
	ATTACHMENT B – DETECTOR NOISE COMPUTATION	443
	ATTACHMENT C – INTEGRATION TIME COMPUTATION	443
	ATTACHMENT D – COMPARISON OF TECHNOLOGIES	444

D.7	SOUNDER DIFFRACTION STUDY	446
D.7.1	Channel specifications	446
D.7.2	Implementation	446
D.7.3	Results	446
E.1	TASK DESCRIPTION	449
E.2	Channel Specifications	449
E.3	Implementation	449
E.4	Results	449

ACRONYMS and ABBREVIATIONS

A/D	Analog-to-digital
ACC	Attitude Control Computer
ACE	Attitude Control Electronics
ACS	Attitude Control System
AEI	Average Error Integrator
AFB	Air Force Base
AIRS	Atmospheric Infrared Sounder
AMAO	Advanced Missions Analysis Office
AOCE	Attitude and Orbit Control Electronics
AP	Aerosol properties
APAR	Absorbed photosynthetically active radiation
APL	Applied Physics Laboratory
ASD	Adaptive slope detection
ATDRSS	Advanced Tracking and Data Relay Satellite Systems
ATS	Applications Technology Satellite
AWIPS	Advanced Weather Information Processing System
AXAF	Advanced X-ray Astronomical Facility
BE	Barnes Engineering
BFL	Back focal length
BLIP	Background limited photodetector
BOL	Beginning of life
BPSK	Binary phase shift key
BRDF	Bi-directional reflectance distribution function
BRTS	Bi-lateral Ranging Transponder System
CA	Course acquisition
C/N	Carrier to noise ratio
CCD	Charged-coupled-Device
CCIR	Consultative Committee on International Radio
CCITT	Consultative Committee on International Telegraph and Telephone
CDA	Command and Data Acquisition
CDR	Critical Design Review
CEI	Coherent error integrator
CIMSS	Cooperative Institute for Meteorological Satellite Studies
CM	Conventional matching
COBE	Cosmic Background Explorer
COSPAS	MORFLOT Search and Rescue Space System (USSR)
CP	Cloud Products
CR	Coefficient of reflection
CRAF	Comet Rendezvous Asteroid Flyby
CSC	Computer Sciences Corporation
CSDL	Charles Stark Draper Laboratory
DADS	Dynamic Analysis and Design System
DAPS	DCS Automatic Processing System
DCP	Data Collection Platform

DCPI	DCP interrogation
DCPR	DCP response
DCS	Data Collection System
DOD	Department of Defense
dof	degree of freedom
DOMSAT	Domestic communications satellite
DRIRU	Dual Redundant & Inertial Reference Unit
DSN	Deep Space Network
DUS	Data Utilization Station
E_b/N_0	Energy per bit to Noise density ratio
ECA	Earth Central Angle
EIRP	Effective isotropic radiated power
EKF	Extended Kalmer Filter
ELT	Emergency Locator Transmitter
ELV	Expendable launch vehicle
EOL	End of life
EOS	Earth Observing System
EPIRB	Emergency Position Indicating Radio Beacon
EPS	Energetic Particle Sensor
ERL	Environmental Resources Laboratory
ES	Earth Sensor
ESA	Earth Sensor Assembly
ESA	European Space Agency
ETS	Engineering Test Satellite (Japanese)
EUV	Extreme ultraviolet
EUVE	Extreme Ultraviolet Explorer
FEM	Finite element model
FHST	Fixed-head star trackers
FLAME	Flight Loads and Matrix Executive
FORS	Fiberoptic rotation sensors
FOV	Field of View
FTS	Fourier Transform Spectrometer
FWHM	Full width half maximum
G/T	Gain-to-temperature ratio
GE	General Electric Company
GEM	Geosynchronous Environmental Mission
GEO	Geosynchronous earth orbit
GFE	Government furnished equipment
GFRP	Graphite fiber reinforced plastic
GOES	Geostationary Operational Environmental Satellite
GPS	Global Positioning Satellite
GR	Ground resolution
GRO	Gamma Ray Observatory
GSFC	Goddard Space Flight Center
GST	GOES-N Study Team
GTO	Geosynchronous Transfer Orbit
GVAR	GOES variable data format

GVHRR	Geosynchronous Very High Resolution Radiometer
H α	Hydrogen-alpha
H α I	Hydrogen-alpha Imager
HAC	Hughes Aircraft Company
HDOS	Hughes Danbury Optical Systems
HEPAD	High Energy Proton and Alpha Detector
HgCdTe	Mercury cadmium tellurium
HIS	High-resolution Interferometer Sounder
HRG	Hemispheric Resonator Gyroscope
HSRS	High Spectral Resolution Sounder
HST	Hubble Space Telescope
I/O	Input/output
I&T	Integration and test
ICD	Interface Control Document
IFOV	Instantaneous field of view
IGFOV	Instantaneous Geometric Field of View
IMAX	Maximum inclination
IMC	Image Motion Compensation
INCA	Interactive Numerical Control Analysis computer program
InGaAs	Indium gallium arsenide
INR	Image Navigation and Registration
INSAT	Indian Satellite
InSb	Indium antimonide
IP	Imagery Products
IPS	Instrument Pointing System
IR	Infrared
IRES	IR Earth Sensor
IRU	Inertial Reference Unit
ITT	International Telephone & Telegraph Company
IUE	International Ultraviolet Explorer
JPL	Jet Propulsion Laboratory
LAS	Loral AeroSYS
LED	Light Emitting Diode
LEO	Low earth orbit
LMS	Lightning Mapper Sensor
LMSC	Lockheed Missile and Space Corporation
LNA	Low Noise Amplifier
LOS	Line of sight
LP	Lightning Products
LPARL	Lockheed Palo Alto Research Laboratory
LPS	Low energy Plasma Sensor
LSB	Least significant bit
LSF	Line spread function
LTR	Loop transfer recovery
LW	Long wave
LWIR	Long wave infrared
MCC	Mission Control Center

MDI	Michelson Doppler Imager
MDL	Multiuse Data Link
MDSSC	McDonnell Douglas Space System Company
MEPED	Medium Energy Proton/Electron Detector
METSAT	Meteorological satellite
MIMO	Multiple input/output
MLI	Multi-Layer insulation
MMC	Mirror Motion Compensation
MMS	Multimission Modular Spacecraft
MORFLOT	Soviet Ministry of Merchant Marine
MP	Moisture Products
MSFC	Marshall Space Flight Center
MSI&T	Mission system integration & test
MTB	Magnetic Torquer Bar
MTF	Modulation transfer function
MW	Mid wave
N/A	Not applicable
NASA	National Aeronautics and Space Administration
NASCAP	NASA Charging Analyzer Program
NASTRAN	NASA Structural Analysis Program
NEAN or NEDN	Noise equivalent delta radiance
NEAT or NEDT	Noise equivalent delta temperature
NEA	Noise equivalent angle
NESDIS	National Environmental Satellite & Data Information Service
NMS	Newton-meter-seconds
NOAA	National Oceanic and Atmospheric Administration
NS	Nanosecond
NWS	National Weather Service
O/A	Orbit/attitude
OATS	Orbit and Attitude Tracking System
OBC	On board computer
OG	Officina Galileo
OGE	Operations ground equipment
OSIP	Operational Satellite Improvement Programs
OSSA	Office of Space Science and Applications
PA	Power amplifiers
PC	Photo-conductive
PDR	Processed data relay
PID	Proportional-plus-Integral-plus-Derivation
POP	Program Operation Plan
PP	Precipitation Products
PPS	Pulse per second
PSD	Power spectral density
PSK	Phase Shift Key
PtSi	Platinum silicon
PV	Photo-voltaic
QPSK	Quadrature Phase Shift Key

RAO	Resources Analysis Office
RC	Ritchey-Chretien
RF	Radio frequency
RFP	Request For Proposal
RH	Relative humidity
RLG	Ring Laser Gyro
RM	Radar matching
RMS	Root mean square
ROM	Rough order of magnitude
RPO	Revolution per orbit
RSS	Root Sum Square
RW	Reaction wheel
RWA	Reaction Wheel Assembly
S&AI	Swales & Associates, Inc.
S/N, SNR	Signal to noise ratio
SA	Solar array
SAR, S&R	Search and Rescue
SAMEX	Solar Activity Measurement Experiment
SARSAT	S&R Satellite
SBRC	Santa Barbara Research Center
SDL	Sounder data link
SEDS	Small Explorer Data Systems
SEL	Space Environmental Laboratory
SEM	Space Environment Monitor
SINDA	System Improved Numerical Differencing Analyzer
SISO	Single input/output
SK	Stationkeeping
SM	Satellite matching
SMC	Spacecraft Motion Compensation
SMM	Solar Maximum Mission
SOCC	Satellite Operations Control Center
SOH	Spacecraft Operations Handbook
SOHO	Solar Heliospheric Observatory
SOW	Statement of Work
SP	Snow and ice Products
SPS	Sensor Processing System
SS	Summer solstice
SSAA	Short span attitude adjustment
SSAI	Science Systems and Applications Incorporated
SSPA	Solid state power amplifier
STI	Stanford Telecommunications Incorporated
SVM	Solar Vector Magnetograph
SW	Short wave
SWF	Spatial weighting function
SXI	Solar X-Ray Imager
SXT	Solar X-Ray Telescope
T&C	Telemetry and command

TBD	To be determined
TDI	Time-delay integration
TDRSS	Tracking and Data Relay Satellite Systems
TEC	Total Electron Content
TED	Total Electron Detector
TIROS	Television Infrared Operational Satellite
TLM	Telemetry
TM	Thematic Mapper
TMAX	Maximum time
TONS	TDRSS Onboard Navigation System
TP	Temperature products
TWTA	Traveling Wave Tube Amplifier
UAQPSK	Unbalanced Asynchronous QPSK
UARS	Upper Atmospheric Research Satellite
UHF	Ultra high frequency
UIT	Ultraviolet Imaging Telescope
ULI	Uplink interface
USAF	United States Air Force
USMCC	United States Mission Control Center
UTC	Universal time coordinated
VAS	VISSR Atmospheric Sounder
VHF	Very high frequency
VHRR	Very High Resolution Radiometer
VISSR	Visible Infrared Spin Scan Radiometer
VP	Vegetation Products
VUV	Vacuum ultraviolet
WD	Whole disk
WEC	Westinghouse Electric Company
WEFAX	Weather facsimile
WFOV	Wide Field of View
WP	Wind Products
WSR	Weather Service Radar
WSR-88D	WSR limited production phase, D for doppler
XRS	X-Ray Sensor

UNITS

μm	micrometer
μr	microradian
A	amperes
arcmin	arcminute (minutes of arc)
arcsec	arcseconds (seconds of arc)
bps	bits per second
$^{\circ}\text{C}$	degree centigrade
ft	feet
Hz	hertz
in	inch
K	degrees kelvin
kbps	kilobit per second
keV	thousand electron volts
km	kilometer
lb	pound
m	meter
mbar	millibar
Mbps	million bits per second
MeV	million electron volts
MeV/n	million electron volts per nucleon
MHz	megahertz
min	minute
mrad	milliradian
ms	millisecond
mW	milliwatt
nm	nanometer
nT	nanotesla
oz	ounce
rad	radian
s	second
sr	steradian
V	volt
W	watt

SYMBOLS

λ	wavelength
σ	standard deviation
ν	wave number
dB	decibel
f#	f-number
RC1, RC2, ...	NOAA Core Requirements
RE1, RE2, ...	NOAA Enhanced Requirements
RO1, RO2, ...	NOAA Option Requirements
R_{\odot}	radius of the sun
Z	atomic number
Δ	delta

LIST OF TABLES

A.1.1-1	Inclination vs. Time On-Station
A.2.2-1	Summary of Attitude Errors as a Result of Specific Inputs (1σ)
A.3.1-1	Candidate CCD Star Trackers
A.3.1-2	Availability of 6 th Magnitude Stars
A.3.1.3-1	Thruster Activity Orbit Error Summary
A.3.1.3-2	GOES-N/Option II and III Orbit Determination Simulation
A.3.1.3-3	GPS Time Transfer Performance for Common-Mode/Common-View Operations
A.3.1.3-4	CDA and Remote Site Ranging Error Sources Using GPS Timing
A.3.1.3-5	One Way Ranging Errors CDA and Remote Site to Spacecraft
A.3.2-1	Estimate of Solar Radiation Torques
A.3.2-2	Maximum Momentum Buildup Over One Orbit; No Magnetic Torque Bars
B.2.1-1	GFRP Mode Set
B.4.5-1	Analysis Input Parameter
B.7.2.2-1	Mounting Accuracy Requirement for High Accuracy Optical Encoders
C.2.1-1	GOES I-M (Option I) Navigation Error Allocation Budget Pixel Location Accuracy
C.2.1-2	GOES I-M (Option I) Within Frame Relative Pixel-to-Pixel Location Error Allocation Budget
C.2.1-3	GOES I-M (Option I) Relative Image-to-Image Registration Error Allocation Budget
C.2.2-1	Option II Navigation Error Allocation Budget: Pixel Location Accuracy
C.2.2-2	Option II Within Frame Relative Pixel-to-Pixel Location Error Allocation Budget
C.2.2-3	Option II Relative Image-to-Image Registration Error Allocation Budget
C.2.2-4	Option III Navigation Error Allocation Budget; Pixel Location Accuracy
C.2.2-5	Option III Within Frame Relative Pixel-to-Pixel Location Error Allocation Budget
C.2.2-6	Option III Relative Image-to-Image Registration Error Allocation Budget
C.4-1	GOES I-M (Option I) Comparison of 3σ Performance for Navigation, Within Frame Registration, and Image-to-Image Registration
C.4-2	GOES I-M (Option II) Comparison of 3σ Performance for Navigation, Within Frame Registration, and Image-to-Image Registration
C.4-3	GOES I-M (Option III) Comparison of 3σ Performance for Navigation, Within Frame Registration, and Image-to-Image Registration
D.1.3-1	Imager Channel Specifications
D.1.3-2	Filter Bandwidths
D.1.4-1	98% Rise Times (No Delay Compensation)
D.1.4-2	Delay Times to Reach 50% Intensity
D.1.4-3	98% Rise Time (Delay Compensation)
D.1.4-4	Duration Periods for 2% Absolute Radiometric Accuracy
D.3.1-1	Sun Angle Relative to Equatorial Plane
D.3.1-2	Sun Shade Length Requirement
ADD.B-2	Defraction Pattern
ADD.B-2	Defraction Pattern
ADD.B-2	Defraction Pattern
ADD.B-4	Defraction Pattern
ADD.B-5	Defraction Pattern

ADD B-6	Defraction Pattern
ADD.B-7	Defraction Pattern
D.5-1	Design Case Studies
D.5-2	Aberration vs Aperture and Field Size
D.5-3	Optical Aberrations of Various Telescope Design Forms
D.7-1	Souder Channel Specifications
E.2-1	Souder Channel Specifications

LIST OF FIGURES

A.1.1-1	Maximum Tolerable Inclination Constraint Circle
A.1.1-2	Inclination vs Time On-Station
A.1.1-3	IMC Signal at 3.1 deg Inclination
A.1.1-4	IMC Signal at 0.5 deg Inclination
A.1.1-5	Servo Error at 0.1 deg Inclination
A.1.1-6	Servo Error at 3.1 deg Inclination
A.1.1-7	GOES East Coverage for Various Orbital Inclinations
A.1.1-8	GOES West Coverage for Various Orbital Inclinations
A.2.1-1	Type II Baseline Configuration
A.2.1-2	Four Bolometer Configuration
A.2.2-1	On-Orbit Pitch Controller
A.2.2-2	On-Orbit Roll/Yaw Controller
A.2.2-3	Covariance for Narrow Band Noise PSD
A.2.2-4	Attitude Errors for Simulation FSCLONG3.PUT
A.2.2-5	Attitude Errors for Simulation PERFESND3.PUT
A.2.2-6	Attitude Errors for Simulation NDNOTKNOIS3.PUT
A.2.2-7	Attitude Errors for Simulation NDNOTQON3.PUT
A.2.2-8	Attitude Errors for Simulation CLEANWH3.PUT
A.2.2-9	Attitude Errors for Simulation THREE3.PUT
A.2.2-10	Power Spectral Density of Theta W.R.T. Tach Noise
A.2.2-11	Imaging V Mode Roll/Yaw Stability
A.2.2-12	Housekeeping V Mode Roll/Yaw Stability
A.2.2-13	Imaging Stability, L-Mode, Roll/Yaw Loop
A.2.2-14	Housekeeping Stability, L-Mode, Roll/Yaw
A.2.2-15	Dynamic Interaction Test Summary of Results
A.2.2-16	Torque Noise Response of Magnetic Wheel Without/With Active Control
A.2.2-17	Power Spectral Density of Theta W.R.T. Tach Noise
A.2.2-18	Power Spectral Density of Theta W.R.T. ESA Noise
A.3.1-1	Star Tracker Boresight Spacing
A.3.1-2	Gyro Model Including Two Noise Sources
A.3.1-3	Attitude Estimation ($T > T_d$)
A.3.1.3-1	Orbit Error for Thruster Misalignment
A.3.1.3-2	Orbit Motion: In-Track Position vs Time
A.3.1.3-3	Orbit Prediction Errors
A.3.1.3-4	Block Diagram of GOES Remote Station Ranging Equipment Configuration
A.3.1.3-5	Equipment Configuration
A.3.2-1	GOES Solar Sail Configurations Studied
A.3.2-2	Moments of Inertia
A.3.2-3	Momentum Buildup-Orbit and Spacecraft Orientation
A.3.2-4	Estimate of Solar Radiation Torques
A.3.2-5	Yaw Momentum Buildup Over One Orbit-No Solar Sail
A.3.2-6	GOES-N Option III (orbit configuration)
A.3.4-1	GOES-N Option II and III Spacecraft Control System Conceptual Block Diagram
A.3.4-2	GOES-N Spacecraft Control
A.3.4.1-1	Root Locus of GOES-N Controller

A.3.4.1-2	Root Locus of GOES-N Controller
A.3.5.2-1	Spacecraft Motion Compensation
A.3.5.1-1	GOES Internal Disturbance Torques
A.3.5.2-2	GOES Internal Disturbance Torques
A.3.5.2-3	Spacecraft Internal Disturbance Torques
A.3.5.4-1	Kalman Filter Algorithm
A.3.5.7-1	Spacecraft Motion Compensation
A.3.5.7-2	Spacecraft Motion Compensation
A.3.5.7-3	Spacecraft Internal Disturbance Torques
A.3.6-1	Attitude Estimation Errors with 2.2 deg X 2.5 deg FOV, 1 Star per Tracker, Updates Every 2 Seconds and No Catalog Errors
A.3.6-2	Attitude Estimation Errors with 2.2 deg X 2.5 deg FOV, 1 Star per Tracker, Updates Every 20 Seconds and No Catalog Errors
A.3.6-3	Attitude Estimation Errors with 2.2 deg X 2.5 deg FOV, 1 Star per Tracker, Updates Every 200 Seconds and No Catalog Errors
A.3.6-4	Attitude Estimation Errors with 2.2 deg X 2.5 deg FOV, 1 Star per Tracker, Updates Every 2 Seconds and 2.5 μ r Catalog Errors
A.3.6-5	Attitude Estimation Errors with 2.2 deg X 2.5 deg FOV, 1 Star per Tracker, Updates Every 20 Seconds and 2.5 μ r Catalog Errors
A.3.6-6	Attitude Estimation Errors with 2.2 deg X 2.5 deg FOV, 1 Star per Tracker, Updates Every 200 Seconds and 2.5 μ r Catalog Errors
A.3.6-7	Attitude Estimation Errors with 2.2 deg X 2.5 deg FOV, 2 Stars per Tracker, Updates Every 2 Seconds and 2.5 μ r Catalog Errors
A.3.6-8	Attitude Estimation Errors with 2.2 deg X 2.5 deg FOV, 2 Stars per Tracker, Updates Every 20 Seconds and 2.5 μ r Catalog Errors
A.3.6-9	Attitude Estimation Errors with 2.2 deg X 2.5 deg FOV, 3 Stars per Tracker, Updates Every 2 Seconds and 2.5 μ r Catalog Errors
A.3.6-10	Attitude Estimation Errors with 2.2 deg X 2.5 deg FOV, 3 Stars per Tracker, Updates Every 20 Seconds and 2.5 μ r Catalog Errors
A.3.6-11	Attitude Estimation Errors with 8 deg Square FOV, 5 Stars per Tracker, Updates Every Second and 5 μ r Catalog Errors
A.3.6-12	Attitude Estimation Errors with 4 deg Square FOV, 1, 3 and 5 Stars per Tracker, Updates Every Second and 5 μ r Catalog Errors
A.3.6-13	Uncontrolled Spacecraft Response to Sounder Disturbance
A.3.6-14	Controlled Spacecraft Response to Sounder Disturbance
A.3.6-15	Uncontrolled Spacecraft Response to Imager Disturbance Over 3 Seconds with Diagonal Spacecraft Moment-of-Inertia Tensor
A.3.6-16	Uncontrolled Spacecraft Response to Imager Disturbance Over 1 Minute with Full Spacecraft Moment-of-Inertia Tensor
A.3.6-17	Controlled Spacecraft Response to Imager Disturbance Over 1 Minute with Full Spacecraft Moment-of-Inertia Tensor
A.3.6-18	Controlled Spacecraft Response to Imager Disturbance Over 5 Minutes With Black-Body Calibration Slew at 2 Minutes
A.3.6-19	Combined Response to Estimation Errors and Imager Disturbance with Black-Body Calibration Slew at 2 Minutes
B.1.2-1	Baseline Instrument FEM
B.1.2-2	GOES Scanner Structure Frequency Response

B.1.2-3	GOES Scanner Structure Frequency Response
B.1.2-4	GOES Scanner Structure Frequency Response
B.1.2-5	GOES Scanner Structure Frequency Response
B.1.2-6	Design Study Results
B.1.2-7	Filter Design Study Results
B.1.2-8	Filter Design Study Results
B.1.2-9	Filter Design Study Results
B.1.2-10	Filter Design Study Results–filter order comparison
B.1.2-11	Filter Design Study Results–example of added damping
B.1.2-12	Filter Design Study Results–lowpass/bandpass comparison
B.1.2-13	Filter Design Study Results–lowpass/bandpass comparison
B.1.3-1	Baseline Controller Block Diagram
B.1.3-2	Uncompensated Frequency Response – Baseline Design
B.1.3-3	Compensated Frequency Response – Baseline Design
B.1.3-4	Test Results from Open Loop Frequency Response Test of Actual Servo
B.1.3-5	Frequency Response with Compensated Baseline Design, 0.3% Damping and No 175 Hz Mode
B.1.3-6	Closed Loop Frequency Response – Baseline Design
B.1.3-7	Time Response of Baseline Design – 140 μ r Step
B.1.3-8	Structure Frequency Response for Co-located Motor/Encoder Design
B.1.3-9	Two Point Mirror Mount Design Structure Frequency Response
B.1.3-10	E/W Controller Block Diagram – Two Point Mirror Mount Design
B.1.3-11	Uncompensated Frequency Response – Two Point Mirror Mount Design
B.1.3-12	Compensated Frequency Response – Two Point Mirror Mount Design
B.1.3-13	Closed Loop Frequency Response – Two Point Mirror Mount Design
B.1.3-14	Time Response of Two Point Mirror Design 140 μ r Step
B.1.3-15	Motor Torque Comparison – Two Point Mirror Mount and Baseline Designs
B.1.3-16	FEM Representation of GFRP Design
B.1.3-17	GFRP Design Structure Frequency Response
B.1.3-18	E/W Controller Block Diagram – GFRP Design
B.1.3-19	Uncompensated Frequency Response – GFRP Design
B.1.3-20	Compensated Frequency Response – GFRP Design
B.1.3-21	Closed Loop Frequency Response – GFRP Design
B.1.3-22	Time Response of GFRP Design
B.1.3-23	Motor Torque Comparison – GFRP and Baseline Design
B.1.3-24	Baseline Prefilter Block Diagram
B.1.3-25	Linear Unit Step Response of Baseline Design with Prefilter
B.1.3-26	Closed Loop Frequency Response – Baseline Design with Prefilter
B.1.3-27	Time Response of Baseline Prefilter Design with Dahl Friction
B.1.3-28	Two Point Mirror Mount Prefilter Block Diagram
B.1.3-29	Linear Unit Step Response – Two Point Mirror Mount Design with Prefilter
B.1.3-30	Closed Loop Frequency Response – Two Point Mirror Mount Design with Prefilter
B.1.3-31	Time Response of Two Point Mirror Mount Prefilter Design – Dahl Friction
B.1.3-32	GFRP Prefilter Block Diagram
B.1.3-33	Linear Unit Step Response of GFRP Design with Prefilter
B.1.3-34	Closed Loop Frequency Response – GFRP Design with Prefilter
B.1.3-35	Time Response of GFRP Prefilter Design with Dahl Friction

- B.2.1-1a,1b Feedback Parallel Compensation and Cascade (series) Compensation
- B.2.1-2 Frequency Response of the Reduced GFRP Mode Set
- B.2.2-1 Stabilization by Observer State Feedback with Matched Plant and Observer Models
- B.2.2-2 Stabilization by Observer State Feedback with Model Mismatch Plant and Observer Models
- B.2.3-1 Step Response for Matched Plant and Controller Model; Modes 1,3,4, Modeled
- B.2.3-2 Difference Between Estimated and Measured Shaft Angles with Modes 1,3,4, Modeled in the Plant and Controller
- B.2.3-3 Control Torque for Matched Plant and Controller Model; Modes 1,3,4, Modeled
- B.2.3-4 Plant States (modal displacements) for Matched Plant and Controller Model; Modes 1,3,4, Modeled
- B.2.3-5 Step Response for Plant with Modes 1,3,4,5,6,8,11,15 and Controller Designed with Modes 1,3,4
- B.2.3-6 Difference Between Estimated and Measured Shaft Angles for Plant with Modes 1,3,4,5,6,8,11,15 and Controller Designed with Modes 1,3,4
- B.2.3-7 Control Torque for Plant with Modes 1,3,4,5,6,8,11,15 and Controller Designed with Modes 1,3,4
- B.2.3-8 Frequency Response for Equivalent Open-Loop System, for Plant with Modes 1,3,4,5,6,8,11,15 and Controller Designed with Modes 1,3,4
- B.2.3-9 Frequency Response for Closed-Loop System for Plant with Modes 1,3,4,5,6,8,11,15 and Controller Designed with Modes 1,3,4
- B.2.3-10 Frequency Response of the Control Torque for Plant with Modes 1,3,5,6,8,11,15 and Controller Designed with Modes 1,3,4
- B.2.3-11 Frequency Response of the Controller (with measured shaft angle as input) and Controller Designed with Modes 1,3,4
- B.2.3-12 Frequency Response of the Estimated Shaft Angle (with measured shaft angle as input) for Controller Designed with Modes 1,3,4
- B.2.3-13 Step Response for Plant with Modes 1,3,4,5,6,8,11,15 (modal frequency increased 20%, damping increased to 0.3%) and Controller Designed with Modes 1,3,4
- B.2.3-14 Difference Between Estimated and Measured Shaft Angles for Plant with Modes 1,3,4,5,6,8,11,15 (modal frequency increased 20% and damping increased to 0.3%) and Controller Designed with Modes 1,3,4
- B.2.3-15 Step Response for Plant Modes 1,3,4,5,6,8,11,15 (modal frequency decreased 20%, damping increased to 0.3%) and Controller Designed with Modes 1,3,4
- B.2.3-16 Difference Between Estimated and Measured Shaft Angles for Plant with Modes 1,3,4,5,6,8,11,15 (modal frequency decreased 20% and damping increased to 0.3%) and Controller Designed with Modes 1,3,4
- B.2.3-17 D≠0. Frequency for Equivalent Open-Loop System for Plant with Modes 1,3,4,5,6,8,11,15 and Controller Designed with Modes 1,3,4
- B.2.3-18 D≠0. Frequency Response for Plant with Modes 1,3,4,5,6,8,11,15 and Controller Designed with Modes 1,3,4
- B.2.3-19 D≠0. Frequency Response of the Control Torque for Plant with Modes 1,3,4,5,6,8,11,15 and Controller Designed with Modes 1,3,4
- B.2.3-20 D≠0. Frequency Response of the Controller (with measured shaft angle as input) and Controller Designed with Modes 1,3,4
- B.2.3-21 D≠0. Frequency Response of the Estimated Shaft Angle (with measured shaft angle as input) for Controller Designed with Modes 1,3,4

B.2.3-22	Step Response for Plant with Modes 1,3,4,5,20,21,23 and Controller Designed with Modes 1,3,4. Modes 20,21 and 23 are Destabilized
B.2.3-23	Frequency Response for Plant with Modes 1,3,4,5,20,21,23 and Controller Designed with Modes 1,3,4. Modes 20,21 and 23 are Destabilized
B.3.2-1	Imager East/West Servo Block Diagram
B.3.2-2	Imager/Sounder North/South Servo Block Diagram
B.3.2-3	GOES-N Imager East/West Servo
B.3.2-4	GOES-N Imager East/West Servo
B.3.2-5	GOES-N Imager East/West Servo
B.3.2-6	GOES-N Imager North/South Servo
B.3.2-7	GOES-N Imager North/South Servo
B.3.2-8	GOES-N Imager North/South Servo
B.3.2-9	Sequence of Events
B.3.2-10	State Space Representation of the Modal Equations
B.3.2-11a	FLAME Run for DAIS State Space Model of Modal Equation
B.3.2-11b	Create modal Damping Vector
B.3.2-11c	Top Right Half of a Matrix
B.3.2-12	Yoke Configuration
B.3.2-13	GOES Scan Assembly
B.3.2-14	Bearing Stiffness for Small Angular Motion (Experimental)
B.3.2-15	Motor/Load Rigid Body Model for Scanner Assuming Viscous Friction Bearing Model
B.3.2-16	Motor/Load Rigid Body Model for Scanner Assuming Spring Stiction Bearing Model
B.3.2-17	IMC Program Parameters
B.3.2-18	IMC signal - 0.5 deg - Inclination 0.0 - NS GIMBAL
B.3.2-19	IMC signal - 0.5 deg - Inclination 0.0 - NS GIMBAL
B.3.3-1	E/W Shaft Error Angle vs Time (Two Axis Simulation)
B.3.3-2	E/W Shaft Error Angle vs Time (Single Axis Simulation)
B.4.1-1	GOES-I Sounder East/West Step and Settle Response
B.4.1-2	GOES-I Sounder East/West Servo Block Diagram
B.4.2-1	Basic Concept
B.4.2-2	Angle, Rate, and Acceleration Profilers
B.4.2-3	Plant Inversion
B.4.2-4	Angle Command, Before and After Notch Filter
B.4.2-5	Overall System Concept
B.4.4-1	Simulation Block Diagram
B.4.4-2	Unloaded Response
B.4.4-3	Response with Notch Filter
B.4.4-4	Response with Notch Filter and Torque Feedforward
B.4.4-5	Response with Notch Filter and Torque Feedforward Detail
B.6.1-1	GOES-I Servo Block Diagram
B.6.2-1	GOES-N. East/West Servo Block Diagram
B.7.2.2-1	Flex Pivot Center Shift
B.7.2.2-2	Flex Pivot Drive Assembly
B.7.2.2-3	Mounting Accuracy Requirements for High Accuracy Optical Encoders
B.7.2.2-4	Readout Error Caused by Flex Pivot Center-Shift

C.4-1	Option I (GOES I-M modified) 3 σ Performance Assessment
C.4-2	Option II 3 σ Performance Assessment
C.4-3	Option III 3 σ Performance Assessment
D.1.2-1(a)	System Block Diagram
D.1.2-1(b)	Equivalent Block Diagram
D.1.4-1(a)	Channel 1 Line Spread Function
D.1.4-1(b)	Channel 2 Line Spread Function
D.1.4-1(c)	Channel 3 Line Spread Function
D.1.4-1(d)	Channel 4 Line Spread Function
D.1.4-1(e)	Channel 5 Line Spread Function
D.1.4-2	Detector Model
D.1.4-3(a)	Channel 1 LSF * Detector
D.1.4-3(b)	Channel 2 LSF * Detector
D.1.4-3(c)	Channel 3 LSF * Detector
D.1.4-3(d)	Channel 4 LSF * Detector
D.1.4-3(e)	Channel 5 LSF * Detector
D.1.4-4(a)	(Expanded Scale) Channel 1 Step Responses
D.1.4-4(b)	(Expanded Scale) Channel 2 Step Responses
D.1.4-4(c)	(Expanded Scale) Channel 3 Step Responses
D.1.4-4(d)	(Expanded Scale) Channel 4 Step Responses
D.1.4-4(e)	(Expanded Scale) Channel 5 Step Responses
D.1.4-5(a)	Channel 1 Pulse Responses
D.1.4-5(b)	Channel 2 Pulse Responses
D.1.4-5(c)	Channel 3 Pulse Responses
D.1.4-5(d)	Channel 4 Pulse Responses
D.1.4-5(e)	Channel 5 Pulse Responses
D.2-1	IMC for -3.5 deg Inclination
D.2-2	IMC for -3.5 deg Inclination
D.2-3	IMC for -3.5 deg Inclination
D.3.1-1	Geometry for Sun Shade Analysis
D.3.1-2	Geometry for Computing Phases
D.3.1-3	Sun Shade Geometry
D.5-1	Reflective Telescope Design Types
D.5-2	Cassegrain and Ritchey-Chretien Aberrations at F/2.5
D.5-3	Cassegrain and Ritchey-Chretien Aberrations at F/5.0
D.5-4	Cassegrain and Ritchey-Chretien Aberrations at F/7.5
D.5-5	Cassegrain and Ritchey-Chretien Aberrations at F/10.0
D.6-1	NE Δ T vs Focal Plane Temperature
D.6-2	Noise Elements (Baseline conditions)
D.6-3	Noise Elements (Extended conditions)
D.6-4	Comparison of Different Ground Resolutions
D.6-5	Comparison of Different Frame Time
D.6-6	Comparison of Different Optics Diameters
D.6-7	Comparison of Different Focal Plane Arrays
D.6-8	Comparison of Different Frame Sizes
D.7-1	Sounder: Short Wave SWF unity area
D.7-2	Sounder: Mid Wave SWF unity area

D.7-3 Sounder: Long Wave SWF unity area
E.4-1 Sounder: Short Wave SWF unity area
E.4-2 Sounder: Mid Wave SWF unity area
E.4-3 Sounder: Long Wave SWF unity area

APPENDIX A

A.1.1 OPERATION WITH INCLINATIONS UP TO 3.5 DEG TO EXTEND LIFE

A.1.1.1 Introduction

A.1.1.1.1 Purpose

The purpose of this alternative spacecraft North/South orbital inclination and North/South stationkeeping study is to assess the potential for eliminating the North/South stationkeeping maneuvers required to keep the spacecraft on station.

It has been demonstrated that, for 24 hour near-equatorial circular satellite orbits, considerable cross-track sustaining velocity can be saved by placing the satellite initially in the maximum allowable orbital inclination (rather than in the nominal equatorial orbit) with an appropriate orbital ascending node location such that the orbit plane inclination decreases towards zero. In placing the satellite at this maximum allowable orbital inclination, the time the satellite remains on-station within a given inclination tolerance without the use of any active control is maximized. This study sought to pursue a maximum allowable orbital inclination (initial and optimum node location) of 3.5 deg (IMAX) with a corresponding maximum time on station (TMAX), and to ascertain the operational considerations/constraints of doing so.

Inserting the spacecraft at an optimum inclination, one where minimal or no stationkeeping maneuvers are required throughout the mission life, has many potential benefits. After the time period TMAX has elapsed, a one maneuver nodal rotation (North/South Stationkeeping maneuver) is required to reestablish the optimal drift cycle, or simply put to ensure the spacecraft remains within the allowable inclination tolerance. This single North/South stationkeeping maneuver after time TMAX is in direct contrast to multiple North/South stationkeeping maneuvers that would be required if the spacecraft were:

1. initially inserted at the nominal equatorial orbit, or
2. maintained within a tighter (smaller) allowable inclination tolerance.

The goal of this study is to place the satellite in an orbital inclination having TMAX greater than the expected mission life. Eliminating North/South stationkeeping maneuvers serves to eliminate the propellant that would be required to perform these maneuvers, and hence to decrease spacecraft weight. In this study, the maximum time (TMAX) of particular interest is given to be approximately seven years.

Another advantage to reducing North/South stationkeeping maneuvering is in the minimization of operational constraints. Serious operational constraints are imposed on a momentum bias spacecraft to support North/South stationkeeping maneuvering. The primary constraint is on the navigation of images, where after a maneuver navigation could be out of specification for eight hours. Additionally, every attempt at sustained firing of thrusters and the associated complex operations increases the risk of spacecraft component and/or operator failure, resulting in jeopardization to the mission.

A.1.1.1.2 Image Motion Compensation (IMC) concerns

Of primary importance to this 3.5 deg inclination study, is whether at this increased inclination Image Navigation and Registration (INR) specification compliance can be met. An increase in orbital inclination serves to increase the amount of IMC signal necessary to correctly navigate/register the instruments' images. This increase similarly increases the IMC signal acceleration, which in turn increases the bandwidth required of the servo control loop. It is therefore of primary consideration that the servo control loop be able to handle the increase in IMC signal generated by the attitude and orbit control electronics for the orbital inclination increase to be considered operationally.

A.1.1.1.3 Feasibility/Other issues under consideration

Other issues must be considered in the determination of the feasibility of the inclination increase. These include:

A.1.1.1.3.1 Communications

Communications capability of the spacecraft and the ground users receiving GOES data and products is of primary concern. A change in the inclination of the spacecraft will change the communications coverage of the Earth and could affect some users located on the edge of the satellite's visibility circle (the area of communications coverage of the ground users). In other words, an increased inclination could potentially exclude some users located on the visibility edge from receiving GOES data/products. Perhaps more important is the fact that many users may have fixed base antennas which would be incapable of providing a good link at high inclinations.

A.1.1.1.3.2 Field of View (FOV)

The FOV of the instruments is of concern. A change in the inclination of the spacecraft will change the instruments capability to view the same surface of the Earth.

A.1.1.1.3.3 Radiative Cooler

The instruments have radiative coolers, whose purpose is to maintain the detector temperature within an allowable range, that are shaded from the sun by a shield for solar elevation angles to a maximum of 25 deg (23.5 deg maximum sun angle above the equatorial plane plus 1.5 deg misalignment). The capacity of the cooler varies with season (sun angle) and length of time on orbit. An increase in inclination angle may under certain circumstances allow solar radiation to interfere with cooler operation by exceeding the maximum allowable sun angle above the equatorial plane. This could have the unacceptable result of radiation hitting the cooler patch. Extension of the sun shade would be necessary under this circumstance.

A.1.1.1.3.4 Polaris Sensor

One option under consideration is to add a Polaris sensor. This could be added to the GOES-1 configuration to sense yaw. Consideration of its FOV must be given.

A.1.1.1.4 Background

A.1.1.1.4.1 Stationkeeping operations for GOES-I

As a starting place, it is necessary to understand the stationkeeping operations of the current GOES-I spacecraft.

A.1.1.1.4.1.1 North/South maneuvers and inclination constraints

The GOES-I spacecraft has an inclination constraint for orbital operations of 0.5 deg about the equator. This constraint is imposed in order for the instruments to meet Image Navigation and Registration (INR) specification. In order to meet this constraint, frequent (about once a year) North/South stationkeeping maneuvers are required. These stationkeeping maneuvers are performed to counteract the lunar-solar effect (the gravitational forces exerted by the Sun and Moon on the spacecraft). The basic strategy consists of starting the stationkeeping cycle with the spacecraft at one edge of the inclination deadband and allowing the spacecraft to drift toward zero inclination and then to the inclination edge, where the maneuver will again be performed at an optimum node to bring the spacecraft back to the beginning of the deadband while minimizing fuel consumption. This minimizes the velocity and hence the propellant requirements. Minimizing the propellant required to conduct North/South stationkeeping maneuvers is vital to the longevity of the mission.

A.1.1.1.4.1.2 Impact on operations

During stationkeeping operations, imaging/sounding do not occur. Thrusters are being fired and INR specification compliance cannot be reliably met. In addition, there are numerous other constraints imposed on operations as a result of the stationkeeping maneuver:

- constraints require that the Solar Array (SA) be positioned nearly perpendicular to the thruster set to minimize plume impingement.
- constraints limit the angle to which the SA can be pointing away from the Sun and still meet power requirements (no North/South stationkeeping maneuver can occur during the eclipse season due to the constraint that the batteries must be fully charged prior to entering each eclipse).

A.1.1.2 Approach

The first step of the study was to verify that the 3.5 deg inclination was feasible with respect to the above mentioned concerns, namely:

1. possible from an orbital mechanics point of view
2. takes into account the FOV coverage
3. takes into account the communications coverage
4. ascertains the effect on the AOCE's capability to process the IMC signals required, and the instruments scan servo control loop's capability to handle these necessary signals.

To address the first concern, a FORTRAN program was written to calculate the relationship of the satellite maximum time kept on-station (TMAX) versus the orbit maximum inclination (IMAX) and the delta velocity required to maintain the orbit for the related maximum times (the velocity change required to enable a North/South stationkeeping maneuver). The program calculates parameters relative to an epoch of interest corresponding to the year 2000 with results imported to a spreadsheet program. Corresponding plots of Delta V and IMAX vs. TMAX were produced.

A Satellite Calculator and Visibility Plotter program (Satplot) was used to observe several visibility circles on a mediocre projection map of the Earth to address the issues #2 and #3 above.

Finally, an IMC simulation program written in FORTRAN was run to calculate the IMC signal resulting from various orbital inclinations from 0.5 deg up to and including the 3.5 deg case. Results of the simulations were then compared. This IMC information in conjunction with IMC servo simulations at 3.1 deg are used to assess the response of the instruments servo control loop to the IMC signal at the maximum inclination.

A.1.1.3 Results/Findings

A.1.1.3.1 Navigation impact

A.1.1.3.1.1 Orbital mechanics

The problem of optimal North/South stationkeeping has been solved by Kamel and Tibbits and is implemented in practice for virtually all geostationary satellites. The method is illustrated with the aid of Figure A.1.1-1 which shows a plot of $x = \sin i \cos \Omega$ versus $y = \sin i \sin \Omega$ where i is the inclination and Ω is the node. The major perturbations which cause inclination error are solar and lunar point mass gravity. The influence of these perturbations alters the inclination and node so that the trajectory in the xy -plane is that of a circle centered at $y = \sin i_s$ (we are free to define the zero longitude for the node to correspond with this point). The inclination i_s is a stable inclination of about 8 deg. The trajectory is that of simple harmonic motion so the rate at which the trajectory is traced out is independent of its amplitude (to first order). In actuality there are other perturbations which cause smaller motions superimposed over the circular trajectory and also East/West drift; however, with frequent East/West stationkeeping the long-term satellite dynamics are well represented by this model. A constraint circle can be drawn in the xy -plane which has radius equal to $\sin i_m$ where i_m is the maximum tolerable inclination. The optimal stationkeeping strategy involves a limit cycle between the two maneuver points shown in Figure A.1.1-1. These maneuver points have been selected such that the angle subtended from the center of the circular trajectory is maximized (hence the time within the constraint circle is maximized). Note that the initial inclination is i_m and that this inclination decreases but not necessarily to zero and then increases back to i_m during the satellite time on station. Maneuvers for optimal stationkeeping actually rotate the node so that the limit cycle can begin again.

Table A.1.1-1 shows the results from the program that calculates TMAX and Delta V for initial node locations or IMAX in the range 0.1 deg to 5.1 deg. Observing column three (TMAX in years) it is seen that for an initial inclination of 3.5 deg the maximum time on-station is 7.9 years. For the mission time-line of particular interest here (seven years), the initial node

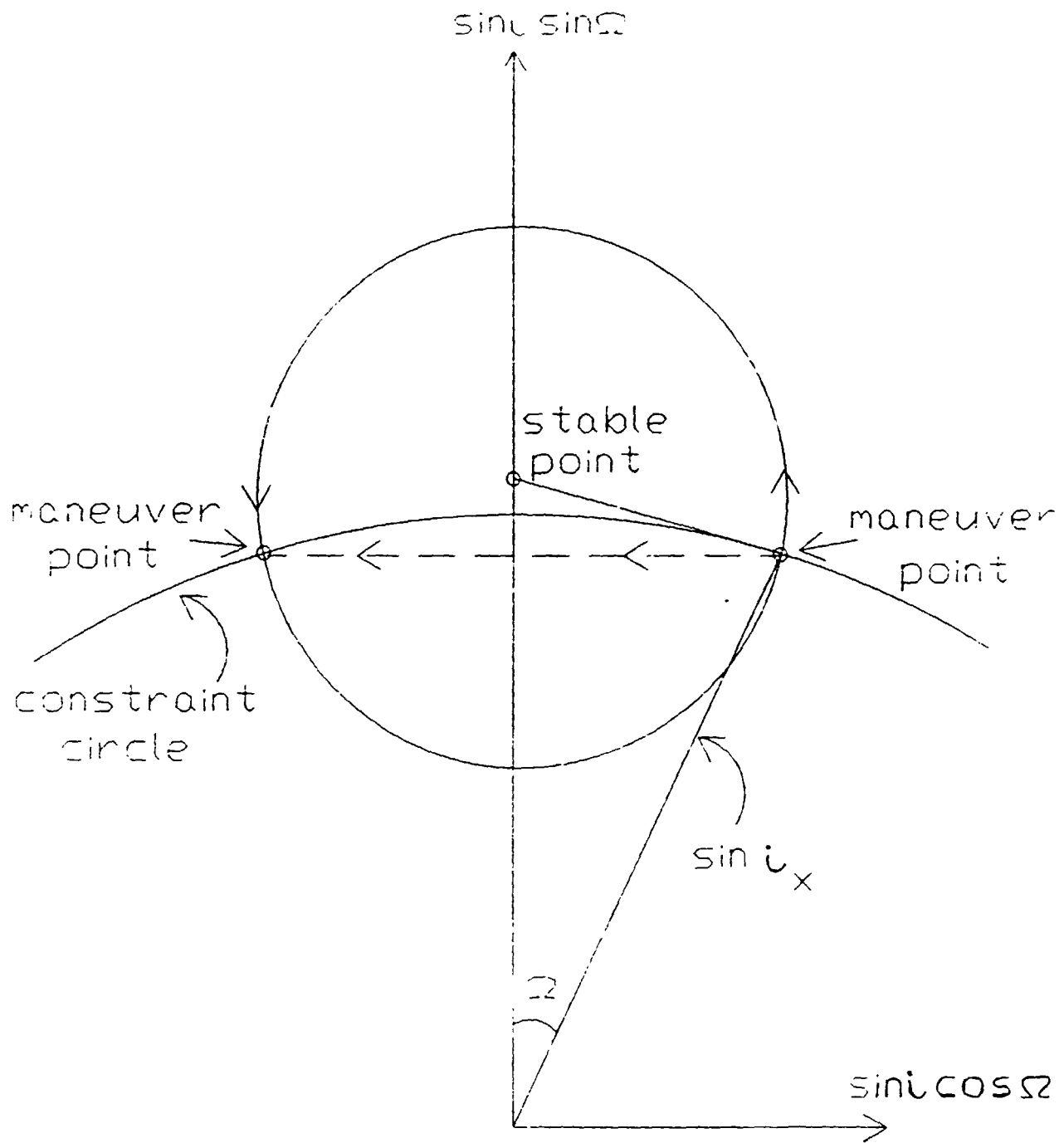


Figure A.1.1-1. Maximum Tolerable Inclination Constraint Circle

location (IMAX) is seen to be at approximately 3.1 deg. This will be the reference IMAX. Note that OHMBEGIN is the node location prior to a North/South stationkeeping maneuver, and OHMEND is the location at the end of the North/South stationkeeping maneuver. DELTA V is the change in velocity required to achieve this node rotation.

In the concept discussed here no North/South stationkeeping maneuvers are planned so the constraining circle radius must be sized such that it is traversed in a period equal to the defined mission lifetime. Figure A.1.1-2 shows the constraining inclination i_c (IMAX) versus lifetime TMAX for an epoch of 2000. As stated earlier, for a seven year lifetime a constraining inclination of 3.1 deg is required. (As an aside note that there is little to be gained by making a few maneuvers at large constraining inclinations less than 3.1 deg versus a single maneuver at 3.1 deg). With this concept the mission life would begin at 3.1 deg and end at the same inclination.

A.1.1.3.1.2 IMC signal and servo response

The high inclination mission has a significant impact on the North/South servo. Figure A.1.1-3 shows the North/South IMC signal required to compensate for inclination when the satellite is at the top of its "figure-8" and the equator is scanned. This is the worst case for IMC magnitudes and accelerations. Figure A.1.1-3 shows the exact IMC required and has a mathematically divergent rate at the limbs. For comparison Figure A.1.1-4 shows the required IMC signal at a 0.5 deg maximum inclination, the baseline inclination for the GOES-I mission. Comparing the maximum IMC signal occurring at an E/W gimbal angle of 0 deg, it is shown that at a North/South maximum inclination of 0.5 deg the maximum IMC signal is 1550 μ r compared to 9530 μ r at a North/South maximum inclination of 3.1 deg (Figure A.1.1-3). Pertaining to Figure A.1.1-3, no servo of any design would be able to follow such a signal without error. Of interest here is the net servo error at some point near the limb (say at 60 deg Earth Central Angle (ECA) which is about 8 deg and 400 msec from center scan). Several simulations (courtesy of ATR) were made with the GOES-I North/South servo to assess these errors. Figure A.1.1-5 shows a servo error of about 1 μ r for an inclination of 0.1 deg at the 60 deg ECA point. This degrades significantly at 3.1 deg inclination where a 31 μ r error is found as shown in Figure A.1.1-6. The main reason for the servo error degradation is that the servo bandwidth is too small to track such high rates and acceleration (i.e., the Fourier transform of the IMC signal has significant power out of band). Another concern for high inclinations is the limiting motor torque. The simulations were configured with several simplifications which probably improve the servo error:

1. No structural modes are included, however, the Chebyshev filter remains in the model.
2. The Analog Error Integrator is turned off.
3. The IMC is generated in the analog domain.

The actual IMC signal generated by the GOES-I AOCE is not that shown in Figure A.1.1-3, rather it is a rational polynomial approximation which lacks the divergent behavior of the rate at the limb. This is a better conditioned signal from the point of view of the servo, however, it will differ from the mathematically correct IMC so that even if no servo errors are present there will still be a navigation error. In our engineering judgment, it would be neither possible to:

IMAX (DEGREES)	TMAX (MONTHS)	TMAX (YEARS)	OHMBEGIN (DEGREES)	OHMEND (DEGREES)	DELTAV (M/S)
0.1	2.5635	0.2136	278.8231	457.2728	10.7030
0.2	5.5822	0.4652	279.7913	456.6084	21.3997
0.3	8.5733	0.7144	280.7345	455.9367	32.0837
0.4	11.5369	0.9614	281.6524	455.2558	42.7490
0.5	14.4731	1.2061	282.5446	454.5674	53.3897
0.6	17.3820	1.4485	283.4112	453.8707	64.0004
0.7	20.2639	1.6887	284.2522	453.1657	74.5758
0.8	23.1194	1.9266	285.0677	452.4524	85.1109
0.9	25.9490	2.1624	285.8579	451.7307	95.6009
1.0	28.7535	2.3961	286.6235	451.0008	106.0414
1.1	31.5338	2.6278	287.3650	450.2625	116.4280
1.2	34.2911	2.8576	288.0830	449.5160	126.7564
1.3	37.0264	3.0855	288.7784	448.7612	137.0226
1.4	39.7412	3.3118	289.4522	447.9984	147.2227
1.5	42.4370	3.5364	290.1055	447.2275	157.3528
1.6	45.1152	3.7596	290.7393	446.4486	167.4089
1.7	47.7776	3.9815	291.3550	445.6619	177.3872
1.8	50.4260	4.2022	291.9539	444.8675	187.2838
1.9	53.0621	4.4218	292.5372	444.0654	197.0946
2.0	55.6878	4.6407	293.1064	443.2557	206.8155
2.1	58.3049	4.8587	293.6628	442.4386	216.4423
2.2	60.9152	5.0763	294.2079	441.6141	225.9707
2.3	63.5206	5.2934	294.7431	440.7823	235.3960
2.4	66.1229	5.5102	295.2695	439.9432	244.7136
2.5	68.7236	5.7270	295.7885	439.0971	253.9185
2.6	71.3243	5.9437	296.3013	438.2437	263.0058
2.7	73.9266	6.1605	296.8090	437.3833	271.9701
2.8	76.5317	6.3776	297.3124	436.5158	280.8060
2.9	79.1410	6.5951	297.8126	435.6412	289.5080
3.0	81.7554	6.8130	298.3102	434.7594	298.0704
3.1	84.3760	7.0313	298.8057	433.8704	306.4875
3.2	87.0029	7.2500	299.2999	432.9741	314.7532
3.3	89.6380	7.4699	299.7929	432.0703	322.8617
3.4	92.2819	7.6902	300.2852	431.1588	330.8068
3.5	94.9340	7.9112	300.7767	430.2394	338.5824
3.6	97.5953	8.1320	301.2676	429.3119	346.1822
3.7	100.2659	8.3551	301.7580	428.3759	353.5998
3.8	102.9476	8.5790	302.2478	427.4310	360.8286
3.9	105.6396	8.8033	302.7369	426.4770	367.8620
4.0	108.3432	9.0286	303.2253	425.5131	374.6926
4.1	111.0593	9.2549	303.7132	424.5390	381.3131
4.2	113.7889	9.4824	304.2005	423.5539	387.7153
4.3	116.5336	9.7111	304.6875	422.5573	393.8905
4.4	119.2953	9.9413	305.1746	421.5484	399.8289
4.5	122.0762	10.1730	305.6625	420.5262	405.5195
4.6	124.8792	10.4066	306.1519	419.4901	410.9505
4.7	127.7076	10.6423	306.6440	418.4390	416.1078
4.8	130.5655	10.8805	307.1400	417.3717	420.9757
4.9	133.4575	11.1215	307.6419	416.2873	425.5366
5.0	136.3890	11.3658	308.1516	415.1846	429.7697
5.1	139.3661	11.6138	308.6716	414.0622	433.6518

Table A.1.1-1 Inclination vs. Time On-Station

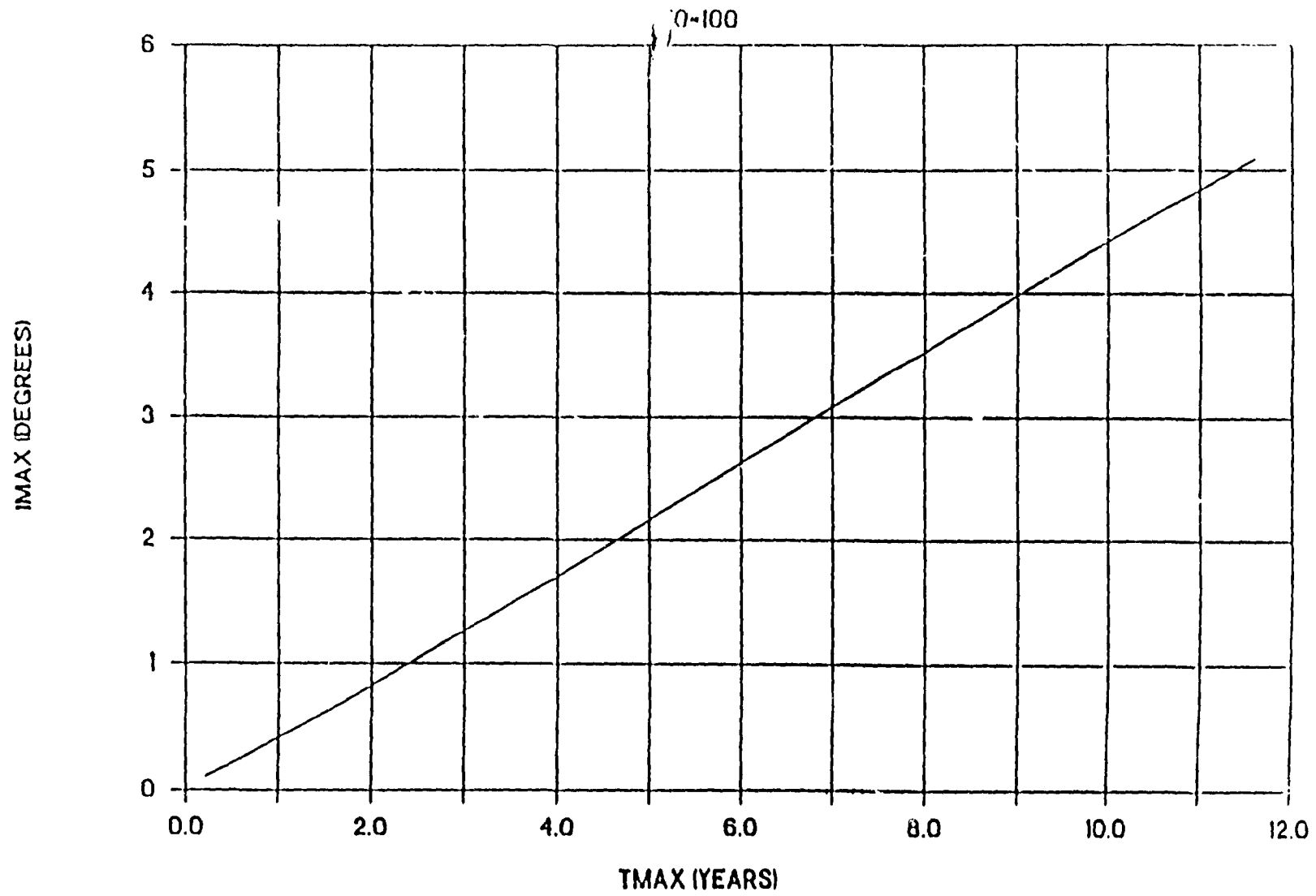


Figure A.1.1-2. Inclination vs. Time On-Station

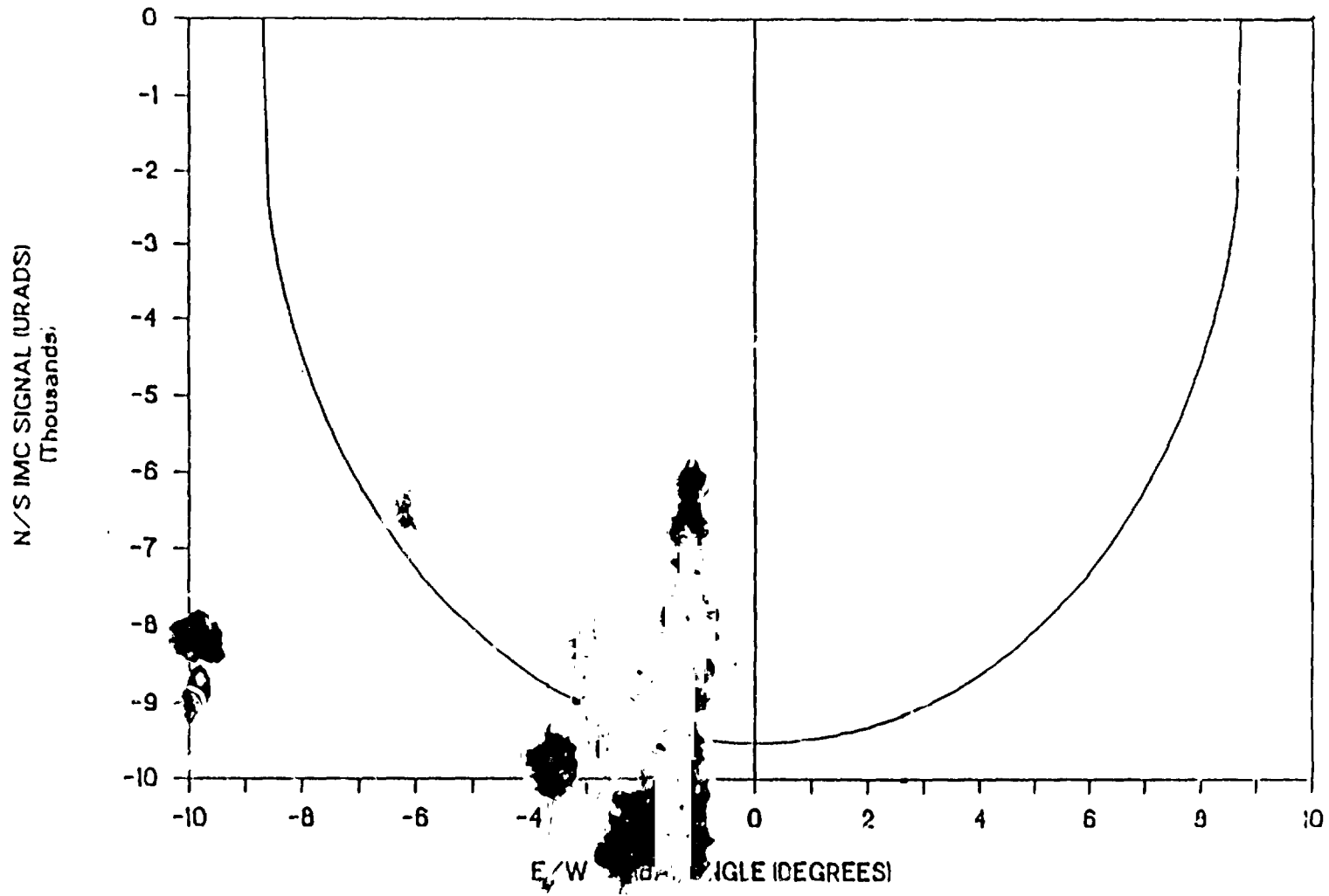


Figure A 1.1-3. IMC Signal at 3.1 deg Inclination.

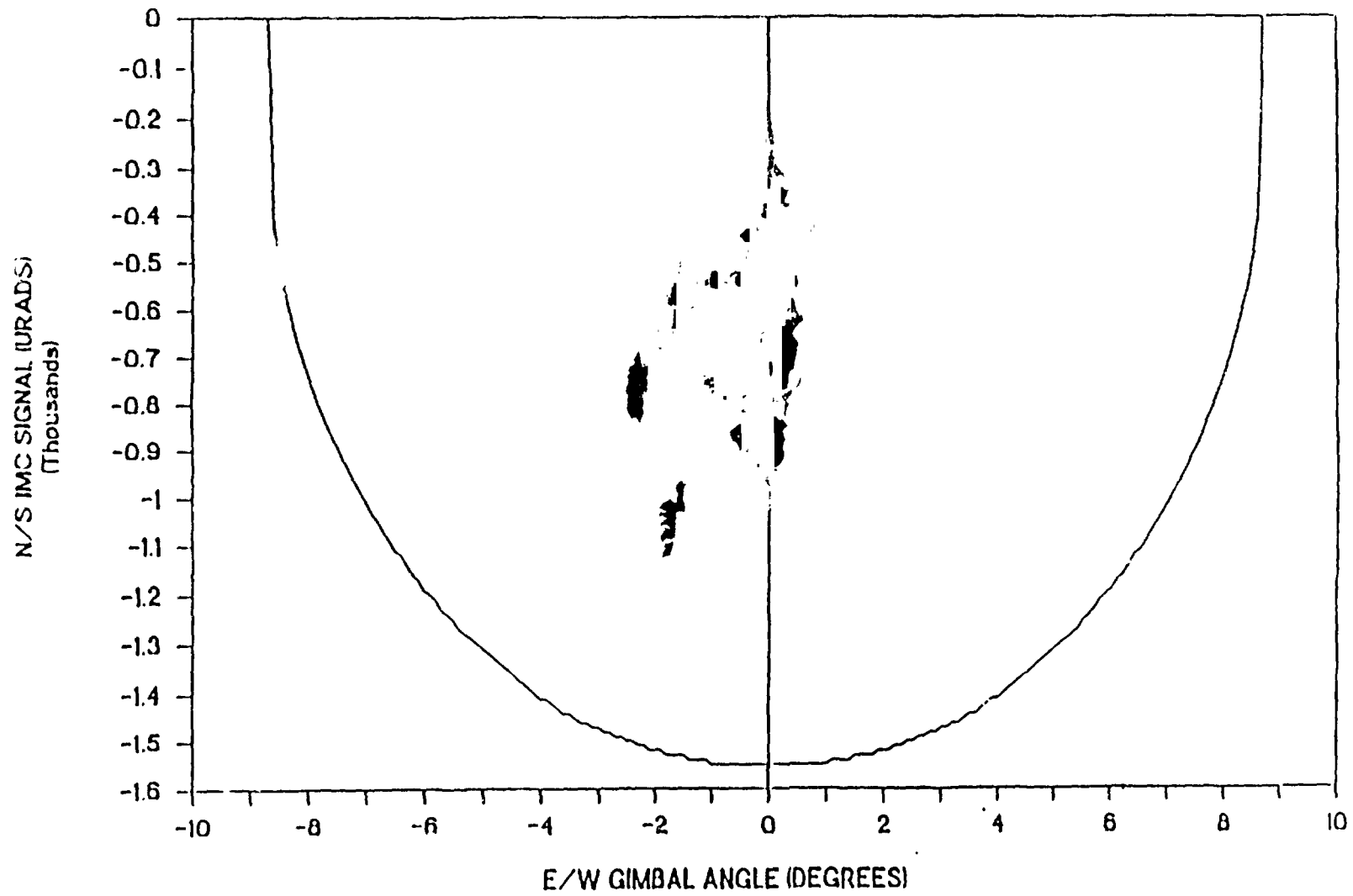


Figure A.1.1-4. IMC Signal at 0.5 deg Inclination.

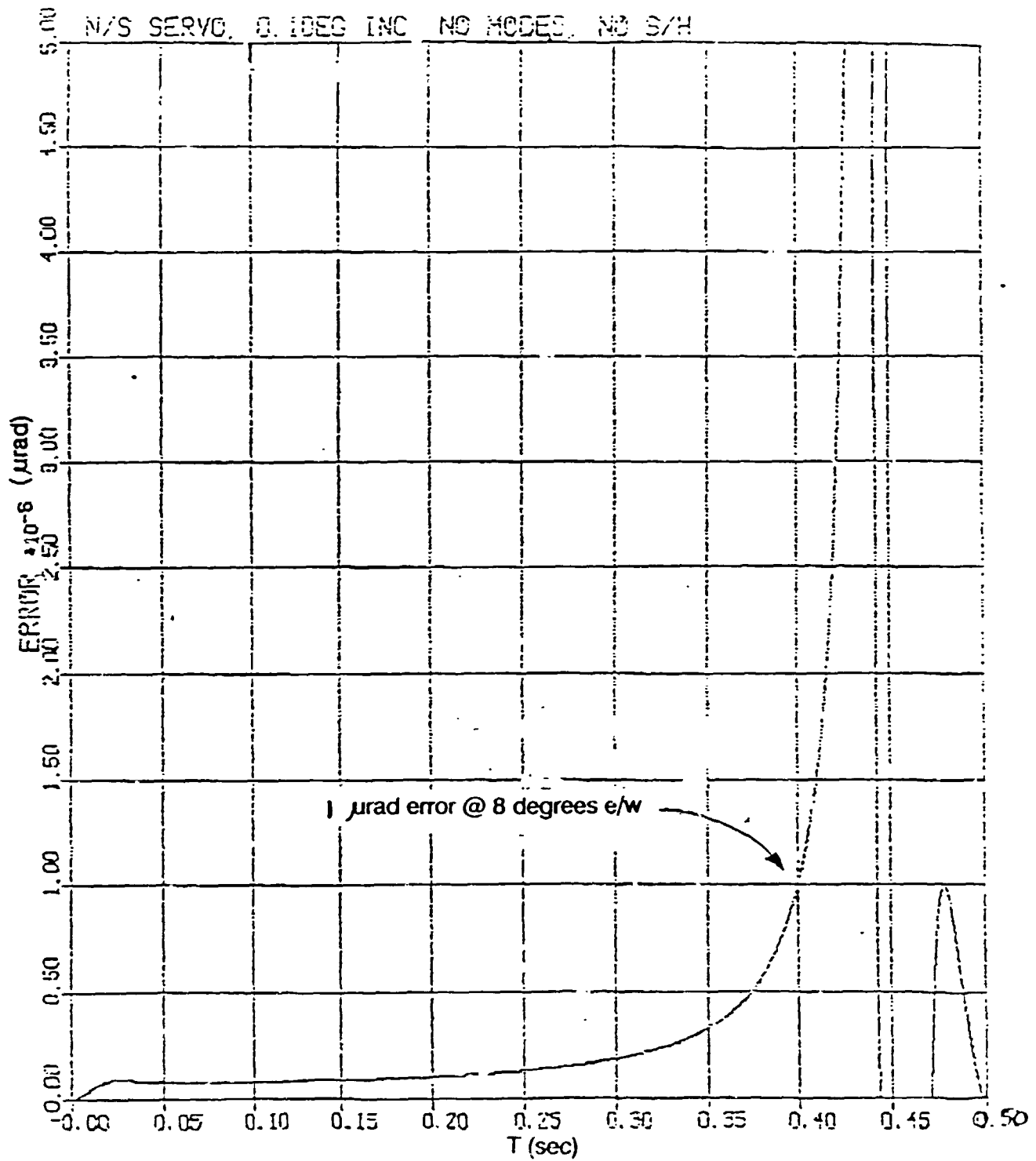


Figure A 1 1-5. Servo Error at 0.1 deg Inclination.

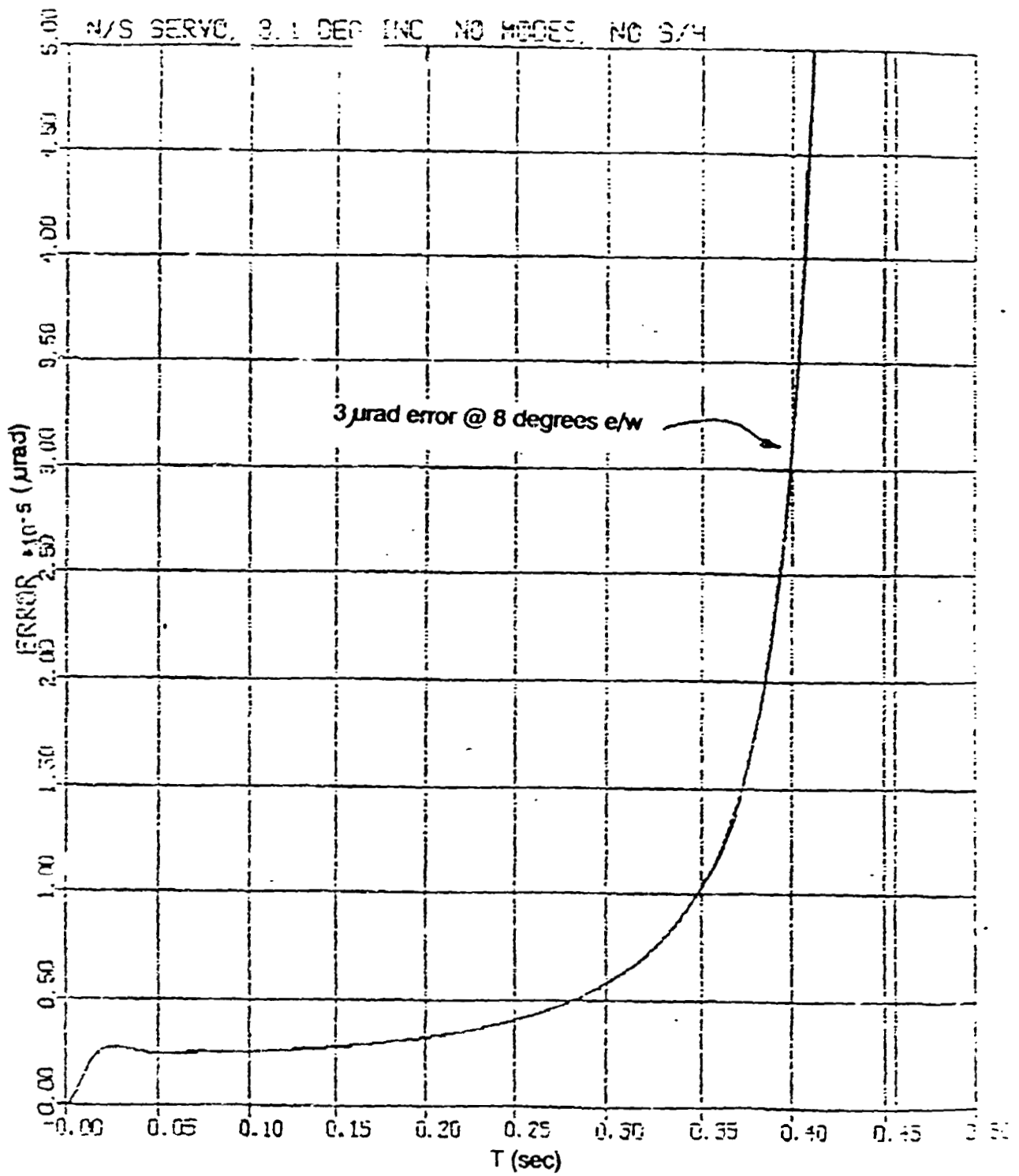


Figure A.1.1-6. Servo Error at 3.1 deg Inclination

1. Tailor the IMC space/earth transition to reduce servo error while keeping tight tolerance on the difference between the tailored IMC and its correct value; nor,
2. Increase the servo bandwidth to the point where the servo error with a 3.1 deg inclination IMC signal can be tracked with tolerable servo error without placing structural modes within the servo bandwidth, resulting in instabilities.

A.1.1.3.2 Impact on other satellite subsystems

A.1.1.3.2.1 Satellite/communications coverage

Satplot was used to address the issue of visibility from the GOES satellite, and communications support for potential users.

Figures A.1.1-7 illustrates the coverage expected from the GOES East spacecraft at 0 deg, 3.5 deg, and -3.5 deg inclinations with Earth Station (ES) elevation angles of 0 deg and 21.9 deg. The 21.9 deg case is equivalent to a 68.1 deg zenith angle which shows the coverage for an Earth Central Angle (ECA) of 60 deg, where IMC in-spec performance gracefully degrades. Figure A.1.1-8 shows the coverage expected from the GOES West satellite for the same cases. The lower (0 deg) ES elevation angle will show greater coverage than will actually be achievable, however. By comparison it can be seen that the GOES users in the North and South American regions should be visible from the East satellite regardless of the inclination, although the coverage will be degraded outside of the 60 deg ECA. For the West satellite, any potential users in the extreme North-eastern United States may be excluded at -3.5 deg inclination taking into account the optimistic ES coverage. Users in Central South America and North-East Canada also could not be visible from the West satellite. Any potential users located at extreme latitudes may be out of the line-of-sight of the spacecraft.

From a communications perspective the ability of the users to receive GOES data is a more serious problem. Most users have fixed based antennas (non-tracking) which are incapable of receiving data from the satellite at inclined orbits of 3 deg or more. Tracking antennas will be required at all ground stations receiving wideband data from GOES-N except perhaps for WEFAX and DCS users.

A.1.1.3.2.2 Cooler performance

An initial assessment indicates that the increase in inclination should have a minimal impact on the cooler performance. Sun radiation will impinge upon the cooler shield, but no radiation should directly or indirectly reflect onto the cooler patch.

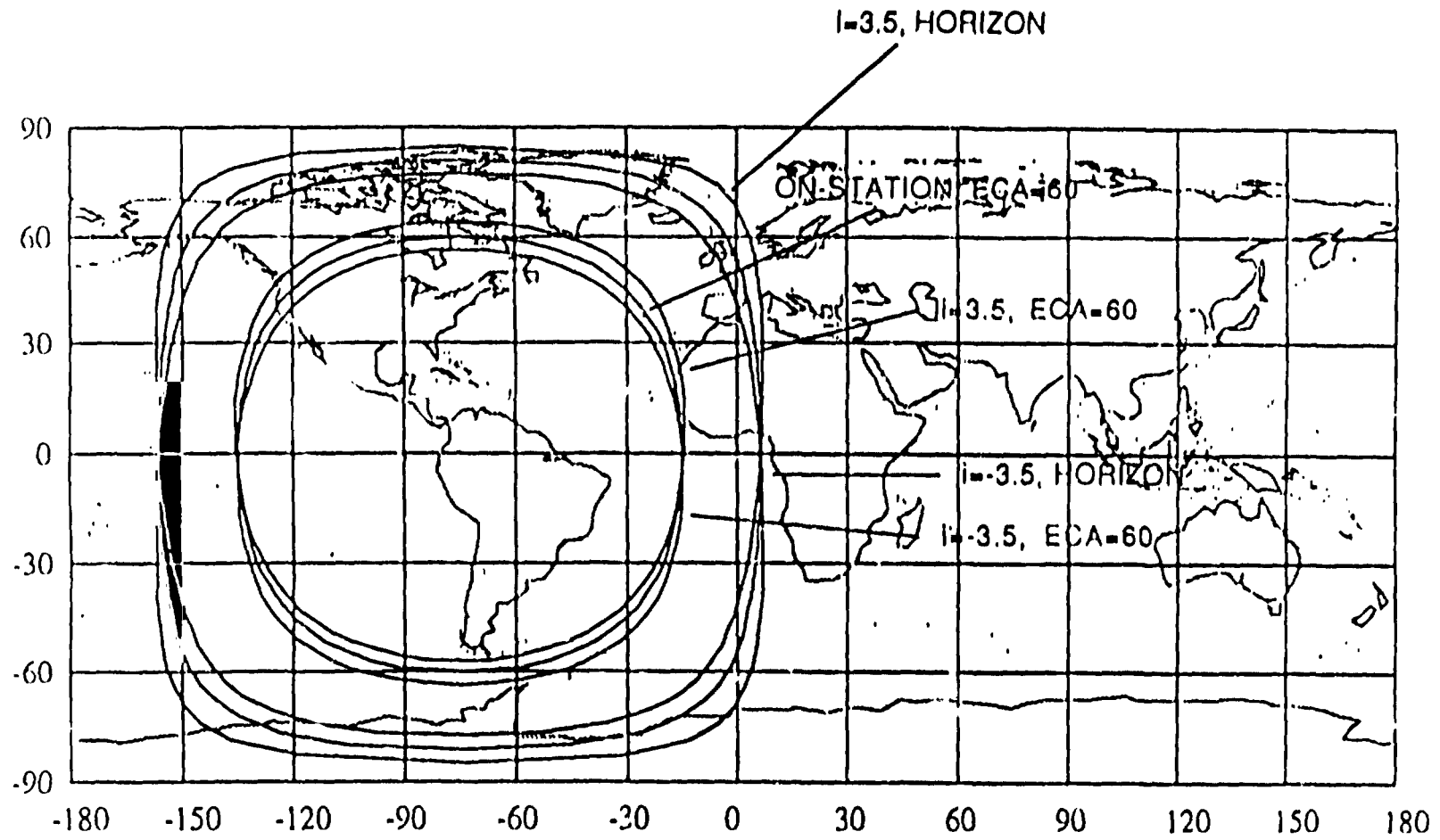


Figure A.1.1-7. GOES East Coverage for Various Orbital Inclinations

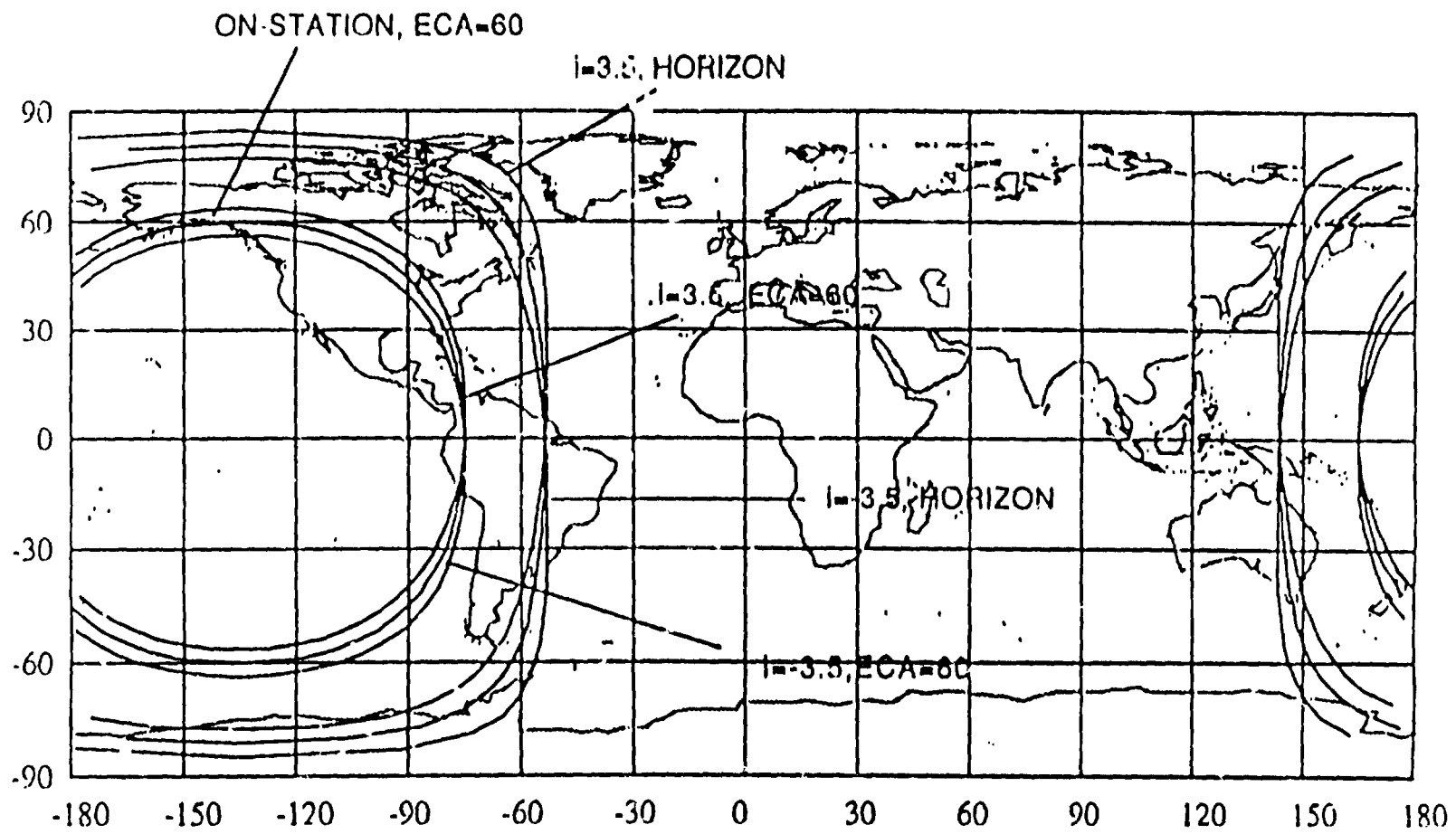


Figure A.1.1-8 GOES West Coverage for Various Orbital Inclinations

A.1.1.3.2.3 Impact on polaris sensor

GOES-N, if it is a momentum bias system where the pitch axis must be perpendicular to the orbit plane and is configured with a Polaris sensor, will have to consider any effect on the Polaris sensor at 3.5 deg inclination. This would require a star tracker having a large enough clear FOV.

A.1.1.4 Assessment

The problem of intolerable servo errors resulting from the high acceleration of the IMC signal necessary to compensate for the increase in orbital inclination renders the high inclination infeasible. Other problems from this high inclination case do arise:

1. reduced visibility by the satellite of weather patterns located in extreme latitudes, and
2. the inability of some potential users to receive GOES data based upon their non-tracking earth station antennas

These difficulties have a similar impact on the feasibility.

The system impacts appear to far outweigh any of the derived benefits. Thus, the use of higher inclination as a means of eliminating North/South stationkeeping is not recommended.

A.1.1.5 References

1. *Some Useful Results on Initial Node Locations for Near-Equatorial Circular Satellite Orbits*, Ahmed Kamel and Richard Tibbitts, Philco-Ford Corp., 20 December 1972.
2. *Spacecraft Operations Handbook (SOH) DRL 503-02, Vol IV, On-Orbit Spacecraft Operation*, Ford Aerospace Corporation, Section 5.2.1, p. 5-22, 30 January 1990.
3. Figures A.1.1-5 and A.1.1-6 are courtesy of Alan Roth, Advanced Technology & Research Corp., June 28, 1990

A.1.2 L-MODE DELETION

A.1.2.1 Introduction

The original impetus for this study was the belief that the L-mode form of control in the GOES-1 spacecraft provides inferior jitter performance relative to the V-mode. The study was to address alternatives to the L-mode backup which could provide similar performance as the V-mode. During the study, Dr. Peter Chu at Loral discovered that the premise of the study is wrong – jitter performance in L-mode is expected to be superior to that in V-mode. There may, however, be some degradation in MMC performance in L-mode relative to V-mode.

A.1.2.2 Approach

The approach to this study involved contacting Loral engineers (such as Dr. Chu) and also those involved in the Intelsat-7 (I-7) program. I-7 is a similar spacecraft to GOES-1 and the I-7 team has examined several alternatives to L-mode backup.

A.1.2.3 Results

The alternatives to L-mode backup considered for I-7 were either a redundant set of V-mode wheels or a single backup wheel which could be latched into place in either of two positions to replace a single failed primary wheel. The redundant V-mode configuration was assessed to cost 11.5 kg in mass and the gimballed backup wheel was assessed to cost 9.75kg in mass. For reasons of mass and the complexity associated with the gimbal mechanism neither of these alternatives was considered attractive for I-7. The later discovery that L-mode performance can be expected to be superior to V-mode obviated the need further consideration of replacing L-mode in the I-7 program.

One consideration not presently addressed is the performance of MMC in the L-mode. There may be some degradation due to the fact that the spacecraft's gyroscopic stiffness is reduced in L-mode (when only a single V-mode wheel is operable); however, this degradation might be overcome by running both V-mode wheels simultaneously.

A.1.2.3 Assessment

Because of the anticipated superiority in jitter performance of the L-mode over the V-mode, consideration should be given to using the L-mode as the primary mode of control. It should of course be verified that MMC performance in the L-mode is satisfactory. Given that L-mode is the primary mode of control, consideration should be given to backing up L-mode with a redundant reaction wheel.

A.2.1 EARTH SENSOR IMPROVEMENTS TO REDUCE NOISE

A.2.1.1 Introduction to the GOFS-I Earth Sensor performance issues

Purpose - The purpose of this study was to determine the feasibility of improving the Earth Sensor beyond its current Type II capabilities in an effort to achieve or exceed the 1983 Image Navigation and Registration (INR) requirements. The 1983 Navigation requirement is 2km and the frame to frame registration requirement is 14 μ .

Background - The Earth Sensor which measures the roll and pitch attitude errors on the GOES I-M is one of the larger sources of navigation and registration errors. The GOES-I system modified for improvements in efficiency or cost savings and the Option I system will continue to use an Earth Sensor for attitude information.

The high frequency noise in the Earth Sensor estimates of the roll and pitch pointing errors of the spacecraft are attenuated and converted into spacecraft jitter or wander of the line of sight by the attitude control system. This jitter then affects the navigation, within-frame and the frame-to-frame registration performance of the data. The Earth Sensor also has some low frequency noise components which are not attenuated by the spacecraft control system and this further degrades the INR performance. The Earth Sensor also responds to clouds and radiance gradients in the earth's atmosphere and generates additional pointing errors due to these causes.

Drift and repeatability of pointing errors with temperature are non-trivial problems but no recommendations for their reduction were developed under this study. These problems are being addressed as part of the GOES-I Earth Sensor development program.

Earth Sensor response to clouds and radiance gradients are accommodated in the GOES-I system by detecting the pointing error in star observations and correcting this error by updating the attitude information in the ground system; the new information is then uploaded to the spacecraft.

This study will present the results of investigations to minimize Earth Sensor noise and thus improve the performance of a GOES-N system that uses Earth Sensors as the primary attitude sensors.

A.2.1.2 Overview

A.2.1.2.1 Approach

Potential modifications to the Lockheed Type II Earth Sensor, which is currently being used on GOES-I, were postulated and analyzed to estimate the resulting improvements in performance, and the associated cost and risk were assessed. Other vendors of Earth Sensors were contacted, and the suitability of their systems were assessed against the GOES-N requirements.

The following approaches were investigated for potential improvements in the Earth Sensor performance:

- Increasing the number of detectors
- Running two Earth Sensors and combining their data
- Reducing low frequency noise
 - Improve filtering of Threshold Control Voltage
 - More digital signal processing
 - Hybrid Type I & II processing
- Minimizing the disturbances due to entering or exiting single chord operation

The following vendors were contacted, and information on their Earth Sensors (available or under development) was assessed as to suitability for the GOES-N mission: EDO Corp./ Barnes Engineering Division, Shelton, CT — Officina Galileo, Florence, Italy

A.2.1.2.2 Brief description of the GOES Type II Earth Sensor

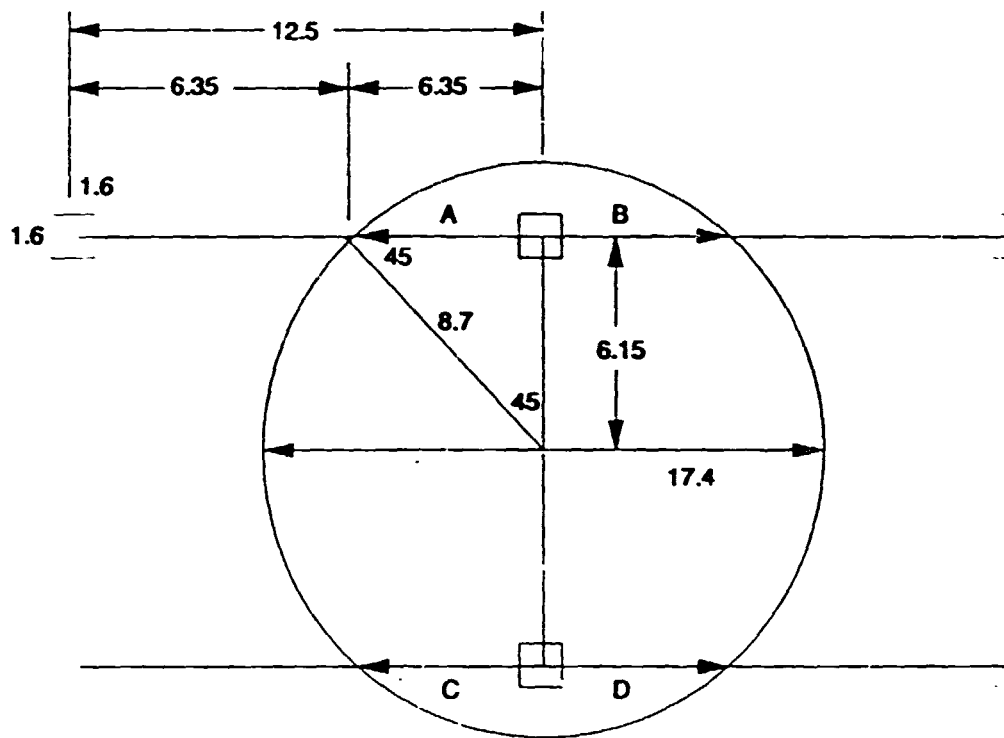
The GOES Type II Earth Sensor derives its information by using an object plane mirror to scan the image of two bolometers, each with a square field of view of 1.6 deg, over an infrared image of the earth. From geostationary orbit the earth's diameter is 17.4 deg and the bolometer scan with a simple harmonic oscillation with an amplitude of 12.5 deg offset ± 6.15 deg from nadir such that the limbs of the earth are at 45 deg to the scan where they cross the earth, Figure A.2.1-1. In this figure the bolometers are shown as a box with solid lines at the rest position or the center of the scan and in dashed lines at the turnaround or DC restore portions of the scan. The information from the space-to-earth transitions are sensed by adaptive threshold circuits to locate the edge of the earth and further processed to generate the roll and pitch errors. An adaptive threshold circuit is used in the Type II sensor which reduces its sensitivity to radiance gradients. The total mass of a Type II Earth Sensor is 2.85 kg and requires less than 6 watts excluding the thermal control plate heater power.

A.2.1.3 Results of studies/analyses

A.2.1.3.1 Modification to reduce the Earth Sensor noise – Use 4 Bolometers

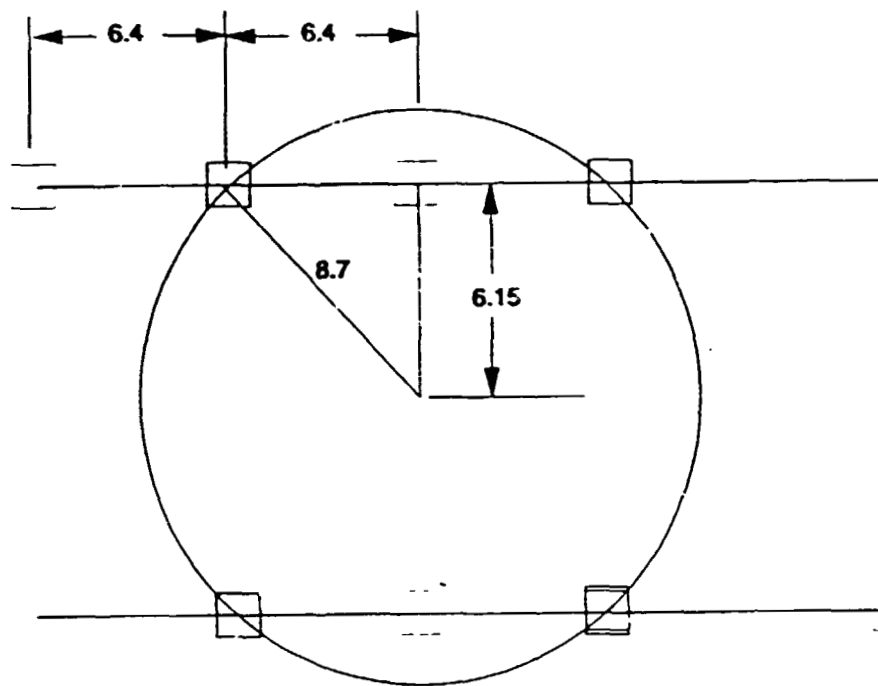
A modification to the Earth Sensor that would reduce the noise in its output is to increase the number of bolometers from 2 to 4. These 4 bolometers would be located at the corners of a square in the focal plane so that when the scan mirror is in its rest position they just sit on the limbs of the earth. Using 4 bolometers the amplitude of the scan can be reduced from 12.5 deg to 6.4 deg and still maintain the same swath coverage for DC restoration on space, Figure A.2.1-2. In this figure the bolometers are drawn with solid lines at the rest position of the scan mirror which is the center of the scan. To simplify the drawing the only the upper left and lower right bolometers are shown in dashed lines at their turnaround or DC restore positions.

The two bolometer Type II sensors scan the detectors across the edge of the earth with a velocity of $9.58 \mu\text{r}$ per microsecond. Keeping the same 8Hz harmonic scan period the four bolometer system scans over the edge of the earth with a velocity of $5.6 \mu\text{r}$ per microsecond. The ratio of these two rates is a measure of the allowable bandwidth reduction in the preamplifier and indicates that a reduction in wide band noise should be achievable. The projected performance of the 4 bolometer system was assessed using an analysis program developed to aid in the



NOTE:
All dimension are in degrees

Figure A.2.1-1. Type II Baseline Configuration



NOTE:
All dimension are in degrees

Figure A.2.1-2. Four Bolometer Configuration

optimization of the Type II sensors to minimize both the low and high frequency noise. To optimize the design for the 4 bolometer configuration the scan rate was reduced from 9.58 to 5.6 $\mu\text{R}/\mu\text{S}$, the bandwidth reduced from 50 to 20Hz, the ASD gain changed from 1.33 to 1.19 and the Tau, or delay, left the same at 0.7 milliseconds. The results of the simulation indicated a significant reduction in both the low and high frequency noise of the sensor. A draft report "LOW FREQUENCY NOISE IN INFRARED EARTH HORIZON SENSORS USING ADAPTIVE SLOPE DETECTION (ASD)" dated 5 October 1990 by James L. Carr which discusses the theory of this noise generation and how it can be reduced along with the total noise is attached.

Officina Galileo of Florence, Italy has developed an Earth Sensor using 4 bolometers in a similar configuration, however its signal processing is different from that proposed here, and that Earth Sensor's performance is not as good as that projected here. (c.f. a more detailed discussion of that Earth Sensor in Section A.2.1.4.2.).

This is a relatively simple modification to the existing design in that the changes require adding 2 more bolometers in the image plane of the system and the associated bias and preamplifier circuits. There are already 4 adaptive threshold circuits in the Type II Earth Sensor. The optic design must be evaluated to assure that the required image quality can be achieved with the detectors 8.7 deg from the optic axis in the 4 bolometer configuration versus 6.1 deg in the 2 bolometer configuration. The design of the logic for generating the attitude information in the transfer orbit and in the acquisition mode must also be revised to reflect the different bolometer locations.

IMPROVEMENT IN PERFORMANCE	
HIGH FREQUENCY NOISE	-28%
LOW FREQUENCY NOISE	-19%
MASS INCREASE	0.5 kg
POWER INCREASE	0.5 WATTS
NON-RECURRING COST	SIGNIFICANT
RECURRING COST INCREASE	MODERATE
TECHNICAL RISK	MODERATE - NEW LOGIC FOR ACQUISITION

A.2.1.3.2 Modification to reduce the effective noise of the Earth Sensor - Run two Earth Sensors and combine their data

It is reasonable to run two Earth Sensors at the same time. The noise, both low and high frequency, in their output estimates of roll and pitch are not correlated, but the errors due to clouds and radiance gradients will be the same in both Earth Sensors. If the AOCE computer

were to average the output of both sensors and use that as the current noisy estimate of the attitude error, the noise in this estimate would be reduced by $\sqrt{2}$ or 40%. This approach will reduce both the high frequency and low frequency noise of the Earth Sensor and also any "random wander" due to mechanical or electrical changes in either of the sensors.

This requires no modification to the Earth Sensor but the AOCE computer system must be modified to accept and combine the data from two sensors. This is a minor modification. To have full redundancy and no single point failures in this mode of operation will require flying 3 Earth Sensors, using two and having one as a backup. This will require developing a new thermal control enclosure since the current enclosure is designed to hold 2 Earth Sensors. This mode of operation may require modifying the input circuits to the AOCE computer to accommodate the third Earth Sensor, but some communication satellites built by Ford Aerospace Corp. with similar Earth Sensors and control computers, have flown with 3 Earth Sensors.

There are nonrecurring costs for increasing the size of the thermal control housing, developing the AOCE software, new harnesses, etc. The major cost will be the recurring cost of flying a third Earth Sensor on each spacecraft. The risks associated with this approach are low. The major risk is that there may be dynamic interactions between the two Earth Sensors operating simultaneously. Prior systems have operated two Earth Sensors at the same time, but they did not require the extreme precision that GOES-N needs.

IMPROVEMENT IN PERFORMANCE	
HIGH FREQUENCY NOISE	-29%
LOW FREQUENCY NOISE	-29%
MASS INCREASE	6 kg
POWER INCREASE	6 WATTS + HEATER POWER
NON RECURRING COST	LOW
RECURRING COST INCREASE	HIGH
TECHNICAL RISK	LOW

A.2.1.3.3 Modifications to reduce the low frequency noise content by improving the filtering of threshold control voltage

The low frequency noise can be reduced by using a digital filter on the Threshold Control Voltage to increase the time constant from the present 12 seconds to 1,200 seconds. This is not feasible using analog techniques. Analysis and simulations have shown that this change will attenuate the low frequency noise to levels essentially equal to that generated by a fixed threshold sensor, such as the Type I Earth Sensor originally proposed for GOES-I-M.

The present integrator could be replaced with an Analog-to-Digital converter (about 14 bits), digital logic to sum and filter the values, and a 14 bit Digital-to-Analog converter to provide the input to the gain set resistors. A single count change in the D/A converter will cause a shift of less than 1 microradian in the threshold. This could be implemented with low speed, low power logic since these values are measured and updated only 8 times per second.

IMPROVEMENT IN PERFORMANCE	
HIGH FREQUENCY NOISE	NONE
LOW FREQUENCY NOISE	SIGNIFICANT
MASS INCREASE	0.5 kg
POWER INCREASE	1 WATTS
NON RECURRING COST	MODERATE
RECURRING COST INCREASE	LOW
TECHNICAL RISK	HIGH

A.2.1.3.4 Modifications to improve stability and reduce noise by using all digital processing of amplified bolometer signals

A 15 bit following type Analog-to-Digital converter running at 10Mhz will generate a digital representation of the bolometer signal with a lag and total error of less than 1 microradian since the scan rate at the limb crossing is about 10 μ r per microsecond. Digital logic using counters, adders, etc. would do the threshold comparison, measurement of the hold voltage after the Tau delay, filtering of the digital hold voltage level and division by the Gain to establish the new threshold value. One set of logic could serve both the East going and West going Space-to-Earth transitions. This modification would replace sensitive analog circuitry largely with digital logic and provide improved stability and performance.

A digital processing of the bolometer signals would also allow easy acquisition of attitude data with both a fixed and adaptive threshold operation on the same signal. This would simplify using the running average substitution technique to further reduce low frequency noise. The fixed threshold processing could be applied to the Earth-to-Space transitions as well as the Space-to-Earth transitions, thus reducing its noise by about a factor of 0.707 or 29%. This could then provide both lower noise and improved rejection of cloud and radiance gradient effects.

An alternative approach to use the Earth-to-Space transitions with the adaptive threshold logic and still minimize cloud and radiance gradient effects would be to store the digital representation of the Earth-to-Space transition, digitally DC restore the signal on the space level, and process backward through the data to locate the transition as if the scan were Space-to-Earth. In this process the distortions of the signal shape due to clouds not near the limb of the earth will be

largely eliminated and thus have minimum effect on attitude estimation. Using a microprocessor further compensation could be applied to correct for the memory effects in the bolometers and filters. This approach has not been analyzed in depth so no precise performance gain can be proposed, but doubling the number limb crossings used in the measuring roll and pitch could potentially reduce the noise by about 29%.

IMPROVEMENT IN PERFORMANCE	
HIGH FREQUENCY NOISE	-29%
LOW FREQUENCY NOISE	SIGNIFICANT
MASS INCREASE	0.5 kg
POWER INCREASE	2 WATTS
NON RECURRING COST	HIGH
RECURRING COST INCREASE	MODERATE
TECHNICAL RISK	MODERATE

A.2.1.3.5 Modification to the GOES-II Earth Sensor to reduce the low frequency noise content - Combine Type I and Type II signal processing

Recent simulations and AUCS Servo Table results have indicated that the Type II Earth Sensor has excessive noise in the frequency range of 1/2 min. to 1/100 min. It is believed that the Type I Earth Sensor does not have this problem, but has a much greater sensitivity to clouds and radiance gradient effects. It appears feasible to build an Earth Sensor that combines the best features of both the Fixed (Type I) and Adaptive Threshold (Type II) Earth Sensors.

The approach is to take the amplified signals from the bolometers and send it to both a fixed threshold and adaptive threshold processors. Roll and pitch measurements would be generated 4 times per second from each set of processors, using the same center reference and 0.01 degree clock for both processors. The output of each of the processors would be used to generate running averages with a length of 16,384 (2^{14}) or 32,768 (2^{15}) covering 1.14 or 2.3 hours. These averaging times were selected to cause the change in the errors due to clouds and radiance gradients in the Type I fixed threshold processor to be small over the interval, but long enough to strongly attenuate the low frequency noise (a 20 Min. period) in the adaptive threshold processor. Making the length an integral power of 2 simplifies the implementation. The value sent to the AOCE computer from this modified Earth Sensor would be generated by subtracting the fixed threshold running average from the fixed threshold value and adding back in the running average

from the adaptive threshold processor. In this manner the slow drift of the fixed threshold processor due to clouds and radiance gradients is suppressed as well as the low frequency noise of the adaptive threshold processor. Any very low frequency noise in the adaptive threshold processor will, of course, pass through this filter.

The cloud and radiance gradient sensitivity of the adaptive threshold processor can be further reduced by setting the G and Tau of this processor to move down the curve to a point where these effects are 1/2 to 1/4 of their present values. This will increase the RMS noise which is counteracted by averaging 16,348 points to reduce the single sample noise by a factor of about 128. If the RMS noise in the processor output increased from 100 to 200 μ r (1 σ) the noise in the running average would increase from 0.78 to 1.6 μ r (1 σ). This would add to the approximately 100 μ r noise from the fixed threshold processor, however the running average noise would not be reduced by the Control System processor because of its very low frequency content.

IMPROVEMENT IN PERFORMANCE	
HIGH FREQUENCY NOISE	-29%
LOW FREQUENCY NOISE	SIGNIFICANT
MASS INCREASE	2 kg
POWER INCREASE	1 WATTS
NON RECURRING COST	HIGH
RECURRING COST INCREASE	MODERATE
TECHNICAL RISK	HIGH

A.2.1.3.6 Modifications to minimize disturbances due To entering/exiting single chord operation

A relatively simple modification to the logic in the Earth Sensor would allow minimizing the attitude offset that occurs when single chord operation is commanded or occurs because of sun or moon detection in the instrument. The present system computes a "standard chord" which is a long term average of both the north and south chords. When single chord operation is commanded the non inhibited chord is compared with the "standard chord" for roll measurement and the semichords of the non inhibited chord compared to develop the pitch error. While the reproducible errors caused by the imperfect location of the detectors could be calibrated out of the system, the errors due to the presence of radiance gradients or clouds in either and/or both chords can not be determined and will occasionally result in a significant change in the spacecraft attitude.

The proposed modification is to keep independent running averages of each of the four semichords, a, b, c and d, which measure the angle between the space-to-earth crossing and the center, or zero, reference in the Earth Sensor. The instantaneous values of the semichords are indicated as A, B, C and D, Figure A.2.1-1. The running average time is long enough to filter the noise in the estimate to less than 20 μ r but short enough that it follows the cloud and radiance gradient effects which have time constants of many hours. The Earth Sensor and/or the spacecraft AOCE system operates on these semichords to estimate the roll and pitch error. Pitch is computed from $(A-B)+(C+D)$ and Roll from $(A+B)-(C+D)$ when both chords are being used. If a single chord is commanded, say the chord generating values A and B is to be used and the chord generating C and D inhibited, then a "standard chord" is computed equal to 1/2 the sum of $a+b+c+d$, and used to compute Roll just using the information in A and B. Pitch is just the difference between A and B. Knowing all of the average values and the "standard chord" value it is then possible to estimate the step error that will occur when a single chord is commanded and this offset can be applied to the Earth Sensor output. This processing could be done in the Earth Sensor, in the AOCE computer or the ground if the appropriate data were sent to the AOCE computer and/or the ground. An offset to compensate for these errors would be applied to the AOCE at the same time that a single chord is commanded to eliminate the step error.

IMPROVEMENT IN PERFORMANCE	
MINIMIZES TIME LOST FROM METEOROLOGICAL OBSERVATIONS WHEN ENTERING/EXISTING SINGLE CHORD OPERATION	
MASS INCREASE	1 kg
POWER INCREASE	1 WATTS
NON RECURRING COST	MODEST
RECURRING COST INCREASE	LOW
TECHNICAL RISK	LOW

A.2.1.4 Comments on Earth Sensors from other vendors

A.2.1.4.1 EDO Corp/ Barnes Engineering Div., Shelton, CT

Barnes Engineering (BE) is currently developing a geosynchronous static Earth Sensor, model 15-405 for use on an advanced communication satellite. This system has a single optical system and redundant detectors and signal processing electronics in a single housing with a mass of about 4.4 kg and requires less than 3 Watts of power. This system uses static thermopile detectors with a time constant of 450 ± 50 msec. This leads to a bandwidth of 0.32 Hz with a maximum readout rate for independent measurements of 1.6 per second. The noise bandwidth of the preamplifiers was not identified in the documentation. Assuming that measurements made at a rate of 1.6 per second are independent the quoted noise in pitch is similar to the LMSC Type II Earth Sensor but

roll has twice the noise of the Type II sensor. The Barnes sensor is projected to have 3 to 7 times the sensitivity to clouds and radiance gradients than that projected for the Type II Earth Sensor. These performance characteristics may be satisfactory for a communications satellite but are not compatible with the GOES-N requirements.

A.2.1.4.2 Officina Galileo, Florence, Italy

Officina Galileo (OG) currently builds an IR Earth Sensor (IRES) which has limited flight experience (specifically on OLYMPUS). It has built 30 to 40 other models with only one significant failure. They are presently working on a second generation IRES. For discussion purposes we indicated that the goals for an Earth Sensor for GOES-N should have the following characteristics.

1. 50 μ R (1σ) short term noise at 4Hz output rate Equivalent to 80 μ R at their 10Hz output rate
2. 50 μ R (3σ) radiance gradient/cloud effect
3. Minimal low frequency noise
4. Minimal single chord operational impact

OG described the operation of its second generation IRES. It uses 4 bolometers sensing in the 14 to 16.25 μ m spectral band (equivalent to the "narrow" spectral filter in the LMSC instruments) scanned at 10 Hz with a harmonic oscillating scan mirror mounted on flex pivots. The present sensor is sensitive to vibrations near 100 Hz. The bolometers have a time constant of about 2.5 milliseconds and their IFOV's are 1.3 deg square. The amplitude of oscillation in the fine pointing mode is ± 5 deg FOV and ± 9 deg FOV in the acquisition mode. The angle encoder uses a pattern with 9 μ m lines with a 0.01 deg pattern resolution and a center reference pattern which are attached to the scan mirror. The output of the bolometer is amplified and the amplifier bandwidth limited so as to differentiate the signal so that it returns to the baseline between space to earth and earth to space transitions. The peak value of the differentiated signal is sensed, sampled, filtered and divided down to develop a threshold value that compensates for level changes in the signal level. The resulting threshold is set between 1/3 and 1/2 of the total signal from the bolometer. The scan amplitude in acquisition mode is less than the LMSC Earth Sensors which will require modifying the earth acquisition procedures in the launch phase.

Threshold detection occurs on both the space to earth and earth to space transitions. The sensor normally uses only 3 of the 4 bolometer outputs to generate the roll and pitch outputs. An east west pair is used to generate pitch and a north south pair for roll. Thus the sensor is always operating in a single chord mode and the appropriate bolometer is inhibited by ground command when the sun or moon would cause interference. By modifying the processing logic and using the signal from all four bolometer when single chord operation is not required the signal-to-noise performance could be improved by about 40%.

OG stated the performance goal of the advanced IRES is 0.0 deg (3σ) at a 10 Hz output rate with a quantization level of 0.0025 deg (44 μ R). This is equivalent to 290 μ R 1σ at 10 Hz or 180 μ R at 4 Hz. By using all four bolometer signals this could be reduced to about 130 μ R equivalent at 4Hz output rate. This performance is not as good as the LMSC GOES-2 Earth Sensor which has

a 1σ noise of about $100 \mu R$ at a 4 Hz output rate. It is not clear as to why the projected performance of this sensor is not better than indicated but it may be due to the noise impact of differentiating the signal as well as using a narrow spectral filter to minimize the impact of clouds.

OG had not done any recent assessment of the cloud and radiance gradient performance of the IRES. Radiance gradient performance may be similar to the GOES-2 sensor because it adapts to radiance level changes by using a percentage of peak algorithm. It uses the earth to space transitions which will probably incur an increased sensitivity to clouds versus the GOES-2 sensor which only uses the space to earth transitions. They had no measurements or analysis concerning very low frequency noise in the IRES. We mentioned that Swales analysis and LMSC experience indicated that they may have similar problems with their IRES.

The IRES is about $14 \times 20 \times 26$ cm, weighs 3 kg and uses 5 W of power.

A.2.1.5 Conclusions and recommendations

The approach combining the data from two Earth Sensors described in Section A.2.1.3.2 is the minimum change that should be used in an Earth Sensor based GOES-N system. The next change should be to reduce the low frequency noise by improving the filtering of the threshold control voltage as described in Section A.2.3.3 in the Earth Sensors. The next most useful modification would be to incorporate the 4 bolometer configuration described in Section A.2.1.3.1. A system combining the data from two Earth Sensors each modified with the two changes recommended should have a high frequency noise level reduced by a factor of about 0.54 or down by 46% from the noise level of the present system with a significant reduction in low frequency noise.

A.2.2 MOMENTUM WHEEL IMPROVEMENTS

A.2.2.1 Wheel noise improvements

A.2.2.1.1 Introduction

In looking for ways to improve pointing performance through minor modifications to existing hardware, one finds that improvements in the wheel tachometer feedback generation could significantly improve spacecraft jitter performance. To see this, one only needs to look at the current GOES pitch and roll/yaw control loops to see the impact of tachometer quantization and noise in each transfer function (Figures A.2.2-1 and A.2.2-2). In each case, momentum commands are used to control each of the two momentum wheels. Thus, the wheels are actually commanded by delta momentum commands, as the original command is different with the tach feedback to create the wheel control command. This study will examine possibilities in reducing noise and quantization errors in order to improve pitch and roll/yaw pointing stability.

The current GOES system employs two momentum wheels built by Teldix. Magnetic tachometers/commutators generate signal which reflect angle changes in the wheels. There are eight commutation windows on the rotor of each wheel, which is powered by a three phase motor. As the windows pass the open ends of a ferrite core, a square wave is generated and the wheel is commutated. The 24 pulses generated are separated for overlapping signals, then divided by two to create the twelve pole pairs. These pole pairs are input to a buffer in the Attitude and Orbital Control Electronics (AOCE), which count pole pairs until 30 revolutions pass. The period of 30 revolutions is timed by a 1.024 MHz clock and is used in processing the wheel speed values. The Teldix tachometer system specification allows for .0167 rpm quantization and .0998 rpm noise, 3σ at 5485 rpm (Addendum A.2.2-1 for derivation of these numbers).

Several methods for tachometer/wheel improvement were studied. These include:

- 1) Increase the number of sensors or poles in order to proportionally reduce the quantization step size (least significant bit) of the feedback signal.
- 2) Change tachometer sensors to reduce sensor noise in the feedback signal. New hardware might include optical sensors, which theoretically output nearly zero noise signals.
- 3) Change signal processing to reduce effects of sensor noise through averaging of tach output over a certain amount of time.
- 4) Reduce (or eliminate) wheel torque quantization within the wheel driver itself.

Each possible improvement was evaluated on the basis of cost, weight and design impacts as well as the pointing performance improvement. Special emphasis was given to methods which can be implemented onto GOES-I without hardware impact (such as changes in computer processing).

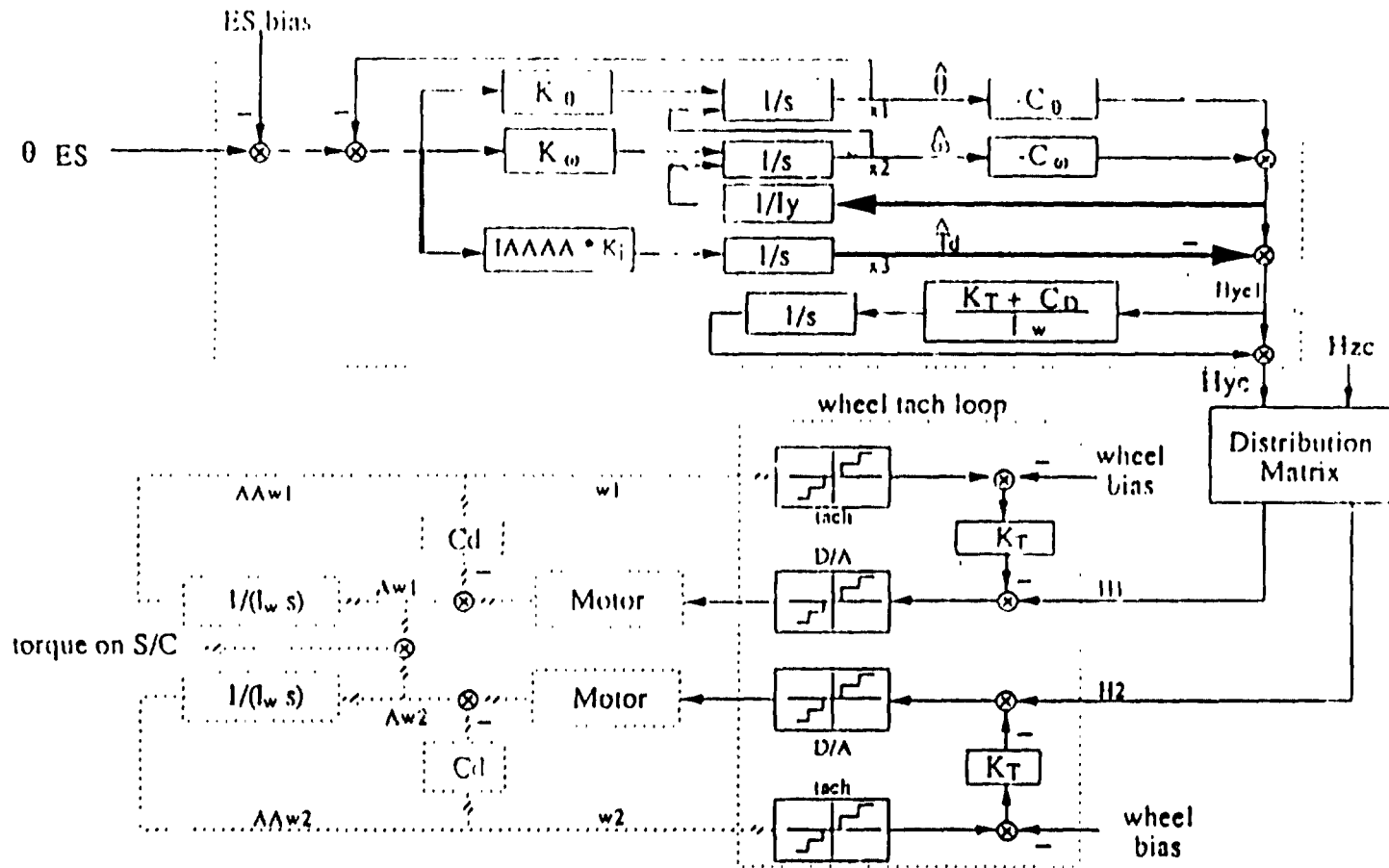


Figure A.2.2-1. On-Orbit Pitch Controller

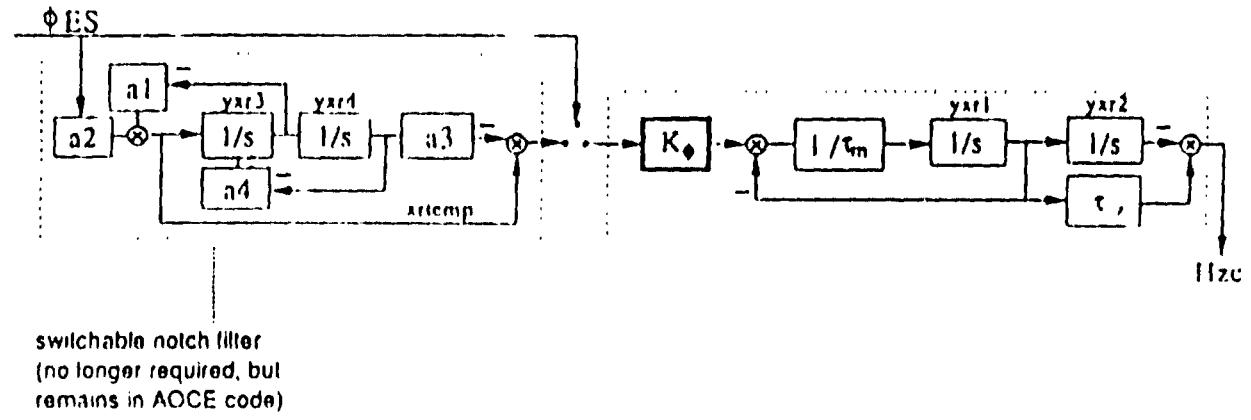


Figure A.2.2-2. On-Orbit Roll/Yaw Controller

A.2.2.1.2 Study methods

Two types of analysis evaluated the estimated pointing performance of each noise improvement with respect to the current spacecraft pointing performance: variance analysis and nonlinear simulation results. Variance analysis provides linear estimates for spacecraft angle jitter as a result of a white noise input. The variance of a system closed loop frequency response is defined to be the square of the standard deviation (1 sigma) of the measured output. This term equals the area found under a Power Spectral Density (PSD) frequency plot for the transfer/ input/output function. The PSD of a transfer function is found by squaring the transfer function over the frequency domain. Thus, one can find the variance of an output function (spacecraft angle) by cascading the PSD of an input onto the PSD of a transfer function.

Variance analysis allows one to approximate the PSD of an input noise source, which may be unknown, as a narrow band noise defined by the variance, sampling frequency, and a constant spectral magnitude (Figure A.2.2-3). Given this input noise source, it is possible to determine the output variance (the co-variance of the spacecraft angle) over the same narrow band frequency range. For example, a variance analysis of the baseline GOES-I system (wheel tachometers and Earth Sensor) is performed in Addendum A.2.2-2. As you can see, GOES-I CDR values are used for tachometer and Earth Sensor 3 σ noise values. Transfer functions for Earth Sensor/theta and tach noise/theta were derived from the GOES-I INR CDR pitch loop (since the pitch axis is the worst case pointing control axis, this report will only discuss pitch results). The analysis shows these inputs will cause 16.3 total μ r of jitter (the Earth Sensor contributes 12.0 μ r and each tachometer contributes 7.8 μ r, which are all root sum squared together). By varying the variance and/or sample frequency of the input noise, one is able to compare spacecraft performance for different noise levels.

The second study method used to verify the performance expectations determined in variance analysis is through a nonlinear computation of the governing equations involved in the spacecraft three axis control loop. The governing equations are determined from the GOES-I INR CDR pitch and roll/yaw control loops and Euler's equations, which are:

- 1) $d(H \text{ system})/dt = T \text{ external} - (W \text{ body} * H \text{ system})$, and
- 2) $H \text{ system} = h \text{ body} + h \text{ wheels}$.

These are listed in a model source file in Addendum A.2.2-3. To solve the equations, the simulation tool MODEL-S is used.

MODEL-S allows for the simulation of several sampling rates in a sampled data system. The modeled GOES-I system uses three sampled systems: the AOCE, which computes and sends commands every .256 seconds (4Hz); the Earth Sensor, which sends roll and pitch error angles every .256 seconds (4Hz); and the wheel tachometers, which fill the tach buffer approximately every .35 seconds (3Hz). Additionally, a white noise generator (gscal.for) is used to create white noise inputs on both wheels and the Earth Sensor in the program. In the simulation, only gravity gradient disturbance torques are input, allowing the noisy inputs generated within the control

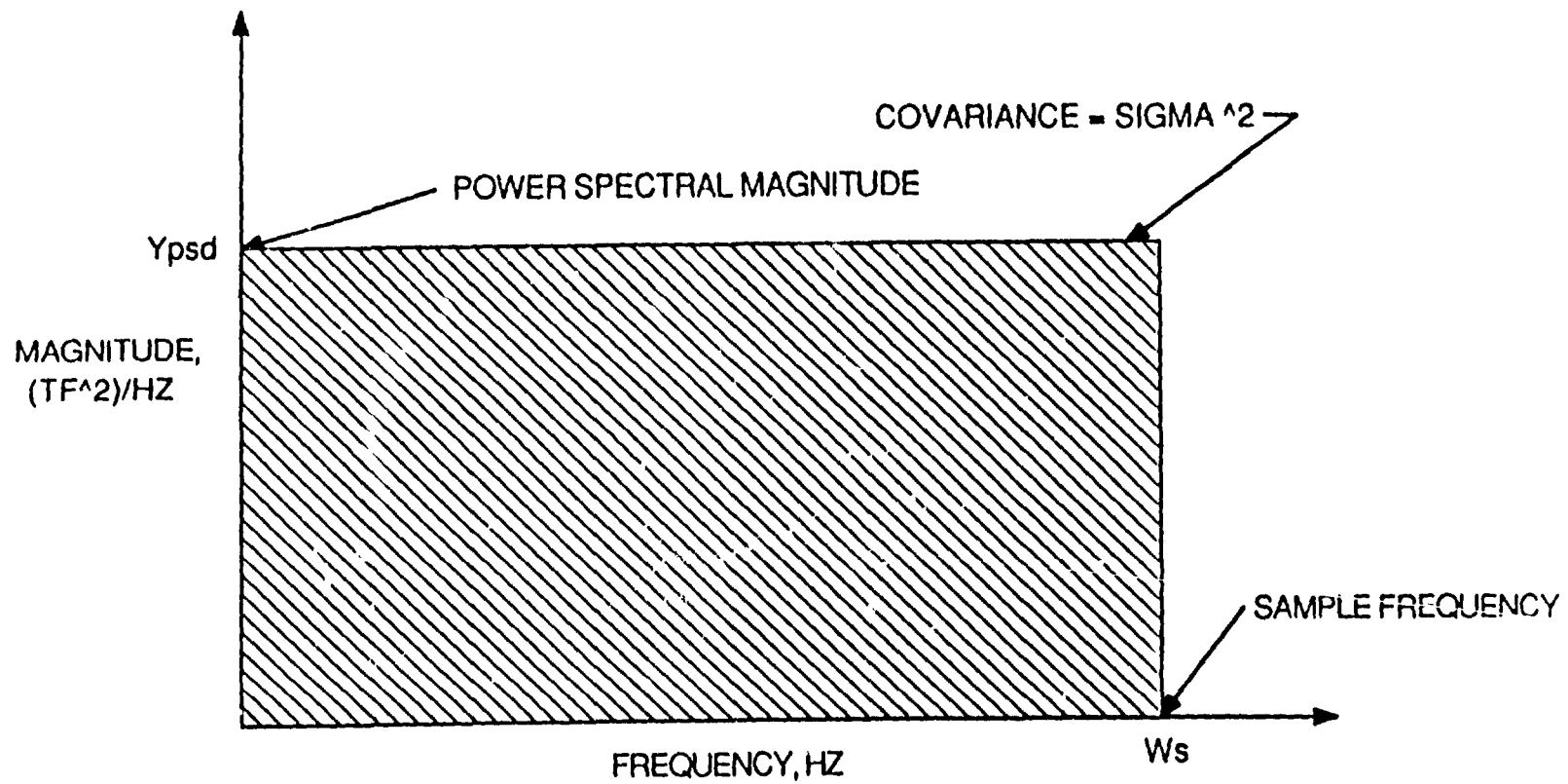


Figure A.2.2-3. Covariance for Narrow Band Noise PSD

loops to be the source of spacecraft jitter. The output roll pitch and yaw angles are used by a statistics program to calculate the variance for each input. Therefore, by turning noise inputs 'on' or 'off' (multiplication by 0 or 1), one sees the effect of each noise on spacecraft jitter.

For example, several different simulation runs have been made for the current GOES-I system, using CDR noise levels. As summarized in Table A.2.2-1, six separate runs characterize spacecraft jitter due to tachometer, Earth Sensor and torque command noise inputs. FSCLONG is a simulation of the spacecraft 'as is', with all noise sources. It is then repeated with realistic Earth Sensor noise. PERFESND deletes Earth Sensor noise, to show that effect on the control system (all other simulations have Earth Sensor noise removed). NDNOTQON removes wheel torque command quantization from the system. NDNOTKNOIS removes tach noise from the system and replaces torque command quantization. CLEANWH removes both torque command quantization and tach noise from the system. It is apparent from baseline results that flight Earth Sensor noise contributes 14.8 μ r to the system error, tachometer noise contributes 1.8 μ r and torque command quantization contributes less than 0.1 μ r (Figures A.2.2-4 through A.2.2-8 for simulation results).

Table A.2.2-1. Summary of Attitude Errors as a Result of Specific Inputs (1 σ)

SIMULATION	ROLL	PITCH	YAW	PITCH 3 σ
FSCLONG (ANALYSIS)	.33	4.12	3.3	12.37
FSCLONG (FLIGHT H/W)	3.94	9.04	4.54	27.14
PERFESND	.17	3.88	3.29	11.65
NDNOTQON	.17	3.87	3.29	11.61
NDNOTICNOIS	.11	1.29	2.35	3.87
CLEAN WH	.09	.71	2.00	2.14
THREE	.16	2.58	3.29	7.75

A.2.2.1.3 Hardware tradeoffs

The first method of improvement studied involved doubling the number of pole pairs for tachometer pulses in order to reduce the quantization step size proportionally. As was mentioned before, tach pulses are generated as a function of commutation frequency. This does not allow for the addition of poles, which would have the effect of increasing the commutation frequency. It is possible to develop a circuit to measure the derivative of the square pulses, effectively counting two pulse edges for each pulse and doubling the number of output signals. This would have the same effect as doubling the pole pairs.

However, the doubling of pulses to the AOCE tach buffer does not halve the quantization step size. The AOCE measures the period for 30 wheel revolutions, rather than the period for movement between two pole pairs. Since the same front edge of the same pole will be used to

count the beginning and end of this period, the other poles have no significance other than for commutation purposes. In other words, from a tachometer viewpoint, there is no pointing difference between a wheel with 12 pole pairs and a wheel with 24 pole pairs.

The second consideration in improving spacecraft pointing performance is to reduce the noise generated by the tachometer signal itself. This noise is a combination of three different noise sources: bearing noise, tachometer input noise and tachometer signal noise. This study focuses on possible improvements in the second noise source, the data collected by the tachometer itself. As mentioned above, each tachometer is not specifically a tachometer, but a window used for the magnetic commutation of the motor. Logically, an improvement on tachometer sensing might be realized through the addition of optical tachometers on the wheels.

However, the improvement realized through the addition of optical tachometers would be small, at a great cost in redesign effort. It is important to remember that the tachometer output signal is limited not only by tachometer noise, but also by tachometer quantization. As mentioned above, spec levels for tach noise and quantization are .0978 rpm and .0163 rpm three sigma, respectively. Since the noise level is six times that of the quantization level, the quantization effect is negligible. However, the spec level for tach noise turns out to be relatively conservative. Based on conversations with the GOES-I spacecraft and wheel vendors and a co-variance analysis of actual wheel time response data, it is more realistic to approximate the actual noise value at a level one third of the spec level. The effect on spacecraft jitter is computed in another variance study and verified in simulation THREE, a copy of PERESND which cuts tach noise to 33% of nominal (Addendum A.2.2-4 for this variance and Figure A.2.2-9 for the simulation output). Therefore, the noise levels are only about twice that of quantization levels.

Assuming a perfectly sensing optical tachometer, the main driver on spacecraft jitter would be the quantization step size, which is a function of the AOCE clock. Thus, by the addition of new tachometers, the wheel tachometer noise would drop from a level around .0326 rpm to .0163 rpm, resulting in spacecraft jitter dropping from 2.4 to 1.2 μ r per wheel. The addition would require redesign of the wheels to include the mounting and support electronics for the optical tachs and possible redesign to the wheel drive electronics which house the tach processing electronics. There is some concern that these mechanical additions could disturb the static and dynamic balance found in the current GOES wheels. This would have the detrimental effect of increasing a disturbance torque on the wheels (Section A.2.2.2). It is therefore recommended that no additions be made to the hardware to improve tachometer sensing performance.

A third method to improve the output data from the tachometer circuit is to lengthen the period of measurement for each sample. As mentioned above, each tach sample measures the period of thirty revolutions of the momentum wheel. Since the tachometer measurement noise is an error in the time of a revolutions completion, the magnitude of the error is reduced proportionally with every additional revolution measured per sample. For example, if tach uncertainty is six microseconds of time, that uncertainty can be compared to the period for one revolution (.0109

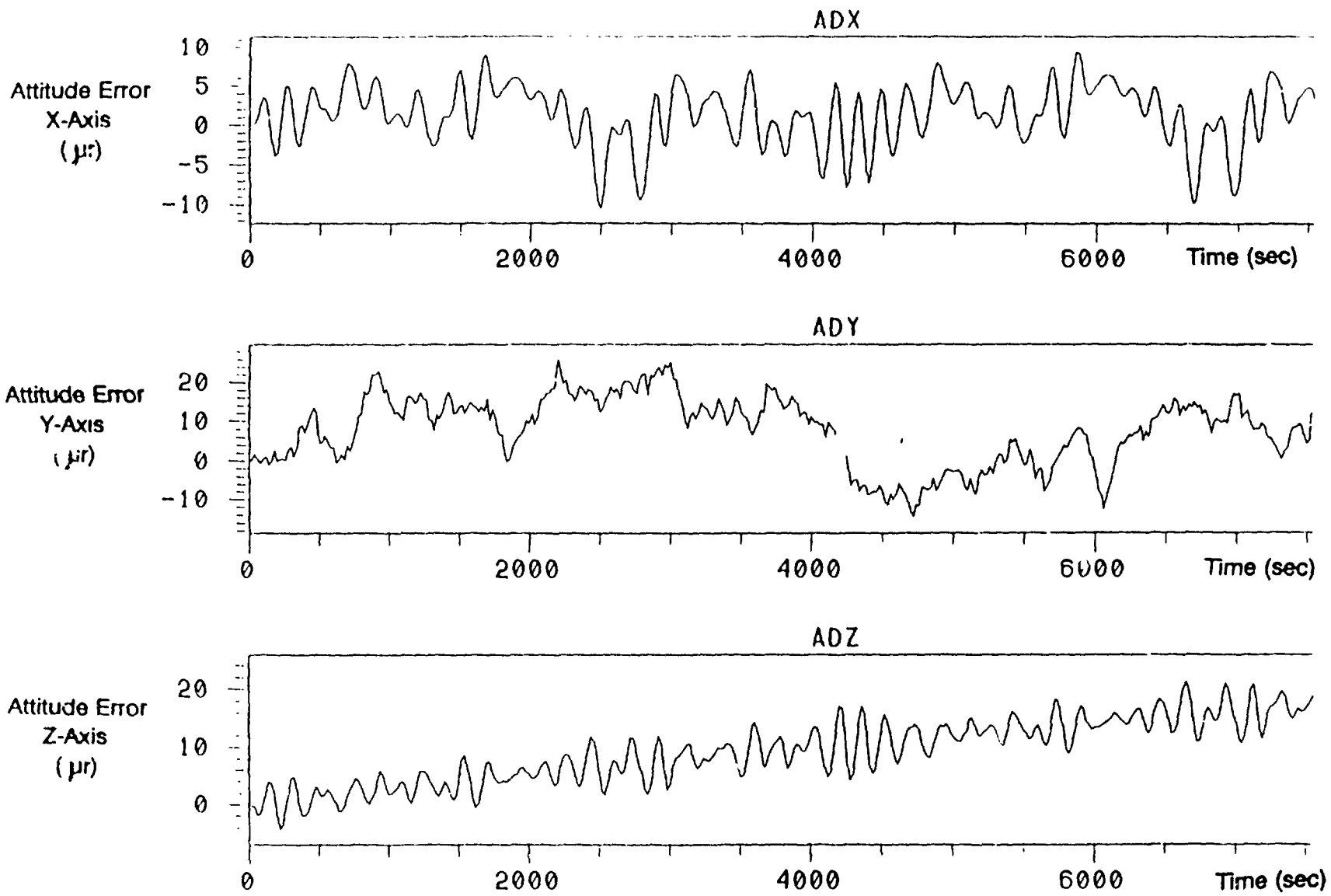


Figure A.2.2-4. Attitude Errors for Simulation FSCLONG3.PUT

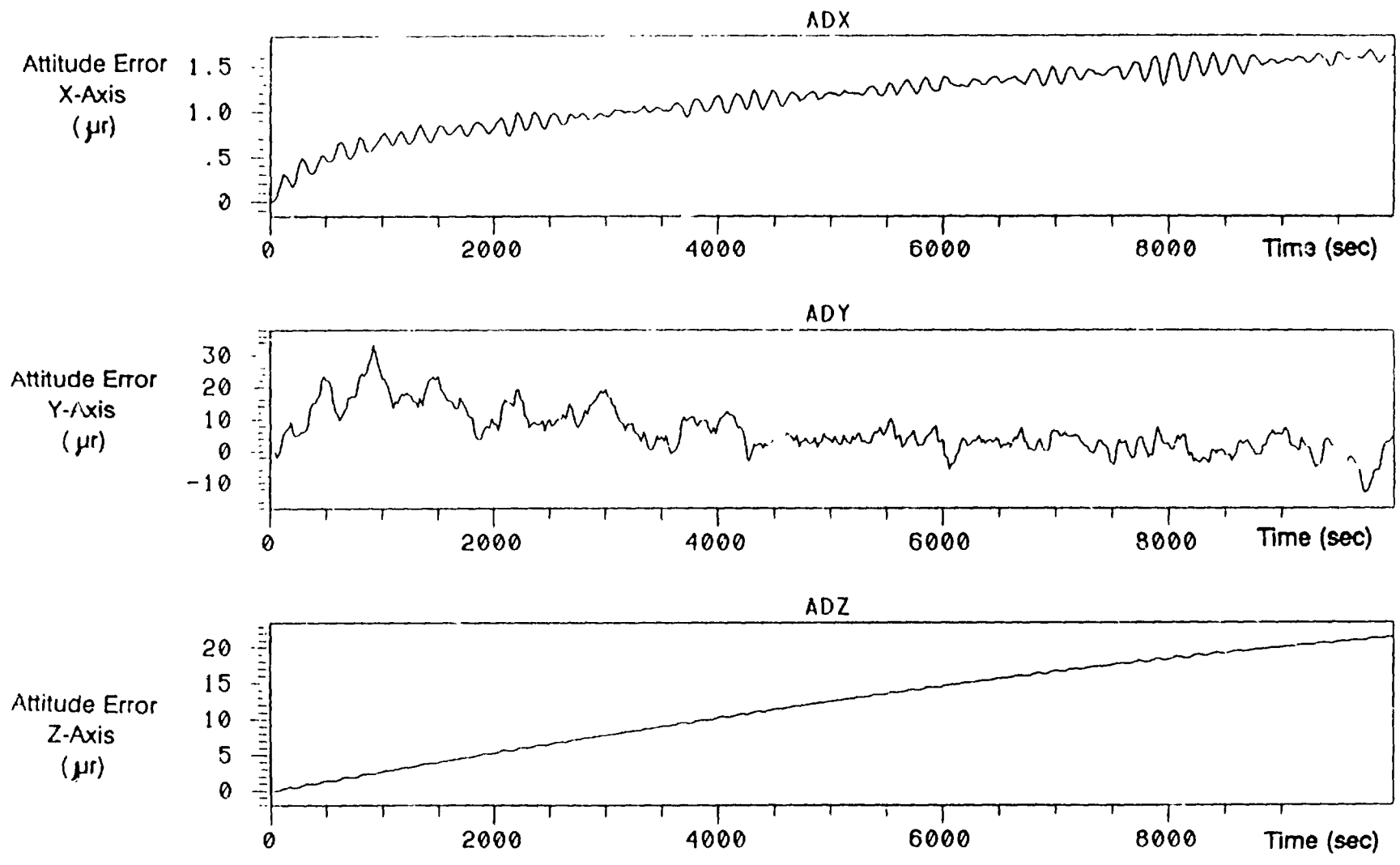


Figure A.2.2-5. Attitude Errors for Simulation PERFESND3.PUT

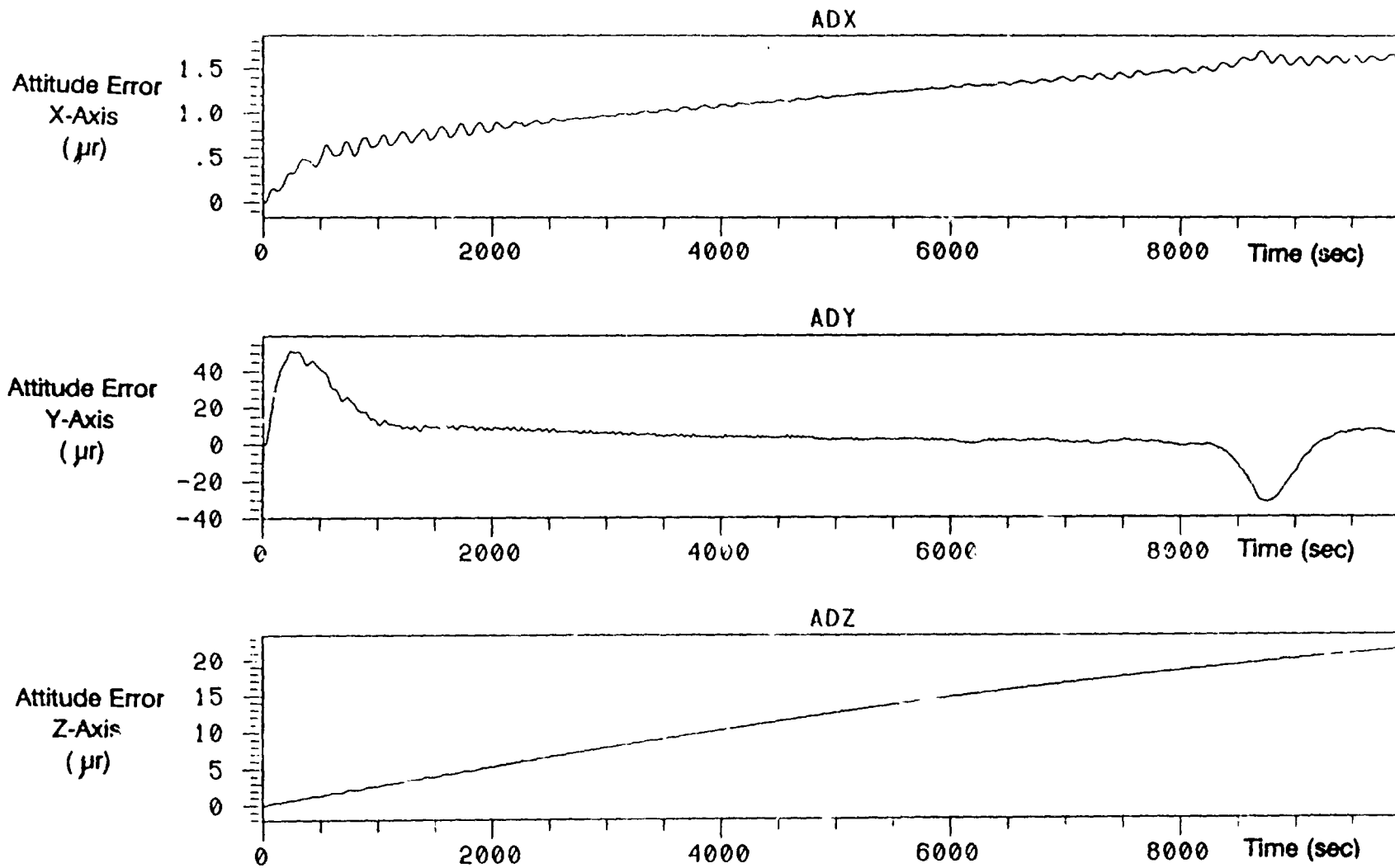


Figure A.2.2-6. Attitude Errors for Simulation NDNOTKNOIS3.PUT

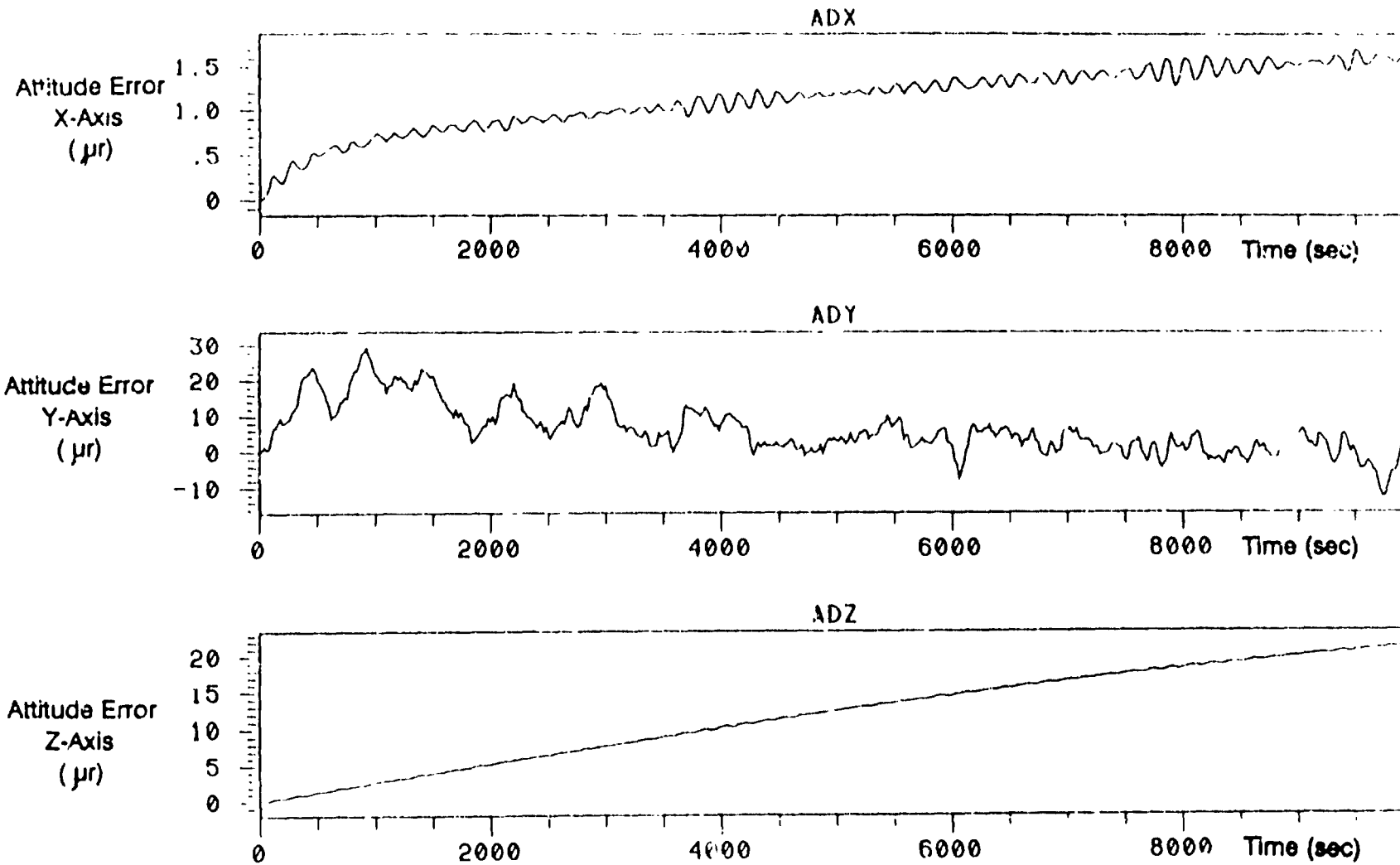


Figure A.2.2-7. Attitude Errors for Simulation NDNOTQQN3.PUT

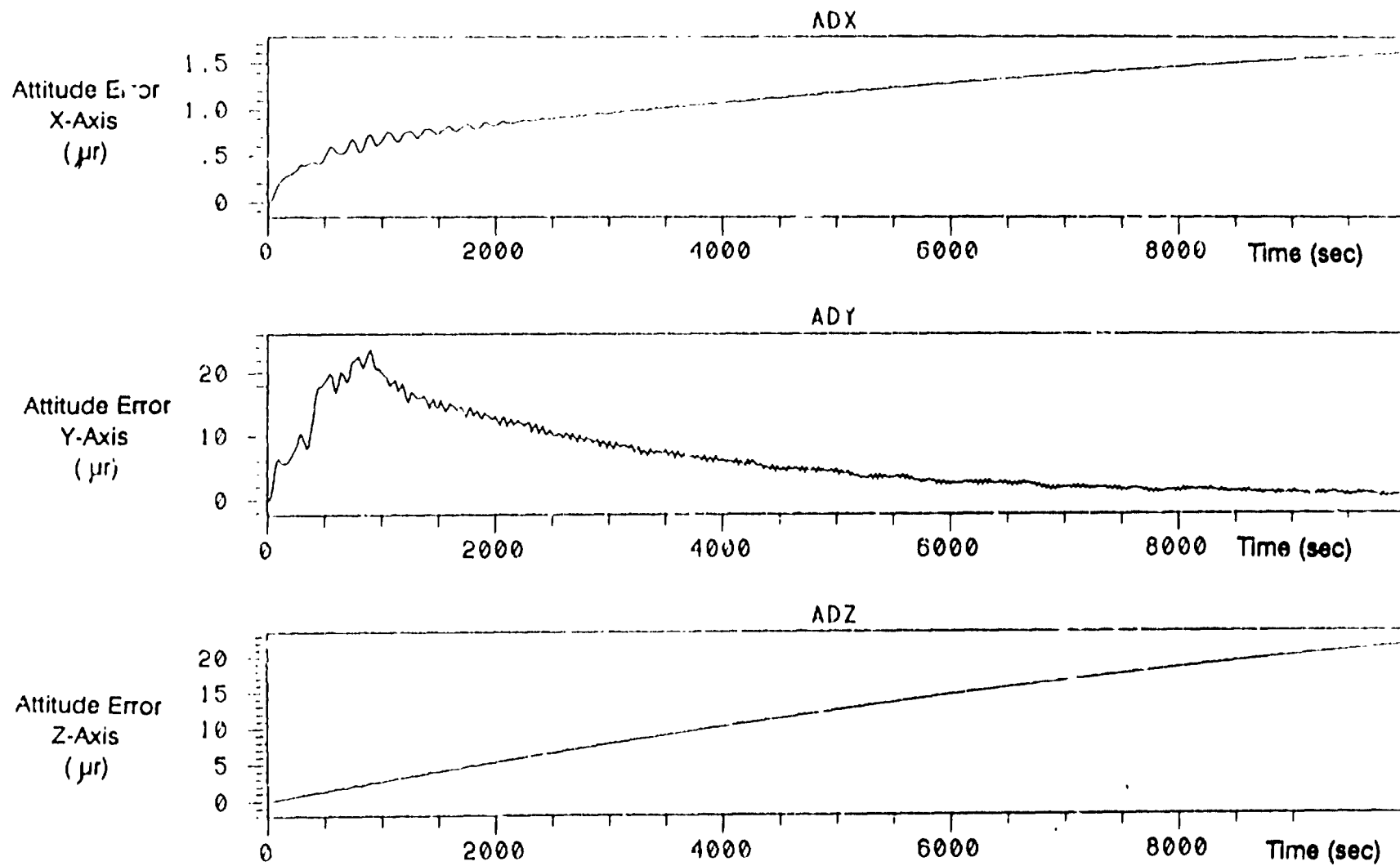


Figure A.2.2-8. Attitude Errors for Simulation CLEANWH3.PUT

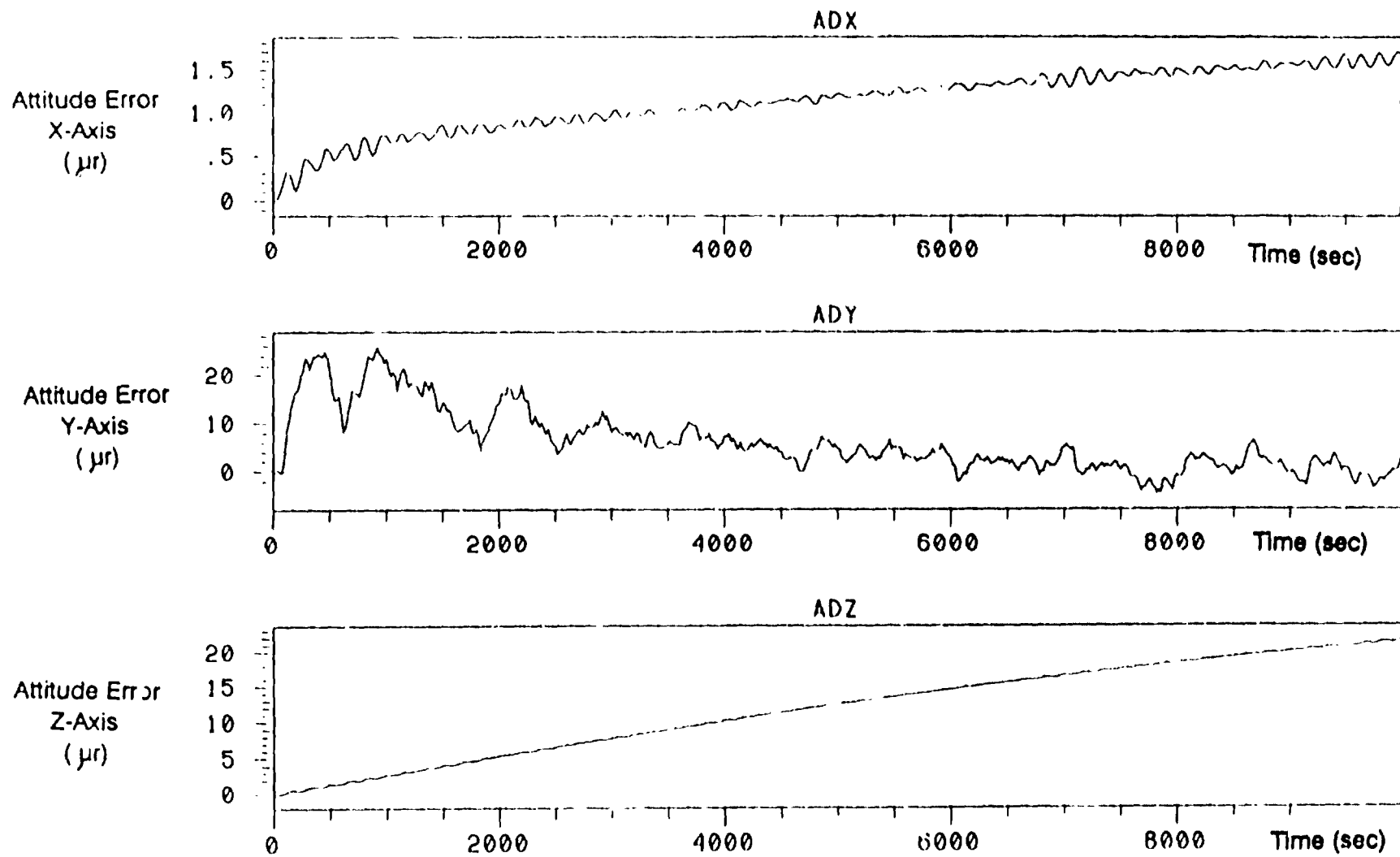


Figure A.2.2-9. Attitude Errors for Simulation THREE3.PUT

seconds) or the period for thirty revolutions (.328 seconds). Logically, it appears that noise improvements can be realized through increasing this period of measurement. It can be proven that the jitter variance change is inversely proportional to the square root of a factor Q, which represents the ratio of wheel revolutions measured versus nominal wheel revolutions measured (Addendum A.2.2-5). For example, on GOES-I there are thirty revolutions counted. If sixty revolutions are counted on the GOES-N system, one would expect the spacecraft jitter to be 1/1.414 (1/square root of 2) of the GOES-I case.

As it has been determined that increasing the period of data sampling theoretically will improve spacecraft jitter, one must determine how much the period should be changed to maximize this improvement. A standard rule of thumb for sampled data control systems is the sample frequency must be twenty times the bandwidth of the system, which is defined to be the -3 dB point on the closed loop frequency response. The closed loop response for each of the control loops (housekeeping and imaging pitch, V mode housekeeping and imaging roll/yaw, L mode housekeeping and imaging roll/yaw and the internal wheel speed vs. torque command loop) was run in order to determine the worst case bandwidth (Figures A.2.2-10 through A.2.2-14). That bandwidth is .04Hz, as defined by the internal wheel control loop that is present in all of the spacecraft control loops. Therefore, for sufficient margin this study assumes a 1Hz sample frequency is feasible. At worst case, the sample frequency is defined by the slowest frequency operational for the momentum wheel. On GOES-I, this frequency is 80 Hz. The maximum number of revolutions that can be counted is therefore 80. This increase by a factor of 2.67 in revolutions counted should decrease the output jitter on the spacecraft by a factor of 1.63.

Finally, some consideration has been given to eliminating the torque command quantization in order to improve performance. It can be seen from the simulation runs that this torque disturbance does not have a significant high frequency effect on spacecraft jitter, but it will cause a "torque jog" over a low frequency. Investigation into the quantization revealed it to be on the order of .0001 newton-meters, approximately equal to the torque resultant from solar pressure imbalance cause by a trim tab failure. Although study limitations did not permit an in-depth study of the effects of this torque quantization, it is believed that the quantization dithers the noisy outputs from the Earth Sensor. Since the control system can handle the effects of the low frequency jogs without going unstable and the high frequency dithering effects apparently do not harm performance, it is recommended that no change be made to the torque quantization size.

A.2.2.1.4 Conclusions

It has been proven that spacecraft pointing performance can be improved by a reduction in noise sources within the wheel and the feedback tachometer. Four possibilities have been studied that may improve this performance. Of the possible improvements, a reduction in the tachometer uncertainty specification and an increase in the period required to sample the tachometer data will both reduce spacecraft pointing jitter at minimal cost, risk and redesign to the present configuration. It is recommended that these improvements be implemented into GOES-N, Option I. Additionally, these improvements may be feasible for implementation into the later spacecraft of this GOES series. This possibility should be explored.

INCA

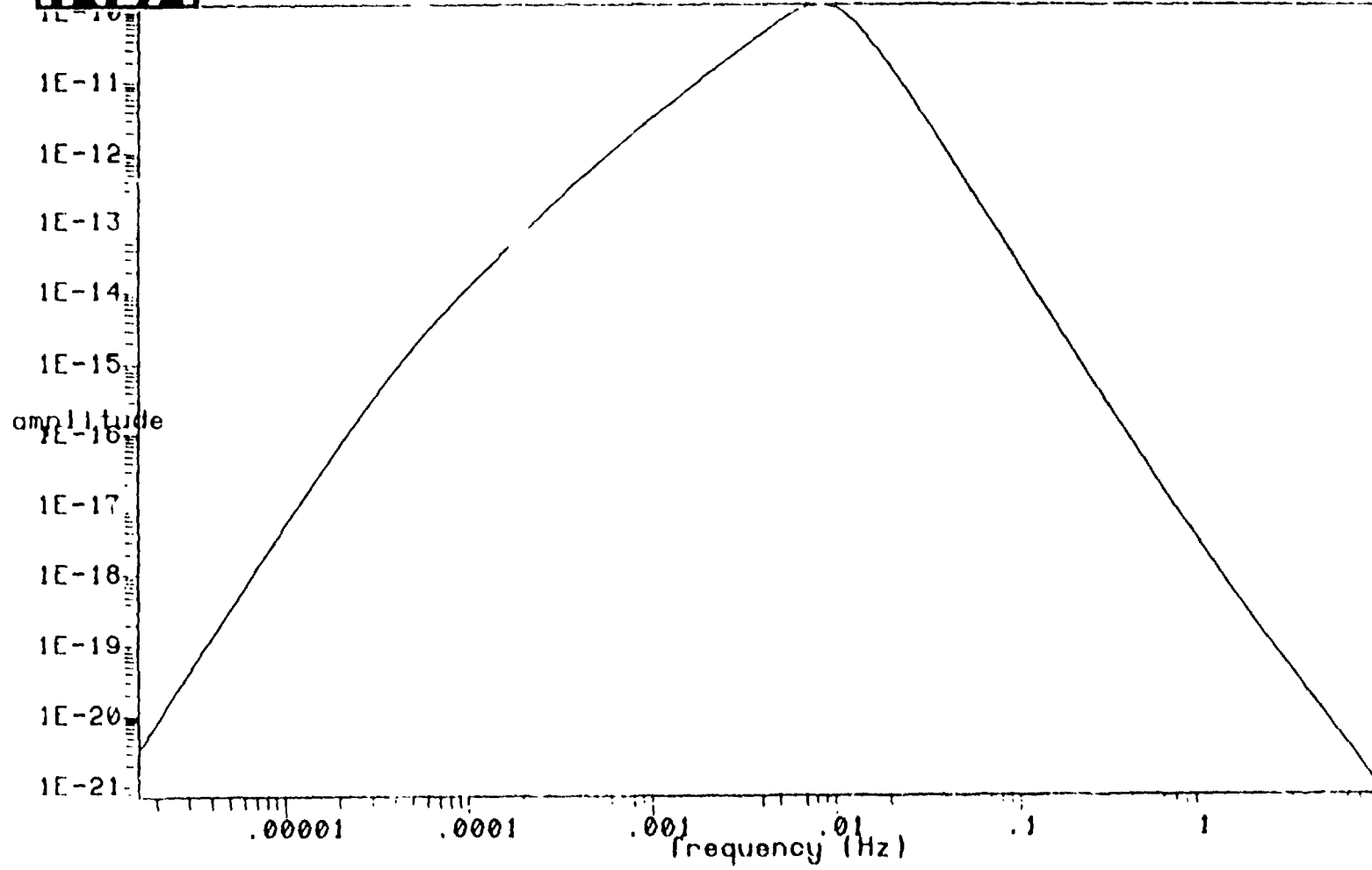


Figure A.2.2-10. Power Spectral Density of Theta W.R.T. Tach Noise

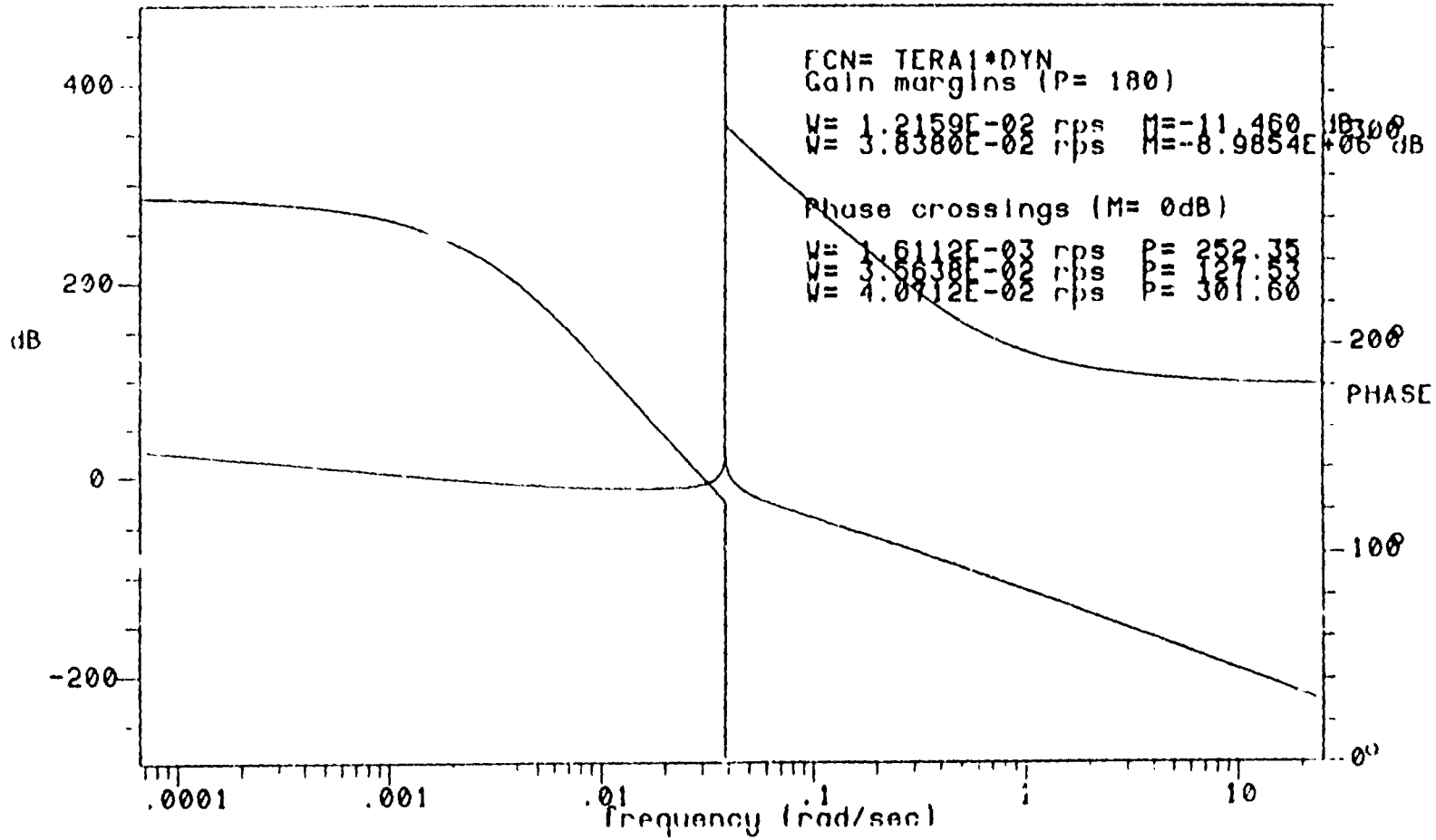


Figure A.2.2-11. Imaging V Mode Roll/Yaw Stability

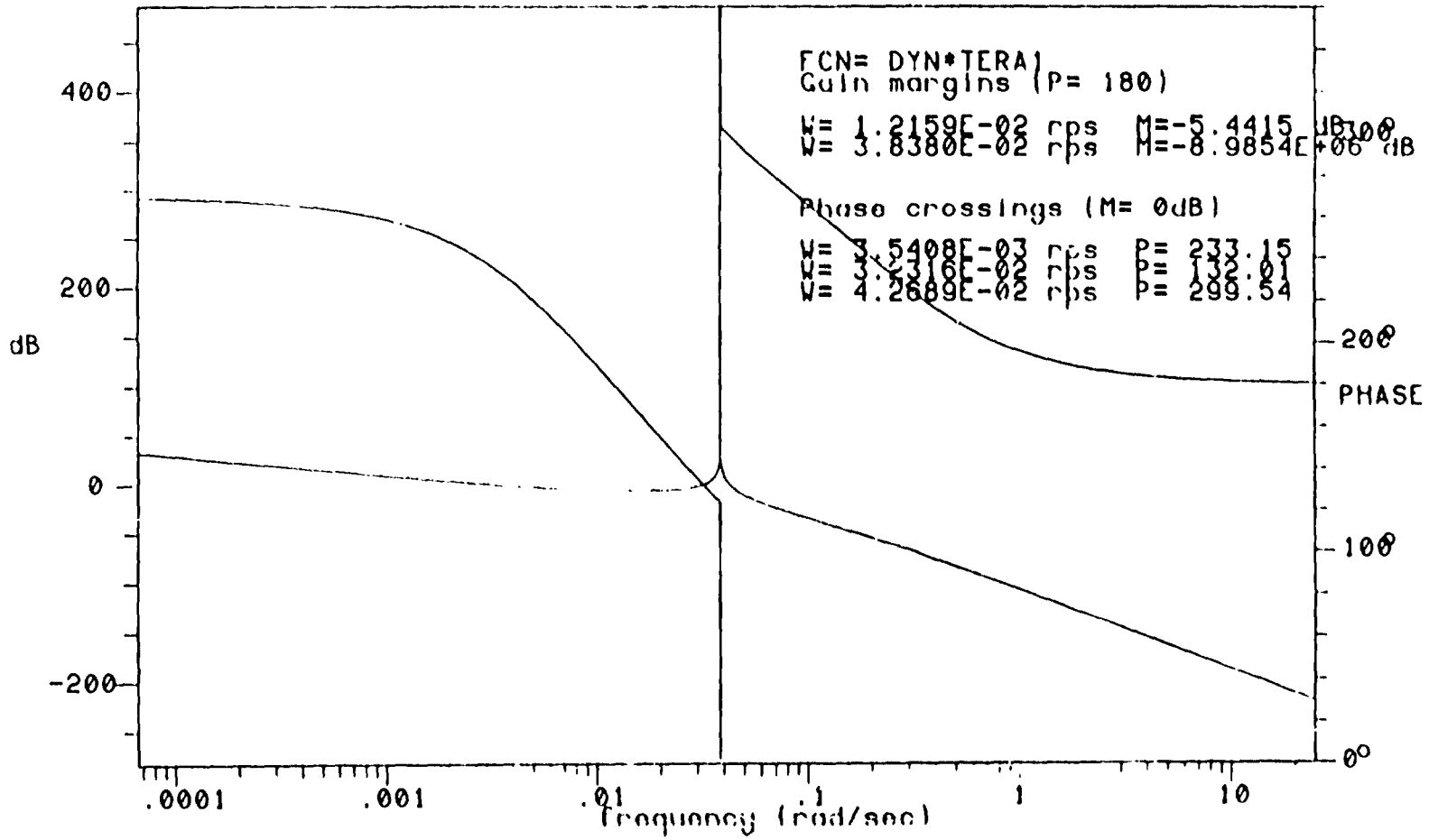


Figure A.2.2-12. Housekeeping V Mode Roll/Yaw Stability

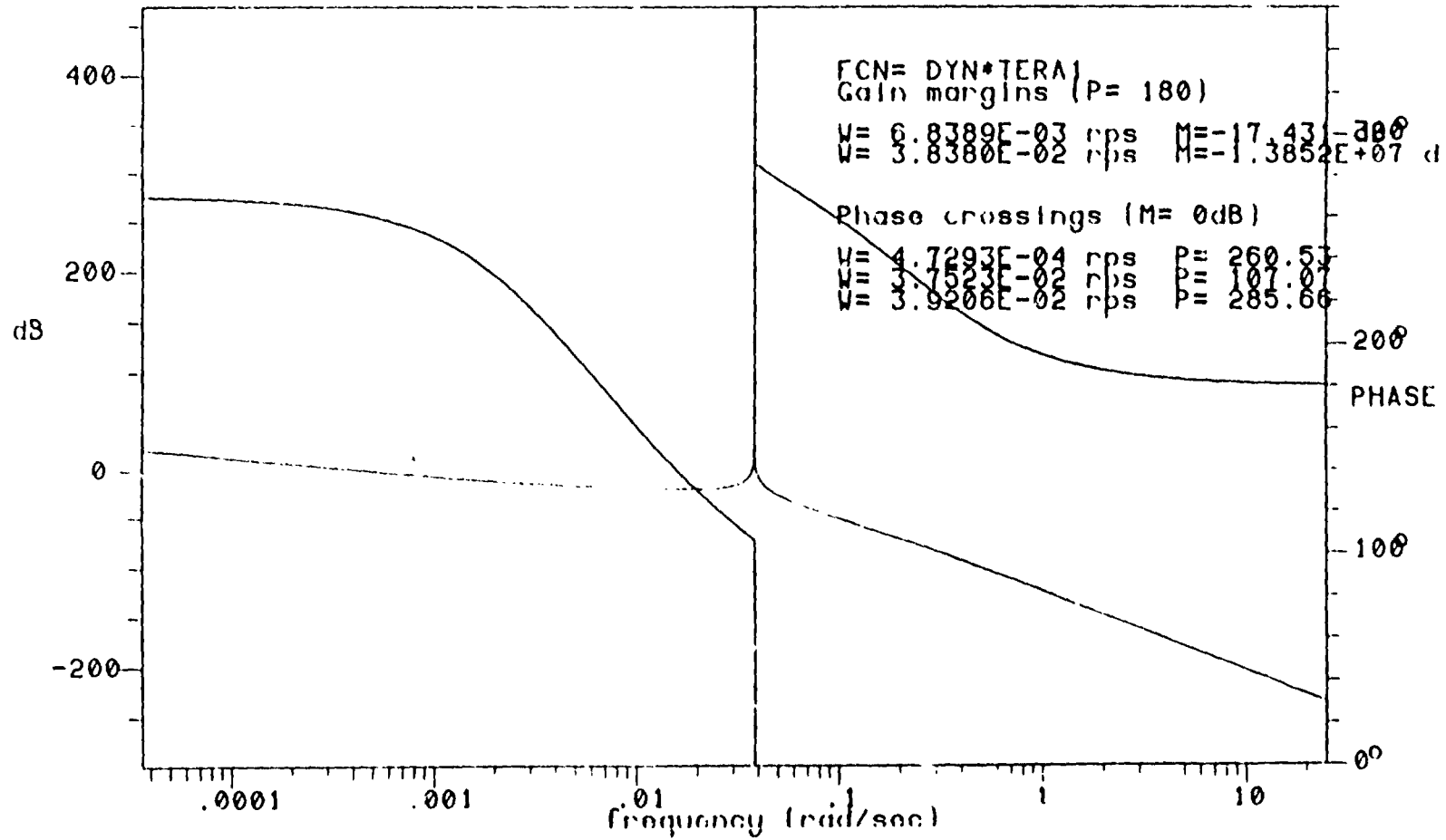


Figure A.2.2-13. Imaging Stability, L-Mode, Roll/Yaw Loop

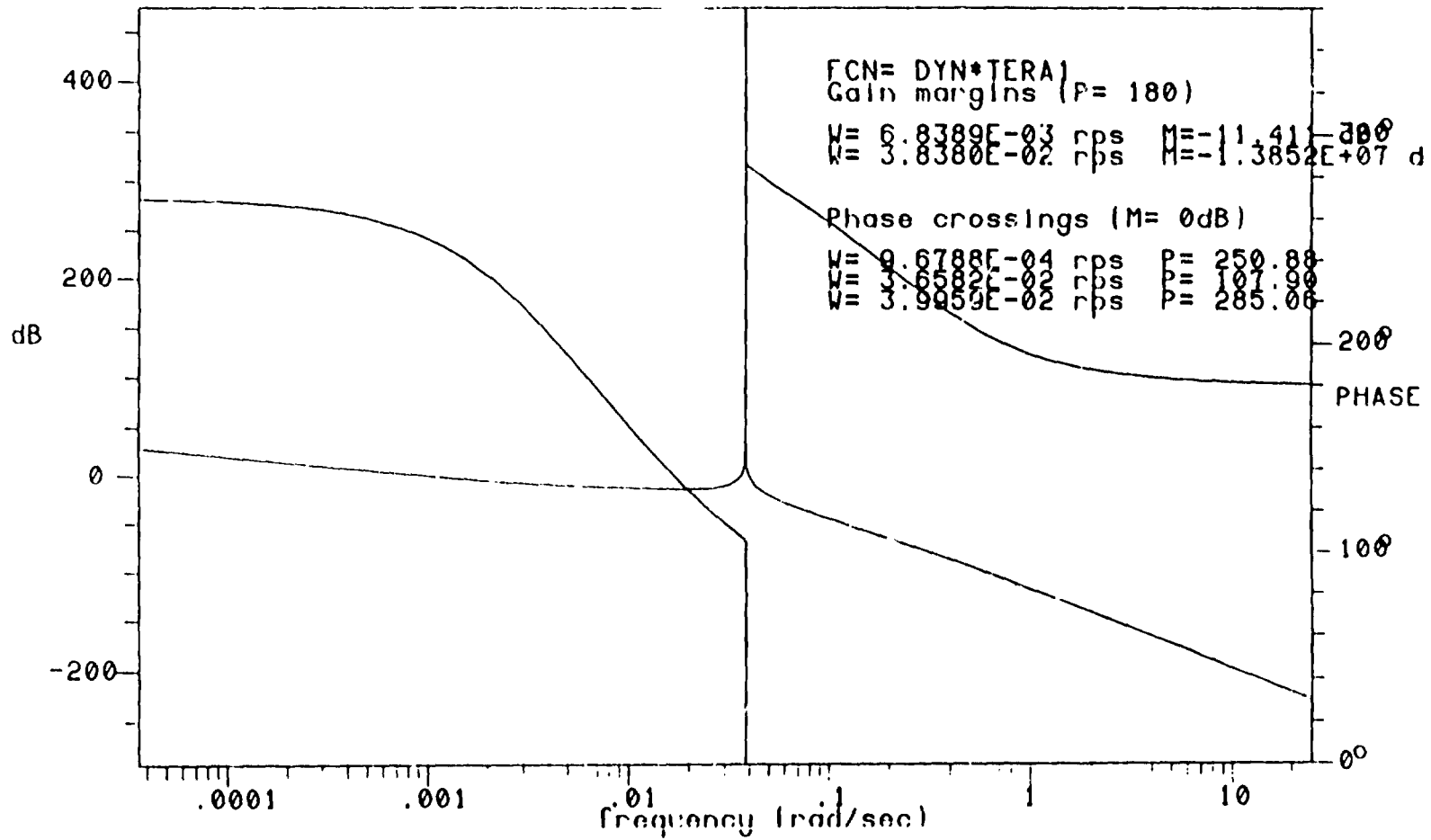


Figure A 2.2-14. Housekeeping Stability, L-Mode, Roll/Yaw

A.2.2.2 Dynamic interaction improvements

A.2.2.2.1 Introduction

The dynamic interaction of mass imbalance properties on a rotating wheel is the source of sinusoidal forces and torques on a spacecraft. The forces and torques are produced by non-uniform properties of inertia along different areas of the wheel. In other words, the momentum wheel wobbles as it reaches high speed. Since this interaction produces a disturbance torque on all three spacecraft axes, pointing performance suffers with a high level of dynamic interaction. This study will examine two methods to improve wheel imbalance properties in order to improve spacecraft pointing performance.

The amount of mass imbalance present in a certain wheel is described by two values, known as static and dynamic imbalance. Static unbalance results from the non-central location of the wheel's center of mass. Dynamic unbalance results from non-zero cross-products of inertia in the plane of rotation. The disturbance forces and torques are also functions of wheel speed and the distances from the wheel center of mass to the spacecraft center of mass.

Given a momentum wheel rotating in the pitch axis at W radians per second, with static unbalance D_s and dynamic unbalance D_d , at center of mass located at point (L_x, L_y, L_z) (spacecraft center of mass defined to be at $(0,0,0)$), the dynamic equations are:

$$F_x = D_s \cdot W^2$$

$$F_y = 0$$

$$F_z = D_s \cdot W^2$$

$$T_x = D_s \cdot W^2 \cdot L_y + D_d \cdot W^2$$

$$T_y = \text{SQRT}(L_x^2 + L_z^2) \cdot D_s \cdot W^2$$

$$T_z = D_s \cdot W^2 \cdot L_y + D_d \cdot W^2$$

Thus, it is obvious that torque disturbances can be reduced through a reduction in static or dynamic unbalance, wheel speed, or distance to the spacecraft center of mass. Since this study assumes the use of the current GOES-I bus with only minor modifications to the control system, it is safe to assume that the wheel dynamic range (usable wheel speed) and the location of the momentum wheels and reaction wheel cannot be changed. Thus, improvements can only be reached through improvements in static and dynamic unbalance.

The pointing performance exhibited by the current GOES-I system during recent dynamic interaction testing is shown in Figure A.2.2-15. As can be seen, dynamic interaction causes in excess of $3 \mu\text{r}$ pointing error and up to $10 \mu\text{r}$ servo error on GOES-I. One would think the GOES wheels are poorly balanced, thus creating the excessive error. On the contrary, the GOES wheels built by Teldix are some of the best balanced wheels in satellite use.

Normally, momentum and reaction wheel vendors will only accept unbalance specifications of $3.6 \times 10^{-3} \text{kg-m}$ static unbalance and $9.1 \times 10^{-6} \text{kg-m}^2$ dynamic unbalance. The GOES specs are $1.08 \times 10^{-3} \text{kg-m}$ static and $1.4 \times 10^{-6} \text{kg-m}^2$ dynamic. In the worst case of six momentum wheels built for GOES already, the specs have been bettered by a factor of two. However, the momentum wheels are run at high speed (near 100 Hz) and a significant flexible body mode exists on the GOES spacecraft near the same frequency. Although there is a range at which the wheels can be used under the present GOES error budget, further advances in wheel balancing might allow for reductions in dynamically induced errors in the GOES-N error budget.

There is reason to believe that two different methods might be useful in improving the static and dynamic unbalance on the GOES wheels. The first would be to allow for further processing in the wheel balancing process. Currently, the GOES wheels are specially balanced to meet the tight unbalance specs required by the GOES-I program. The special balancing process is considered a proprietary and has allowed Teldix to improve dynamic balancing by a factor of three over standard space flight wheels. There is some belief that further enhancements can be made to the two momentum wheels through use of other wheel balance processes. Another approach to improve balance is to use magnetic suspension in place of ball bearings. These methods will both be examined with respect to feasibility, cost, design effort and risk.

A.2.2.2.2 Study results and system tradeoffs

The first method of possible improvement is through additional processing during wheel balancing by the manufacturer. By choosing this method, NASA would task Teldix to determine other methods for improving balancing of momentum wheels. There is reason to believe the dynamic unbalance on the large momentum wheels can still be significantly improved. Prior to the GOES wheel balancing process, the normal range of dynamic balance was $2.7 \times 10^{-6} \text{Kg-m}^2$. With one step in processing, that figure has been dropped to a worst case of $5.38 \times 10^{-7} \text{Kg-m}^2$ in the first six GOES momentum wheels. It is feasible that additional research might turn up another process that might again reduce the dynamic unbalance performance.

But further reductions in dynamic unbalance do not appear to be worth the extra effort they would require. On the current GOES bus, the values for L_x , L_y , and L_z , the distance from wheel to spacecraft center of mass, are all on the order of 1 meter. For that distance and the GOES values of static and dynamic unbalance, the contribution of dynamic unbalance is an order of magnitude smaller than that of static unbalance. The value of static unbalance has remained unchanged since the GOES processing began, and it is less likely that real improvements can be made in this value. Therefore, the additional processing effort is not recommended. Although the cost would only be 10% higher than the current system and risk would be minimal, there simply is not a significant performance benefit from the additional processing to warrant the additional costs.

The second method of reducing unbalance disturbances would be through the use of a magnetic suspension system in place of ball bearings. Magnetic suspension wheels use Lorenz forces to suspend and actively control the rotor of the wheel. There are several special advantages to using magnetic bearing systems. There is no restriction force, which would cause a disturbance torque as the wheel speed reversed direction (important for reaction wheels). There are no ball bearings

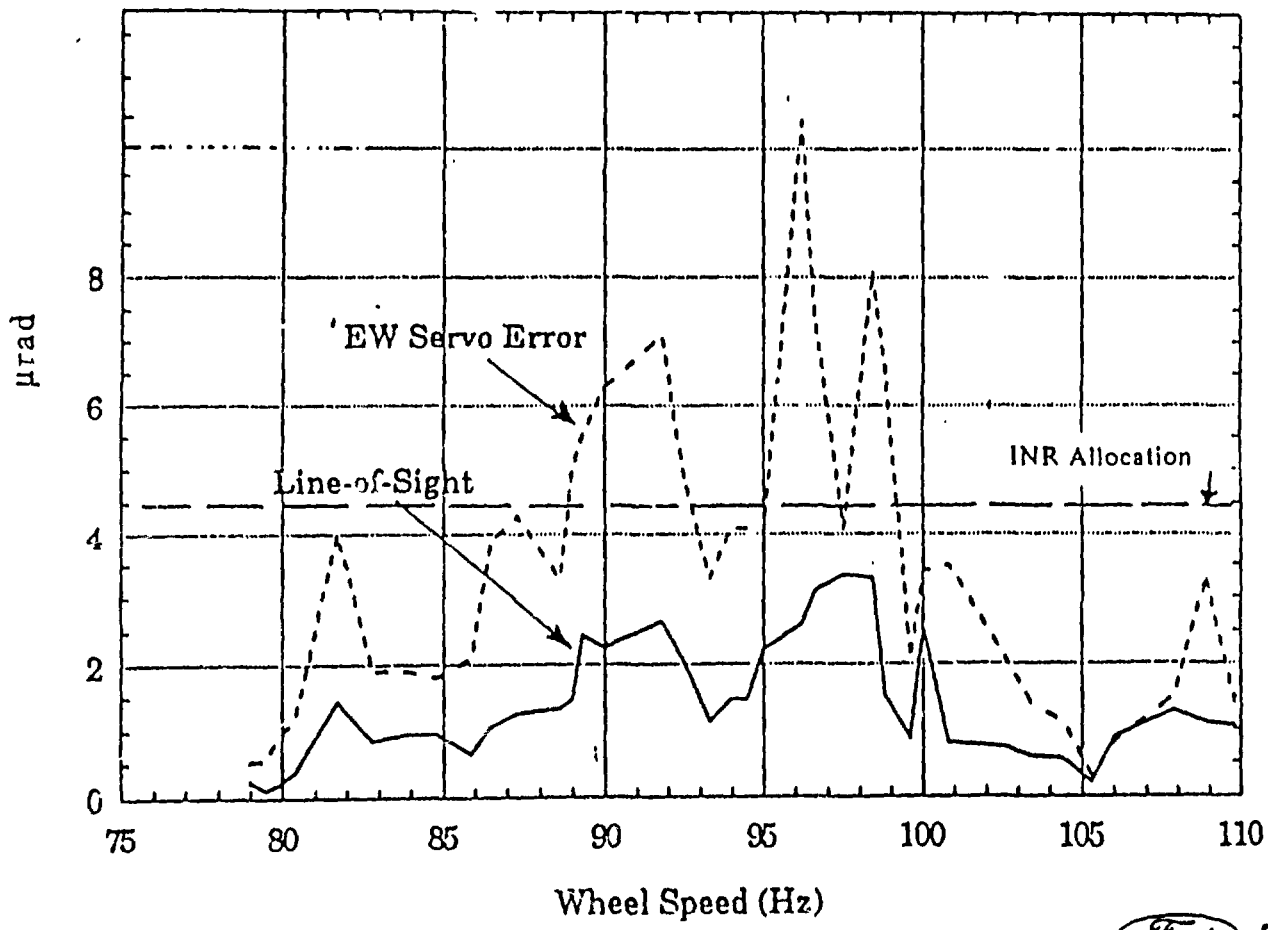


Figure A.2.2-15. Dynamic Interaction Test Summary of Results

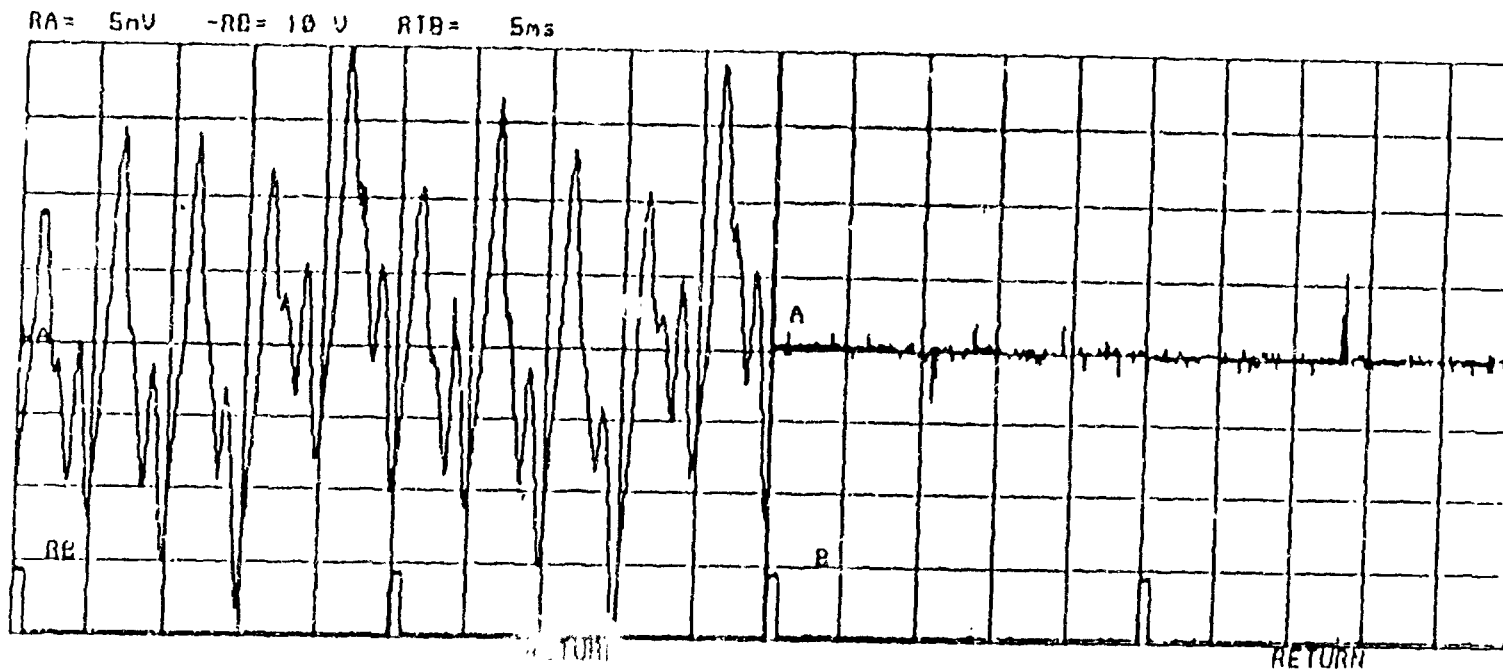
or lubrication systems that might fail. Finally, although magnetic bearing wheels are more difficult to balance, they do not transmit disturbance torques onto the spacecraft. This principle is demonstrated in Figure A.2.2-16. On the left is the torque transferred onto the test set from a wheel with magnetic suspension without active control. This value is roughly on the same order of magnitude as torques caused by a similar wheel using ball bearings. On the right is the same wheel with active control. The Teldix literature approximates a 40 dB noise attenuation (two orders of magnitude) by use of active magnetic control. It is apparent that substantial disturbance torque improvement can be realized by use of an actively controlled magnetic suspension system.

Although the use of magnetic bearings in the momentum and reaction wheels is an attractive improvement, there are drawbacks in its implementation. The most important is a lack of existing flight-qualified hardware on the market. Teldix will have an engineering unit bearing system completed by next year, but there would be risks involved in qualifying new technology for space flight. Secondly, there is a prohibitive cost increase in using magnetic bearings. Teldix estimates the cost per wheel will double by using the new technology. This is a deceptive increase since magnetic suspension wheels can be used as control moment gyros, which allows for an operational system that employs only two momentum wheels: one for operations and one for redundancy. The extra reaction wheel would not be needed. However, there would still be a substantial increase in wheel system costs. Finally, there would be considerable redesign required to use magnetics in the GOES wheels. Essentially, GOES-N would use an entirely new wheel, rather than one with minor improvements.

A.2.2.2.3 Conclusions

This study has examined the feasibility of improving the static and dynamic unbalance values for the GOES momentum and reaction wheels in order to improve pointing stability for the GOES-N spacecraft. Two methods of improvement were studied. The first involved supporting further research into wheel balancing at the wheel vendor, Teldix. Investigation has revealed improvements from this additional processing might only improve dynamic unbalance characteristics. The disturbance improvement from this method is too slight to merit an expected 10% increase in wheel costs.

The second method involved a redesign to use actively controlled magnetic suspension in place of ball bearings. There are several benefits: torque disturbances seen by the spacecraft may be reduced by two orders of magnitude; there is no danger of torque ripple due to reversing wheel rotational direction; there are no ball bearings or lubrication systems to fail; and momentum can be better gimballed so that the momentum wheels can be used like control moment gyros. However, by using magnetic suspension, GOES-N assumes the cost, schedule and design risks of flying a component that has not been space qualified before. I cannot recommend magnetic suspension under the guidelines of the Option 1 study. This is not a minor improvement to an existing system, it is the complete redesign of the wheel system. However, it is a development that must be carefully considered for use on any spacecraft that is willing to accept the start-up risks. By Phase-B, NASA will be able to determine the feasibility of qualification in time for use on GOES. I suggest that magnetic suspension be reexamined at that time.



Axial Controller Output at 2400 rpm
without MFC _____ **with MFC**

Figure A.2.2-16. Torque Noise Response of Magnetic Wheel Without/With Active Control

ADDENDUM A.2.1 1: CALCULATION OF QUANTIZATION & NOISE LEVELS

(DATA PROVIDED BY LAS AOCS DYNAMICS AND CONTROLS CDR PACKAGE)

NOMINAL WHEEL SPEED: $W_n = 5485 \text{ rpm}$
 QUANTIZATION LEVEL: $Q = .0163 \text{ rpm}$
 NOISE (3 Sigma) LEVEL: $N = .0978 \text{ rpm}$

DATA PROVIDED BY TELDIX MOMENTUM WHEEL SPEC

TACHOMETER STABILITY: $S_t = 6 \text{ microseconds} = .000006 \text{ seconds}$

(DATA PROVIDED BY CONVERSATIONS WITH LAS (P. CHU, T. HENTHORN))

CLOCK RATE: $T_c = 1.024 \text{ microsecond} = .000001 \text{ second}$
 REVOLUTIONS COUNTED $R = 30 \text{ revolutions}$

Allow tach quantization, Q, to be driven by the AOCS clock, T_c , and tach noise, N, to be driven by the tachometer stability, S. Both levels will be driven by the wheel speed, W_n . The study uses a nominal wheel speed (485 rpm - 91.4 Hz) for the calculations of the levels and assumes the levels to be constant afterwards.

$$T_{\text{buffer}} = \text{time to fill tachometer buffer} = \frac{R}{W_n} = \frac{30}{91.4167} = 3281677 \text{ seconds}$$

$$W_q = \text{worst case quantization wheel speed} = \frac{R}{(T_{\text{buffer}} + T_c)} = \frac{30}{.3281687} = 91.416387 \text{ Hz} \\ = 5484.9833 \text{ rpm}$$

$Q = W_n - W_q = .0167 \text{ rpm}$ (compares well with GOES CDR value)

$$W_{\text{no}} = \text{worst case noise wheel speed} = \frac{R}{(T_{\text{buffer}} + S_t)} = \frac{30}{.3281737} = 91.415004 \text{ Hz} \\ = 5484.90022 \text{ RPM}$$

$N = W_n - W_{\text{no}} = .0998 \text{ rpm}$ (also compares well with GOES CDR value)

This calculation also proves, since T_{buffer} is inversely proportional to both wheel speed and noise/quantization level, that proportionally higher noise/quantization levels will result from higher wheel speeds

ADDENDUM A.2.2-2: VARIANCE ANALYSIS OF TACHOMETER/EUROPEAN SPACE AGENCY (ESA) NOISE

(DATA PROVIDED BY LAS DYNAMICS & CONTROLS CDR)

ESA SAMPLE RATE: $W_s(e) = 4 \text{ Hz}$

(DATA PROVIDED BY CONVERSATIONS WITH FORD (P. CHU, T. HENTHORN))

TACH SAMPLE RATE @ 5484 rpm: $W_s(t) = 3.04 \text{ Hz}$

ESA NOISE LEVEL (3 σ): $N(e) = 275 \mu\text{r}$

SPACECRAFT ANGLE VS. TACH NOISE TRANSFER FUNCTION (NUMBERS FROM INR CDR)

(DATA DERIVED IN ADDENDUM A.2.2-1)

TACH NOISE (3 σ): $N(t) = .0988 \text{ rpm} = .0103463 \text{ rad/s}$

Define the variance of a noise function to be the square of the standard deviation, such that:

$$\text{VAR}(x) = \text{SD}(x)^2$$

and the variance of the same function can be defined by the area under a power spectral density frequency response defined by sample frequency and power spectral magnitude. If the noise is assumed to be white and there is a finite sample frequency, then this equation can be expressed as:

$$\text{VAR}(x) = \text{PSM}(x) * W_s(x).$$

Define the co-variance of a transfer function or the square of the magnitude of the transfer function, such that:

$$\text{COVAR}(x,y) = \text{TF}(x,y)^2.$$

Then the variance of an output function can be found by the following equations:

$$\text{PSM}(y) = \text{COVAR}(x,y) * \text{PSM}(x)$$

$$\text{VAR}(y) = \text{PSM}(y) * W_s(y).$$

In this application, we will assume $W_s(y)$ approaches infinity.

VARIANCE OF TACH NOISE

$$N(t) = .0988 \text{ rpm} = .010346 \text{ rad/s}$$

$$\text{SD}(t) = N(t)/3 = .003449 \text{ rad/s}$$

$$\text{VAR}(t) = \text{SD}(t)^2 = .00001189 \text{ rad}^2/\text{sec}^2$$

$$\text{VAR}(t) = \text{PSM}(t) \cdot W_s(t) \text{ (assuming band-limited noise)}$$

$$\text{PSM}(t) = \text{VAR}(t)/W_s(t) = .00001189/3.04 = .0000039112 \text{ rad}^2/(\text{sec}^2 \cdot \text{Hz})$$

The power spectral magnitude is cascaded into the square of the transfer function spacecraft angle vs. tach noise to develop the co-variance of spacecraft angle with respect to tach noise (see Figure A.2.2-17). This area is the variance of the output angle. From this variance, one can find the standard deviation and the three sigma jitter.

$$\text{VAR}(y) = \text{area under curve} = 6.8\text{E-}12 \text{ radians}^2$$

$$\text{SD}(y) = \text{SQRT}(\text{VAR}(y)) = 2.6\text{E-}6 \text{ radians}$$

$$\text{Jitter} = 3 \cdot \text{SD}(y) = 7.8\text{E-}6 \text{ radians}$$

VARIANCE OF EARTH SENSOR NOISE

$$N(e) = 275 \text{ microradians} = 275\text{e-}6 \text{ radians}$$

$$\text{SD}(e) = N(e)/3 = .000091667 \text{ radians}$$

$$\text{VAR}(e) = \text{SD}(e)^2 = 8.402777\text{e-}9 \text{ rad}^2$$

$$\text{PSM}(e) = \text{VAR}(e)/W_s(e) = 8.402777\text{e-}9/4.0 = 2.10069\text{e-}9 \text{ rad}^2/\text{Hz}$$

Once again, the power spectral magnitude is cascaded into the transfer function for spacecraft angle vs. ESA noise to create the output variance (Figure A.2.2-18).

$$\text{VAR}(y) = \text{area under curve} = 1.6\text{E-}11 \text{ radians}^2$$

$$\text{SD}(y) = \text{SQRT}(\text{VAR}(y)) = 4.0\text{E-}6 \text{ radians}$$

$$\text{jitter} = 3 \cdot \text{SD}(y) = 1.2\text{E-}5 \text{ radians}$$

INCA

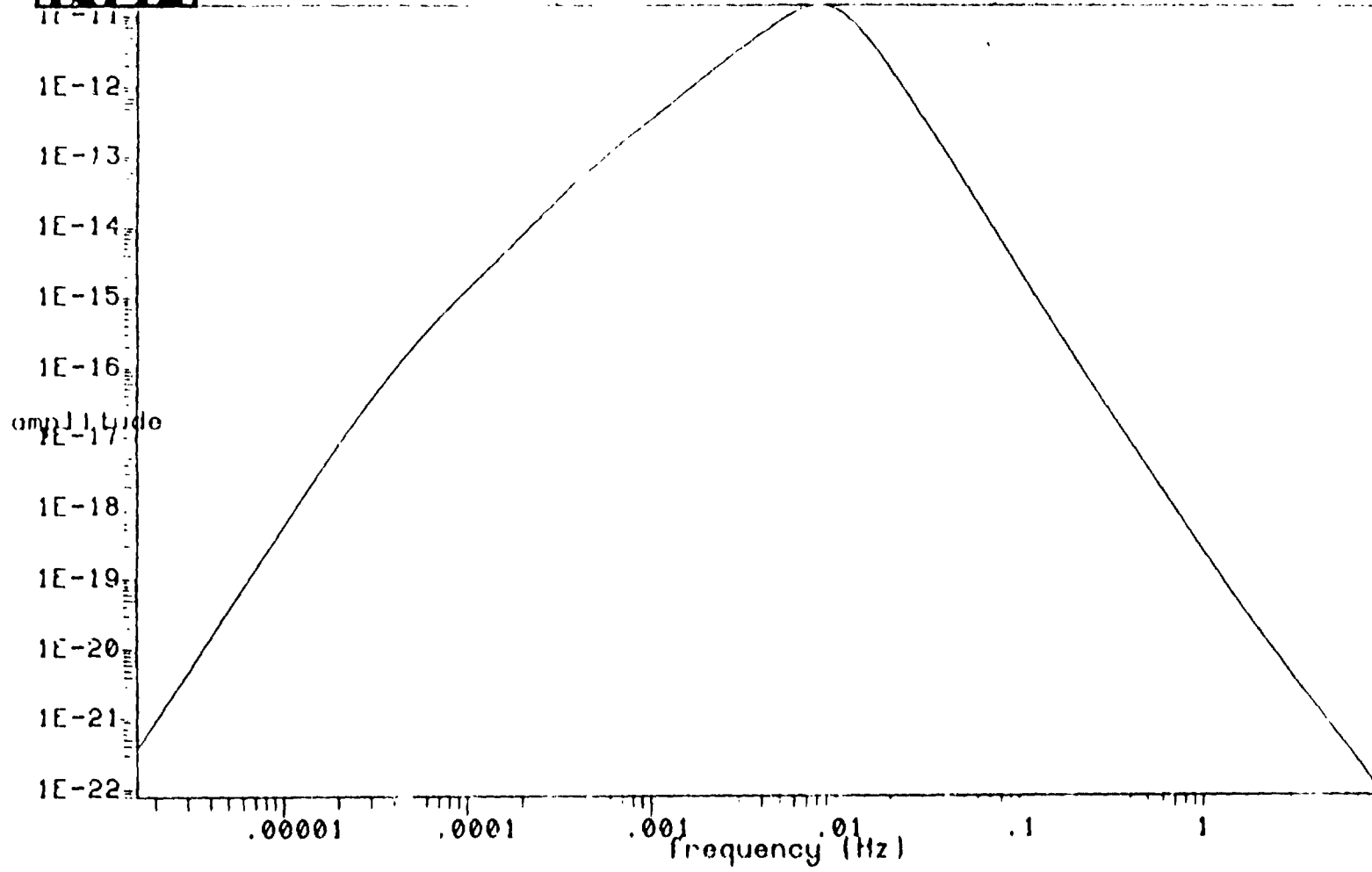


Figure A.2.2-17. Power Spectral Density of Theta W.R.T. Tach Noise

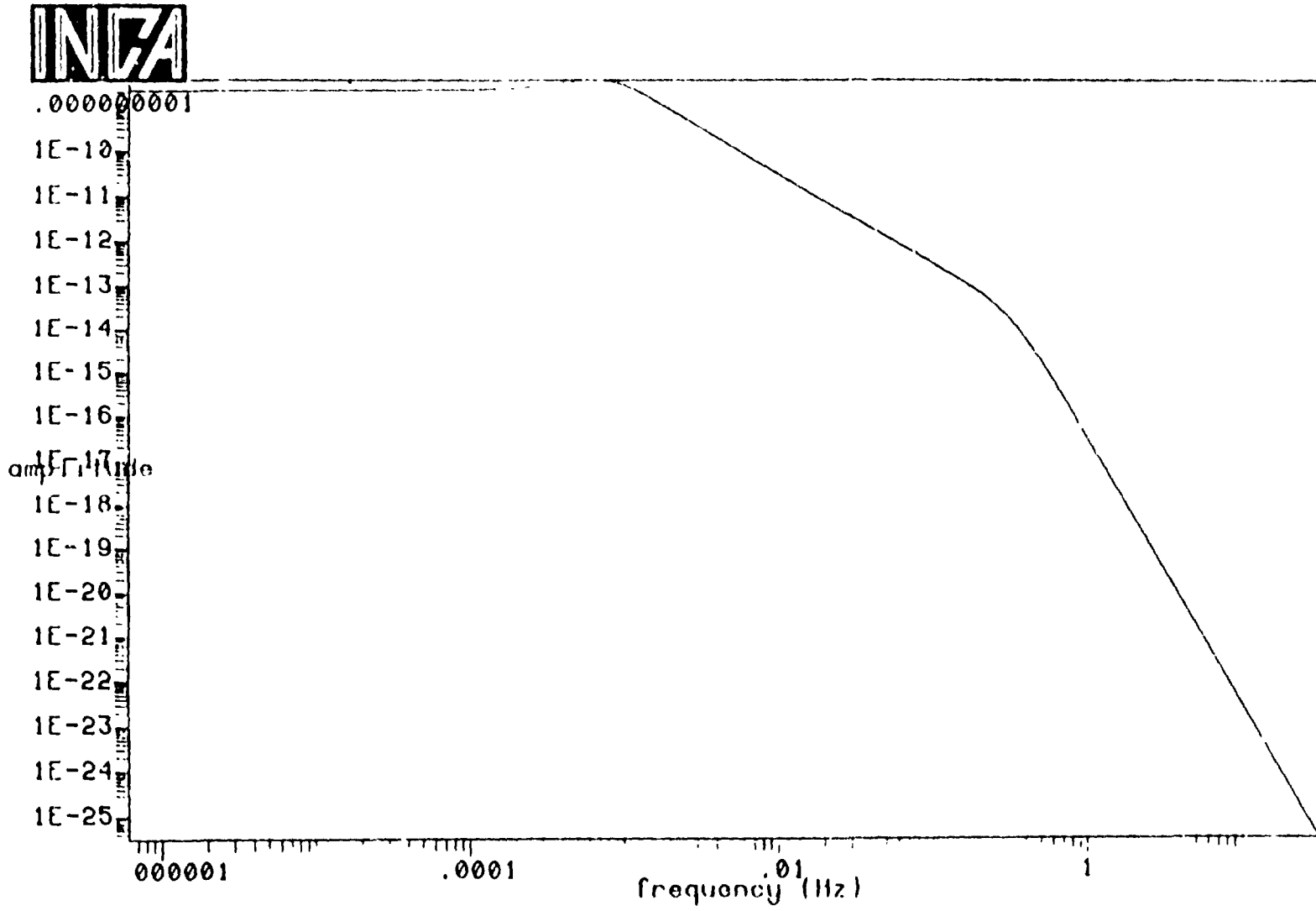


Figure A.2.2-18. Power Spectral Density of Theta W.R.T. ESA Noise

ADDENDUM A.2.2-3: MULTIRATE SAMPLING

```

* ONORB.MOD
*23456789012345678901234567890123456789012345678901234567890123456789012
*      10      20      30      40      50      60      70
* SAMPLING VARIABLES
* DT IS DEFINED BY *MODEL* AS TC/NC = .002
* SAMP. RATE .256 SEC EARTH SENSOR NOISE USED IN REM & PEM SUBROUTINES
* EARTH SENSOR SAMPLING RATE IS FROM GOES-PCC-TM-2205 DATED 1/20/88
* EARTH SENSOR ALTERNATELY MODELED AS 275 MICRORAD WHITE NOISE
* SIGNAL AT SAME SAMPLE RATE (SAMPLING RATE # 1)
* SAMPLING RATE 1 = MS1*TC , (.256 SEC) USED IN AOCE
* AOCE SAMPLING RATE IS FROM GOES-PCC-TM-2205 DATED 1/20/88
* SAMPLING RATE 2 = MS2*TC , (.33 SEC) USED IN MOM. WHEEL TACH.
* THIS RATE DERIVED FROM TALKS W/ TOM HENTHORNE SEP 1990
* ALTERNATE RATE FROM CDR IS 2 HZ (.5 SEC)
* MOM. WHEEL TACH. SAMPLING RATE IS FROM AOCS ANALYSIS CDR 3/8/88
  TC = .002 // SAMPLING CLOCK
  NC = 1.0 ; MS1 = 128.0 ; MS2 = 145.0
##### SET CONSTANTS
  W0 = -7.3E-05 ! RAD/SEC ORBITAL RATE (BODY AXES)
  IW = .2082 ! kg.m^2 MOMENTUM WHEEL INERTIA
##### TORQUE DISTURBANCES
##### INTERNAL TORQUE DISTURBANCES (from WDL-TR10729 6/27/86) NEW # FROM
##### WHEEL IMBALANCES K.P BHAT
  DSM = 1.08E-5 ! MOM. WHEEL STATIC IMBALANCE ( kg.m )
  DDM = 1.40E-6 ! MOM. WHEEL DYNAMIC IMBALANCE ( kg.m^2 )
  LXM1 = -.077 ; LYM1 = .439 ; LZM1 = -.607 ! MOM. WHEEL LOCATION
  LXM2 = -.061 ; LYM2 = .262 ; LZM2 = -.697 ! REL. TO S/C C.M.(meters)
  MWMX1 = DSM*WMW1**2*LYM1 + DDM*WMW1**2 !
  MWMY1 = DSM*WMW1**2*(LXM1**2+LZM1**2)**.5 ! MOMENTUM WHEEL M.X.
  MWMZ1 = DSM*WMW1**2*LYM1 + DDM*WMW1**2 ! TORQUE IMBALANCES
  MWMX2 = DSM*WMW2**2*LYM2 + DDM*WMW2**2 ! ( N.m )
  MWMY2 = DSM*WMW2**2*(LXM2**2+LZM2**2)**.5 !
  MWMZ2 = DSM*WMW2**2*LYM2 + DDM*WMW2**2 !
  PWMW1' = WMW1 ; PWMW2' = WMW2 ! WHEEL POSITION (radians)
  MWDF = 0.0 ! MOMENTUM WHEEL DISTURBANCE FLAG
  MWTX1 = MWDF*MWMX1*SIN(PWMW1) ; MWTZ1 = MWDF*MWMZ1*COS(PWMW1)
  MWTY1 = MWDF*MWMY1*SIN(PWMW1) ! MOM. WHEEL #1 IMB. TQS.
  MWTX2 = MWDF*MWMX2*SIN(PWMW2) ; MWTZ2 = MWDF*MWMZ2*COS(PWMW2)
  MWTY2 = MWDF*MWMY2*SIN(PWMW2) ! MOM. WHEEL #2 IMB. TQS.
  TWIX = MWTX1 + MWTX2 ; TWIY = MWTY1 + MWTY2 ; TWIZ = MWTZ1 + MWTZ2
##### SOLAR ARRAY STEPPING
  STEPF=0.0 ! SOLAR ARRAY STEP TORQUE FLAG
  TSTY=STEPF*STOR(T)
##### SOUNDER FILTER WHEEL
  SFWF = 0.0 ; SFW' = 62.832 ; SFWM = 6.5E-6 ; TSFWX = SFWF*SFWM*SIN(SFW)
  TSFWY = SFWF*SFWM*SIN(SFW) ; TSFWZ = SFWF*SFWM*COS(SFW)
##### IMAGER TORQUES
  IMAGF = 0.0 ! IMAGER TORQUE FLAG
  TIMX = IMAGF*AINX(T) ! IMAGER NORTH/SOUTH SCAN TORQUE
  TIMY = IMAGF*AIW(T) ! IMAGER EAST/WEST SCAN TORQUE
  TIMZ = 0.0 !IMAGF*0.0 ! ASSUME NO IMAGER TORQUE IN THE Z-AXIS
##### SOUNDER TORQUES
  SOUF = 0.0 ! SOUNDER TORQUE FLAG
  TSRX = SOUF*0.0 ! SOUNDER NORTH/SOUTH STEP & SETTLE TORQUE
  TSRY = SOUF*ASEW(T) ! SOUNDER EAST/WEST STEP & SETTLE TORQUE
  TSRZ = SOUF*0.0 ! ASSUME NO SOUNDER TORQUE IN THE Z-AXIS
##### TOTAL TORQUES INTO S/C
  TKXI = TWIX + TSFWX + TIMX + TSRX ! N.m
  TKYI = TWIY + TSFWY + TIMY + TSRY + TSTY ! N.m

```

```

TKZI = TWIZ + TSFWZ + TIMZ + TSRZ ! N.m
IF(T.LT.21.0)TKX = 0.0 ; ELSE, TKX = TKXI
IF(T.LT.21.0)TKY = 0.0 ; ELSE, TKY = TKYI
IF(T.LT.21.0)TKZ = 0.0 ; ELSE, TKZ = TKZI
##### DYNAMICS
*** DEFINE INERTIA INVERSE MATRIX
PIF = 1.0 ; IXX = 3256.7 ; IYY = 1025.5 ; IZZ = 3200.0 ! kg.m^2
IXY = -23.8*PIF; IXZ = 38.8*PIF; IYZ = -15.86*PIF ! kg.m^2
IAI = (IXX*IYY-IXY**2)*IZZ-IXX*IVZ**2+2.0*IXY*IXZ*IZZ-IXZ**2*IYY
IXXI = (IYY*IZZ-IYZ**2)/IAI ; IXYI = -(IXY*IZZ-IXZ*IZZ)/IAI
IXZI = (IXY*IZZ-IXZ*IYY)/IAI ; IYXI = (IXX*IZZ-IXZ**2)/IAI
IYZI = -(IXX*IZZ-IXY*IXZ)/IAI ; IZZI = (IXX*IYY-IXY**2)/IAI
* S/C BODY MOMENTUM
HSCX = IXX*WRX + IXY*WRY + IXZ*WRZ ! N.m.s
HSCY = IXY*WRX + IYY*WRY + IYZ*WRZ ! N.m.s
HSCZ = IXZ*WRX + IYZ*WRY + IZZ*WRZ ! N.m.s
* S/C WHEEL MOMENTUM
H1W = IW1*(WMW1) ; H2W = IW2*(WMW2) ! N.m.s
HWXA = 0.0 ! WHEEL MOM. VECTOR IN THE Y-Z PLANE ONLY
HWYA = (-H1W-H2W)*COSB ; HWZA = (H1W-H2W)*SINB ! N.m.s
HWTA = (HWXA**2 + HWYA**2 + HWZA**2)**.5 ! N.m.s
* TOTAL S/C MOMENTUM
HTX = HSCX + HWXA ; HTY = HSCY + HWYA ; HTZ = HSCZ + HWZA ! N.m.s
* TOTAL S/C GYROSCOPIC TORQUE
TGYX = WRY*HTZ - WRZ*HTY ; TGYI = WRZ*HTX - WRX*HTZ ! N.m.s
TGYZ = WRX*HTY - WRY*HTX ! N.m.s
* S/C GRAVITY GRADIENT TORQUE
TG1X = IXX*ADY - IXY*ADX - IXZ
TG1Y = IXY*ADY - IYY*ADX - IYZ
TG1Z = IXZ*ADY - IYZ*ADX - IZZ
TGGX = 3.0*W0**2*(-ADX*TG1Z + TG1Y) ! N.m
TGGY = 3.0*W0**2*(-ADY*TG1Z - TG1X) ! N.m
TGGZ = 3.0*W0**2*(ADY*TG1Y + ADX*TG1X) ! N.m
* TOTAL S/C TORQUES
IF(T.LT.20.0) REL = 0.0 ; ELSE, REL = 1.0
TRXX = TKX+TGGX-TGYX; TRYI = TKY+TCYA+TGGY-TCYI ! N.m
TRZZ = TKZ+TGGZ-TGYZ-TCZA ! N.m
* ABSOLUTE S/C ROTATIONAL ACCELERATIONS
WRX' = REL*(IXXI*TRXX + IXYI*TRYI + IXZI*TRZZ) ! rad/sec^2
WRY' = REL*(IXYI*TRXX + IYXI*TRYI + IYZI*TRZZ) ! rad/sec^2
WRZ' = REL*(IXZI*TRXX + IYZI*TRYI + IZZI*TRZZ) ! rad/sec^2
* RELATIVE BODY RATES
ADX' = WRX-W0*ADZ ; ADY' = WRY-W0 ; ADZ' = WRZ+W0*ADX ! rad/sec
THEA = ADY ; PHIEA = ADX ! radians
##### GAUSSIAN RANDUM NUMBER GENERATOR
* INITIALIZE FLAG FOR RANS FUNCTION: EFFECTS THE READING OF TABLE LOOKUP
GF = 0.0
* SEED VALUES FOR CALLS TO RANDUM NO. GENERATOR
IGS1 = 1123.0 ; IGS3 = IGS1 + 10.0 ; JGS3 = IGS3 + 1.0
* CALL RANS FOR RAND. NO. GAUSSIAN DISTRIBUTION
GRN3 = FTT(RANS(IGS3,JGS3,T,GF)) ; GSCAL = GRN3/2.85023
##### EARTH SENSOR
RF = 0.0 ; PF = 0.0 ! E.M. NOISE DATA READ IN FLAGS
ESSR = 0.0 ; ESSP = 0.0 ! E.M. NOISE DATA SWITCH/SCALERS
PHIE = PHIEA + REM(T,RF)*ESSR*1.0E-6 ! radians
THE = THEA + PEM(T,PF)*ESSP*1.0E-6 ! radians
##### CONTROLLERS ! GAIN PARAMETERS ARE FROM AOCs ANALYSIS CDR
* PITCH CONTROLLER *
WOBS = .005 ; KTH = (1.414*WOBS)+(1/2500) ; KTY = 1.0
CTH = 3967.2 ; CW = 2805.2 ; CTY = .3937*WCBS*WOBS

```

```

KW=(WOBS+.0005656)*WOBS
* OPTIMAL ESTIMATOR AND CONTROLLER
IF(T.LT.20.0) PBIAS = 0.0 ; ELSE,PBIAS = W0*(T-20.0)*PBF;PBF=0.0
TH1=-THE+PBIAS-TH4; TH2=KTH*TH1 ; TH3 = TH2 + TH8 ; TH4' = TH3
TH5 = -CTH*TH4 ; TH6 = KW*TH1 ; TH7 = TH6 + TH15 ; TH8' = TH7
TH9 = -CW*TH8 ; TH10 = TH5 + TH9 ; TH12 = CTY*TH1
TH13' = TH12 ; TH15 = TH10/IYY
TH14 = TH10 - TH13 ; VY = TH14*ZZZ; ZZZ=1.0
* WHEEL CONTROL COMPENSATION
KT = .02705 ; CD = 4.05E-05 ; UYE = ((KT+CD)/IW)*VY ; ER' = UYE
IF(T.LT.20.0) HYC = 0.0 ; ELSE, HYC = -1.0*(ER + VY)#1 ! N.m
* ROLL / YAW CONTROLLER *
* TERASAKI CONTROLLER
KPH = .1938 ; TM = 40.0 ; TZ = 150.1 ; TW = 4.0
PH1 = PHIE - PH3 ; PH2 = PH1/TM ; PH3' = PH2
PH4 = PH3 ; PH5 = KPH*TZ*PH4 ; PH6' = PH4
PH7 = KPH'PH6 ; HZC = ((PH5 - PH7)/TW)#1 ! N.m
##### MOMENTUM COMMAND DISTRIBUTION MATRIX (V MODE)
BETA = 1.6 ; COSB = COSD(BETA) ; SINB = SIND(BETA)
H1C = .5*( HYC/COSB + HZC/SINB ) ! N.m
H2C = .5*( HYC/COSB - HZC/SINB ) ! N.m
##### MOMENTUM WHEELS
* MOMENTUM WHEEL #1 FEEDBACK LOOP
WT1(0)=571.055 ; WMWA(0)=571.055
H1F(0)=-2.3142E-02
W1BI = 571.913725 ; KS1 = 1.0 ; CD1 = 4.05E-05 ; IW1 = .1082
T1A = H1C - H1F ; T1B = T1A*KS1 ; WMF = 0.0 ; W1QT = 1.74E-4 ! N.m
IF(WMF.EQ.0.0) T1C=T1B ; ELSE, T1C = AINT(T1B/W1QT)*W1QT
WMW1(0)=571.054 ; T1C(0) = 2.3142E-02 ; TC1(0) = 0.0
TC1 = T1C/KS1 - WMW1*CD1 ; WMW1' = TC1/IW1
* TACH. NOISE
WMWA = WMW1 + GSCAL*.01024*TM ; TFL = 0.0
* TACH QUANTIZATION & SAMPLE RATE
* wt1=wmwa
W1QNT = 1.707E-3 ; WQ1 = AINT(WMWA/W1QNT)*W1QNT ; WT1 = WQ1#2
H1F = KT*(WT1 - W1BI)
* MOMENTUM WHEEL #2 FEEDBACK LOOP
WT2(0)=571.055 ; WMWB(0)=571.055
H2F(0)=-2.3142E-02
W2BI = 571.913725 ; KS2 = 1.0 ; CD2 = 4.05E-05 ; IW2 = .1082
T2A = H2C - H2F ; T2B = T2A*KS2 ; W2QT = 1.74E-4 ! N.m
IF(WMF.EQ.0.0) T2C = T2B ; ELSE, T2C = AINT(T2B/W2QT)*W2QT
WMW2(0)=571.054 ; T2C(0) = 2.3142E-02 ; TC2(0) = 0.0
TC2 = T2C/KS2 - WMW2*CD2 ; WMW2' = TC2/IW2
* TACH. NOISE
WMWB = WMW2 + GSCAL*.01024*TFL
* TACH QUANTIZATION & SAMPLE RATE
* wt2=wmwb
W2QNT = 1.707E-3 ; WQ2 = AINT(WMWB/W2QNT)*W2QNT ; WT2 = WQ2#2
H2F = KT*(WT2 - W2BI)
* TOTAL WHEEL MOMENTUM & TORQUE VECTORS
TCXA = (TC1 - TC2)*SINB ; TCYA = (TC1 + TC2)*COSB ! N.m
TCZA = (TC1 - TC2)*SINB ! N.m
##### OUTPUT
ADXM = ADX*1.0E+06 ; ADYM = ADY*1.0E+06 ; ADZM = ADZ*1.0E+06
WRITE (T,TKXI,TKYI,TKZI,TRXX,TRYX,TRZZ,VY,HYC,H1W)
WRITE (HZC,H1C,H2C,WMWA,WMWB,TC1,TC2,T1A,T1B,T1C)
WRITE (T2A,T2B,T2C,TCXA,TCYA,TCZA,HWA,HWA,HWA,HWA)
WRITE (HXA,HYA,HZA,HTOT,ADXM,ADYM,ADZM,TGYX,TGYX,TGYZ)
WRITE (HTX,HTY,HTZ,HSCX,HSCY,HSCZ,ADX',ADY',ADZ',H2W)

```


ADDENDUM A.2.2-4: VARIANCE ANALYSIS OF REALISTIC TACHOMETER NOISE

(DATA PROVIDED BY CONVERSATIONS WITH LAS (T. HENTHORN) AND TELDIX (W. AUER))

TACH SAMPLE RATE @ 5485 rpm: $W_s(t) = 3.04 \text{ Hz}$
TACH NOISE (approximately 1/3 spec) $N(t) = .0329 \text{ rpm} = .0034488 \text{ rad/s}$

VARIANCE OF REALISTIC TACH NOISE

$N(t) = .0034488 \text{ rad/s}$
 $SD(t) = N(t)/3 = .0011496 \text{ rad/s}$
 $VAR(t) = SD(t)^2 = .000001321 \text{ rad}^2/\text{s}^2$
 $PSM(t) = VAR(t)/W_s(t) = .000001321/3.04 = .000000434 \text{ rad}^2/(\text{s}^2 \cdot \text{Hz})$

Use this power spectral magnitude to find the variance of the output, as was performed in Addendum A.2.2-2 (Figure A.2.2-18).

$VAR(y) = \text{area under curve} = 6.64\text{E-}13 \text{ radians}^2$
 $SD(y) = \text{SQRT}(VAR(y)) = 8.0\text{E-}7 \text{ radians}$
 $\text{Jitter} = 3 \cdot SD(y) = 2.4\text{E-}6 \text{ radians}$

ADDENDUM A.2.2-5: RATIO OF NOISE IMPROVEMENT FROM INCREASED SAMPLE

Assume the same GOES pitch transfer function and control system except that the number of revolutions counted by the tachometer buffer is multiplied by a factor of K. Since the sample period is longer, the 6 microsecond (spec value) tach uncertainty noise results in a standard deviation that is a factor of K smaller than the nominal GOES-I configuration.

T_b = time to fill tachometer buffer

W_n = nominal wheel speed

N = tachometer uncertainty

W_{worst} = worst case noise wheel speed

K = ratio new revolutions counted vs. nominal revolutions counted

R = revolutions counted (nominal)

SD = standard deviation of noise (Add. A.2.2-1 uses 3σ numbers throughout, so 3σ numbers are calculated)

$$W_n = \frac{R}{T_b} \quad W_{sk} = \frac{KR}{KT_b} \quad W_{unc} = \frac{R}{T_b + N} \quad W_{worst} = \frac{KR}{KT_b + N}$$

$$SD = W_n - W_{worst}$$

$$SD_1 = \frac{R}{T_b} - \frac{R}{T_b + N} = \frac{RN}{T_b^2} \quad SD_2 = \frac{KR}{KT_b} - \frac{KR}{KT_b + N} = \frac{RN}{KT_b^2}$$

It is easy to see that the standard deviation will be reduced by approximately a factor of K. This reduction will also increase the sample period by a factor of K and reduce the sample frequency by the same factor of K.

By variance analysis, one sees that $VAR(n) = SD(n)^2$, so the variance of the noise will be reduced by a factor of K squared. This will result in a change of power spectral magnitude cascaded into the co-variance transfer function.

$$VAR(n) = PSM(n) * Ws(n)$$

$$PSM(y) = PSM(n) * COVAR(n,y)$$

Since the variance decreases by K^2 and the sample frequency decreases by a factor of K, the power spectral magnitude will be a factor of K smaller. This will result in the output area being a factor of K smaller. This area represents the variance of spacecraft jitter. By taking the square root, one finds the standard deviation to be a factor of square root of K smaller than the nominal case.

A.3.1 SENSOR CONFIGURATIONS STUDIED

A.3.1.1 Alternative configurations

A.3.1.1.1 Inertial reference units

The sensor configurations studied for Options II and III include an accurate inertial reference unit (IRU), or gyro package, which provides complete rotational rate information on the three spacecraft axes. This information is available for spacecraft attitude control in the normal mission mode and for rapid recovery from the attitude disturbances caused by stationkeeping maneuvers (typically in 5 - 10 minutes rather than the 5 - 10 hours required for the Option I configuration). The IRU outputs are also employed for real-time commanding of the instrument mirror gimbal drives to compensate for spacecraft attitude disturbances; this is called spacecraft motion compensation (SMC).

The baselined IRU is the Teledyne DRIRU-II gyro package, which is a fully redundant package including three dry-tuned two-axis gyros and associated electronics. There is extensive flight experience with this unit, including Solar Maximum Mission (SMM), Landsats 4 and 5, ETS-1, and at least two Department of Defence (DOD) missions. Only one in-flight failure has been experienced, an electronic (not mechanical) failure of one of the six output channels on SMM. The DRIRU-II has excellent drift and noise characteristics, as discussed in Section A.3.1.2 below.

Alternative advanced-development IRUs involve higher risk but potential payoff in lower power, weight, increased accuracy, or greater lifetime. Principal among these is the Fiber Optic Rotation Sensor (FORS) being developed by the Jet Propulsion Laboratory (JPL) and the Charles Stark Draper Laboratory (CSDL) for the Comet Rendezvous Asteroid Flyby (CRAF) mission. This sensor is designed to have performance comparable to the DRIRU-II, but with reduced weight and power requirements and increased lifetime. Another alternative is the ring laser gyro (RLG), models of which are provided by various vendors for use in aircraft. Space experience with this sensor is not extensive, however, and it has the additional risk of requiring high voltage. A third option is the Hemispheric Resonator Gyroscope (HRG), currently under development by the Delco Electronics subsidiary of GM Hughes Electronics. This sensor shows promising performance, but there is no flight experience whatsoever, so the risk factor is high.

If the IRUs were perfect, no further sensing would be necessary, but additional attitude sensors are required to compensate for the inevitable gyro drifts. The information from these sensors can be optimally combined with the IRU data using an extended Kalman filter (EKF) [1,2]. This technology is quite mature, and has been used or is planned on several NASA missions including Landsats 4 and 5, Gamma Ray Observatory (GRO), Upper Atmosphere Research Satellite (UARS), and Explorer Platform (EJVE).

A.3.1.1.2 Star trackers

In the applications referred to above, the additional sensors are fixed-head star trackers (FHSTs), and the first choice for the GOES-N Options II and III ACS includes three FHSTs. Two star trackers are needed for accurate attitude determination, since a single star tracker provides very

poor information about attitude rotations about its boresight. The principal reason for including the third tracker is redundancy, but performance is improved if all three star trackers are employed simultaneously. The trackers must be oriented so that their fields of view (FOVs) are shielded from interference by the Sun, Moon, and Earth. The Sun, being the brightest of these objects, constitutes the most significant problem. A reasonable requirement for a sunshield is to allow FHST operation except when the Sun is within 30 deg of the FHST boresight; this requirement can be satisfied by a sunshade 50cm to 80cm in length, depending on the size of the objective of the FHST optics. Since the Sun is never farther than 23.44 deg from the Earth's equatorial plane, orienting the FHST boresights at 35 deg from the North or South pole will avoid Sun interference completely. Earth and Moon interference are also avoided by this configuration. The baselined GOES-N configuration has the tracker boresights equally spaced in azimuth at an angle of 35 deg from the spacecraft -y (negative pitch) axis, as shown in Figure A.3.1-1. The North face is chosen to avoid interference by reflections from the solar array; deletion of the solar sail from the South face is quite desirable to avoid interference with the FHST.

Candidate star trackers are the Ball Aerospace CT-601 [3], the Hughes Danbury Optical Systems (HDOS) ASTRA-II [4], and the JPL ASTROS. The characteristics of these three trackers are summarized in Table A.3.1-1. The CT-601 and ASTRA-II have been designed as replacements for the NASA Standard Star Tracker, which uses an image dissector tube rather than a solid state focal plane detector; they have similar fields-of-view and sensitivities. The ASTROS tracker, on the other hand, was designed for a shuttle attached payload (Astro) requiring an extremely small noise-equivalent angle (NEA) and very accurate small-scale linearity. The resulting requirements for thermal stability, along with the shuttle environment, lead to the large weight and power figures for the ASTROS tracker. These could be reduced in a redesign for a free-flying mission, but either the CT-601 or the ASTRA-II seems a better choice for GOES-N. This is especially true in view of the large 19 μ r global calibration errors allowed in the ASTROS tracker. In fact, the limiting parameter for star tracker performance is not noise, but calibration errors. Discussions with both Ball and HDOS personnel indicated that calibration to better than 1 arcsec (4.848 μ r) is beyond current capabilities, owing to atmospheric effects in ground testing, limitations of collimated light sources, etc.

There is a tradeoff between brightness sensitivity of a tracker and its FOV, if the requirement is to have a minimum probability of seeing some desired number of stars in the FOV. This is discussed in [4] and in more detail in [3]. There are approximately ten times as many stars of magnitude 8.2 or brighter than there are of magnitude 6.0 or brighter. Thus a star tracker with 2.5 deg square FOV and sensitivity to magnitude 8.2 will see approximately the same number of stars as a star tracker with 8 deg square FOV and sensitivity to magnitude 6.0. There is also a tradeoff between FOV and NEA, since the NEA is determined by the ability to interpolate a star position to a certain fraction of a pixel of the CCD array. Thus changing the optics while retaining the same focal plane detector gives an NEA that is linearly proportional to the FOV. It might be desirable for GOES-N to redesign the optics of the CT-601 or the ASTRA-II to give a 4 deg square FOV while reducing the NEA to 4 μ r. Reducing the NEA further is not beneficial, however, since the calibration error of about 5 μ r cannot be reduced by this method. The average number of stars, n_{ave} , and the probability $P(n)$ of having n stars in the FOV are given for two cases in Table A.3.1-2. The probabilities follow a Poisson distribution

$$P(n) = \exp(-n_{ave}) (n_{ave})^n / n!$$

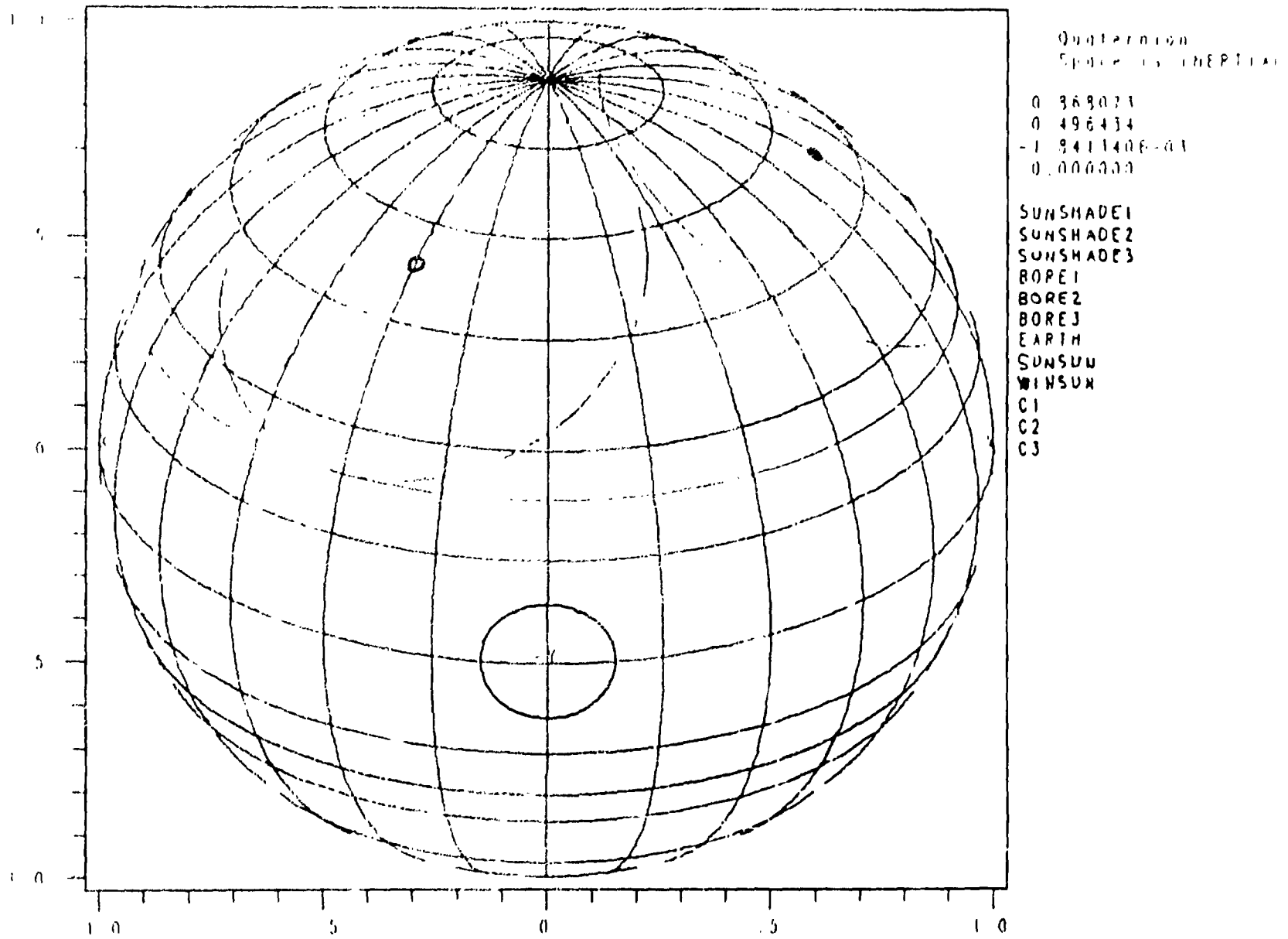


Figure A.3.1-1 Star Tracker Boresight Spacing

Device	CT-601	ASTRA-II	ASTROS
Manufacturer	Ball Aerospace	Hughes Danbury	JPL
CCD Chip	TEK 512 × 512	RCA 504	RCA 501
FOV	8° × 8°	8° × 8°	2.2° × 2.5°
limiting magnitude	6	6	8.2
# of stars tracked	5	5	3
NEA	8 μrad	8 μrad	1.5 μrad
power	5 -10 watts	15 watts	170 watts
weight	8.8 kg	7 - 9 kg	41 kg
proposed use	MMS Shuttle	TOPEX Space Station	ASTRO-1 (STS-35)

Table A.3.1-1. Candidate CCD Star Trackers

n_{ave} is the average number of stars in a FOV. $P(n)$, the probability of having n stars in a FOV, follows a Poisson distribution. The requirement is to have at least one star in at least two of the three FOVs.

FOV	4' × 4'		8' × 8'	
	galactic pole	galactic equator	galactic pole	galactic equator
n_{ave}	1	4	4	16
P(0)	0.37	0.02	0.02	10^{-7}
P(1)	0.37	0.07	0.07	10^{-6}
P(2)	0.18	0.15	0.15	10^{-5}
P(3)	0.06	0.20	0.20	0.0001
P(4)	0.015	0.20	0.20	0.0003
P(> 4)	0.004	0.37	0.37	0.9996

The performance of a star tracker with 2.5' × 2.5' FOV and sensitivity to star magnitudes to 8.2 is the same as with an 8' × 8' FOV and magnitudes to 6.

Table A.3.1-2. Availability of 6th Magnitude Stars

There are approximately four times as many stars per unit solid angle near the galactic equator than there are near the galactic poles, which are at declination 27.4 deg, right ascension 192.25 deg and declination -27.4 deg, right ascension 12.25 deg in Earth-centered inertial coordinates. It is important to note that at most one of the three tracker FOVs, in the configuration of Figure A.3.1-1, can be located closer than 30 deg from a galactic pole at any time. Table A.3.1-2 shows that two of three CT-601 or ASTRA-II trackers in this configuration will almost certainly have five or more stars in their FOVs, while the third will very probably have three or more. Reducing the FOVs to 4 deg square reduces these numbers to three or more in two trackers and zero or one in the third, if it is near a galactic pole.

An advantage of having the three FHST boresights at equal angles to the pitch axis is that the tracker fields of view will sweep out the same band in the celestial sphere as the spacecraft rotates during its 24 hour orbit, so that the three trackers can share a common star catalog. The size of the catalog depends on both the minimum magnitude of stars included and on the size of the FHST FOV. An estimate of the size of the on-board star catalog required is given by

$$n_{on} = n_{ave} \times (360 \text{ deg}) \times \sin(35 \text{ deg}) / d$$

where n_{ave} is the average number of stars in a tracker field of view over the 12 hour orbit period and d is the length of a side of the tracker FOV in degrees. Reference [3] indicates that the average density over the celestial sphere is about 3/4 of the density at the galactic equator. Using this estimate gives a catalog size of 155 stars for a 4 deg square FOV with sensitivity to magnitude 6.0, 620 stars for an 8 deg square FOV with sensitivity to magnitude 6.0, and 1000 stars for a 2.5 deg square FOV with sensitivity to magnitude 8.2. If a 180 degree yaw maneuver is performed semiannually as in Option II, then two catalogs of this size are required, one for each yaw attitude. They can either be simultaneously resident in the on-board computer memory, or else the catalog can be reloaded at the time of the yaw maneuver. The above estimates must be verified by detailed simulations using real star catalogs, but the results should differ only in detail. The assessment of the location errors of stars in actual catalogs will also be necessary. For this study, it suffices to note that there is a catalog of International Reference Stars, uniformly distributed at one star per square degree over the celestial sphere, with location errors of 1.5 μ rad or less. These reference stars have magnitudes between 7.5 and 10.5, and it is generally true that the locations of brighter stars are better known than those of dimmer stars.

A.3.1.1.3 Earth beacon trackers

A gyro-star tracker attitude system provides an attitude referenced to inertial space, i.e., to the fixed stars. Thus an in-track or cross-track error in spacecraft location results in a 1:1 error in the registration of a pixel in an instrument FOV relative to a fixed grid on the Earth. It would be preferable to have an Earth-referenced attitude keeping the spacecraft z axis nadir-pointing. In this case, the registration error resulting from an in-track or cross-track ephemeris error would be reduced by the ratio of the Earth's equatorial radius to the spacecraft orbit radius, 6378/42164 = 0.15. In an effort to achieve this 85 percent reduction in the effect of ephemeris errors both optical beacons and radio-frequency (RF) beacons were investigated. Infrared Earth Sensors were not considered for Options II and III because their sensitivity to cold clouds and radiance gradients does not allow the attitude accuracy required for GOES-N.

Either visible or infrared optical beacons can be detected by a focal-plane array similar to a CCD star tracker or by a quadrant detector. In order to improve the signal-to-noise ratio, to allow detection against the Earth background, it is advisable to chop the laser signal. This, unfortunately, is inconsistent with the use of CCD arrays as integrating devices. The most promising sources are infrared lasers, either CO₂ with a 10.6 micron wavelength or Neodymium Yttrium Garnet (YAG) with a 1 micron wavelength. At least two beacons are needed for attitude determination, and at least three must be provided at separated locations to allow for cloud cover. For redundancy, four trackers should be provided on the spacecraft, three locked to the locations of the beacons and one spare. All the trackers should be steerable to allow for changing the spacecraft longitude, but the trackers should be locked in use since the accuracy of gimbal angle encoders is inconsistent with the attitude accuracy required for GOES-N. After the gimbals are locked, the trackers can be aligned to the imager by using landmarks found by the imager as in the GOES-I OATS. Other than the mechanical complication of the sensors, a disadvantage of optical beacons is the possibility of interference with overflying aircraft.

RF beacons would be detected by interferometry from several antennas on the spacecraft. This configuration has the advantage of also providing enhanced search-and-rescue (SAR) capability and also providing ephemeris information. Locating four antennas at the corners of the Earth-pointing face of GOES-N provides some redundancy, since only three antennas are needed to provide the necessary attitude reference. With this configuration, roll and pitch are obtained from antenna pairs with baselines of approximately 3 m. In order to provide 10 μ m attitude accuracy, the $\pm z$ motion of these antennas must be known to approximately $10^{-5} \times 3 \text{ m} = 30 \text{ microns}$. Controlling or predicting the thermal distortions of the Earth-pointing face of the spacecraft to this level appears to be an insurmountable problem, which would preclude the use of RF beacons.

A further disadvantage of both optical and RF beacons is that they require tended Earth sites at widely dispersed locations. This has negative implications for both cost and risk.

A.3.1.1.4 Polaris tracker with Earth beacon tracker

This option uses one Earth reference and one star reference, so it is a combination of the two previous cases. The Earth reference is used for pitch and roll, which means that the 85 percent reduction in the effect of ephemeris errors is achieved for these angles. Polaris is used mainly as a yaw reference, although it also contains roll information corrupted by ephemeris errors. The advantage of this configuration over the all-beacon configuration is that only one Earth reference is needed, rather than two. The -y axis of GOES-N always points to the North celestial pole, within the allowed attitude errors, and Polaris is within one degree of this pole, so a star catalog of a single star suffices. This is a significant simplification over the all-star reference case. Since only one star is used, some of the FHST calibration errors can be removed, corrections due to star color, for example.

To allow for cloud cover, at least two Earth references must be provided. For redundancy, three Earth beacon trackers and two Polaris sensors are required. Thus this configuration requires more sensors than either the all-star or all-beacon configuration. In addition, the 180 degree yaw maneuver of Option II cannot easily be accommodated, since there is no counterpart to Polaris near the South celestial pole.

A.3.1.1.5 Landmarks

In principle, landmarks could be substituted for beacons as Earth references. Either two landmarks or one landmark and Polaris would provide the needed attitude references. The potential advantage of this is that the landmarks could be sensed at the imager focal plane, therefore avoiding sensor co-alignment errors. Also, landmarks, being passive, avoid many of the operational problems of optical or RF beacons. Early studies using an analytical method of Farrenkopf [5] indicated that attitude references are needed very frequently, at about one every two seconds. There are no known methods of acquiring and processing landmarks at this rate, so this option was not pursued further. If gyros were available with drift performance orders of magnitude better than DRIRU-II, the landmark option would be viable. Relying on the development of such gyros entails higher risk than allowed for GOES-N, though.

A.3.1.2 Attitude determination (navigation) performance

In order to accurately estimate the spacecraft attitude, the sensor data from the IRU and star trackers described above must be processed in an on-board computer (with a math co-processor) using a Kalman filter attitude estimation algorithm as discussed in this section.

The gyro noise model is:

$$\begin{aligned}d(\theta)/dt &= \omega + n_r + b(t) \\d(b)/dt &= n_b\end{aligned}$$

where θ is the gyro output angle, ω is the true angular rate about the gyro input axis, b is the gyro drift rate, and n_r and n_b are gaussian-distributed white noise sources with zero means and standard deviations σ_r and σ_b , respectively. The process n_r models the instantaneous white rate noise, while n_b accounts for the long-term drift rate variation as an integrated white noise process. This widely-accepted gyro noise model [1,2,5,6] is illustrated in Figure A.3.1-2. The Teledyne DRIRU-II has a drift rate stability of 0.0145 $\mu\text{r}/\text{sec}/6$ hours, rate white noise (σ_r) of 0.206 $\mu\text{r}/\text{sec}^{1/2}$, and rate random walk (σ_b) of 2.15×10^{-4} $\mu\text{r}/\text{sec}^{3/2}$. These values were derived by TRW for the AXAF fine pointing study in 1988, based on 50 hours of gyro rate data collected at the Holloman AFB. They represent extremely low-noise gyros, probably the best of the SDG-5 gyros, used in DRIRU-II, that Teledyne can manufacture. The star sensor noise n_T is modeled as white, gaussian, and zero-mean with standard deviation σ_T .

The inertial attitude is estimated as follows. The vehicle three-axis attitude is maintained in the flight computer as a quaternion q . The output gyro rate data is sampled every T_g seconds (where T_g is typically equal to 0.1 sec, the value assumed here for GOES-N), processed to remove the estimated drift rate bias, and used to propagate the quaternion q . At an update period T , which is some multiple of T_g , the star tracker measurements are used in an Extended Kalman Filter (EKF) to optimally compute a six-component state vector comprising the errors in the three estimated gyro drift rate biases and three attitude error angles. The Kalman filter outputs are then used to update the inertial attitude quaternion q and the three gyro biases, as illustrated in Figure A.3.1-3 and discussed in detail in references [1] and [2].

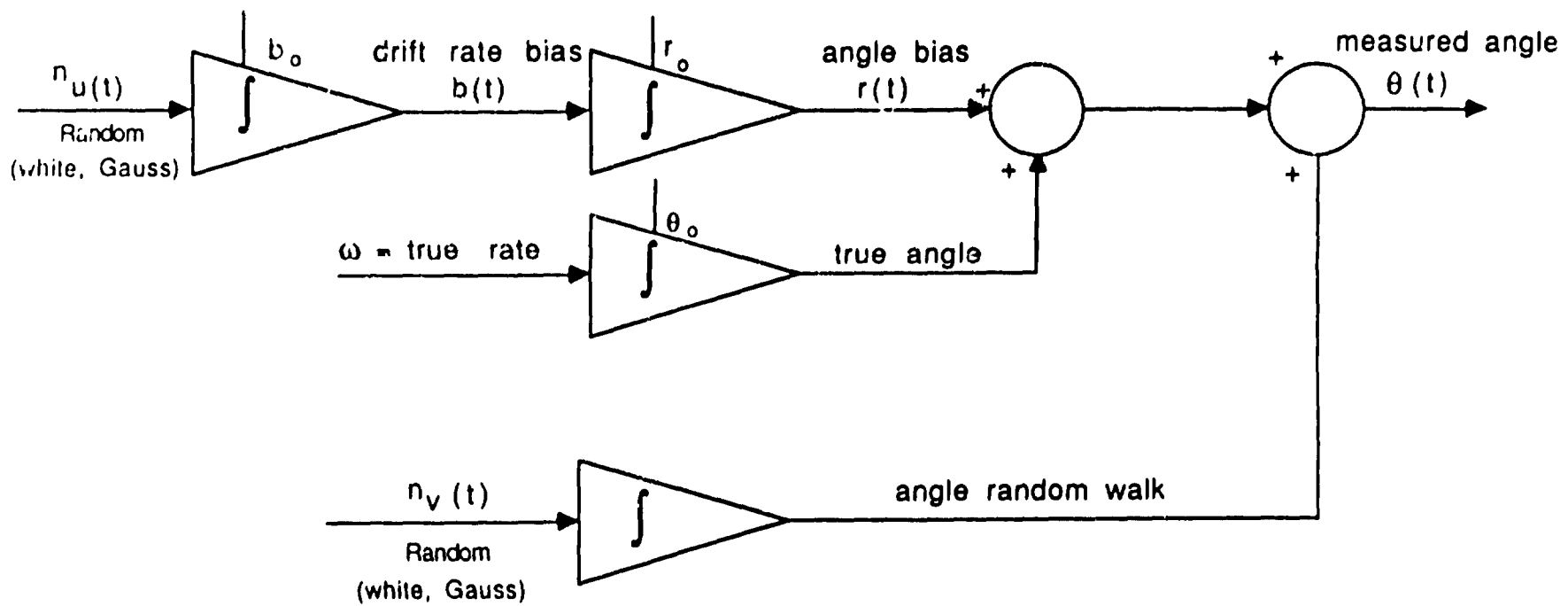
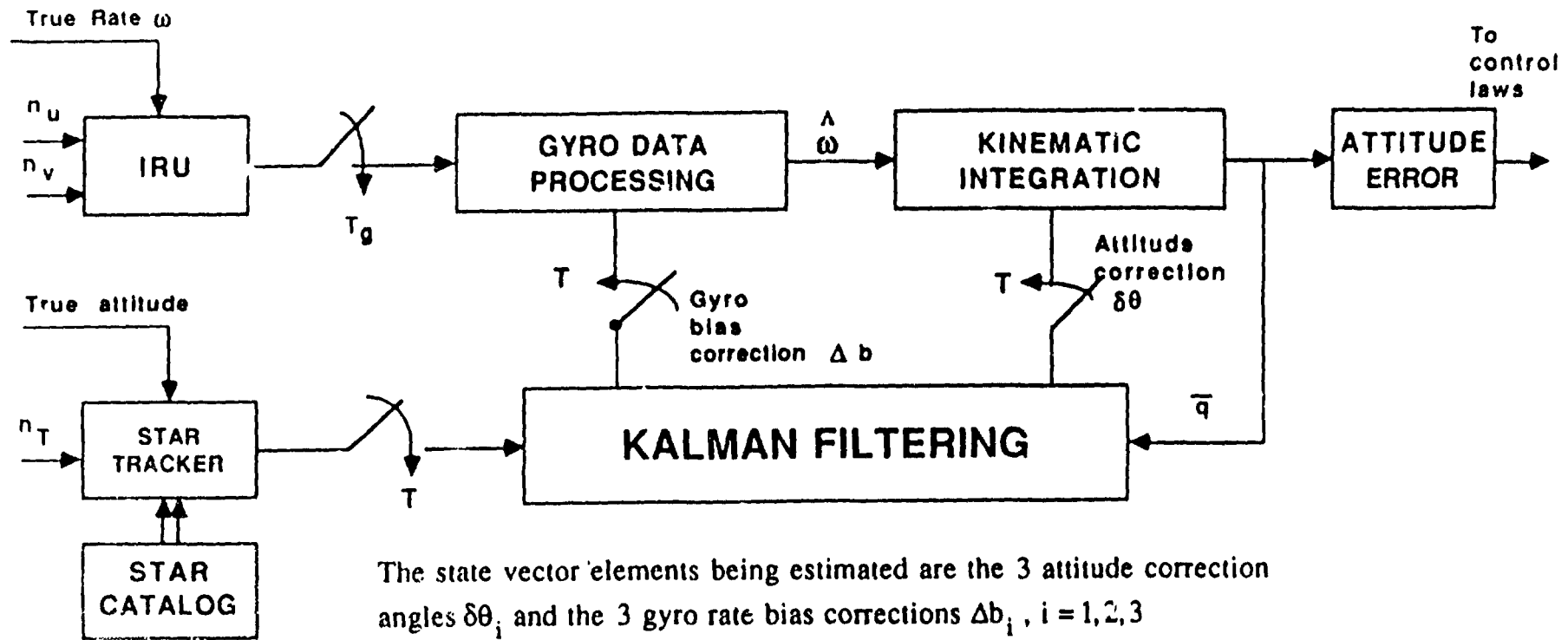


Figure A.3.1-2. Gyro Mode' including Two Noise Sources



The state vector elements being estimated are the 3 attitude correction angles $\delta\theta_i$ and the 3 gyro rate bias corrections Δb_i , $i = 1, 2, 3$

where $\delta\theta_i = 2\delta q_i$ $\delta q_i =$ i th component of δq

$\delta q = \hat{q}^{-1} \bar{q}$, $\bar{q} =$ true attitude quaternion, $\hat{q} =$ estimated \bar{q}

$\omega =$ true rate, $\hat{\omega} =$ estimated rate

$b(t) =$ random walk drift rate $= b_0 + \int n_u(t)$

$b = \hat{b} + \Delta b$ $\hat{b} =$ kalman-filter-estimated drift rate

Figure A.3.1-3. Attitude Estimation ($T > T_g$)

The predicted performance of the attitude estimation can be found by iterating the EKF equations to steady-state, when the pre-update and post-update co-variances stop changing. This must generally be done numerically, but Farrenkopf [5] obtained analytic solutions for the case when the three attitude error angles can be assumed to be uncoupled so that the estimation process reduces to three single-axis problems. His results for the pre-update and post-update attitude error standard deviations, denoted by $\sigma_\theta(-)$ and $\sigma_\theta(+)$, respectively, are:

$$\begin{aligned}\sigma_\theta(-) &= \sigma_\theta \left(\frac{x}{S_\theta} \right)^2 - 1)^{1/2} \\ \sigma_\theta(+) &= \sigma_\theta \left(1 - \left(\frac{S_\theta}{x} \right)^2 \right)^{1/2}\end{aligned}$$

where:

$$\begin{aligned}x &= -(1/2)\{(S_\theta^2/2 + \beta) + [(S_\theta^2/2 + \beta)^2 - 4S_\theta^2]^{1/2}\}, \\ \beta &= [S_\theta^2(4 + S_\theta^2) + S_\theta^4/12]^{1/2}, \\ S_\theta &= \sigma_\theta T^{3/2} / \sigma_\omega \\ S_\omega &= \sigma_\omega T^{1/2} / \sigma_\theta\end{aligned}$$

In the limiting case of very frequent updates, the pre-update and post-update attitude error standard deviations approach the common limit (the continuous-update limit):

$$\sigma_c = T^{1/4} \sigma_\theta^{1/2} (\sigma_\omega^2 + 2 \sigma_\theta \sigma_\omega T^{1/2})^{1/4}$$

Assuming the IRU standard deviations σ_θ and σ_ω given above for the DRIRU-II, and using the ASTROS NEA value of $1.5 \mu\text{r}$ (the best possible value) for σ_ω , gives the following standard deviations as a function of update time T:

UPDATE TIME (SEC)	$\sigma_\theta(-)$ (μRAD)	$\sigma_\theta(+)$ (μRAD)	σ_c (μRAD)
1.0	0.57	0.52	0.55
2.0	0.69	0.62	0.65
10.0	1.12	0.88	0.98
100.0	2.67	1.28	1.79

Setting σ_θ to $4.8 \mu\text{r}$, corresponding to the estimated best calibration accuracy of 1 arcsec (which, however, is not really a source of gaussian noise) gives:

UPDATE TIME (SEC)	$\sigma_\theta(-)$ (μRAD)	$\sigma_\theta(+)$ (μRAD)	σ_c (μRAD)
1.0	1.03	1.02	1.01
2.0	1.25	1.21	1.21
10.0	1.97	1.83	1.84
100.0	4.29	3.21	3.49

In all but the 100 second update cases, the continuous-update limit gives a reasonably accurate, and relatively simple, estimate of the attitude estimation errors. The even simpler limiting form:

$$\sigma_e = T^{1/4} \sigma_a^{1/2} \sigma_v^{1/2}$$

is valid when the contribution of σ_a to the attitude estimation errors is negligible; it shows a 1/2 power dependence on both σ_a and σ_v and a 1/4 power law dependence on the update time T. This shows why it is extremely difficult to improve the attitude determination performance by increasing the update frequency.

These analytic results are strictly true only if all the star observations are at the same point in the star tracker FOV, and the resulting error estimates are for rotation errors about the two axes perpendicular to the line-of-sight (LOS) to the star; the errors for rotations about the LOS are infinite. The results are quite accurate for a single small-FOV star tracker, with effectively infinite attitude uncertainties for rotations about the tracker boresight. The results for several trackers can be obtained by adding the information (inverse variance) obtained by the different trackers, but this will not be pursued further, since the full-up simulation described in Section A.3.6 gives these results. The purpose of the analysis of this section is to provide order-of-magnitude estimates that establish the validity of the gyro/star tracker system and justify its further study.

A.3.1.3 Orbit ephemeris performance implications for inertial reference sensing systems

Accurate orbit determination is required for the image navigation of all GOES-N configurations; however, it is particularly important for the Options II and III because their attitudes are derived from inertial sensors (star trackers and gyroscopes) rather than an earth referenced attitude sensor (Earth Sensor). In fact it is quite impossible to properly control the attitude of the Options II and III spacecraft without knowledge of the orbital ephemeris.

Several orbit determination methods were considered for the GOES-N Options II and III. Consideration was given to accuracy, recovery time after thruster firings, operational complexity, and technical risk. Frequent thruster activity is anticipated for the purpose of momentum management in the referred deleted solar sail configurations (Section A.3.2). While initial assessments show that the firing of coupled thruster pairs for the purpose of momentum dumping will not cause orbit errors to exceed allocations, it is prudent to utilize an orbit determination system which has a quick transient recovery time. Transient recovery is especially important after stationkeeping maneuvers. There is an advantage to tightly controlling the inclination if an extended focal plane is employed in the imager instrument (Section TBD). Tight inclination control may imply daily stationkeeping which can be combined with momentum management function. Quick transient recovery along with the need for high accuracy is the justification for our recommendation that a multi-station ranging system be employed for orbit determination.

A.3.1.3.1 Importance of orbit determination

A goal of the GOES-N control system is to point the yaw axis directly at the nadir. An Earth Sensor system will always do this (subject to jitter and drifts due cloud and radiance gradient effects) regardless of the orbit. In an Earth Sensor system an effect of the orbit on image

navigation is that the true nadir deviates from the nominal nadir of a fixed grid. IMC is intended to correct for this, and does to the extent that the orbit is known. It is easy to show that the nadir pointing error is related to orbit position error by:

$$\text{Nadir pointing Error} = \frac{\text{Earth radius}}{\text{Satellite Altitude}} \times \frac{\text{Orbit position error}}{\text{Orbit radius}}$$

Off-nadir for an equatorial orbit, the pointing error diminishes (in fact it vanishes at the horizon to linear order in the orbit error). When there is an inclination error there will also be an orbit yaw effect which is vanishing at nadir and grows towards the horizon. The maximum orbit yaw pointing error is approximated by:

$$\text{Maximum orbit Yaw error} = \frac{\text{Earth radius}}{\text{Orbit radius}} \times \text{Inclination error}$$

In all cases, the orbit error expressed in dimensionless terms (orbit position error normalized to the orbit radius or the inclination error in radians) is attenuated by the ratio of the earth radius to either the satellite altitude or the satellite orbit radius. These ratios are on the order of 1/6 for geostationary satellites. For the inertially controlled GOES-N Options II and III, the attitude control system must have a time varying target inertial attitude which properly orients the yaw axis towards nadir. This target attitude is a function of orbital position. If there is an error in the orbital position, in the along-track direction for example, there will be a corresponding error in the nadir location which is equivalent to a pitch error of:

$$\text{Equivalent pitch Error} = \frac{\text{Orbit position error}}{\text{Orbit radius}}$$

Here, there is no attenuation factor of 1/6, and we conclude that for the inertially controlled Options II and III, orbit determination must be about 6 times better than for Option I if the same level of performance is required. An allocation of 10 μ r has been made for Options II and III (Appendix C) which according to the above formula corresponds to an ephemeris error of about 400 m (3- σ) for the Option II and III orbit determination.

A.3.1.3.2 Orbit errors due to thruster activity

When radiative coolers are used in the instruments, the preferred configurations for the GOES-N Options II and III satellites have no solar sails. This results in a solar torque imbalance which causes a secular build-up of roll-yaw momentum. To dump this momentum magnetically has been deemed undesirable and momentum management using thrusters has been selected. These considerations are reviewed in Section A.3.2 and an assessment is made of the worst case ΔV caused by the thrust mismatch and thrust vector misalignment of a coupled thruster pair. It was assumed that the worst case thrust mismatch is 10% and that the misalignment is 1 deg. Thruster activity to dump momentum may occur daily and involve 0.5 s firings of 5 lb thrusters. An orbit integrator was used to evaluate the impact on the orbit of such ΔV 's. Figure A.3.1.3-1 shows the orbit error for a thruster pair firing along the pitch axis with misalignments in their

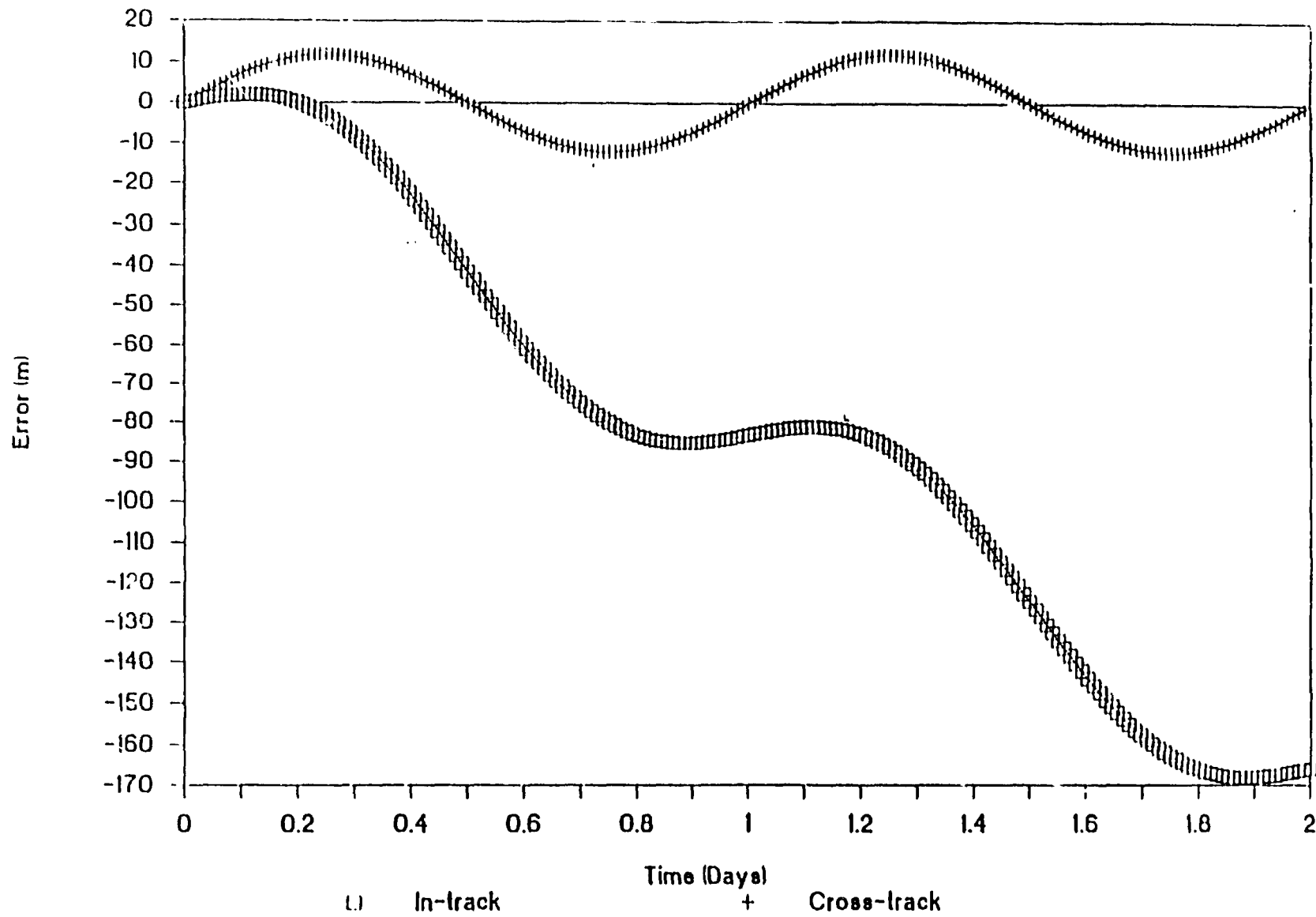


Figure A.3.1.3-1. Orbit Error for Thruster Misalignment

thrust vectors such that a ΔV is generated along the roll axis. The thruster activity occurred at $t=0$ and the figure shows a slow in-track drift away from the satellite's desired station, however, the error remains within allocations even after two days.

Table A.3.1.3-1 summarizes the combinations of thruster pair firings considered in the study and their resultant orbit errors (worst case during the day following the event) assuming worst case thruster mismatch and misalignment. Because the solar array tracks the sun the solar pressure torque and hence the secular momentum, are inertially fixed and oriented in the orbit lane and perpendicular to the sun line. Therefore, the momentum rotates in the body frame with it being in the roll direction at 12 noon and 12 midnight (local solar time) and the yaw direction at 6 A.M. and 6 P.M. Roll momentum may be canceled with a coupled pair in either the pitch or yaw axes, and yaw momentum may be canceled with a coupled pair in either the roll or pitch axes. In all cases the allocation of 400 m is not exceeded, however, thruster configurations which tend to generate less roll-axis ΔV are clearly preferred.

The tabulated orbit errors are for a control strategy where momentum is canceled. If an optimal limit cycle is employed where the momentum vector is inverted, twice the torque is required which should double the tabulated errors, however, momentum dumps will occur only half as often. In which case all errors remain within allocations except for the case where a roll axis pair is used. This may be avoided unless other spacecraft configuration or operational issues allow this as the only option.

One interesting possibility is to combine momentum management with station keeping. With the proper configuration of thrusters the inclination, longitude, and eccentricity of the satellite may be maintained with daily firings with designed torque imbalances. The lifetime fuel use required for a few large station keeping maneuvers is nearly the same as that required for many small maneuvers so the momentum management function may be achieved with little or no fuel penalty. Tight control of satellite station also has other benefits such as reducing the reliance on IMC to compensate for orbital effects. This simplifies instrument focal lane (larger extended focal lanes with smaller co-registration errors) and servo requirements.

The mean rate of inclination growth is 0.002 deg/day. To cancel this growth requires about 0.2 m/s ΔV along the pitch axis daily. Worst case 10% thrust error and 1 deg thrust vector misalignment will cause ΔV errors of 0.02 m/s along the pitch axis and 0.0035 m/s errors will cause the in-track error to exceed the 400 m allocation about 9 hours after the maneuver (Figure A.3.1.3-2). Of course there will be orbit knowledge errors at the time of the maneuvers and hence the total orbit error may exceed allocation prior to 9 hours after the event. Assuming that the satellite is tracked prior to the maneuver, this error should be on the order of the error at the end of the definitive arc. It will be shown in Section A.3.1.3.3 that such errors are on the order of 100 m which if subtracted from the 400 m allocation still allows orbit errors to remain within allocation for at least 6 hours.

<u>To Cancel A</u>	<u>At Local Time</u>	<u>With A</u>	<u>Worst Case 1 - Day Error</u>
Roll Momentum	12 AM/12 PM	Pitch Axis Pair	90 m
		Yaw Axis Pair	110 m
Yaw Momentum	6 AM/ 6 PM	Roll Axis Pair	250 m
		Pitch Axis Pair	90 m

ASSUMES COUPLED PAIR FIRING WITH 10% THRUST MISMATCH AND 1° THRUST VECTOR MISALIGNMENT

Table A.3.1.3-1. Thruster Activity Orbit Error Summary

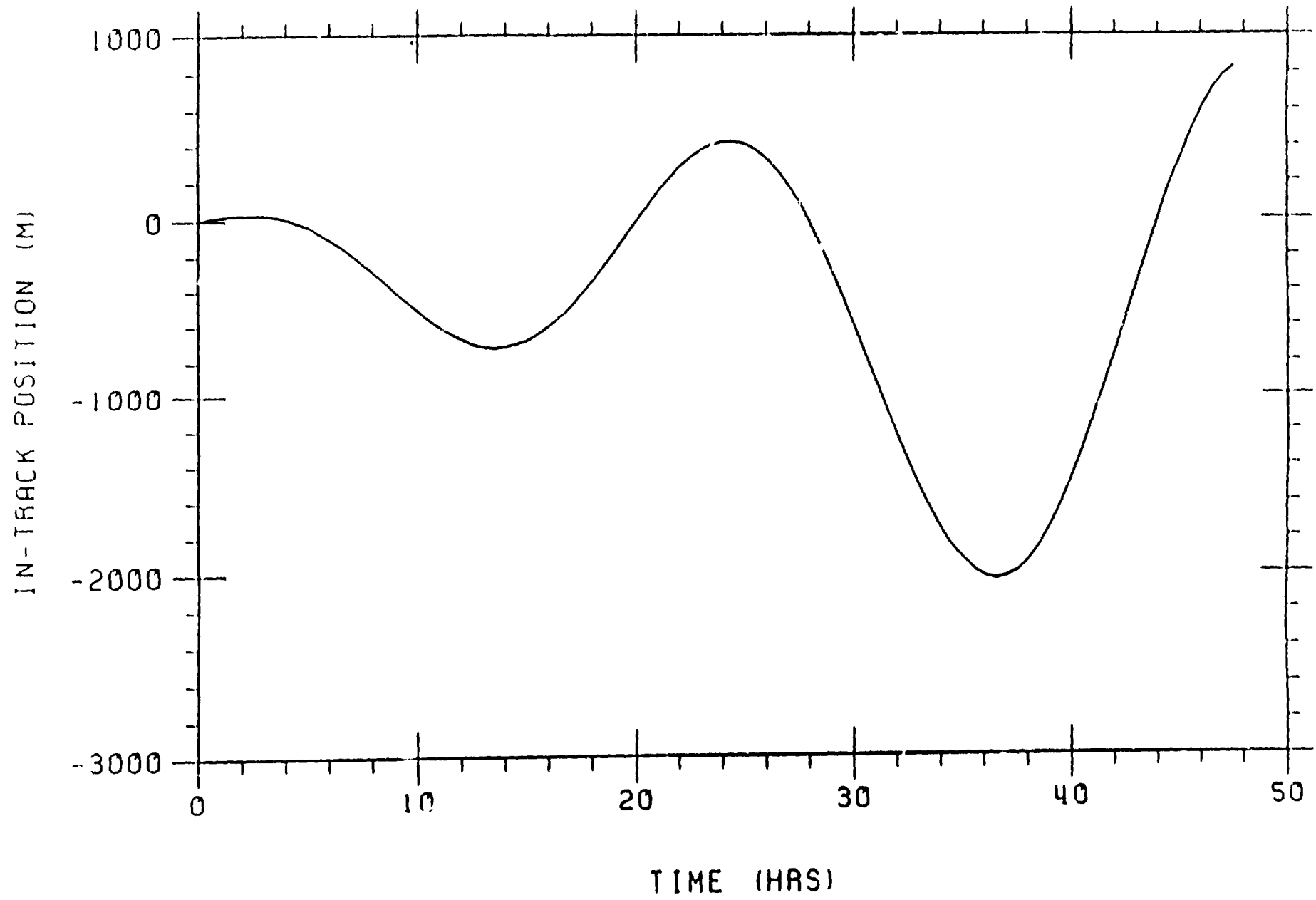


Figure A 3.1.3-2 Orbital Motion: In-Track Position vs Time

A.3.1.3.3 Orbit determination options

Systems for orbit determination for Options II and III must deliver at least 400 m accuracy ($3-\sigma$) and should offer rapid recovery after thruster firings. Since any deviation from the satellite's desired station can be compensated for with IMC, the 400 m accuracy refers to the accuracy in the knowledge of the orbit; however, it may also be desirable to restrict absolute errors to accommodate extended instrument focal planes. Several Options were considered in the study, including:

1. Multistation ranging
2. Landmarks with one station ranging
3. Deep Space Network (DSN)
4. Global Positioning System (GPS)
5. Advanced TDRSS (A-TDRSS) with the TDRSS On-board Navigation System (TONS)

A.3.1.3.3.1 Landmark and range orbit determination

The landmark and single station ranging system will be used for the GOES-I program. Simulations using the INRSIM¹ computer code have shown that orbit determination using landmarks and single station ranging can be expected to produce orbit errors on the order of 2 km ($3-\sigma$) which is plenty accurate for the GOES-I application but insufficient for the GOES-N application. The operation of acquiring large numbers of landmarks immediately after a maneuver or momentum dump in order to rapidly re-determine an orbit was also deemed burdensome.

When landmarks are augmented with two-station ranging, there is an improvement in orbit errors to about the 500 m ($3-\sigma$) level; however, the landmarks appear to contribute little to the orbit determination accuracy since, when they are deleted, orbit accuracy degrades only slightly.

A.3.1.3.3.2 DSN orbit determination

Consideration was given to the possibility of calling on the DSN infrequently to determine an orbit (100 m to 200 m ($3-\sigma$) accuracy) and to propagate between updates using a high fidelity orbit integrator. The limiting factor in geostationary orbit propagation is the modeling of solar pressure forces². Realistically it is questionable whether the solar pressure can be modeled to better than 10% ($3-\sigma$) as a matter of routine operation. This means that orbits can not be propagated beyond about 5 days before the 400 m allocation is exceeded (assuming an area-to-mass ratio similar to GOES-I's). Frequent usage of the DSN would then be required. This was deemed operationally undesirable.

¹ Ca , J.L., H.W. Dunhill, D.W. Gamble, A.A. Kamel, "Simulation Studies of the GOES-I Image Navigation and Registration (INR) System", *Advances in the Astronautical Sciences*, Vol. 72, 1990.

² Treder, A.J., "Autonomous Navigation - When Will We Have It?", *Navigation*, Vol. 34, No. 2, 1987.

A.3.1.3.3 GPS orbit determination

The GPS system is certainly capable of being effectively utilized for low earth orbit determination. In theory it may also be used for geostationary orbit determination³, however, there are several impediments which makes this approach technically risky. The GPS constellation occupies orbits significantly below geostationary altitude. The satellites have also been designed with antenna gain directed towards earth, therefore, the GPS satellites may be in contact with GOES-N only when they are on the far side of the earth and traversing a small annulus around the earth limb. This severely limits the statistics for satellite visibility and instantaneous determination of position is not possible (unlike in low earth orbit). The constraints imposed by orbital mechanics and the use of high stability clocks will, however, allow for the determination of an orbit after a number of contacts. The referenced paper claims that 300 m (3- σ) accuracy is achievable based on a co-variance analysis. While this is within allocations there would be considerable risk associated with this approach since, to our knowledge, there is no practical experience with such a system. Moreover, the poor satellite visibility statistics slows recovery after maneuvers and momentum dumps. Indeed there may be periods longer than an hour during which no GPS satellites are visible.

Because of this consideration and the fact that, to our knowledge, nobody has ever used GPS at geostationary altitude, this option was deemed technically risky. However, there is discussion about equipping the next block of GPS satellites with antennas capable of providing convenient service to geostationary satellites. A fully populated constellation of such satellites would make GPS an attractive Option.

A.3.1.3.4 ATDRSS/TONS orbit determination

The TDRSS satellite provides a tracking service to low earth orbits. It cannot provide this service to geostationary satellites in general. As with GPS there are discussions regarding upgrades to support geostationary satellites. If such a capability is provided with ATDRSS, an on-board system called TONS⁴ could be used for orbit determination. Since the present TDRSS does not support geostationary satellites, this Option was deemed programmatically risky.

A.3.1.3.5 Multistation ranging orbit determination

The use of a multistation ranging system was considered and found to be the most attractive option for GOES-N orbit determination because of its high accuracy and its ability to rapidly recover ephemeris accuracy after maneuvers and momentum dumps. At least two stations are required to determine an orbit, a third station provides redundancy and substantially improves

³ Jorgensen, P., "Autonomous Navigation of Geosynchronous Satellites using the NAVSTAR Global Positioning System", IEEE CH 1824-2/82/0000-0306, 1982.

⁴ Gramling, C.J., R.S. Hornstein, A.C. Long, M.V. Samii, B.D. Elrod, "TDRSS Onboard Navigation System (TONS) Experiment for the Explorer Platform (EP)", AIAA-90-3365-CP, Portland Oregon, 1990.

accuracy. Such a system may be configured in several ways to reduce operational complexity, recurring and non-recurring costs. Discussion of system architecture is deferred until Section A.3.1.3.4.

To assess the capabilities of a multistation ranging system in terms of accuracy and transient recovery time, a computer simulation was constructed. The simulation consisted of an orbit integrator with earth point mass gravity and non-eclipse solar pressure modeled. Higher order earth gravity, lunar and solar point mass gravity are certainly also important for geostationary orbit modeling, however, they are relatively well known and do not limit orbit determination and propagation accuracy. The simulation models the acquisition of range observations with white noise and bias, solves for the orbit state vector at epoch (position, velocity, and optionally solar pressure) using a batch nonlinear least squares filter and propagates the orbit beyond the definitive period.

Table A.3.1.3-2 shows the assumed conditions for a simulation. Two stations, in addition to the CDA, were selected at Santiago, Chile and Ascension Island. Good geographic diversity is desirable in a multistation ranging system. Ranging measurement gaussian noise of 15 m (3- σ) and biases of 5 m were assumed for the one-way range measurements. These errors result predominantly from ionospheric effects and clock synchronization errors as will be discussed in Section A.3.1.3.4.

To assess the potential for rapid recovery after maneuvers and momentum dumps, a simulation was done using only 6 hours of range data during the definitive arc with no *a priori* knowledge of the position or velocity. Ranging triples were assumed to be acquired every 10 minutes. Figure A.3.1.3-2 shows the simulated orbit determination errors. During the definitive arc the orbit error shown indicates how well the ranging data fit the ultimate orbit solution. The assumed range biases are reflected in the indicated biases in the in-track and altitude components. During the definitive arc the satellite must be operated with an *a priori* orbit. For a momentum dump event additional orbit errors resulting from the thruster activity should be negligible during the 6 hour definitive period as reflected in Figure A.3.1.3-1.

For a maneuver, the errors will largely be a function of the calibration of the satellite thrusters. As a worst case it has been assumed that a 10% error in thrust and a 1 deg error in thrust vector alignment may exist. With daily stationkeeping it has been shown that these errors will result in orbit errors which may exceed allocations within 6 to 9 hours (Section A.3.1.3.2). The orbit determination simulation has been exercised under the daily stationkeeping scenario and the results do not deviate significantly from those shown in Figure A.3.1.3-3 for the momentum dumping event.

- **ORBIT DETERMINATION SIMULATION DEVELOPED FOR THE GOES-N PHASE-A STUDY**
- **SIMULATION CASE ASSUMPTIONS**
 - **GOES-EAST SATELLITE**
 - **RANGING STATIONS AT**
 - WALLOPS ISLAND (CDA)**
 - SANTIAGO CHILE**
 - ASCENSION ISLAND**
 - **15m (3- σ) RANGING NOISE WITH 5m BIASES**
 - **10% SOLAR PRESSURE MODELING ERROR**
 - **6 HOUR DEFINITIVE ARC WITH ONE RANGING TRIPLE EVERY 10 MINUTES**
 - **MOMENTUM UNLOAD THRUSTER ACTIVITY AT BEGINNING OF DEFINITIVE ARC**

Table A.3.1.3-2. GOES-N/Option II and III Orbit Determination Simulation

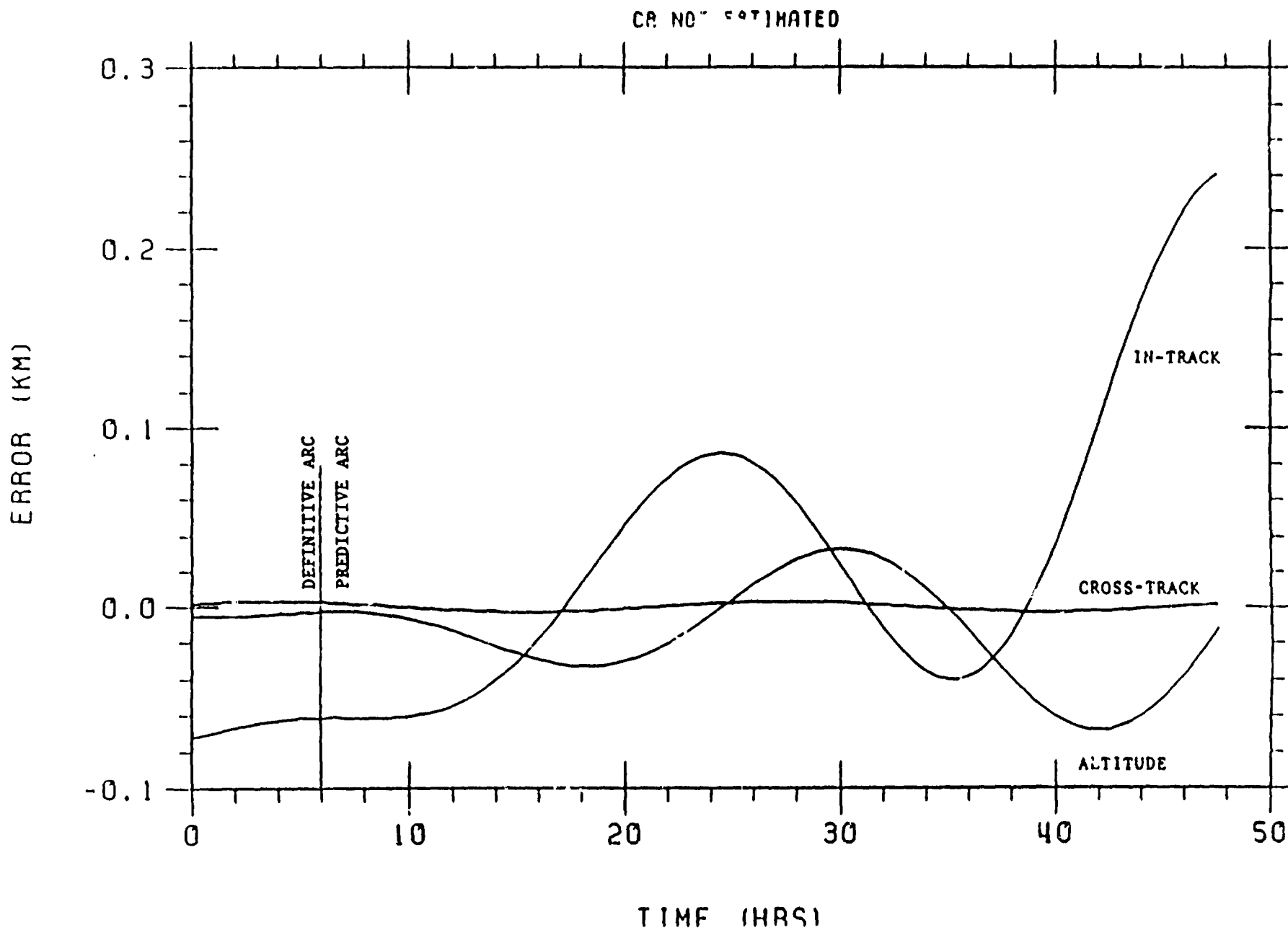


Figure A.3.1.3-3. Orbit Prediction Errors

The definitive arc shown in Figure A.3.1.3-3 shows that orbit errors remain under allocations for at least two days. In this simulation the solar pressure (represented by the reflection coefficient CR) was not solved for. Longer definitive arcs generally allow for better definition of CR. It was assumed that previous tracking had determined CR to an accuracy of 10%. The growing oscillations in the in-track and altitude components are the signature of increasing eccentricity error associated with the 10% solar pressure error. Including solar pressure as a solve-for parameter does not improve performance unless the definitive arc is lengthened. Shortening the definitive arc has the effect of degrading orbit determination even when CR is not estimated. The 6 hour definitive arc used in the simulation represents a reasonable trade-off between orbit determination accuracy and transient recovery time.

Comparing these simulation results with the actual performance achieved in tracking the TDRSS satellites using the BRTS system (a two-station ranging system with 100 m to 200 m (3- σ) performance) indicates that the simulation results are reasonable.

The simulation studies conducted have shown that the 400 m allocation for orbit error may be met with a multistation ranging system and that transient recovery is possible within a 6 hour period. Since orbit disturbances tend to grow with time it is likely that the 400 m allocation will be met even during the definitive period when the disturbance is characterized only by an *a priority* value.

A.3.1.3.4 Multistation ranging system implementation

Several architectures for a multistation ranging system may be imagined—turn-around ranging with remote sites, down-link only one-way ranging with GPS time transfer equipment, and up-link only one-way ranging. Only the GPS time transfer system was considered in detail as part of this study.

A.3.1.3.4.1 Multistation ranging options

The most straightforward and accurate configuration would be to have dedicated remote ranging sites which would participate in turn-around ranging events involving the CDA, the satellite, and the remote site. The present GOES-I ranging system utilizes the GVAR link for CDA to satellite turn-around ranging. To enable a remote site to participate would require communications system modifications such as including a dedicated ranging transponder for the remote site to satellite link. Several measures may be taken to minimize recurring and non-recurring costs associated with remote ranging sites. These include co-location with other government facilities, and the use of automated equipment requiring human intervention for maintenance only.

A promising concept that would provide less accurate rangings, but at substantially reduced cost, would be to equip several existing GVAR user sites with timing equipment accurate enough to perform one-way rangings. This concept ("Hybrid" ranging) is described in detail later in this section where use of commercial GPS time transfer equipment is proposed. Some consideration to such a system was given early in the GOES-I program.

A third possible architecture is to use remote sites for uplink only and to perform all the orbit determination computations on-board or in a ground computer at CDA or SOCC semi-autonomously. This would require accurate clocks at the remote sites. Timing bias for a single clock (for example the on-board clock if processing is placed on-board) may be solved for as part of the orbit determination process.

A.3.1.3.4.2 Hybrid ranging system

Like the GOES-I ranging system, the CDA would transmit a pulse in the GVAR data and receive it, noting both the transmit and receive times. The only change to the current implementation would be to substitute an off-the-shelf GPS receiver and atomic frequency standard (clock) in lieu of the current clock. A common clock reference is required at both the transmit and receive sites in order to determine the one way ranging time to the remote site.

At one or more remote sites, the received ranging bit in the GVAR data would be time tagged using a similar GPS receiver/atomic clock and ranging recovery equipment similar to that in the current CDA. By limiting the number of ranging transmissions to one every few seconds, the time of reception at a remote site could be unambiguously related to the time of transmission. Once or several times a per day the GPS ranging bit reception times would be forwarded to the CDA (or SOCC) for processing to determine the ephemeris for the following day.

The following assumptions are made:

- The timing uncertainties associated with the current CDA equipment and delineated in the References ^{5,6} are essentially correct.
- The GPS equipment will be used in the coarse (C) mode; if required in the future, permission to use the precision (P) mode could probably be obtained.

A number of companies currently build GPS equipment, and it is available "off-the-shelf." The GPS equipment discussed in the remainder of this document is the STI (San Jose, CA.) GPS Time Transfer System 502B (TTS-502B). This equipment is thought to be representative of this type of equipment/performance based on a number of discussions held with company representatives. The TTS-502B has the following capabilities:

- Tracking of the Course Acquisition (CA) code on the L1 carrier, with acquisition times of less than 90 seconds.
- Determination of the ground location of the system to reduce location uncertainties.
- Automatic computation of all GPS satellite locations from information contained in the data stream.
- Either UTC or GPS as a time reference.

⁵ "OGE System Description, Analysis and Implementation Plan" DRL 504-01, Volume 1, 27 April 1987

⁶ FAC response to Technical Direction Number 18 (CCR/2010) of 26 June, 1987

- User selection from a "shopping list" of twelve categories of data for transfer, including time transfer data, fault diagnostics, satellite visibility times, and satellite tracking schedule.
- Interfaces with atomic frequency and time standards.
- Time transfer random errors of less than 3 nanoseconds (1 σ) with 4 minute smoothing.
- RS-232-C port for data output.
- Keyboard entry and video display.

At the CDA and remote sites, the TTS-502B equipment in the operational mode would generate time pulses (probably in UTC) from the timing information derived from the GPS satellites (Figure A.3.1.3-4). An atomic frequency standard would be used as the clock and would be continuously updated by the GPS. The GPS based clock time would be routed to a time interval counter (e.g., a Hewlett-Packard) to determine the time that the range pulse was received by the ranging equipment. At a remote site the time of this range pulse would then be recorded for subsequent transmission to the SOCC. The system would probably be implemented to transmit all the ranging times once or several times per day to the SOCC. Then, all the range pulse received times from the CDA and remote sites would be different from the range pulse transmit times and the ephemeris determined.

Although the TTS-502B system will automatically track GPS spacecraft indefinitely without need for operator intervention, the common-mode/common-view mode of operation (i.e., when the same spacecraft can be seen simultaneously from two locations) requires that an operator manually input the GPS spacecraft that are to be tracked. The TTS-502B aids the operator in determining GPS common-view times by calculating the visibility times of the GPS spacecraft for any point on the Earth. The tracking schedule would need to be entered about once a week. It is also possible to get nearly the same common-view (timing) performance from two widely separated locations by "daisy chaining" (e.g., from Hawaii to California or White Sands to the CDA at Wallops Island)

The expected timing performance for common-mode/common-view operation using just the CA code on the L1 carrier is given in Reference ⁷ and summarized in Table A.3.1.3-3. An unknown location requires that four satellites be within view simultaneously to solve for location and time. For a known location it is only necessary that one GPS spacecraft be in view to determine the time: this is the method of operation that would be used in the GOES system to determine ranging. The location of each site would be determined prior to the start of operation using the TTS-502B equipment, which would provide location to an accuracy of about 2 meters. The same TTS-502B equipment would then be used operationally to determine the ranging times.

A more detailed block diagram incorporating the TTS-502B into the current GOES I-M CDA and showing the remote site configuration of the appropriate GOES I-M downlink equipment with the TTS-502B is shown in Figure A.3.1.3-5.

⁷ "Application of Time Transfer Using NAVSTAR GPS," A.J. Van Dierendonck and A. C. Melton, The Institute of Navigation., Volume II, page 133

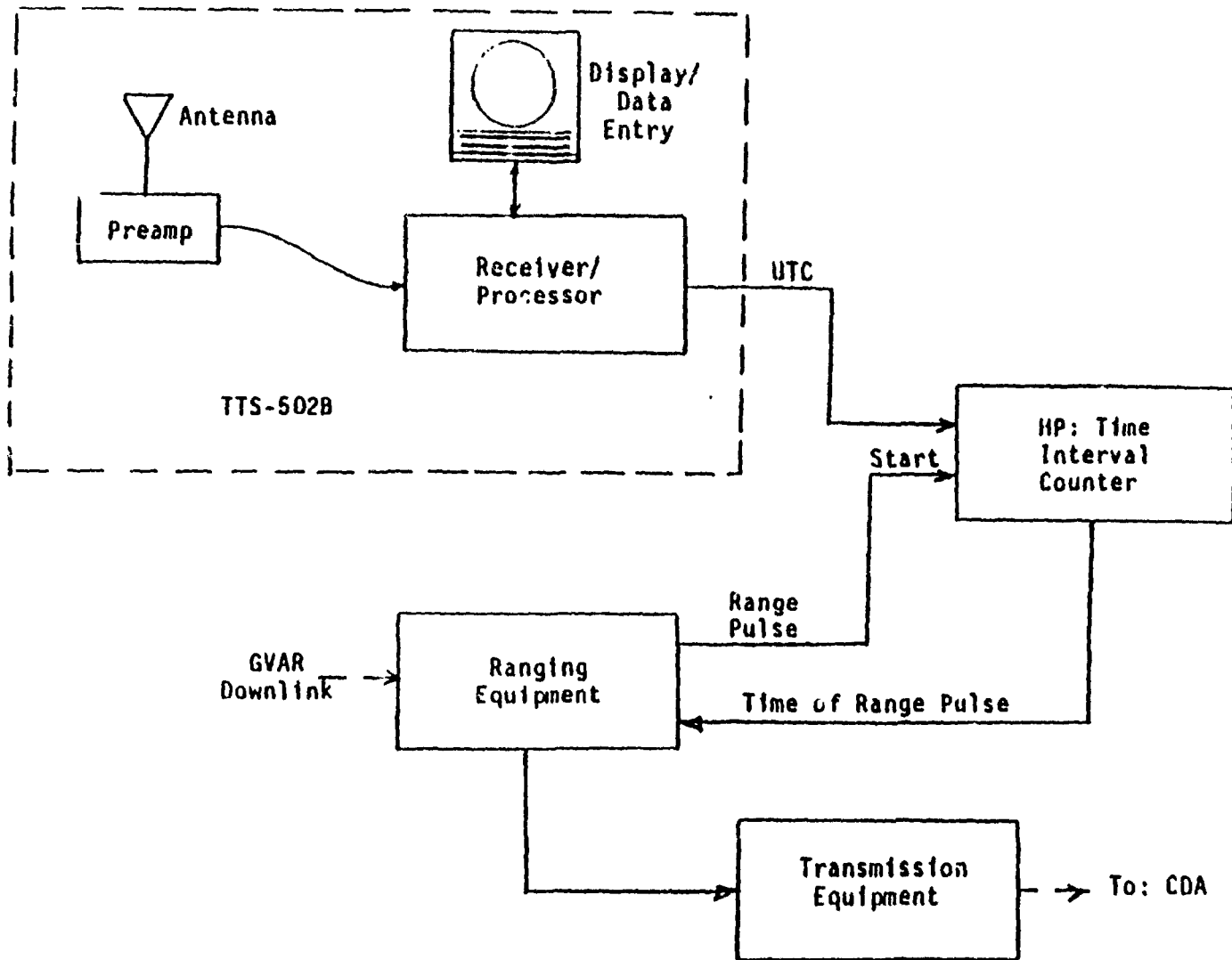
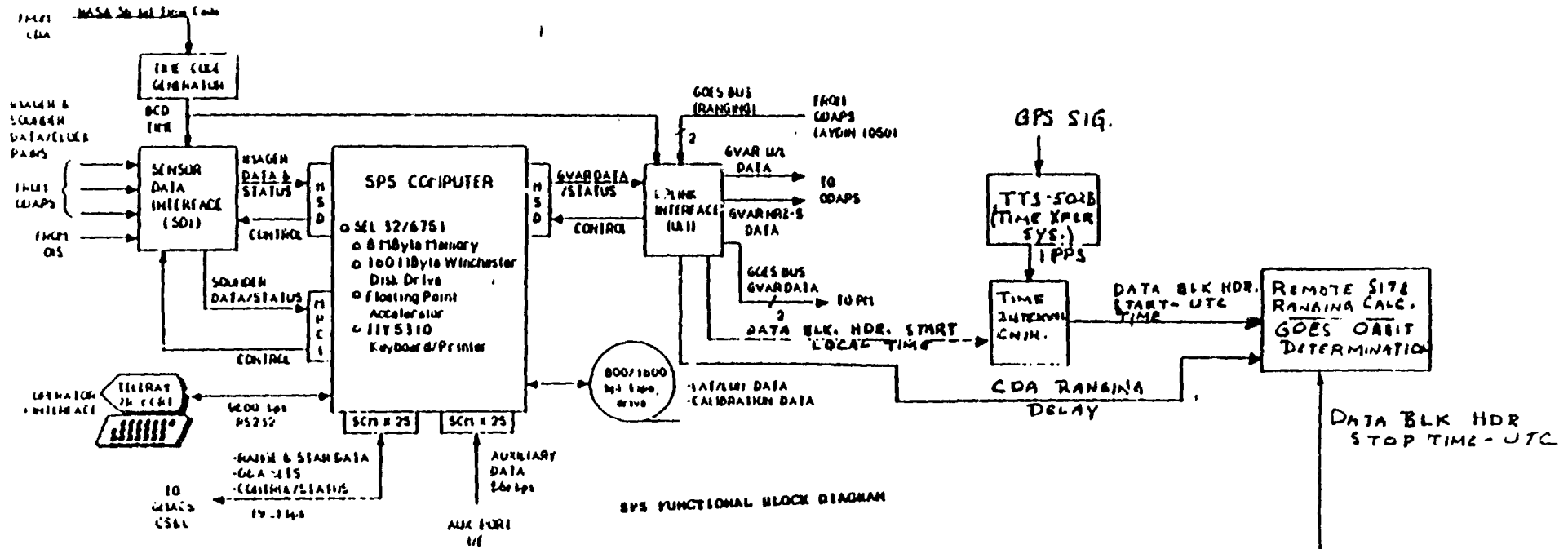


Figure A.3.1.3-4. Block Diagram of GOES Remote Station Ranging Equipment Configuration.

CDA EQUIPMENT



REMOTE SITE EQUIPMENT

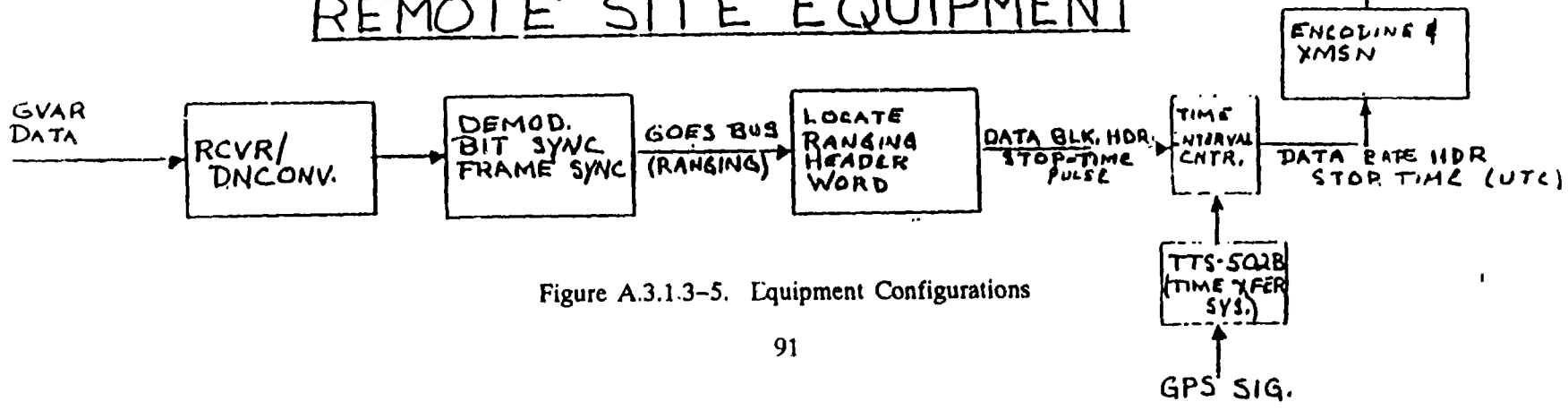


Figure A.3.1.3-5. Equipment Configurations

The only major change at the CDA would be the incorporation of a GPS time based clock using an atomic frequency standard in place of the current clock. The atomic frequency standard will provide more than two orders of magnitude improvement in the timing uncertainty associated with the current GOES I-M clock.

The remote sites would use the same downlink design as in the CDA to recover the ranging pulse from the GVAR data stream. To minimize costs the remote site should be at a location that is already receiving GVAR data; the added cost in this case would be for the addition of the downlink range recovery equipment and equipment to transmit the received range data back to the Spacecraft Operational Control Center (SOCC). It is possible that a telephone link may be the least expensive transmission medium for this data. The determination of the ephemeris would be done in the Operational Ground Equipment (OGE).

The present OGE design has the ranging measurement made in the Uplink Interface (ULI) under the control of the Sensor Processing System (SPS). In this design, the SPS controls the ULI by setting the ranging bit in the ULI's mode control word, and also setting the ranging bit in the GVAR header data to be sent out in the next block of data to be uplinked. The ULI starts the ranging time measurement at the start of the uplinking of the data block header. For the received GVAR downlink, since the ranging bit can be in any data block header, the timer value is latched for every header start pulse received by the ULI, but the timer is permitted to continue running until the header word is verified to contain the ranging bit.

For ranging measurements to a remote site, the proposed system would not have to alter the current ranging implementation at the CDA. However, a second pulse coincident with the start of the uplinking of the data block header would need to be routed to the GPS time transfer equipment. From this the uplink transmission start time would be determined and stored. The actual measurement of the uplink start time would be determined by measuring the time interval between the uplink start pulse and the very accurate 1 pulse per second (pps) clock from the TTS-502B. This uplink start time would be stored for comparison with the ranging reception times received from the remote sites. By limiting the ranging pulses to no more than one every half second, the round trip transmission time to/from a geosynchronous spacecraft, the transmit and receive times can be unambiguously paired. It should be noted that the entire design can be simplified by restricting the ranging bit to be in a specific GVAR data block in all frames.

TABLE A.3.1.3-3 GPS TIME TRANSFER PERFORMANCE FOR
COMMON-MODE/COMMON-VIEW OPERATION

ERROR SOURCE	RAW MEASUREMENTS (NS)	SMOOTH MEASUREMENTS OVER 4 MIN. (NS) ^a
SATELLITE EPHEMERIS AND CLOCK	0 - 5 $\sqrt{2}$	0 - 5 $\sqrt{2}$
ATMOSPHERIC DELAY	0 - 40 $\sqrt{2}$	0 - 40 $\sqrt{2}$
RECEIVER NOISE	10 $\sqrt{2}$	1.5 $\sqrt{2}$
QUANTIZATION NOISE	15 $\sqrt{2}$	2.5 $\sqrt{2}$
POSITION ERROR	5 $\sqrt{2}$ - 15 $\sqrt{2}$	5 $\sqrt{2}$ - 15 $\sqrt{2}$
TOTAL ERROR (RSS)	6.5 - 66	8.2 - 61
TOTAL ERROR (METERS)	8 - 20	2.5 - 18.3

Although this proposed implementation does not require the current ULI ranging design to be changed, for design consistency it might be worthwhile to have the CDA turn-around ranging time determined in the same way as the ranging time at the remote sites. It will be necessary to use the GPS derived clock for the CDA ranging. As well as for determining the ranging times to remote sites, because the current clock would be a major error source (24 nanoseconds) instead of being negligible (< 0.24 nanoseconds - Table A.3.1.3-4).

At the remote site, the GVAR data would be received, down converted, demodulated, and synchronized, and the ranging header word located by equipment/software similar to that designed for the ULI. This assumes that the ranging bit is not restricted to a specific GVAR data block, which would significantly simplify the design. Note that the addition of the ranging function processing would not affect the normal processing of the GVAR data at an existing GVAR receiving facility. (Figure A.3.1.3-5)

Assuming that the ranging bit is not restricted to a specific GVAR data block, the remote site ULI implementation would differ from the CDA implementation in the way that the valid ranging headers were identified. Specifically, since the header identification in the received GVAR data stream occurs after the receipt of a ranging stop-time pulse (i.e., the ranging stop-time must be coincident with the reception of the data block header), provision must be made to discard all data

^a. Smoothed measurements are based on samples taken every 6 seconds over a 4 minute (240 second) period.

TABLE A.3.1.3-4 CDA AND REMOTE SITE RANGING ERROR SOURCES
USING GPS TIMING

SUBSYSTEM/ITEM	ERROR SOURCES	ESTIMATED ERROR	
		NANOSEC	METERS
CDA UPLINK	IF MODULATOR	3.2	
	MULTIPLEXER	2.1	
	CABLE	5.0	
	POWER AM.	0.7	
	UNCONV. XLATOR	1.3	
	DIPLEXER	0.7	
	CALIBRATOR	1.3	
CDA UPLINK SUBTOTAL (RSS)		6.6	2.0
SATELLITE	CHANNEL FILTER	0.4	
	OUTPUT MUX.	0.3	
	RECEIVER	0.4	
	POWER AM.	0.4	
	CABLE	0.3	
	PRESELECT FILTER	0.2	
SATELLITE SUBTOTAL (RSS)		0.84	0.25
CDA DOWNLINK	DIPLEXER	0.7	
	LNA	0.7	
	RF DNCONV.	0.7	
	CABLE	5.0	
	MUX	2.1	
	AYDIN 1050	5.0	
	CLOCK	0.3	
	COMPARATOR	10.0	
CDA DOWNLINK SUBTOTAL (RSS)		12.6	3.8
CDA ANTENNAL LOCATION ANTENNA LOCATION		16.7	5.0
REMOTE SITE DOWNLINK	LNA	0.7	
	RF DNCONV.	0.7	
	CABLE	5.0	
	MUX	2.1	
	TIME INTERVAL CNTR	5.0	
	CLOCK	0.3	
	COMPARATOR	10.0	
REMOTE SITE DNLINK SUBTOTAL (RSS)		12.5	3.7
REMOTE SITE TIME DIFFERENCE		8.2 - 61.0	2.5 - 18.3
REMOTE SITE ANTENNA LOCATION		16.7	
REMOTE SITE SUBTOTAL (RSS)		22.4 - 64.5	6.7 - 19.3

block header stop-time pulses that do not show the associated ranging bit to be "set." Again, this would not be a design problem if the ranging bit were restricted to a specific data block in all GVAR frames.

The times of occurrence of the ranging stop-time pulses at the remote sites also would be determined using the GPS time transfer equipment in the same manner as the start-time transmission determination at the CDA. The amount of data to be sent to the SOCC for each received ranging bit is very modest: day, hour, minute, and seconds to the nearest nanosecond (ns). This could be done with 16 characters.

After uniquely associating each stop-time pulse with its start-time, the one way ranging times from the CDA to the spacecraft and from the spacecraft to the remote site would be calculated. These values for an entire day would be sent to the OGE, where the ephemeris would be calculated.

Operation of the remote sites will require an initial and periodic calibrations every six months to maintain the required ranging measurement accuracy. A potential method for performing these calibrations would use a remote site ranging test generator to be developed, and inclusion of a coupling point (e.g., a diplexer) in the existing RF or IF downlink for inserting the test signals. This ranging test generator would utilize the GPS time transfer signals for the calibration. Another approach would be to take the remote site equipment to the CDA for initial calibration; subsequent calibrations would use separate or redundant time transfer equipment that was interchanged with the in-place equipment.

Conservative estimates have been made for the various errors affecting the overall determination of one way range measurements using the GOES-I or a similar system. The equipment error contributions are taken from Reference 6.

Table A.3.1.3-4 summarizes the timing/location error uncertainties for the CDA and remote site equipment. Table A.3.1.3-5 provides the expected one way ranging errors from the CDA to the spacecraft and from the spacecraft to the remote site.

Summarizing the results of Table A.3.1.3-5, the uncertainty in the CDA to spacecraft ranging measurement is 18.2 nanoseconds (5.4 meters); and the uncertainty in the spacecraft to remote site ranging error is about 30.2 nanoseconds (9.1 meters). These estimated results are increased to 10 meters for both ranging estimates in the simulations discussed in the previous section.

A.3.1.3.5 Summary of orbit determination requirements and options

This section has shown that the GOES-N Options II and III satellites will require more accurate orbital ephemeris knowledge than will be provided by the GOES-I system. This is mainly due to a change from earth referenced attitude sensors to inertial attitude sensors. Another GOES-N requirement is rapid ephemeris knowledge recovery from transient events such as maneuvers and thruster momentum unloads which may occur once per day. An allocation of 400 m (3- σ) for orbit error can be met by a multistation ranging system and orbital ephemeris knowledge may be recovered within 6 hours of a transient event. During the recovery period the errors associated

with the thruster activity are not expected to cause the ephemeris error to exceed its 400 m allocation. Combining stationkeeping and momentum management functions may be feasible and will result in the expenditure of no additional fuel over that which would be spent for stationkeeping. Tight constraints an inclination has the benefit of reducing IMC dynamic range (a benefit for extend focal plane instruments) but requires frequent, perhaps daily, maneuvers.

The use of a hybrid ranging system utilizing GPS time transfer equipment at remote GVAR sites has been studied in detail. Non-recurring costs associated with the remote stations would be minimized by using existing GVAR sites. Recurring costs would be modest since the remote site equipment requires human intervention infrequently.

TABLE A.3.1.3-5 ONE WAY RANGING ERRORS CDA AND REMOTE SITE TO SPACECRAFT

LINK	SUBSYSTEM/LINK	ESTIMATED ERROR	
		NANOSEC	METERS
CDA SPACECRAFT	CDA UPLINK	6.6	2.0
	SATELLITE	0.84	0.25
	CDA DNLINK	12.6	3.8
LINK SUBTOTAL (RSS)		14.3	4.3
	ONE WAY LINK	7.2	2.2
	CDA ANTENNA LOCATION	16.7	5.0
CDA SPACECRAFT (RSS)		18.2	5.4
SPACECRAFT - REMOTE SITE	CDA SPACECRAFT REMOTE SITE	18.2	5.4
		22.4 - 64.5	6.7 - 19.3
CDA REMOTE SITE (RSS)		28.9 - 67.0	8.7 - 20.1
SPACECRAFT REMOTE SITE (1/2 OF CDA REMOTE SITE)		14.5 - 33.5	4.4 - 10.1
GEOMETRIC MEAN		30.2	9.1

THIS HAS A LARGE PACKAGE OF GRAPHICS AND CHARTS THAT GOES WITH IT

A.3.1.4 Sensor configuration recommendations

The recommended configuration employs a DRIRU-II inertial reference unit and three star trackers oriented as in Figure A.3.1-1. Either the Ball CT-601 or the HDOS ASTRA-II would be an acceptable star tracker. Improved performance could be obtained by reducing the FOV of either tracker from 8 deg square to 4 deg square, which would require redesigned optics. This is

straightforward in principle, but does increase the cost and risk. Although involving higher cost and risk, advanced-technology IRU options should be followed closely owing to their potentially superior performance, reliability, power, and weight characteristics.

A.3.1.5 Power, volume, weight, and cost impacts

The estimated power, volume, weight, and cost of the added components for Options II and III are as follows:

	POWER (WATTS)	VOLUME (M ³)	WEIGHT (KG)	COST (\$M)
DRIRU-II	22.5	0.025	17	2.1
TRACKER	10-15	0.01	9	1.25

The star tracker costs quoted are the estimated recurring costs per tracker. The estimated non-recurring cost for developing new star tracker optics for a 4 deg square FOV are \$2M - \$3M.

The four reaction wheels for this option are lighter than the two momentum wheels and one reaction wheel of Option I. The horizon sensors of Option I are deleted, also, but some simpler horizon sensors are probably desirable for acquisition and safehold operations; so this represents a cost savings but probably not a significant power, volume, or weight saving. Deletion of the solar sail in Options II and III saves cost, weight, volume.

A.5.1.6 Risks

The risk is very low for the recommended system. The DRIRU-II inertial reference unit has been employed on several missions with great success. The risk would be somewhat higher if advanced-technology IRUs are employed in place of DRIRU-II. The star trackers have not been space-tested as of this date, but they are based on proven technology and should be well tested long before they are needed for GOES-N. The algorithms for combining the IRU and star tracker data have been extensively tested in space. The data system required for these computations is well within the bounds of current technology; a data system similar to the Small Explorer Data System (SEDS) would certainly be sufficient. The SEDS employs Intel 8086 and 80386 microprocessors with a 1773 optical data bus architecture. Deletion of the solar sail is a significant risk-reduction factor.

A.3.2 MOMENTUM MANAGEMENT SYSTEM DESIGN

A.3.2.1 Introduction

A.3.2.1.1 Requirements overview

The momentum management system must be designed to handle both cyclic and secular torques and momentums. Secular torques are constant in magnitude and direction in an inertial (non-accelerating) coordinate system, whereas cyclic torques vary sinusoidally in a coordinate system. The momentums the torques cause are also cyclic or secular, depending on the nature of the torques. Torques and momentums that are secular in an inertial coordinate system can be cyclic in a rotating coordinate frame, and the momentum management system, which is rotating with the spacecraft in orbit, must be able to control these momentum buildups. Secular momentums will build up continually, and the wheels must be unloaded periodically, whereas cyclic momentums only need to be absorbed by the reaction wheels.

A.3.2.1.2 Spacecraft configurations studied

Several spacecraft designs were used in the tradeoff studies performed. The first option considered was a GOES-I style bus, with a straight extendable boom, a conical solar sail, and a trim tab on the end of the solar array. The second option had a cylindrical solar sail on the end of a canted boom, and a trim tab attached to the solar array. The cant was used to get the sail further away from the spacecraft bus to reduce the thermal load on the bus. The third option was a GOES-I style bus with no solar sail; this configuration was examined with two momentum management systems, described below. The solar array, on the south side of the bus, was rotated such that it was perpendicular to the Sun-satellite vector to give the maximum solar exposure at all times. Each option was three-axis stabilized (nonspinning, rotating once per orbit), nadir-pointing (same side pointing towards the Earth at all times) satellite with a four reaction wheel assembly (RWA) control system. See Figures A.3.2-1 and A.3.2-2 for a diagram of each configuration, along with the estimated mass properties.

A.3.2.1.3 Geostationary disturbance torque overview

There are several sources of external torques on this spacecraft. External disturbances come primarily from the solar radiation pressure on the off-center solar array. The gravity-gradient torques (these tend to rotate the spacecraft to point its long axis towards Earth) are less than 1/1000th as strong as the maximum solar radiation torques, and aerodynamic torques are practically nonexistent at geostationary altitude (35700km, or 19300 nmi). The magnitude of the solar radiation at Earth is constant, independent of orbital position for an equatorial orbit. The geometry of the spacecraft and the sun's angle above or below the orbit plane are the deciding factors in the amount of torque that is produced. The straight solar sail configuration produces the least torque of the designs studied, while the canted solar sail and the no solar sail design created similarly large solar radiation torques, although in different directions. For comparison, the largest component of gravity gradient torque is about the same magnitude as the solar radiation torque magnitude of the straight solar sail configuration.

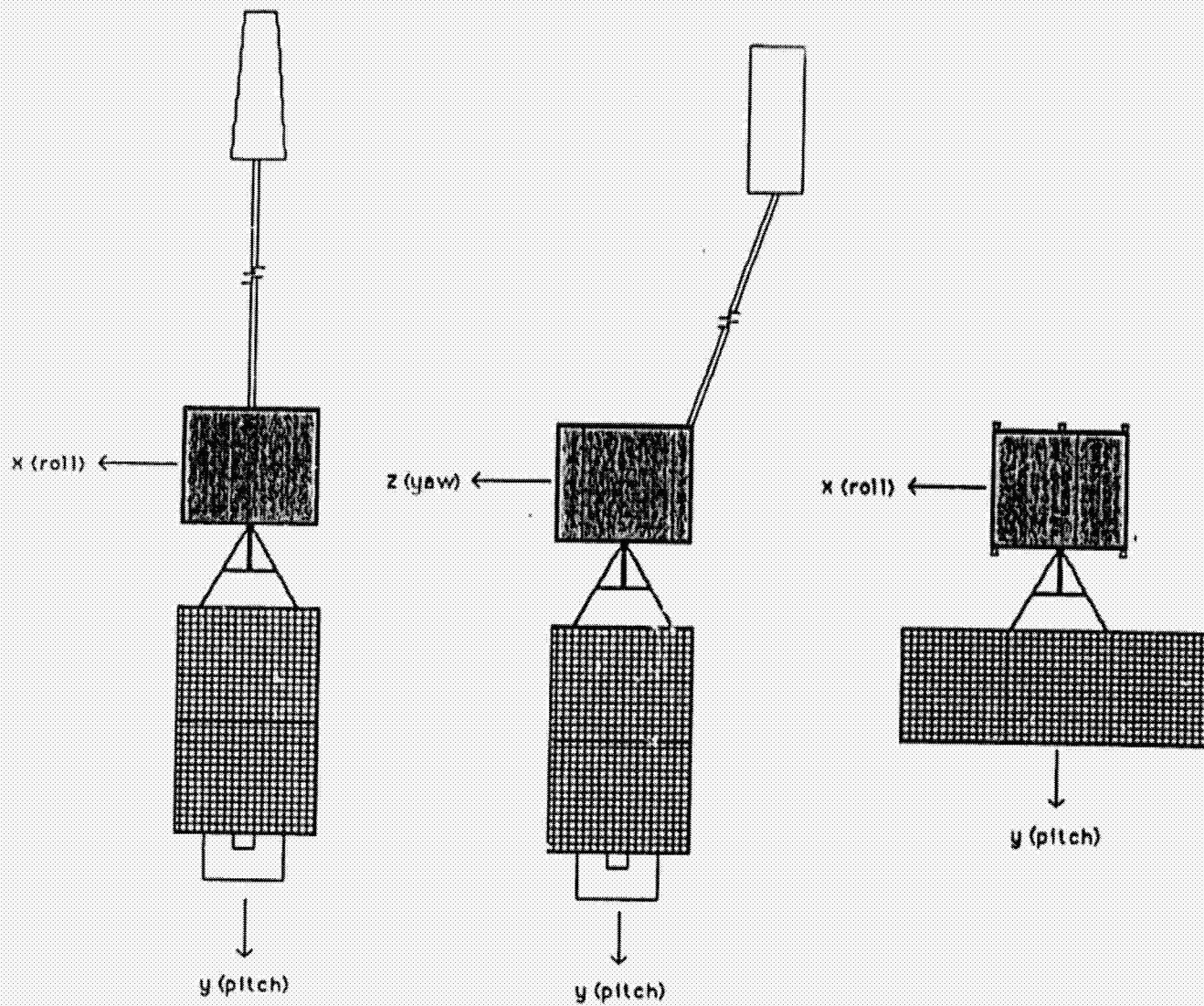


Figure A.3.2-1. GOES Solar Sail Configurations Studied

<u>Configuration</u>		Inertias	
		<u>sl-ft²</u>	<u>kg-m²</u>
Straight Solar Sail	I_{xx}	2402	3257
	I_{yy}	756	1026
	I_{zz}	2360	3200
No Solar Sail	I_{xx}	2168	2940
	I_{yy}	1269	1721
	I_{zz}	2140	2900

Figure A.3.2-2. Moments of Inertia

In an inertial, Sun-centered coordinate system, the solar radiation is always in the same direction: towards Earth. The torque on the spacecraft is always in the same inertial direction for the same reason (also because the solar array is south of the spacecraft bus). This is the secular solar radiation torque. The spacecraft rotates once per orbit, however, keeping the same side towards the Earth at all times. The result is that the torque (and thus the momentum buildup) trades off between the yaw (Earth-pointing) axis and the roll (velocity vector) axis every quarter orbit. This is called quarter-orbit gyroscopic coupling, and the cycling has a period of one orbit. See Figure A.3.2-3 for a diagram of the axes and the torques. Cyclic torques are produced with the canted solar sail; the moment arm to the sail produces a pitch torque that varies sinusoidally between two fixed values. The torque does not build up momentum continuously over successive orbits, thus it is neither a secular torque nor a secular momentum. For either torque, the momentum that is built up must be absorbed, and unloaded, if necessary. If the momentum is unloaded with thrusters, there is the possibility of disturbance torques due to thruster force imbalance and/or thruster misalignment. These disturbances produce changes in the spacecraft's orbit and ephemeris, and were studied in more detail in Section A.3.1 of this appendix.

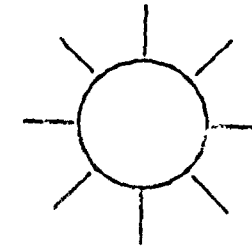
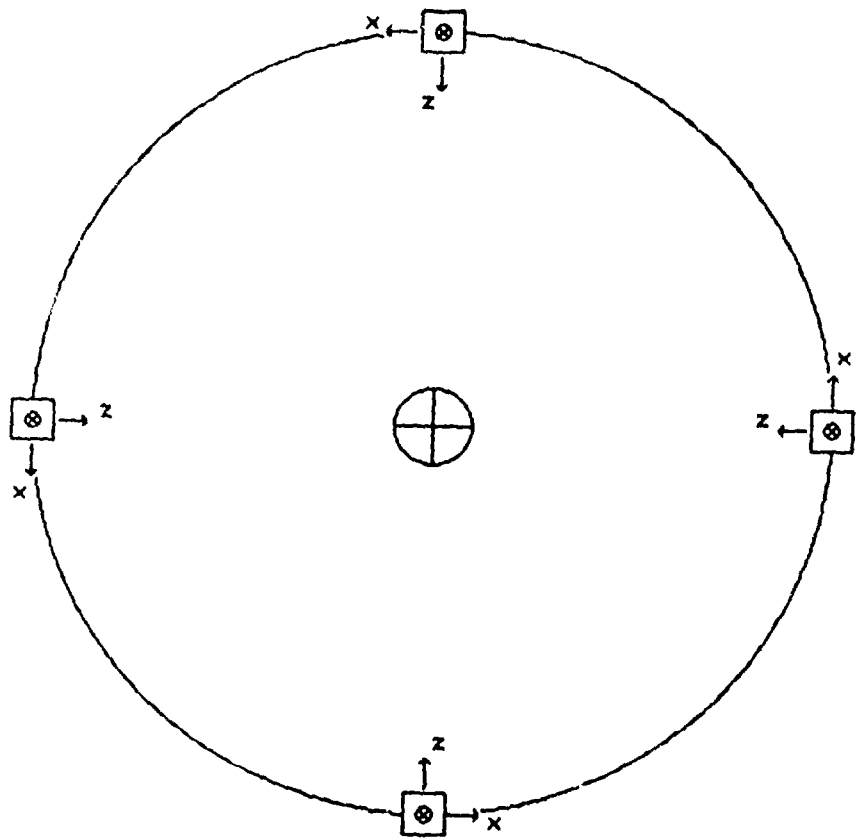
A.3.2.1.4 Momentum management hardware configurations studied

Each spacecraft design had its own momentum management system configuration, and the no solar sail option had two system configurations that were studied. The solar sail option used four RWA and magnetic torquer bars (MTB) to unload momentum buildups because the torque magnitudes (and therefore the momentum buildups) were small; the solar torque due to the solar array was balanced by the solar sail, as expected. The satellite with the canted solar sail used the same design except that the reaction wheels had to be larger than the ones on the straight solar sail spacecraft, due to the addition of a pitch axis torque. The first configuration of the no solar sail option satellite used MTB to unload the momentum, and used thrusters for stationkeeping only. The other configuration used thrusters firing in pairs to unload the momentum, reducing in size or even eliminating the MTB. Four RWA would be used in both options for torque and momentum management as described below.

A.3.2.2 Design description and analysis results

A.3.2.2.1 Wheel design criteria

The spacecraft will use the GOES-I system performances for baseline performance criteria. The similarities of and differences between momentum wheels and reaction wheels should be noted first. Both are devices used for the storage of angular momentum. There are several reasons for using these devices: they add stability against disturbance torques; they allow operation at one revolution per orbit by providing variable momentum, they absorb cyclic torques, and they transfer momentum to the satellite body for the execution of slewing maneuvers. A momentum wheel is designed to operate at a nonzero (biased) momentum. It provides a stable momentum axis with a variable-momentum storage capability. It is fixed in the spacecraft, and spins in one direction only. A reaction wheel, on the other hand, is designed to operate at zero spin and can spin in both directions. They are used primarily for absorbing cyclic torques, during slew (reorientation) maneuvers. Reaction wheels also are needed to provide control and momentum storage capability in several axes along with redundancy for safety reasons.



Constraints

- circular orbit
- no inclination
- array perp. to sun-sat. line
- at vernal equinox; sun in orbit plane
for max. solar pressure

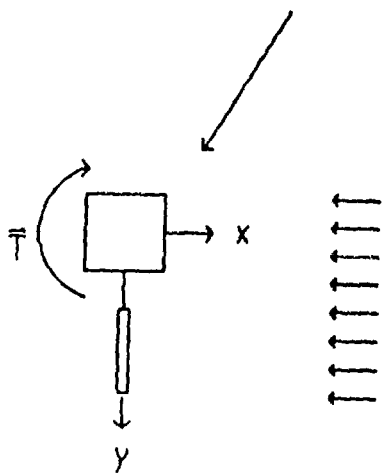


Figure A.3.2-3. Momentum Buildup - Orbit and Spacecraft Orientation

A.3.2.2.1.1 Torque requirements

The reaction wheels will be used for the slew (pointing) maneuvers, and must be sized to rotate the entire spacecraft. The design torque capability is .09 N-m (12.8 in-oz); this is the same capacity as the GOES-I spacecraft.

A.3.2.2.1.2 Momentum storage requirements

For momentum storage capability, the wheels must be sized to absorb roughly four times the momentum buildup the spacecraft is expected to encounter. There are a number of reasons for this factor. First, the momentum (like the torques) can be both positive or negative, depending on the orientation of the satellite, and the wheels must handle the maximum momentum in either direction. In addition, unpredictable disturbance momentums, whether from mechanical or environmental causes, dictate the need for a conservative wheel design to absorb any excess momentum.

A.3.2.2.1.3 Weight, cost, power

The wheels will be designed to minimize the impact of any weight, cost, or power change on the satellite, compared to the GOES-I configuration.

A.3.2.2.2 Momentum management characterization

The orbit was assumed to be a circular, geostationary, 86164 second (23 hours 56 minutes 4 seconds) orbit period. The determination of the solar radiation torque magnitude is outlined in Figure A.3.2-4, taken from Section 17.2 in Wertz' "Spacecraft Attitude Determination and Control". The resulting values of torque can be found in Table A.3.2-1, along with the axis of each torque. These values were taken to be the maximum amplitude of a sinusoidally-varying (in the body axes) torque with a period of one orbit. The orbit was started at the vernal equinox, so initially only positive yaw torque was present. After approximately six hours (or 90 degrees of orbit), the torque was all positive roll; after about 12 hours (180 degrees), all negative yaw, and so forth. Refer to Figure A.3.2-3 again for a diagram of the situation.

A.3.2.2.2.1 Solar torque estimation

a. With Solar Sail

1. straight boom

With the straight solar sail, and with nominal trim tab performance, the maximum solar radiation torque magnitude is 1.399×10^{-7} N-m (1.032×10^{-7} ft-lbf). This value came from the equation presented in Figure A.3.2-4, and from Ford Aerospace's GOES-I analysis. The torque is produced about the roll/yaw axes, since there is no imbalance about the pitch axis.

<u>Satellite Configuration</u>	<u>Solar Radiation Torque</u>		<u>Torque Axes</u>
	<u>English</u>	<u>Metric</u>	
Straight Solar Sail	1.032x10 ⁻⁷ ft-lbf	1.399x10 ⁻⁷ N-m	roll/yaw
Canted Solar Sail	2.880x10 ⁻⁴ ft-lbf	3.900x10 ⁻⁴ N-m	pitch
No Solar Sail	2.580x10 ⁻⁴ ft-lbf	3.498x10 ⁻⁴ N-m	roll/yaw

Table A.3.2-1. Estimate of Solar Radiation Torques

2. canted boom

The canted boom caused a more complicated motion to develop. In addition to the larger (when compared to the straight solar sail) coupled roll/yaw torques, there was a sinusoidally varying pitch torque that developed. The pitch torque magnitude was calculated to be 3.9×10^{-4} N-m (2.88×10^{-4} ft-lbf) (memo to F. Bauer, Aug. 27, 1990, "Canted Solar Sail Configuration for GOES-N", from J. Carr). This is approximately 2800 times as large as the torque developed by the straight boom. That is the maximum amplitude of the cyclic torque described above. There is also the problem of mechanical complexity (the shape and deployment of the sail), risk in deploying a boom, and weight. Also, it did not appear that the primary goal of the canted solar sail, reducing thermal loads on the coolers, was adequately met.

b. Without Solar Sail

The solar torque on the spacecraft was also large when there was no solar sail. In this design, the maximum solar radiation torque magnitude was found to be 3.498×10^{-4} N-m (2.58×10^{-4}), a factor of 2500 larger than the solar torque of the straight solar sail option. It is easy to see that this torque is about the roll/yaw coupled axes.

A.3.2.2.2 Momentum management computer program description

The computer code written to determine the effects of the external disturbances and the size of the magnetic torquer assembly was written by D. Henretty of Goddard Space Flight Center's Design Analysis Section in the Guidance and Control Branch. The FORTRAN program determines the radius vector, the velocity vector, aerodynamic torque, gravity gradient torque, magnetic unloading torque, solar radiation torque, and momentum buildup of a spacecraft in the body frame of the spacecraft. The torques and momentums are integrated forward to give the history of the torques and momentums over any number of orbits. The program can use either English or metric units, and parameter variation is accomplished by changing variables such as magnetic gain constants, magnetic coil strength, solar radiation torque, spacecraft mass and inertia properties, and the integration length and step size within a data file.

A.3.2.2.3 Analysis results

The computer program was run for two spacecraft configurations: with a straight solar sail and without a solar sail. The magnetic coil strength was varied to determine uncontrolled (no momentum unloading) and controlled (unloading) momentum buildups. The sinusoidal variation of the momentum (due to the spacecraft's slow rotation about the earth) and the gradual buildup (due to a secular torque) can be seen clearly in Figure A.3.2-5. The maximum momentum buildup (no unloading of the wheels) over one orbit can be seen in Table A.3.2-2. The cyclic pitch torque did not build up momentum over each orbit, the value shown is the calculated maximum momentum buildup over one orbit. That value is the amplitude of a sinusoidally-varying momentum.

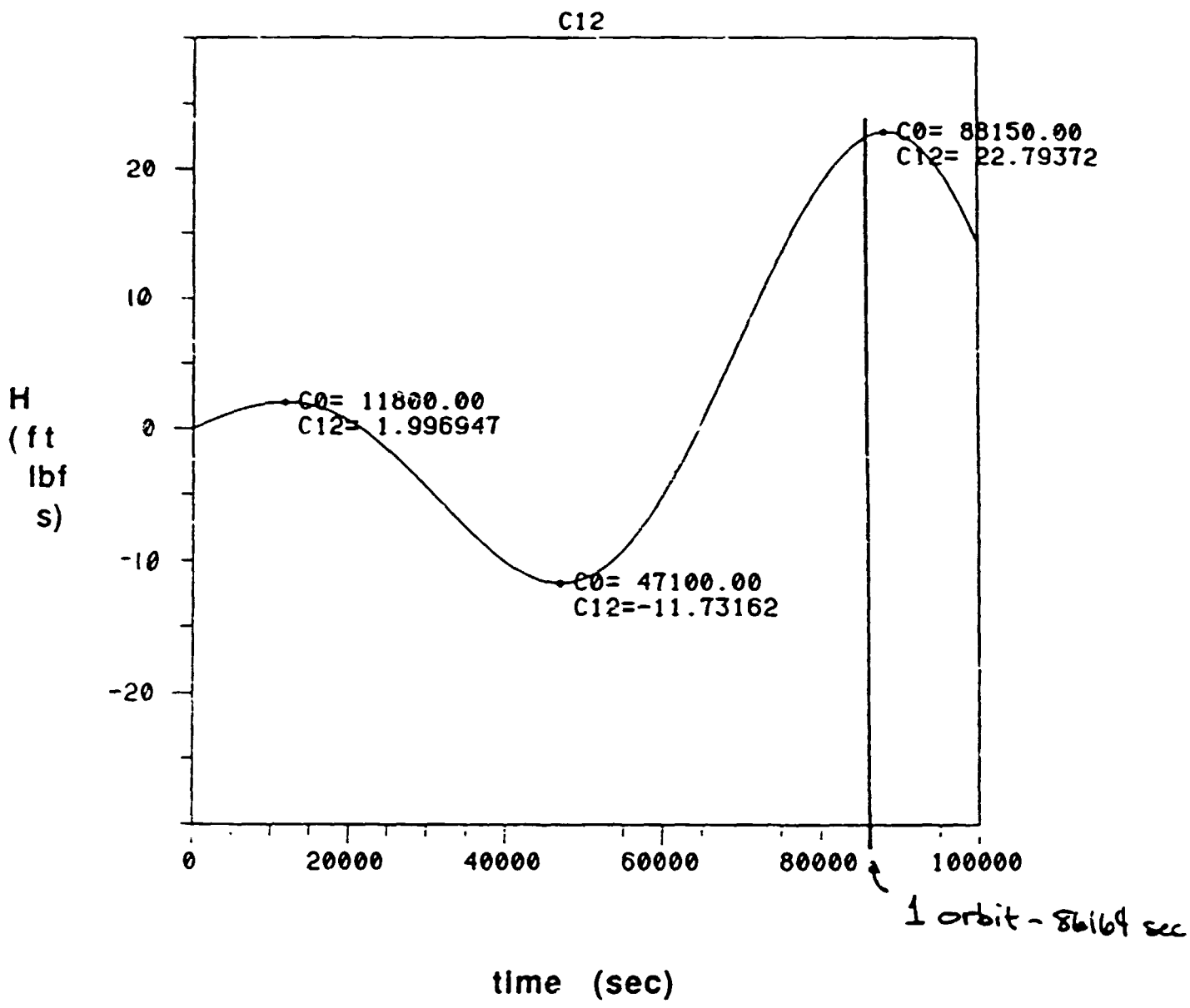


Figure A.3.2-5. Yaw Momentum Buildup Over One Orbit-No Solar Sail

<u>Configuration</u>	<u>Momentum</u>		<u>Axis</u>	<u>Torque variation</u>
straight sail	-.009	ft-lbf-s (.012 N-m-s)	roll	secular
	0.04	ft-lbf-s (.054 N-m-s)	pitch	cyclic
	-.009	ft-lbf-s (.012 N-m-s)	yaw	secular
canted sail	-0.01	ft-lbf-s (.014 N-m-s)	roll	secular
	3.98	ft-lbf-s (5.40 N-m-s)	pitch	cyclic
	-0.01	ft-lbf-s (.014 N-m-s)	yaw	secular
no sail	-22.8	ft-lbf-s (30.9 N-m-s)	roll	secular
	0.05	ft-lbf-s (0.07 N-m-s)	pitch	cyclic
	22.8	ft-lbf-s (30.9 N-m-s)	yaw	secular

Table A.3.2-2. Maximum Momentum Buildup Over One Orbit—No Magnetic Torquer Bars

a. Straight Solar Sail Configuration

With a solar sail, the satellite experienced a solar radiation torque magnitude of 1.399×10^{-7} N-m (1.032×10^{-7} ft-lbf). Since the thrusters were not going to be used for momentum unloading, MTB's were the only devices studied. Without momentum unloading, the maximum momentum buildup was 0.271 N-m-s (0.2 ft-lbf-s). For a magnetic coil strength of 10,000 pole-cm (10 Amp-turn-m², or 10 ATM²), the maximum momentum buildup was less than 0.136 N-m-s (0.1 ft-lbf-s) about the pitch (cross-track, or out of orbit plane) axis over five orbits. A magnetic coil strength of 1,000,000 pole-cm (1000 Amp-turn-m²) was also tested, which resulted in a maximum momentum buildup of less than .108 N-m-s (.08 ft-lbf-s) about the pitch axis. The roll/yaw coupled torque was almost completely balanced by the solar sail, as designed. Small MTE's (10 ATM²) could be used to unload any momentum buildup over five orbits, since the larger MTB's do not greatly reduce the momentum buildup.

b. Canted Solar Sail Configuration

The program did not run this configuration because no inertia properties were available. There was a numerical calculation done that determined the maximum momentum buildup based on the amount of solar radiation torque and the geometry of the satellite. The details can be found in J. Carr's memo of Aug. 27, 1990: the peak amplitude of the cyclic pitch momentum was found to be 5.4 N-m-s. The size of a magnetic unloading system was not established because the program was not able to be run.

c. No Solar Sail Configuration

This configuration was tested twice, once using only magnetics to unload the momentum, and once using thrusters to unload the momentum, with no magnetic torquers. Without wheel unloading, the coupled yaw momentum builds up to about 31 N-m-s (23 ft-lbf-s) after one orbit, as seen in Figure A.3.2-5. In this situation, a magnetic coil strength of 100,000 pole-cm (100 ATM²) was not enough to prevent the coupled roll/yaw momentum from building to greater than 136 N-m-s (100 ft-lbf-s) over five orbits. The momentum buildup was reduced to approximately 3.25 N-m-s (2.4 ft-lbf-s) when extremely large 3,000,000 pole-cm (3000 ATM²) magnetic torquer devices were used.

The maximum momentum the thrusters would have to unload after one orbit occurred at the end of the orbit, in the yaw (Earth pointing) axis; the magnitude was approximately 23 ft-lbf-s (31 N-m-s). Thruster unloading of the reaction wheels is not available with the computer program so it was handled in a separate study; those results are in Section A.3.1.

A.3.2.2.3 Configuration tradeoffs

(Several configuration tradeoff studies were performed.)

A.3.2.2.3.1 Solar sail trades

The first solar sail configuration studied was essentially the GOES-1 structure. The solar sail was at the end of a long straight deployable boom, and was shaped like a frustum of a cone. The solar array was on the south side (along the pitch/orbit normal axis), and the sail was aligned along the north axis. It was designed to be a simple balance for the solar radiation pressure on the solar array. There was little solar torque generated; for example, the gravity gradient torque was of the same magnitude. That performance was compared to the performance of the canted solar sail configuration. The boom was canted to put the sail further from the coolers, reducing the thermal loads seen. The boom would be attached to the north face of the bus, and could be on the anti-Earth edge. The proposed shape for the sail is a cylinder, because the sail is not aligned along an axis of symmetry, but would still need to generate the same balancing torque at all times in the orbit. There are several potential problems with this design, and there are several questions that have to be answered for this option to be considered viable. First, it is not clear that the thermal benefits are large enough to offset the increased mechanical risk associated with a canted boom and sail compared to a straight assembly. Also, there is a pitch torque (and momentum) produced with the canted solar sail, as explained above. This would require a larger pitch reaction wheel, increasing the weight of the system. There is also uncertainty about the thermal performance of the boom material and coating. A solar sail in general is inherently risky, as it is a single point failure mechanism. If any part of the deployment went wrong, there would be no way to balance the solar torques, and no way to unload the momentum with the small torquer bars.

Eliminating the solar sail altogether would have several advantages. The immediate savings would be in spacecraft weight. There would also be a reduced thermal load on the satellite bus and coolers, as there would be no boom to radiate heat. The solar sail pitch torque (canted boom) and the solar array trim tab (straight and canted boom) would be eliminated also. The tradeoff is that the coupled roll/yaw torque magnitude would increase by a factor of 2500; note that this is less than the factor of 2800 increase of the pitch torque with the canted boom compared to the straight solar sail configuration. Thus, with no solar sail, the choice becomes whether to use thrusters to unload the momentum, or to use large magnetic torquers to do the job. The additional fuel required by the thrusters and the added mass have to be considered, but if a thruster failed, there would be redundancy built into the system, and other thrusters could still be used. The magnetic torquers would save on fuel, but torquer assemblies of the necessary size have never been flown, they would be large and heavy, and they would use power that could be budgeted to the instruments.

A.3.2.2.3.2 Thruster firing to dump momentum

There are several items to consider when using thrusters to unload momentum. The thrusters are not perfect; they will not always thrust at their nominal force levels. A worst case estimate is to assume a 10% thrust mismatch between any given pair of thrusters. Also, the axis of the thruster nozzle is not exactly the axis of the thrust vector; a worst-case one degree misalignment is usually assumed for any thruster used. The net result is that to unload the 31 N-m-s

(23 ft-lbf-s) momentum buildup, the jets would have to be fired for about .5 seconds once per day (once per orbit). The thruster imbalance and the thrust misalignment produce force imbalances that change the velocity of the satellite. As discussed in Section A.3.1 of this appendix, this changes the orbit, but not enough to cause ephemeris inaccuracy.

A.3.2.2.3.3 Magnetic torquer sizing

The size of the MTB depends on the design configuration chosen. Based on the results presented above, the straight solar sail design will require 10,000 pole-cm torquer bars. This is an average-sized magnetic system of a type that has been used before. A similar system could be used on the canted sail satellite because the roll/yaw torques and momentums are similar to those of the straight sail. A reaction wheel could handle the cyclic momentum, since it does not build up over several orbits. Using only magnetics to unload the momentum of the no solar sail configuration however, will require large 3,000,000 pole-cm magnetic torquers. This is equivalent to a magnetic coil strength of 3000 Amp-turn-m². Torquers of this size would not be torquer bars, but would be torquer plates, and would have to be wrapped around the satellite bus of the solar array to develop the needed dipole moment. A magnetic system of that size would have a mass of approximately 500 kg - obviously a severe mass penalty. Also, the system would interfere with the magnetometer, and there would be resistive heating, adding to the thermal rejection needs of the system. More power would be needed to keep the magnetics on long enough to unload the momentum.

A.3.2.2.3.4 Configuration selection

Based on the above configurations and analyses, the no solar sail design is the option selected as the baseline configuration. A tentative design is shown in Figure A.3.2-6. There are four momentum unloading thrusters on both the north face and the south face of the spacecraft bus. They are placed at the edges of the face, along the principal axes to minimize cross-coupling torques. The thrusters are not canted. There should be a small magnetic torque capability in the system to unload residual momentums and to counteract small disturbance torques such as the gravity gradient torque. The four reaction wheel assemblies will be set in a tetrahedral arrangement for better momentum storage and torque capability and for redundancy.

A.3.2.3 Conclusions

There are still some issues that need to be addressed. The degree of possible instrument contamination due to thruster firings needs to be determined, as the current thruster locations were chosen only from a momentum management point of view. In addition, the time in the orbit of the momentum unloading must be decided. There may be a location in the orbit to unload a roll/yaw momentum that is more preferable than unloading only when the momentum has reached its maximum value about either the roll or the yaw axis. As the design matures the mass properties will change and will have to be taken into account when determining the attitude effects of the thruster firings and the general dynamics of the satellite. Finally, a more detailed study of the orbit ephemeris must be done, since the thruster firings will affect the orbit of the satellite.

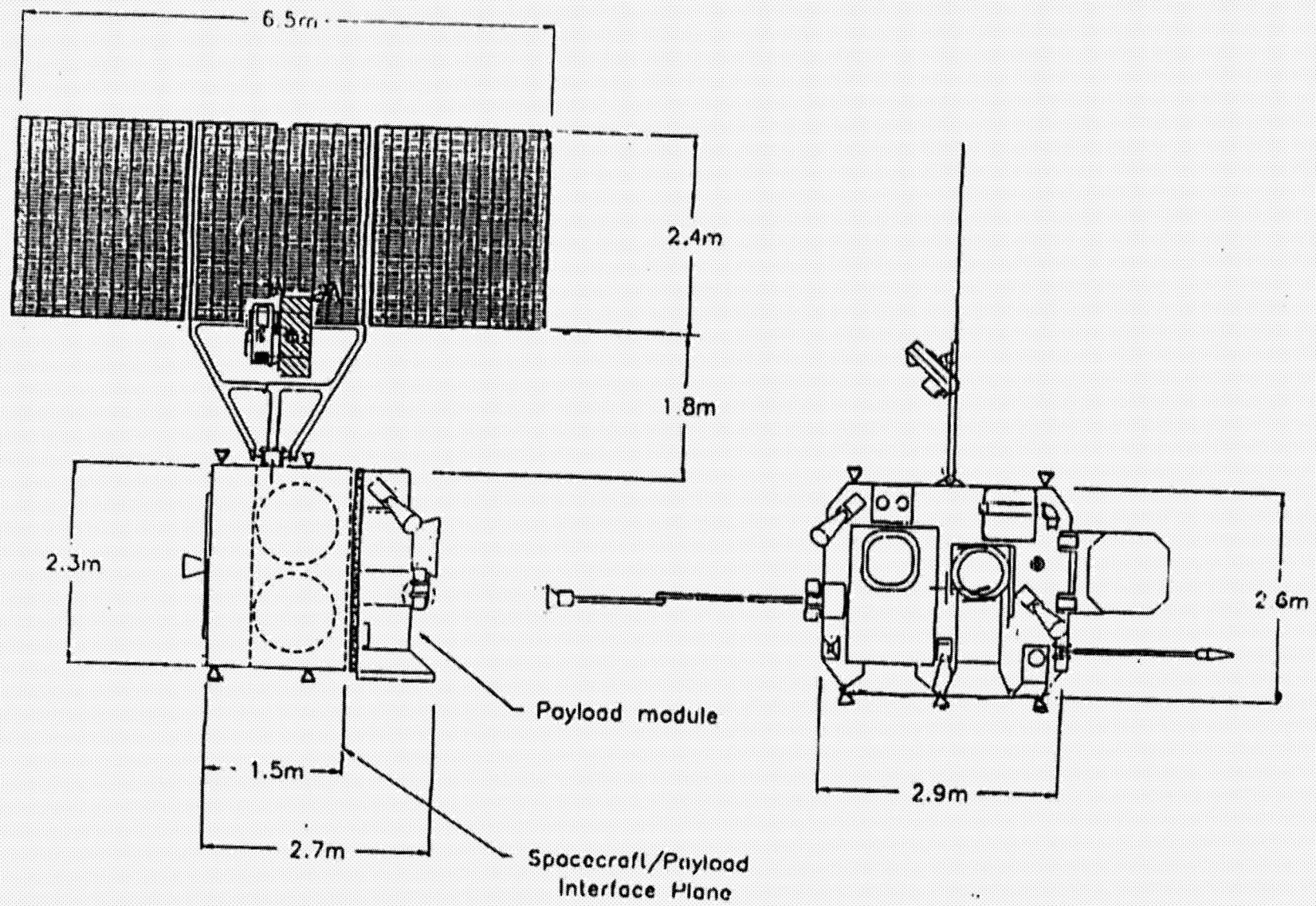


Figure A.3.2-6. GOES-N Option III (orbit configuration)

A.3.3 REACTION WHEEL INDUCED DYNAMIC INTERACTION

A.3.3.1 Introduction

As mentioned in Section A.2.2.2, mass unbalance properties in momentum and reaction wheels impart a sinusoidal disturbance force and torque onto the spacecraft. These unbalance properties are divided into two values: static unbalance and dynamic unbalance. Static unbalance results from the alignment of the wheel center of mass away from the point of rotation. Dynamic unbalance results from the non-zero cross products of inertia in the plane of rotation. Spacecraft disturbances are also related to the rotational velocity of the wheel and the distance from the spacecraft center of mass to the wheel. Given a wheel rotating at W radians per second in the pitch axis, with static unbalance D_s and dynamic unbalance D_d , located at a center of mass L_x , L_y , L_z away from the spacecraft center of mass, the disturbance equations are:

$$F_x = D_s \cdot W^2$$

$$F_y = 0$$

$$F_z = D_s \cdot W^2$$

$$T_x = D_s \cdot W^2 \cdot L_y + D_d \cdot W^2$$

$$T_y = \text{SQRT}(L_x^2 + L_z^2) \cdot D_s \cdot W^2$$

$$T_z = D_s \cdot W^2 \cdot L_y + D_d \cdot W^2$$

This study will examine the range over which the GOES-N reaction wheels will be used and their dynamic disturbance profile as a result of mass unbalance. The mass properties of several flight proven wheels will be discussed, as well as the possible improvements to those properties by use of magnetic suspension wheels. This study will discuss wheels suitable to each of the configurations studied in Section A.3.2.

For each of the configurations studied above, a four wheel, zero momentum control system is assumed. Four wheels are used to provide redundancy along the three axes in case of a single wheel failure. The wheels are sized to provide enough momentum capability to handle twice the momentum buildup possible per orbit in each direction. Each wheel therefore has four times the momentum range of the total spacecraft orbital momentum buildup. This fact allows for one to specify the dynamic operating range that each momentum wheel will see. From the equations above, it is apparent that disturbance torque is proportional to the square of the rotational velocity. Therefore, by limiting the dynamic range of each reaction wheel, it is possible to cut the output torque by a square of the amount the range is limited.

Dynamic interaction is of consequence on the present series of GOES spacecraft due to flexible body modes that are significant at ranges near 100Hz (the dynamic range of the GOES-I momentum wheel). By limiting the dynamic range to 50Hz, one not only lessens output torque by 75%, he will reduce the likelihood of flexible mode interactions that will increase the amount

of torque that is seen by the spacecraft. For those two reasons, this study will attempt to minimize the amount of output torque by limiting the dynamic range for every reaction wheel to 50Hz (3000 rpm).

A.3.3.2 Study results

Two classes of wheels were studied to match the two significant spacecraft configurations (with and without a solar sail). For the configuration that included a solar sail, reaction wheels that provide on the order of 5 Newton-meter-seconds (NMS) of momentum are recommended. In this class of wheel, one finds products from two major vendors: Bendix and Teldix. Bendix has built wheels for the INSAT program that provide approximately 4 NMS momentum capability at a maximum velocity of 3000 rpm. Generally, the static and dynamic unbalance spec values are 3.6×10^{-5} kg-m and 9.15×10^{-6} kg-m² for this wheel. Assuming a moment arm of 1 meter, the cross axis torque produced by this wheel running at 50 Hz would be 4.45 N-m.

Another candidate would be the Teldix GOES reaction wheel. It provides three NMS momentum capability at 3000 rpm. The static and dynamic unbalance specs on the GOES reaction wheel are 1.08×10^{-5} kg-m and 1.4×10^{-6} kg-m². Again assuming a one meter moment arm, this creates a cross axis torque of 1.2 N-m. In this case, the torque seen by the spacecraft is less than that seen by a momentum wheel on the present GOES-I system. As expected, the torque disturbance caused by the smaller wheels is generally smaller than seen on the present system, which has cross axis disturbance torques of 7.46 N-m due to the contribution of two momentum wheels in the pitch axis. However, variations in static and dynamic unbalance cause the Bendix reaction wheel to actually produce more torque than the larger Teldix reaction wheel.

The second spacecraft configuration would remove the solar sail completely. Since momentum buildup per orbit would be on the order of 30 NMS, the wheels would be sized to provide 60 NMS momentum storage in each direction. Three vendors build wheels in this class: Bendix, Honeywell and Teldix. The Bendix and Teldix wheels would be modified versions of the INSAT and GOES momentum wheels to allow for bi-directional commutation and sensing. Since each provides for almost 60 NMS at 6000 rpm, there would be ample momentum storage capability at 3000 rpm in each type of wheel. In each case, the wheel vendor uses the same spec for both large momentum wheels and small reaction wheels. Thus, the values for torque at 3000 rpm due to the reaction wheels computed above is the correct value for these larger modified momentum wheels.

The third vendor, Honeywell, has built larger reaction wheels for several Multimission Modular Spacecraft (MMS) in the past. For example, the UARS reaction wheel can provide almost 80 NMS momentum storage at a velocity of 6000 rpm. Limiting dynamic range at 3000 rpm gives the UARS wheel a storage capacity of 40 NMS at a disturbance torque of 4.45 N-m (spec values are the same as Bendix values). In each of the three large wheel cases, disturbance torque is similar to torques found in the smaller reaction wheels if the dynamic range is limited to 50 Hz (3000 rpm). Thus, only differences in static and dynamic unbalance values causes differences in torque profiles between wheels rotating at the same velocity.

A.3.3.3 Magnetic bearing merits

Another way to reduce disturbance torque as a result of mass unbalance is by use of actively controlled magnetic suspension as opposed to ball bearings. Magnetic suspension systems are discussed at length in Section A.2.2.2. In review, magnetic suspension allows disturbance torques to be isolated from the spacecraft. Also, magnetics allows for vernier gimbaling of the spinning mass so that the wheel can be used as a control moment gyro. There are no effects of torque ripple as the wheel changes direction. In fact, magnetic suspension may allow for a two order of magnitude decrease in disturbance torque caused by various wheel characteristics, including mass unbalance. Obviously, a space qualified magnetic suspension system is preferable to a mechanical ball bearing system in terms of failure risk, disturbance torque and mission adaptability.

However, as mentioned in Section A.2.2.2, there are no space qualified magnetic bearings in production at this time. Vendors are currently building engineering "proof" models that may or may not be applicable to reaction wheel technology in the next decade. There is some risk in choosing new hardware over existing technology for the GOES-N mission. This risk may be outweighed by the vast improvements that will be gained through the use of magnetics. The use of magnetics is not recommended for Option I since the guidelines specified only minor modifications to existing hardware. In order to minimize assumed risk at the Phase-A level, magnetics cannot be recommended as a baseline to the Option II or III spacecraft. As mentioned before, we must continue to monitor technology progress during Phase-B to keep our options open with regards to magnetic suspension bearings. (See Section A.2.2.2 for more on magnetic bearings.)

A.3.3.4 Conclusions

This study has examined the various disturbance torques created by nominal use of candidate Option III reaction wheels. The dynamic range has been specified not to exceed 50Hz (3000 rpm) in order to prevent high mass u.balance torques. Of the candidate wheels selected, only the present GOES wheels were able to meet or exceed the torque output of the present GOES-I system. Since no significant flexible modes are in the 50Hz range, pointing performance is expected to be improved over the present system (which has a significant mode near 100Hz) for any of the wheels chosen. Further enhancements (on the order of two orders of magnitude) can be realized through the use of magnetic bearings. This system isolates the disturbance torques on the rotating mass of the wheel, vastly improving pointing performance. However, no magnetic bearings are presently space qualified. It is recommended that these systems be studied in Phase-B for schedule and cost assessment, since there will be more information as to actual costs and the possibility of space qualification after engineering units currently in development are completed and tested.

A.3.4 CONTROLLER DESIGN

The spacecraft control function for GOES-N Options II/III is provided by a fully redundant gyro-star tracker-reaction wheel system illustrated in Figure A.3.4-1. The control system will employ the DRIRU II dually-redundant inertial reference package for attitude sensing with a set of three Charged-coupled-device (CCD) star trackers to provide updates to the DRIRU II. The DRIRU II will provide attitude data in all three spacecraft axes to the Attitude Control Electronics (ACE). The ACE computes a control torque level and sends this value to the reaction wheel electronics as a torque command. The reaction wheel electronics receives the torque command and adjusts the reaction wheels' speeds to provide the commanded level of control torque to the spacecraft. The control actuation is achieved with a set of four (4) reaction wheels in a pyramidal arrangement which provides redundant torque capability in all spacecraft axes. The mass properties used in the design of the spacecraft controller are listed below. The control law which computes the control torque command is resident in the ACE. The control law is a standard Proportional-Integral-Derivative (PID) controller. (Figure A.3.4-2) The PID controller gains for each spacecraft axis KI, KP, and KR for a standard PID controller are functions of the spacecraft's inertia in the particular axis and the bandwidth of the controller which is chosen by the designer. The gains were computed using the standard PID forms as follows:

$$\begin{aligned}K_p &= (2 \cdot \pi \cdot I \cdot W)^2 \cdot I \\K_d &= (4 \cdot \pi \cdot 0.707 \cdot BW) \cdot I \\K_i &= (2 \cdot \pi \cdot I \cdot W)^3 \cdot 0.06436 \cdot I \\B_w &= 0.1 \text{ Hz Controller Bandwidth} \\I_{xx} &= 2939 \quad I_{yy} = 1720 \quad I_{zz} = 2900 \text{ (kg-m}^2\text{)}\end{aligned}$$

The controller bandwidth was chosen to be 0.1Hz. At this point in the design 0.01Hz provides a proper balance between spacecraft pointing performance and pointing stability as well as avoiding the significant low frequency flexible modes of the spacecraft. The controller is able to operate at a much higher bandwidth than the GOES-I controller because there is no need to filter out the large magnitude noise of the GOES-I Earth Sensor. Increasing the controller bandwidth improves performance and speeds the recovery from maneuvers such as stationkeeping. However the first significant flexible mode of the spacecraft solar array is expected to be between 0.5 and 1.0 Hz. The controller therefore will not be capable of exciting this mode.

A.3.4.1 Stability analysis

The GSFC INCA program was utilized to perform stability analysis of the Option II/III spacecraft controller. For the stability analysis the reaction wheels were modeled as a first order lag, the spacecraft as a rigid body, and the DRIRU II as a 15Hz bandwidth device with a second order lag. Figures A.3.4.1-1,2 show the root locus of the roll axis controller with an upper gain margin of 24 dB at 1.9Hz and a lower gain margin of 26 dB at 0.02Hz. The controller has 58 degrees of phase margin at the gain crossover frequency of 0.16Hz. The controller is deliberately robust at this point in the design because the plant dynamics modeled in the analysis did not include structural flexibility. The stability margins will not be as high when a more complete flexible model of the spacecraft structure is included.

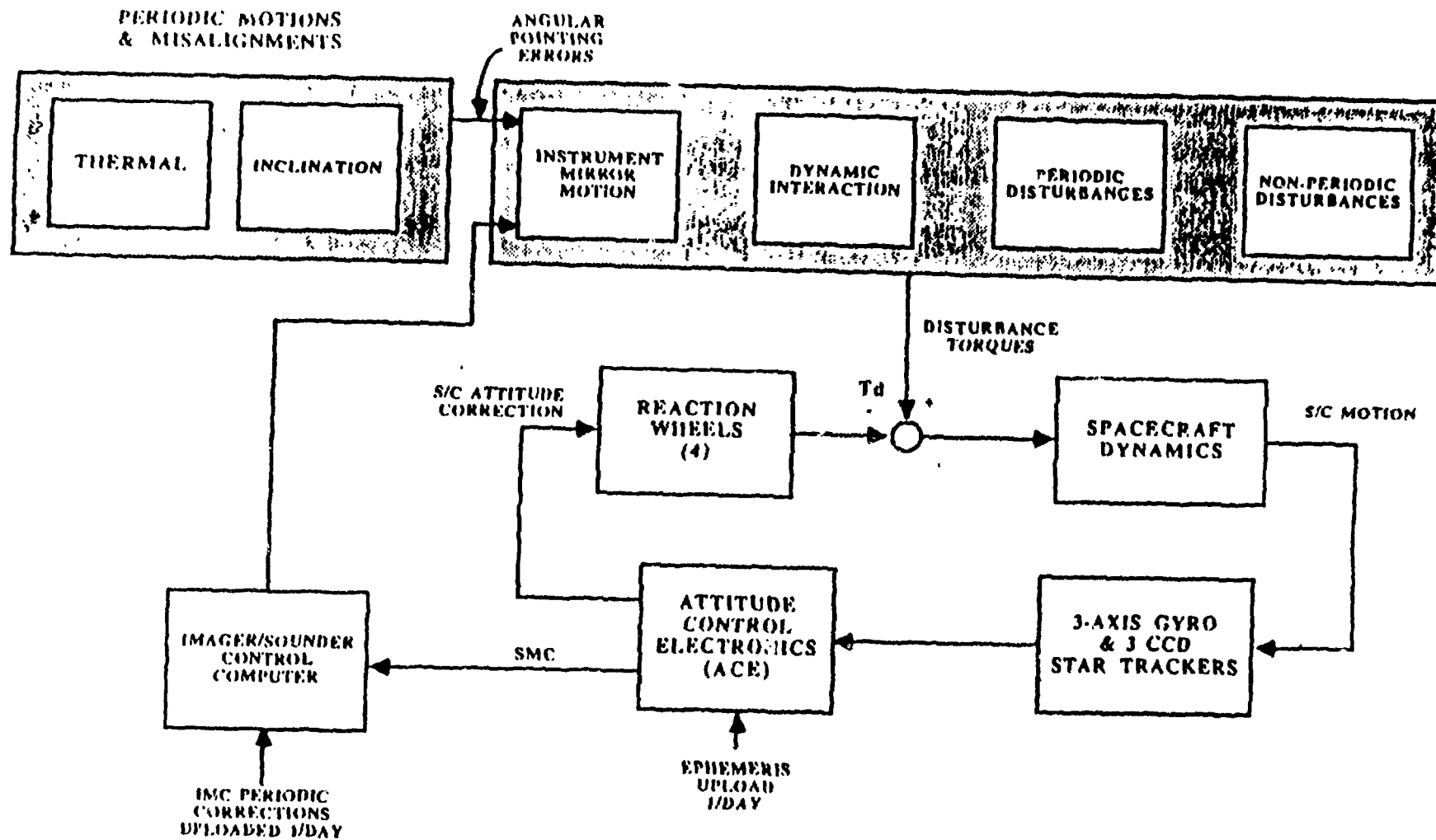
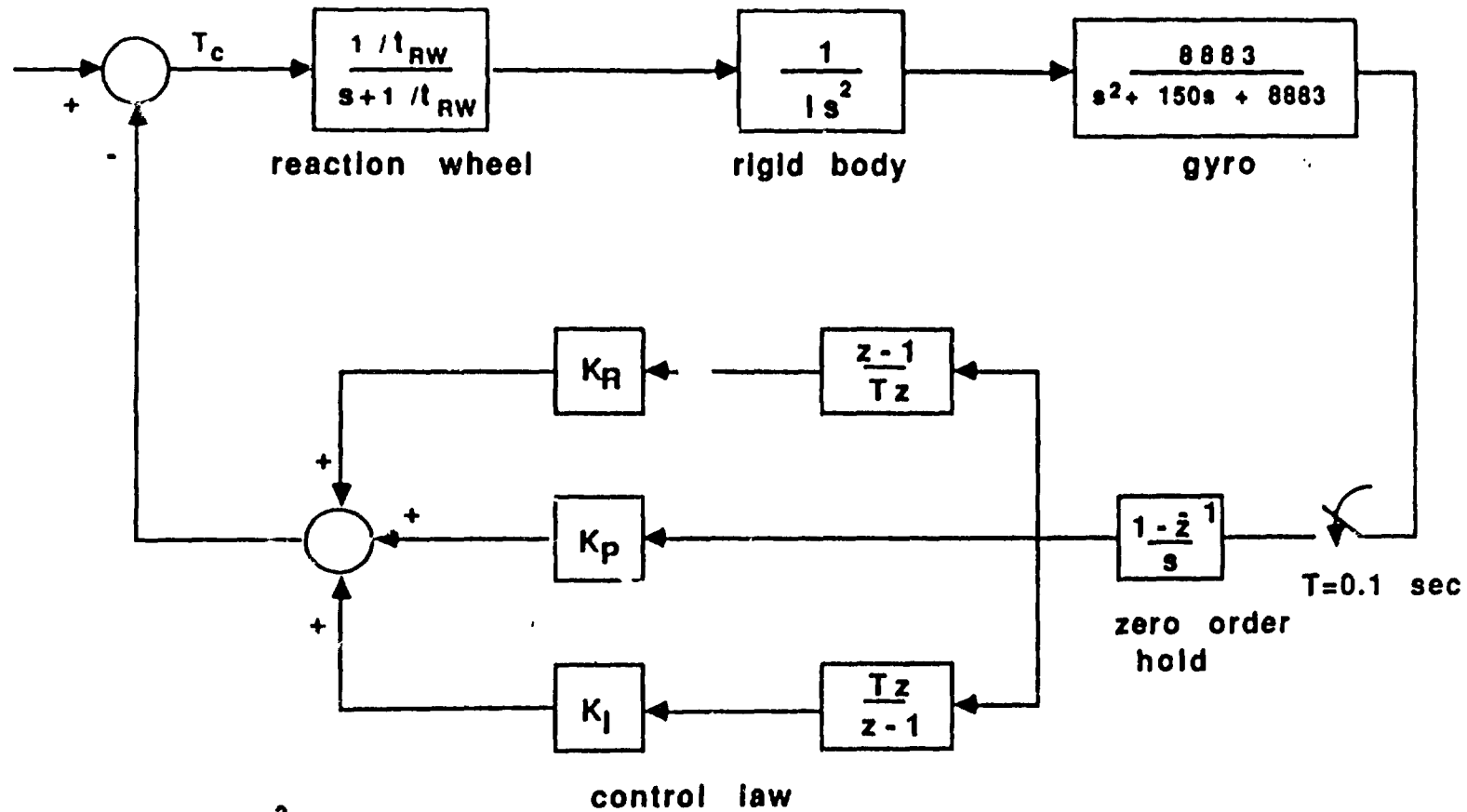


Figure A.3.4-1. GOES-N Options II & III Spacecraft Control System Conceptual Block Diagram



$$K_p = (2 \cdot \pi \cdot BW)^2 \cdot I$$

$$K_i = 4 \cdot \pi \cdot 0.707 \cdot BW \cdot I$$

$$K_d = (2 \cdot \pi \cdot BW)^3 \cdot 0.06436 \cdot I$$

Note: Controller Bandwidth = 0.1 Hz (BW=0.1)

Figure A.3.4-2. GOES-N Spacecraft Control

INCA

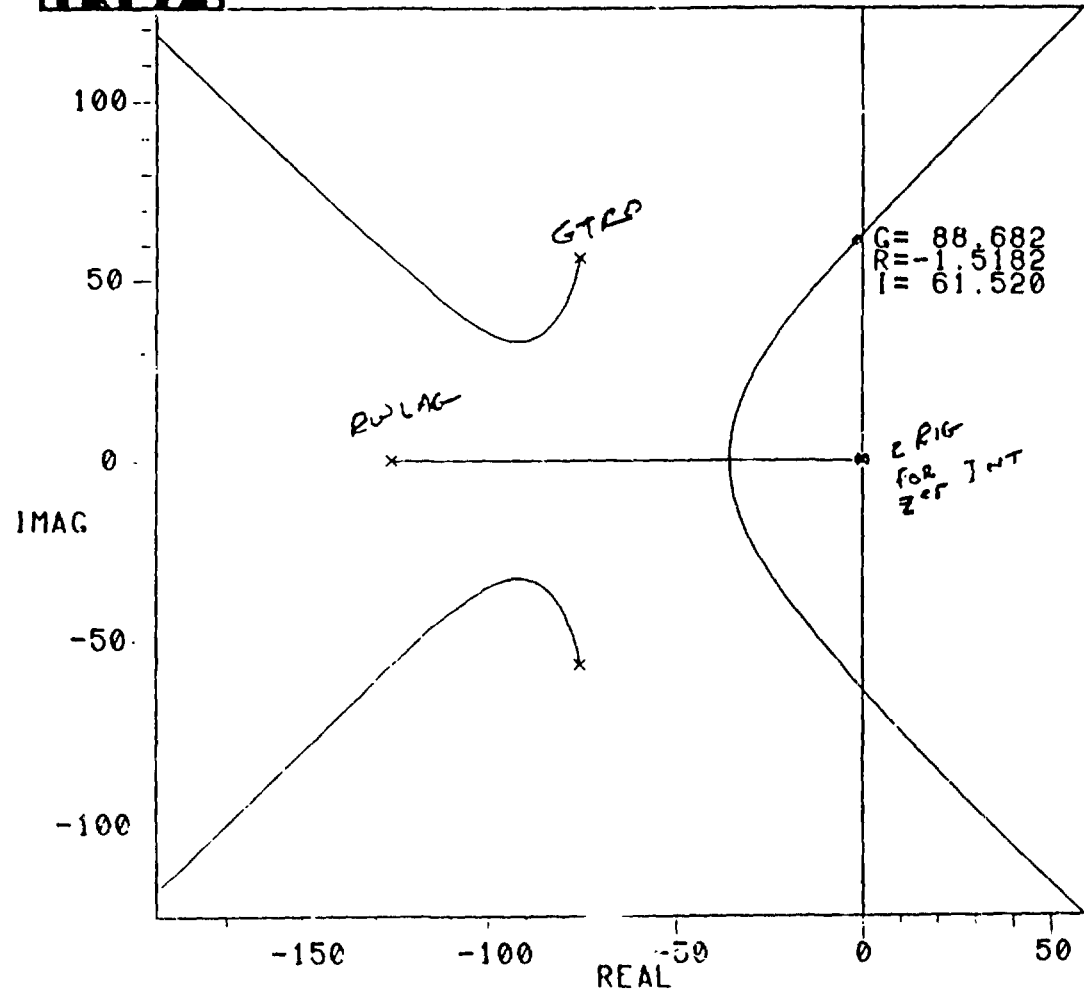


Figure A.3.4.1-1. Root Locus of GOES-N Controller

INFA

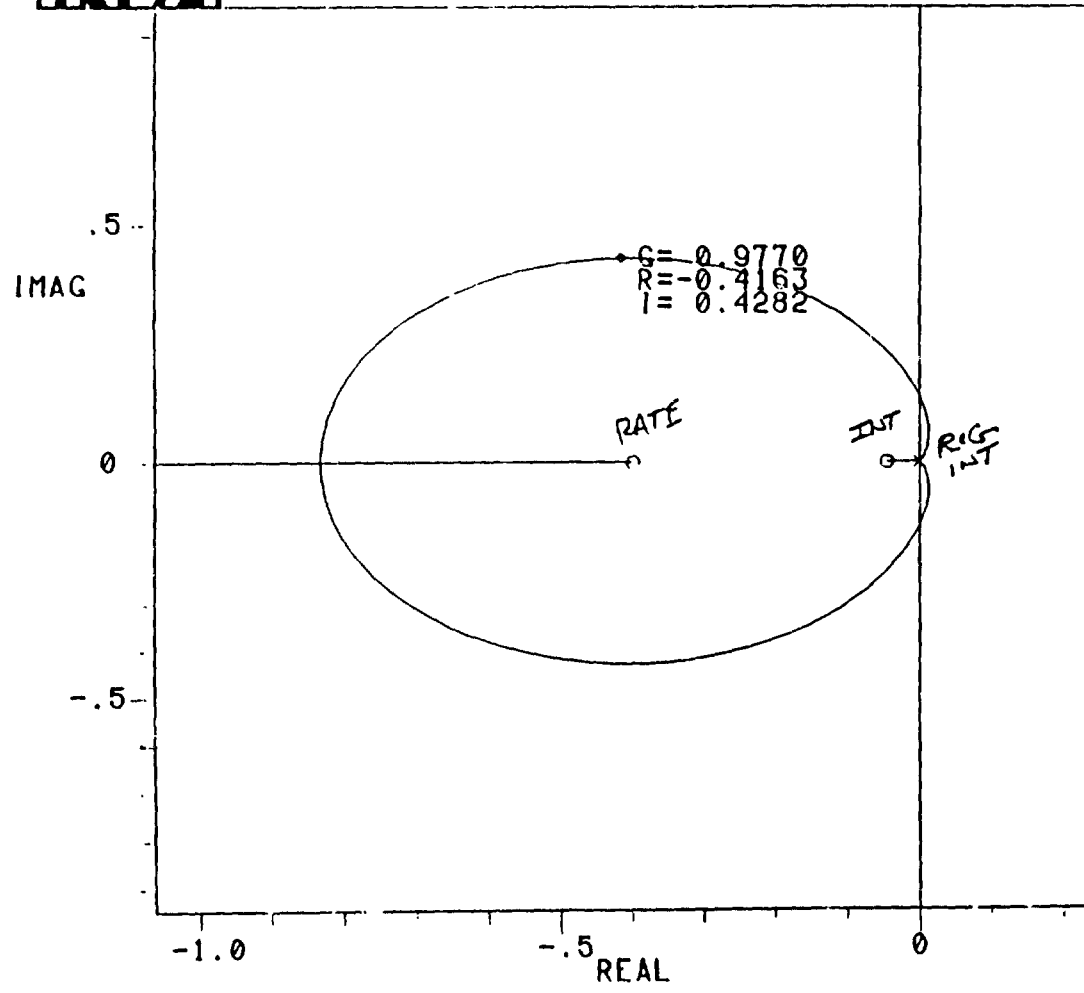


Figure A.3.4.1-2. Root Locus of GOES-N Controller

A.3.5 SPACECRAFT MOTION COMPENSATION

A.3.5.1 Introduction

The spacecraft controller with its bandwidth of 0.1Hz will be capable of an impressive level of spacecraft line of sight pointing. However, the GOES-N instruments will require a compensation system to attenuate disturbances of frequencies that are above the controller's capability. Therefore, on GOES-N, a Spacecraft Motion Compensation (SMC) system will be utilized. The SMC concept attempts to sense at a high frequency, the residual motion of the spacecraft with the DRIRU II/star tracker system and calculate and feed forward to the instrument servos a real-time gimbal correction to compensate for the spacecraft motion.

Heritage for the SMC comes from the Image Motion Compensation System developed for the ASTRO-1 payload that will fly on STS-35. The ASTRO-1 STS-35 Spacelab payload consists of four telescopes mounted on two pointing systems. Three ultraviolet viewing telescopes are end-mounted through a cruciform structure on the ESA designed Instrument Pointing System (IPS). The Ultraviolet Imaging Telescope (UIT) built by Goddard Space Flight Center was one of the telescopes on the IPS. UIT required better pointing performance than the IPS was capable of. Thus, an Image Motion Compensation (IMC) capability was incorporated into UIT to improve the jitter performance at the telescope focal plane. The IMC concept is unique in that the payload motion is sensed by a gyro/star tracker pair and the sensed motion is fed "open loop" to articulate the UIT secondary mirror. Through this technique the payload motion, observed by the sensors, is compensated at the instrument focal plane to jitter levels which are well below its specified requirements.

A similar technique called Spacecraft Motion Compensation (SMC) will be employed on GOES-N. The DRIRU II/star tracker combination will provide attitude information to the spacecraft at 10Hz. The attitude information will also be transformed to instrument servo coordinate frames and sent to the instruments at 50Hz. This information will be used by the servo controller loops as a position correction command to attenuate disturbances up to 5Hz. (Figure A.3.5.1-1).

A.3.5.2 Disturbance environment

In developing the SMC for GOES-N, an attempt was made to get a feel of the possible disturbance environment the spacecraft may experience. Ford Aerospace Co. document TR107:9 attempts to quantify the torques the GOES-I spacecraft is expected to encounter. Figures A.3.5.2-1,2 show the approximate profiles of the torque sources. The solar array stepping and blackbody calibration of the instrument mirrors exert the largest magnitude torques. The disturbances contain frequency components as low as 0.1Hz for part of the blackbody calibration to above 10 Hz for mirror scan motions.

As the frequency of a disturbance becomes higher it can more and more be accurately modeled as a sinusoidal function:

$$T = KT \sin \omega t$$

- Direct (Gyro/Star Tracker) Sensing of Spacecraft motion at High Rate
 - 50 Hz DRIRU
 - 1 Hz Star Tracker
- Feed forward command signal computation and output to Imager and Sounder servos

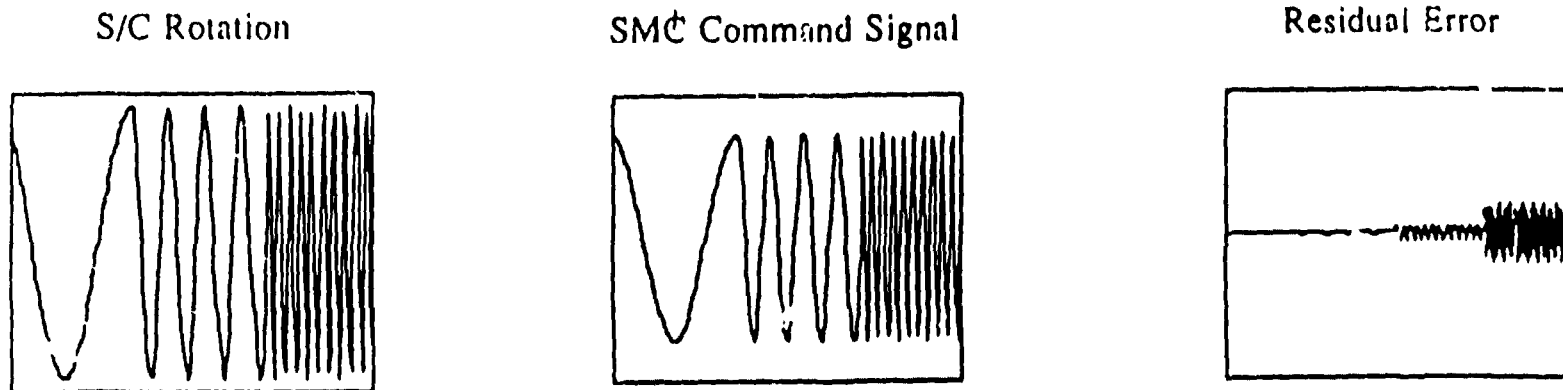
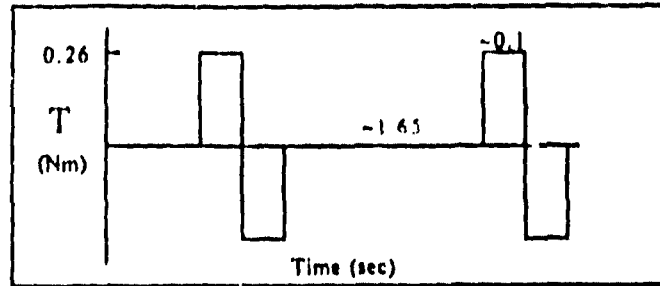


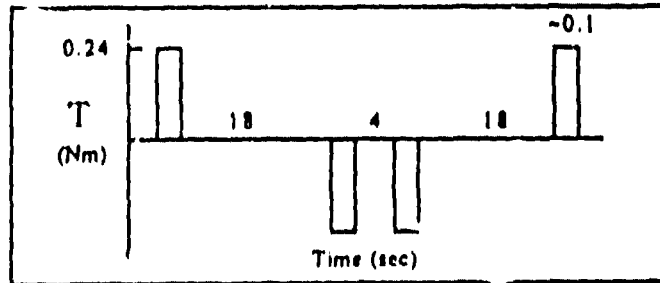
Figure A.3.5.1-1. Spacecraft Motion Compensation

Solar Array Stepping
(Pitch E/W)



$T \approx 0.26 \text{ Nm}$
 $f \approx 0.60 \text{ Hz}$
 $\approx 10 \text{ Hz}$

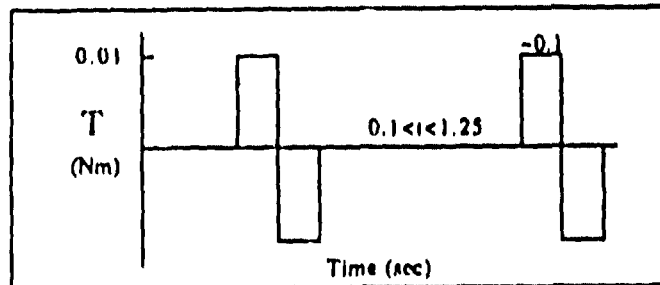
Black Body Calibration
(Roll N/S)



Note: Event repeated every 10-20 min

$T \approx 0.24 \text{ Nm}$
 $f \approx 0.25 \text{ Hz}$
 $\approx 0.056 \text{ Hz}$

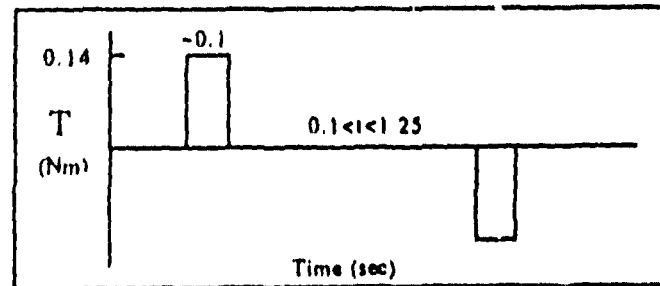
imager
(Roll N/S)



$T \approx 0.01 \text{ Nm}$
 $f \approx 0.80 \text{ Hz}$
 $\approx 10 \text{ Hz}$

Figure A.3.5.2-1. GOES Internal Disturbance Torques

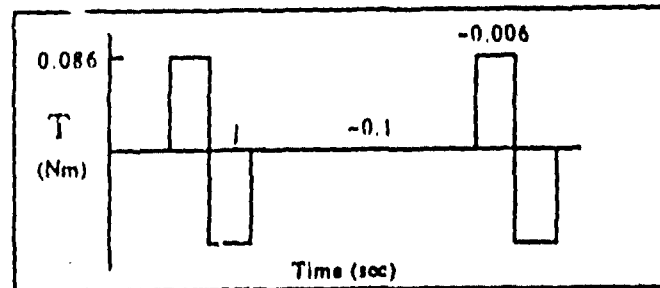
Imager
(Pitch E/W)



Note: Event repeated for every scan line

$T \approx 0.14 \text{ Nm}$
 $0.78 \text{ Hz} < f < 10 \text{ Hz}$

Sounder
(Pitch E/W)



$T \approx 0.086 \text{ Nm}$
 $f \approx 10 \text{ Hz}$

Figure A.3.5 2-2. GOES Internal Disturbance Torques

An uncontrolled system's response to such an input is inversely proportional to its frequency squared:

$$\begin{aligned} T &= KT/w \cdot \sin wt \\ \dot{\theta} &= -KT/W^2 \cdot \sin wt \\ \theta &= -KT/w^2 \cdot \sin wt \end{aligned}$$

Therefore, for a given level of torque, if it is applied at increasing frequencies, the system's response will decrease:

$$\theta = -KT/I \cdot w^2 \cdot \sin wt$$

and thus compensation for this disturbance may not be required to preserve the system's performance.

The spacecraft controller has a bandwidth of 0.1Hz and is not capable of attenuating disturbances above that frequency. Disturbances above that level are uncontrolled by the controller. The disturbances identified in Figures A.3.5.2-1,2 contain frequency components across a range of frequencies above the 0.1Hz controller bandwidth.

The spacecraft cannot attenuate these disturbances, and they will cause spacecraft jitter. Therefore a Spacecraft Motion Compensation (SMC) system was developed in an attempt to compensate for disturbances in a mid-range of frequencies above the spacecraft controller and below the frequency levels that the spacecraft will not respond to significantly.

Looking at the east/west imager scan as an illustration, the rigid body momentum exchange can be approximated by the following relations:

$$ISC \cdot WSC = IEW \cdot WEW$$

The imager moves at 10 o/s, the spacecraft pitch inertia is 1720, and the imager pitch inertia is 0.035 kg-m². This gives

$$\begin{aligned} 1720 \cdot WSC &= 0.035 \cdot 10 \text{ deg o/s} \\ WSC &= 0.000203488 \text{ deg o/s} = 3.55 \mu\text{s} \end{aligned}$$

A scan of 1 second would rotate the uncontrolled spacecraft 3.55 μr which translates into spacecraft line-of-sight error. However, if a 0.1 second scan was approximated by a torque sinusoid:

$$\begin{aligned} T &= 0.14 \cdot \sin 62.8t \quad (\text{N-m}) \\ \theta &= 0.14 / (62.8^2 \cdot 1720) = 0.021 \mu\text{r} \end{aligned}$$

Obviously the higher frequencies motions are less of a concern. Figure A.3.5.2-3 summarizes the torque environment for the spacecraft in frequency range in question.

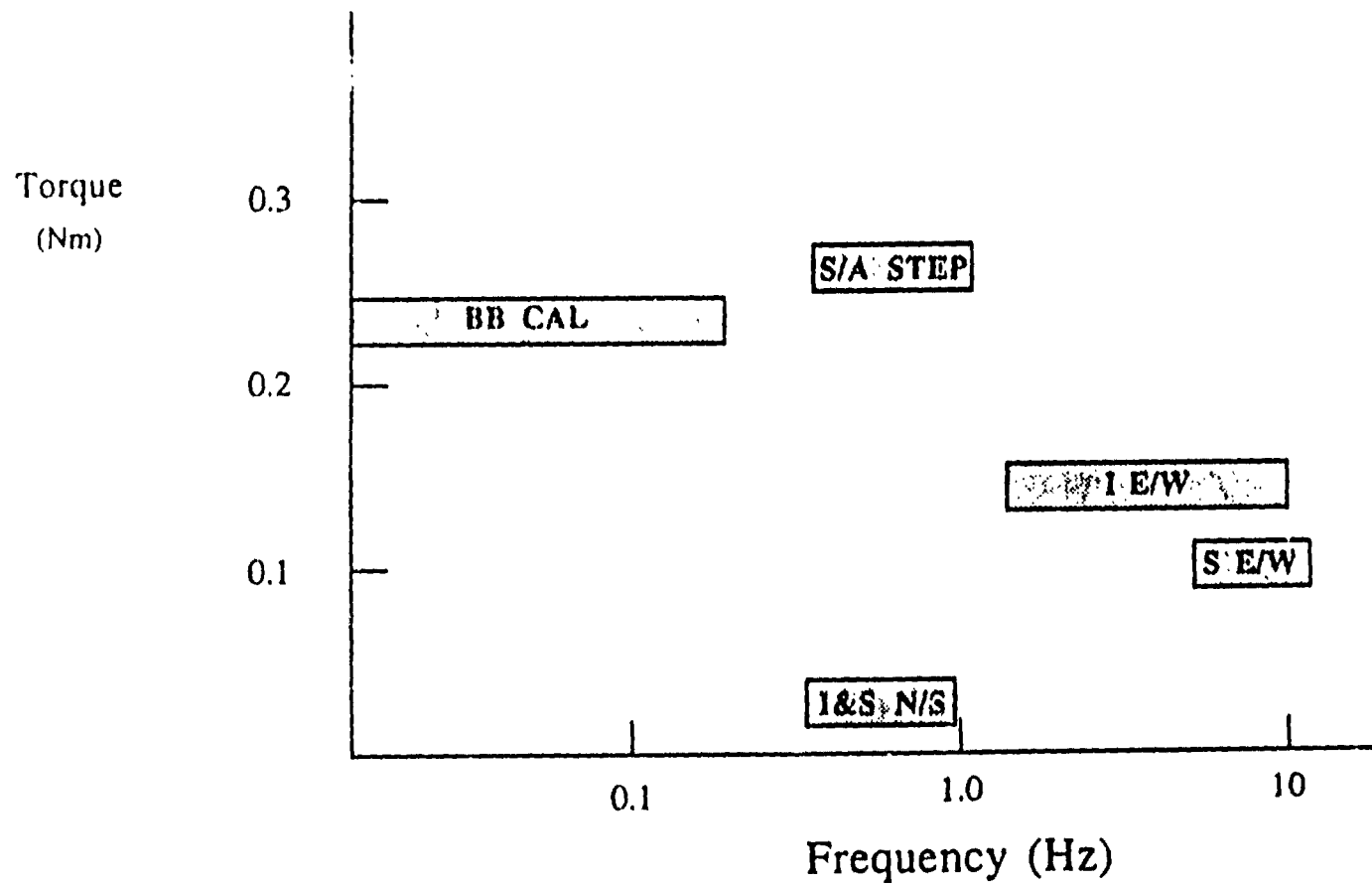


Figure A.3.5.2-3. Spacecraft Internal Disturbance Torques

A.3.5.3 SMC configuration

The SMC system enhances the instrument pointing performance at the focal plane by sensing spacecraft jitter and compensating for these errors by modifying the gimbal angle commands in the instrument servos. Attitude motion of the payload is sensed using a combined gyro/star tracker system. The Dry Rotor Inertial Reference Unit DRIRU II, developed by Teledyne, is used to provide high rate (50Hz) attitude data. Gyro drift estimation and thermal drift updates will be provided by the star tracker.

A.3.5.4 Software algorithm description

A Kalman filter algorithm embedded in the AOCE combines the sensor data to provide attitude error estimates to the spacecraft at 10Hz and the SMC at 50Hz. These digital errors are sent open loop to the instrument servos. The DRIRU II is sampled at 50Hz and the ASTROS star tracker is sampled at 1Hz to remove drift from the DRIRU II signal. Within the AOCE the error signals undergo a coordinate transformation to the gimbals' coordinate frame. Figure A.3.5.4-1.

A.3.5.5 Interface definition

The SMC requires the SMC error signal generated in the AOCE to be transferred to the digital controller resident in the instruments. Before being transmitted, the AOCE transforms the attitude correction to the gimbals' coordinate frame. The gimbal correction is sent at 50 Hz to the instrument servo controller. The interface is defined as an AOCE serial output through a cable to the instruments.

A.3.5.6 Command and telemetry requirements

The instrument telemetry system will relay servo and gimbal information to the ground. The output of the AOCE will be telemetered and the AOCE will receive commands from the ground to switch SMC operating modes.

A.3.5.7 Performance expectations

The INCA program was utilized to estimate the disturbance attenuation of the SMC. The closed loop transfer function of the East/West servo was rearranged to form a transfer function of servo error response to AOCE position correction command. (Figure A.3.5.7-1) Figure A.3.5.7-2 shows the Bode diagram of such a transfer function. The transfer function includes a lag due to the gyro dynamics and computational delay of the command signal. The figure depicts the SMC attenuation achieved using the gyro/star tracker pair to supply the gimbal correction at 50Hz to the GOES-I instrument servos. Below a disturbance frequency of 5Hz, disturbances are attenuated, and at 0.1Hz an order of magnitude performance improvement is achieved. Figure A.3.5.7-3 summarizes the enhanced disturbance rejection of the GOES-N spacecraft with the SMC capability for jitter at the instrument focal plane.

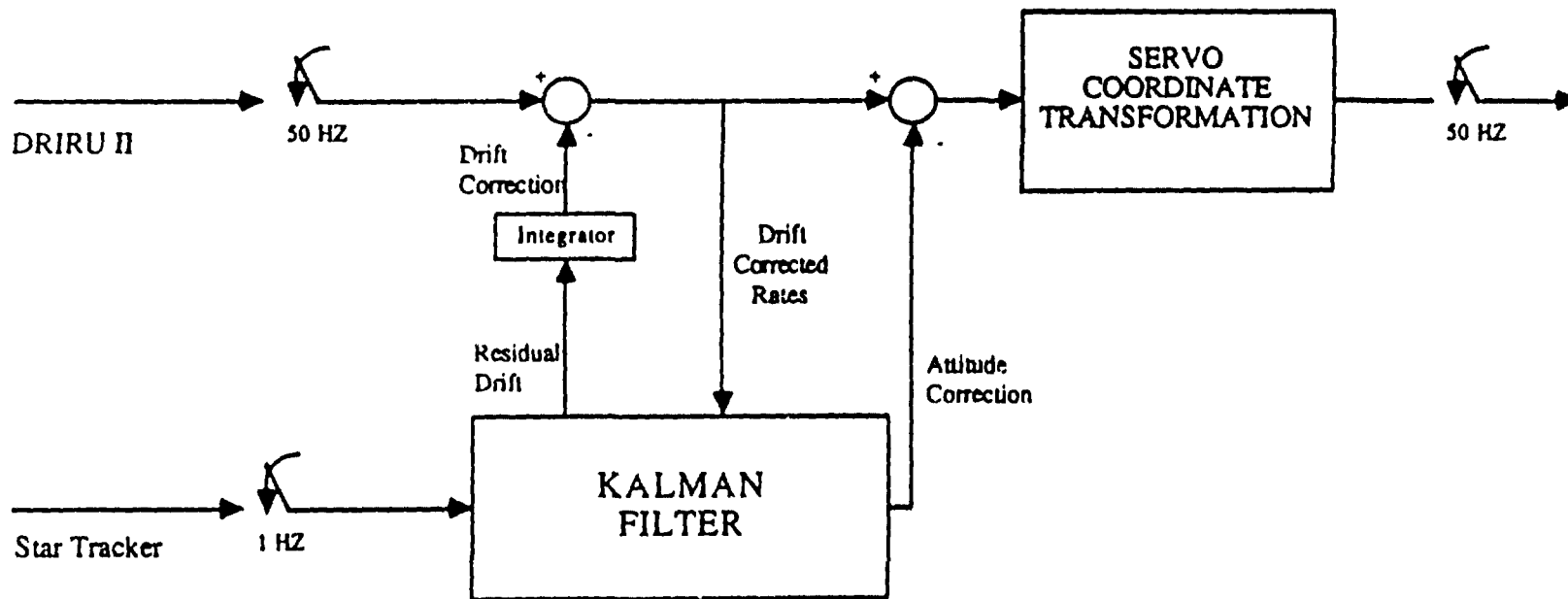
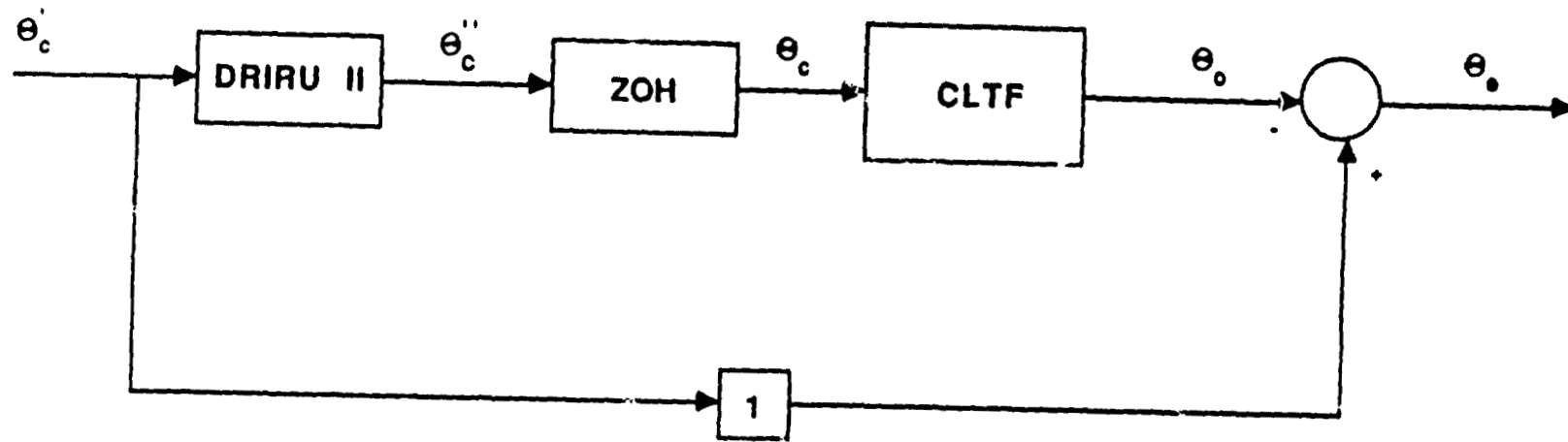


Figure A.3.5.4-1. Kalman Filter Algorithm



$$\ddot{\theta}_o = \ddot{\theta}_c - \ddot{\theta}_c \cdot \text{DRIRU} \cdot \text{ZOH} \cdot \text{CLTF}$$

$$\frac{\ddot{\theta}_o}{\ddot{\theta}_c} = 1 - \text{DRIRU} \cdot \text{ZOH} \cdot \text{CLTF}$$

Figure A.3.5.7-1. Spacecraft Motion Compensation

INBA

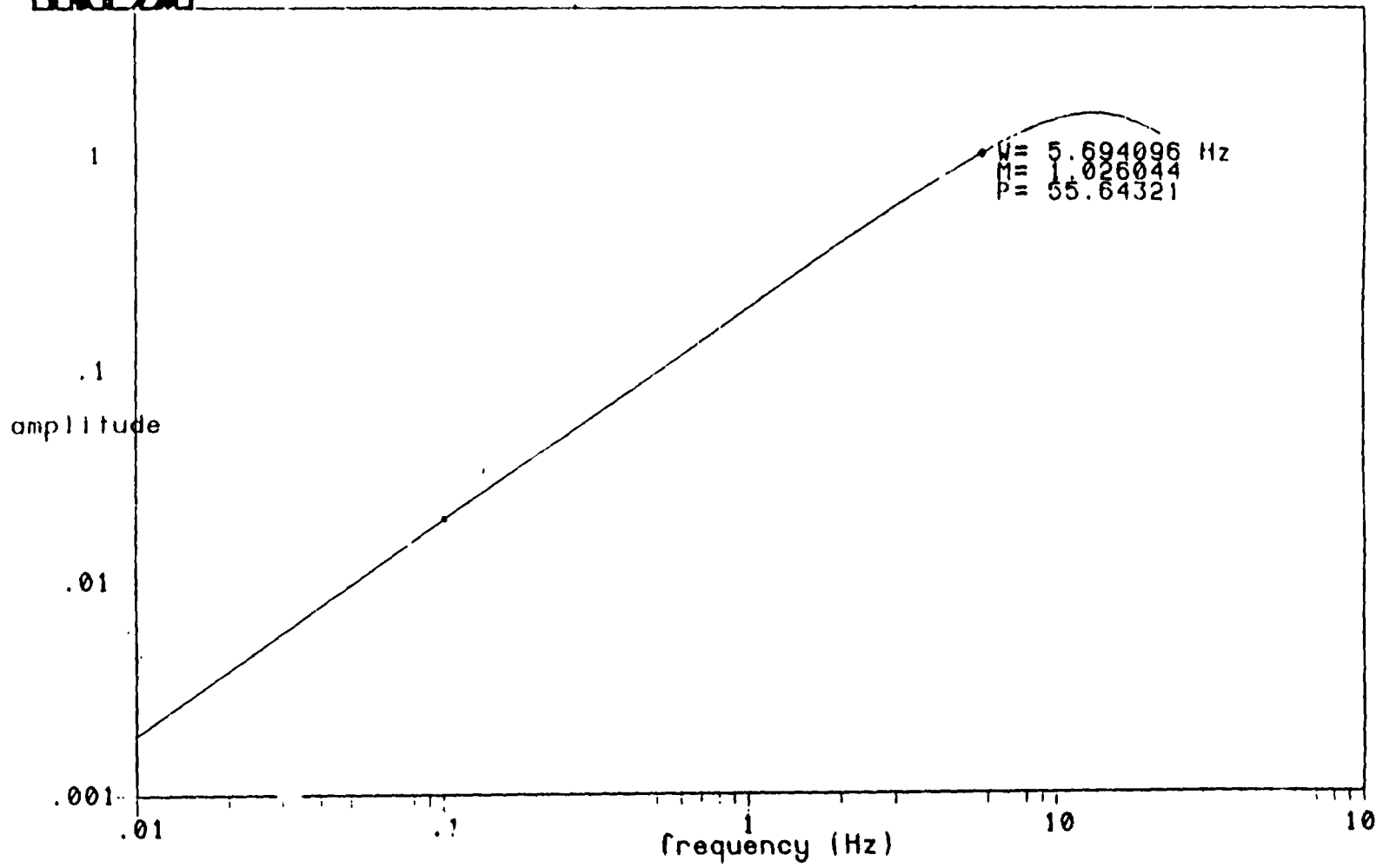


Figure A.3.5.7-2. Spacecraft Motion Compensation

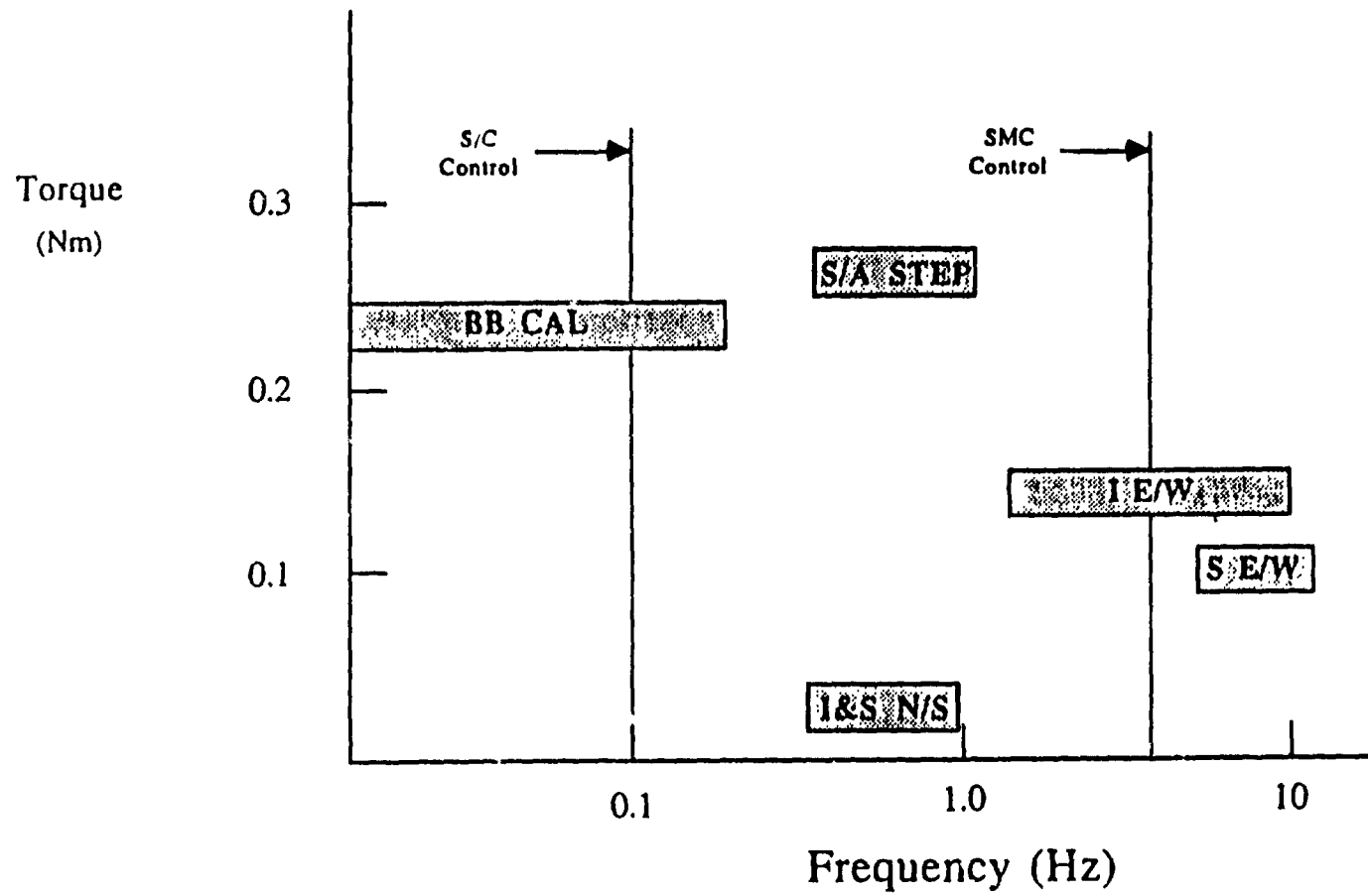


Figure A.3.5.7-3. Spacecraft Internal Disturbance Torques

A.3.5.8 Spacecraft impacts

The impacts on the spacecraft appear to be minimal. No additional sensors are required. The AOCE has more than enough capability to handle the computational burden of spacecraft control and SMC. All that would be required is the cabling to transmit the gimbal correction from the AOCE to the instrument servos.

A.3.5.9 Conclusions

The Spacecraft Motion Compensation is a very effective method to enhance the instrument pointing performance with little impact on the spacecraft system.

A.3.6 OPTION II & III CONTROLLER PERFORMANCE

A.3.6.1 Baseline controller overview (Discussed in Vol. 1, Section 10)

A.3.6.2 Simulation description, limitations, etc.

A.3.6.2.1 Dynamic models

The heart of the simulation is a numerical integration of the spacecraft equations of motion. A classical fourth-order Runge-Kutta integrator with fixed stepsize is used for this purpose. The stepsize was taken to be 0.1 sec, the gyro update interval, for simulations of the undisturbed motion. A smaller stepsize was used when imager and sounder disturbances were modeled, since these effects have variations on time scales shorter than 0.1 sec. The integration state has 26 components as follows in the next table:

The equations of motion are the rigid body equations as given, for example, in Reference [6]. In particular, the rate of change of H is given by the total *external* torque on the spacecraft. The rate of change of the reaction wheel momenta are given by the commanded reaction wheel torques, less a viscous friction term, which was set equal to zero for the results presented here. The internal disturbances from the imager and sounder are given as internal angular momenta with prescribed time histories, these are the time integrals of the torque disturbance profiles given above in Section A.3.5. The true spacecraft body rate vector, which comprises the components along the spacecraft body axes of the angular velocity of the spacecraft relative to inertial space, is given by:

$$\omega = I^{-1} (H - h_{wheel} - h_{dist})$$

where I^{-1} is the inverse of the spacecraft moment-of-inertia tensor and h_{wheel} and h_{dist} are the vector sums of the reaction wheel and disturbance angular momenta, respectively. This body rate vector is used to propagate the true attitude quaternion.

COMPONENTS	DESCRIPTION
1-4	Inertially-referenced true attitude quaternion
5-7	Cartesian components of total spacecraft angular momentum H along spacecraft body axes
8-11	Angular momenta of roll, pitch, yaw, skew reaction wheels
12-14	True spacecraft inertial position vector
15-17	True spacecraft inertial velocity vector
18-20	Spacecraft on-board model of position vector
21-23	Spacecraft on-board model of velocity vector
24-26	Integrated angles along gyro input axes

The true and estimated spacecraft ephemerides are integrated using Newton's laws of motion, with a simple force term consisting of the Earth's mass and J_2 , J_3 , and J_4 oblateness terms. This was chosen as an easily-implemented model that allows for some non-trivial orbit dynamics, without necessarily being an accurate representation of the dynamics. In particular, lunisolar perturbations and resonance terms in the Earth geopotential are not included in the model. Both the force model constants and the initial conditions can be chosen separately for the true ephemeris and the on-board ephemeris, but the two ephemerides were identical for all the simulations presented in this report.

A.3.6.2.2 Star measurements, attitude estimator and error sources

At the beginning of the simulation, a fixed, pre-specified number of stars is randomly placed in the FOV of each star tracker. The positions of the stars are mapped back into inertial space using the true star tracker alignment matrices and the true spacecraft attitude matrix. A gaussian "catalog" error is placed on each star vector to simulate the finite accuracy of star catalogs. As the simulation progresses, the inertial star positions are held fixed, and these are mapped back into the tracker FOV coordinates by using the true attitude matrix (computed from the true attitude quaternion) and true star tracker alignment matrices. The actual star tracker measurements are taken to be two components of the star vector perpendicular to the tracker boresight; gaussian noise is added to these and they were quantized to the least significant bit (LSB) of the star tracker data to give the simulated tracker output. Each star is tracked until it leaves the tracker FOV, at which point another star is randomly placed in the FOV to replace it, thus keeping a constant number of stars in each FOV.

The simulation includes an on-board estimator of the type described in Section A.3.1.2 above. The updates are based on the difference between the measurements described above and predicted star tracker measurements. The predicted measurements are computed in the same way as the actual measurements, except that the estimated attitude matrix (computed from the estimated spacecraft attitude quaternion) and estimated star tracker alignment matrices are used in place of

the true matrices, and the estimated values are neither corrupted with noise nor quantized. The estimated attitude quaternion is propagated in the same manner as the true quaternion, but using the bias- and noise-corrupted gyro estimates of the spacecraft body rates rather than the true body rate vector. The Kalman gain matrix for the attitude and bias updates uses constant values for the attitude state transition matrix and process noise co-variance matrix computed at the beginning of the simulation, based on the constant update interval T and constant body rate of one revolution per orbit about the spacecraft negative pitch axis.

As stated above, the star measurements use a set of true star tracker alignment matrices while the data processing in the on-board computer uses a set of estimated alignment matrices. It is possible to use different values for these matrices in the simulation in order to simulate the effect of star tracker misalignments, but the alignment knowledge was assumed to be perfect for all the results presented in this report. The estimator state vector could be enlarged to include star tracker misalignment parameters, but this enhancement is left for future studies.

A.3.6.2.3 Controller

The controller model in the simulation is the controller described in Section A.3.4.2 above. This involves separate PID controllers on each of the spacecraft body axes. It is only necessary here to describe the computation of the attitude angle and rate errors that are input to the controller. The desired inertial attitude matrix has rows that are related to the spacecraft position vector and the Earth's North pole (inertial z-axis) as:

$$A_{\text{commanded}} = [\mathbf{u} \ \mathbf{v} \ \mathbf{w}]^T$$

where superscript T denotes the matrix transpose and

$$\begin{aligned} \mathbf{u} &= \mathbf{k} \times \mathbf{r} / |\mathbf{k} \times \mathbf{r}| \\ \mathbf{v} &= \mathbf{k} \times (\mathbf{k} \times \mathbf{r}) / |\mathbf{k} \times \mathbf{r}| \\ \mathbf{w} &= -\mathbf{r}, \text{ the nadir vector} \\ \mathbf{k} &= [0 \ 0 \ 1]^T = \text{Earth's North pole vector.} \end{aligned}$$

The attitude error angles are the elements of the skew-symmetric matrix:

$$A_{\text{err}} = (1/2) [A_{\text{commanded}} (A_{\text{est}})^T - A_{\text{est}} (A_{\text{commanded}})^T].$$

The commanded rates are similarly given by the elements of the skew-symmetric matrix:

$$\Omega_{\text{commanded}} = [d(A_{\text{commanded}})/dt][A_{\text{commanded}}]^T.$$

The rate errors are then the difference of the commanded rates and the estimated rates. It is important to note that both the attitude angle errors and the rate errors must be computed from the estimated attitude and rates, since the true attitude and true rates are not known to the on-board computer.

The controller outputs are sent as torque commands to the roll, pitch, and yaw reaction wheels. The command to each wheel is limited to a maximum magnitude of 0.3 Nm and quantized to an LSB of 1.5×10^{-4} Nm, corresponding to a 12-bit wheel command. The skew wheel is not used in the present simulation, although it would be easy to include a torque distribution matrix to simulate a four-wheel controller or a three-wheel controller omitting one of the orthogonal wheels.

A.3.6.3 Quiescent registration performance

Several runs were made with different star tracker parameters and with no attitude disturbances to test the performance of the attitude estimation. The IRU parameters were taken to be the DRIRU-II parameters presented in Section A.3.1.2 for all these runs, as well as for the runs with attitude disturbances to be presented below. The error curves show three errors on each axis: the estimation error, the control error, and the actual pointing error. These can be understood as the differences among three distinct spacecraft attitudes: the true attitude, the attitude estimated by the gyro/star tracker system, and the commanded Earth-pointing attitude. The relations are:

$$\begin{aligned} \text{estimation error} &= \text{estimated attitude} - \text{true attitude} \\ \text{control error} &= \text{commanded attitude} - \text{estimated attitude} \\ \text{pointing error} &= \text{commanded attitude} - \text{true attitude}. \end{aligned}$$

These errors are not independent, but satisfy the relation:

$$\text{pointing error} = \text{estimation error} + \text{control error}.$$

The pointing error, being the difference between the commanded and actual attitudes, is the quantity of greatest significance. The curve of this error is always the smoothest of the three curves, since the estimated attitude has high frequency sensor noise, which neither the true attitude nor the commanded attitude contains (the rigid body dynamics acts as a low-pass filter to keep this noise out of the true attitude). The three error curves are difficult to distinguish in the plots, but this smoothness property can be used to distinguish the pointing error curve. In all the plots of the undisturbed motion presented in this section, the control error curve is always the curve that stays closest to the horizontal axis, since the estimation errors are always larger than the control errors in these cases. When only two curves can be distinguished, it is because the estimation error and pointing error plots are too close to be resolved.

The six runs illustrated in Figures A.3.6-1 to A.3.6-10 all use the star tracker parameters appropriate to the ASTROS tracker, specifically the 2.2 deg x 2.5 deg FOV and the 1.5 μ rad NEA. The cases shown in Figures A.3.6-1,2,3 do not include any star tracker calibration or star catalog errors; but they show the effect of changing the filter update times. The peak-to-peak range of the curves can be taken as six standard deviations; with this identification the results agree quite well with the predictions of Section A.3.1.B.

The next three runs, illustrated in Figures A.3.6-4,5,6 include Gaussian-distributed zero-mean random star catalog errors of 2.5 μ on each of the two axes perpendicular to the LOS to each star. When these catalog errors are taken into account, the performance of the estimator at 2 sec

and 20 second updates is similar because the catalog errors cannot be averaged out by taking repeated measurements, since they are constant for a given star. The performance of the system with a 200 sec update frequency is clearly inferior, however, so this case was not considered further. The need for updates at a frequency of at least one per minute eliminated landmarks from serious consideration in the study.

The next four plots, Figures A.3.6-7 through A.3.6-10, show the effects of having multiple stars in each tracker. There is some improvement, since the catalog errors of the different stars tend to average out, but it is not as great as might have been hoped for

Figure A.3.6-11 shows the best estimate of the performance achievable with an off-the-shelf CT-601 or ASTRA-II star tracker. This estimate assumes a 14.5μ NEA and a 16-bit star tracker data word, giving an LSB of 2.13μ . There were assumed to be five stars in each tracker FOV, and the star catalog errors were 5μ on each axis perpendicular to the LOS. These errors are taken to represent the combined effect of actual catalog errors and calibration errors. The latter are hard to model more accurately, since they are neither random nor constant for a given star. The Kalman filter update interval was reduced to 1 sec, since this is within the capabilities of both the star trackers and the on-board processor and provides slightly better performance than that obtained with a 2 sec update interval. The curves show that the standard deviation of the attitude error is about 1.7μ on each axis, which is only about two times as great as the best of the runs with star tracker parameters characteristic of ASTRO. The CT-601 or ASTRA-II are otherwise preferable to ASTRO since they are more readily available and their use of brighter stars allows a smaller on-board star catalog.

Figure A.3.6-12 shows the results obtained by redesigning the optics of the CT-601 or ASTRA-II to reduce the FOV from 8 deg square to 4 deg square. The NEA and data LSB are thereby reduced to 7.25μ and 1.065μ , respectively, but the catalog errors remain unchanged at 5μ rad. Table A.3.1-2 shows that the FOVs will probably not all contain 5 stars, so 1, 3, and 5 stars were assumed in the three FOVs. Other input parameters are unchanged from the 8 deg FOV case. The performance is slightly better than with the 8 deg square FOV, and the smaller swath swept out in the sky allows the size of the on-board star catalog to be cut roughly in half. The disadvantages of reducing the FOV include the cost and risk of redesigning and recalibrating the optics and the increased probability that no stars will be in a FOV at some times during the orbit. More detailed modeling is needed to resolve these issues.

The conclusion of these simulations is that the Option II and III attitude control system employing gyro/star tracker sensing and active three-axis control with reaction wheels is capable of maintaining attitude errors of 1.7μ or less (1 standard deviation) on all axes in the absence of attitude disturbances.

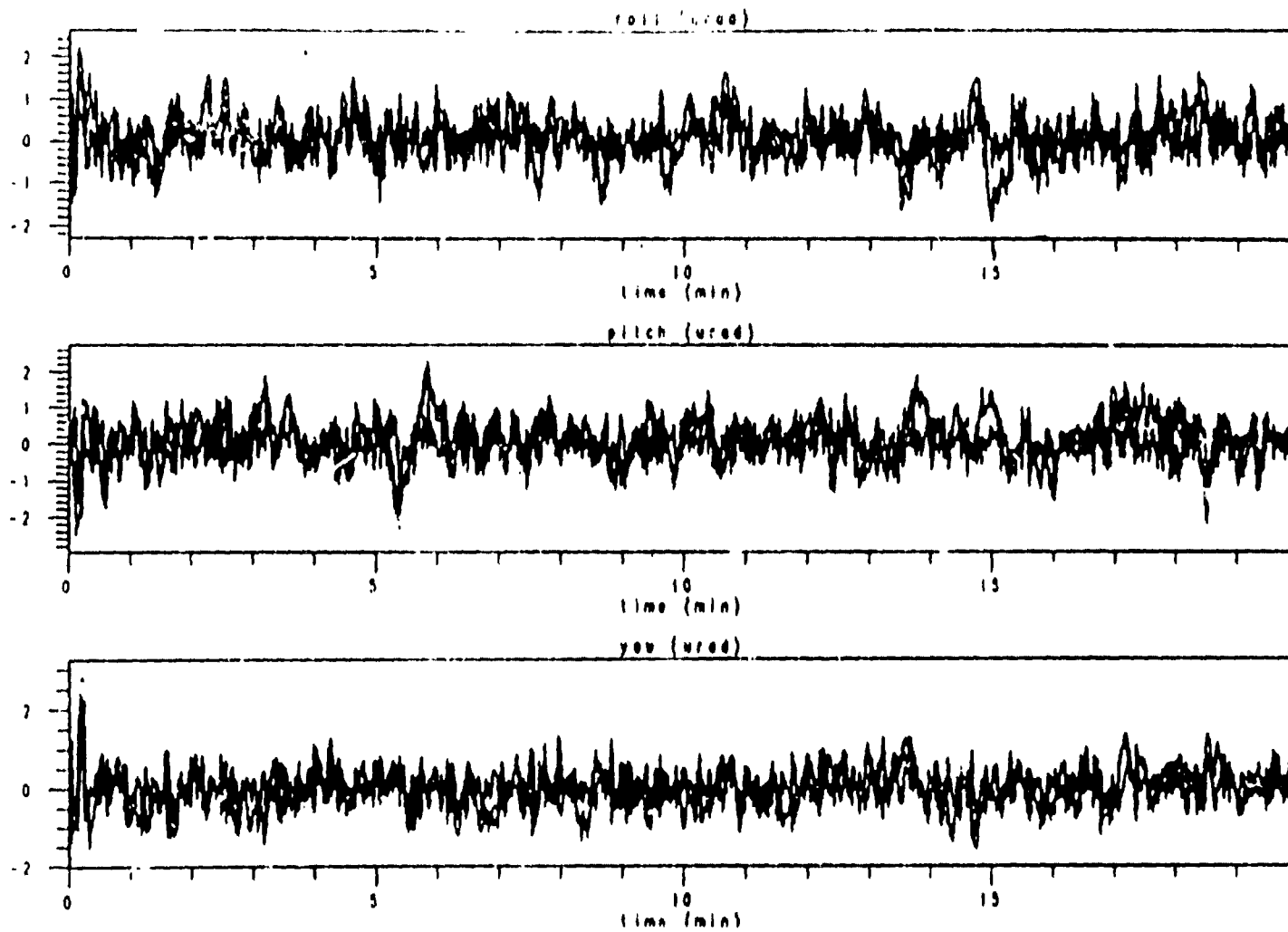


Figure A.3.6-1. Attitude Estimation Errors with 2.2 deg x 2.5 deg FOV, 1 Star per Tracker, Updates Every 2 Seconds, and No Catalog Errors

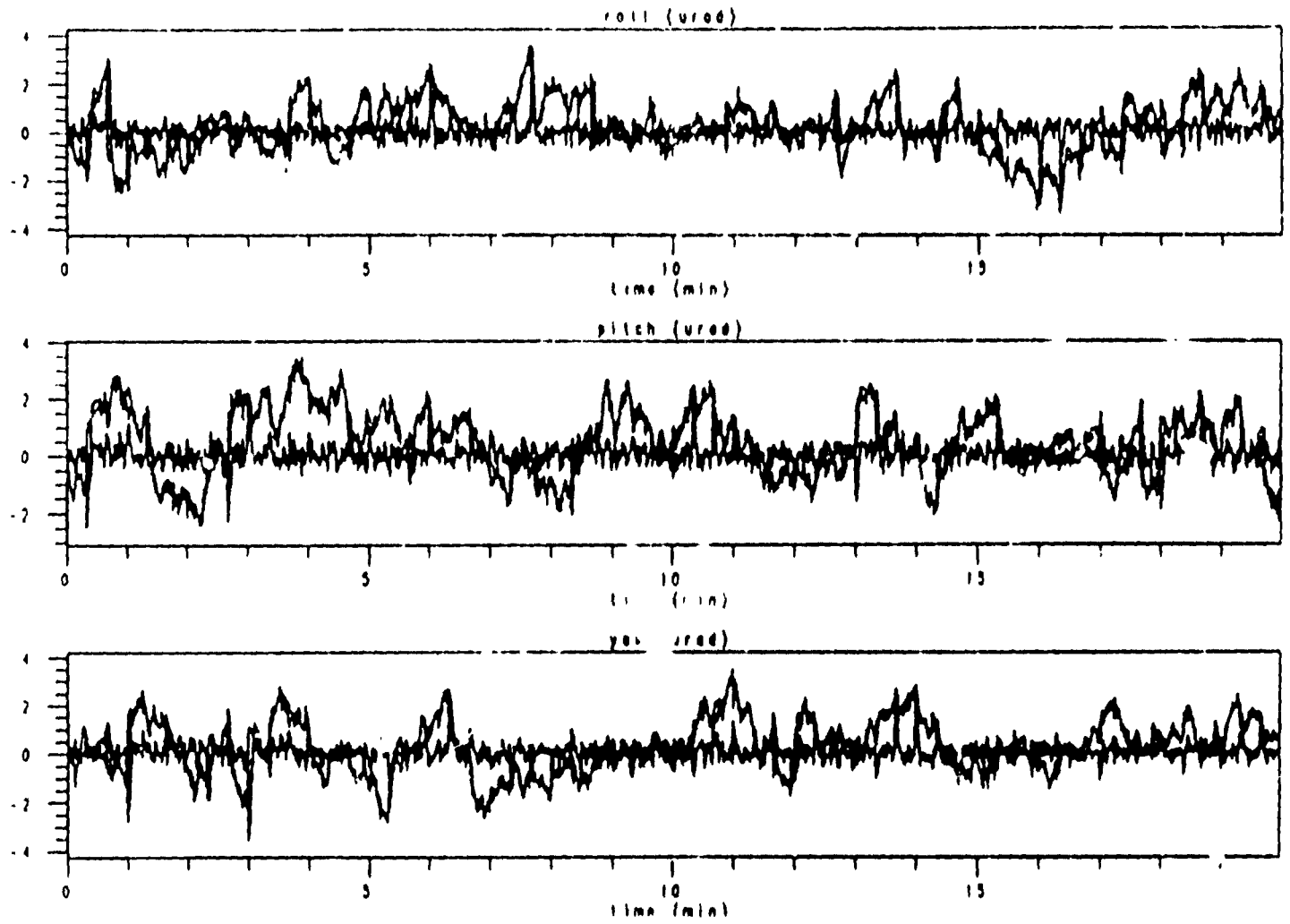


Figure A.3.6-2. Attitude Estimation Errors with 2.2 deg x 2.5 deg FOV, 1 Star per Tracker, Updates Every 20 Seconds, and No Catalog Errors

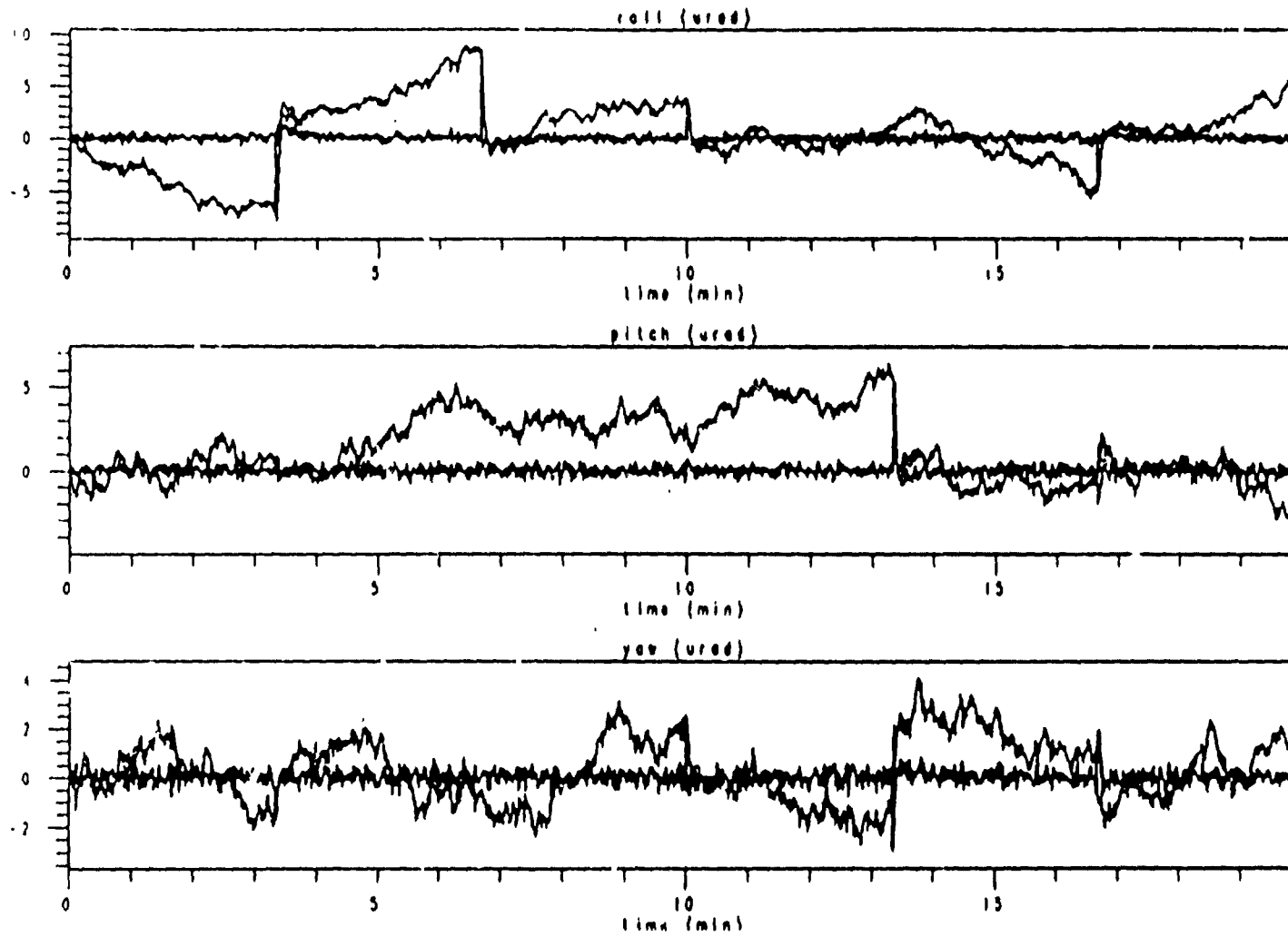


Figure A.3.6-3. Attitude Estimation Errors with 2.2 deg x 2.5 deg FOV, 1 Star per Tracker, Updates Every 200 Seconds, and No Catalog Errors

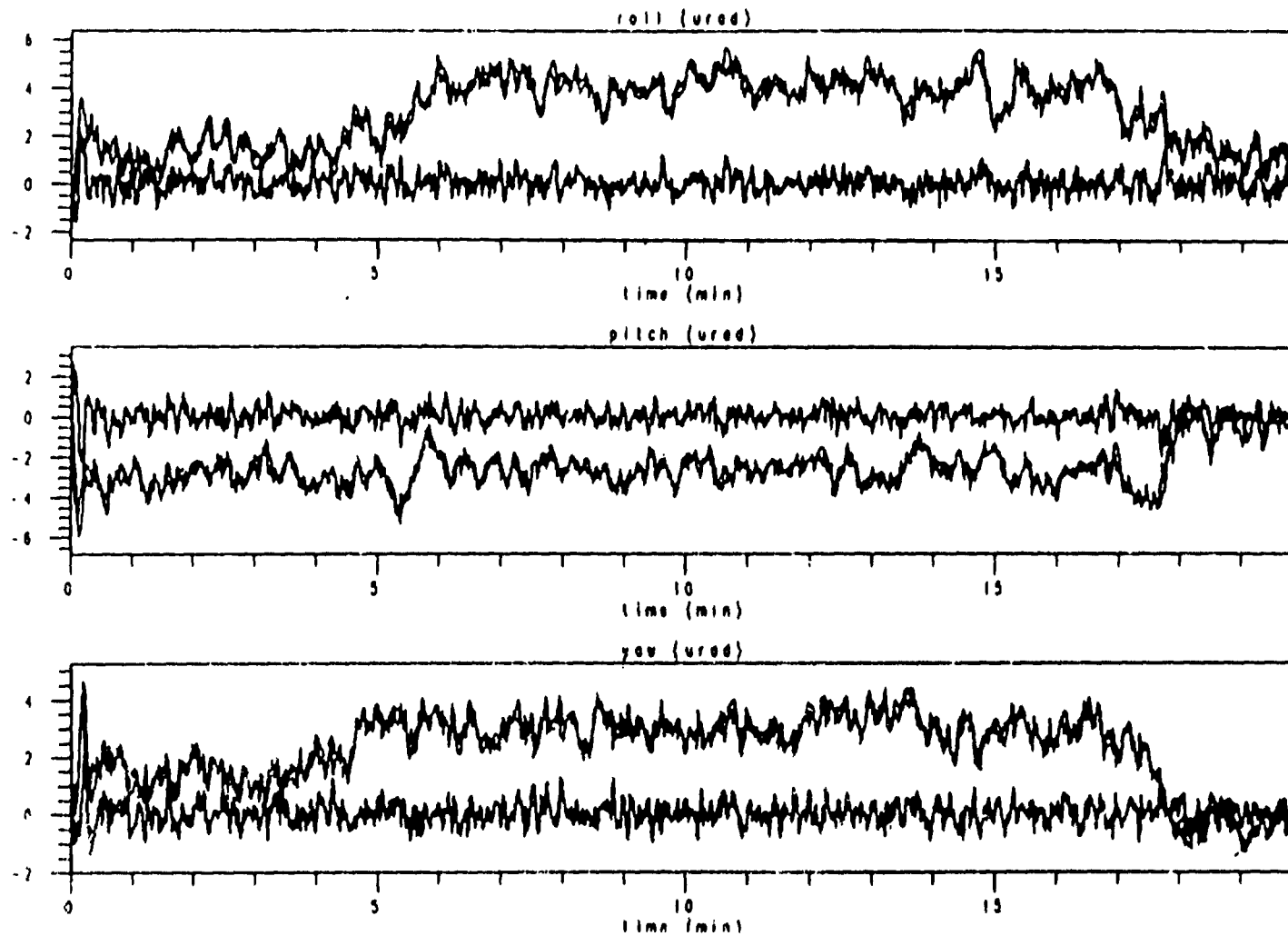


Figure A.3.6-4. Attitude Estimation Errors with 2.2 deg x 2.5 deg FOV, 1 Star per Tracker, Updates Every 2 Seconds, and 2.5 μ r Catalog Errors

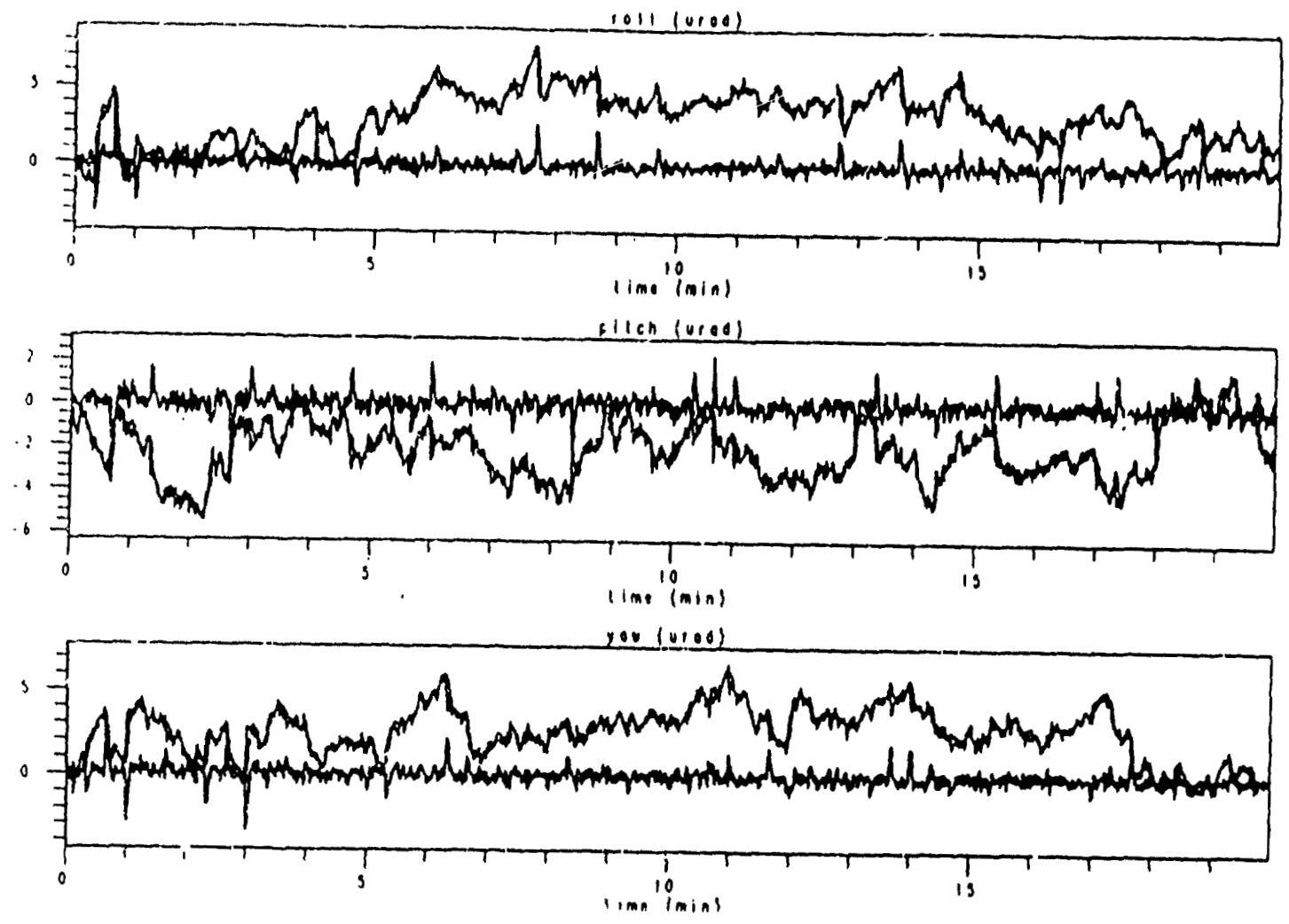


Figure A.3.6-5. Attitude Determination Errors with 2.2 deg x 2.5 deg FOV, 1 Star per Tracker, Updates Every 20 Seconds, and 2.5 μ r Catalog Errors

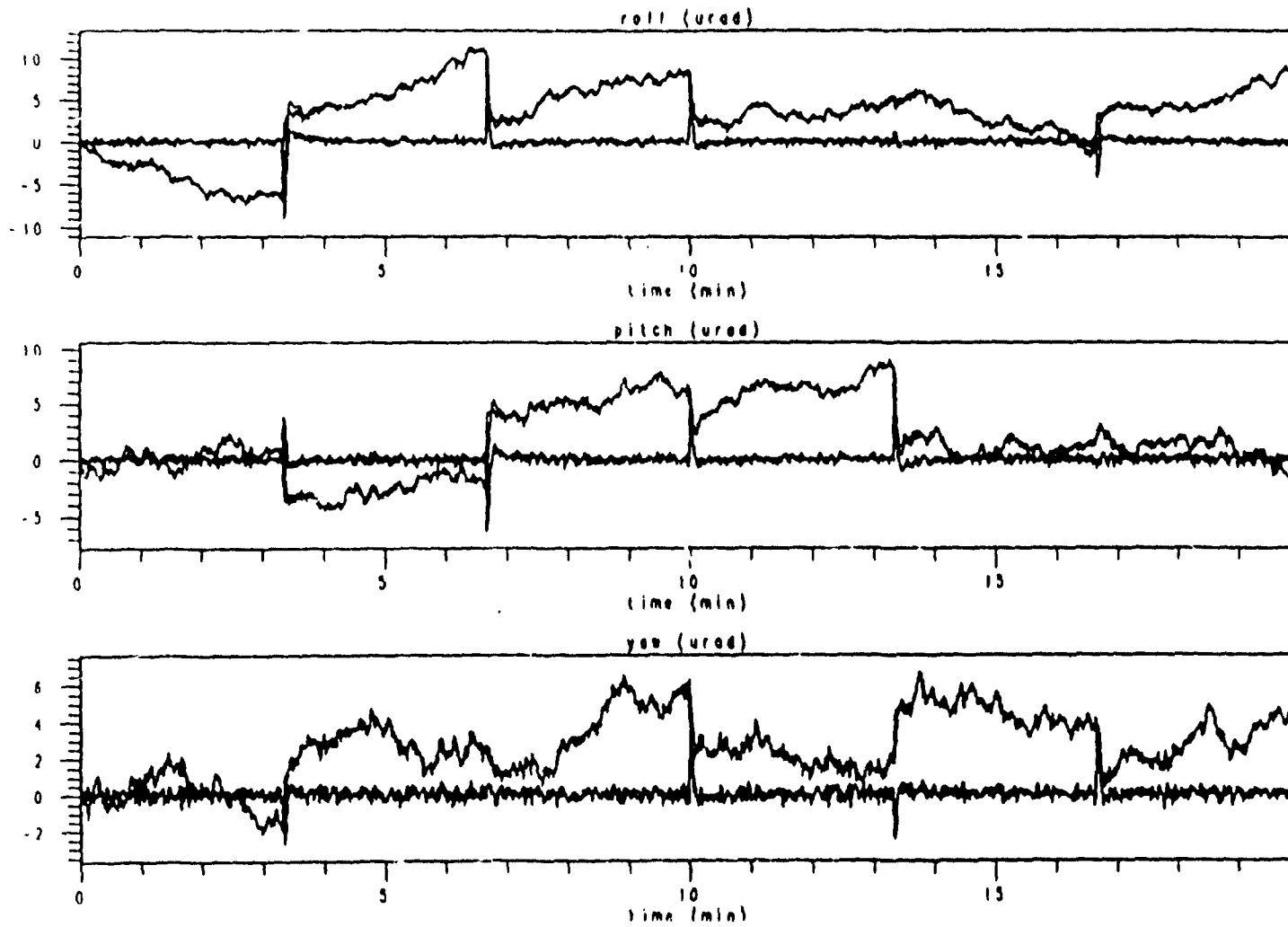


Figure A.3.6-6. Attitude Estimation Errors with 2.2 deg x 2.5 deg FOV, 1 Star per Tracker, Updates Every 200 Seconds, and 2.5 μ r Catalog Errors

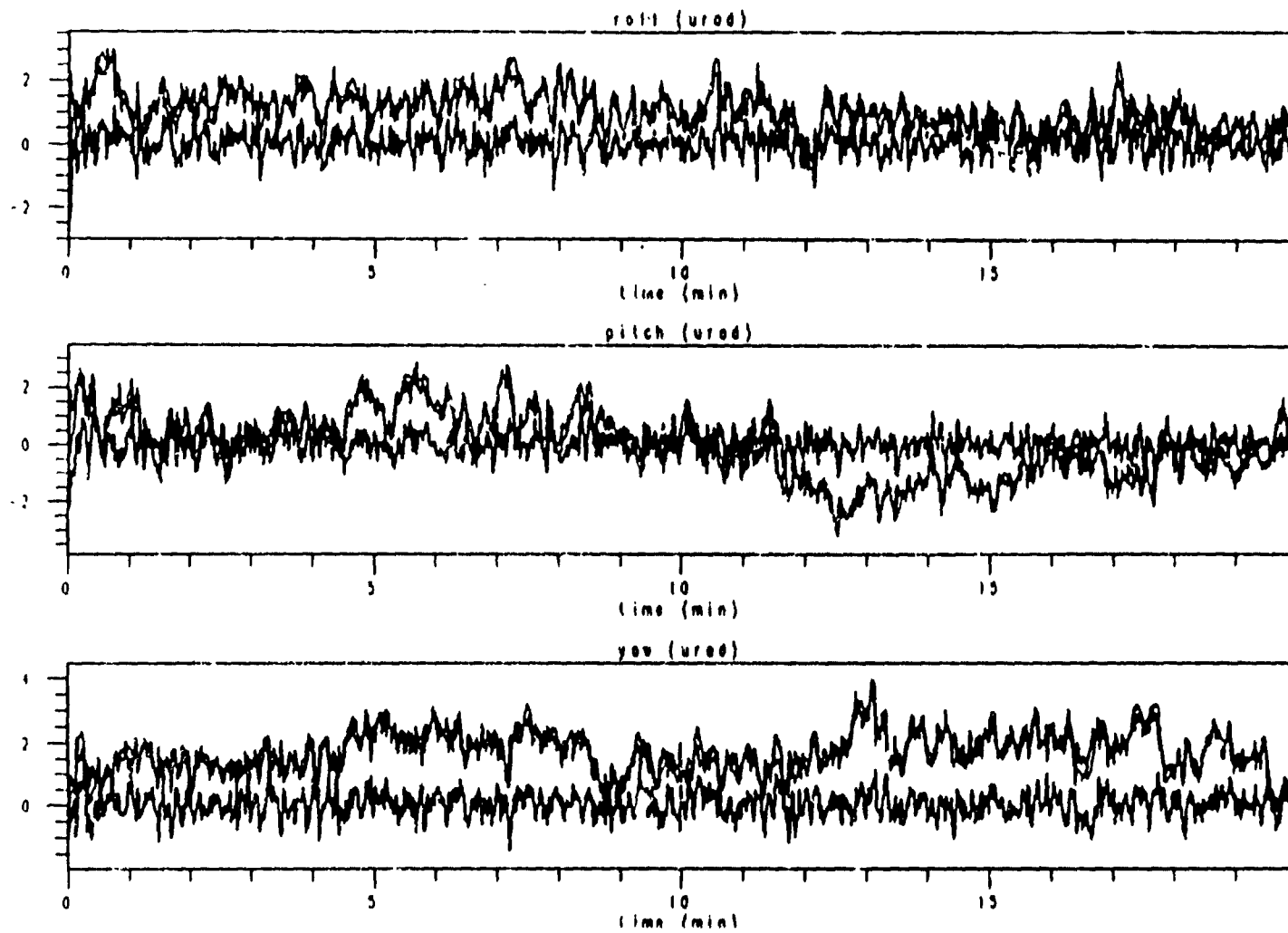


Figure A.3.6-7. Attitude Estimation Errors with 2.2 deg x 2.5 deg FOV, 2 Stars per μ rad, Updates Every 2 Seconds, and 2.5 μ rad Catalog Errors

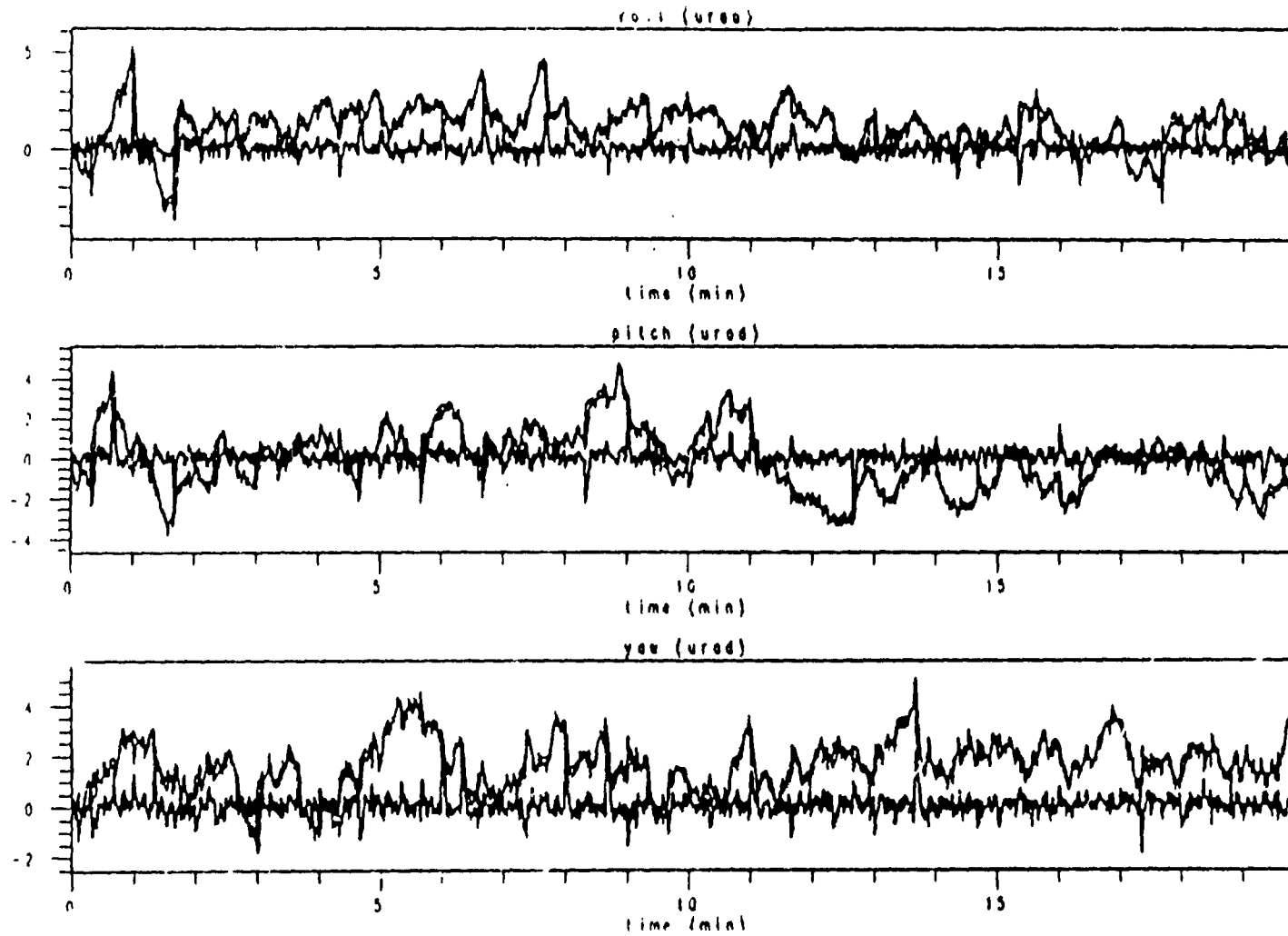


Figure A.3.6-8. Attitude Estimation Errors with 2.2 deg x 2.5 deg FOV, 2 Stars per Tracker, Updates Every 20 Seconds, and 2.5 μ r Catalog Errors

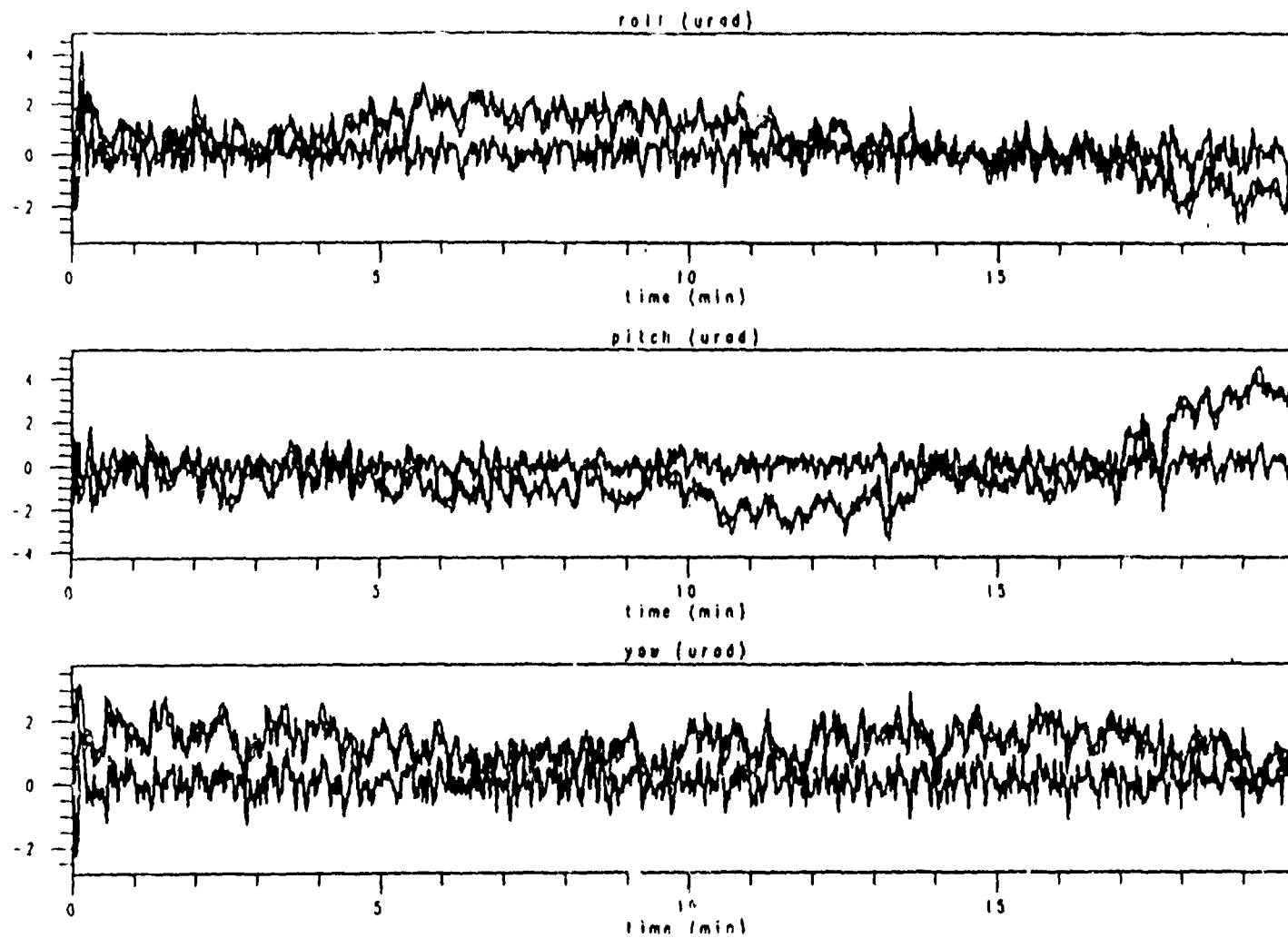


Figure A.3.6-9. Attitude Estimation Errors with 2.2 deg x 2.5 deg FOV, 3 Stars per Tracker, Updates Every 2 Seconds, and 2.5 μ r Catalog Errors

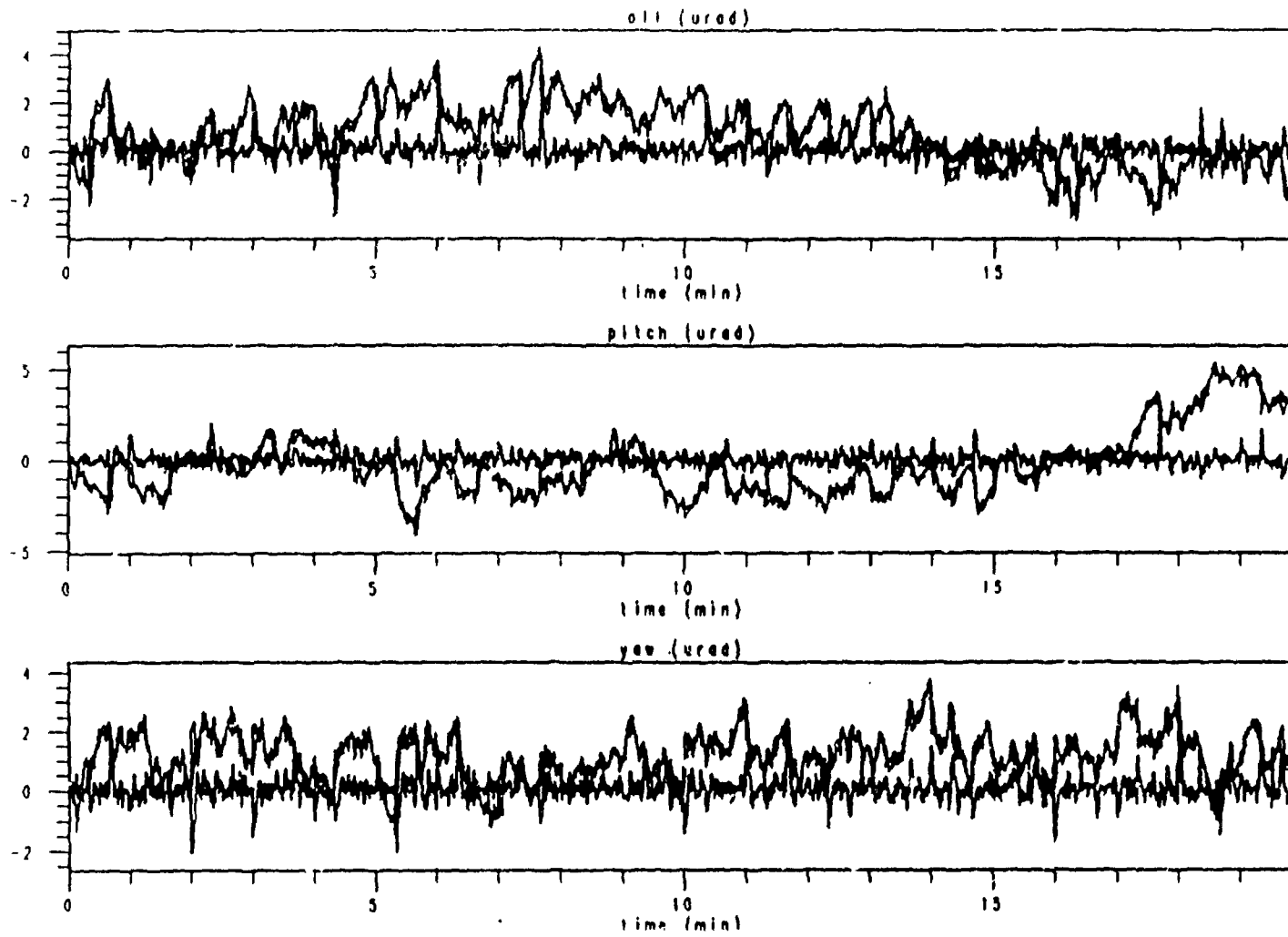


Figure A.3.6-10. Attitude Estimation Errors with 2.2 deg x 2.5 deg FCV, 3 Stars per Tracker, Updates Every 20 Seconds, and 2.5 μ r Catalog Errors

8x8 fov

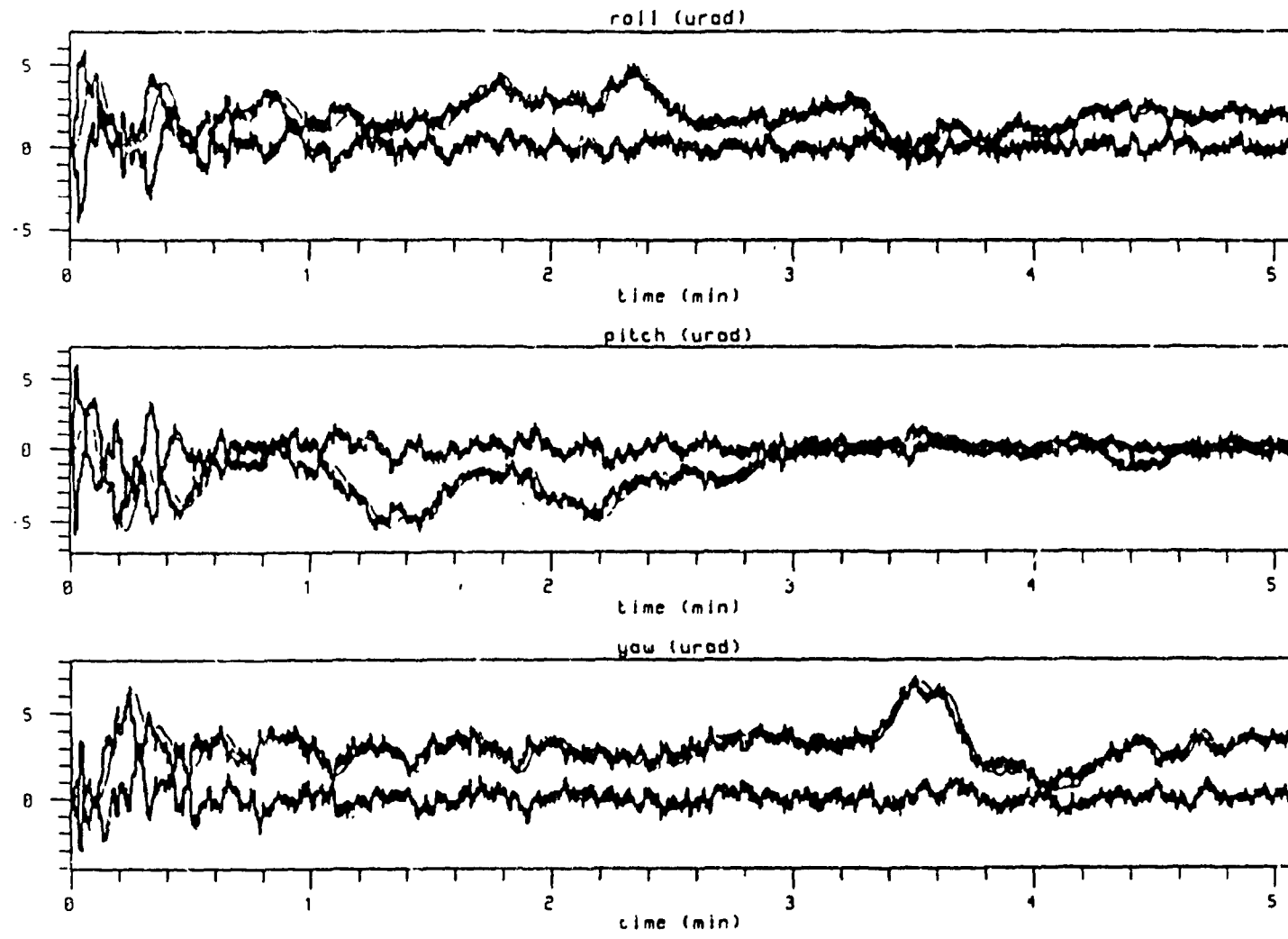


Figure A.3.6-11. Attitude Estimator Errors with 8 deg Square FOV, 5 Stars per Tracker, Updates Every Second, and 5 μ r Catalog Errors

4x4 fov

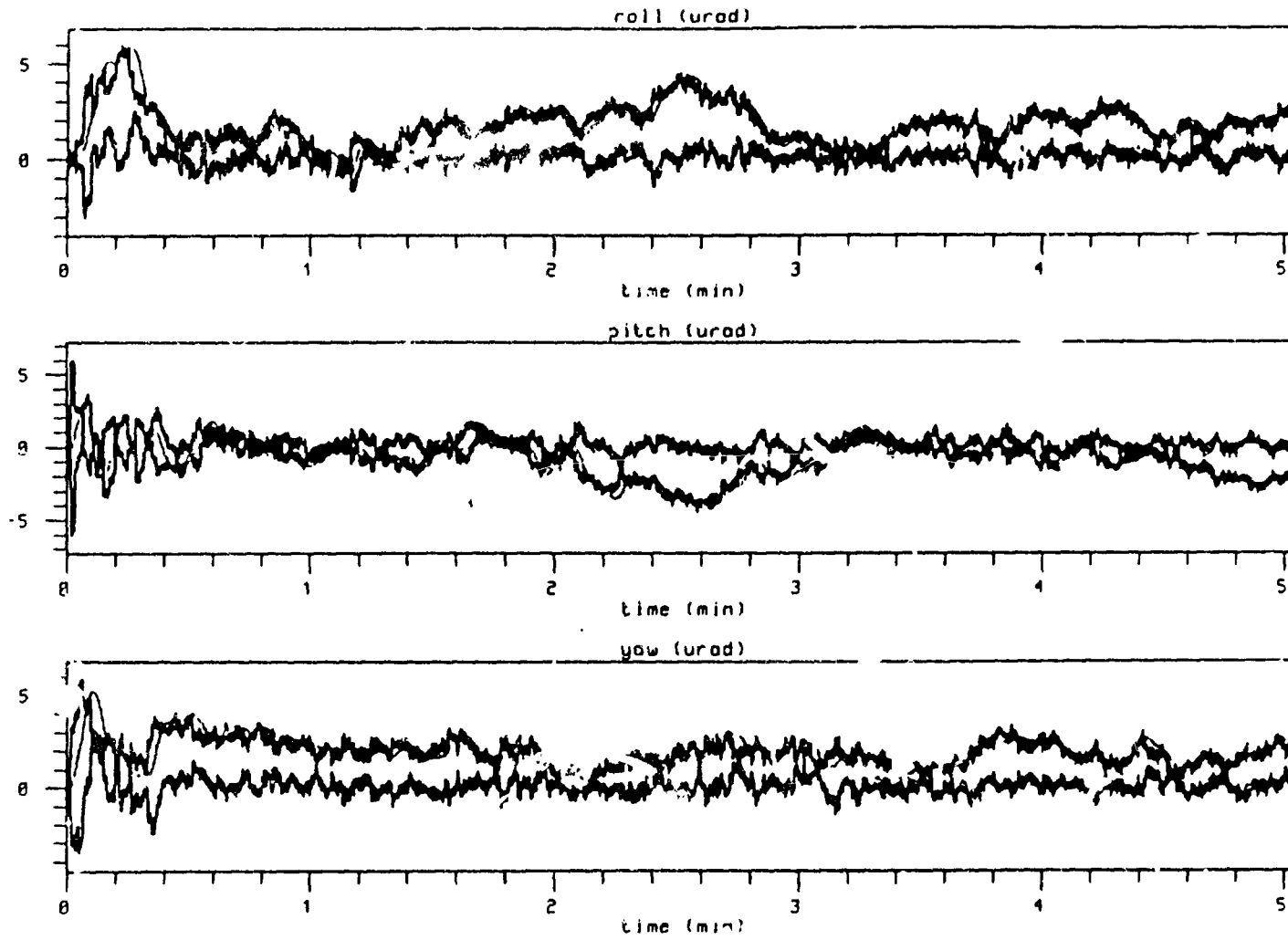


Figure A.3.6-12. Attitude Estimation Errors with 4 deg Square FOV, 1, 3, and 5 Stars per Trackers, Updates Every Second, and 5 μ Catalog Errors

A.3.6.4 Spacecraft disturbance accommodation

This section shows the simulated response of the control system to imager and sounder disturbances, which were included in the form of internal angular momenta, as described in Section A.3.6.A.1 above. As also mentioned there, the integration stepsize was reduced so that the details of the disturbance profiles would not be missed. The same three error curves are plotted as for the quiescent registration performance.

All the runs presented here but the last were made with zero initial attitude estimation errors and perfect gyros, to exhibit the performance of the controller unmasked by estimation errors. In these runs, the Kalman update time was set to a time longer than the length of the simulation, since star references are not needed if the initial attitude estimate and the gyros are perfect. Also in these runs the estimation error is zero and the pointing and control errors are equal to one another. Thus only two curves are visible on each plot, one of which lies exactly on the horizontal axis.

The first two runs show the response to the sounder disturbances. The products of inertia (off-diagonal elements of the spacecraft moment-of-inertia tensor) were set equal to zero in these simulations, in order to eliminate cross-axis coupling effects that would mask the effects of interest. There still is some coupling between the roll and yaw axes arising from the 1 RPO pitch motion for Earth pointing. Figure A.3.5-13 shows the uncontrolled spacecraft response. The N/S mirror motion is about the spacecraft roll axis, so the pitch response is to the 1120 μ r steps at the end of the E/W scan. The E/W mirror step-and-settle correspondingly shows up as a pitch disturbance. The uncontrolled response assumes the unrealistic value of 20 step-and-settle moves between N/S moves in order to show both effects on a convenient time scale. The simulation of the controlled response to the sounder disturbance shown in Figure A.3.6-14 uses a more realistic value of 750 step-and-settle moves, which corresponds to a total of about 6 deg of E/W motion between N/S steps. The attitude errors are extremely small, never exceeding 0.1 μ r, so the sounder disturbance is negligible in the absence of black-body calibration slews. Since the disturbance profiles of imager and sounder black-body slews are identical, we defer consideration of this perturbation until the discussion of imager disturbances below.

The last five simulations, shown in Figures A.3.6-15 through A.3.6-19, show the response to imager disturbances. The imager scan time was set equal to 0.6 sec, giving a scan length of approximately 6 deg, allowing for mirror acceleration and deceleration. The first of imager runs, Figure A.3.6-15 shows the uncontrolled spacecraft response to the E/W scan and N/S step. The diagonal spacecraft moment-of-inertia tensor used in the sounder simulations was used in this run, also, so the roll-yaw coupling is due to the 1 RPO pitch motion. Figure A.3.6-16 shows the uncontrolled spacecraft response on a different time scale, and Figure A.3.6-17 shows the controlled response with perfect attitude estimation. These and the following runs used the full moment-of-inertia tensor, so the roll motion shows the combination of the direct response to the N/S steps and the coupling of the E/W scan through the xy product of inertia. Figure A.3.6-18 is the same case as Figure A.3.6-17 except that a longer time span is shown, including a black-body calibration at 2 minutes. The black body calibration gives a large attitude disturbance, as expected, with pointing errors as large as 10 μ r. The response of the control system to sounder black body calibrations is similar, so these results have not been shown.

20 steps
sounder - no control

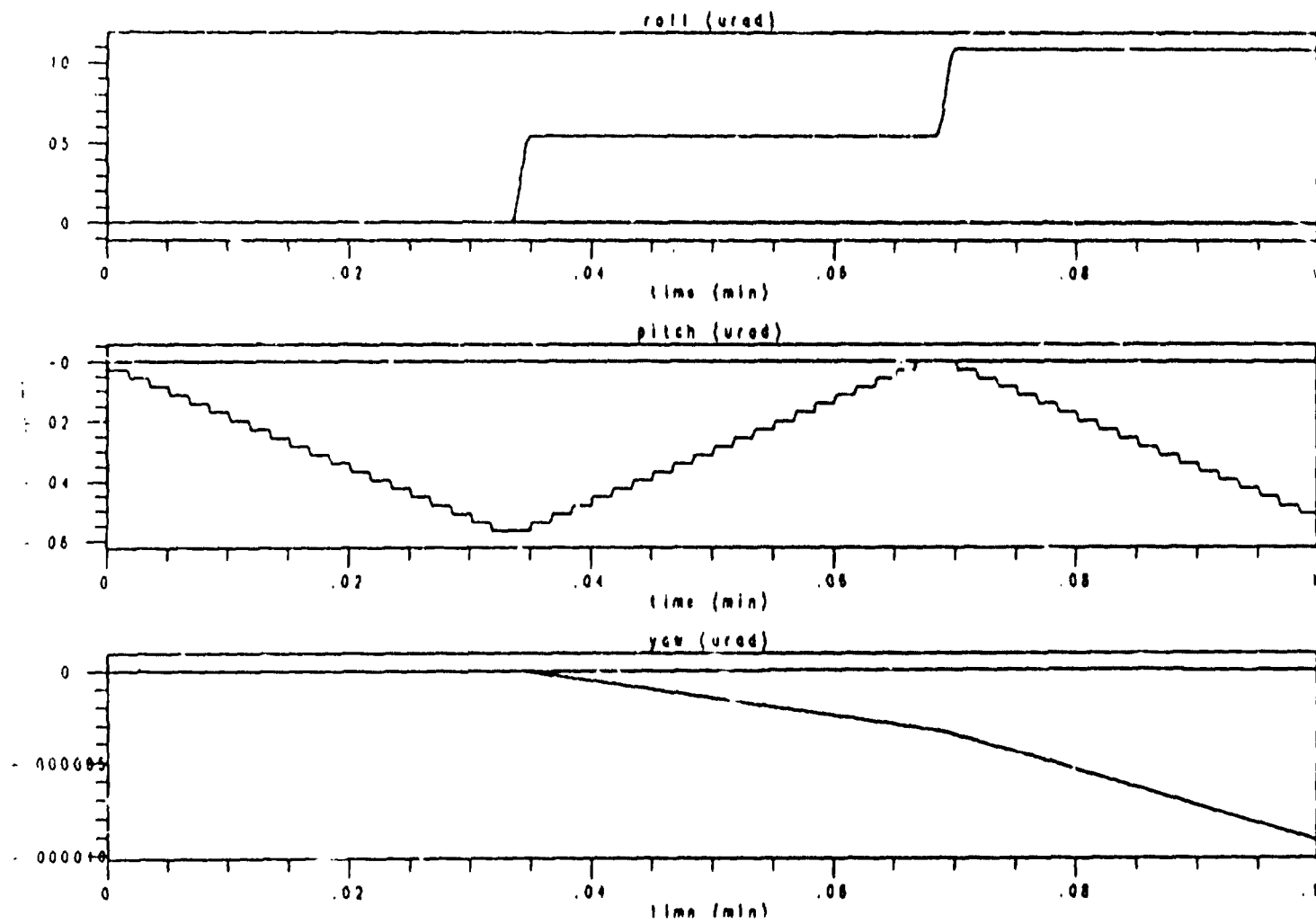


Figure A.3.6-13. Uncontrolled Spacecraft Response to Sounder Disturbance

750 steps $\approx 6^\circ$
soudner - control on - 100 msec control step
 λ

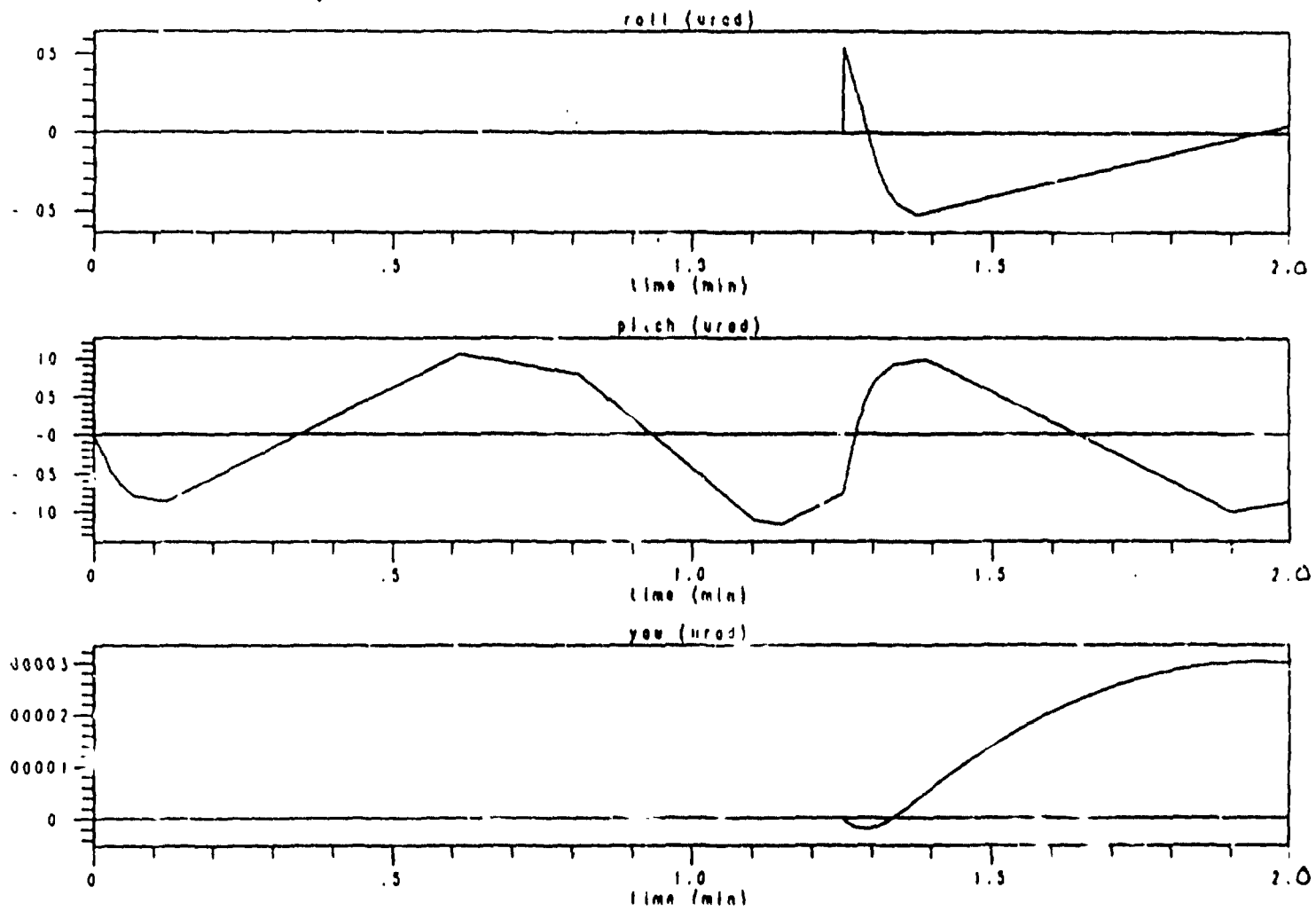


Figure A.3.6-14. Controlled Spacecraft Response to Soudner Disturbance

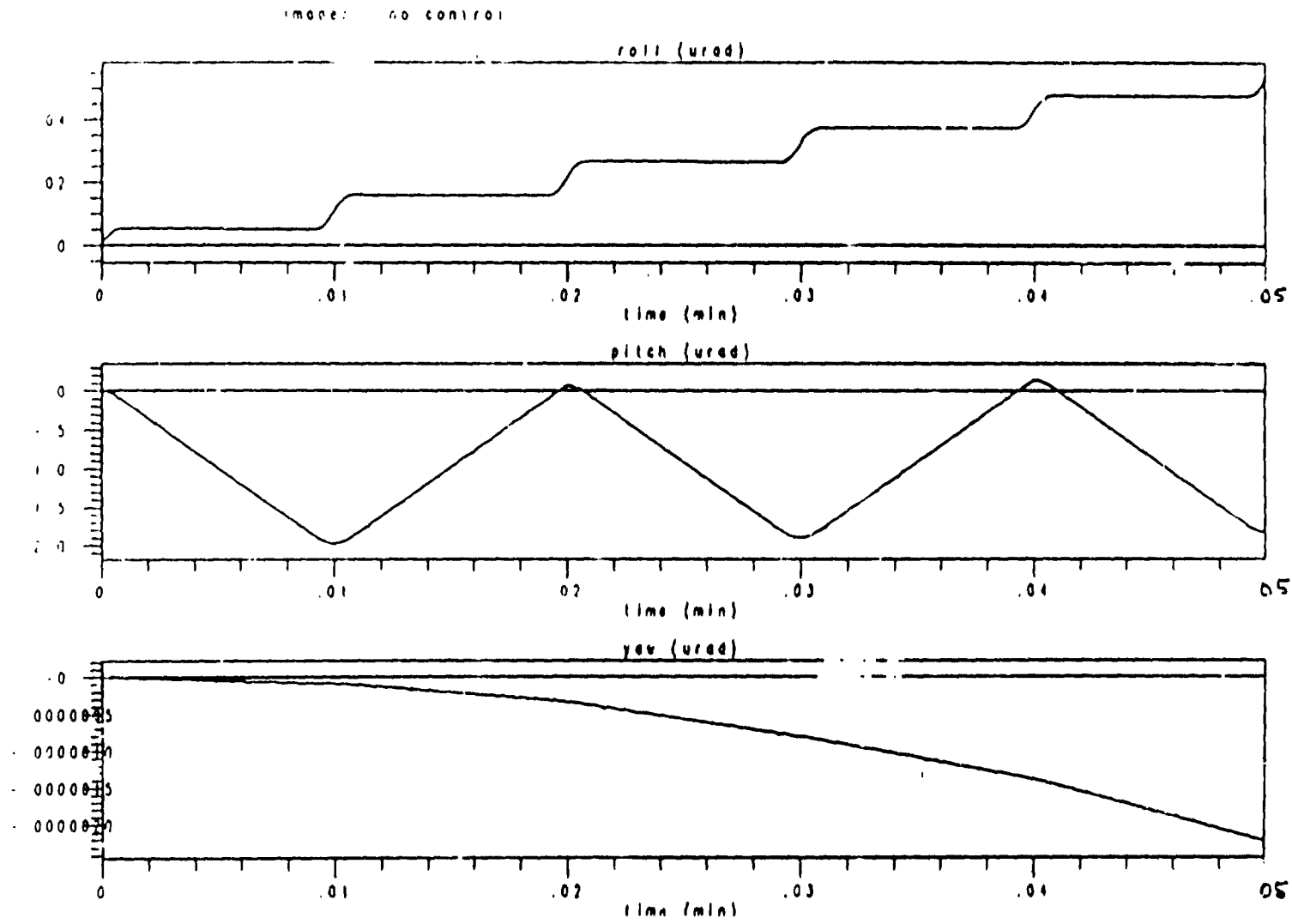


Figure A.3.6-15. Uncontrolled Spacecraft Response to Imager Disturbance over 3 Seconds with Diagonal Spacecraft Moment-of-Inertia Tensor

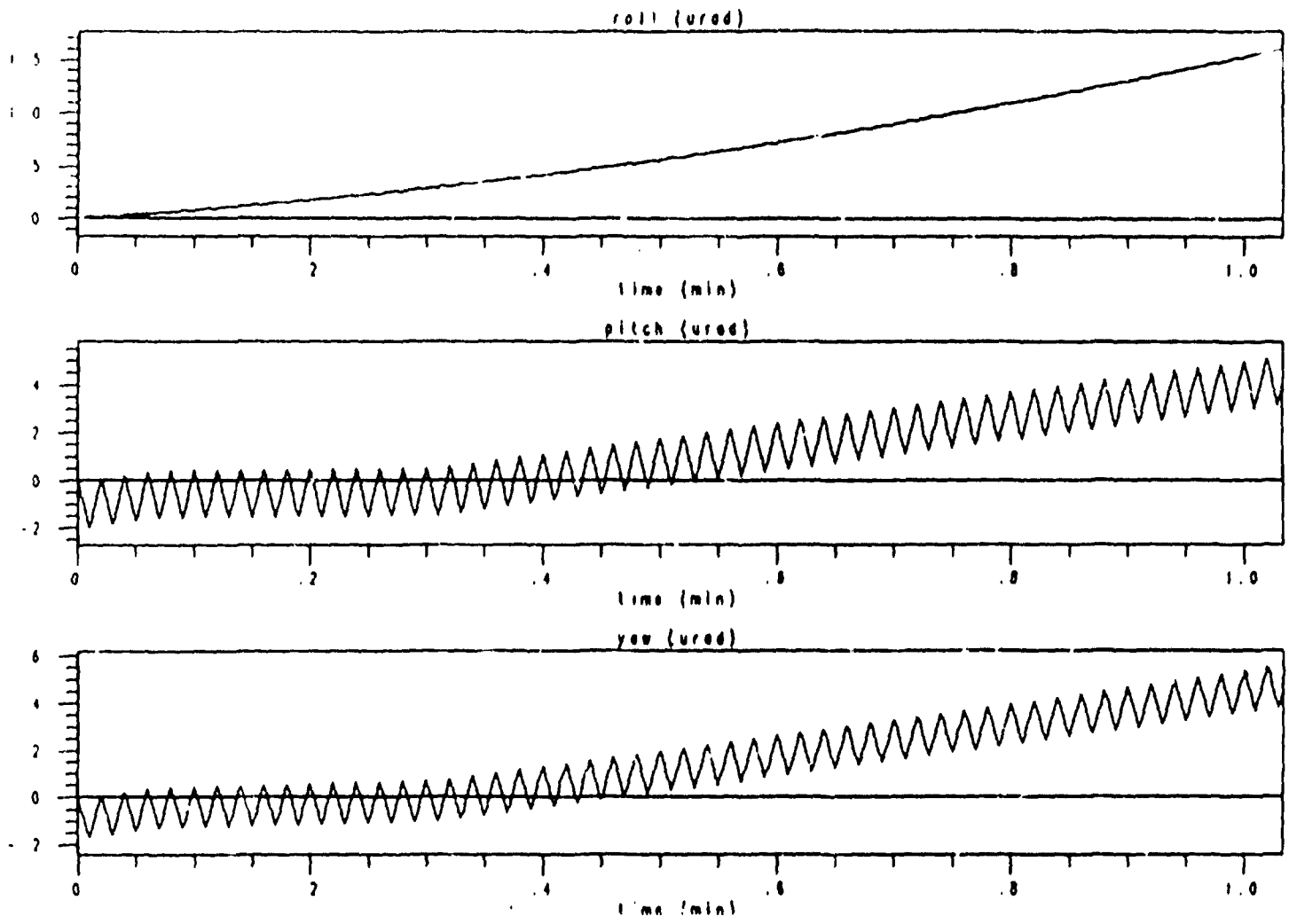


Figure A.3.6-16 Uncontrolled Spacecraft Response to Imager Disturbance over 1 Minute with Full Spacecraft Moment-of-Inertia Tensor

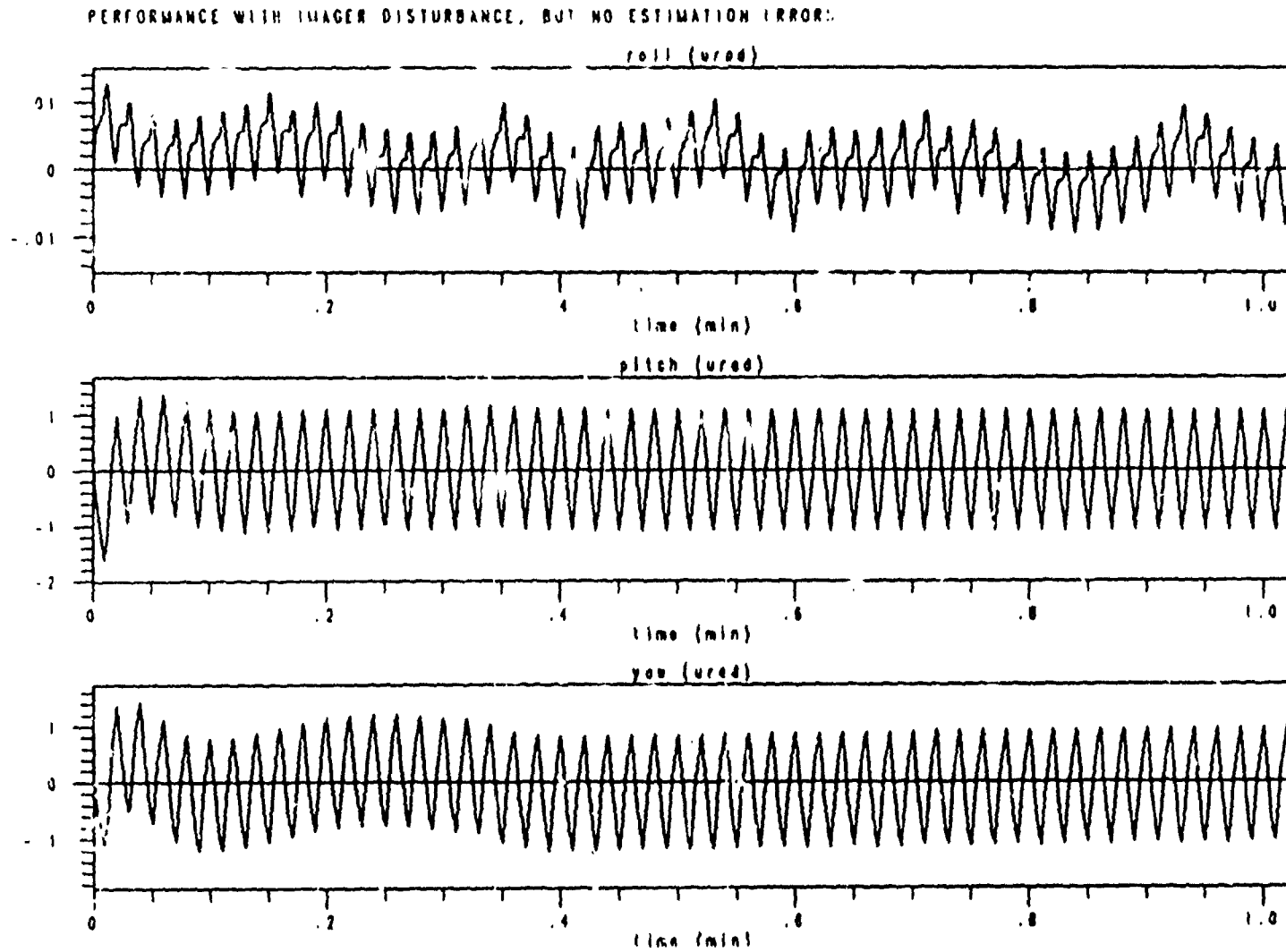


Figure A.3.6-17. Controlled Spacecraft Response to Imager Disturbance over 1 Minute with Full Spacecraft Moment-of-Inertia Tensor

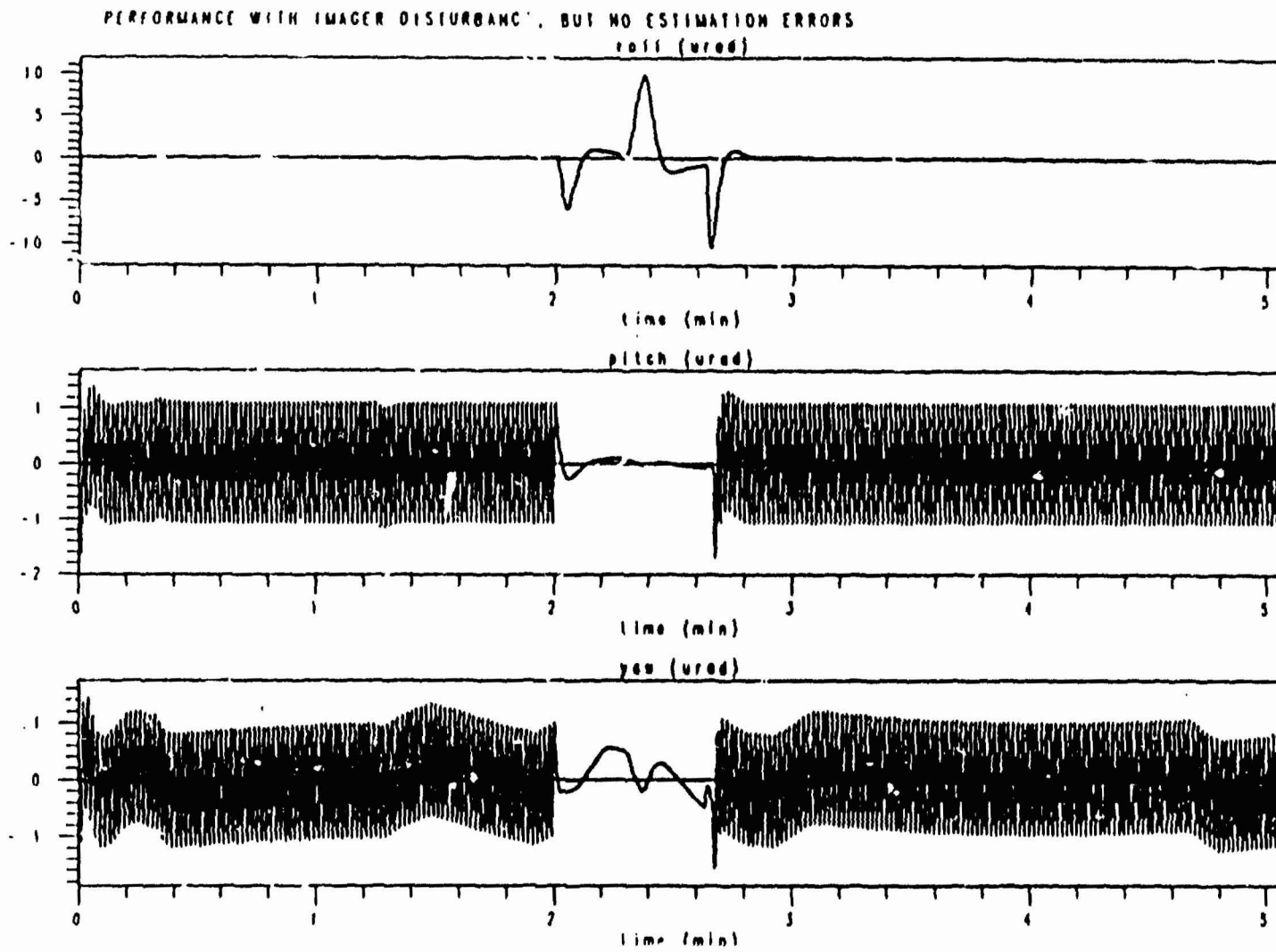


Figure A.3.6-18. Controlled Spacecraft Response to Imager Disturbance over 5 Minutes with Black-Body Calibration Slew at 2 Minutes

4.4 (ov 0) ser integration step

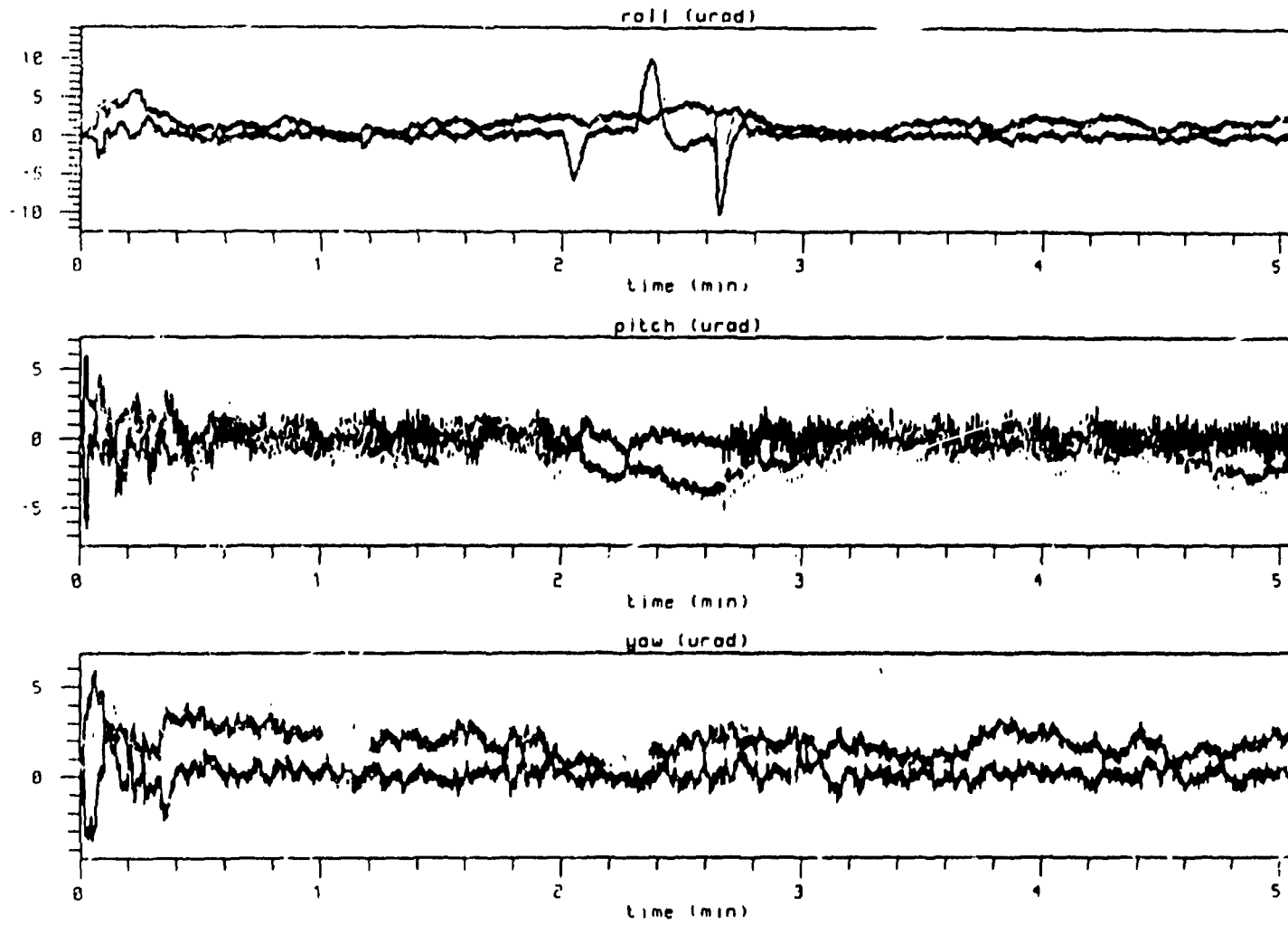


Figure A.3.6-19. Combined Response to Estimation Errors and Imager Disturbance with Black-Body Calibration Slew at 2 Minutes

The overall conclusion of the simulations with perfect estimation is that the control errors are about 1μ except during black-body calibration slews, at which times they are as large as 10μ (both of these are maximum deviations from zero). These errors can further be reduced by spacecraft motion compensation (SMC), as explained in the following section.

The last simulation, illustrated in Figure A.3.6-19, shows the combined effect of estimation errors and imager disturbances. The estimation model used the star tracker with 4 deg square FOV and with the same performance parameters as the run shown in Figure A.3.6-12. The estimation error, control error, and pointing error are all non-zero in this run. Comparison of the curves in these two figures shows that the estimation errors dominate the control errors except during the black-body calibration maneuver, as expected. The control errors can be further reduced by SMC while the estimation errors cannot, since they are unknown to the controller, so the effective overall performance in presence of attitude disturbances is the same as in the quiescent case, with pointing errors of 1.7μ (1 standard deviation) per axis.

A.3.6.5 SMC disturbance accommodation

A.3.6.6 References

- [1] Murrell, J.W., "Precision Attitude Determination for Multimission Spacecraft," AIAA Paper 78-1248, August 1978
- [2] Lefferts, E.J., F.L. Markley, and M.D. Shuster, "Kalman Filtering for Spacecraft Attitude Estimation," *Journal of Guidance, Control, and Dynamics*, Vol. 5, September-October 1982, pp. 417-429
- [3] McQuerry, J.P., M.A. Radovich, Jr., and R.A. Deters, "A Precision Star Tracker for the Nineties: A System Guide to Applications," AAS Paper 90-014, February 1990
- [4] Stanton, R.H., J.W. Alexander, E.W. Dennison, T.A. Glavich, P.M. Salomon, and R.E. Williamson, "ASTROS: A Sub-Arcsec CCD Star Tracker"
- [5] Farrenkopf, R.L., "Analytic Steady-State Accuracy Solutions for Two Common Spacecraft Attitude Estimators," *Journal of Guidance and Control*, Vol. 1, July-August 1978
- [6] Wertz, J.R., editor, *Spacecraft Attitude Determination and Control*, D. Reidel 1978

APPENDIX B

B.1 ANALOG FILTERING

B.1.1 Introduction

B.1.1.1 Purpose

The pointing performance of the existing GOES-I servo controller is limited by the structural modes of the instrument. The purpose of this study was to determine if the pointing performance of the servo could be improved by modifying the structure and then redesigning the controller using the same analog filtering approach that is used in the current design.

B.1.1.2 Design requirements

The stability requirements for the instrument servo are 8 dB gain margin for the rigid body, 12 dB for the modes, and 30 deg of phase margin. The design is also required to remain stable if any of the modes are shifted in frequency by as much as 20 percent.

The servo is implemented in two instruments, the Sounder and the Imager. The Sounder input is a series of step and settle commands, while the Imager follows a ramp position input. The instrument performance requirements used in the analysis were generated from the error budget for the GOES-N servo. Based on the budget, the Sounder is required to settle to within $2.75 \mu\text{r}$ of a $140 \mu\text{r}$ step command in 28 milliseconds, which represents a 1.96% settling level. The settling level was rounded to 2% for the analysis. The Imager shaft angle error is required to be less than $1.72 \mu\text{r}$ 0.2 seconds after the start of each slew.

B.1.2 Analysis approach

B.1.2.1 Finite element model correlation

At the initiation of this effort, a finite element model (FEM) that had been correlated to modal test data was not available. The existing uncorrelated FEM (Figure B.1.2-1) and data from a modal survey test of the existing GOES-I instrument were obtained, and an effort to perform a reasonable correlation was made.

After examining the available FEM, two areas for concern arose. First, the GOES-I FEM incorporates several modeling techniques which are not recommended. The effect of these techniques on the results could not be individually evaluated; although it is possible that their combined effects could cancel, the use of these techniques is not desirable as they can only act as possible sources of inaccuracy.

The second concern was the quality of the modal survey test data. The FEM was modified to reflect the structure that was tested in the modal survey, and an analytical mass matrix was obtained for correlation purposes. The mass matrix was used to mass normalize the test modes,

SPRINGS REPRESENTING H-S SHAFT BEARING

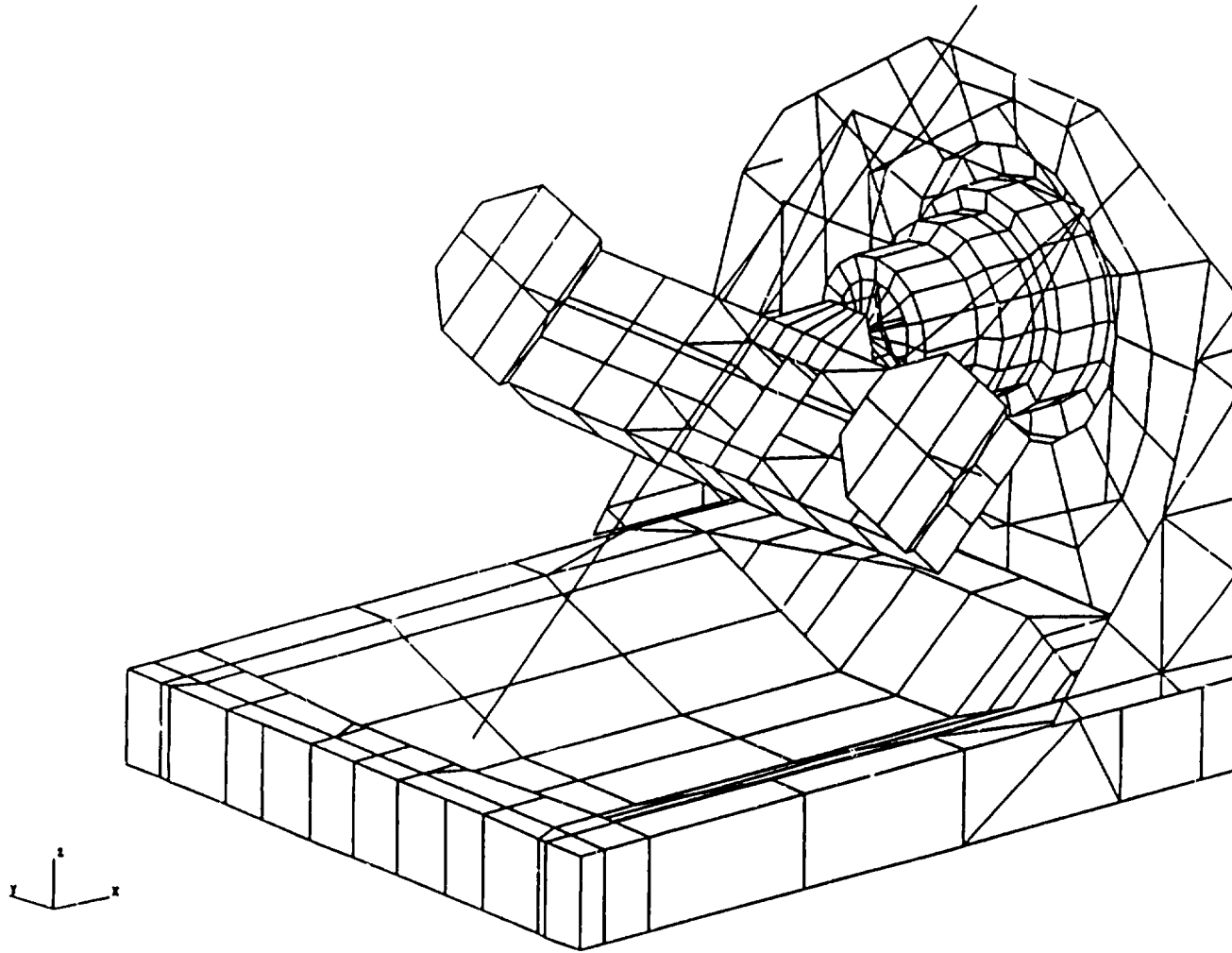


Figure B.1.2-1. Baseline Instrument FEM

and then the mass orthogonality of the test modes against themselves was calculated. The results show a high degree of coupling among the low order modes which should in general be the easiest to capture.

Since the modal survey test data did not include rotational displacements, a FORTRAN program was written to use geometry to calculate the rotations from the available translations. To check the procedure, translations from the FEM modes were input to the program, and the rotations output from the program were compared to the rotations in the original modes. The program was successful in reproducing the original rotations, so the modal test data displacements were input to calculate rotations as if they had been measured in the test. Having found the rotations, it was possible to calculate a structure transfer function for the controller from the modal test data for use in the correlation. A plot of the frequency response of the transfer function is shown in Figure B.1.2-2 using the modal damping values measured in the test.

Because of the shortcomings of both the FEM and the modal survey data, a precise correlation was not possible. Instead, the FEM was corrected only to the degree of attempting to produce some type of modal response in the same frequency ranges shown by the modal survey test data. A frequency response of the correlated FEM modes is shown in Figure B.1.2-3, using 0.1% modal damping. A comparison of Figures B.1.2-2 and 3 indicates that the modes of the correlated FEM reflect for the most part the same gross behavior as those in the modal survey test data. The conservative value of 0.1% modal damping used in the study causes the FEM modes to exhibit larger, sharper peaks than those of the test, where the measured damping was typically on the order of 1.0%.

B.1.2.2 Mode sorting procedure

Because the FEM contains thousands of degrees of freedom, the dynamic analysis of the model produces a large number of modes. Including all of these modes in the controller design process is impractical due to numerical constraints, and is also unnecessary because many of the modes have little or no effect on the controller's performance. A sorting procedure was therefore used to select only the significant modes for inclusion in the controller design and performance analysis.

Before initiating the sorting process, the mode sets were normalized to unity modal mass so that valid comparisons among the modal displacements could be made. Next, the mode sets were truncated to only include modes below 3000 Hz. Because the rigid body characteristics of the structure naturally attenuate high frequencies, the conservative assumption was made that the system would safely attenuate modes above 3000 Hz into insignificance.

Since the model typically contained about 200 modes below 3000 Hz, further sorting was required. Several established methods are available for determining modal significance. Based on the locations of the controller's inputs and outputs in the structure, the methods calculate a significance factor for each mode in a set. The results are normalized so that the mode with the highest significance is assigned a value of 100 percent, and all of the others are expressed as a percentage of the highest value. The modes can then be sorted based on the significance factors. Unfortunately, none of the methods gives a foolproof procedure for interpreting the results of the significance calculation. It is difficult to establish the significance level at which the mode set

FROM ITT TEST DATA USING MEASURED MODAL DAMPING - LAST MODE 715 HZ

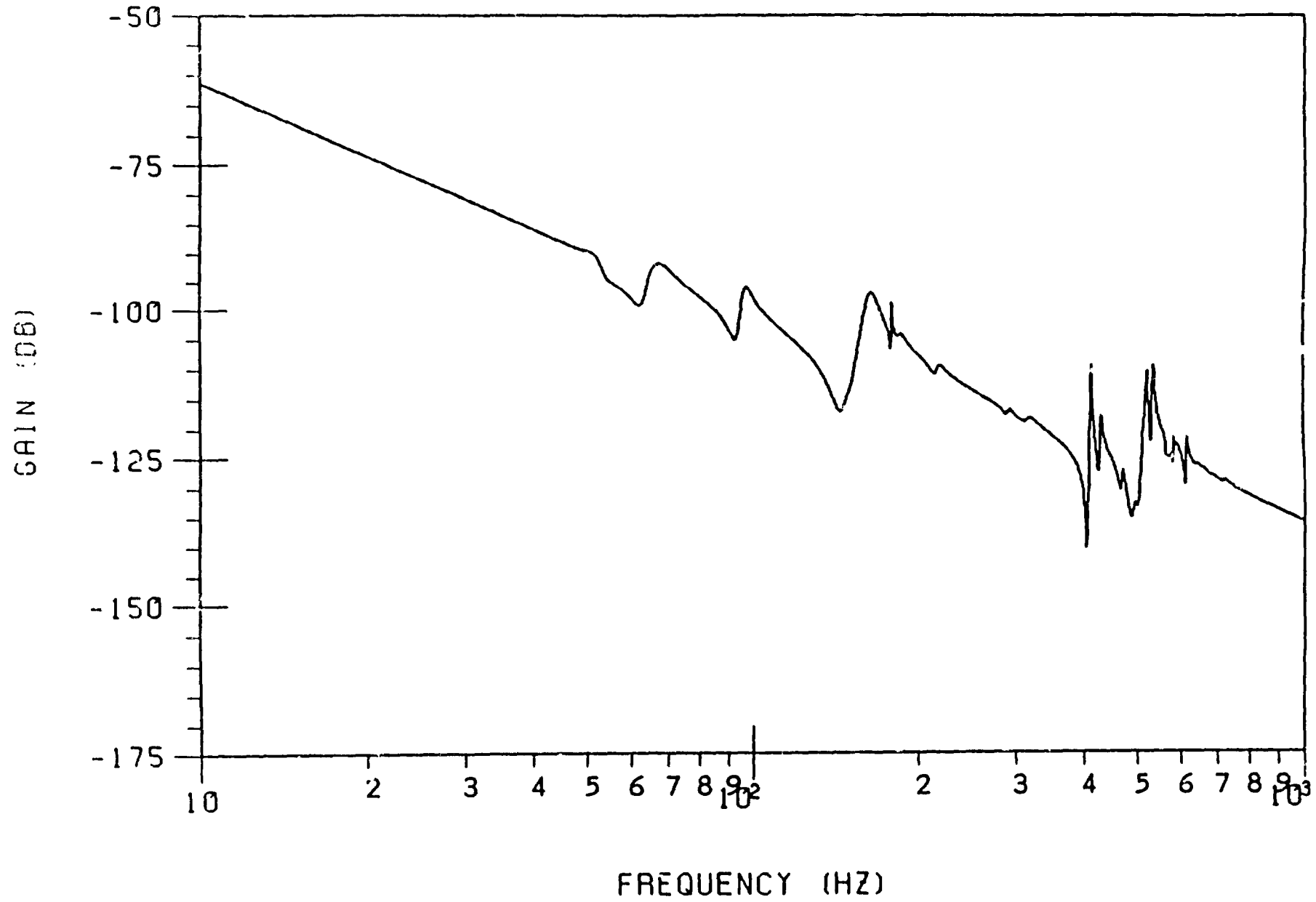


Figure B.1.2-2. GOES Scanner Structure Frequency R sponse

BASELINE NASTAR MODEL - MODES UP TO 1 KHZ

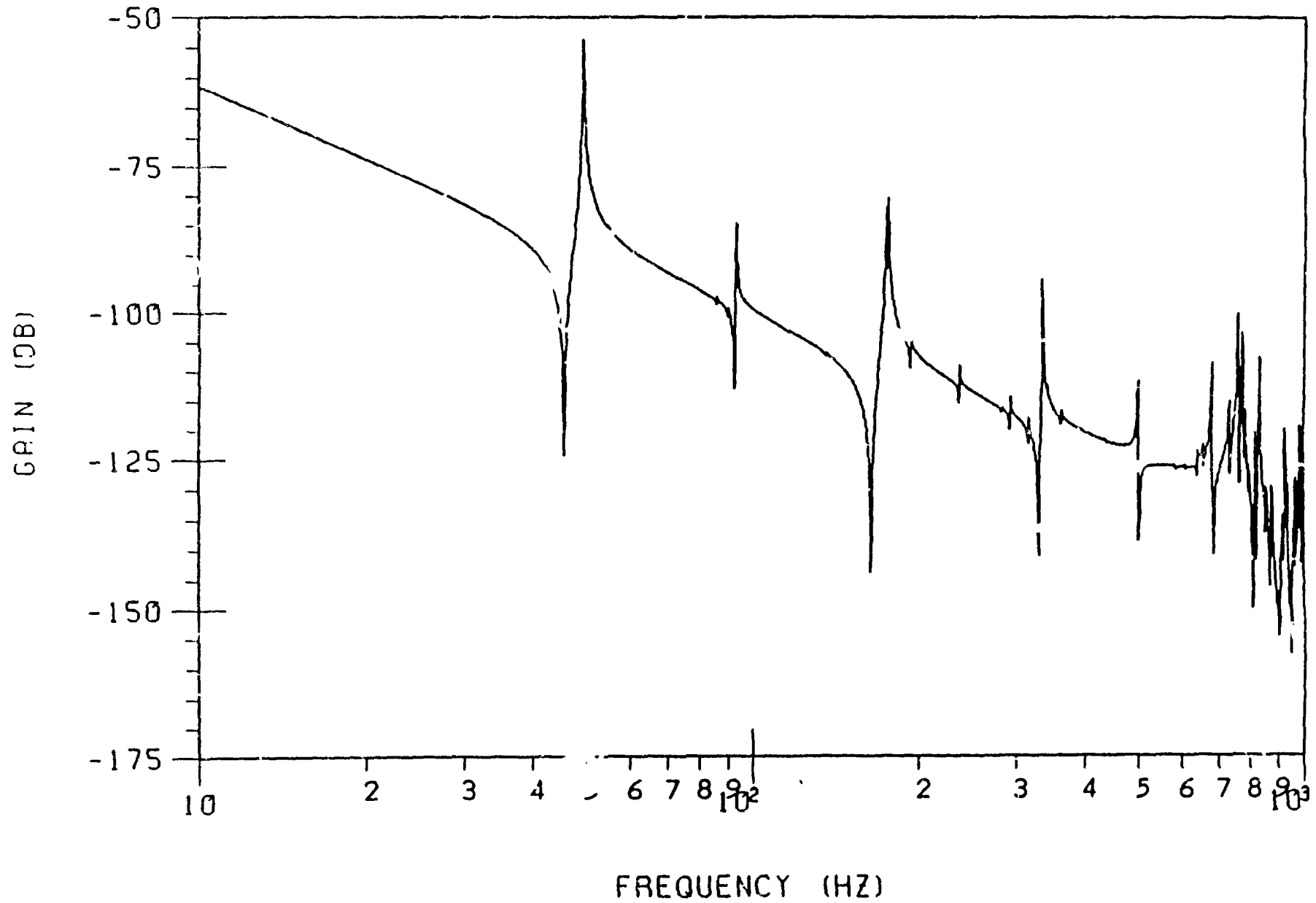


Figure B.1.2-3. GOES Scanner Structure Frequency Response

should be truncated, and it is also possible for a method to 'miss' significant modes by assigning them significance factors which are too small. These problems arise because the methods calculate significance based only on mathematical aspects of the modes, without considering the type of controller that is to be designed or the configuration of the system under study.

In order to minimize the possibility of missing significant modes, as a conservative approach it was decided to employ four different sorting methods and merge the results. The four methods consisted of three single input/output (SISO) methods (Modal Gain, Peak Amplitude, and a SISO version of Gregory's method) and one multiple input/output (MIMO) version of Gregory's method. These methods are documented in detail in References 1 and 2. The three SISO methods assigned significance using the relative rotation of the motor rotor with respect to the motor stator as the input and the relative rotation of the inductosyn rotor with respect to the inductosyn stator as the output. The MIMO version of Gregory's method assigned significance using the same degrees of freedom as in the SISO cases, but also included the rotation of the scan mirror about the East/West shaft as an additional output.

Each of the sorting methods was used to evaluate all of the modes below 3000 Hz. In order to get a preliminary reduction of the number of modes, a minimum normalized significance level was set for the output of each sort. From experience, values of 0.1% for Peak Amplitude and Gregory's Methods and 1.0% for Modal Gain have been found to work well. Modes with normalized significance below these values are generally not needed.

After applying each of the sorting methods, the results were combined into a table for easy comparison. The table typically contained between 50 and 100 modes. The modes to be used in the analysis were selected from the table by examining the level of agreement between the various methods. Modes showing a normalized significance of at least one percent in more than one method were selected first. Next, the remaining modes were examined on a case by case basis to decide if they should be selected. The selection among these remaining modes was performed with the controller design in mind; therefore modes in a critical frequency range (such as the region of the anticipated phase crossover frequency) were given highest priority.

The final set generally contained between 15 and 25 selected modes. As a last check of the sorting process, frequency response plots of the structure were made by first using the reduced mode set and then using the entire mode set. The plots were compared to ensure that the reduced mode set captured all of the important frequency domain characteristics of the full mode set. To illustrate the sorting procedure, Figures B.1.2-4 and 5 provide frequency response plots of the full and sorted mode sets for the baseline design.

B.1.2.3 Compensation design considerations

Both the imager and sounder are based on the same instrument structure design; only the scan profile required of each instrument is different. The sounder is required to follow a series of step and settle commands, while the imager slews to follow a ramp position input. A single controller design suitable for both instruments was attempted. The sounder presents the more challenging requirement of meeting a 2% settling time goal of 28 milliseconds. This requirement exceeds the

BASELINE NASTRAN MODEL - MODES UP TO 3 KHZ

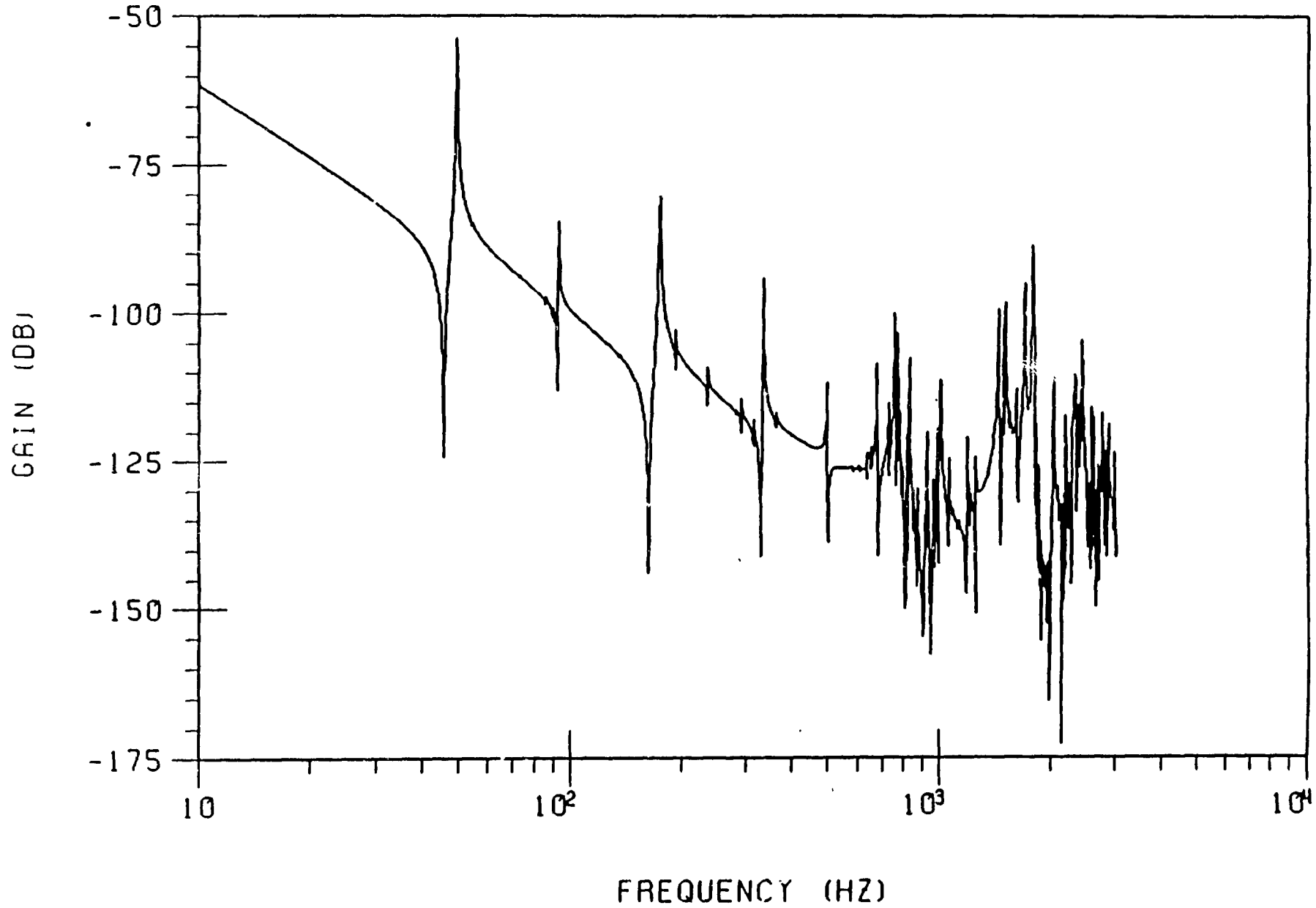
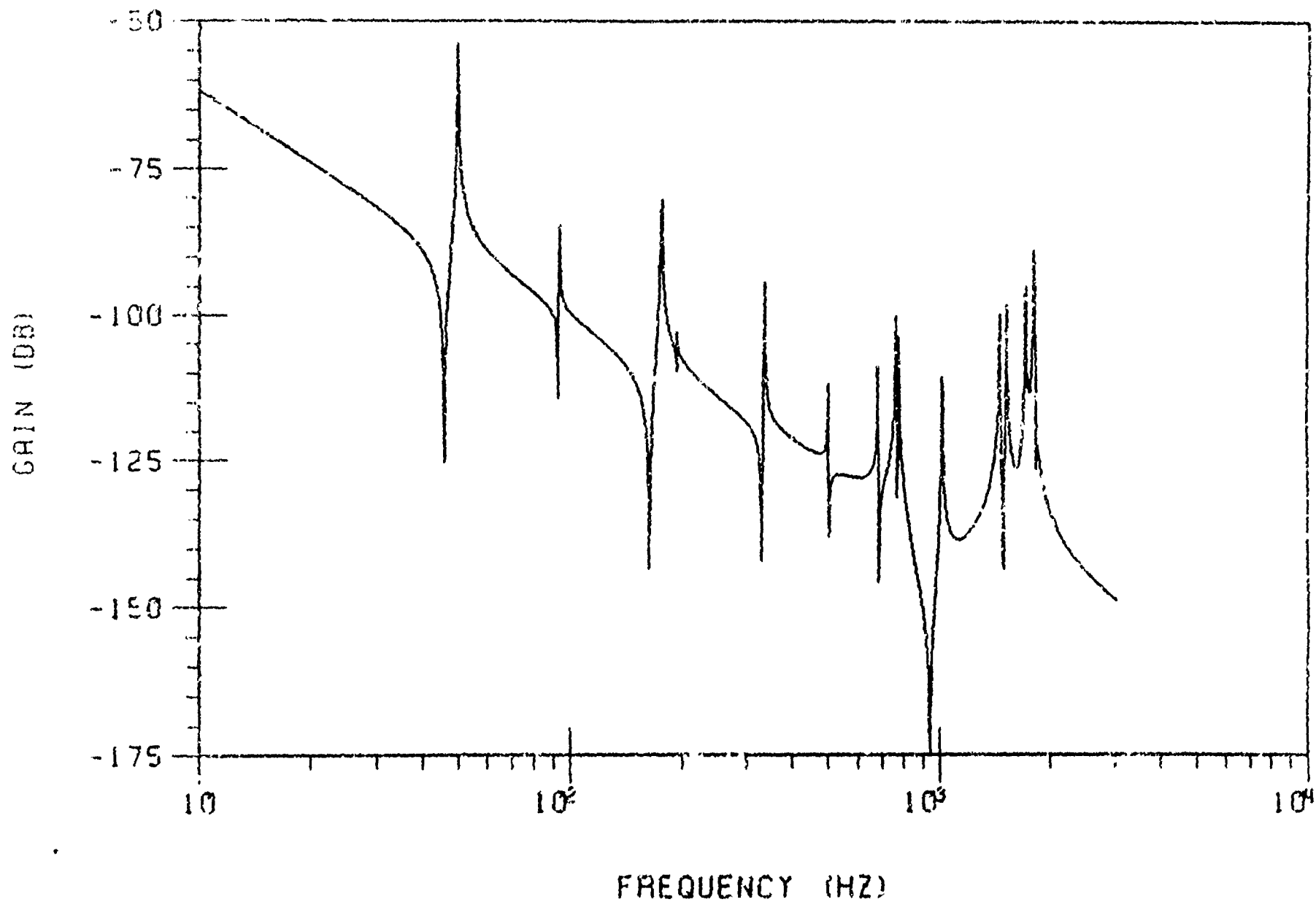


Figure B.1.2-4. GOES Scanner Structure Frequency Response

BASELINE NASTRAN MODEL - REDUCED MODE SET SELECTED FOR CONTROLLER ANALYSIS



Figur. B.1.2-5. GOES Scanner Structure Frequency Response

current instrument's capability, which is a 6% settling time of 28 milliseconds, according to test data from the actual servo (Figure B.1.3-7, Section B.1.3). The controller was therefore designed to meet the Sounder's step and settle requirement. A design which meets the step and settle is anticipated to meet the Imager's slew requirement, so analysis of the Imager was left for additional study. The Imager, however, does impose one requirement on the design. Due to the presence of friction, a proportional-plus-integral controller was included in the compensation designs to produce a Type II system which will have zero steady state error for the ramp input.

The design effort sought to maximize the bandwidth of the closed loop system while maintaining adequate stability margins. Since the design is primarily carried out using the open loop frequency response, the open loop crossover frequency was monitored as an approximate measure of the closed loop bandwidth. An examination of the structure transfer function for the baseline case, shown in Figure B.1.2-5, illustrates the typical problem that arises in designing the servo controller. Structural modes of large gain exist over the 50-1800 Hz frequency range, and must either be stabilized with a 30 deg phase margin or attenuated to -12 dB using some type of filtering.

Phase stabilization of modes at high frequencies is risky in practice because of uncertainty in the ability of the model to predict the actual phase of the system at high frequencies. The modes also tend to become more closely spaced on a log scale with increasing frequency, which increases the difficulty of phase stabilization. Phase stabilization of modes above 200 Hz was therefore not attempted. The adoption of this approach results in the frequency scale being broken into two regions consisting of a lower region where modes are phase stabilized, and an upper region where modes are attenuated. A transition region which does not contain modes of significant gain is needed to divide the two regions.

Generally, some type of filtering is required to attenuate modes in the upper region. Filtering also has the undesirable effect of introducing phase lag at low frequencies, which tends to erode the system's phase margins. The amount of phase lag produced by the filtering in the lower region increases as the filter attenuation increases and as the cutoff frequency gets lower.

Usually, lead compensation is also needed to establish phase margins in the lower region. Lead compensation also has two undesirable effects. First, it produces high frequency amplification which tends to cancel the attenuation of the filter in the upper region. Second, the slope of the gain curve is reduced in the lower region, which tends to reduce the rigid body gain margin. The amount of amplification produced by the lead network in the upper region increases as the amount of phase lead produced by the network increases.

For a given structure (mode set), the competing nature of the effects described above limits the bandwidth that can be achieved using a compensation design that is based on the analog design approach employed here. Maximizing the system bandwidth is analogous to maximizing the open loop gain. As the open loop gain is increased, the amount of attenuation required in the upper region increases, and finding a combination of filtering and lead compensation that produces a stable system becomes more difficult. At some point, it becomes impossible to both attenuate modes in the upper region and maintain phase and gain margins in the lower region.

The maximum gain, and hence bandwidth, at which the system can be stabilized clearly depends on the modes of the structure. If the structure has modes of very large gain at high frequencies, a large amount of attenuation will be required. If a mode set has a small transition region, the filter cutoff frequency will have to be placed close to the lower region, which causes a large phase penalty per unit filter attenuation. If many modes exist in the lower region, where a 30 degree phase margin must be maintained, then a lead network that produces a large phase lead is required. All of these cases illustrate ways in which the structure can impose undesirable limits on system performance. The structural modifications considered in this study were intended to produce favorable changes in the mode set. The compensation was then designed to use the highest open loop gain for which the resulting system could be made stable.

B.1.2.4 Filter design study

From the preceding discussion, it is apparent that the phase lag produced by the filtering below its cutoff frequency should be minimized because it is one of the factors which limits system performance. In an effort to identify an efficient filtering scheme, three common filter types (Butterworth, Type I Chebyshev, and Inverse Chebyshev) were compared for phase performance.

Filter specifications often arise as an attenuation requirement above a certain frequency (e.g., -30 Db for $f > 300$ Hz). Two factors govern the phase performance of the filters: the attenuation required, and the filter order used. Four test cases were chosen to form a test matrix that would characterize the effect of each factor on phase performance. In each test case, filters of the same order and attenuation level were compared. The four cases considered were: third order filters providing -15 dB at 1 Hz, third order filters providing -30 dB at 1 Hz, sixth order filters providing -15 dB at 1 Hz, and sixth order filters providing -30 dB at 1 Hz. Each of the cases compares filters that achieve the specified attenuation level at the same frequency, thus providing a net effect of normalizing the filters to a stopband edge of 1 Hz. Type I Chebyshev filters have the additional parameter of passband ripple, so two different values of the ripple were considered. The resulting set of filter designs used in the test cases consisted of Butterworth, Inverse Chebyshev, and Type I Chebyshev with 0.1 dB and 3.0 dB ripple.

The filter designs for the test cases are presented in Figures B.1.2-6 through B.1.2-9. As shown in the figures, the Inverse Chebyshev differs from the Butterworth and Type I Chebyshev due to the presence of zeros in the stopband which cause an equiripple effect. For odd orders, there is one extra pole which causes a -20 dB/decade slope at high frequencies.

A comparison of the third order cases with the sixth order cases indicates that the phase lag of the Butterworth and 0.1 dB Chebyshev increases as the filter order increases and that the phase lag of the 3.0 dB Chebyshev and Inverse Chebyshev decreases as the filter order increases. A comparison of the -15 dB cases with the -30 dB cases indicates that the phase lag gets larger as the attenuation level increases for all filter types. This result indicates that the filter attenuation should be kept to the minimum needed to meet a requirement. Finally, it can be seen that as the required attenuation doubles from -15 dB to -30 dB, the phase lag of the filters increases by less than a factor of two. Therefore, using two third order filters producing -15 dB each is not a better alternative to using one 6th order filter producing -30 dB.

THIRD ORDER FILTERS PROVIDING -15 DB AT 1 HZ

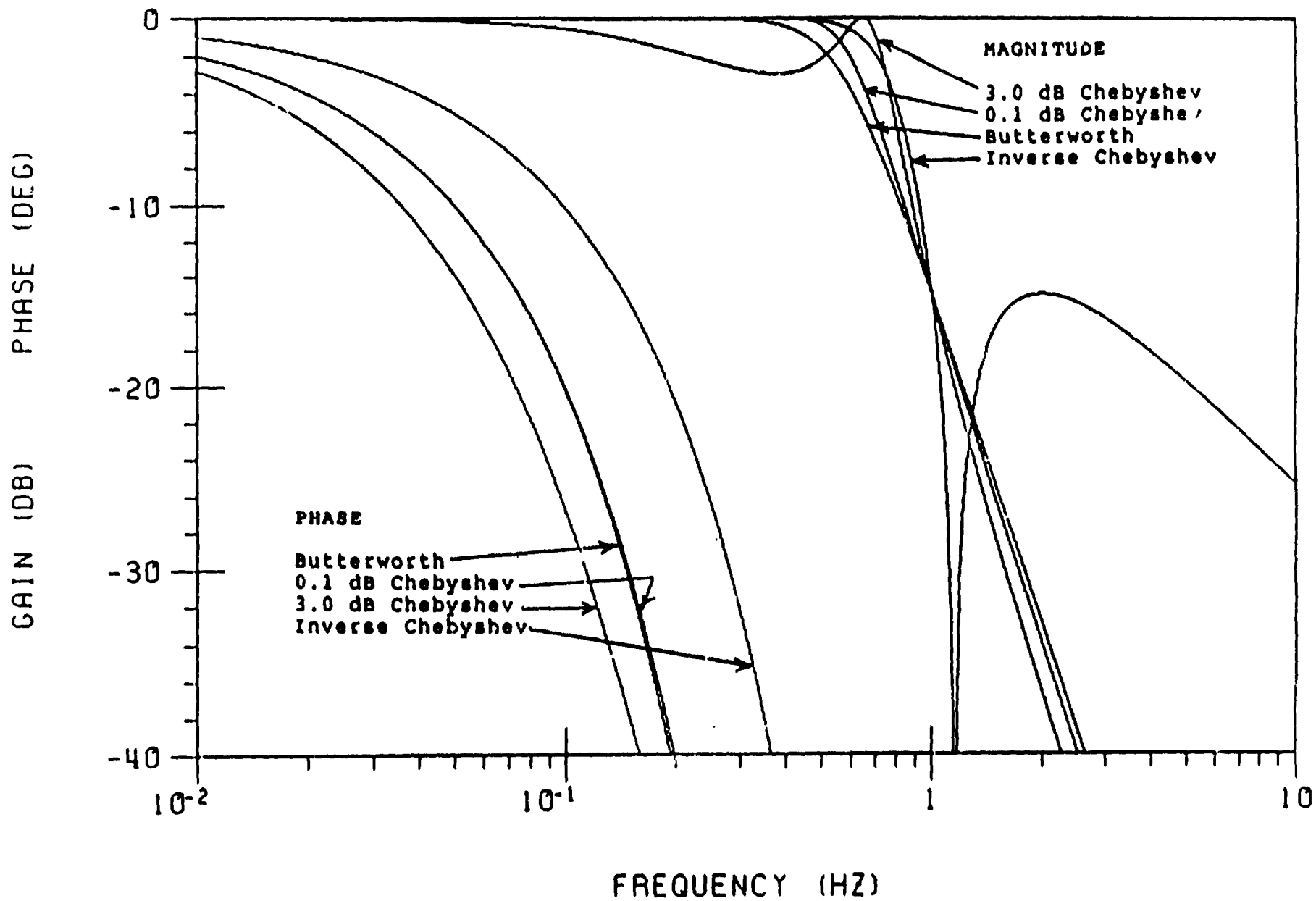


Figure B.1.2-6. Design Study Results

THIRD ORDER FILTERS PROVIDING -30 DB AT 1 HZ

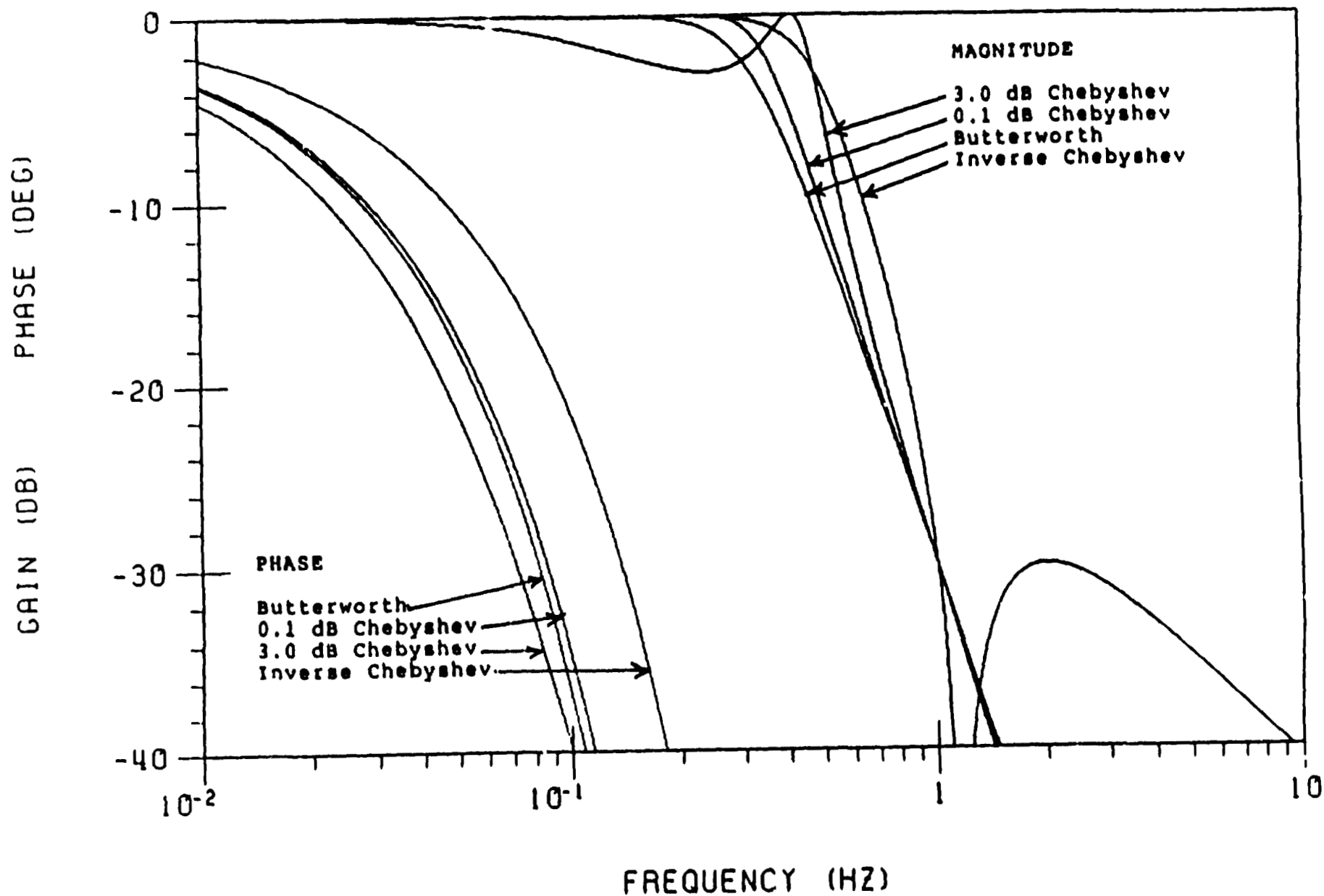


Figure B.1.2-7. Filter Design Study Results

SIXTH ORDER FILTERS PROVIDING -15 DB AT 1 HZ

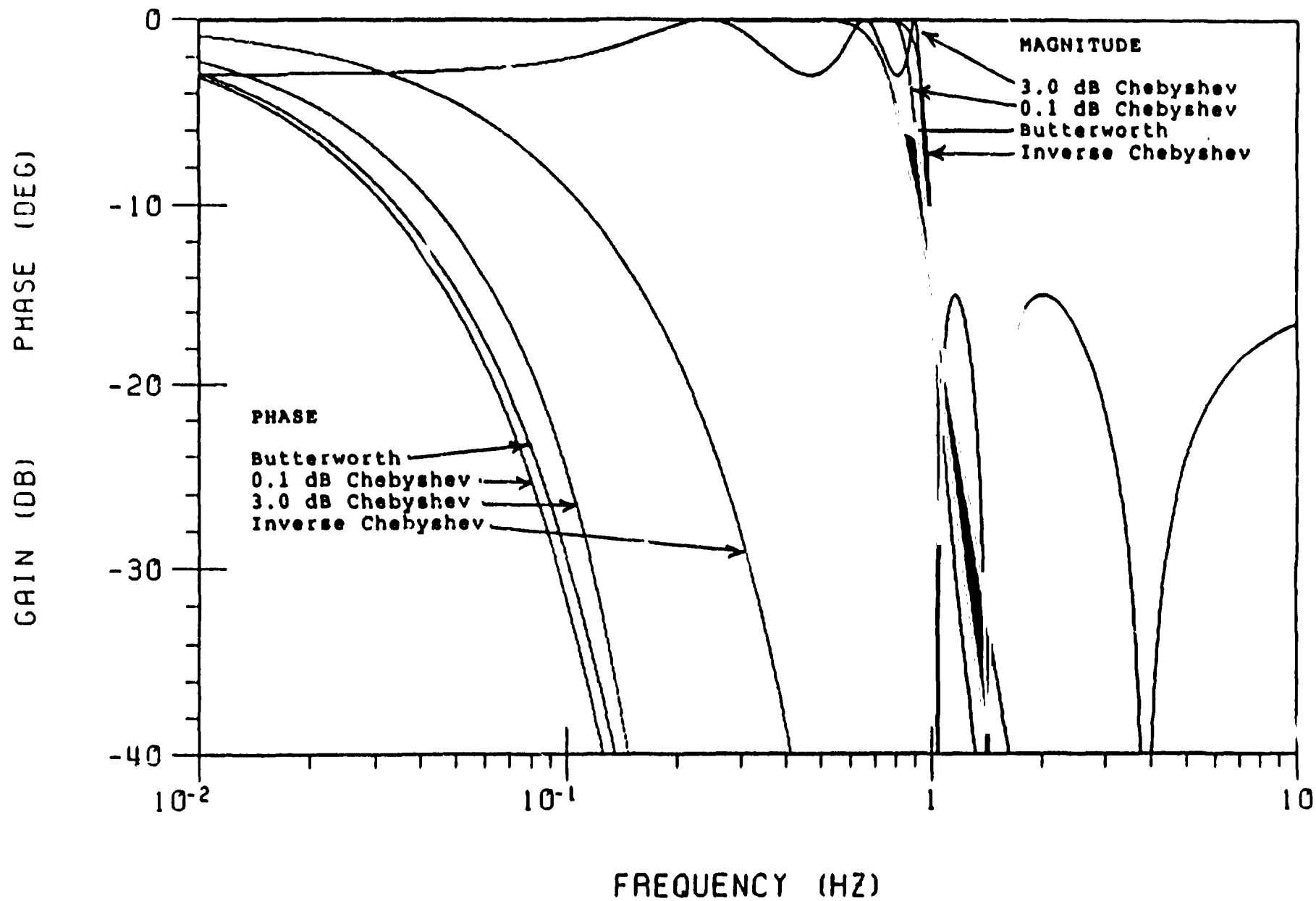


Figure B.1.2-8. Filter Design Study Results

SIXTH ORDER FILTERS PROVIDING -30 DB AT 1 HZ

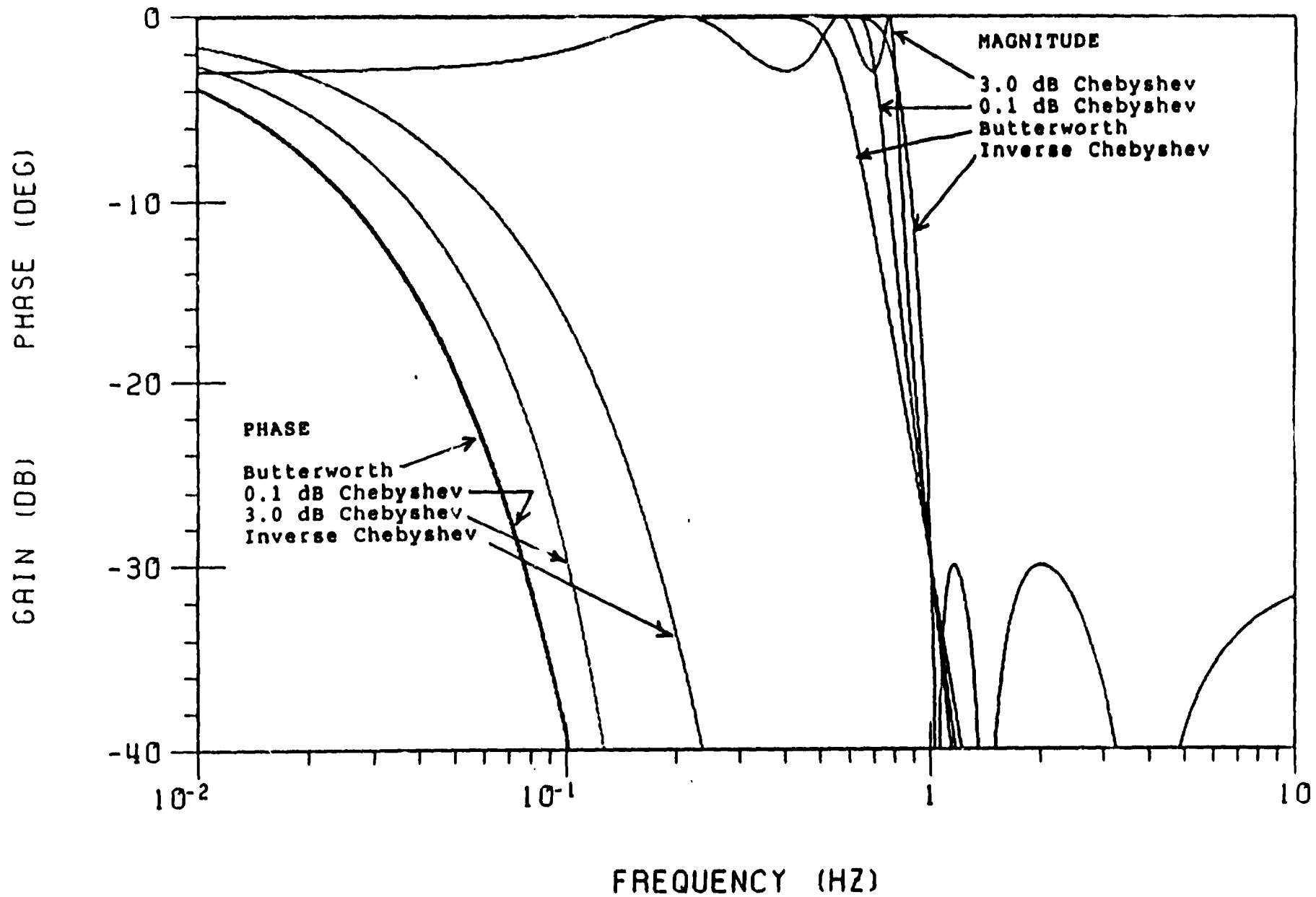


Figure B.1.2-9. Filter Design Study Results

The figures also indicate that the Inverse Chebyshev has the best phase performance by a significant margin in all cases. The Inverse Chebyshev was therefore selected as the preferred filter type when designing compensation in this study. The selection of the Inverse Chebyshev was based on the need for a constant attenuation because that was the considered to be the most likely requirement in the study. It should be noted, however, that in other cases the Inverse Chebyshev may not be the best choice. Mode sets that require attenuation which increases with increasing frequency or varies greatly with frequency are examples of these situations.

Having selected the Inverse Chebyshev, the filter characteristics were examined more closely in an effort to obtain additional performance improvement. First, to better understand the effect of filter order on phase performance, 3rd, 6th, 9th, and 12th order filters were generated to give -30 dB at 1 Hz. The results are shown in Figure B.1.2-10. As noted previously, the phase lag decreases as the filter order increases, but the performance gained by increasing the order appears to have an asymptotic limit. It is apparent that raising the filter order above a certain level is not worth the added system complexity. Therefore, in a given application the filter order should be chosen just high enough to get nearly the asymptotic performance, but no higher than required to minimize the filter complexity.

The second option for improving the Inverse Chebyshev was to add damping to the zeros. The 'textbook' Inverse Chebyshev filter is generated with undamped zeros, all of which occur after the cutoff frequency of the filter. Each undamped pair of zeros introduces 180 degrees of phase lead at the frequency at which the zeros occur. With the addition of damping to the zeros, however, the phase lead is introduced more gradually, extending into the passband region where it partially counteracts the phase lag of the poles. Adding damping to the zeros also has the undesirable effect of increasing the gain in the vicinity of the zeros, so that the gain can become greater than unity near cutoff in the passband, and can give less attenuation than prescribed in parts of the stopband. The more damping is added, the more the gain increases. The extent to which this effect can be tolerated by the system being compensated defines the improvement that can be obtained. Essentially, adding damping to the zeros is similar to adding second order lead compensation. By trial and error, it was found that adding damping in small amounts has minor effects on the gain curve, but still produces worthwhile improvements in phase. The gain problem is minimized in the passband by adding very little damping to the zeros closest to the filter cutoff frequency, and adding progressively more damping to the zeros as they move out in frequency from cutoff. An illustration of this technique is provided in Figure B.1.2-11, where a 7th order filter providing -30 dB at 1 Hz is shown with and without the added damping. The figure shows that the added damping has produced a moderate improvement in phase performance.

Finally, the option of using a bandstop filter based on the Inverse Chebyshev instead of a lowpass filter was investigated. An examination of bandstop filter behavior showed that the phase lag produced by these filters increases as the width of the stopband increases. For a narrow stopband, the bandstop gives better phase performance than a lowpass of the same order. At some width, the bandstop and lowpass give identical performance. As the stopband becomes very wide, the performance approaches that of a lowpass of half the order, which is worse than that for a lowpass of the same order. Bandstop filters are therefore preferable when the range of frequencies to be attenuated is sufficiently narrow. To get a preliminary assessment of the bandstop filter's usefulness, a 12th order filter was generated to give -30 dB for frequencies from

INVERSE CHEBYSHEV FILTERS PROVIDING -30 DB AT 1 HZ

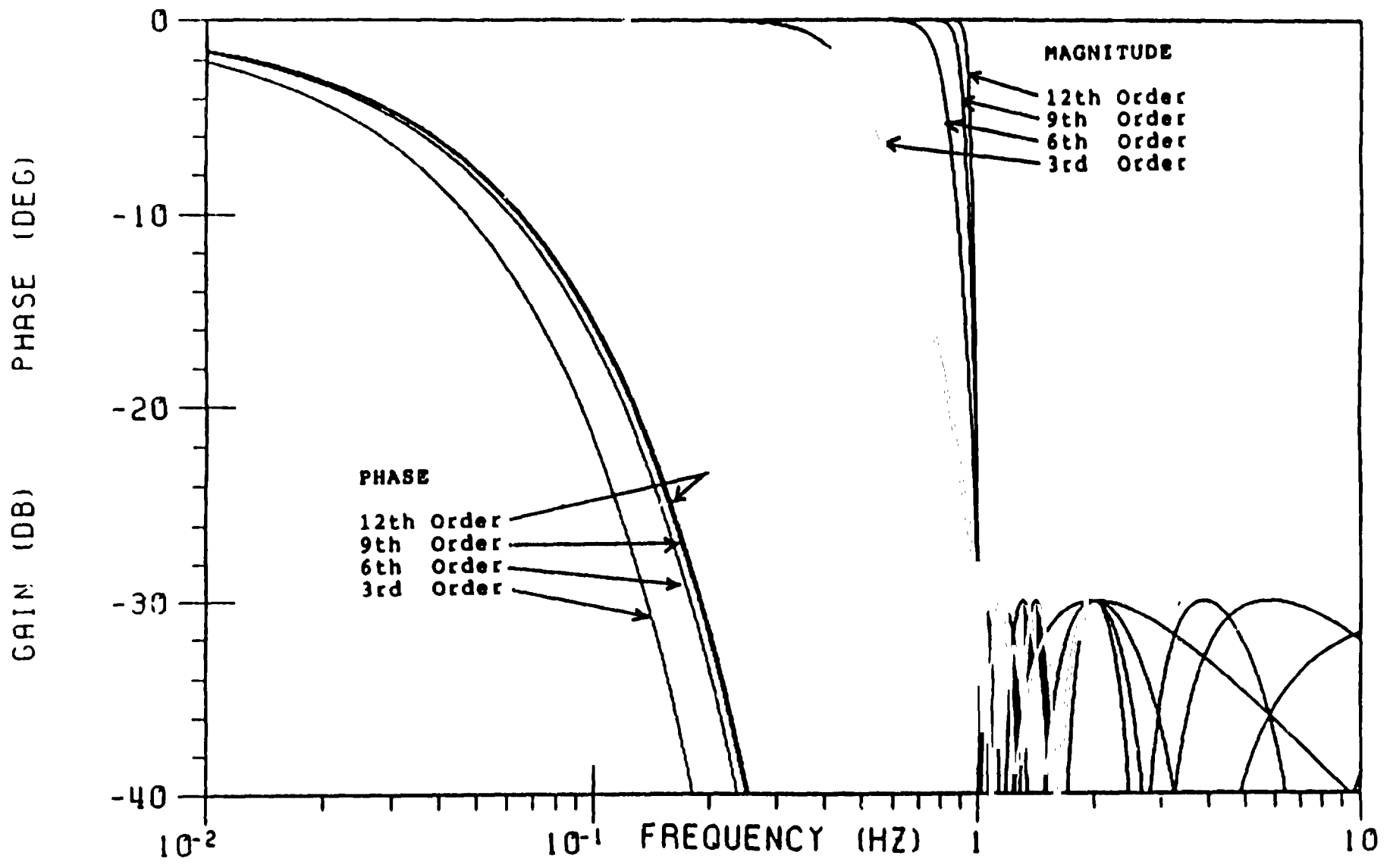


Figure B.1.2-10. Filter Design Study - Results filter order comparison

7TH ORDER INVERSE CHEBYSHEV FILTERS PROVIDING -30 DB AT 1 HZ

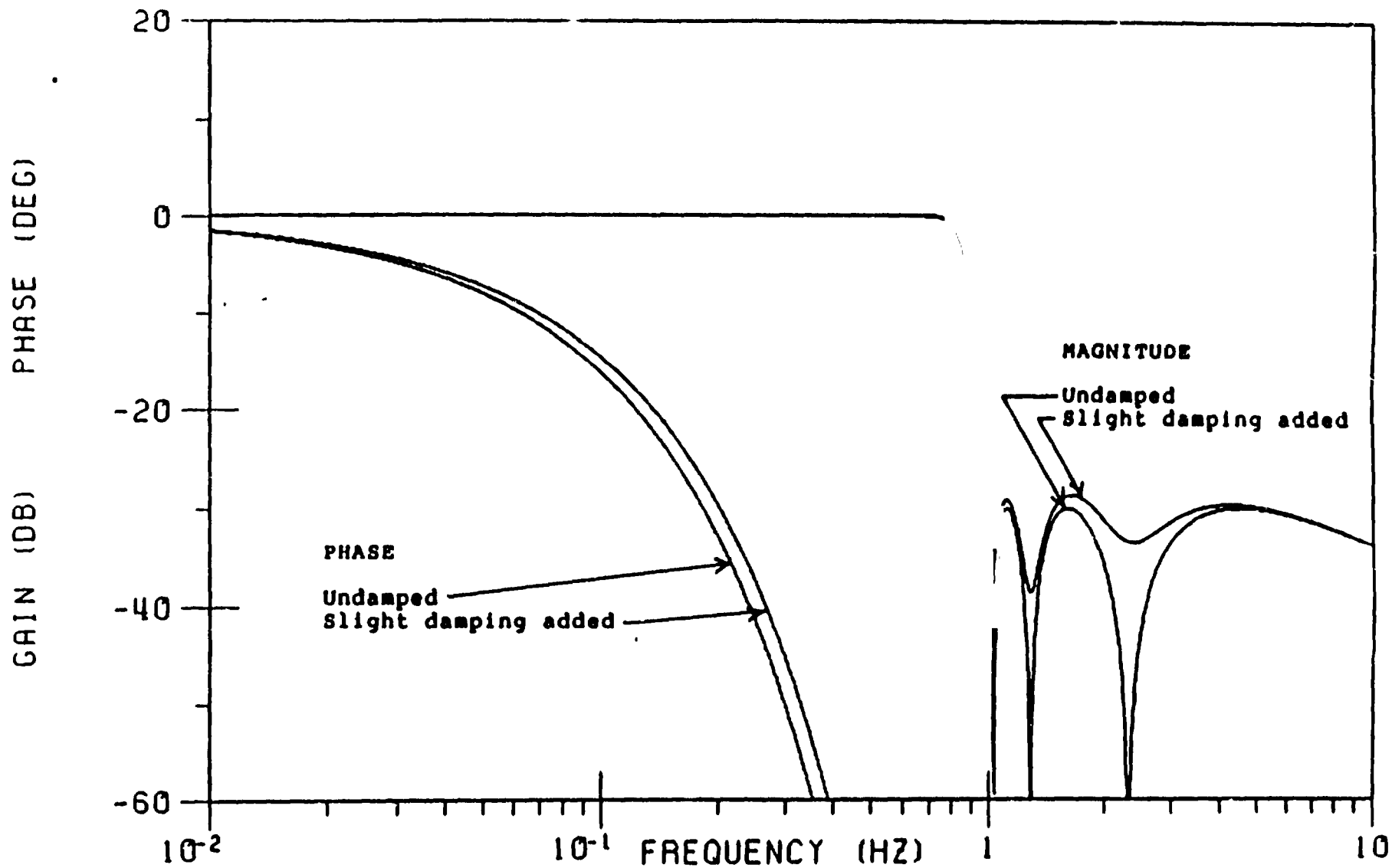


Figure B.1.2-11. Filter Design Study - example of added damping

40 to 2200 Hz, which is the largest range that was likely to be needed in the study. A 12th order lowpass giving -30 dB at 40 Hz was also generated for comparison. The frequency response of the filters is plotted in Figure B.1.2-12. It can be seen that for a stopband of this width, the lowpass provides slightly better phase performance.

The order of the filters used in Figure B.1.2-12 was limited to twelve because an analog implementation is currently used. Constructing reliable high order filters using analog electronics is difficult because filter performance becomes increasingly sensitive to variations in component properties as the order increases. If a digital implementation is ultimately selected for GOES-N, it may be possible to consider higher order filters. Although the phase performance of the lowpass in Figure B.1.2-12 cannot be improved by raising the order (Figure B.1.2-10), the bandstop may still exhibit room for improvement. To examine this further, a 48th order bandstop filter was generated, and damping was added to the zeros to give a 'best case' version of the bandstop for comparison with the previously generated lowpass. (results are in Figure B.1.2-13). It can be seen that the high order bandstop now shows moderately better performance than the lowpass. The improvement was possible because at order twelve the asymptotic limit on phase performance of the bandstop had not yet been reached. The comparison therefore shows that if a digital implementation is used, or if the frequency range to be attenuated is narrower than the one used here, then a bandstop may be more effective.

B.1.3 Analysis results

B.1.3.1 Baseline case

An analysis of the existing instrument was performed using the baseline FEM and the current GOES-I servo controller design. The analysis was performed to compare the results with data from hardware tests of the actual system. This comparison was used to evaluate the ability of the analysis to predict the behavior of the actual system. The fidelity with which the baseline analysis reproduced the test results was used to gauge the reliability of the results for modified structure designs, for which no test data would be available.

B.1.3.1.1 Structure transfer function

The modes resulting from a dynamic analysis of the baseline FEM were sorted using the procedure previously described. The modal damping used was 0.1% percent, which is a standard value used for design. A frequency response plot using the significant modes selected by the sorting process is shown in Figure B.1.2-5.

B.1.3.1.2 Block diagram

A block diagram of the baseline system is presented in Figure B.1.3-1. The design contains an average error integrator (AEI), which acts as a PI controller to give zero steady state error for the Imager ramp input. The motor is voltage controlled, and therefore has back EMF included. The limiters were ignored in the frequency response analysis, but were included in the non-linear time response simulation of the system.

12TH ORDER INVERSE CHEBYSHEV FILTERS

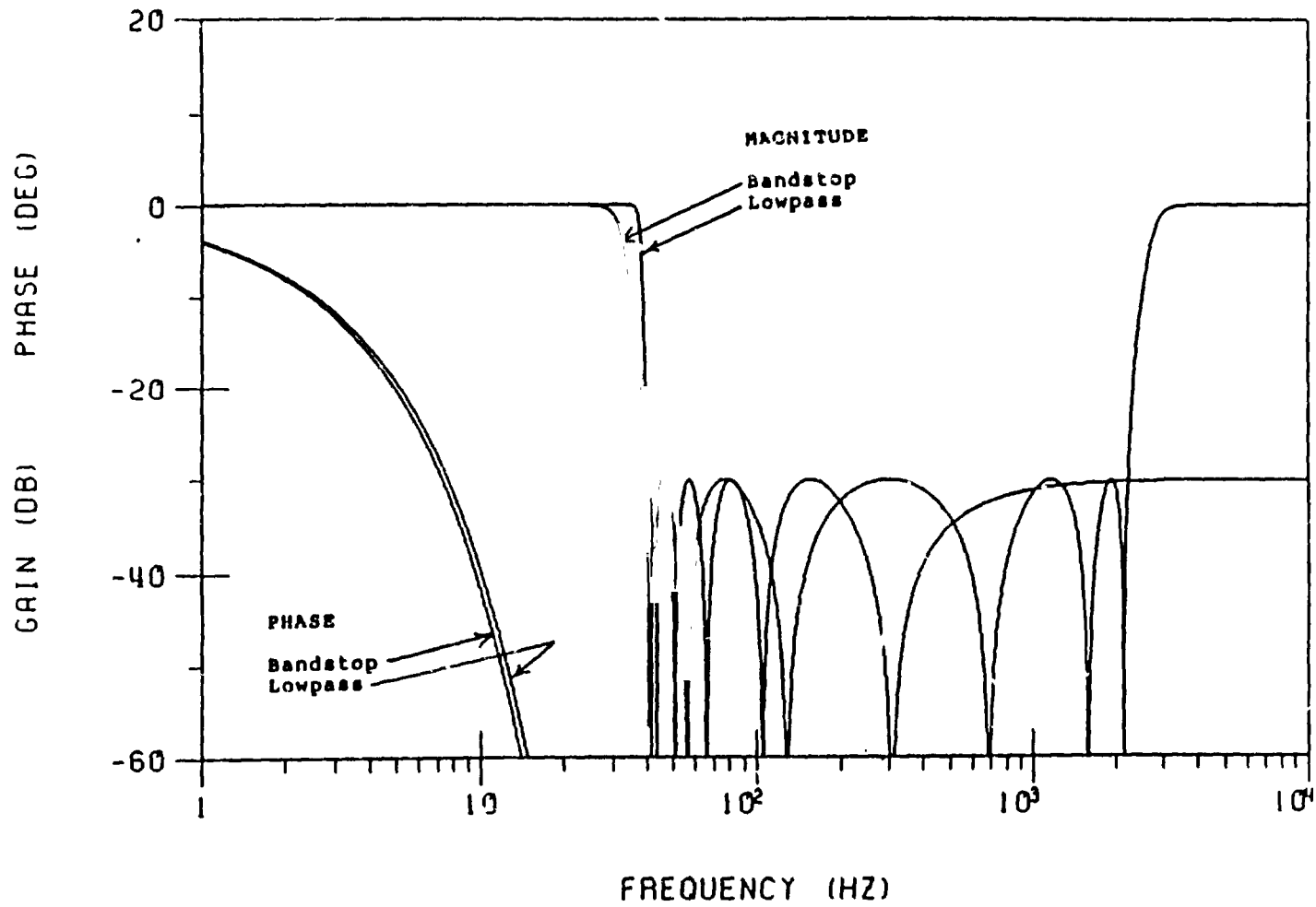


Figure B.1.2-12. Filter Design Study - lowpass/bandpass comparison

INVERSE CHEBYSHEV FILTERS -30 DB AT 40 HZ. LOWPASS ORDER=12, BANDSTOP ORDER=48

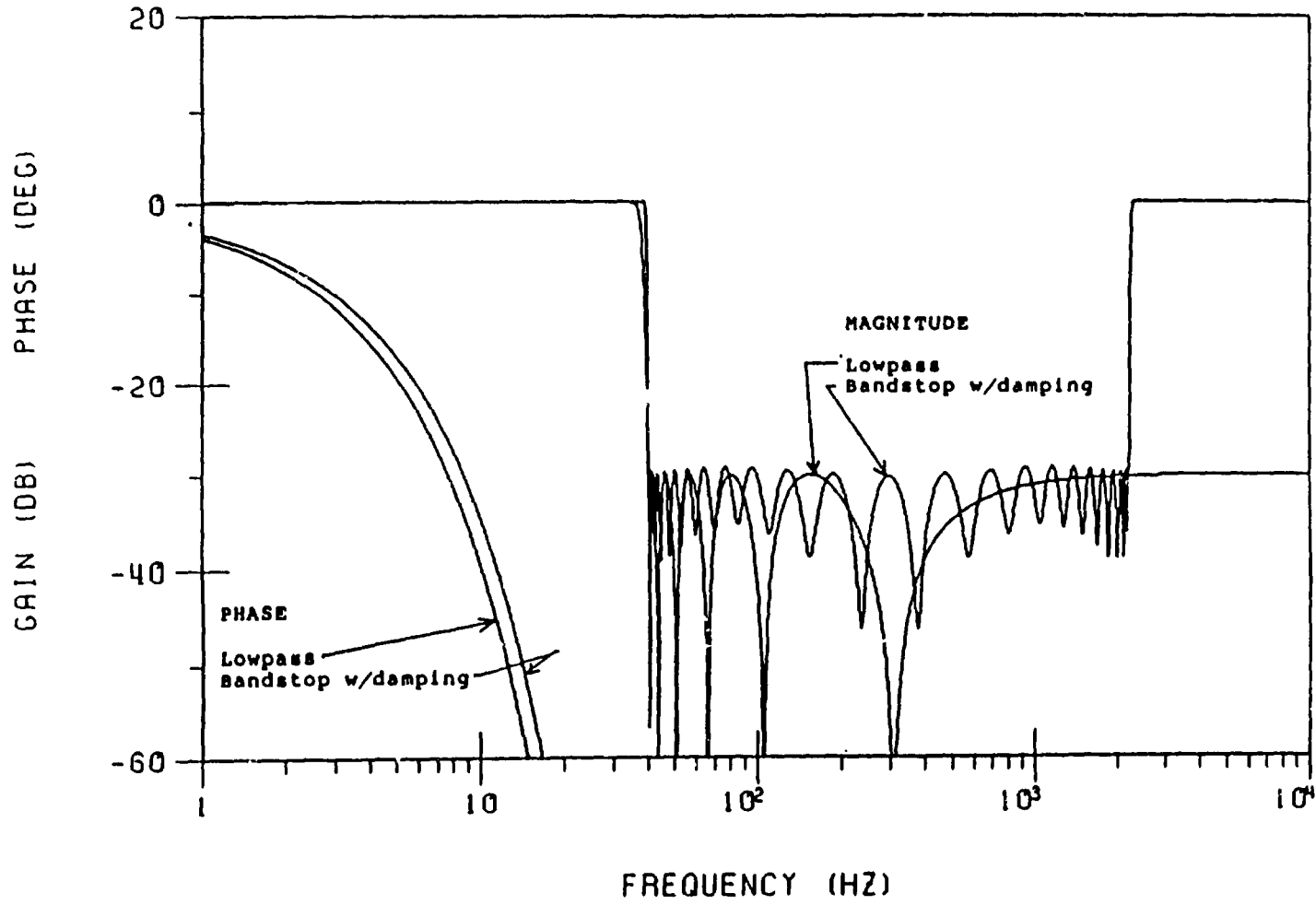


Figure B.1.2-13. Filter Design Study - lowpass/bandpass comparison

EAST/WEST SERVO BLOCK DIAGRAM

Reproduced from best available copy.

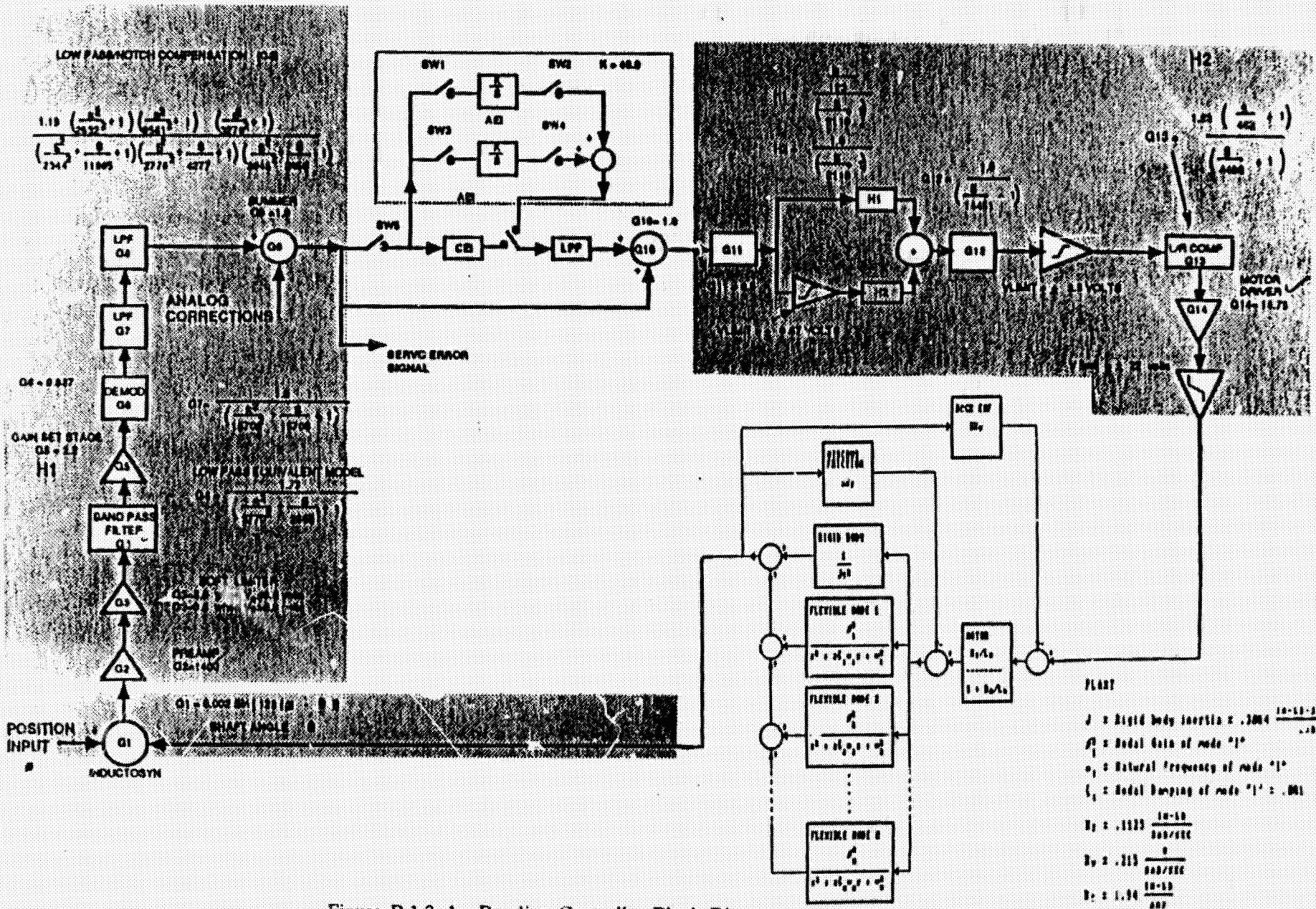


Figure B 1.3-1. Baseline Controller Block Diagram

B.1.3.1.3 System frequency response

The open loop frequency response of the plant before and after compensation is shown in Figures B.1.3-2 and 3. The compensation for the system includes a 6th order Inverse Chebyshev filter and two first order lead compensators.

Figure B.1.3-3 indicates that the system comprised of the baseline FEM modes and the existing controller design is unstable, mainly due to a mode of the FEM with large gain at 175 Hz. The modal survey test data for the actual instrument (Figure B.1.2-2) did show a significant mode near this frequency (163 Hz), but the mode has not been observed in open loop frequency response tests of the actual servo (Figure B.1.3-4). An investigation of the discrepancy between the modal survey and open loop test data found possible explanations for the disparity, but could not establish the specific cause. The actual system is known to be stable; therefore, based on the open loop test data it was decided that the 175 Hz mode would be left out of the baseline controller analysis. For subsequent cases involving hardware modifications, however, the mode was left in when it appeared because no supporting test data was available to justify its deletion. One additional modification was required to obtain adequate stability margins; the structural damping had to be raised from 0.1% to 0.3%. This action was justified by the results of the modal survey test of the hardware (Figure B.1.2-2), in which the measured damping was considerably greater than 0.3% for nearly all of the modes. Again, in analyzing other cases for which no test data was available, the damping was conservatively left at 0.1%.

The compensated open loop frequency response with the modifications to the mode set included is shown in Figure B.1.3-5. The system now shows adequate gain and phase margins of 8.2 dB and 31 deg, with an open loop crossover frequency of 14.6 Hz. The closed loop frequency response is given in Figure B.1.3-6. The presence of phase stabilized modes makes it difficult to interpret a value for the closed loop bandwidth. It can be seen, however, that the gain rises above 0 dB, which in a second order interpretation indicates a tendency of the step response to overshoot.

B.1.3.1.4 Time response simulation

A non-linear simulation of the baseline case was used to evaluate the step and settle performance of the system. The Dynamic Analysis and Design System (DADS), a non-linear simulation software package, was used to construct a model of the system. The simulation was based on the block diagram with the limiters included and a non-linear Dahl model used to represent the actual friction in the East/West shaft bearings. The simulation deliberately used Dahl friction instead of viscous friction (which was assumed in the compensation design) so that the effect of inaccuracies in modeling the real friction could be examined. The model was used to generate the response of the system to a 140 μ r step input. The resulting shaft error is plotted in Figure B.1.3-7 along with the response measured in a test of the actual servo.

The analysis results show a slowly decaying component in the error that is due to the Dahl friction model, which for a step of this magnitude acts like a retarding spring. The test data and the analysis results show similar decay characteristics and ringing of the lowest structural mode.

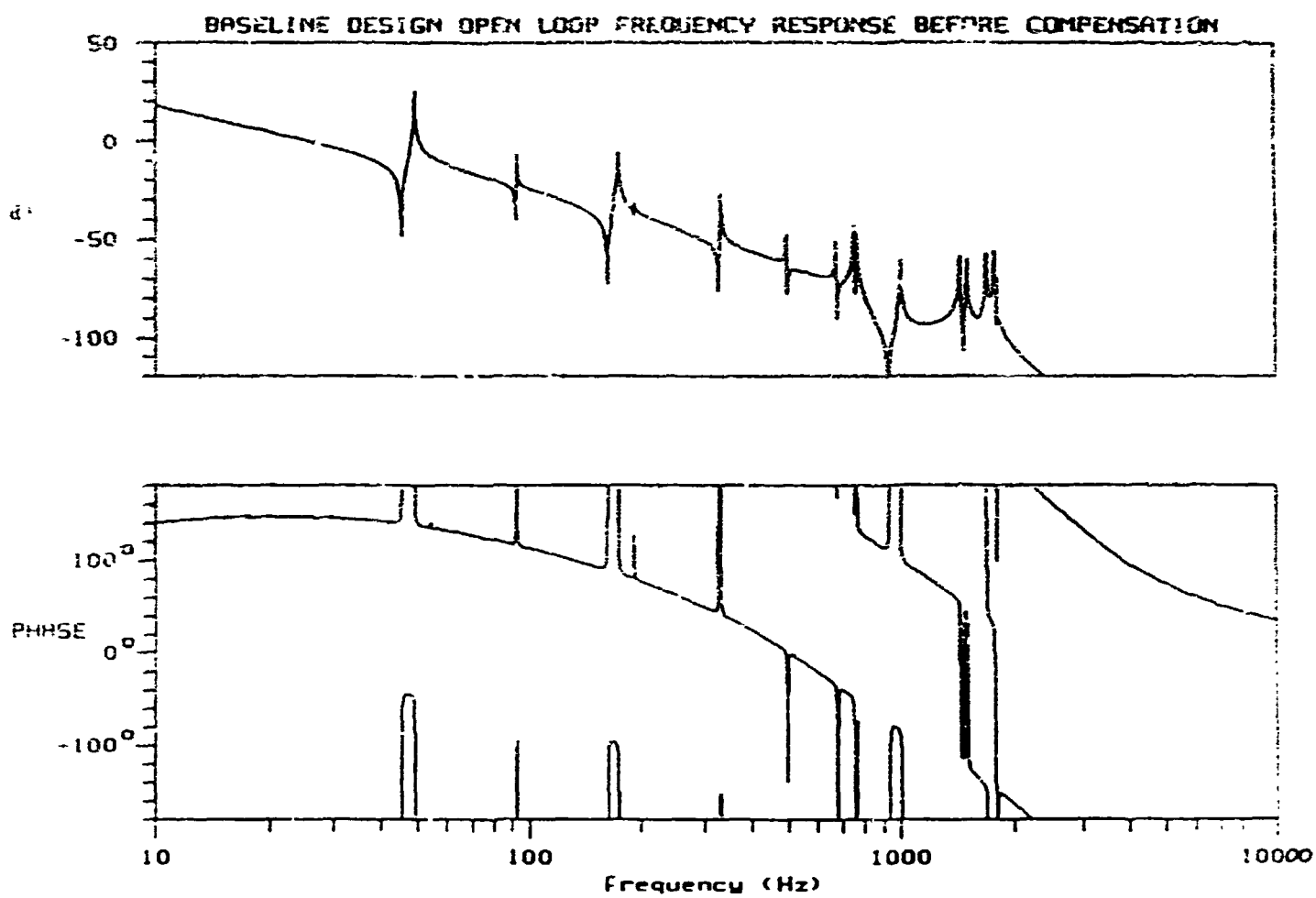
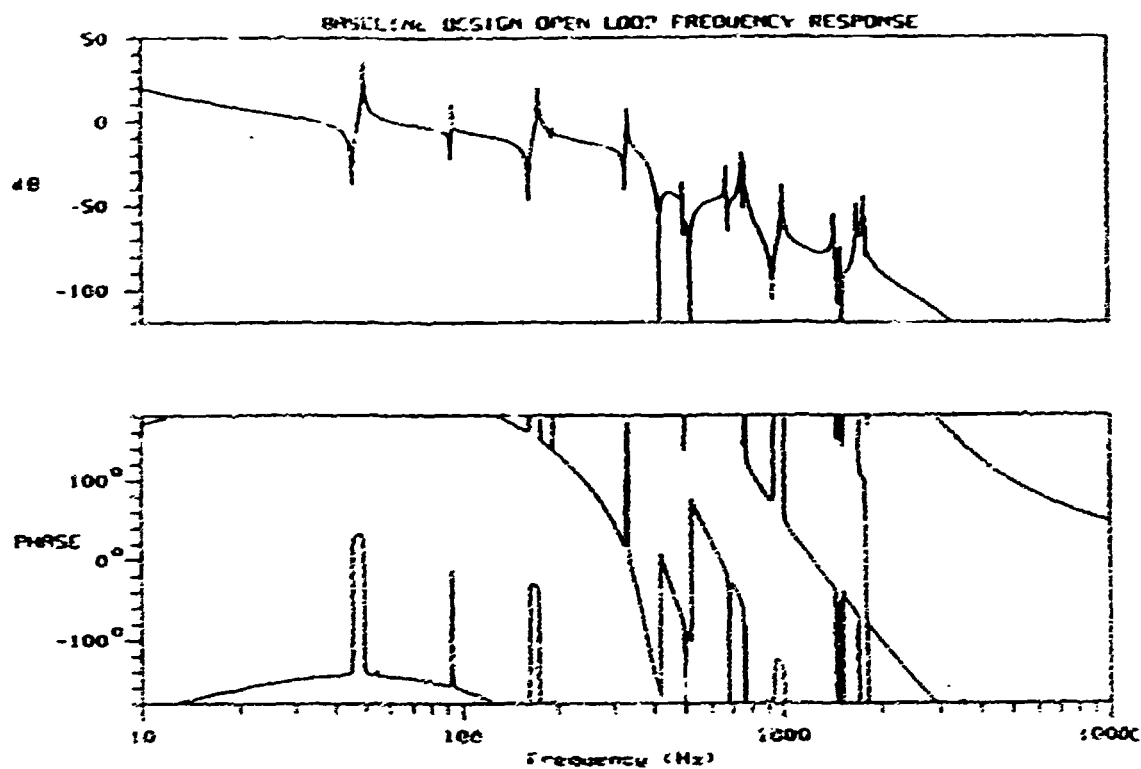


Figure B.1.3-2. Uncompensated Frequency Response - Baseline Design



Gain margins (P= 180)

W:	12.522 Hz	M:	15.097 dB
W:	127.58 Hz	M:	-9.8225 dB
W:	162.71 Hz	M:	-39.910 dB
W:	175.74 Hz	M:	17.745 dB
W:	152.86 Hz	M:	-9.3502 dB
W:	192.99 Hz	M:	-4.9647 dB
W:	418.90 Hz	M:	-7.4398E+05 dB
W:	496.52 Hz	M:	-37.229 dB
W:	499.13 Hz	M:	-67.432 dB
W:	521.39 Hz	M:	-5.0046E+06 dB
W:	756.14 Hz	M:	-20.911 dB
W:	752.94 Hz	M:	-51.583 dB
W:	769.91 Hz	M:	-22.799 dB
W:	935.82 Hz	M:	-106.02 dB
W:	1006.7 Hz	M:	-41.006 dB
W:	1448.7 Hz	M:	-60.679 dB
W:	1479.5 Hz	M:	-165.57 dB

Phase crossings (M= 0dB)

W:	34.426 Hz	P:	-147.24
W:	47.493 Hz	P:	32.423
W:	59.886 Hz	P:	-146.29
W:	92.793 Hz	P:	-15.339
W:	93.666 Hz	P:	-156.21
W:	172.10 Hz	P:	-34.298
W:	179.97 Hz	P:	146.80
W:	353.47 Hz	P:	150.89
W:	235.08 Hz	P:	15.550

Figure B.1.5-3 Compensated Frequency Response - Baseline Design

E/W BODE WHEN N/S AXIS AT NADIR

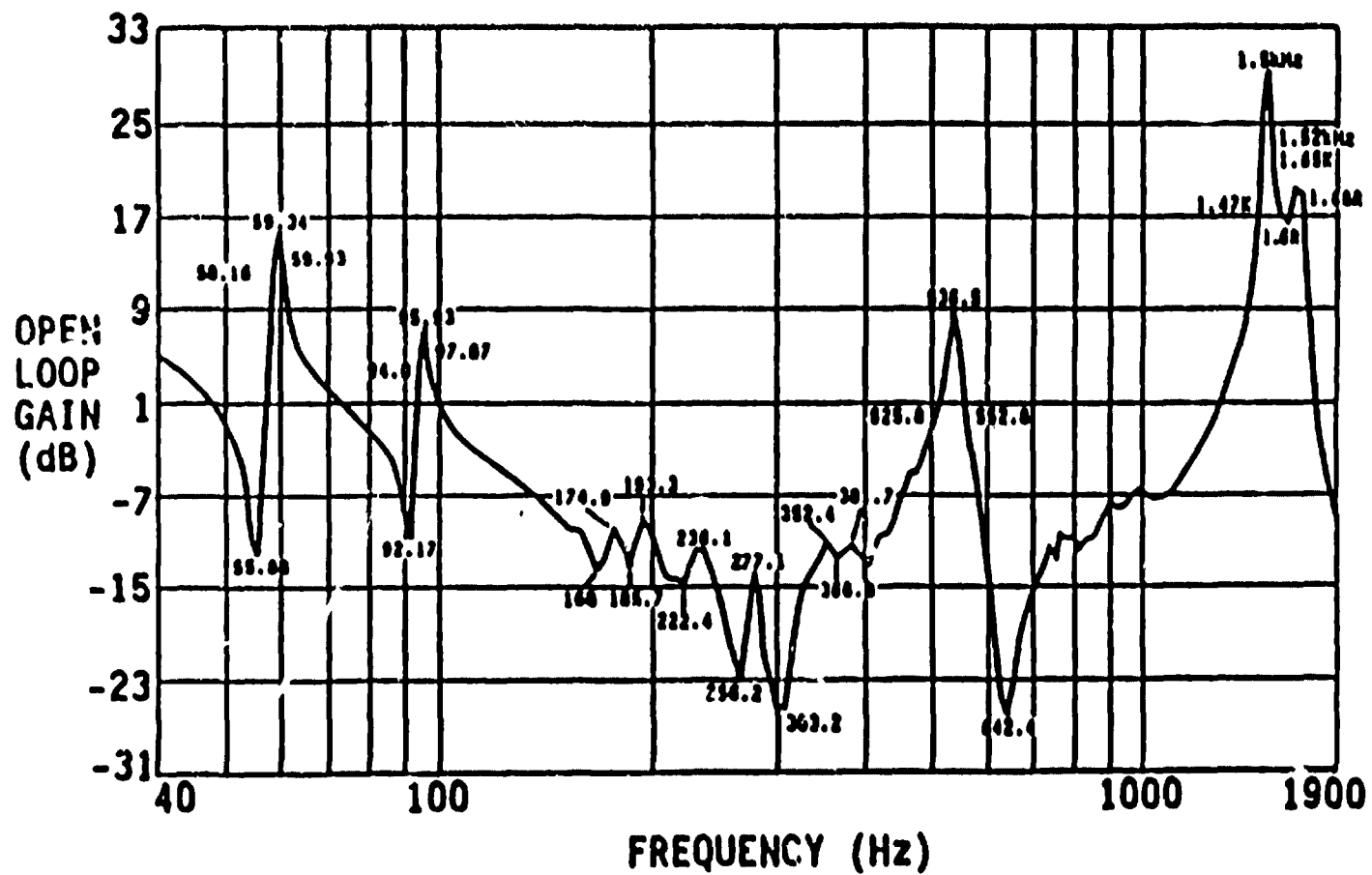
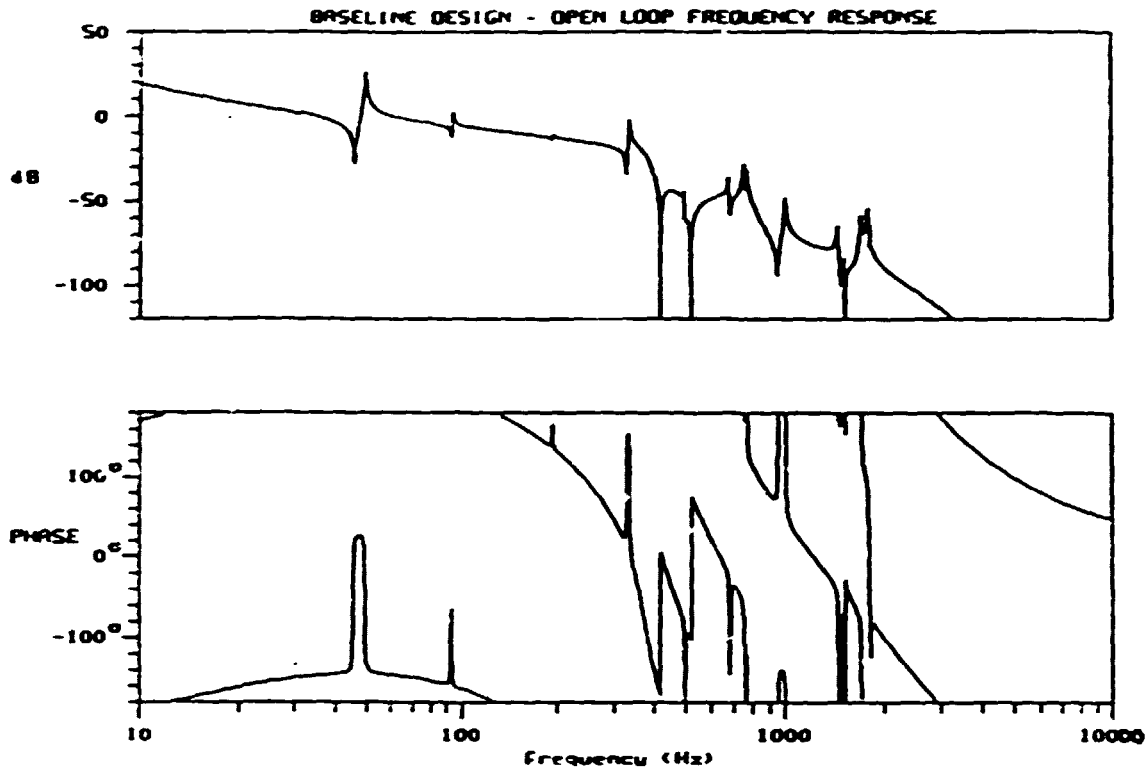


Figure B.1.3-4. Test Results from Open Loop Frequency Response Test of Actual Servo

The time is 14:03:24.89 12-SEP-1990
 Project: REPORT



FCN: G
 Gain margins (P= 180)

LF= 12.521 Hz	M= 15.106 dB		
LF= 127.57 Hz	M= -8.2334 dB		
LF= 418.90 Hz	M= -7.4516E+05 dB		
LF= 521.39 Hz	M= -5.9793E+06 dB	Phase crossings (M= 0dB)	
LF= 757.85 Hz	M= -32.324 dB	LF= 34.578 Hz	P= -147.10
LF= 761.82 Hz	M= -42.170 dB	LF= 47.505 Hz	P= 26.886
LF= 770.36 Hz	M= -31.386 dB	LF= 60.235 Hz	P= -146.18
LF= 953.72 Hz	M= -93.134 dB	LF= 92.880 Hz	P= -74.948
LF= 1004.4 Hz	M= -51.159 dB	LF= 93.623 Hz	P= -148.47
LF= 1453.5 Hz	M= -72.161 dB		
LF= 1475.3 Hz	M= -94.708 dB		
LF= 1517.7 Hz	M= -89.675 dB		
LF= 1524.9 Hz	M= 3.5750E+06 dB		
LF= 1701.9 Hz	M= -58.772 dB		
LF= 2916.2 Hz	M= -111.96 dB		

Figure B.1.3-5. Frequency Response with Compensated Baseline Design, 0.3% Damping and No 175 Hz mode

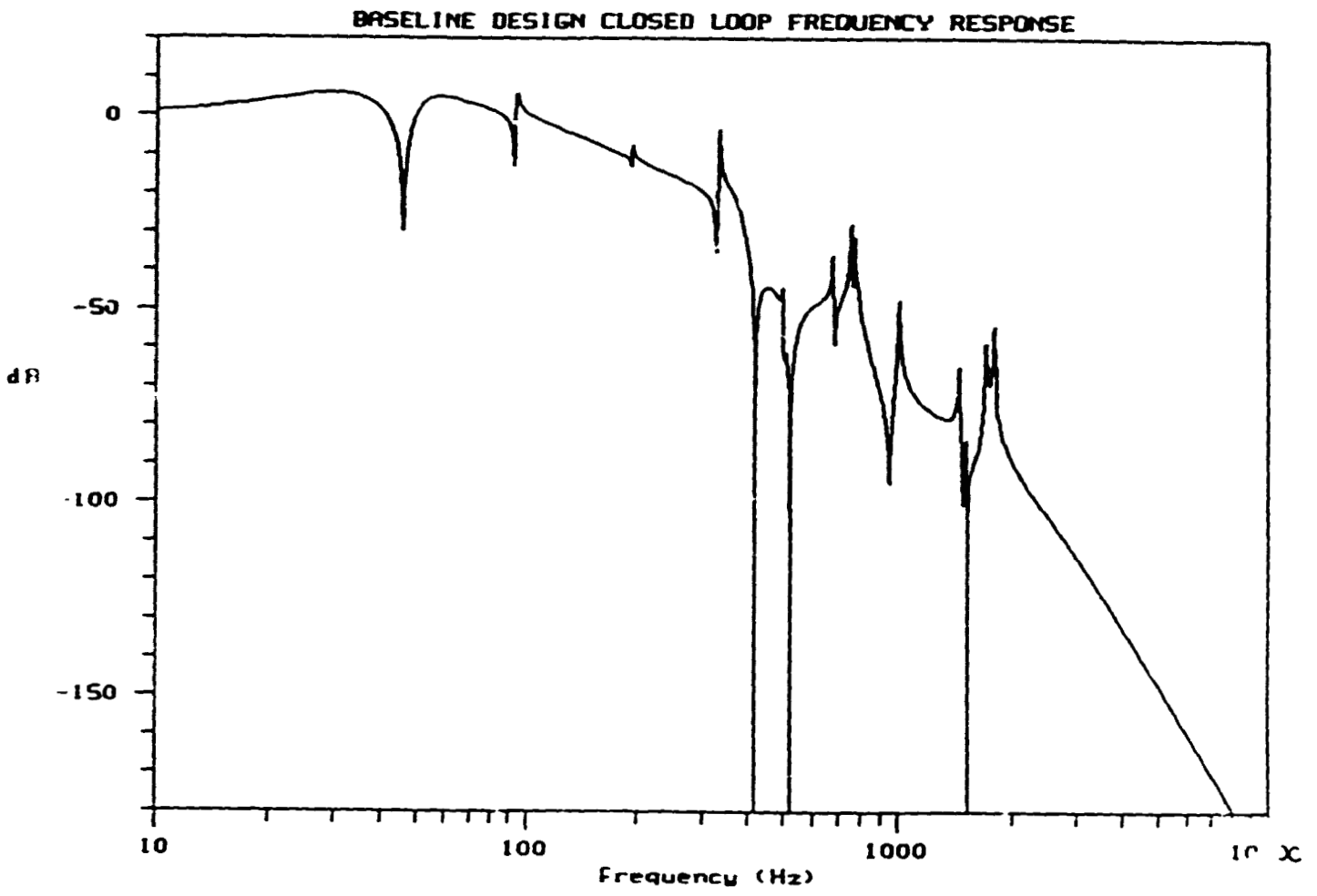


Figure B.1.3-6. Closed Loop Frequency Response - Baseline Design

140 MICRORADIAN STEP RESPONSE - BASELINE DESIGN AND ACTUAL SERVO

$\times E^{-5}$

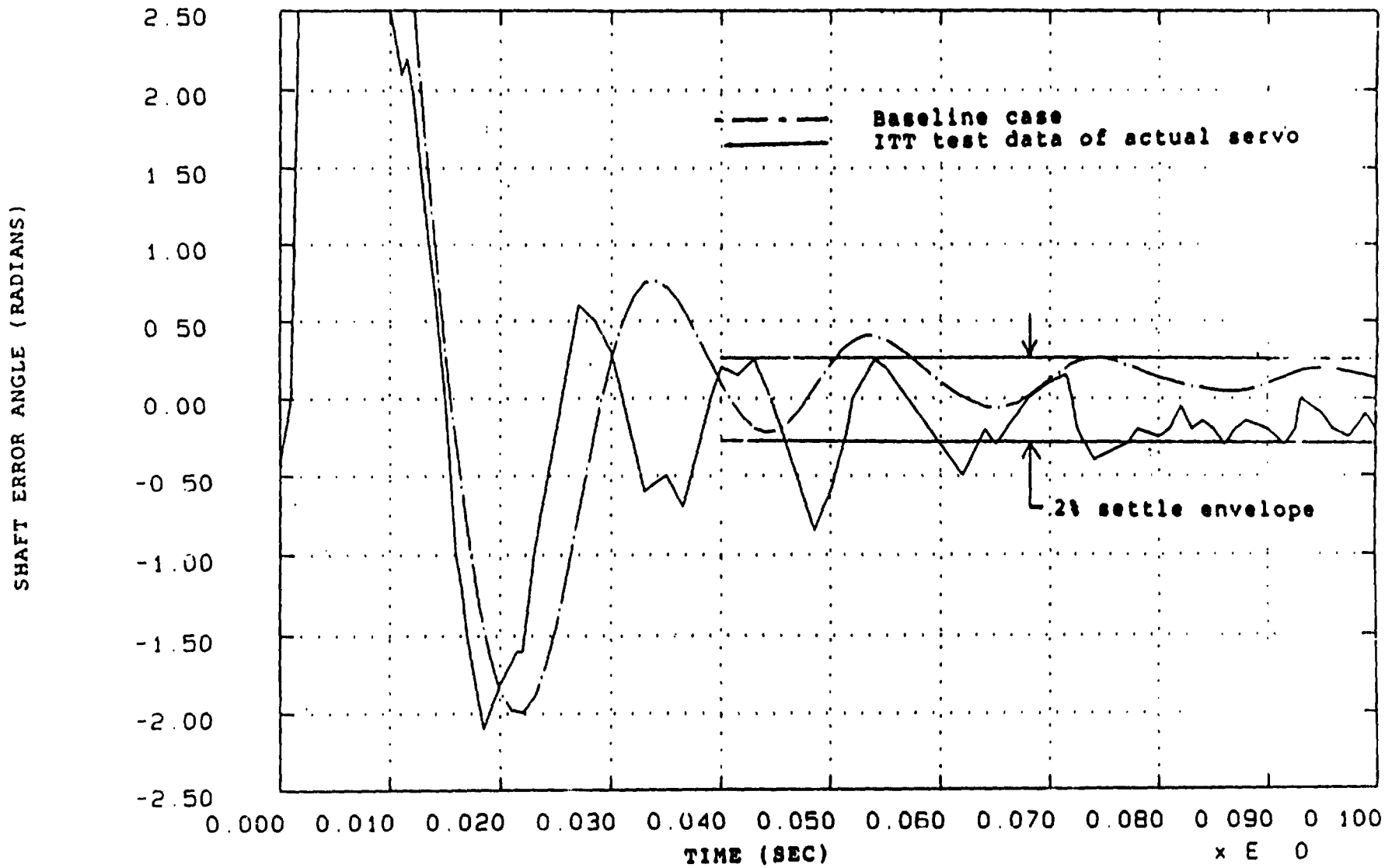


Figure B.1.3-7. Time Response of Baseline Design - 140 μ r Step

The bandwidth of the actual system appears to be slightly higher than in the analysis, but the analysis results are of acceptable accuracy for this study. It is apparent that this design does not meet the 2% step and settle requirement.

B.1.3.2 Co-located motor/encoder design

The baseline structure frequency response exhibits a mode of large gain at 1786 Hz, which was determined to be a torsional mode of the E-W shaft. Having a mode of large gain at this frequency makes it difficult to achieve a large bandwidth because the frequency is too high to consider phase stabilization, but is not high enough for the rigid body poles of the system to attenuate the large gain of the mode sufficiently. In an attempt to eliminate this problem, the idea of moving the inductosyn shaft angle sensor to the same side of the shaft as the motor was proposed. It was anticipated that the influence of the shaft flexibility would be reduced by this modification.

To analyze this configuration, the modes from the baseline model were resorted with the controller output location redefined to be at the motor end. A frequency response plot of the resulting plant transfer function is plotted in Figure B.1.3-8. Contrary to what was expected, the plot shows that the gain of the mode has increased by 25 dB, indicating that the relocation of the sensor has amplified the original problem. An examination of the shaft torsion mode shape provides a physical explanation for this result. The inertia of the mirror is approximately 100 times that of the motor, and 1000 times that of the inductosyn. The shaft torsion mode at 1786 Hz was actually a 'half-shaft' torsion mode, with the motor end having a large rotation, and the mirror and inductosyn end barely moving. The effect occurring in this mode shape, then, was the motor winding the E-W shaft up against the inertia of the mirror. The inductosyn does not show a large displacement because the large mirror inertia located midway between the motor and inductosyn acts as a buffer for the motion. The gain of a mode in a sensor/torquer system such as this servo depends on the magnitude of the relative motion occurring at the input and output. The motion at the input indicates how much a unit force will excite a mode, and the motion at the output indicates the observability of the mode. The product of these relative motions defines the total gain of the mode. Therefore, the original system tended to excite this mode greatly, with the mirror isolating the inductosyn somewhat from observing the motion. The net effect was a fairly large gain. Moving the inductosyn to the motor side caused both the excitation of the mode and the observability of the mode to be large, resulting in a very large gain.

Since the relocation of the inductosyn made the design problem worse, it was clear that the idea should be abandoned, and no controller redesign was attempted.

B.1.3.3 Two point mirror mount design

Another strategy for reducing the effect of the shaft flexibility was to change the mirror mount on the East/West shaft from a one point attachment at the center of the shaft to a two point attachment near the ends of the shaft. The goal of the new design was to reduce the effective shaft length and raise the frequency of the half-shaft torsion mode. Moving the mode to a higher frequency would allow the rigid body attenuation of the system to reduce the gain of the mode.

MOTOR/ENCODER ON SAME SIDE - NASTRAN MODEL MODES TO 3 KHZ

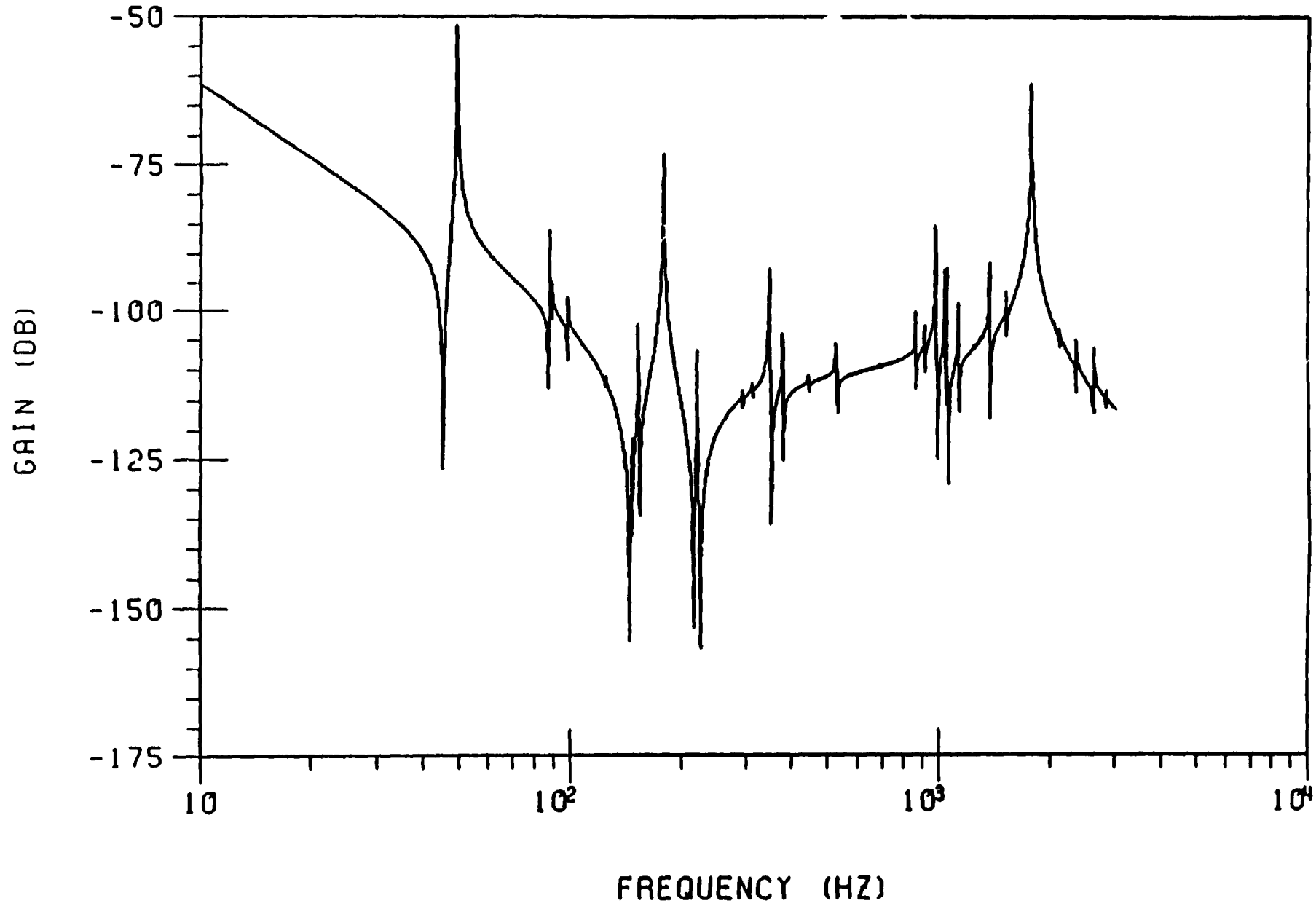


Figure B.1.3-8. Structure Frequency Response for Co-located Motor/Encoder Design

The new mount was designed with the end near the motor fixed to the shaft to prevent both rotations and translations, while the other end was a collar type joint that only prevented translations normal to the shaft. This configuration avoided using the mirror to carry torsional loads in the E-W axis, which could produce undesirable deformations of the mirror.

B.1.3.3.1 Structure transfer function

The baseline FEM was modified to reflect the new mirror mount and was then analyzed to produce the modes and frequencies of the new system. The modal sorting procedure was used to select the significant modes using a modal damping value of 0.1%. The frequency response of the resulting structure transfer function is plotted in Figure B.1.3-9.

An examination of Figure B.1.3-9 shows that modes of significant gain still exist in the 1800 Hz frequency range. Closer study of the mode shapes corresponding to these peaks showed that the frequency of the half-shaft torsion mode for the motor end was raised as expected.

Unfortunately, at the same time the half-shaft mode for the inductosyn end, which had been near 2500 Hz, dropped to 1800 Hz because the effective shaft length for this mode was made longer by moving the mirror East/West torsion constraint to the motor end. The net effect is an exchange of one half-shaft torsion for the other.

An unforeseen benefit of moving the mirror attachment points to the ends of the shaft was the reduction or elimination of some shaft bending modes in the 300-500 Hz range. The absence of problem modes in this frequency range creates the opportunity to phase stabilize the lower modes and attenuate the higher modes. Although the 175 Hz mode was still prominent and could not be dropped from the design, the possibility for improved performance was noted, and a controller redesign was performed to see if gains could be realized.

B.1.3.3.2 Block diagram

The block diagram for the two point mirror design is presented in Figure B.1.3-10. The average error integrator is still included, and a viscous model of the friction in the East/West shaft bearings is employed. Two modifications to the baseline design have been incorporated. First, a current controlled motor is included which essentially acts as a constant gain at the frequencies of this system. The motor pole and back EMF are therefore removed. Second, an optical encoder has been assumed, which removes the inductosyn dynamics from the system. Limiters have not been included because they represent constraints imposed by the implementation of the system, and this is a preliminary look at a design concept. Instead, the time domain simulation was used to examine the motor torque level required by this design.

B.1.3.3.3 System frequency response

The open loop frequency response of the system before and after compensation is given in Figures B.1.3-11 and 12. The compensation consists of a structural filter and a lead compensation network. An examination of the uncompensated frequency response shows that the need for attenuation in the 400-2000 Hz range increases with increasing frequency. The structural filter therefore includes a two pole filter to equalize the attenuation required by these modes, and

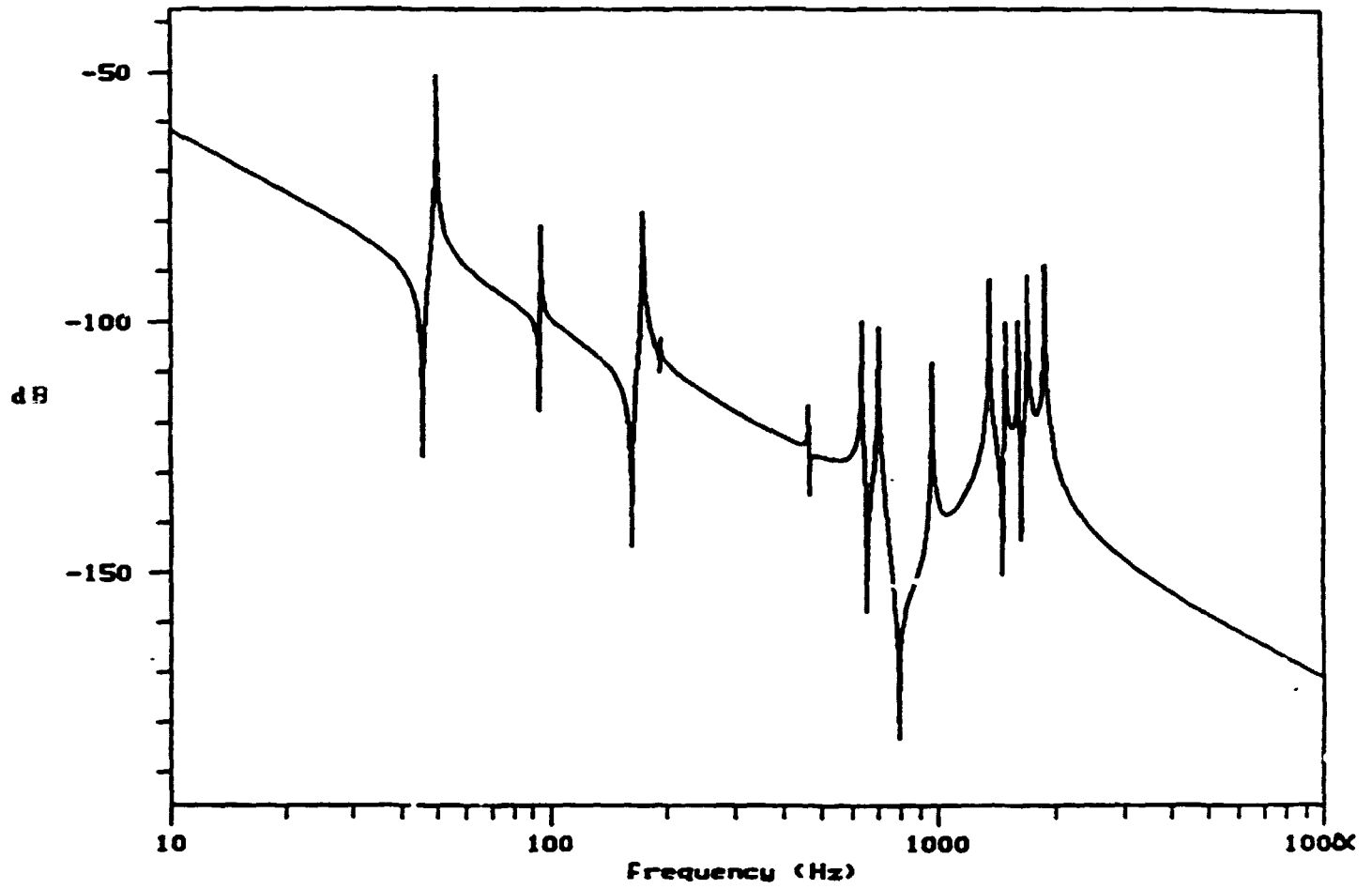
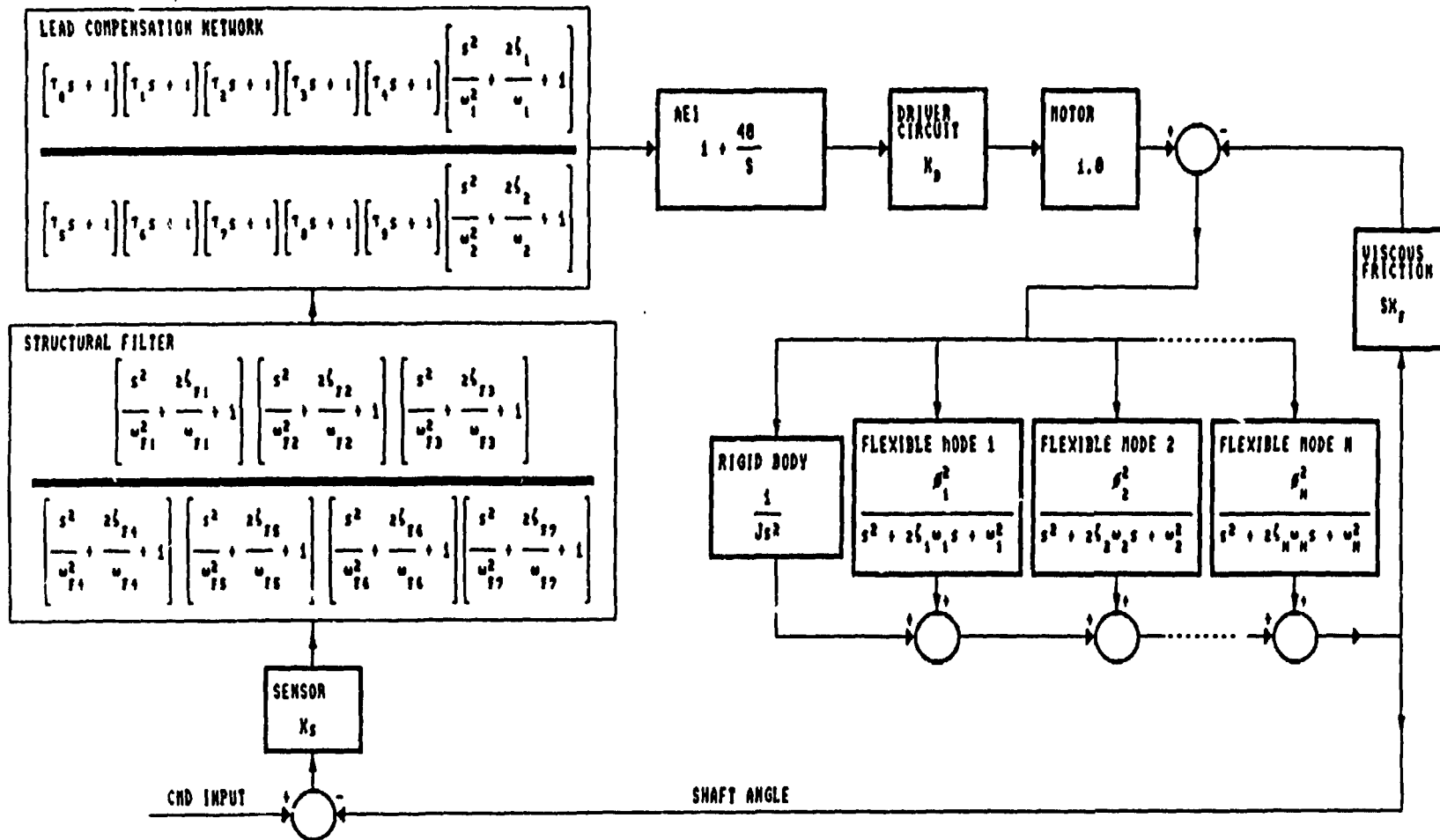


Figure B.1.3-9. Two Point Mirror Mount Design Structure Frequency Response



SENSOR	STRUCTURAL FILTER ZEROS	STRUCTURAL FILTER POLES	LEAD COMPENSATION ZEROS	LEAD COMPENSATION POLES	DRIVER CIRCUIT	VISCIOUS FRICTION	PLANT
$K_s = .256 \frac{V}{RAD}$	$\omega_{z1} = 2601.9$ $\omega_{z2} = 3554.3$ $\omega_{z3} = 9710.5$	$\omega_{p1} = 2333.3$ $\omega_{p2} = 2947.1$ $\omega_{p3} = 4633.4$ $\omega_{p4} = 2513.0$ $\omega_{p5} = 2513.0$	$\omega_1 = 146.90$ $\tau_1 = 1/725.6$ $\tau_2 = 1/191.2$ $\tau_3 = 1/102.6$ $\tau_4 = 1/615.7$ $\tau_5 = 1/338.3$	$\omega_2 = 210.60$ $\tau_6 = 1/2176.0$ $\tau_7 = 1/252.9$ $\tau_8 = 1/153.9$ $\tau_9 = 1/410.5$ $\tau_{10} = 1/5002.5$	$K_D = 20257.4$	$K_f = .1123 \frac{IN-LB}{RAD/SEC}$	$J = \text{Rigid body Inertia} = .3004 \frac{IN-LB-SEC^2}{RAD}$ $\beta_i^2 = \text{Nodal Gain of mode "i"}$ $\omega_i = \text{Natural frequency of mode "i"}$ $\zeta_i = \text{Nodal Damping of mode "i"} = .001$

Figure B.1.3-10. E/W Controller Block Diagram - Two Point Mirror Mount Design

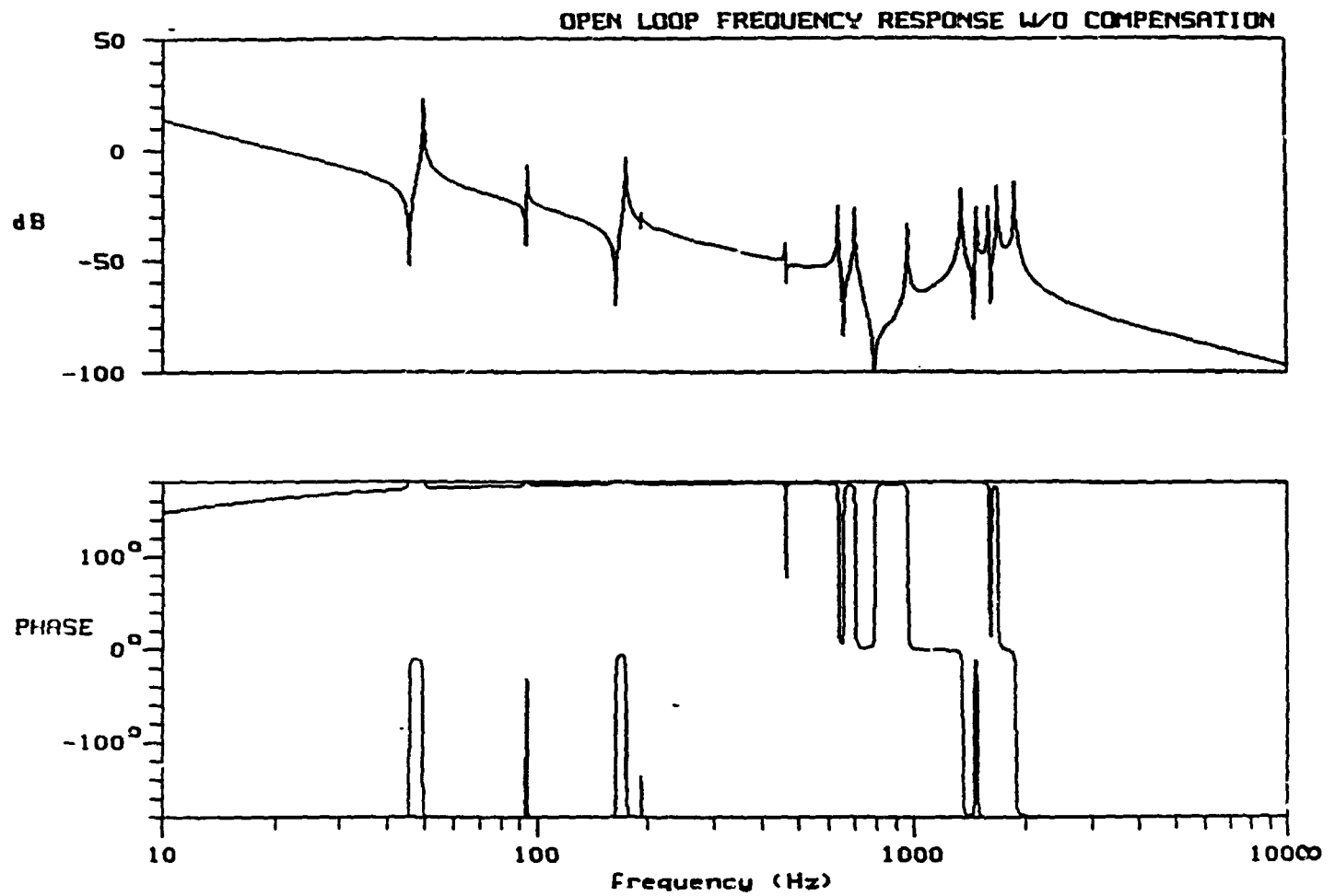
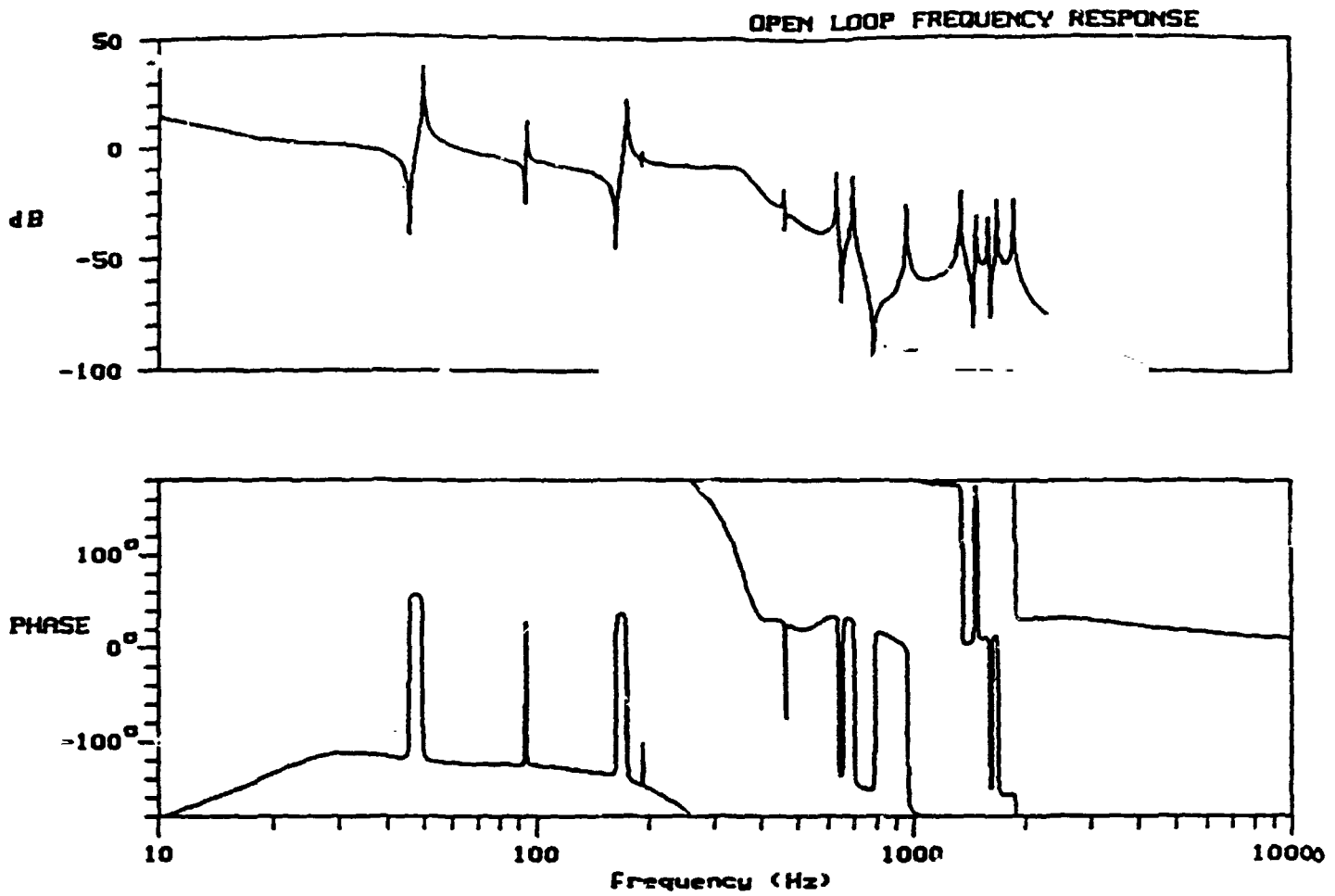


Figure B.1.3-11. Uncompensated Frequency Response - Two Point Mirror Mount Design



Gain margins (P= 180)

W= 10.271 Hz	M= 14.181 dB
W= 259.03 Hz	M= -8.5408 dB
W= 1047.3 Hz	M= -58.455 dB
W= 1882.1 Hz	M= -29.918 dB

Phase crossings (M= 0dB)

W= 34.270 Hz	P= -113.22
W= 47.643 Hz	P= 57.091
W= 60.723 Hz	P= -122.90
W= 93.804 Hz	P= 22.971
W= 94.721 Hz	P= -121.23
W= 171.87 Hz	P= 34.188
W= 180.66 Hz	P= -142.45

Figure B.1.3-12. Compensated Frequency Response - Two Point Mirror Mount Design

then a 6th order Inverse Chebyshev filter is used to provide the required attenuation. Damping was added to the zeros of the Inverse Chebyshev filter to improve its phase performance. The lead network is composed of three first order lead compensators and one lead-lag compensator which provide 30 deg phase margins for the lower modes while minimizing high frequency amplification. Finally, a second order lead compensator is included to increase the phase margin at the gain crossover frequency in an attempt to secure better damping in the time response. Although the compensation is of high order, it is composed of lower order elements and therefore should be feasible.

The compensated frequency response shows that the system has adequate gain and phase margins of 8.5 dB and 37 deg. with an open loop crossover frequency of 34.2 Hz. The closed loop frequency response is shown in Figure B.1.3-13. As in the baseline case, the phase stabilized modes make the identification of bandwidth unclear, but a tendency to overshoot is indicated. It is also apparent that this system has not achieved any improvement in open loop crossover frequency over the baseline. The requirement to phase stabilize the 175 Hz mode (which was dropped in the baseline case) balanced the structural improvement obtained in the 300-500 Hz range.

B.1.3.3.4 Time response simulation

A DADS simulation of the block diagram shown in Figure B.1.3-10 was constructed and then used to calculate the step response of the system for a 140 μ r step input. As in the baseline case, a Dahl model was used to represent the actual friction in the East/West shaft bearings. The shaft angle error is plotted in Figure B.1.3-14.

The calculated response contains considerable poorly damped ringing from the low frequency structural modes, resulting in a poor response that is inferior to the baseline case.

The motor output torque for the step is shown in Figure B.1.3-15, along with the motor torque for the baseline case for comparison. It can be seen that this design requires more control torque than in the baseline case. The larger control torque in this design is due in part to the larger number of modes that required phase stabilization.

B.1.3.4 GFRP design

The low frequency modes of the current structure are associated with bending of the scan mounting plate. The object of the GFRP modification was to increase the scan plate's stiffness and subsequently raise the frequencies of the lower modes to the point where they would no longer interfere with the bandwidth of the controller.

In the GFRP design, the instrument's baseplate and enclosure assembly are replaced by a much stiffer cylindrical structure made of the GFRP material. The scan mounting plate, which attaches the North/South housing to the baseplate, is replaced by a stiffer GFRP triangular plate which attaches the scan assembly to the circumference of one end of the cylinder.

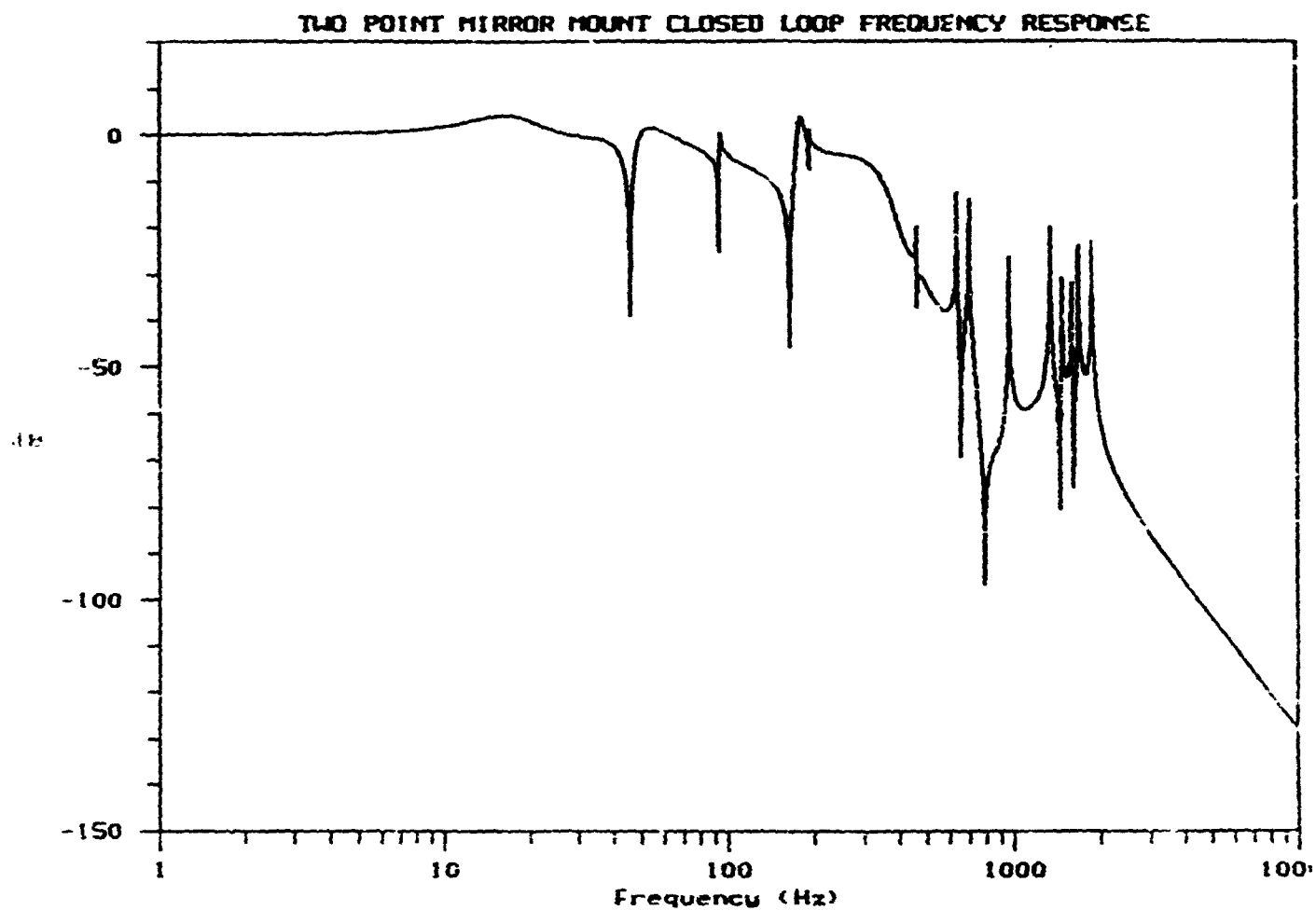


Figure B.1.3-13. Closed Loop Frequency Response - Two Point Mirror Mount Design

140 MICRORADIAN STEP RESPONSE - VISCOUS AND DAHL FRICTION

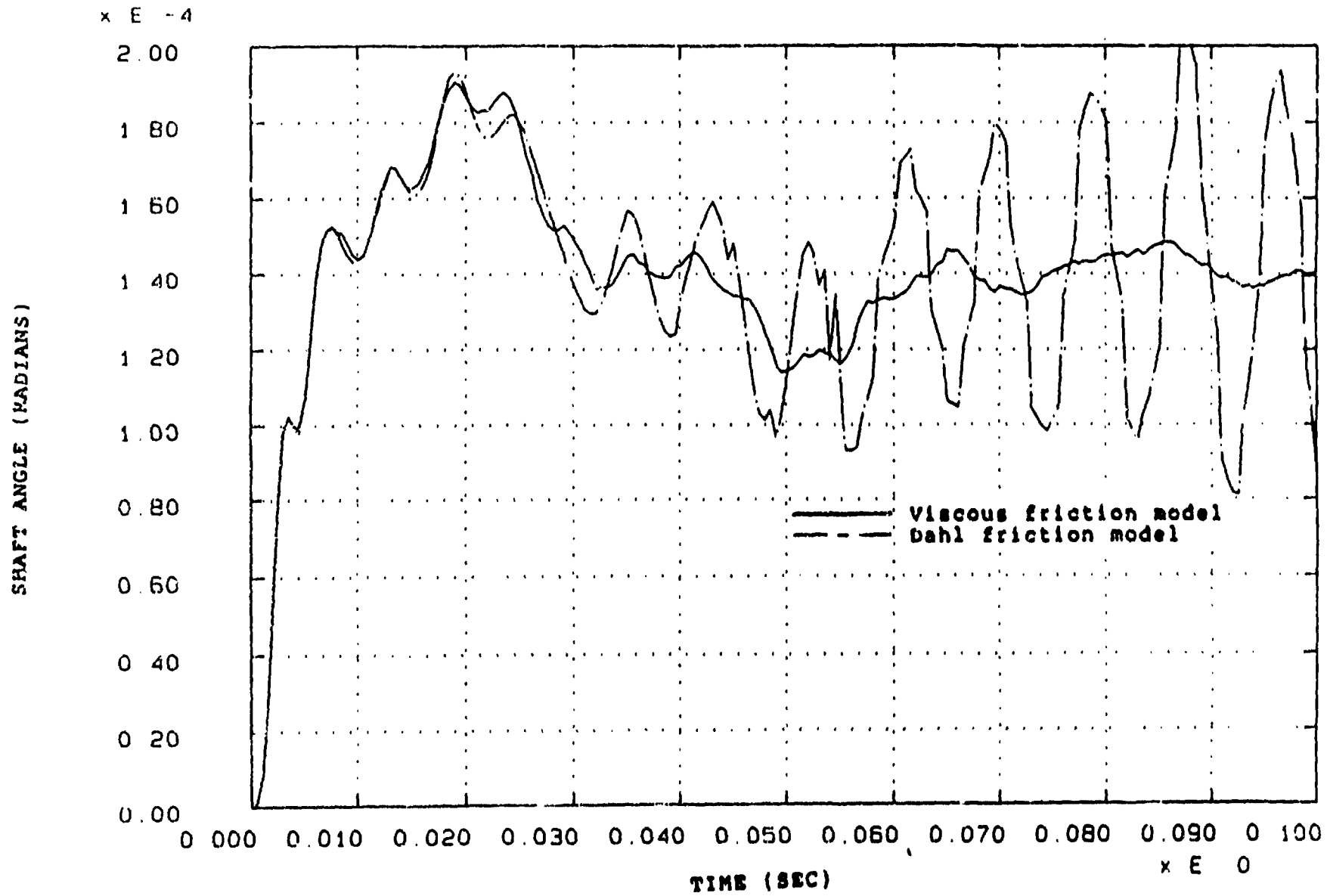


Figure B.1.3-14. Time Response of Two Point Mirror Design 140 μ r step

140 MICRORADIAN STEP MOTOR TORQUE FOR TWO PT MIRROR AND BASELINE

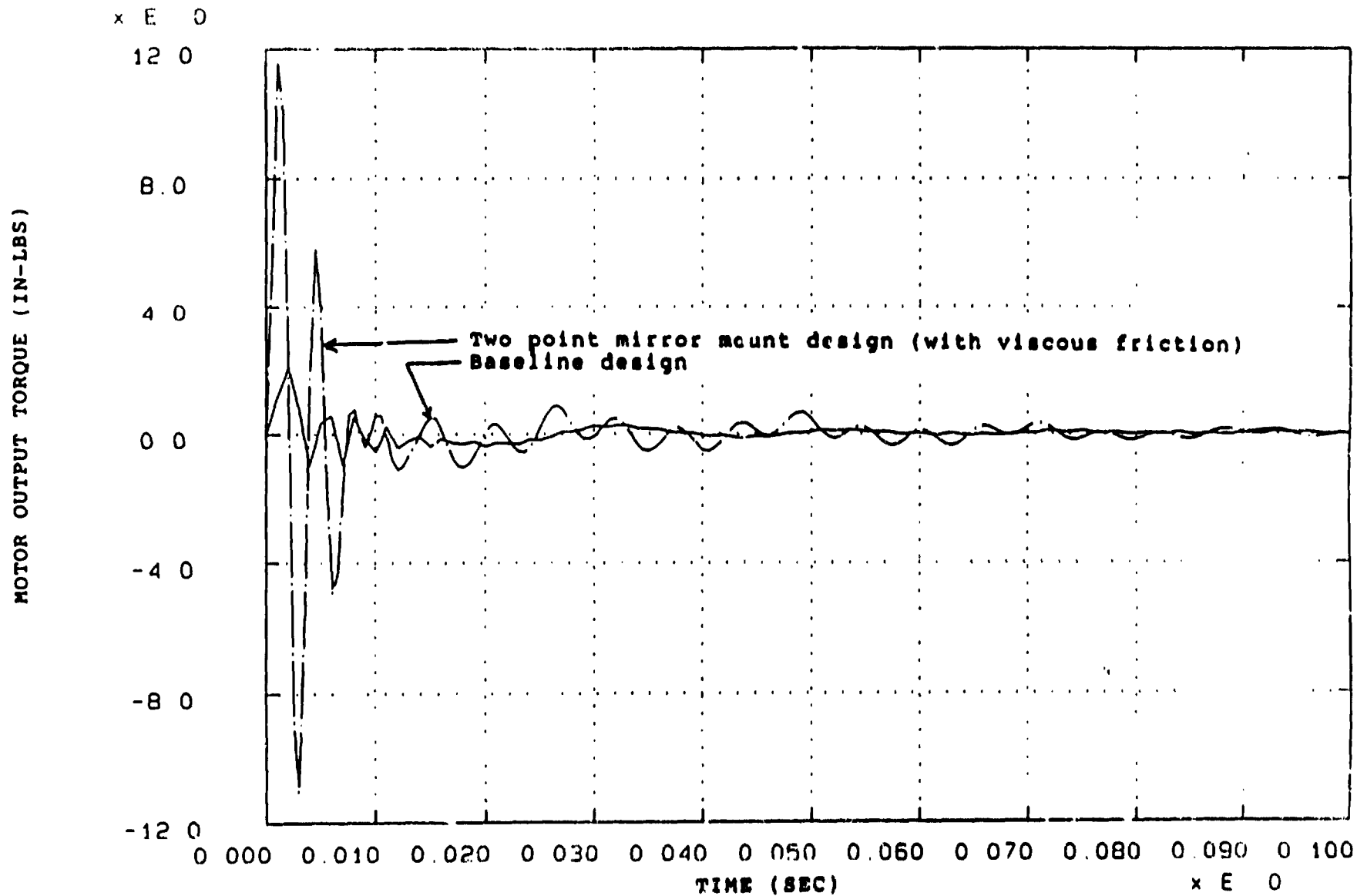


Figure B.1.3-15. Motor Torque Comparison - Two Point Mirror Mount and Baseline Designs

Time constraints prevented the creation of an entirely new FEM for this design, so the existing model was modified for a preliminary investigation of the concept. The cylinder is very stiff compared to the other elements of the system, and was therefore assumed to be infinitely rigid as far as the controller was concerned. With that approximation made, the FEM consisted only of a scan plate and the scan assembly. The detailed design of the scan plate had not been determined, but the goal of the design would be to make the plate as stiff as possible. The scan plate in the FEM was therefore replaced with a stiff triangular plate (aluminum, 2" thick honeycomb with .0625" facesheets) which would simulate the stiffness of the new GFRP scan plate. For the dynamic analysis, the triangular plate was rigidly supported at its three corners to simulate the interface to the cylinder. Although the FEM representation of the GFRP design was of low fidelity, the load paths and relative stiffness were of sufficient accuracy to evaluate the feasibility of the GFRP concept. The FEM used in the analysis is shown in Figure B.1.3-16.

B.1.3.4.1 Structure transfer function

The modes resulting from a dynamic analysis of the FEM were sorted, and the significant modes were used to form a structure transfer function for use in the controller design. A frequency response plot of the structure is given in Figure B.1.3-17. A value of 0.1% percent was used for modal damping.

Figure B.1.3-17 shows that the first significant mode of the structure has been raised to 95 Hz. It is also apparent that modes of significant gain are spread throughout the frequency range, so phase stabilization will not be possible because no transition region is available for a phase crossover point. All of the modes must therefore be attenuated. With the increased frequency of the first mode, however, performance improvement may still be possible using this approach. A compensation design for the mode set was therefore performed.

B.1.3.4.2 Block diagram

A block diagram of the GFRP design is shown in Figure B.1.3-18. As in the two point mirror mount case, a current controlled motor has replaced the voltage controlled motor, and an optical encoder has been used in place of the inductosyn. A viscous model of the friction in the East/West shaft bearings has been used.

B.1.3.4.3 System frequency response

The open loop frequency response of the system before and after compensation is given in Figures B.1.3-19 and 20. The compensation consists of a 7th order Inverse Chebyshev filter with damping included in the zeros, and an extra zero to cancel the viscous friction and provide phase lead at low frequencies.

The compensated system shows adequate gain and phase margins of 8.0 dB and 36 degrees, with an open loop crossover frequency of 16.1 Hz. The low value of the gain crossover frequency is a consequence of the need to attenuate all of the modes, including a provision for a 20% shift in frequency. Stability margins could not be maintained if the filter cutoff was moved higher in frequency.

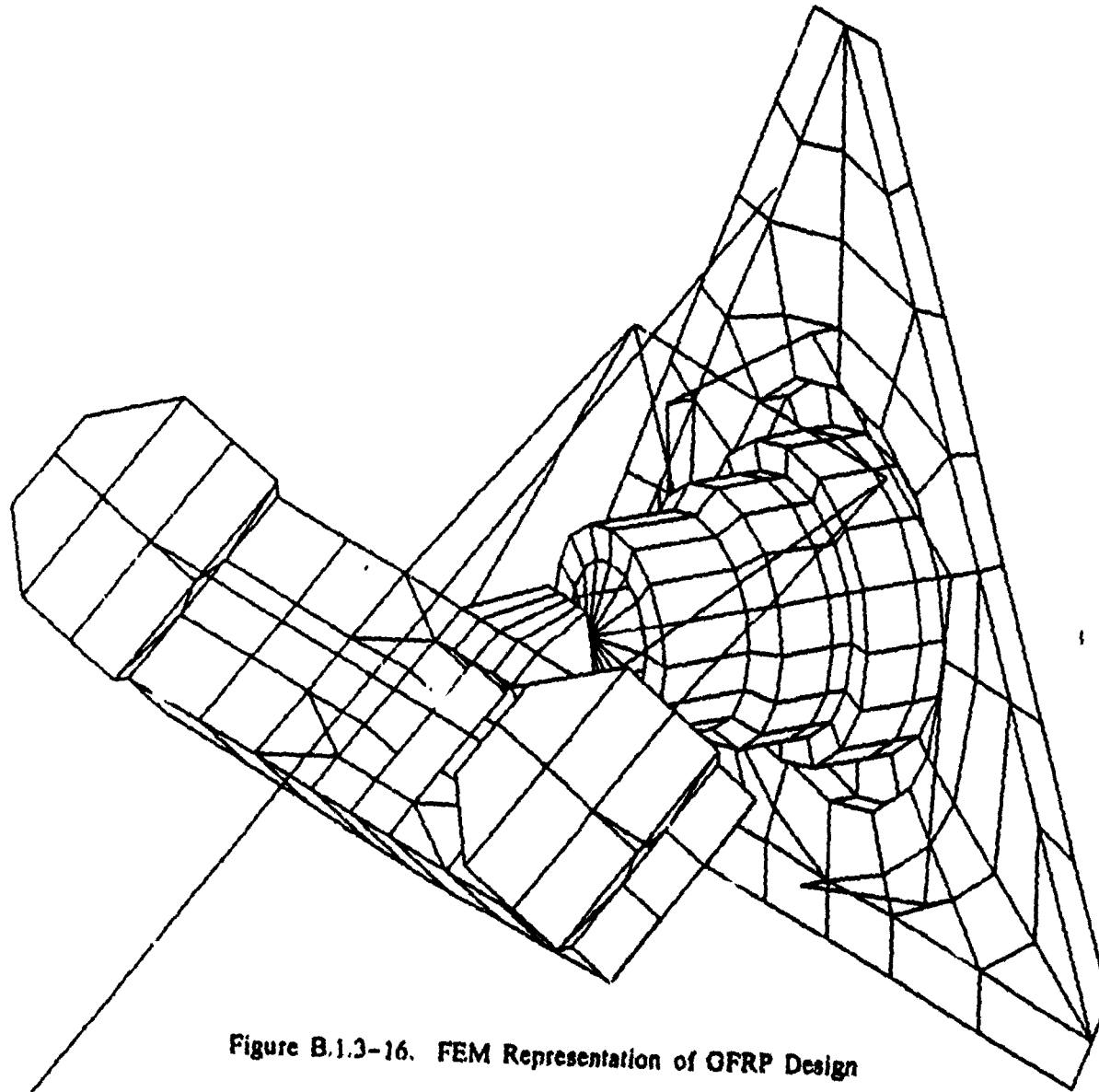


Figure B.1.3-16. FEM Representation of GFRP Design

GFRP DESIGN - STRUCTURE FREQUENCY RESPONSE

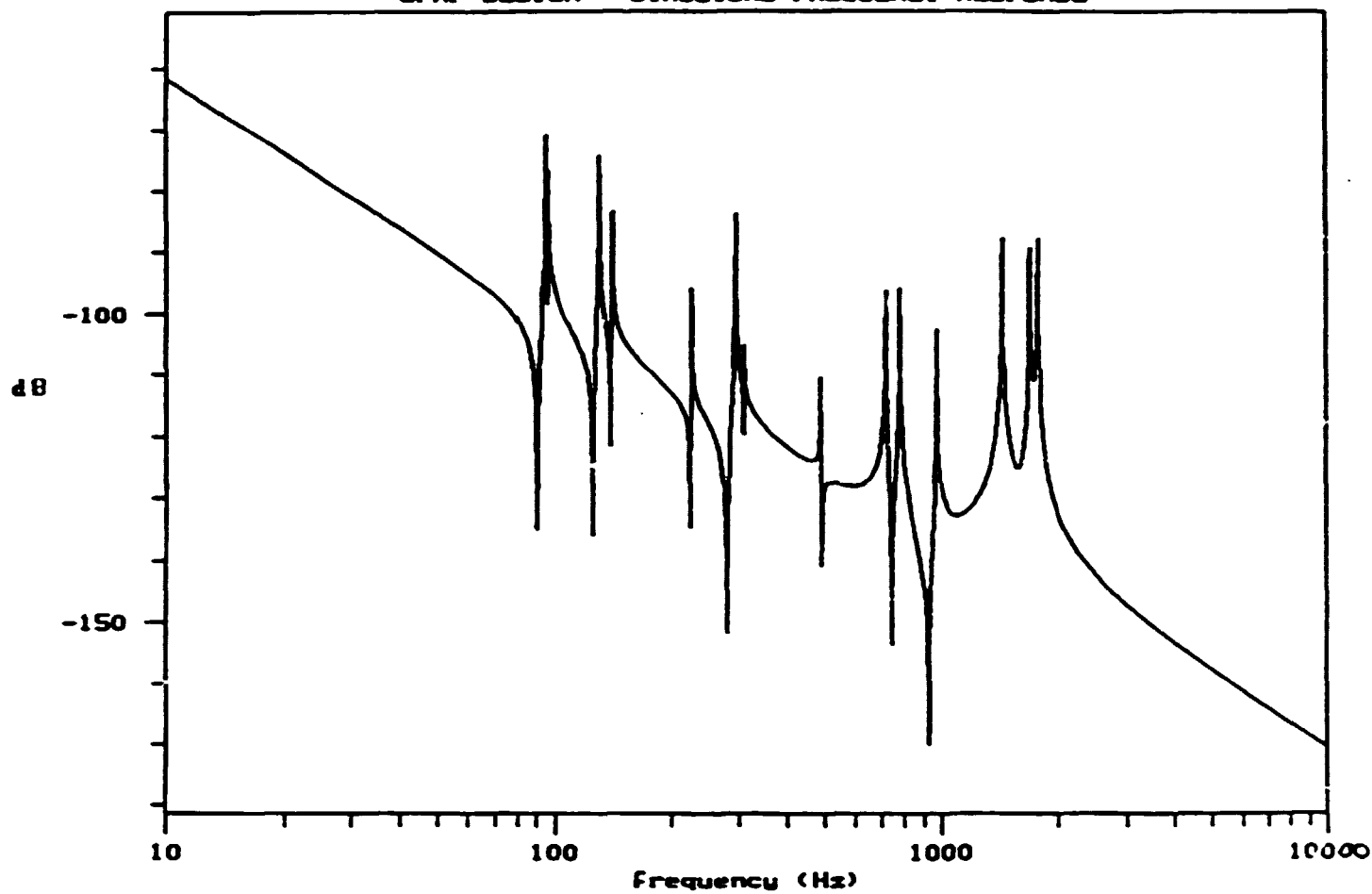
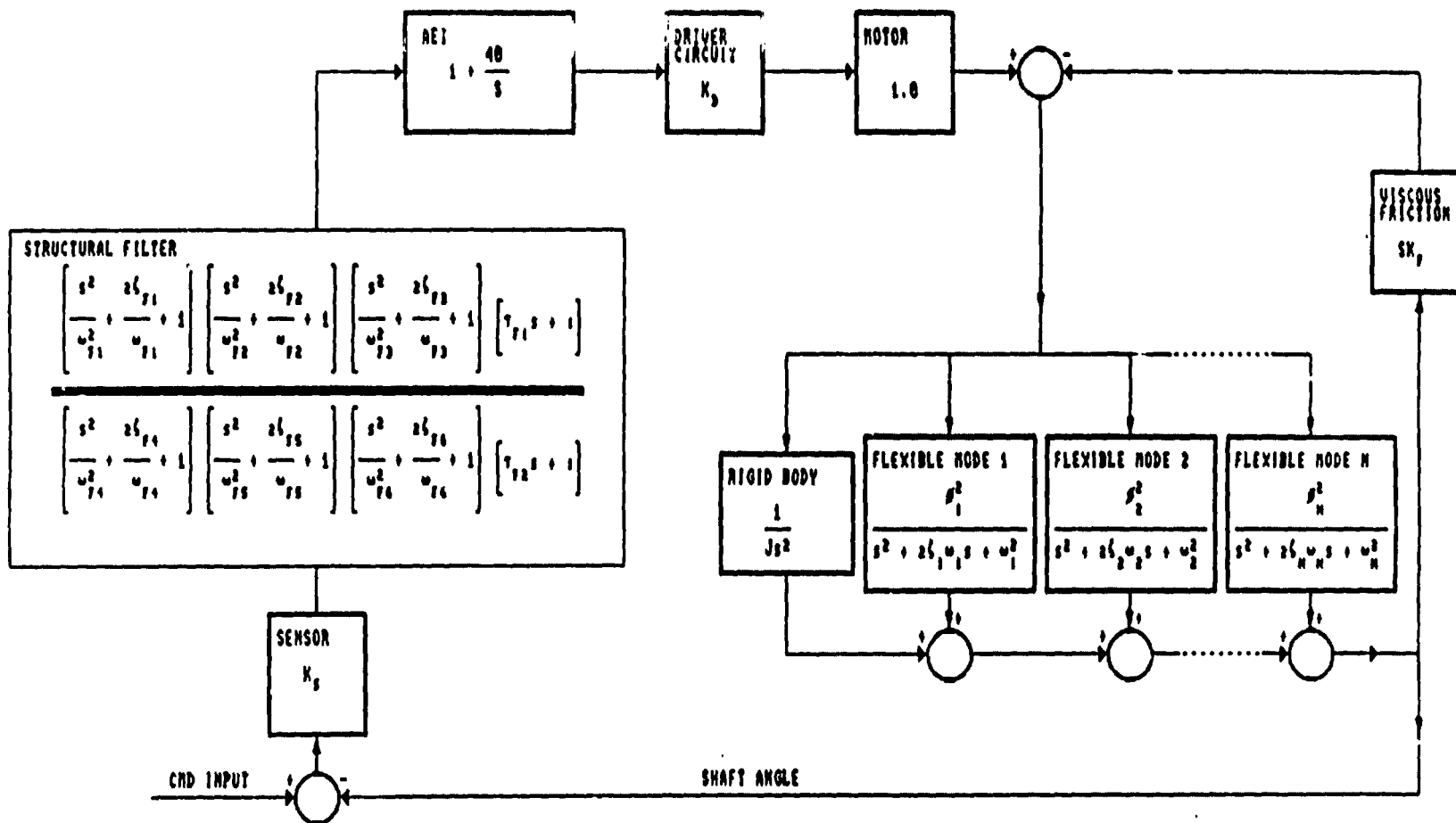


Figure B.1.3-17. GFRP Design Structure Frequency Response



SENSOR	STRUCTURAL FILTER ZEROS	STRUCTURAL FILTER POLES	DRIVER CIRCUIT	VISCOUS FRICTION	PLANT
$K_s = .256 \frac{V}{RAD}$	$\omega_{F1} = 582.69 \quad \zeta_{F1} = .020$ $\omega_{F2} = 626.84 \quad \zeta_{F2} = .025$ $\omega_{F3} = 1129.54 \quad \zeta_{F3} = .100$ $\tau_{F1} = 1/.400$	$\omega_{F4} = 422.67 \quad \zeta_{F4} = .120$ $\omega_{F5} = 400.02 \quad \zeta_{F5} = .390$ $\omega_{F6} = 642.30 \quad \zeta_{F6} = .741$ $\tau_{F2} = 1/700.00$	$K_D = 45.520$	$K_f = .1125 \frac{IN-LB}{RAD/SEC}$	$J = \text{Rigid body inertia} = .3004 \frac{IN-LB-SEC^2}{RAD}$ $\beta_i^2 = \text{Modal Gain of mode "i"}$ $\omega_i = \text{Natural frequency of mode "i"}$ $\zeta_i = \text{Modal Dampings of mode "i"} = .001$

Figure B.1.3-18. E/W Controller Block Diagram - GFRP Design

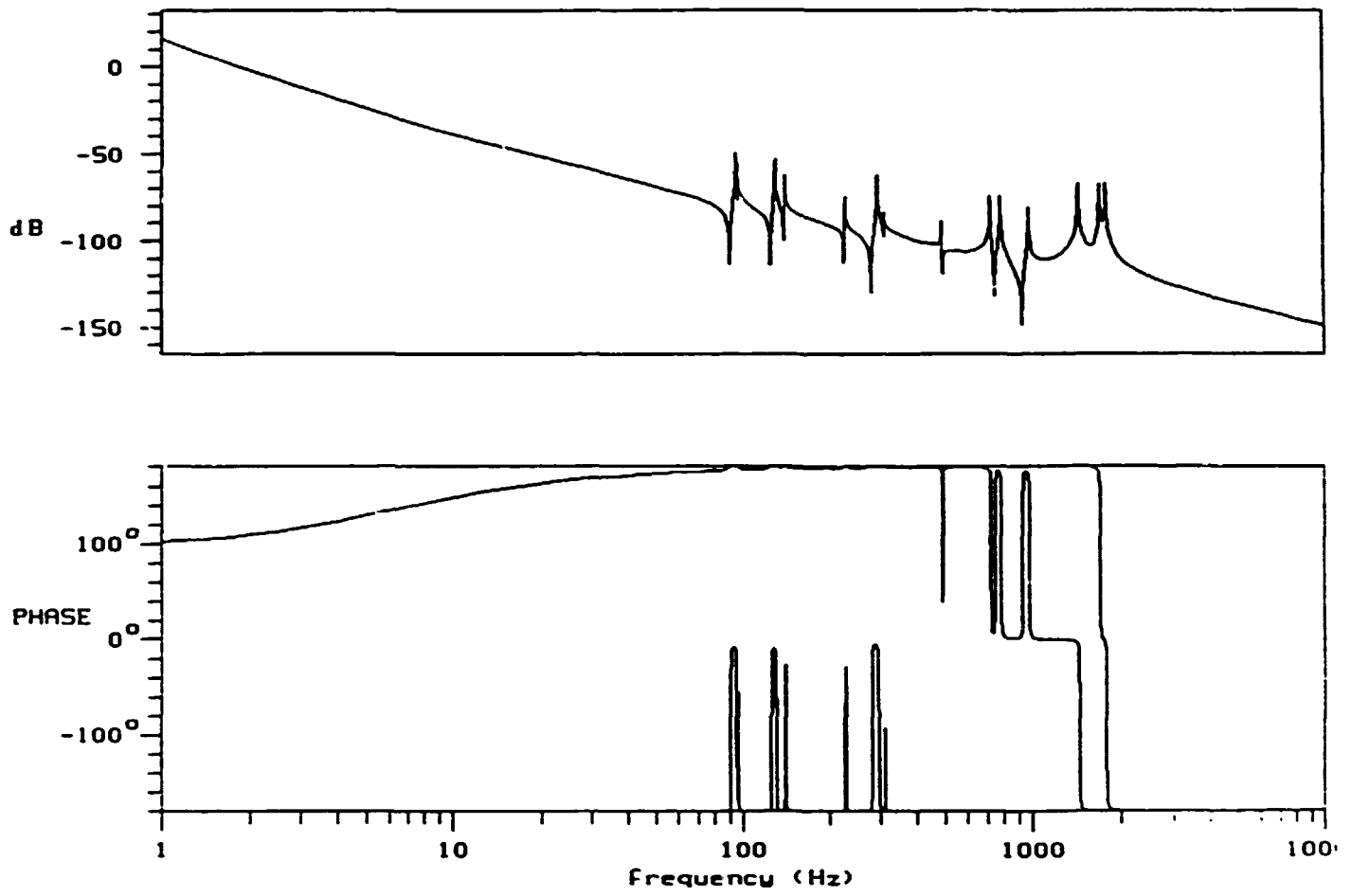
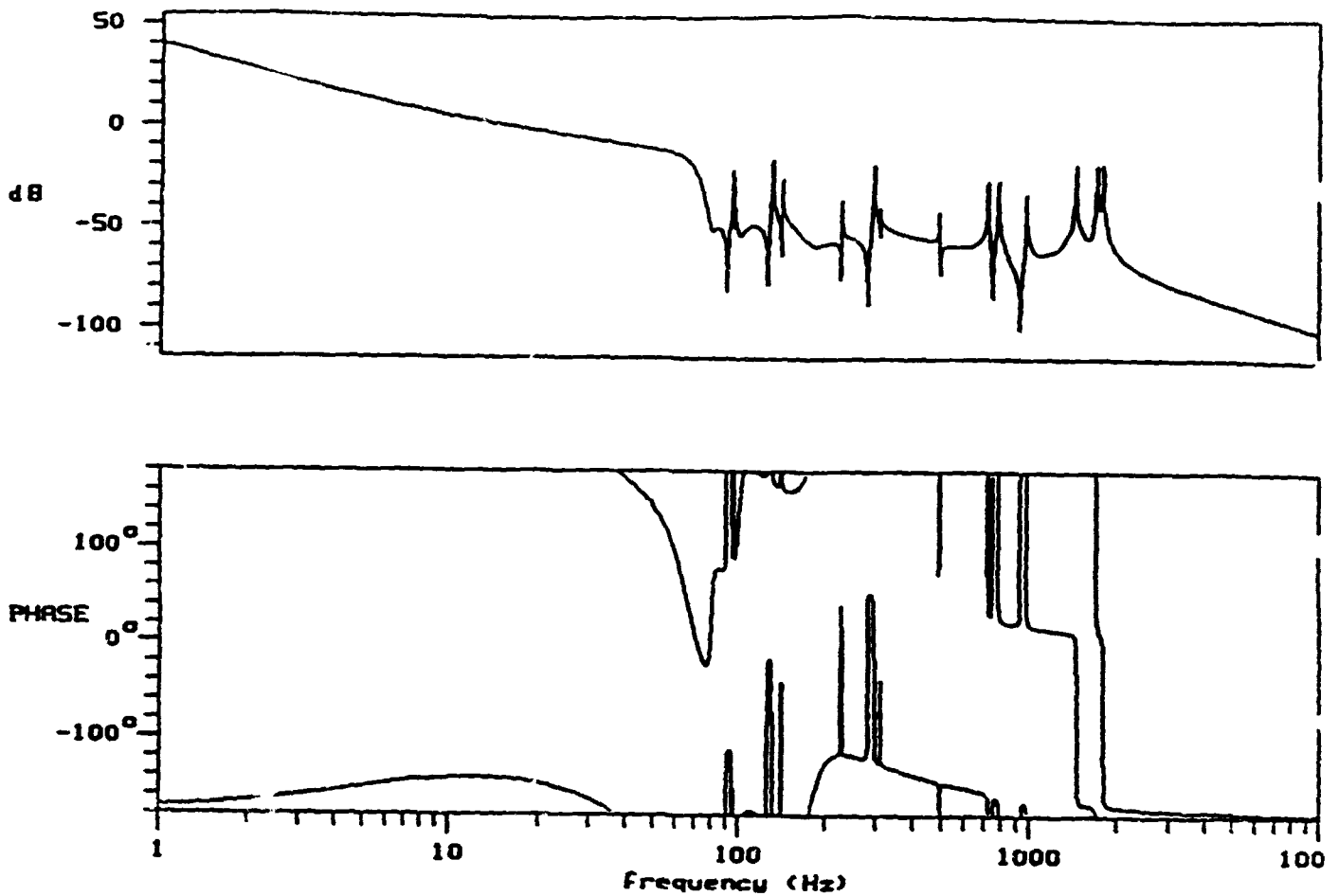


Figure B.1.3-19. Uncompensated Frequency Response - GFRP Design



Gain margins (P= 180)

W= 37.246 Hz	M=-8.0020 dB
W= 90.475 Hz	M=-81.121 dB
W= 94.793 Hz	M=-22.020 dB
W= 95.799 Hz	M=-49.099 dB
W= 96.080 Hz	M=-31.156 dB
W= 104.57 Hz	M=-51.423 dB
W= 115.95 Hz	M=-49.443 dB
W= 124.76 Hz	M=-63.691 dB
W= 130.76 Hz	M=-28.129 dB
W= 139.18 Hz	M=-57.612 dB
W= 141.15 Hz	M=-32.504 dB
W= 171.94 Hz	M=-57.194 dB
W= 491.8 Hz	M=-44.097 dB
W= 495.69 Hz	M=-70.745 dB
W= 722.49 Hz	M=-34.244 dB
W= 749.58 Hz	M=-76.754 dB
W= 784.02 Hz	M=-35.306 dB
W= 932.83 Hz	M=-89.628 dB
W= 977.06 Hz	M=-44.377 dB
W= 1690.6 Hz	M=-35.872 dB

Phase crossings (M= 0dB)

W= 16.094 Hz P=-143.53

Figure B.1.3-20. Compensated Frequency Response - GFRP Design

The closed loop frequency response of the system is shown in Figure B.1.3-21 and indicates a closed loop bandwidth of approximately 30 Hz. Even though the open loop crossover frequency is only half that for the baseline, the closed loop bandwidth is nearly the same. The closed loop response also has a second order appearance, with the slight bulge in the gain curve at 20 Hz indicating the potential for overshoot.

B.1.3.4.4 Time response simulation

A DADS simulation of the GFRP system was constructed and used to calculate the response of the system to a 140 μ r step input. As in the baseline and two point mirror mount cases, the time domain simulation used a Dahl model to represent the actual friction in the East/West shaft bearings. The shaft error angle is plotted in Figure B.1.3-22. As in the baseline case, the error can be seen to exhibit a slowly decaying component due to the Dahl friction. The response has the expected second order appearance, and as in the previous cases, the response does not meet the step and settle requirement.

The motor output torque is shown in Figure B.1.3-23, along with the baseline results for comparison. The absence of phase stabilized modes in this design has caused the control torque required to drop from the levels seen in the baseline design.

B.1.3.5 Prefilter concept

An observation of the step response from each of the preceding designs indicates that the settling time goal might have been achieved if the responses had been critically damped. A method for improving the damping in the time response consists of cascading a prefilter with the closed loop system. The prefilter's frequency response is used to modify the closed loop frequency response of the system. With a careful choice of prefilter, the frequency response of the total system can be shaped to give the desired result. An added benefit of the prefilter approach is that it has no effect on the stability of the system.

The analytical design of a prefilter is straightforward, because the closed loop poles and zeros of the system are known. The prefilter zeros are selected to cancel undesirable poles of the closed loop, and the prefilter poles are used to cancel undesirable zeros and to insert desirable poles. The number of poles and zeros that must be canceled by the prefilter gives an indication of the robustness of the design in an actual application. For example, it is possible to get a 1000 Hz bandwidth for any of these systems using this technique, but the prefilter will be required to cancel nearly all of the poles and zeros of the plant. With this type of design, the slightest bit of modeling error (which is inevitable) will cause the response to deteriorate completely probably to a level which is worse than with no prefilter at all. The prefilter should therefore be designed using the minimum order that will accomplish the performance goals.

Prefilters for the baseline, two point mirror mount, and GFRP designs were constructed to compare the complexity required and performance obtained in each case. In order to shorten the design time, the prefilters were designed using a linear simulation to see that the 2% settling was

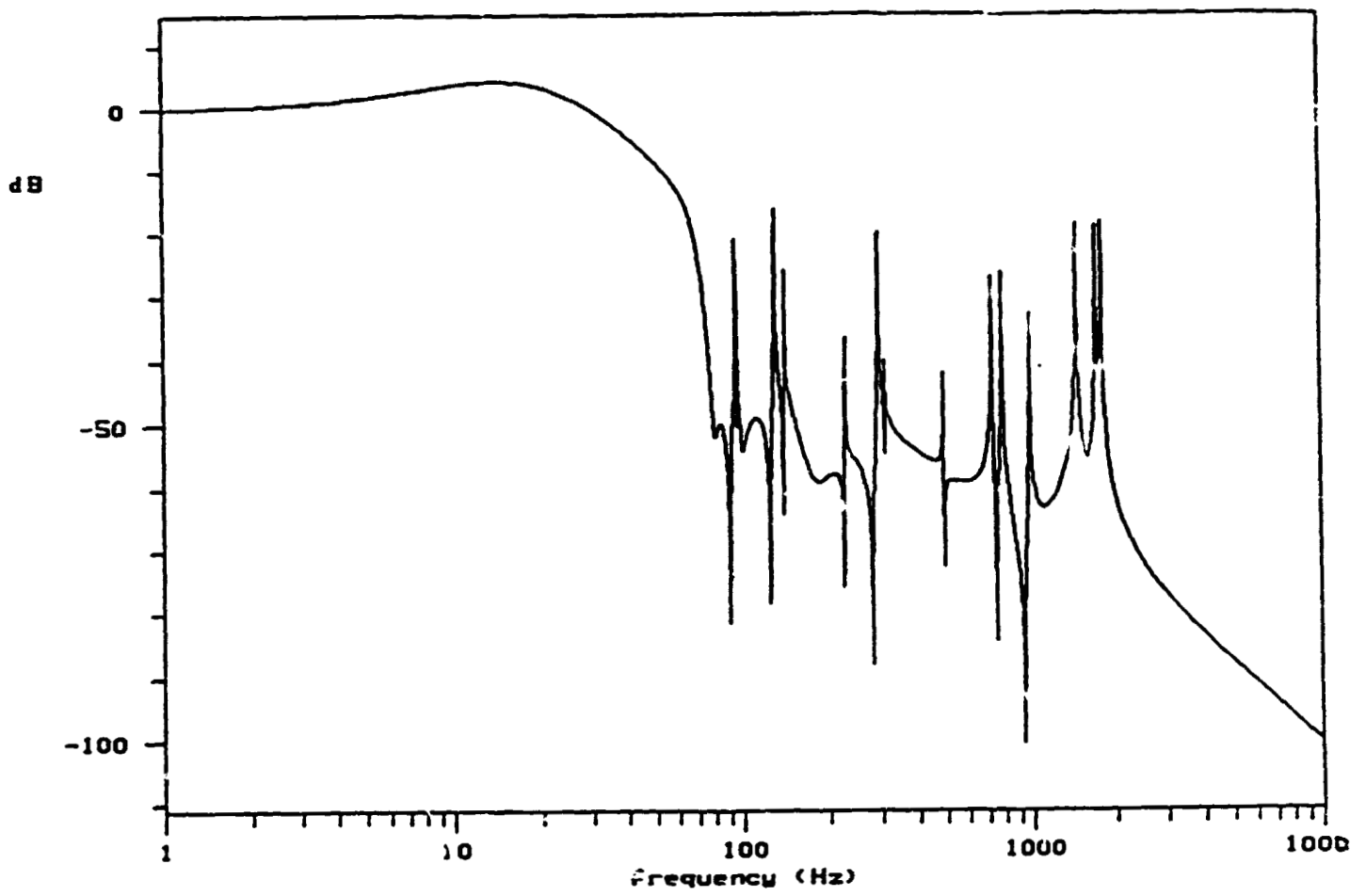


Figure B.1.3-21. Closed Loop Frequency Response - GFRP Design

140 MICRORADIAN STEP RESPONSE - GFRP DESIGN

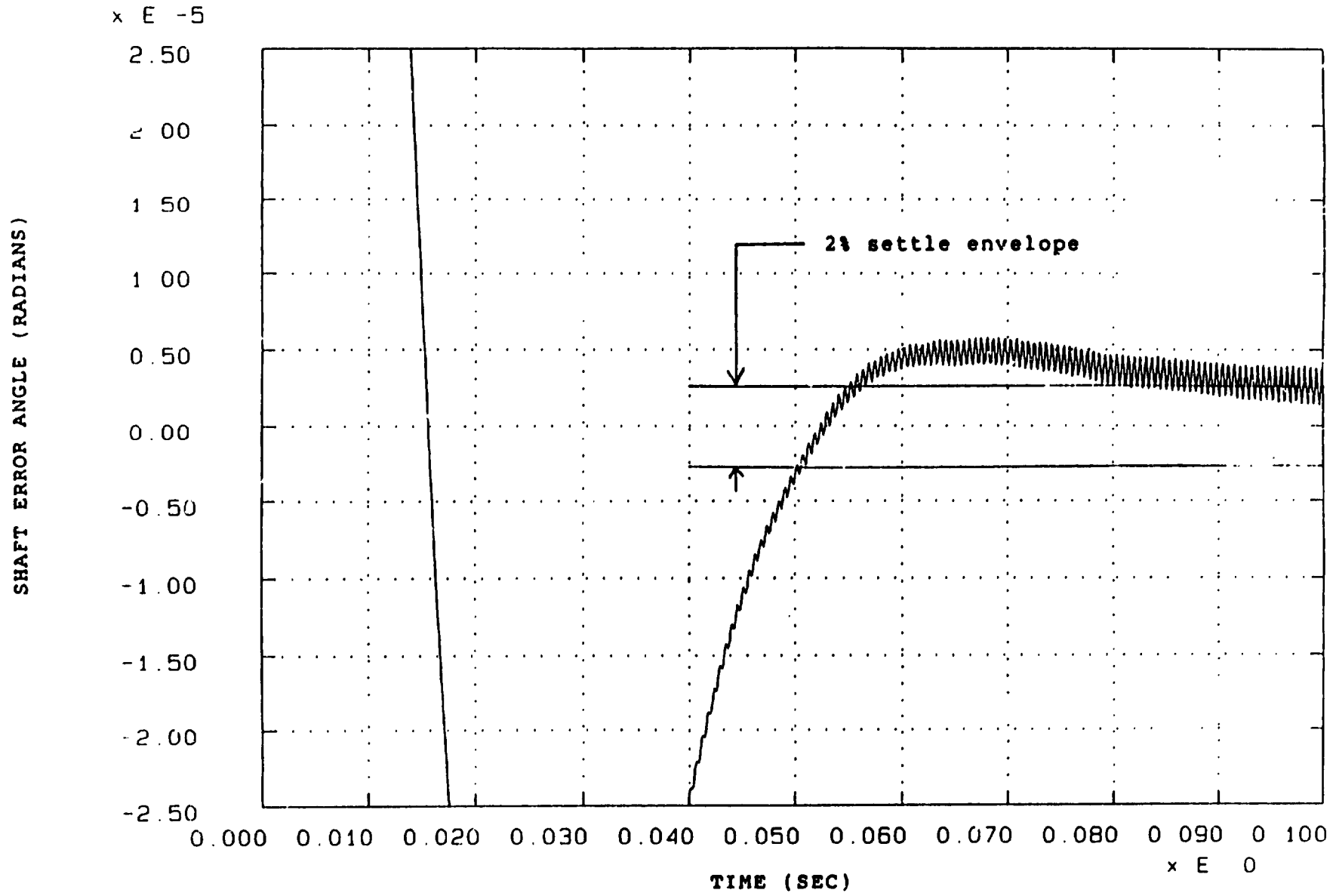


Figure B.1.3-22. Time Response of GFRP Design

140 MICRORADIAN STEP MOTOR TORQUE FOR GFRP AND BASELINE

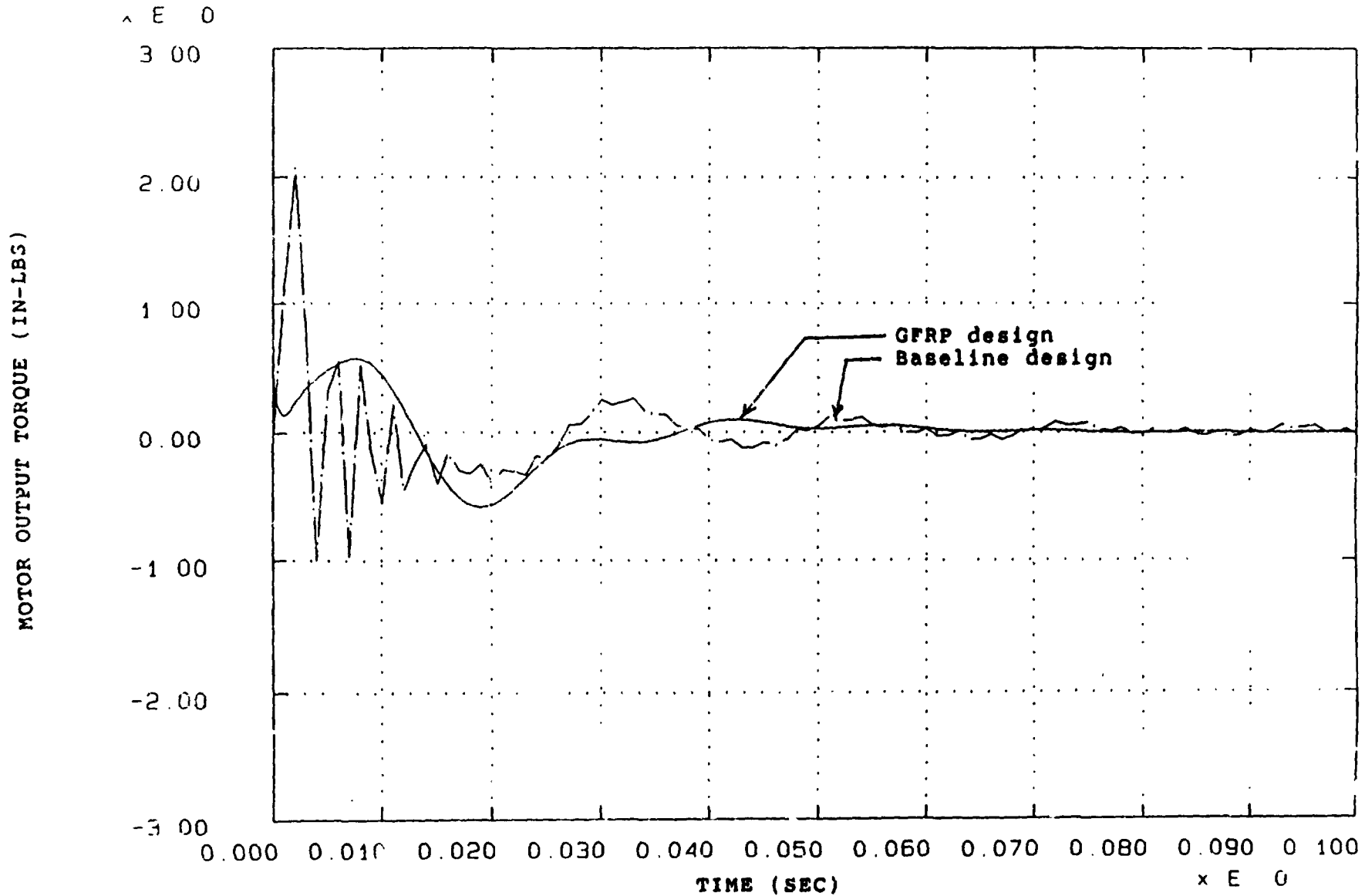


Figure B.1.3-23 Motor Torque Comparison - GFRP and Baseline Design

achieved. Later, a non-linear simulation using Dahl friction (which is more time consuming to implement) was used to examine the performance of the completed designs. This approach avoided the need to use a lengthy iterative development process which would be required to develop designs for actual hardware.

B.1.3.5.1 Baseline case with prefilter

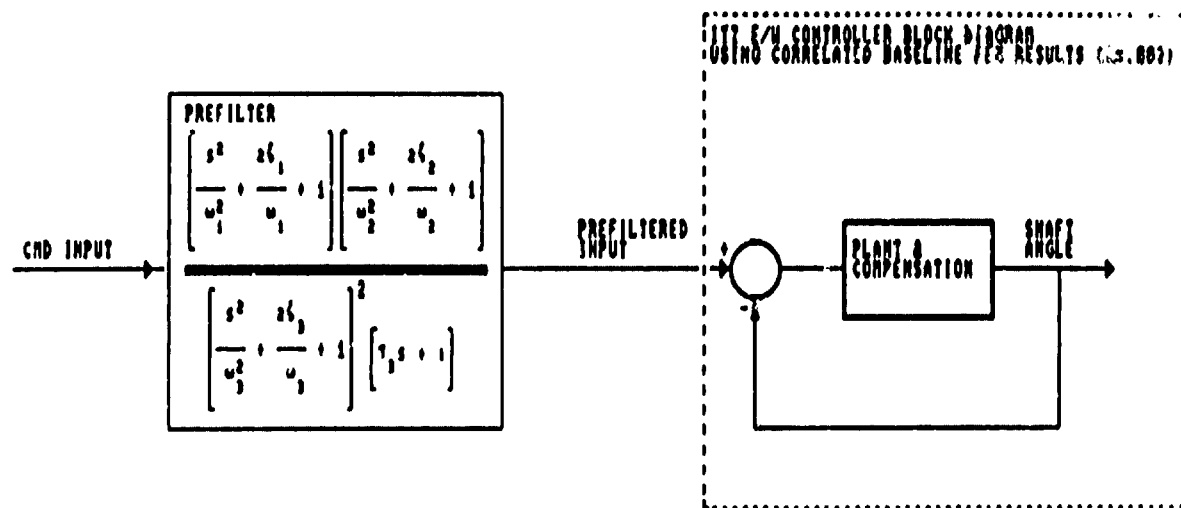
A block diagram of the completed baseline prefilter design is presented in Figure B.1.3-24. A fifth order prefilter was required to achieve the 2% settling time. The prefilter contains a zero to cancel the pole of the first flexible mode, which indicates that this design is probably sensitive to variations in the frequency of that mode. The result of a linear unit step response (no limiters, viscous friction) is given in Figure B.1.3-25. Note that the response meets the 2% settling time goal. The closed loop frequency response with the prefilter included is shown in Figure B.1.3-26. The result of a DADS simulation using Dahl friction is presented in Figure B.1.3-27. It can be seen that the Dahl friction causes a slight degradation in performance by introducing a steady state error that the AEI removes slowly.

B.1.3.5.2 Two point mirror mount with prefilter

A block diagram of the completed two point mirror mount prefilter design is given in Figure B.1.3-28. A ninth order prefilter was required to achieve the 2% settling time. Similar to the baseline case, the prefilter has zeros that are used to cancel poles due to modes of the plant, which indicates that this design will probably be sensitive to variations in the frequencies of the modes. The linear unit step response is given in Figure B.1.3-29, and shows that the new system meets the 2% settling time goal. The closed loop frequency response with the prefilter included is shown in Figure B.1.3-30. The result of a DADS simulation with Dahl friction is presented in Figure B.1.3-31. As in the baseline case, the Dahl friction causes a slight degradation in performance.

B.1.3.5.3 GFRP design with prefilter

A block diagram of the GFRP prefilter design is given in Figure B.1.3-32. In this case, the prefilter required to achieve 2% settling is only third order, and does not contain any zeros to cancel poles due to modes. The poles canceled by the prefilter zeros are due to rigid body characteristics of the plant, which are easier to characterize analytically than flexible dynamics. This design should therefore be insensitive to variations in the modal frequencies. The linear unit step response of the system is shown in Figure B.1.3-33. The closed loop frequency response including the prefilter is given in Figures B.1.3-34, and 35 shows the results of a DADS simulation with Dahl friction. The DADS simulation shows that the Dahl friction degrades the performance more than in the previous two cases. The Dahl friction's retarding torque has a greater impact in this case, because the system has a lower bandwidth and also has a lesser tendency to overshoot. The AEI has such a long time constant that the difference is made up slowly.



PREFILTER
ZEROS

$\omega_1 = 214.60$ $\zeta_1 = 2.433$
 $\omega_2 = 313.40$ $\zeta_2 = 2.160$

PREFILTER
POLES

$\omega_3 = 234.47$ $\zeta_3 = 2.715$
 $\tau_1 = 1/123.0$

Figure B.1.3-24. Baseline Prefilter Block Diagram

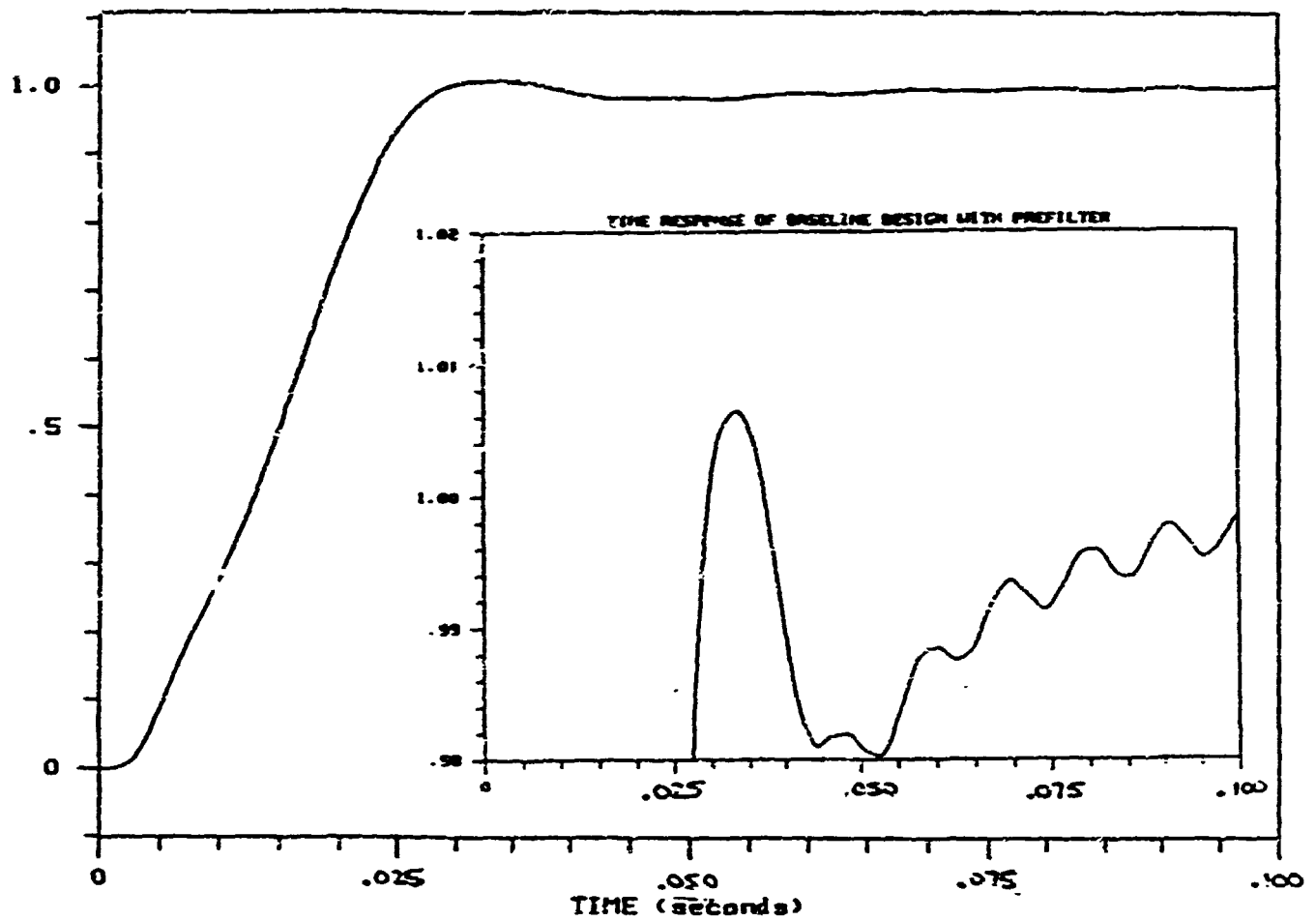


Figure B.1.3-25. Linear Unit Step Response of Baseline Design with Prefilter

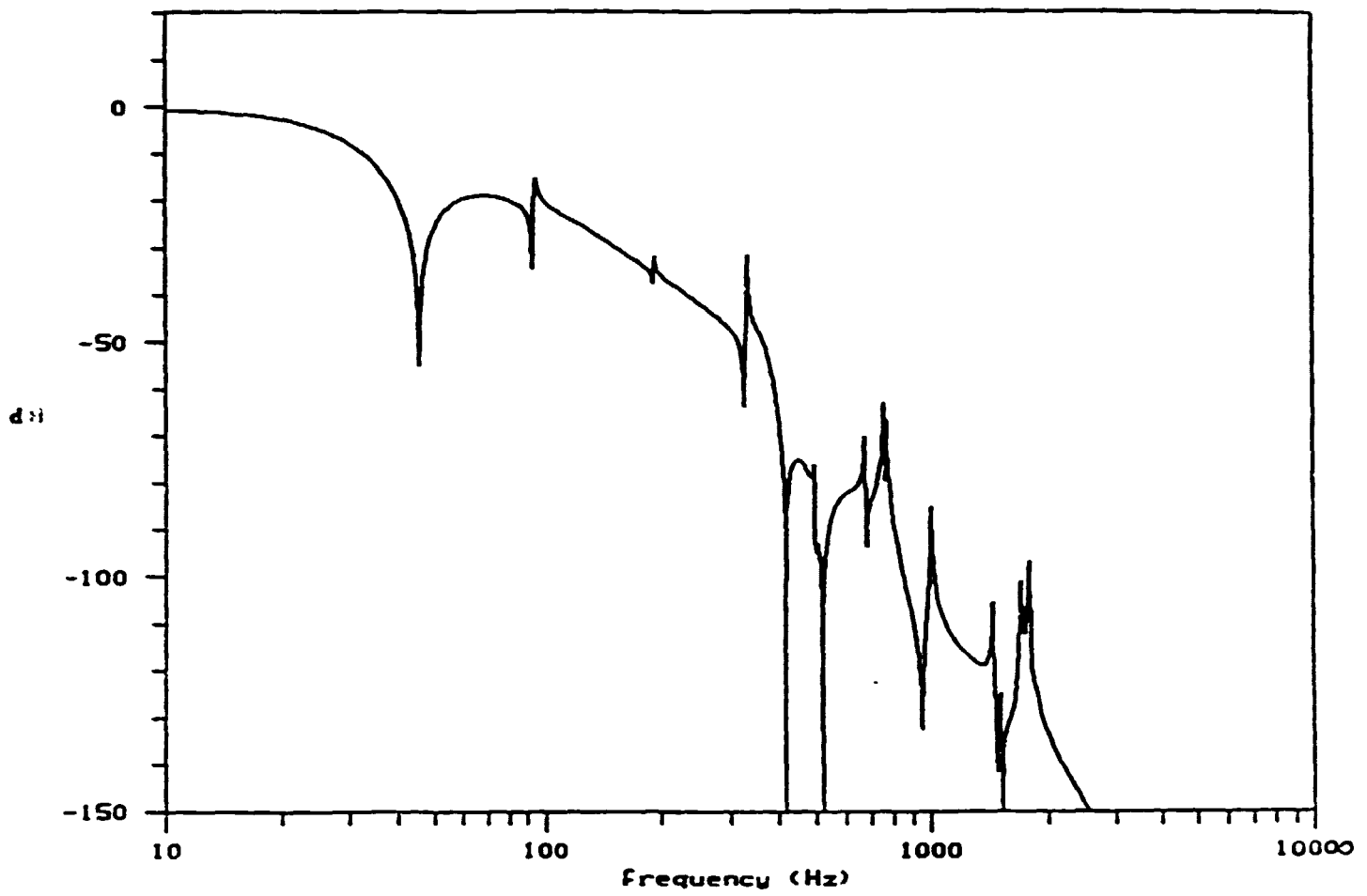


Figure B.1.3-26. Closed Loop Frequency Response - Baseline Design with Prefilter

140 MICRORADIAN STEP RESPONSE - BASELINE DESIGN WITH PREFILTER

$\times E - 5$

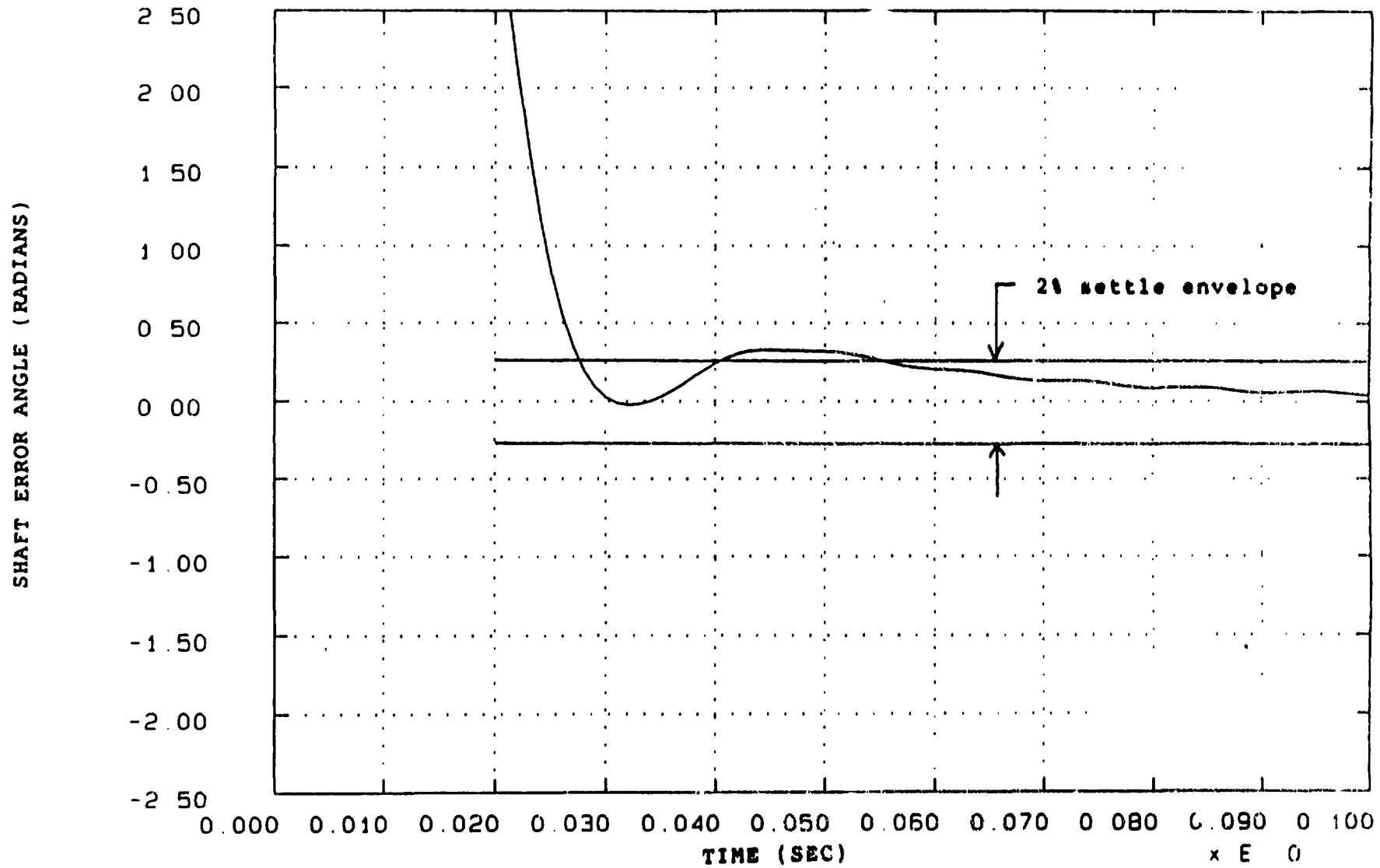


Figure B.1.3-27. Time Response of Baseline Prefilter Design with Dahl Friction

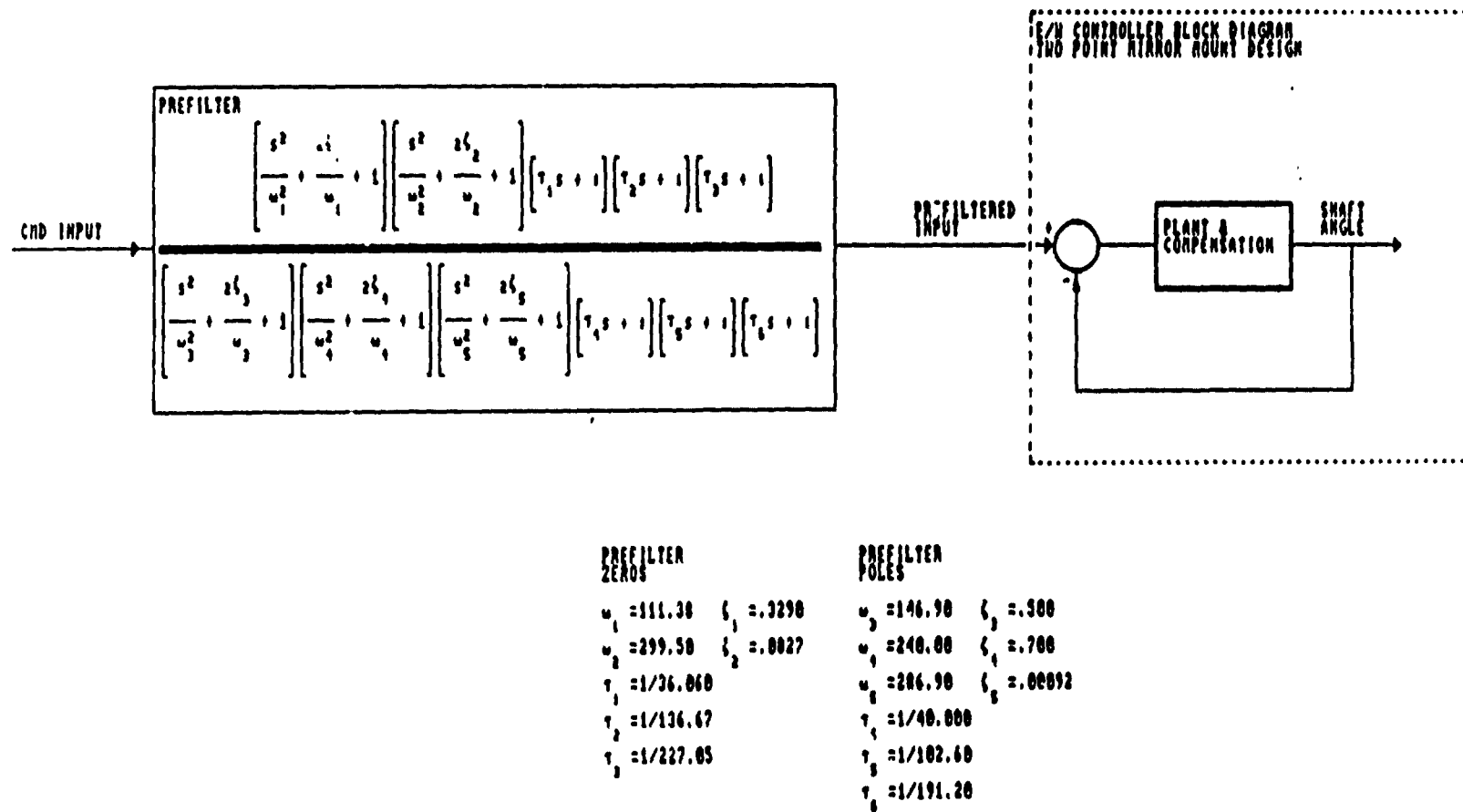


Figure B.1.3-28. Two Point Mirror Mount Prefilter Block Diagram

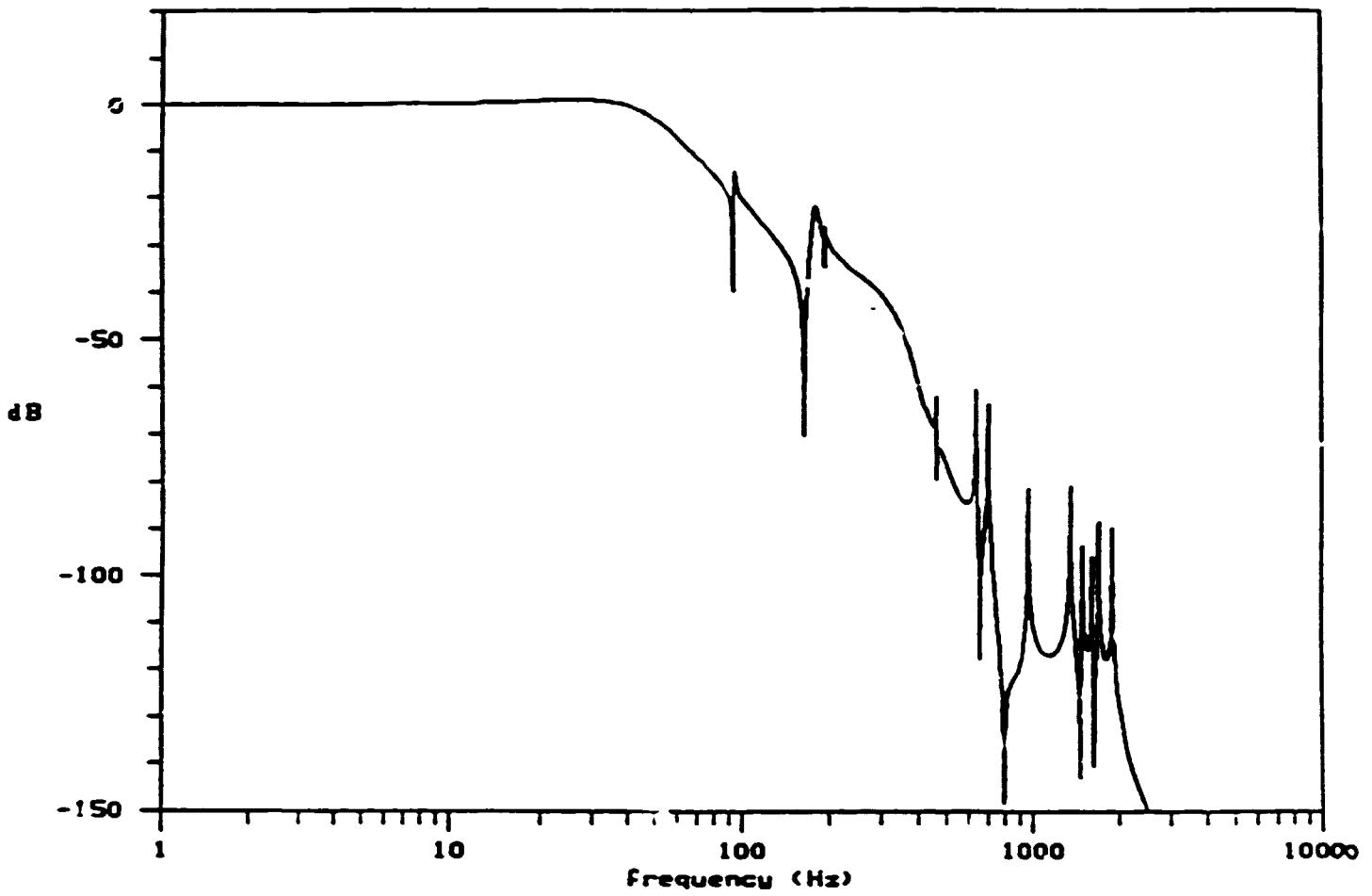


Figure B.1.3-29. Linear Unit Step Response - Two Point Mirror Mount Design with Prefilter

This page intentionally blank

140 MICRORADIAN STEP RESPONSE - TWO PT MIRROR MOUNT WITH PREFILTER

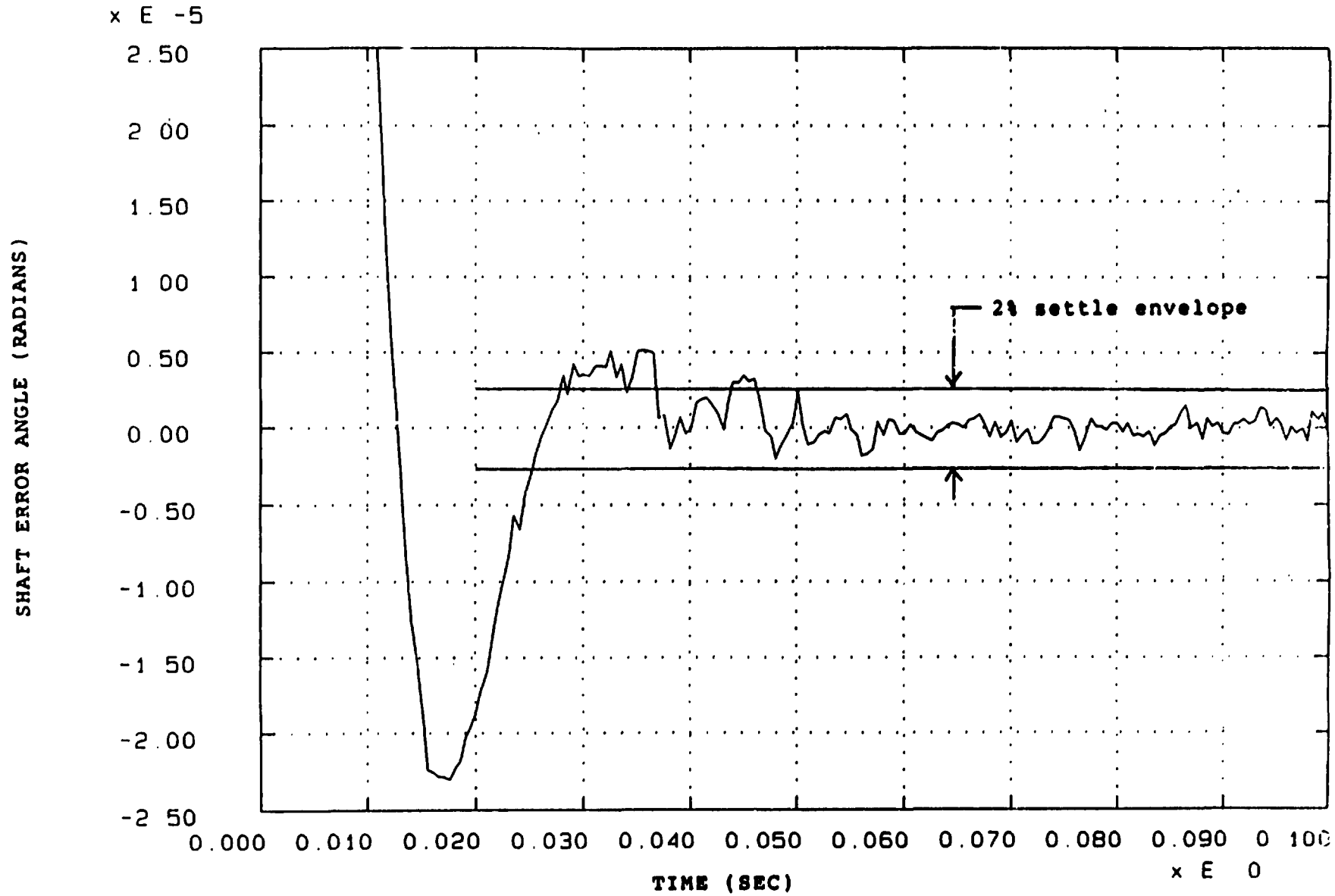
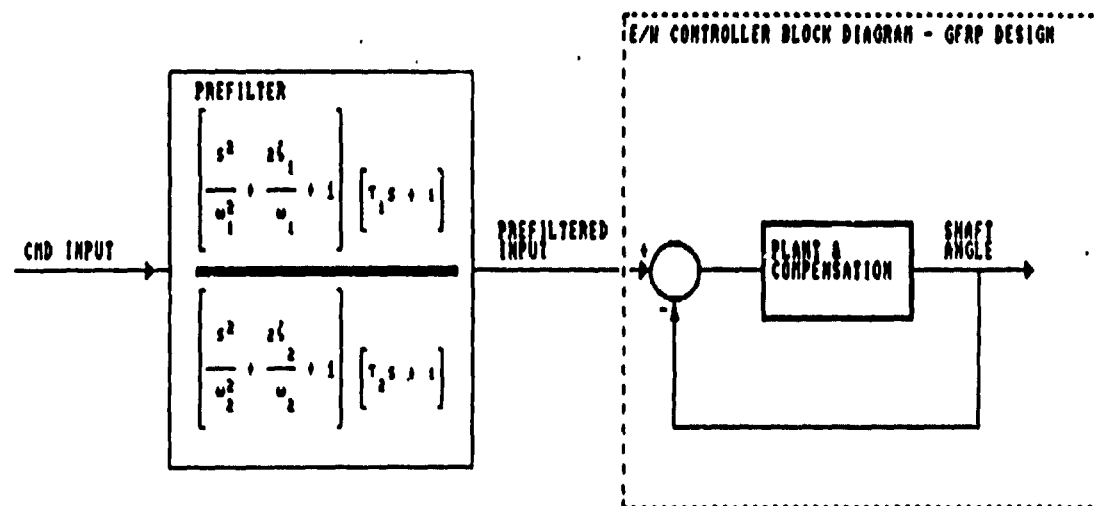


Figure B.1.3-31. Time Response of Two Point Mirror Mount Prefilter Design - Dahl Friction



PREFILTER
ZEROS

$$\omega_1 = 127.10 \quad \zeta_1 = .770$$

$$\tau_1 = 1/122.3$$

PREFILTER
POLES

$$\omega_2 = 100.50 \quad \zeta_2 = .000$$

$$\tau_2 = 1/40.0$$

Figure B.1.3-32. GFRP Prefilter Block Diagram

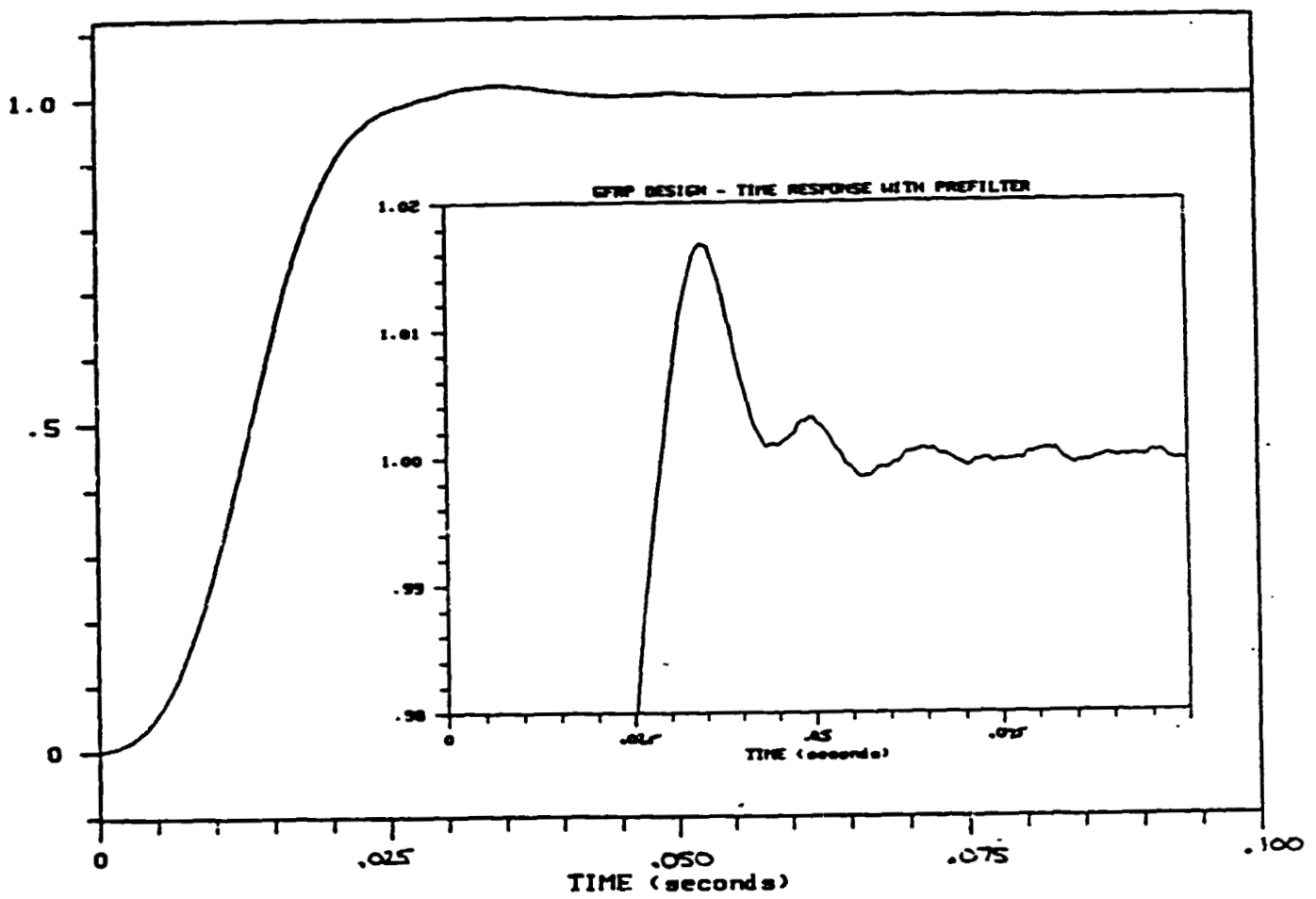


Figure B.1.3-33. Linear Unit Step Response of GFRP Design with Prefilter

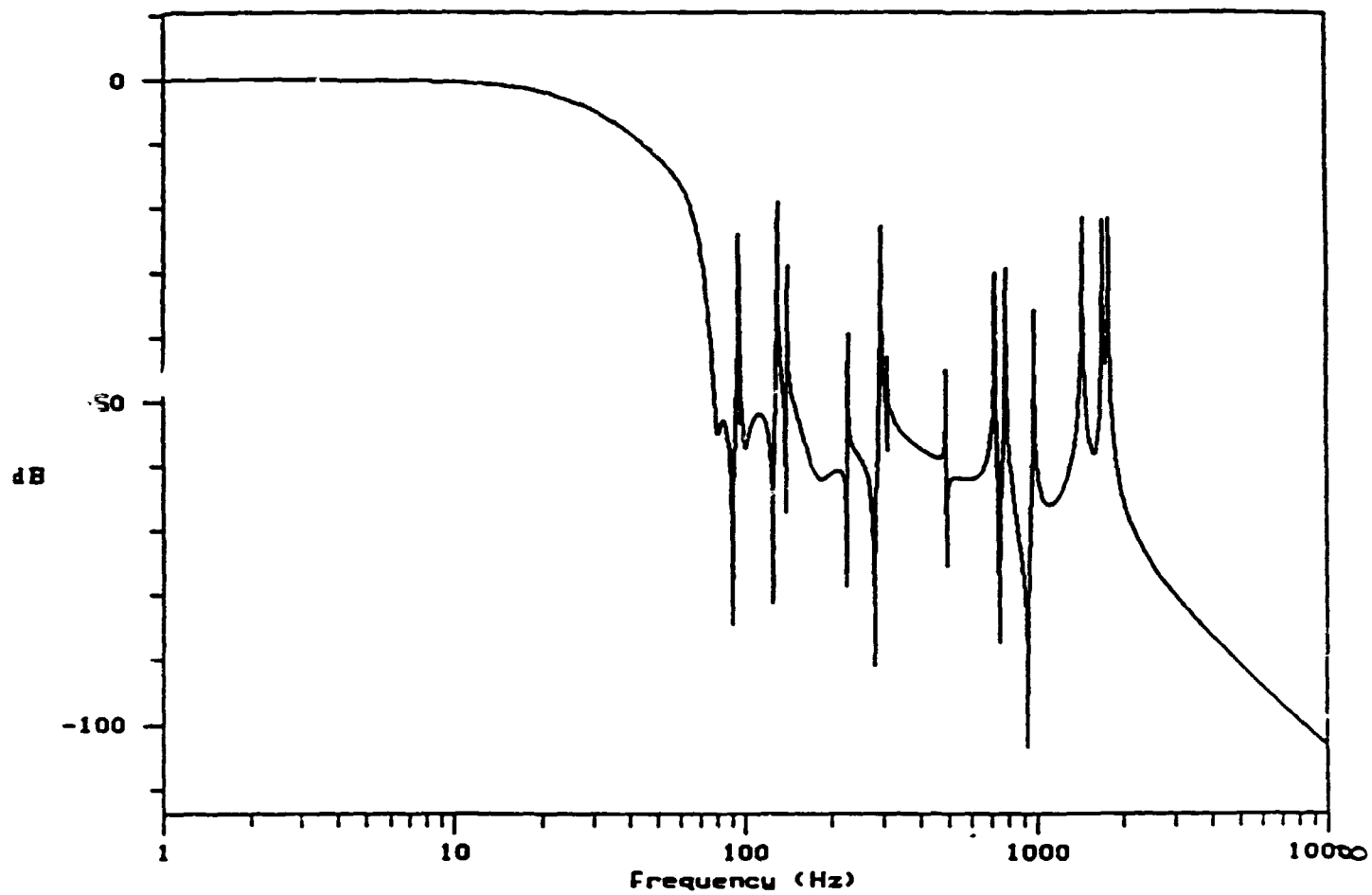


Figure B.1.3-34. Closed Loop Frequency Response - GFRP Design with Prefilter

140 MICRORADIAN STEP RESPONSE - GFRP DESIGN WITH PREFILTER

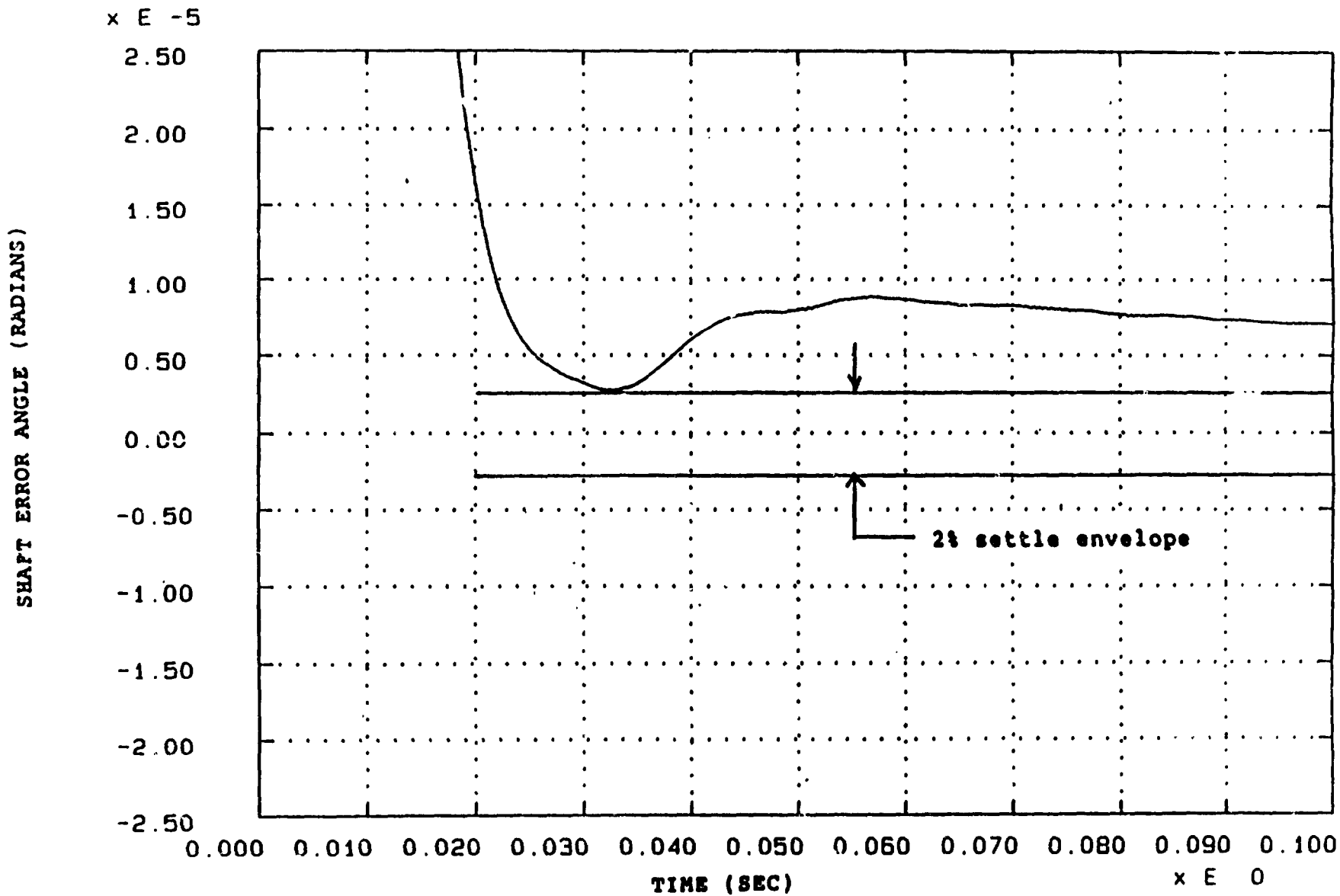


Figure B.1.3-35. Time Response of GFRP Prefilter Design with Dahl Friction

B.1.4 Discussion

B.1.4.1 Conclusions

Of the cases examined, it appears that the GFRP design with the prefilter included shows the greatest promise for achieving the 2% settling time goal in an actual implementation. The GFRP design's simplicity of compensation and insensitivity to variations in modal parameters are desirable features that are not possible with the other concepts. A disadvantage of the GFRP approach is that its low bandwidth caused the design to show the greatest sensitivity to friction. However, ground testing of the hardware can be used to obtain an accurate friction model for use in the design. In addition, a digital implementation of the prefilter would also allow on-orbit tuning of the system to further reduce implementation risk.

The two point mirror mount design did not show any particular advantage over the baseline case and is, therefore, not recommended. If a resolution to the 175 Hz mode discrepancy shows that the mode is not real because of some deficiency in the FEM, it may be worthwhile to revisit this concept. It is still likely, however, that the required performance will be difficult to obtain because of the first few modes which will still interfere with the controller's bandwidth.

A preliminary study of the Imager slew requirement using the GFRP prefilter design indicated that the 1.72 μ r error requirement can be met, but the prefilter imposes a delay in the command signal which delays the entire system response. A Sounder prefilter design is therefore not appropriate for the Imager.

In summary, it appears that the Sounder 2.75 μ r error requirement in the GOES-N budget should be achievable using this technique. It is anticipated that the Imager requirement can also be met.

B.1.4.2 Areas for additional study

Further effort in this area can be directed at obtaining a FEM that is fully test correlated. Because the analyses in this study were concerned only with basic behavior of the structure, the existing FEM was sufficient to get results. However, a more detailed examination leading to actual component selection will require a fully test correlated model.

With additional effort, the prefilter concept can be refined. The sensitivity of such designs to variations in the plant should be quantified, and a closer examination of friction effects is needed using friction models which are correlated to test data.

Finally, the performance of the designs should be evaluated for the Imager requirements and for other qualities such as disturbance rejection and the ability to follow image motion compensation signals.

B.1.5 References

1. Gregory, C. Z., "Reduction of Large Flexible Spacecraft Models Using Internal Balancing Theory", *Journal of Guidance and Control*, Volume 7, No. 6, Nov-Dec 1984, pp. 725-732.
2. Smagala, T.J., Class, B.F., Bauer, F.H., and Lehair, D.A., "Dual Keel Space Station Payload Pointing System Design and Analysis Feasibility Study", *SPIE Proceedings: Acquisition, Tracking, and Pointing II*, Volume 887, 1988.

B.2 GFRP SERVO DESIGN - MODERN CONTROL APPROACH

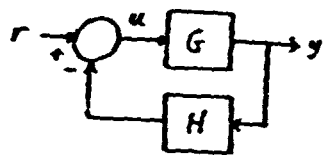
B.2.1 Introduction

Changes to the structure of the sounder (an infrared imaging device) in the GOES spacecraft were made to increase the resonant frequencies of the structure on which the mirror is mounted (the backplate) so that mirror position control performance requirements may be met. The change is largely the substitution of graphite fiber reinforced plastic (GFRP) for aluminum. This report addresses the development of a controller for the GFRP structure. As it turned out, the classical cascade compensator design for the GFRP mode set was difficult [1]. The final design was of 7th order with a closed-loop bandwidth of 35 Hz and required a prefilter to achieve the desired step and frequency response. This report addresses an alternative approach to the development of a controller for the GFRP structure. Only the "step and settle" requirements of the sounder are addressed. This should provide insight into controlling East-West slewing of the imager and performance with the Image Motion Compensation (IMC) signal.

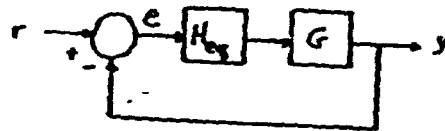
Because of the difficulties in designing a stabilizing compensator for the GFRP, a modern control approach was taken. The modern control approach provides a systematic way to design a dynamic compensator. In this approach, a Luenberger observer is used to estimate the states of certain significant modes for the purpose of state feedback. As is generally known [2], feedback (or parallel) compensation (Figure B.2.1-1a) is, among other advantages, more robust to modeling error than is cascade (or series) compensation (Figure B.2.1-1b). Thus, state feedback is generally more robust than cascade compensation.

Since the modeling uncertainties in the mode set are significant, particularly with respect to modal damping and frequency, the most important quality that the controller must possess is robustness. Measured data tends to verify the modeled parameters, but it is certain that these change when the spacecraft is placed on orbit.

The GFRP plant transfer function has poorly damped poles and zeros over a wide frequency range. A frequency response plot of the plant for the reduced mode set given in Table B.2.1-1 is shown in Figure B.2.1-2. The zeros of the open-loop system are zeros of the closed-loop system. The low-frequency zeros cause significant overshoot because of their low damping and because they are close to the passband of the controller. Thus, poles of the closed-loop system which are located adjacent to these zeros are shifted slightly via appropriate choice of a feedback gain vector to cancel these zeros. This results in an interesting property of the motor torque command signal, which will be discussed later. Although most textbooks warn against complex pole-zero cancellation in the context of cascade compensation, this is much less of a problem with state feedback. Robustness is improved by the apparent property that the open-loop pole-zero separation does not change significantly with perturbations in frequency or damping of the poles. This property carries over to the closed-loop pole-zero separation. These properties were observed in simulation studies, but have not yet been verified analytically. However, this does not detract from the inherent robustness of feedback compensation compared to cascade compensation. The remaining poles of the open-loop system are rigid-body poles (two poles at zero frequency); the feedback gain vector is chosen so that these are shifted to pole locations that give a desired second-order response, namely a specified overshoot, settling time, and accuracy.



(a)



(b)

Figure B.21-1a. Feedback Parallel Compensation and
Figure B.21-1b. Cascade (series) Compensation

TABLE B.2.1-1. GFRP Mode Set

MODE	FREQUENCY (Hz)
1	0 (rigid body mode)
2	79.97
3	94.82
4	96.12
5	130.22
6	140.81
7	204.05
8	227.98
9	244.22
10	285.35
11	295.97
12	311.39
13	336.86
14	365.74
15	492.37
16	500.46
17	724.04
18	786.00
19	980.38
20	1447.05
21	1700.71
22	1747.10
23	1786.61

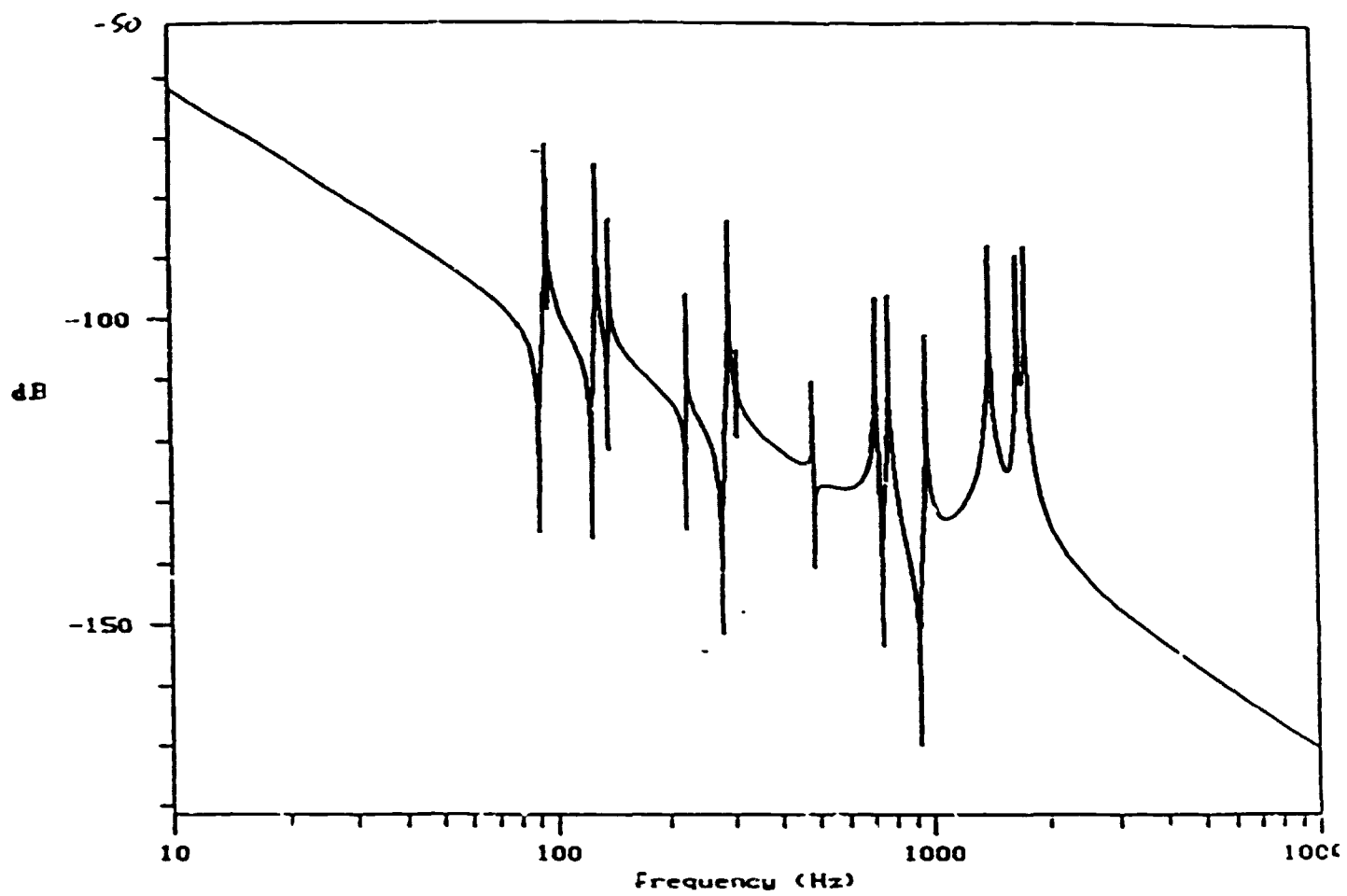


Figure B.2.1-2. Frequency Response of the Reduced GFRP Mode Set

The pole placement design procedure and the development of the observer are outlined in the next section. Special attention is given to time scaling, numerical problems in the design process, and model order reduction. In the third section, input/output relations (transfer matrices) between various points in the control system are given and numerical results are presented in graphical form. The last section contains conclusions and suggests topics for further study.

B.2.2 Pole placement design procedure

Pole placement via state feedback has several advantages over classical cascade compensation. Since the compensator is in the feedback path, rather than in series with the plant (Figure B.2.1-1), the closed-loop system is less sensitive to modeling errors. Closed-loop poles can be specified to cancel plant zeros and to specify dominant poles and other poles to meet certain specific performance criteria such as settling time and overshoot. The design process is algorithmic, rather than trial and error. The pole placement design procedure using state feedback is outlined in this section. Since all the states are not directly measured, a Luenberger observer is developed so that modal states can be estimated. Computation of the input gain from the plant and controller matrices is also given. A singular perturbation approach to reduced-order modeling shows that even though the feedthrough term D_p is zero for the full plant model, the reduced-order model from which the controller is designed has $D \neq 0$. Thus, the reduced-order model is proper, but not strictly proper, even if the plant is strictly proper. Some results are given in Section 3 to demonstrate the effect of this feedthrough term.

B.2.2.1 State equations

The state and output equations representing the rigid body and flexible body dynamics of the mirror pointing system are of the form

$$\begin{aligned} \dot{x} &= Ax + Bu \\ y &= Cx + Du, \end{aligned} \quad (1)$$

where u is the torque command input and y is the shaft angle output as measured at the end of the shaft opposite the motor (the mirror is mounted between). The D matrix is zero for the time being. The A , B , and C matrices, of dimensions $2n \times 2n$, $2n \times 1$, and $1 \times 2n$, respectively (where n is the number of modes) are of the form

$$A = \begin{bmatrix} -2z\Omega & -\Omega^2 \\ I_n & 0 \end{bmatrix} \quad B = \begin{bmatrix} B_1 \\ 0 \end{bmatrix} \quad C = [0 \quad C_2] \quad (2)$$

where Ω is an $n \times n$ diagonal matrix of modal frequencies (in radians/second) and Z is an $n \times n$ diagonal matrix of damping coefficients. For the purpose of design, a very conservative value of $\xi = 0.001$ is the required damping for each flexible body mode, and the modal frequencies may vary $\pm 20\%$. The matrices B_1 and C_1 are computed from the mass-normalized eigenvector matrix as Φ

$$B_1^T = [1 \ -1 \ 0 \dots 0] \Phi \quad (3a)$$

$$C_2 = [0 \ 0 \ 1 \ -1 \ 0 \dots 0] \Phi \quad (3b)$$

These matrices represent the difference between the stator and rotor torques of the motor and the difference between the rotation angles of the yoke and the shaft (at the end opposite the motor), respectively.

B.2.2.2 Time scaling

Because of the wide range of modal frequencies, the system (1) must be scaled. Appropriate scaling will improve the numerical properties of the pole placement and the observer design procedures. Internal balancing [3,4] is one way to scale the system, but is not used in the present design. The simplest scaling is time scaling (or equivalently, frequency scaling), where time t is scaled by $\tau = \omega_f t$ so that the derivative operator is $d-d\tau = 1 - \omega_f d-d\tau$. Let $S_0 = 1 - \omega_f$, I , and let

$$S_1 = \begin{bmatrix} S_0 & 0 \\ 0 & I \end{bmatrix}, \quad S_2 = \begin{bmatrix} S_0^2 & 0 \\ 0 & S_0 \end{bmatrix} \quad (4)$$

Because the system represents n uncoupled second-order systems, (1) can be scaled as

$$\begin{aligned} S_2 \dot{x} &= S_2 A S_1^{-1} S_1 x + S_2 B u \\ y &= C S_1^{-1} S_1 x + D u, \end{aligned} \quad (5)$$

This can be written as

$$\begin{aligned} \bar{x} &= \bar{A} \bar{x} + \bar{B} u \\ y &= \bar{C} \bar{x} + D u \end{aligned} \quad (6)$$

where $x = S_1 \bar{x}$, $A = S_2 A S_1^{-1}$, $B = S_2 B$, and $C = C S_1^{-1}$. This scaling process amounts to replacing the modal frequencies ω_i by ω_i / ω_0 in (2). Note that (6) is of the same form as (1); for ease of notation and clarity in what follows, the overbars are omitted and the system is assumed to be scaled. The scaling frequency ω_0 is chosen to give good numerical properties, as will be discussed later.

B.2.2.3 State feedback

State feedback takes the form $u = -Kx + Er$, where K is a feedback matrix, E is a feedforward matrix, and r is a reference input. In the present work, E is a scalar and is chosen to give the closed-loop system a unity gain. Substituting this expression for u into (1) yields

$$\dot{X} = (A - BK)x + BEr \quad (7)$$

If the pair (A, B) is completely controllable, K can be chosen so that each eigenvalue of $A_c = A - BK$ can be assigned any desired value. The following approach was taken to compute K . The system (1) can be converted to phase variable form by the transformation

$$\begin{aligned} P\dot{x} &= PAP^{-1}Px + PBu \\ y &= CP^{-1}Px + Du \end{aligned} \quad (8)$$

which can be written

$$\begin{aligned} \dot{x}_o &= A_o x_o + B_o u \\ y &= C_o x_o + Du \end{aligned} \quad (9)$$

where $x = Px$, $B = PB$, $C = CP^{-1}$, and

$$A_o = PAP^{-1} = \begin{bmatrix} 1 & 0 & \dots & 0 \\ 0 & 1 & \dots & 0 \\ \dots & \dots & \dots & \dots \\ -a_0 & -a_1 & \dots & -a_{n-1} \end{bmatrix}, \quad B_o = PB = \begin{bmatrix} 0 \\ 0 \\ \dots \\ \dots \\ 0 \\ 1 \end{bmatrix} \quad (10)$$

The transformation matrix P is given by

$$P = \begin{bmatrix} P_1 \\ P_1 A \\ \vdots \\ \vdots \\ P_1 A^{2^{n-1}} \end{bmatrix} \quad (11)$$

where

$$S = \begin{bmatrix} B & AB & A^2 B & \dots & A^{2^{n-1}} B \end{bmatrix} \quad (12a)$$

and

$$P_1 = [0 \ \dots \ 0 \ 1] S^{-1} \quad (12b)$$

Equation (12a) is the controllability matrix and is of full rank if (A, B) is completely controllable.

Let the feedback be given by $u = -Kx$, where $K = [k_0 \ k_1 \ \dots \ k_{n-1}]$ is the state feedback gain vector. Substitution of this into (9) gives the matrix

$$A_{c_0} = A_0 - B_0 K_0 = \begin{bmatrix} 1 & 0 & \dots & 0 \\ 0 & 1 & \dots & 0 \\ \cdot & \cdot & \cdot & \cdot \\ -(a_0 + k_0) & -(a_1 + k_1) & \dots & -(a_{n-1} + k_{n-1}) \end{bmatrix} \quad (13)$$

The last row defines the characteristic equation of the closed-loop system.

Now, the companion matrix A_ϕ (and thus its characteristic equation) does not have to be computed, and the gain K can be obtained directly. Consider the relation $A_{c_0} = A_\phi - B_\phi K_\phi$ from (13). Rearrange this equation with the substitution $A_\phi = PAP^{-1}$ to get

$$B_\phi K_\phi = PAP^{-1} - A_{c_0} \quad (14)$$

and let A_{c_0} contain the coefficients of the desired characteristic equation. Post multiplication of (14) by P yields

$$B_\phi K = PA - A_{c_0} P \quad (15)$$

where the relation $K = K_\phi P$ was used. Since B_ϕ is zero except for the last entry, K is given by the last row of the right-hand side of (16). Then

$$K = (P)_{n..} A - (A_{c_0})_{n..} P \quad (16)$$

where $(M)_{n..}$ indicates the n^{th} row of a matrix M . This method is more accurate than the first approach described in this section since the solution to a system of equations is not required and the final transformation to get K is not required. For implementation, K is time-scaled to real time by post-multiplication by S_1 .

The approach given above is satisfactory for the low-order plant models being considered when appropriate scaling is used. However, for high-order systems or poorly scaled systems, this approach can yield inaccurate results since P in (11) and S in (12a) can be poorly conditioned. Brogan's approach [5] may be numerically more accurate (though scaling is still important) and will be considered in future developments. (For a fourteenth order system, the approach described above was compared with results from the POLEPLACE routine in MATRIX-X, and the resulting gains had small relative error. Although MATRIX-X documentation says very little about its algorithms, it appears that Brogan's approach may be used.)

B.2.2.4 The Luenberger Observer

Given a model of the plant and measured inputs and outputs, the states of the plant can be estimated. The estimator equations are where L is the observer gain. The state estimation error,

$$\begin{aligned}\dot{\hat{x}} &= A\hat{x} + L(y - \hat{y}) + Bu \\ \hat{y} &= C\hat{x} + Du\end{aligned}\quad (17)$$

defined by $\tilde{x} = x - \hat{x}$, is governed by the differential equation

$$\dot{\tilde{x}} = (A - LC)\tilde{x} \quad (18)$$

The observer gain L is chosen such that $A_o = A - LC$ is asymptotically stable so that $\tilde{x} \rightarrow 0$. The placement of eigenvalues of A_o by selection of L is quite similar to that of A_c in (7), with A replaced by A^T , B replaced by C^T , K_p replaced by L_p^T , and P replaced by T . (Thus the pair (A^T, C^T) must be completely controllable, which is equivalent to (A, C) being completely observable.) Once L_p is computed, it is transformed to the coordinates of the original system (1) by $L = T^T L_p$. For implementation, L is time-scaled to real time by pre-multiplication by S_2^{-1} .

B.2.2.5 Input gain calculation

The closed-loop system is shown in Figure B.2.2-1. This $2n^{\text{th}}$ order system is represented by

$$\begin{bmatrix} \dot{x} \\ \dot{\hat{x}} \end{bmatrix} = \begin{bmatrix} A & -Bk \\ LC & A-LC-Bk \end{bmatrix} \begin{bmatrix} x \\ \hat{x} \end{bmatrix} + \begin{bmatrix} BE \\ BE \end{bmatrix} r \quad (19a)$$

$$y = [C \quad -Dk] \begin{bmatrix} x \\ \hat{x} \end{bmatrix} + DEr \quad (19b)$$

With the transformation

$$\begin{bmatrix} x \\ \tilde{x} \end{bmatrix} = \begin{bmatrix} I & O \\ I & -I \end{bmatrix} \begin{bmatrix} x \\ \hat{x} \end{bmatrix} \quad (20)$$

an equivalent representation of (19) is

$$\begin{bmatrix} \dot{x} \\ \dot{\tilde{x}} \end{bmatrix} = \begin{bmatrix} A-BK & BK \\ O & A-LC \end{bmatrix} \begin{bmatrix} x \\ \tilde{x} \end{bmatrix} + \begin{bmatrix} BE \\ O \end{bmatrix} r \quad (21a)$$

$$y = [C-DK \quad -DK] \begin{bmatrix} x \\ \tilde{x} \end{bmatrix} + DEr \quad (21b)$$

The left-hand side of (21) is zero in steady state (and r is taken to be a unit step), so this yields an equation that can be solved for the steady-state value of the state vector. Note that the closed-loop system is not completely controllable, namely the observer states are not controllable.

Since $A - LC$ is stable, and the input does not affect these states, x also goes to zero. Then, in steady state, (21a) and (21b) reduce to $0 = (A - BK)x_{ss} + BE$ and $y_{ss} = (C - DK)x_{ss} + DE$. Solving for x_{ss} yields

$$y_{ss} = (D - (C - DK)(A - BK)^{-1}B)E \quad (22)$$

which can be solved for E .

The procedure above can be "simplified" somewhat by noting the special structure of the system (2), in particular $x^T = [x_1^T \ x_2^T]$ where $x_1^T = x_2^T$. Then $x_{1ss} = 0$, which yields

$$y_{ss} = \left[D - (C - DK) \begin{pmatrix} 0 \\ (-\Omega^2 - B_1 K)^{-1} B_1 \end{pmatrix} \right] E \quad (23)$$

B.2.2.6 Model order reduction

In the block diagram of Figure B.2.2-1, the A , B , C , and D matrices of the observer and plant are the same only for the purpose of design. In reality, these matrices may be somewhat different, and in general the model plant is of lower order than the true plant or the plant used for analysis. It is common (and necessary) practice to neglect high-frequency modes of the plant and to use a reduced-order model for the purpose of design. The closed-loop system with the full-order plant model (A_p , B_p , C_p , D_p) is shown in the block diagram of Figure B.2.2-2. Before writing equations for the closed-loop system, where the plant is of higher order than the observer, it is necessary to derive a reduced-order model and to examine the effect of unmodeled high-frequency modes on the closed-loop system. Let the full-order plant and state vector be partitioned as

$$A_p = \begin{bmatrix} A_{11} & A_{12} \\ A_{21} & A_{22} \end{bmatrix} \quad B_p = \begin{bmatrix} B_{01} \\ B_{02} \end{bmatrix} \quad C_p = [C_{01} \ C_{02}] \quad X_p = \begin{bmatrix} x \\ z \end{bmatrix} \quad (24)$$

so that the state and output equations can be written

$$\begin{aligned} \dot{x} &= A_{11}x + A_{12}z + B_{01}u \\ \dot{z} &= A_{21}x + A_{22}z + B_{02}u \\ y &= C_{01}x + C_{02}z + D_p u \end{aligned} \quad (25)$$

where the eigenvalues of A_{11} and A_{22} are approximately equal in magnitude, and where x and z are state vectors and μ is a small time-scaling parameter [6,7]. Assuming the fast modes are stable (as they are in the present problem), the fast modes will damp out more quickly than the slow modes. Setting $\mu = 0$, one obtains equations for the slow states x_s and z_s . Then

$$z_s = -A_{22}^{-1}A_{21}x_s - A_{22}^{-1}B_{02}u_s \quad (26)$$

where u_s , u is the slow-state input. Substituting this into

$$\begin{aligned}\dot{x}_s &= A_{11}x_s + A_{12}z_s + B_{01}u_s \\ y_s &= C_{01}x_s + C_{02}z_s + D_p u_s\end{aligned}\quad (27)$$

yields

$$\begin{aligned}\dot{x}_s &= A_o x_s + B_o u_s \\ y_s &= C_o x_s + D_o u_s\end{aligned}\quad (28)$$

where

$$\begin{aligned}A_o &= A_{11} - A_{12}A_{22}^{-1}A_{21} \\ B_o &= B_{01} - A_{12}A_{22}^{-1}B_{02} \\ C_o &= C_{01} - C_{02}A_{22}^{-1}A_{21} \\ D_o &= D_p - C_{02}A_{22}^{-1}B_{02}\end{aligned}\quad (29)$$

The fast state and output is defined by

$$\begin{aligned}\mu \dot{z}_f &= A_{22}z_f + B_{02}u_f \\ y_f &= C_{02}z_f + D_p u_f\end{aligned}\quad (30)$$

where $u_f = u - u_s$ is the fast-state input.

The initial conditions are $x(0)_s = x(0)$, and $z_f(0) = z(0) - z_s(0) = z(0) + A_{22}^{-1}A_{21}x_s(0) + A_{22}^{-1}B_{02}u_s(0)$. Equations (22) define a reduced-order model, i.e., the (A, B, C, D) matrices in (1). These expressions simplify considerably since $A_{12} = 0$ and $A_{21} = 0$ in the present problem. Note, however, that even though $D_p = 0$ in the present problem, the reduced-order model has a non-zero feedthrough term D_o . As it turns out, this term is significant since some of the neglected high-frequency modes have large modal gains. The controller was initially designed without consideration of this feedthrough term.

It is shown in [8] and [9] that if A_{22} is stable, then there exists a (computable) $\mu^* > 0$ such that if the reduced-order system is stabilized with state feedback and a strictly proper observer, then the singular perturbation (25) of (28) is stabilized for all $\mu \in (0, \mu^*]$. (Thus, eigenvalues of $1 - \mu A_{22}$ must be more negative than those of $1 - \mu A_{22}$.) If A_{22} is not stable or is not sufficiently damped, the fast states can also be stabilized with state feedback and an observer, where z_f is estimated. (The condition on μ must still be satisfied.) This latter configuration is known as a two-time scale system and has numerical advantages over a single observer incorporating both slow and fast states. In the present work, only the slow state observer was considered.

In many early papers that quote the theorem stated above, it was thought that μ was arbitrary and that a system in which high frequency modes were neglected could always be stabilized with observer-state feedback. Since the parameters are fixed once the system is specified, the theorem should be interpreted to say that the system is stable when $\mu \in (0, \mu^*]$, which is not always the case.

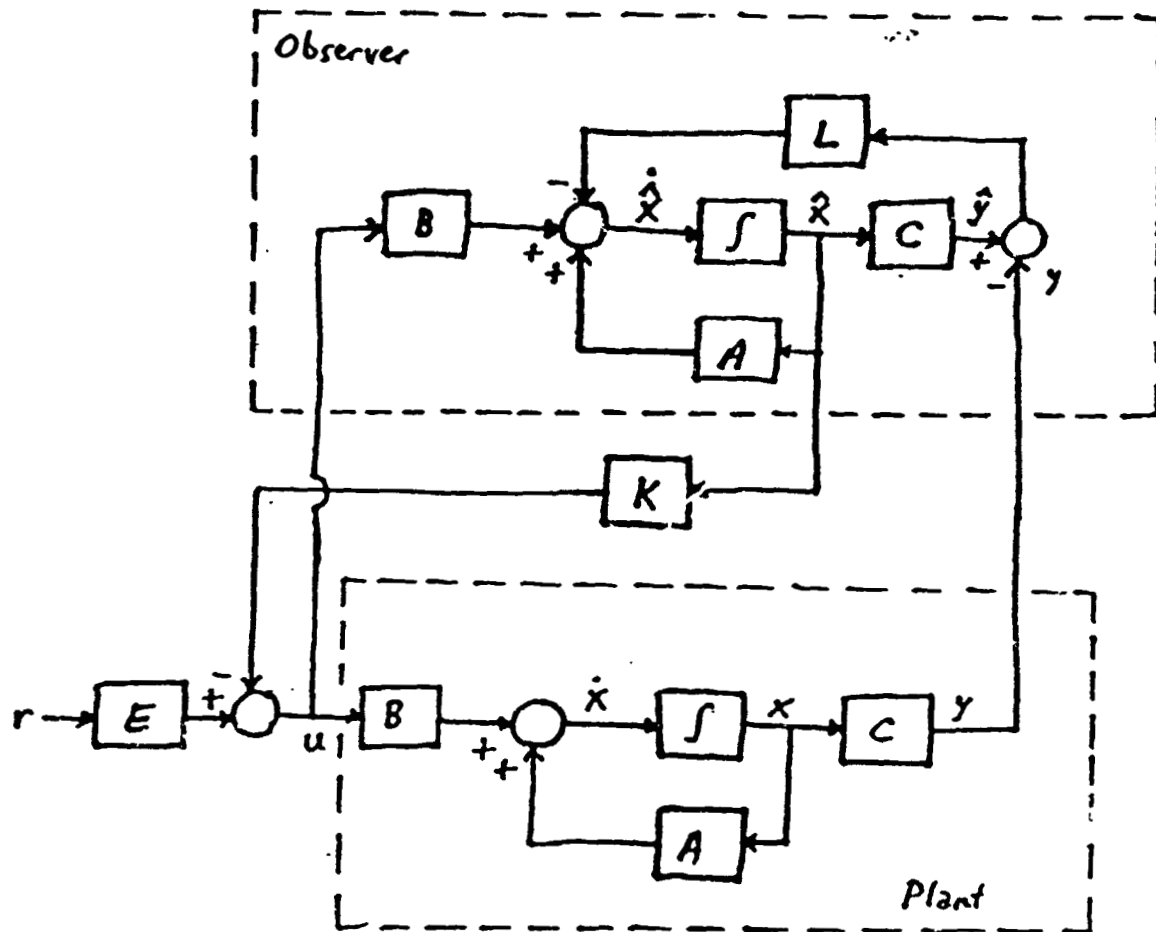


Figure B.2.2-1. Stabilization by Observer State Feedback with Matched Plant and Observer Models

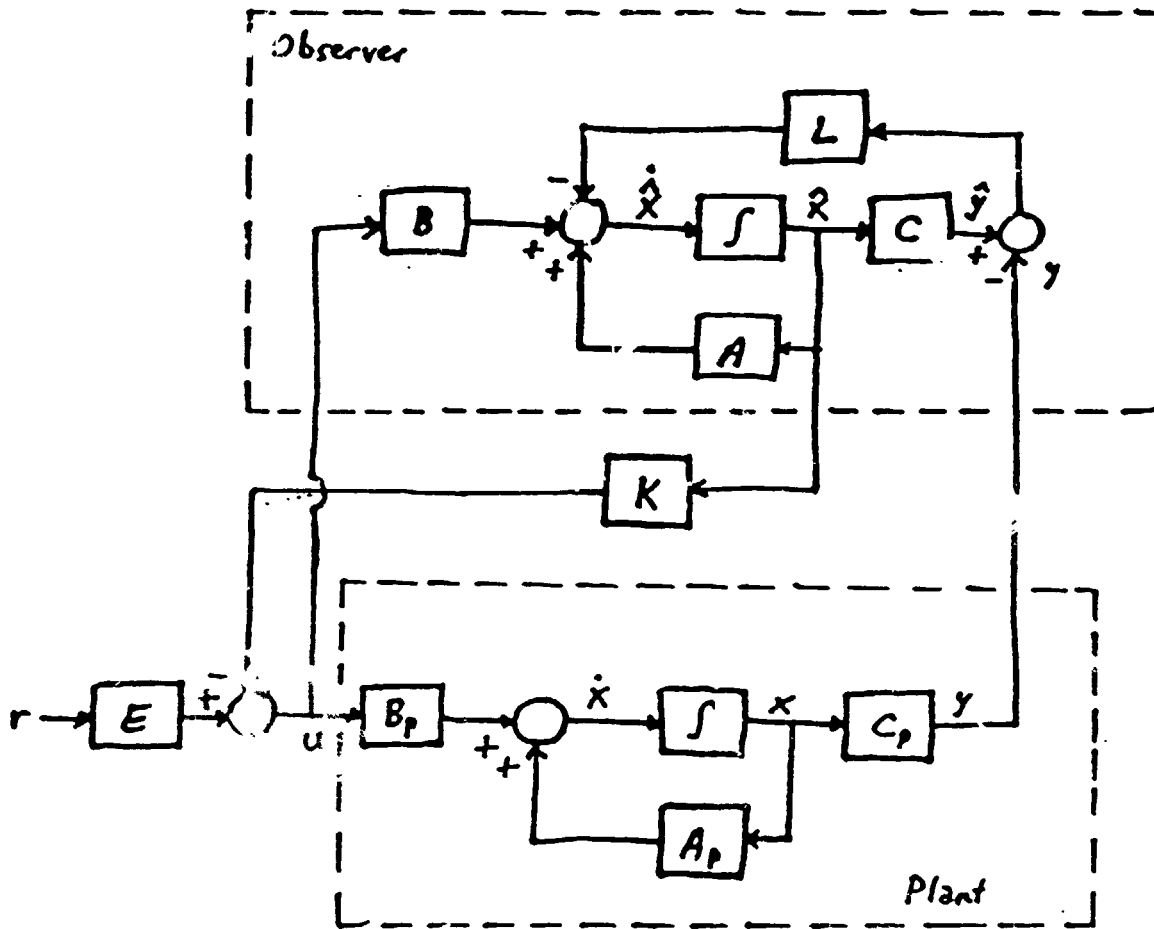


Figure B.2.2-2. Stabilization by Observer State Feedback with Model Mismatch
Plant and Observer Models

Further consideration to deriving a reduced-order model is needed. In particular, it is important to retain the dominant zeros of the plant. The introduction of a non-zero D causes a shift in these zeros in both frequency and damping, and this should be taken into account in the controller design, as shown in results to follow. This topic is discussed further in [10].

B.2.3 Controller design and analysis

Design data and gains are given in this section along with system equations that relate various signals in the system. Considerations for choosing the controller and observer gains are given. Results include time and frequency response data for the controller with the reduced-order plant (matched plant and design model where two flexible-body modes are modeled) and the controller with the full plant model (where the controller design model is of lower order than the full plant model). Results are also given for a reduced-order model that includes several high-frequency modes.

B.2.3.1 Controller design

The mode set for the GFRP structure is provided in Table B.2.1-1. The mode selection for the reduced-order model was based on Gregory's criterion [1], where modes that are poorly observable and poorly controllable are excluded from the design model. Friction and nonlinear effects were ignored. The design incorporates modes 1, 3, and 4 (the rigid body modes and modes at 94.82 Hz and 96.12 Hz). Thus the reduced order model contains six poles and four zeros, aside from the feedthrough term D_0 (which was taken to be zero in the initial design). The zeros of the plant, which are also closed-loop zeros if they are not canceled, are poorly damped and can cause significant overshoot and sensitivity to disturbances, particularly since they are almost within the bandwidth of the closed-loop system. Therefore, the poles of the closed-loop system were chosen to cancel the zeros. The remaining two poles are dominant poles and were chosen to meet the settling error requirement of $e = 1.9\%$ error in $T_s = 28$ milliseconds for a unit step input. Analysis of a second-order system shows that the damping ratio ξ and natural frequency ω_n are related to the error and settling time by

$$\xi \omega_n = \frac{-\ln(e\sqrt{1-\xi^2})}{T_s} \quad (31)$$

Although the observer will be faster than the controller, 2 milliseconds of the specified settling time are allowed for error contributed by the observer. The controller must then give the required accuracy in 26 milliseconds. Choosing $\xi = 0.9$ gives $\omega_n = 205$ radians/second specifies dominant complex conjugate poles for the closed-loop system. (The resulting closed-loop bandwidth is then 152.9 radians/second with a crossover frequency at 109.2 radians/second.) The frequency scaling was set to 603.96 radians/second.

The three complex conjugate poles of the observer are placed at a natural frequency of 1000 radians/second with damping ratios of 0.7, 0.8 and 0.9. (A faster observer is desired but limitations of Matrix-X, which was used for design and analysis, were encountered.)

In analyzing the performance and robustness of the controller, the time response of the shaft angle ($y(t)$), torque command ($u(t)$), and the observer output error ($y(t) - \hat{y}(t)$) were plotted. Also, the frequency response was computed for each of the following: closed-loop system (y/r), the torque command (u/r), the plant (y/u), the controller (y/y and r/y), and the equivalent open-loop unity-feedback system ($y/e = y/(r-y)$). The system equations for computing these are as follows:

$$\begin{bmatrix} \dot{x} \\ \dot{\hat{x}} \\ y \\ u \end{bmatrix} = \begin{bmatrix} A_p & -B_p K & B_p E \\ LC_p & A-LC-BK+LDK & BE-LDE \\ C_p & 0 & 0 \\ 0 & -K & E \end{bmatrix} \begin{bmatrix} x \\ \hat{x} \\ r \end{bmatrix} \quad (32)$$

for computing the time responses $y(t)$ and $u(t)$ to a step input and the frequency responses y/r and u/r ,

$$\begin{bmatrix} \dot{x} \\ y \end{bmatrix} = \begin{bmatrix} A_p & B_p \\ C_p & 0 \end{bmatrix} \begin{bmatrix} x \\ u \end{bmatrix} \quad (33)$$

for computing the frequency response y/u of the plant;

$$\begin{bmatrix} \dot{\hat{x}} \\ \dot{y} \\ \hat{y} \end{bmatrix} = \begin{bmatrix} A-LC-BK+LDK & L \\ K & 0 \\ C-DK & 0 \end{bmatrix} \begin{bmatrix} \hat{x} \\ y \end{bmatrix} \quad (34)$$

for computing the frequency responses r/y and y/y of the observer;

$$\begin{bmatrix} \dot{x} \\ \dot{\hat{x}} \\ y \end{bmatrix} = \begin{bmatrix} A_p + B_p E C_p & -B_p K & B_p E \\ (L+BE-LDE) C_p & A-LC-BK+LDE & BE-LDE \\ C_p & 0 & 0 \end{bmatrix} \begin{bmatrix} x \\ \hat{x} \\ r-y \end{bmatrix} \quad (35)$$

for computing the frequency response y/e of the equivalent open-loop unity-feedback system.

The closed-loop step and frequency response of the shaft angle and the torque command indicates overall performance, while the frequency response of the equivalent open-loop system shows the phase and gain margins. The response of the controller gives some insight into its performance and characteristics.

B.2.3.2 Simulation results

Results are presented for the controller design that models modes 1, 3, and 4. Results for a matched plant and controller model are given in Figures B.2.3-1 through B.2.3-5 with $D = 0$. Figure B.2.3-1 is the response of the shaft angle to a step input, and shows that the desired response time and settling accuracy are achieved. The undershoot at the start is due to the initial

controller state being set to $(0 \ 0 \ 0 \ -0.1 \ -0.1 \ -0.1)^T$, while the initial plant state vector was zero. The estimated shaft angle (from the observer) is compared in Figure B.2.3-2 to the shaft angle from the plant model, and is seen to converge rapidly to zero. The torque input to the plant is shown in Figure B.2.3-3. After the observer settles, it produces a torque input to the plant that shifts the flexible body modes to match the plant zeros. This results in disturbances from these modes being unobservable in the output. The control torque is lightly damped but stable since the plant zeros are lightly damped and stable. Merits and demerits of this control method with regard to the control torque is reconsidered in the Conclusions. Figure B.2.3-4 shows the response of the plant states (displacements only) to the step input, where x_1 is the motor rotor angle, and x_2 and x_3 are the flexible body states corresponding to modes 3 and 4.

Figures B.2.3-5 through B.2.3-12 are results where the controller was designed using modes 1, 3, and 4, and the analysis incorporates modes 1, 3, 4, 5, 6, 8, 11, and 15. Figures B.2.3-5 through B.2.3-7 show the effect of the unmodeled modes on the step response. These figures indicate that the system remains stable and that the unmodeled modes give rise to disturbances at the shaft output that are within the required error tolerance. Figures B.2.3-8 through B.2.3-12 give, respectively, the frequency responses for the open-loop system, the closed-loop system, the control torque, the observer control output, and the estimated plant output. The upper graph is the log magnitude plot and the lower graph is the phase plot. (The frequency responses were generated using Matrix-X. Its BODE routine was not used because of problems with the phase tracker and because of memory limitations; the FREQ routine was used instead, but the phase was not unwrapped by FREQ. The peaks in the frequency response were found manually.) Figure B.2.3-8 gives the open-loop frequency response of the plant and equivalent unity-feedback cascade compensator. Figure B.2.3-12 shows that the observer can produce accurate estimates of the plant state up to frequencies of about 1000 radians/second. In summary, the unmodeled modes do not have a significant effect on the output and the output error does not exceed the accuracy requirement. Figures B.2.3-13 and B.2.3-14 give the step response when the modal frequencies used in the analysis were increased 20% and the damping was increased from 0.001 to 0.003. Figures B.2.3-15 and 16 give the step response when the modal frequencies used in the analysis were decreased 20% and the damping was increased from 0.001 to 0.005. In these cases, the closed-loop system remained stable, and although the error increased, it is still within bounds.

Figures B.2.3-17 through B.2.3-21 are similar to the case of Figures B.2.3-8 through B.2.3-12, but D is computed using singular perturbation theory. Comparing Figure B.2.3-8 with Figure B.2.3-17 shows that the first zero is shifted slightly so that it is no longer exactly canceled by the pole. Although this does not cause a problem, the shift of the zero could be anticipated in the placement of the closed-loop poles. The other effect of a non-zero D is a decrease in the gain and phase above the gain crossover frequency (Figure B.2.3-17) and an increase in the damping of the poles of the controller (Figure B.2.3-20).

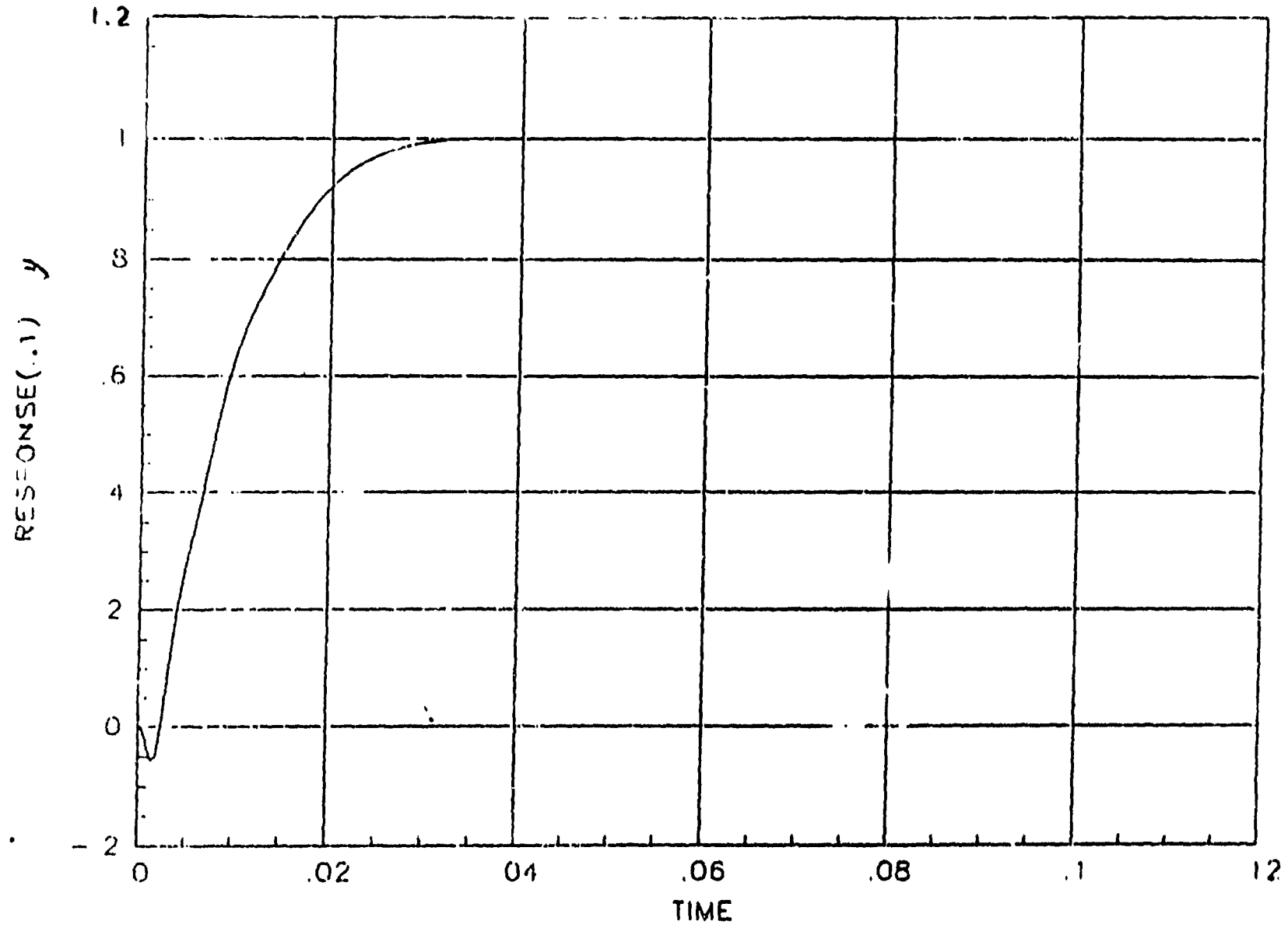


Figure B.2.3-1. Step Response for Matched Plant and Controller Model; Model 1,3,4, Modeled

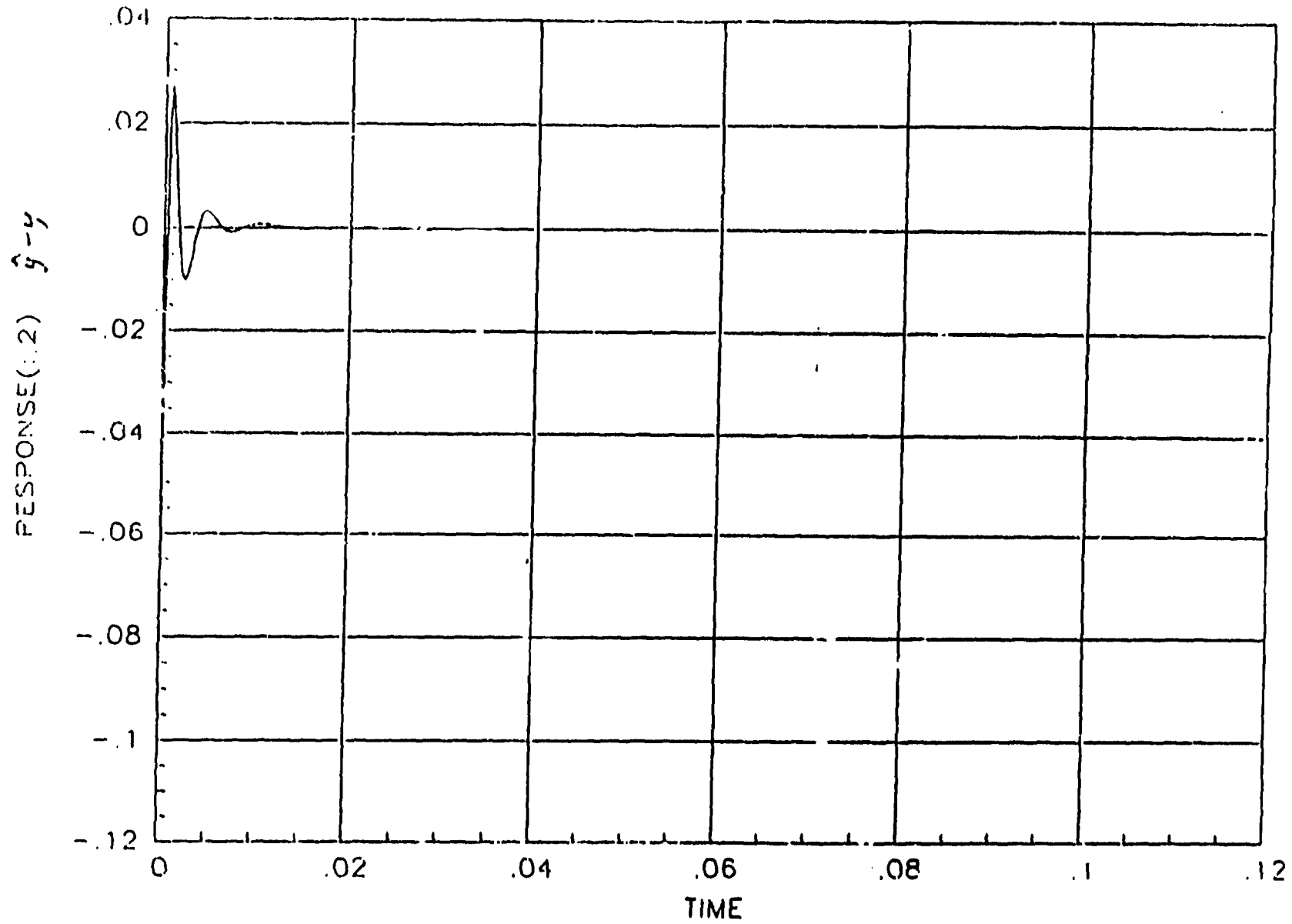


Figure B.2.3-2. Difference Between Estimated and Measured Shaft Angles with Modes 1,3,4 Modeled in the Plant and Controller

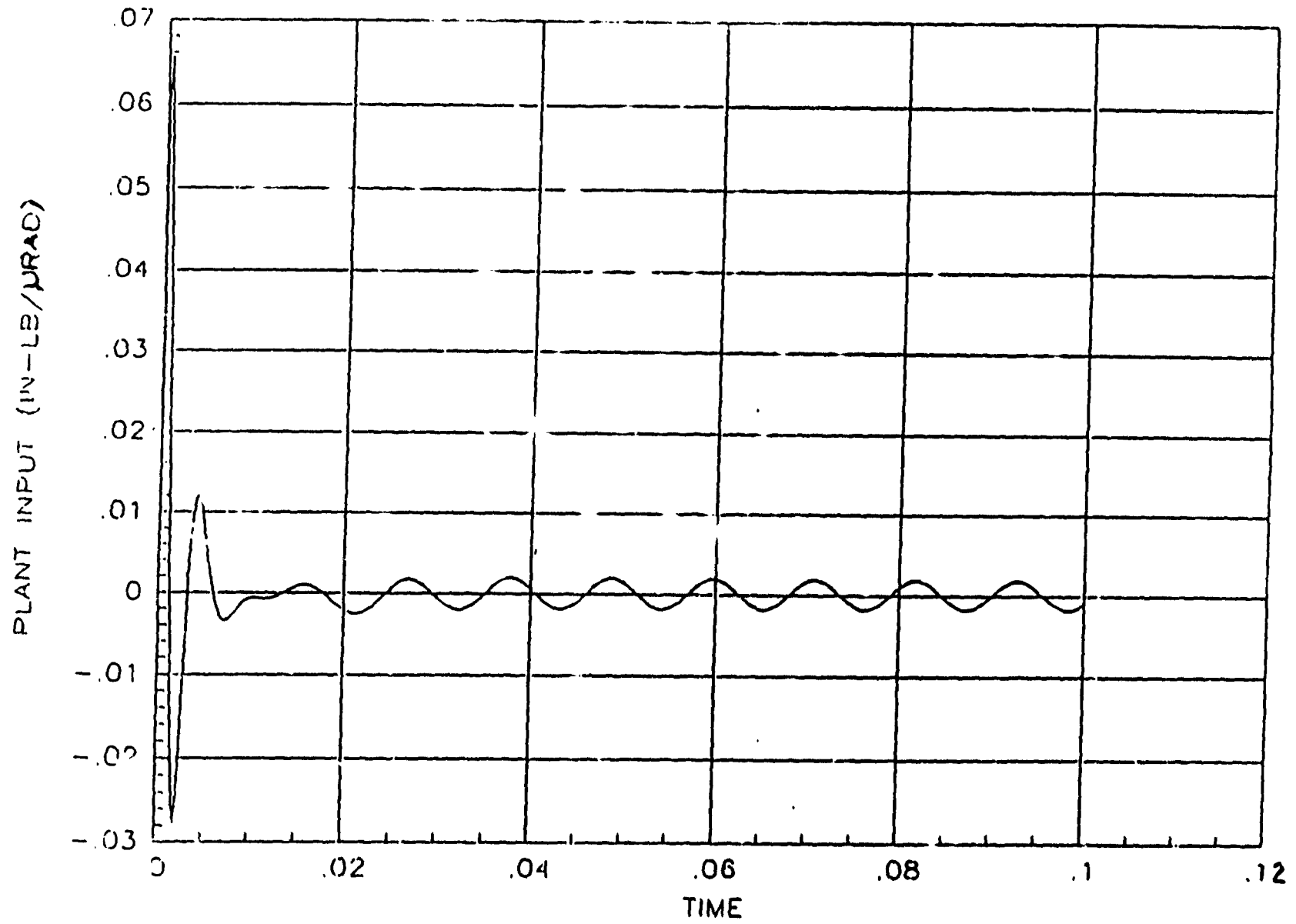


Figure B.2.3-3. Control Torque for Matched Plant and Controller Model; Modes 1,3,4 Modeled

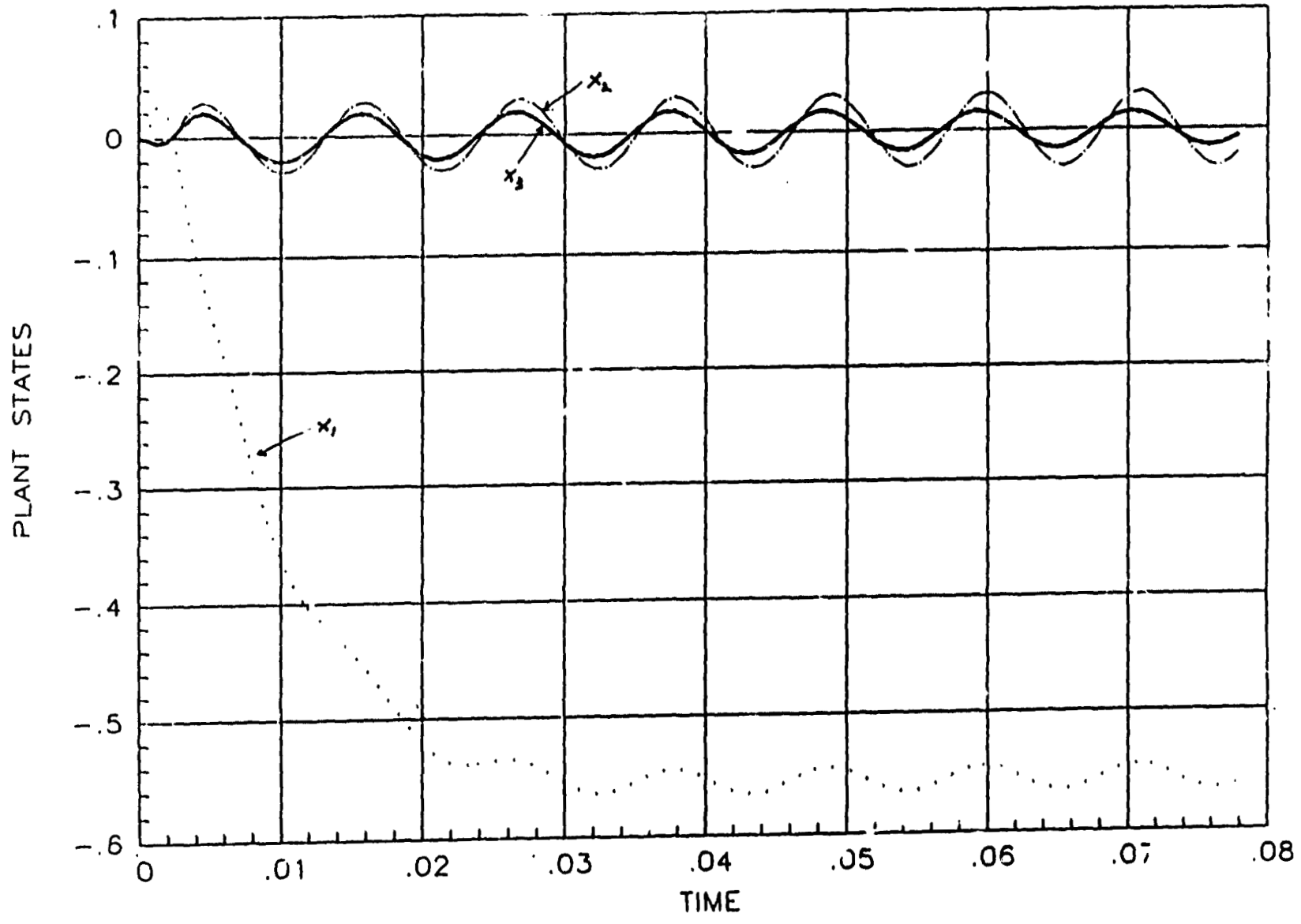


Figure B.2.3-4. Plant States (modal displacements) for Matched Plant and Controller Model; Modes 1,3,4 Modeled

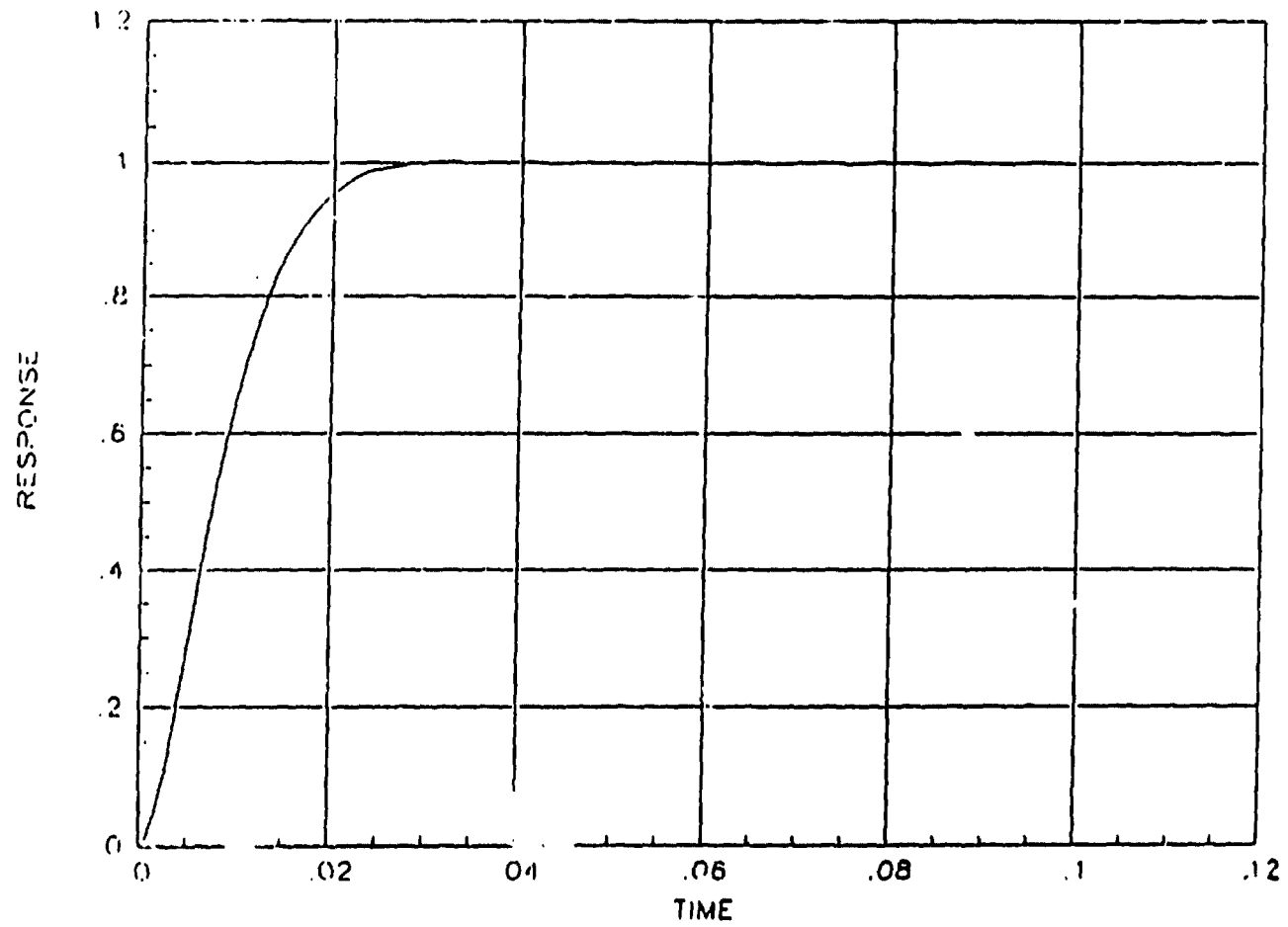


Figure B.2.3-5. Step Response for Plant with Modes 1,3,4,5,6,8,11,15 and Controller Designed with Modes 1,3,4

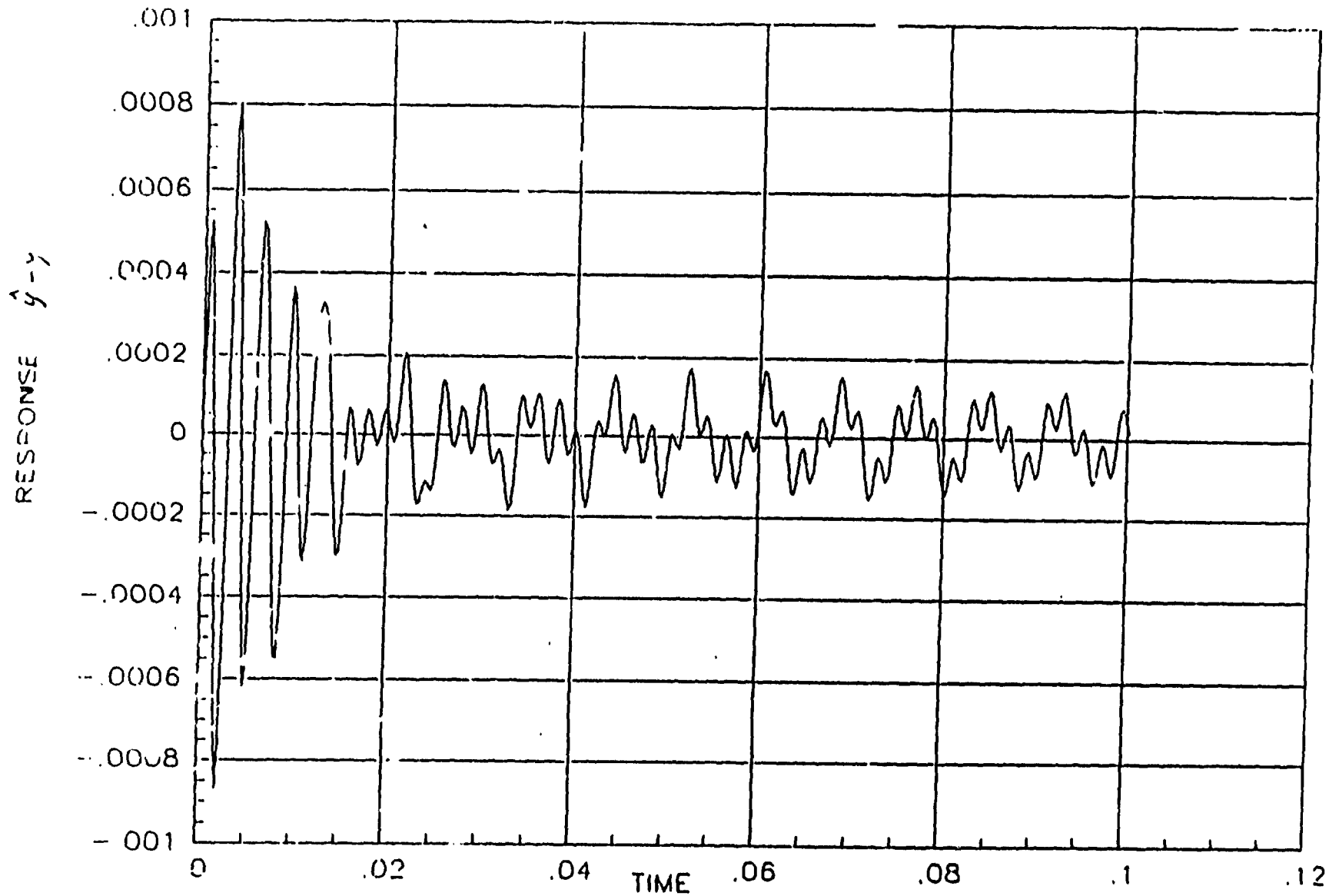


Figure B.2.3-6. Difference Between Estimated and Measured Shaft Angles for Plant with Modes 1,3,4,5,6,8,11,15 and Controller Designed with Modes 1,3,4

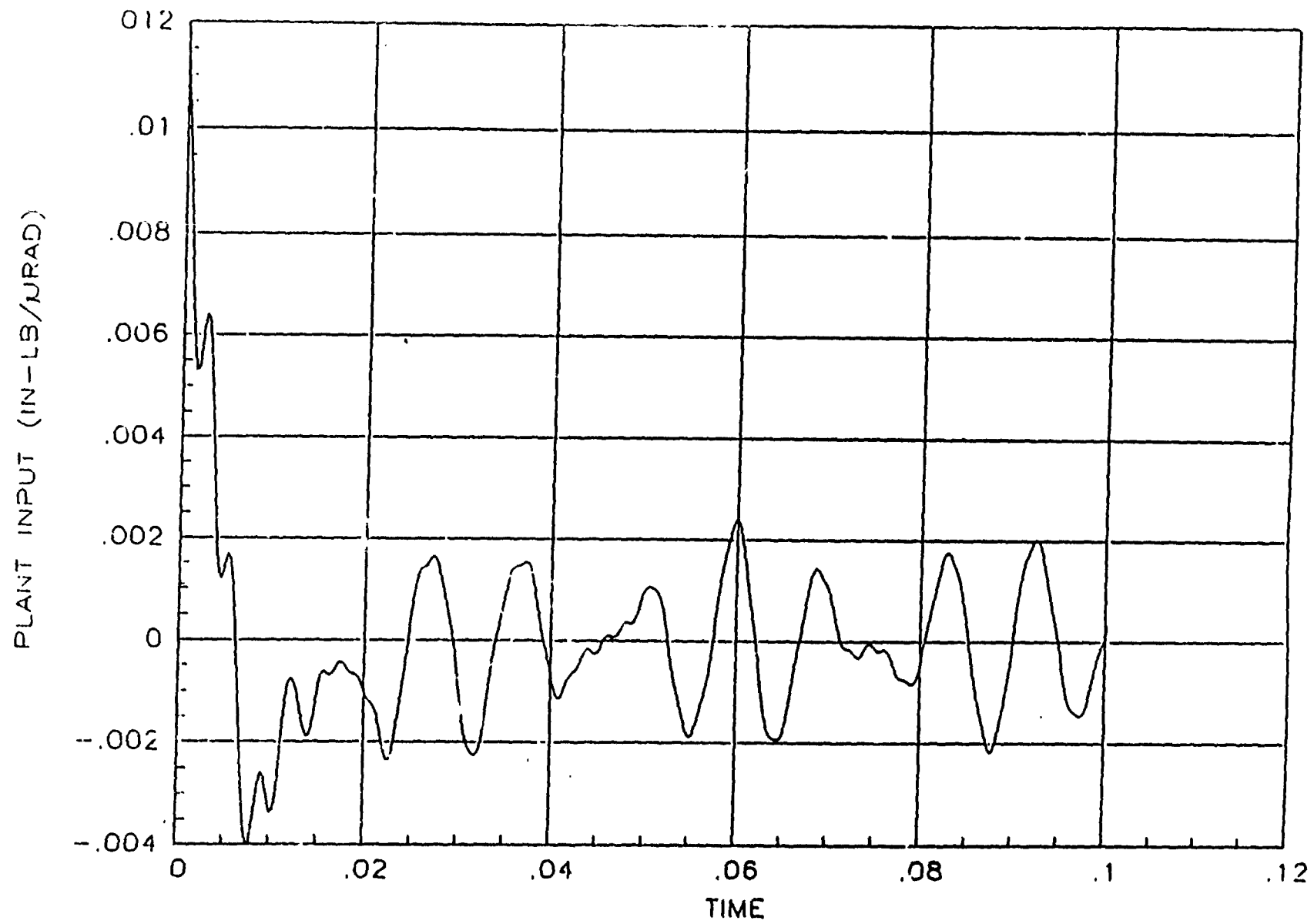


Figure B.2.3-7. Control Torque for Plant with Modes 1,3,4,5,6,8,11,15 and Controller Designed with Modes 1,3,4

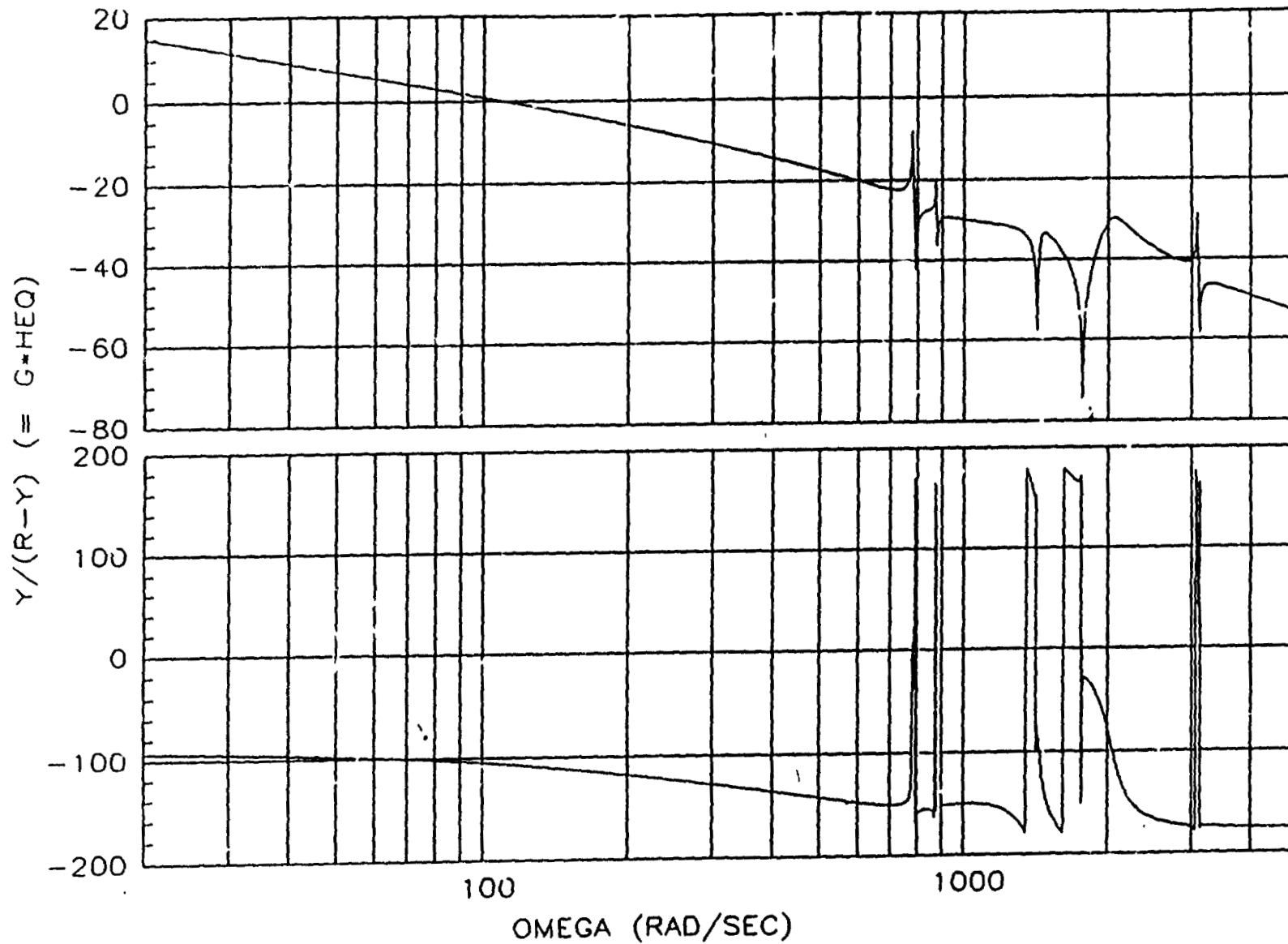


Figure B.2.3-8. Frequency Response for Equivalent Open-loop System for Plant with Modes 1,3,4,5,6,8,11,15 and Controller Designed with Modes 1,3,4

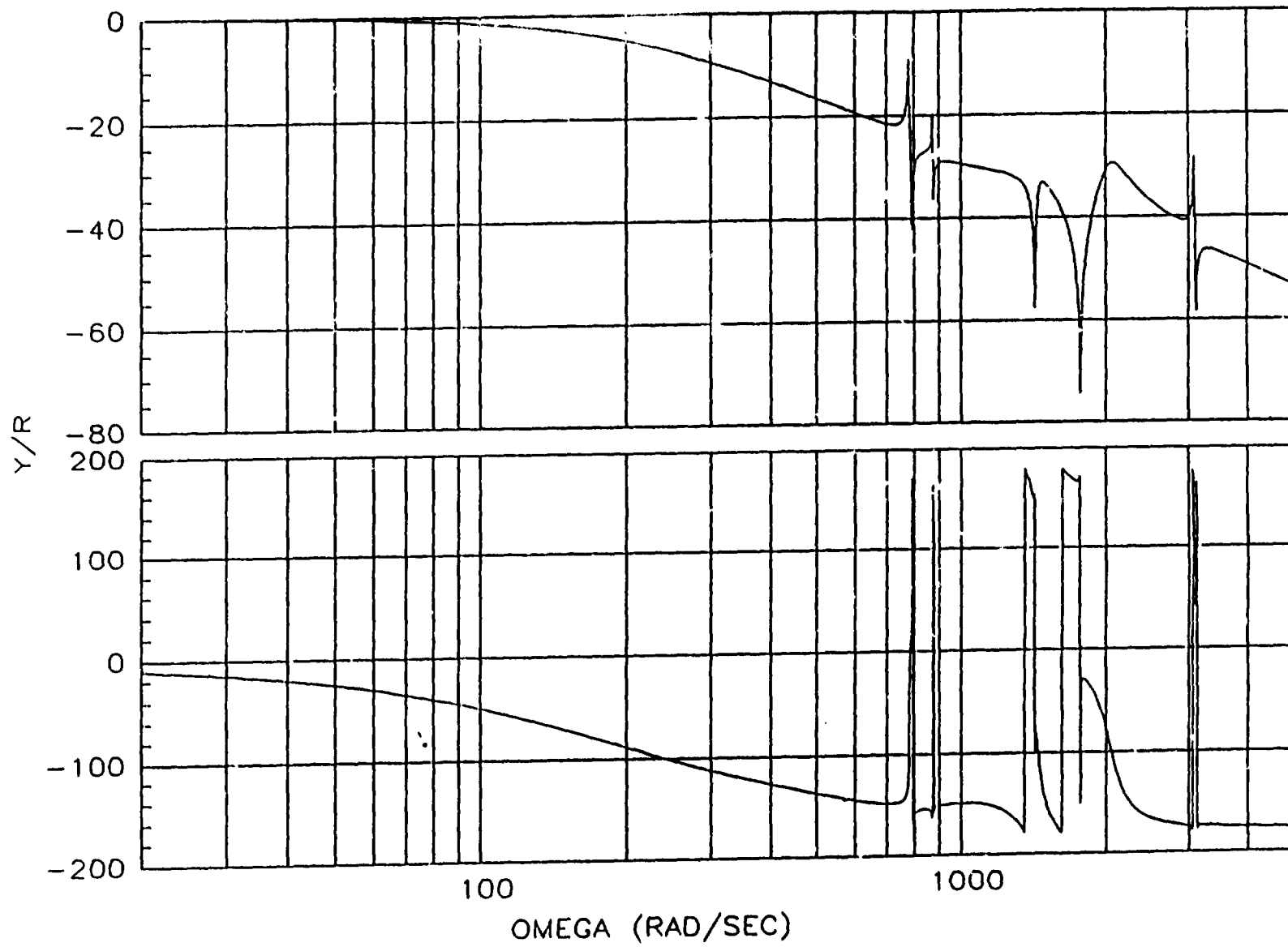


Figure B.2.3-9. Frequency Response for Closed-loop System for Plant with Modes 1,3,4,5,6,8,11,15 and Controller Designed with Modes 1,3,4

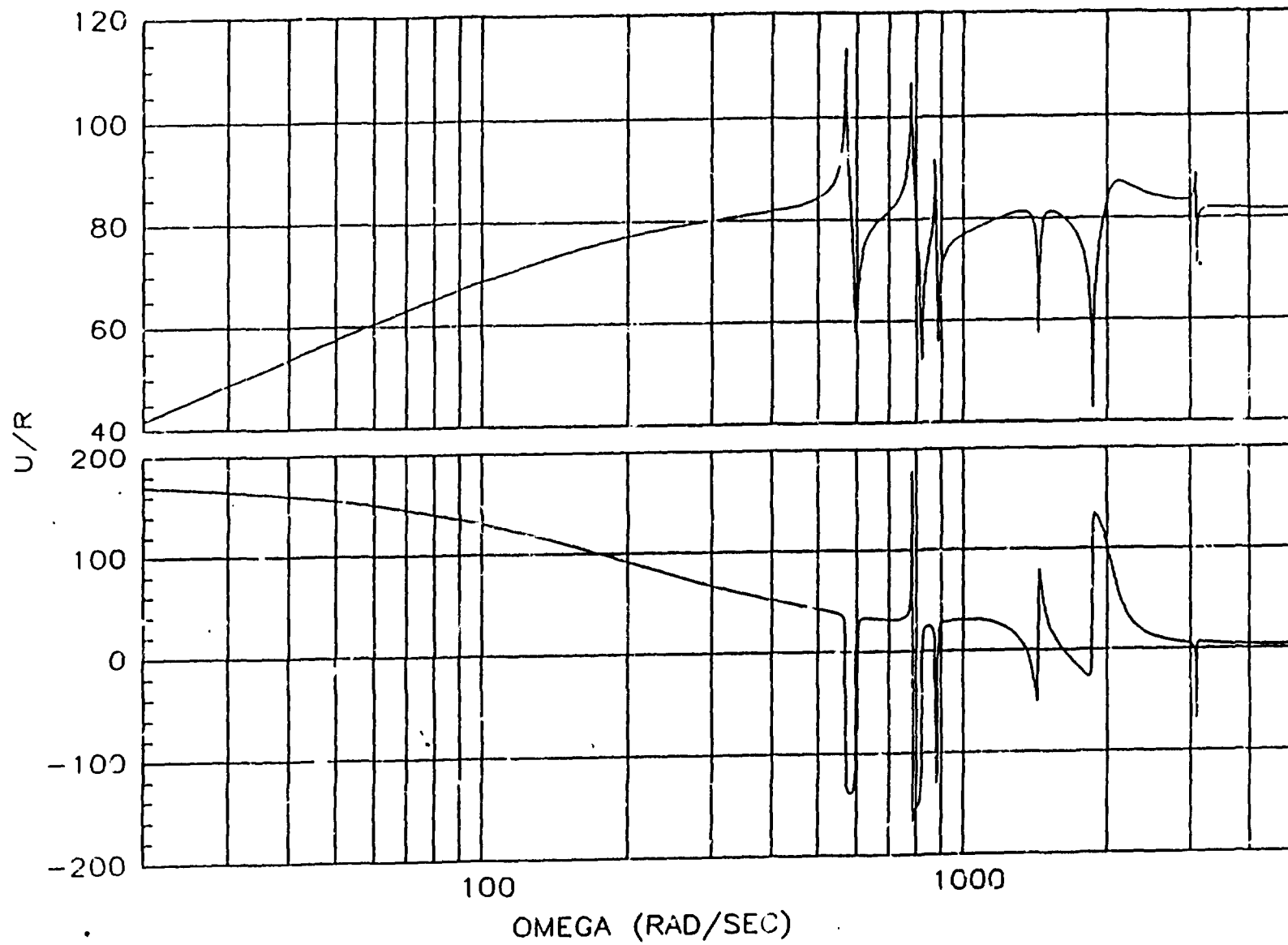


Figure B.2.3-10. Frequency Response of the Control Torque for Plant with Modes 1,3,4,5,6,8,11,15 and Controller Designed with Modes 1,3,4

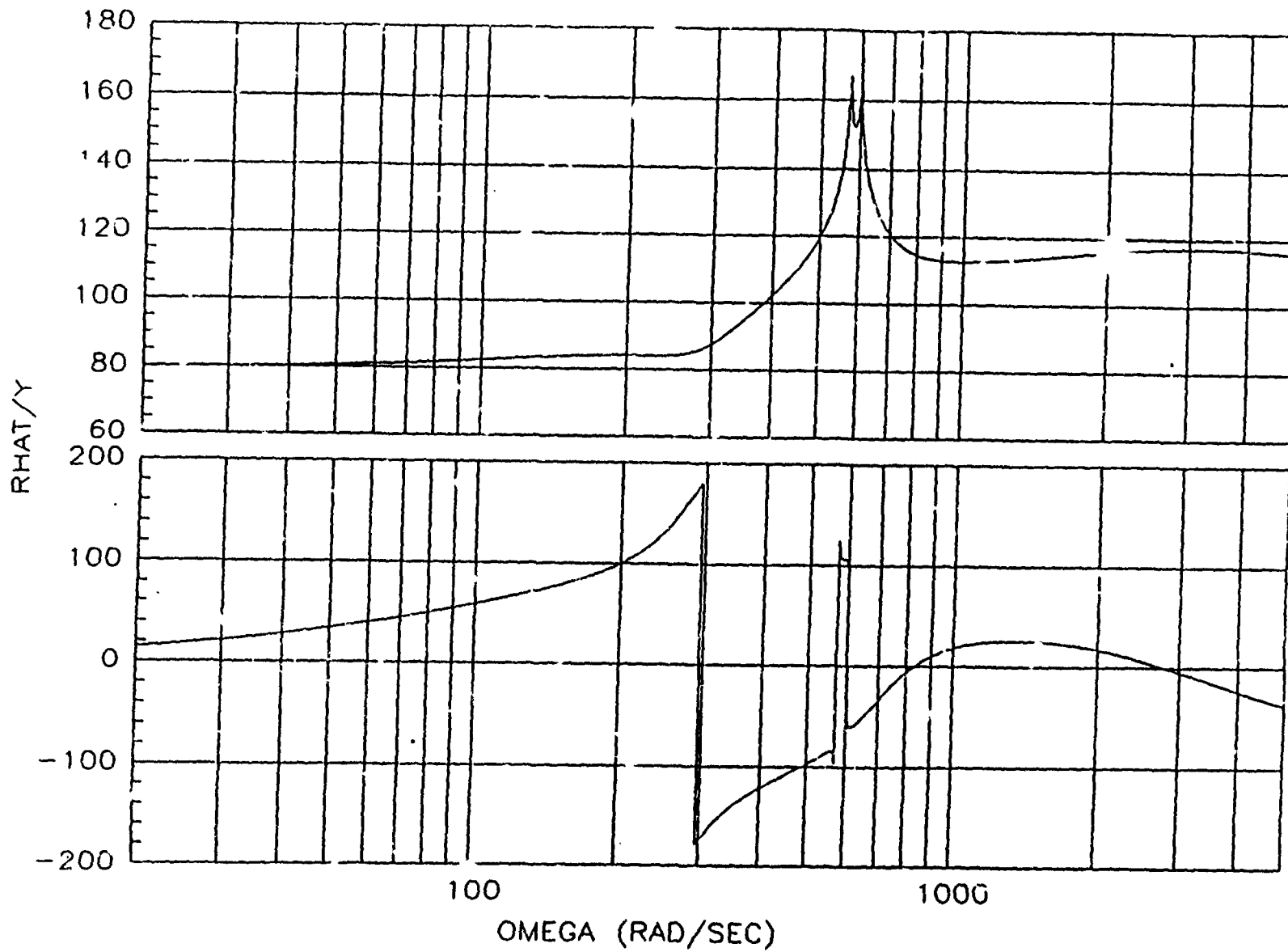


Figure B.2.3-11. Frequency Response of the Controller (with measured shaft angle as input) and Controller Designed with Modes 1,3,4

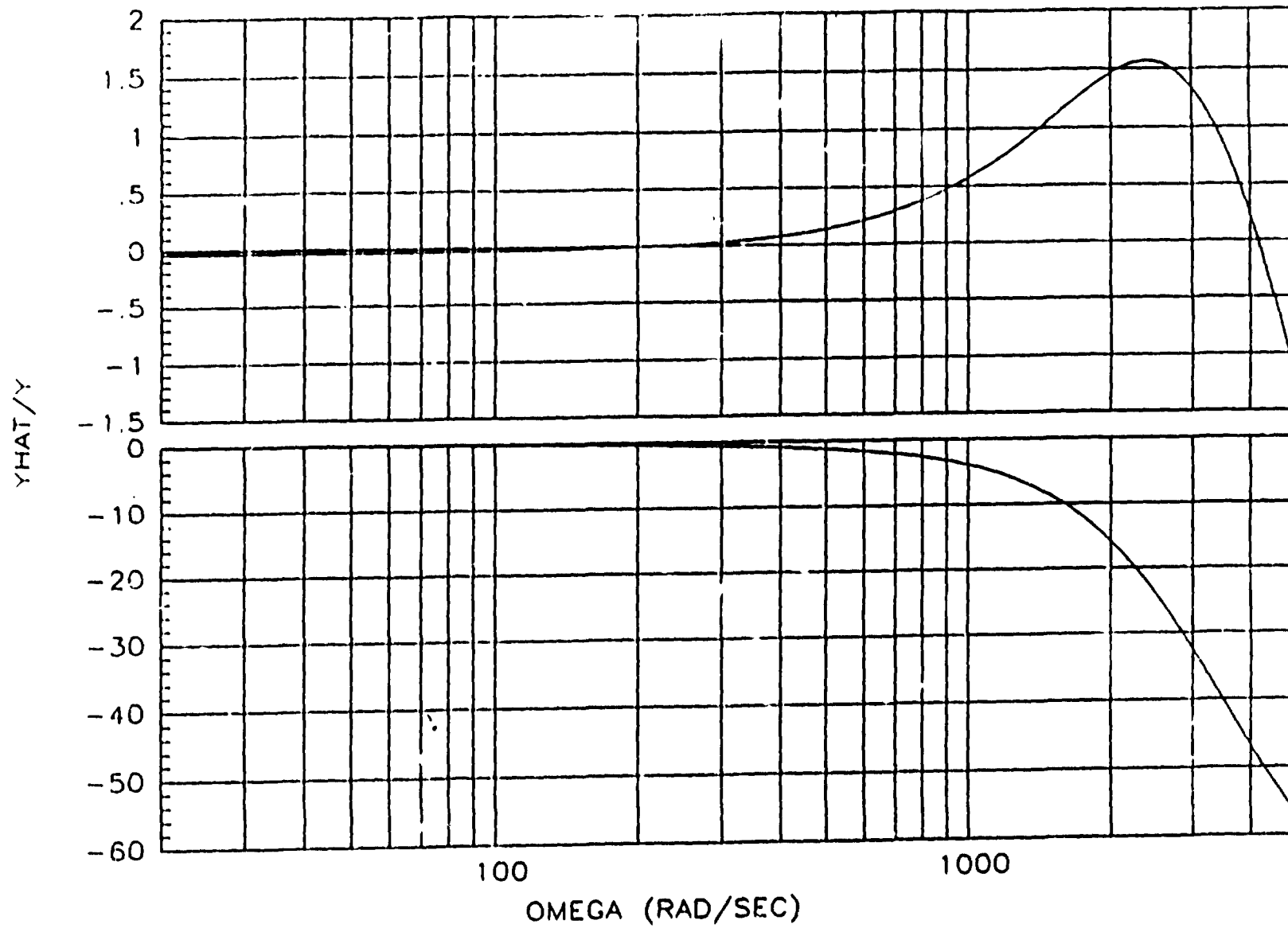


Figure B.2.3-12. Frequency Response of the Estimated Shaft Angle (with measured shaft angle as input) for Controller Designed with Modes 1,3,4

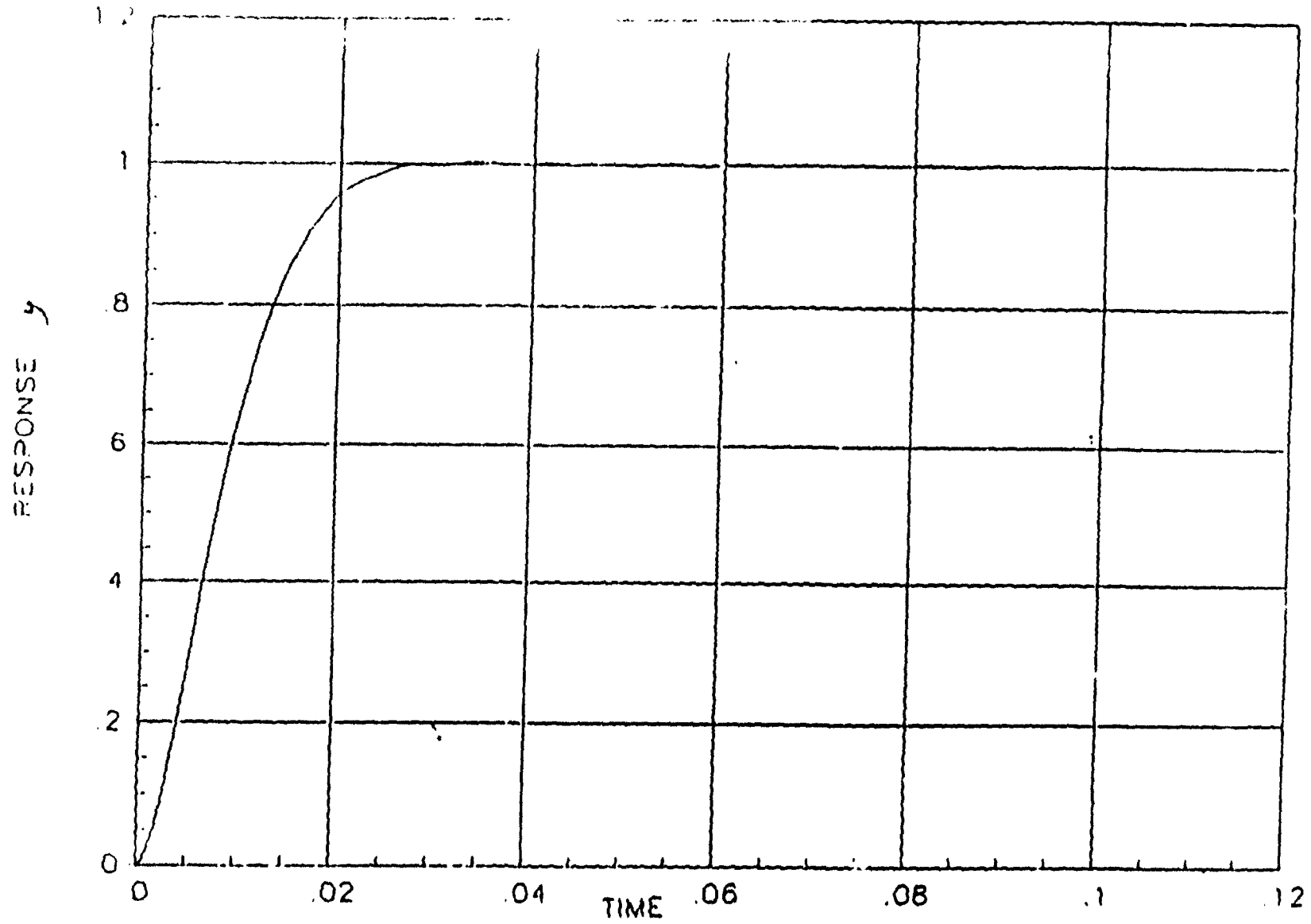


Figure B.2.3-13. Step Response for Plant with Modes 1,3,4,5,6,8,11,15 (modal frequency increased 20%, damping increased to 0.3%) and Controller Designed with Modes 1,3,4

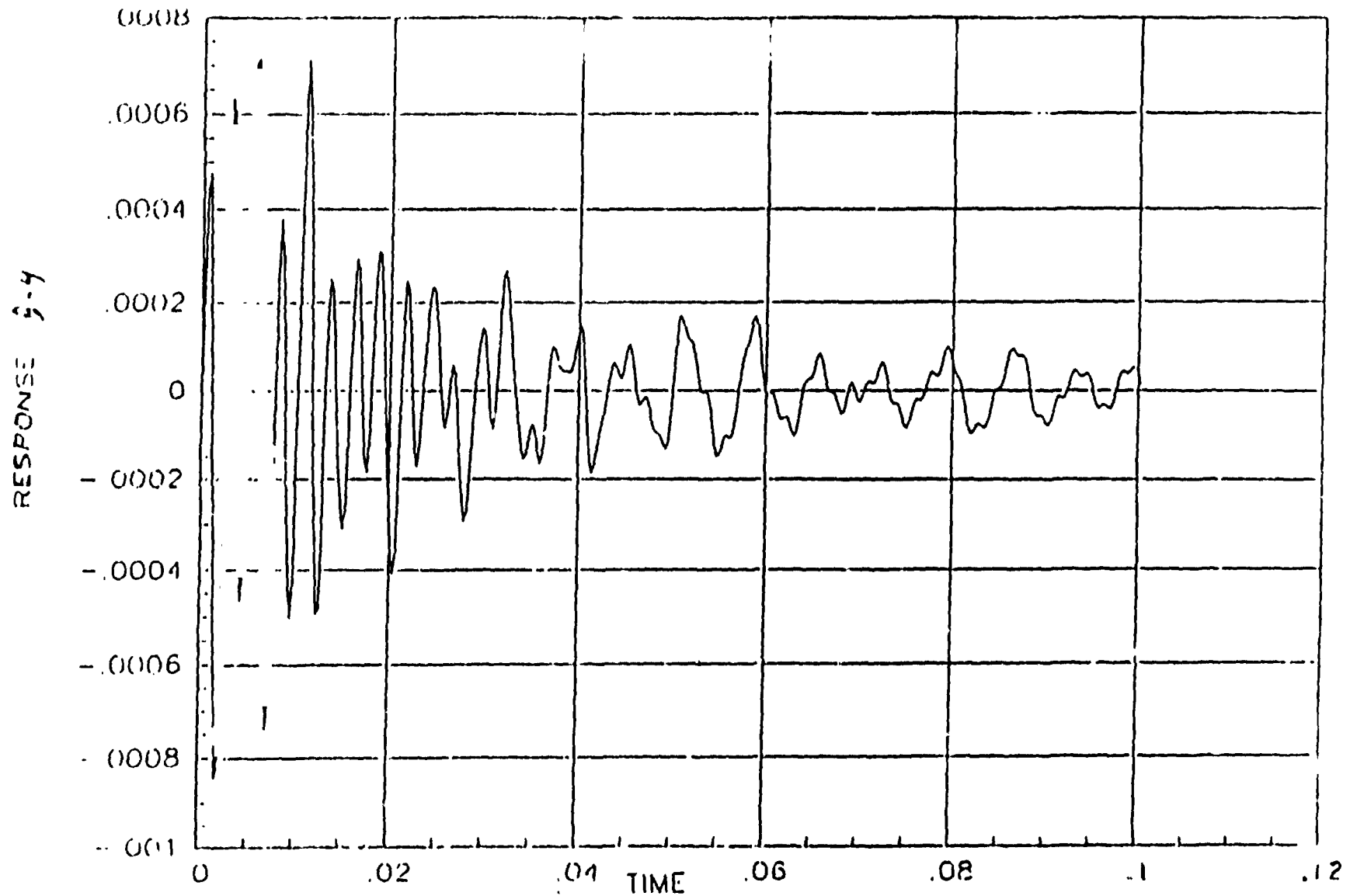


Figure B.2.3-14. Difference Between Estimated and Measured Shaft Angles for Plant with Modes 1,3,4,5,6,8,11,15 (modal frequency increased 20% and damping increased to 0.3%) and Controller Designed with Modes 1,3,4

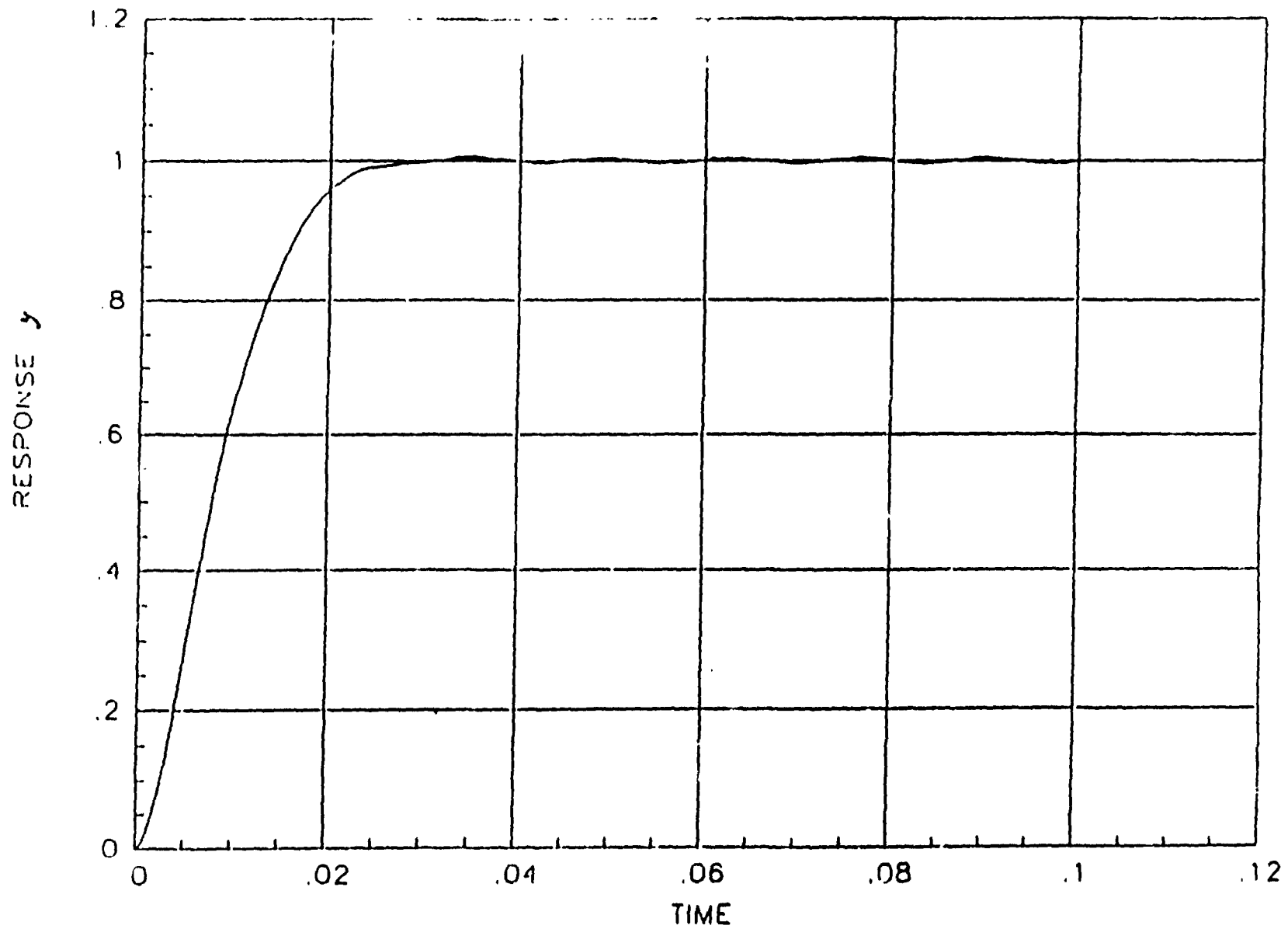


Figure B.2.3-15. Step Response for Planar Modes 1,3,4,5,6,8,11,15 (modal frequency decreased 20%, damping increased to 0.3%) and Controller Designed with Modes 1,3,4

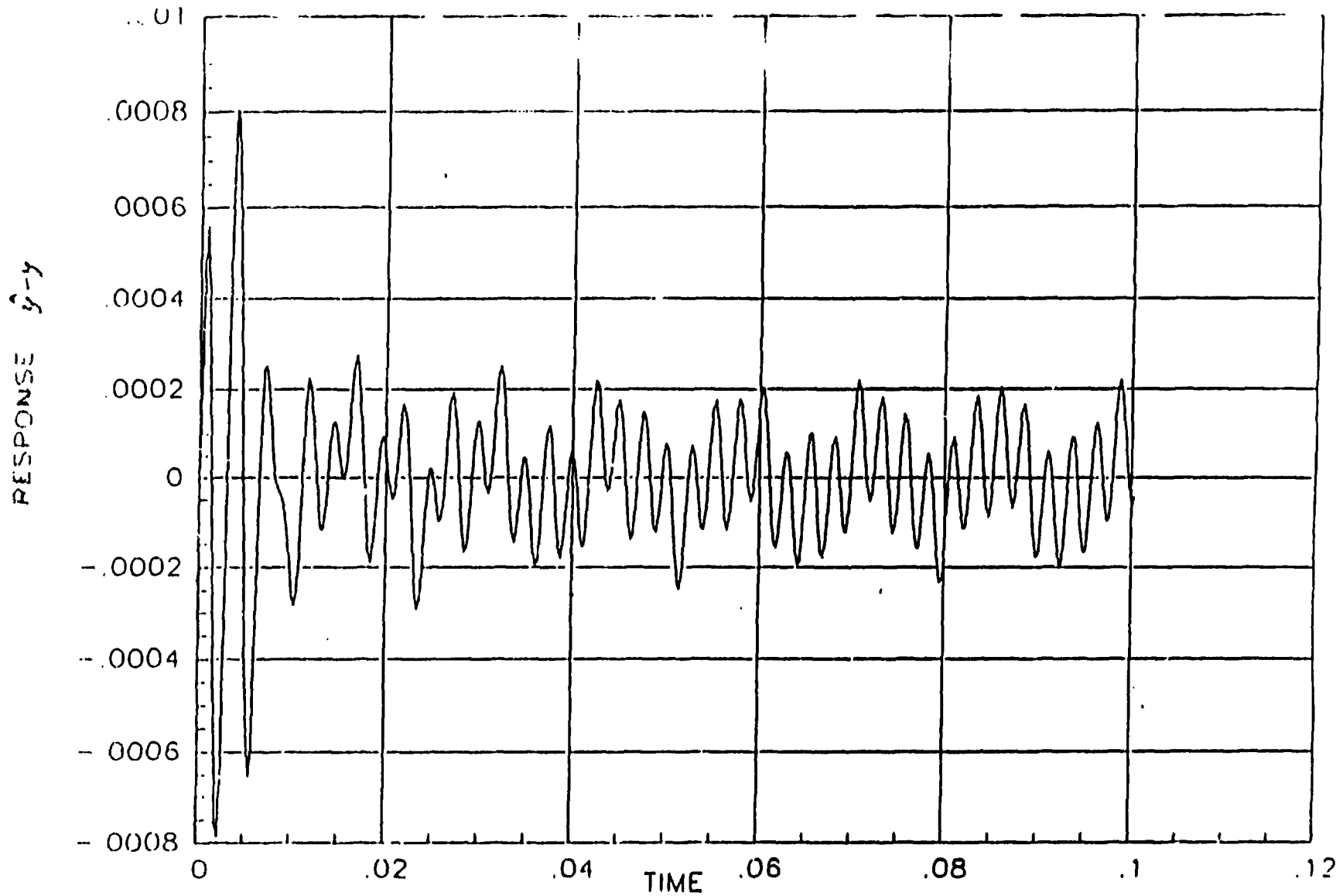


Figure B.2.3-16. Difference Between Estimated and Measured Shaft Angles for Plant with Modes 1,3,4,5,6,8,11,15 (modal frequency decreased 20% and damping increased to 0.3%) and Controller Designed with Modes 1,3,4

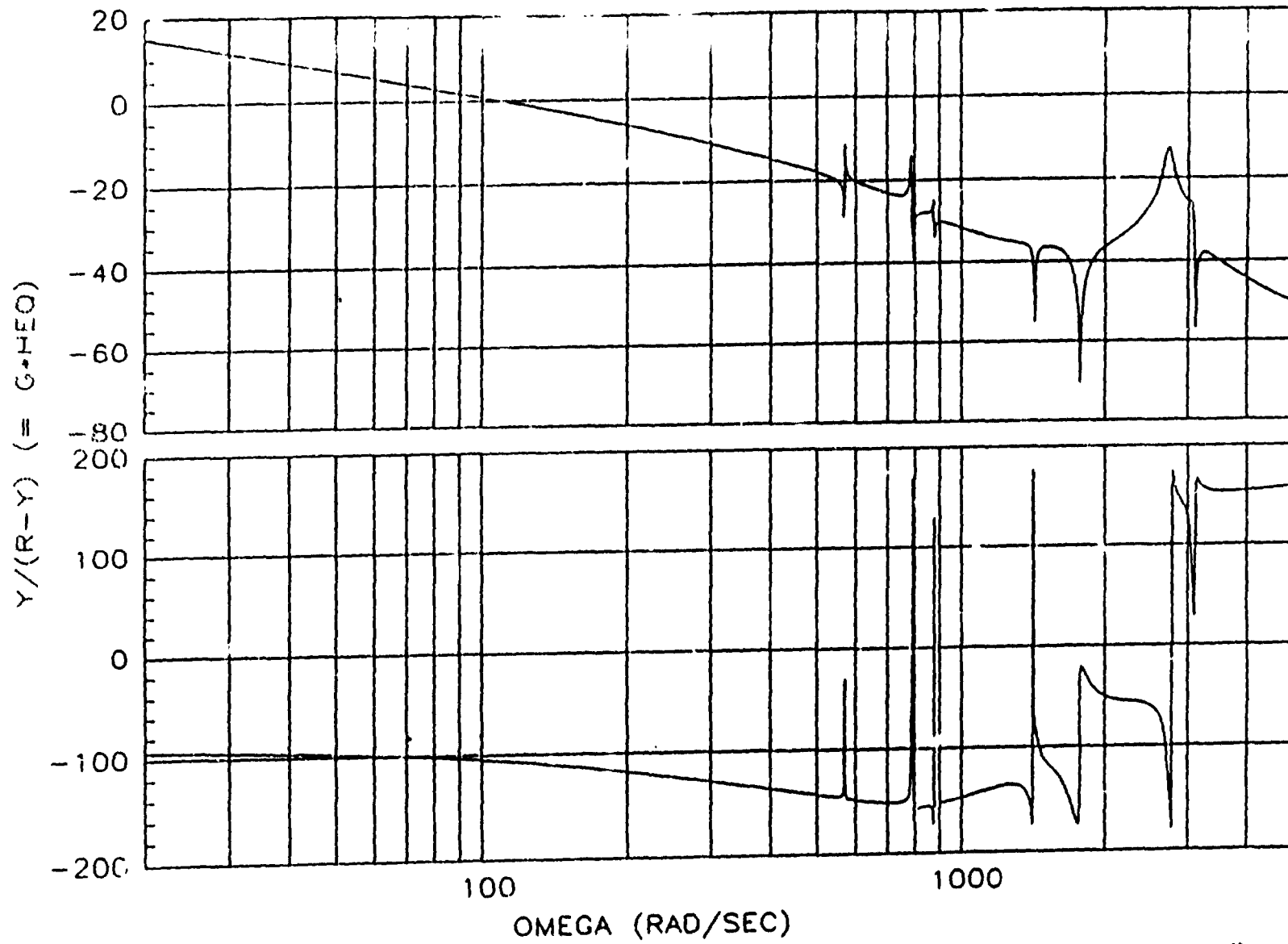


Figure B.2.3-17. D=O. Frequency for Equivalent Open-loop System for Plant with Modes 1,3,4,5,6,8,11,15 and Controller Designed with Modes 1,3,4

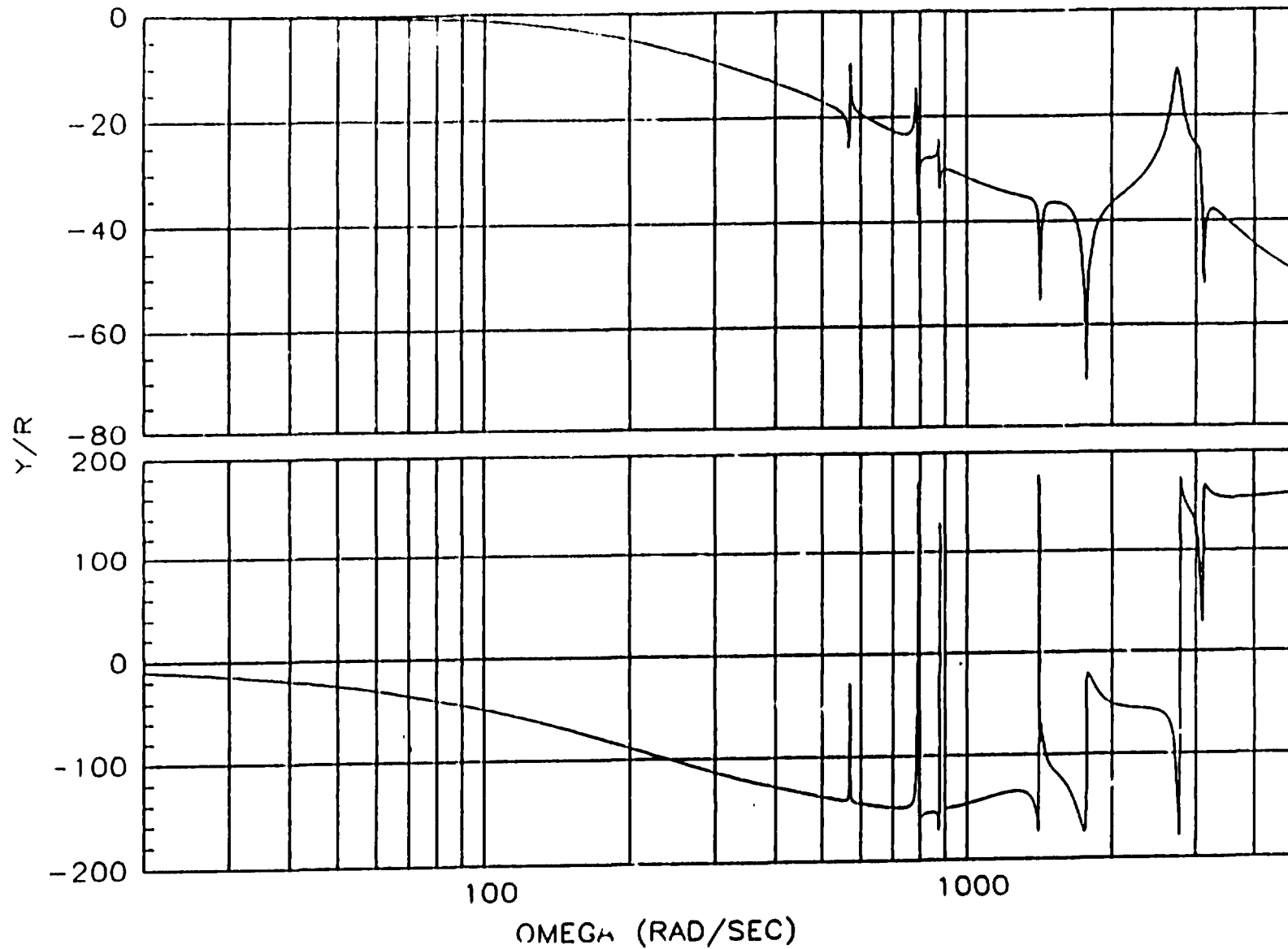


Figure B.2.3-18. D=O. Frequency Response for Closed-loop System for Plant with Modes 1,3,4,5,6,8,11,15 and Controller Designed with Modes 1,3,4

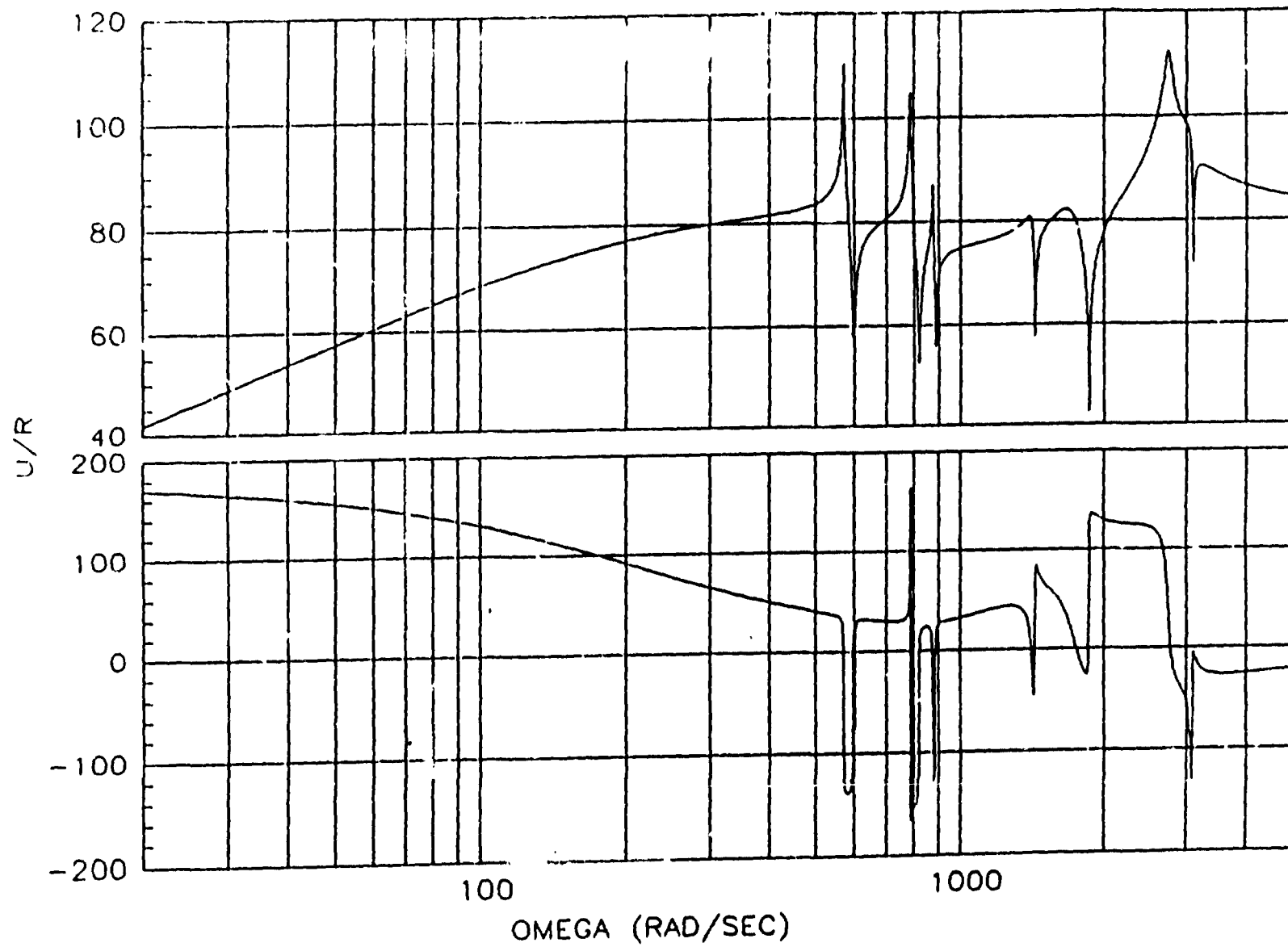


Figure B.2.3-19. D=O. Frequency Response of the Control Torque for Plant with Modes 1,3,4,5,6,8,11,15 and Controller Designed with Modes 1,3,4

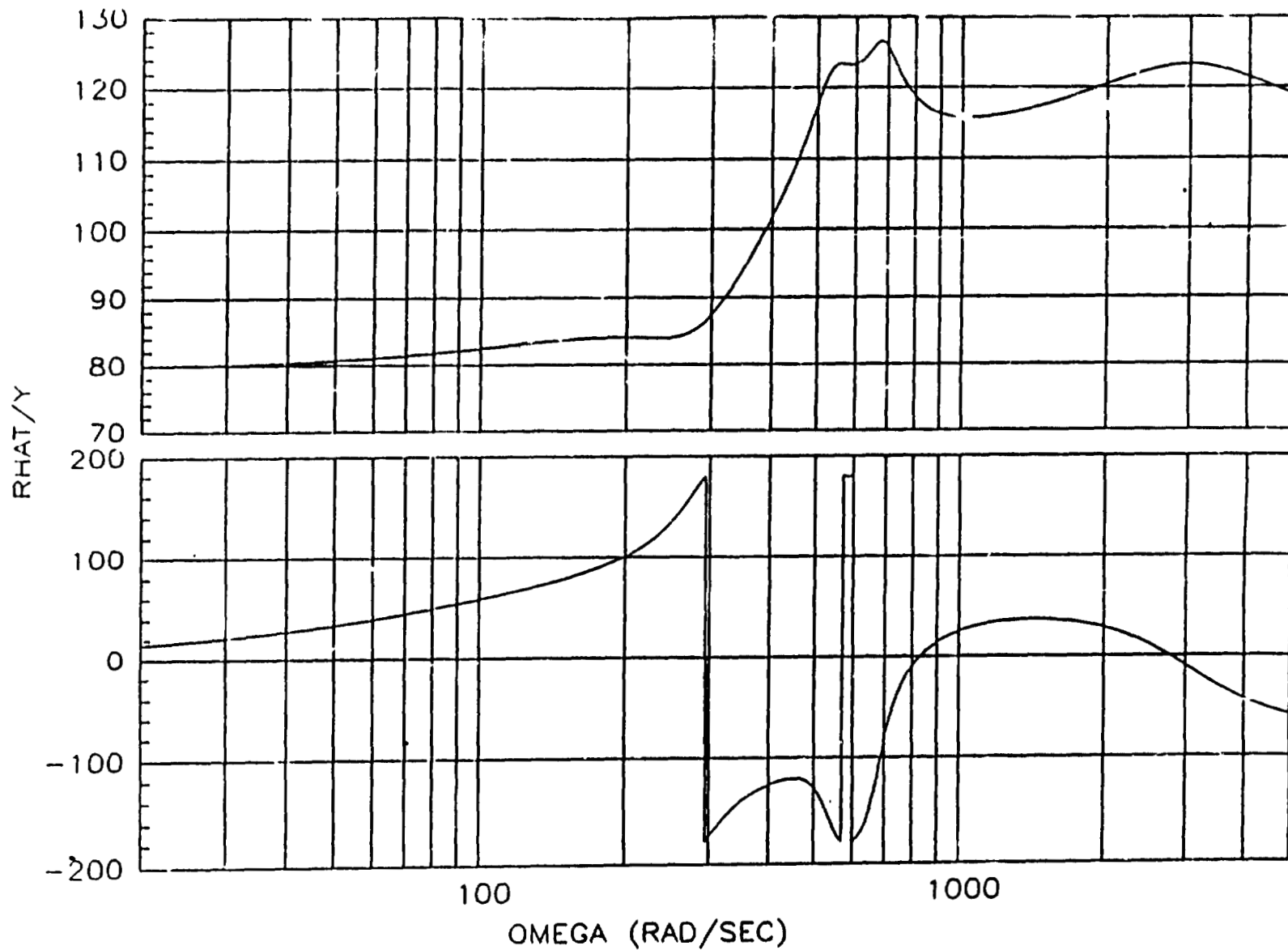


Figure B.2.3-20. D=O. Frequency Response of the Controller (with measured shaft angle as input) and Controller Designed with Modes 1,3,4

It is now shown that other modes that have large modal gain, but are insignificant by Gregory's criteria, are significant and can cause instability. Modes 1, 3, 4, 5, 20, 21, and 23 were used in the analysis shown in Figures B.2.3-22 and 23. Although instability is difficult to deduce from the Bode plot in Figure B.2.3-23 (and indeed a Nyquist plot would be better, keeping in mind that there are two non-minimum phase zeros), the step response in Figure B.2.3-22 clearly shows that the closed-loop system is unstable. This highlights the importance of presenting results using at least several carefully chosen significant modes. However, this does not detract from the advantages of an observer-based controller design, although further investigation is warranted. Eigen-analysis of the closed-loop system shows that modes 20, 21, and 23 were unstable. It was found that reducing the band-width of the observer to 600 radians/second gave a stable closed-loop system, but error due to the (rather slow) observer threw the settling error a bit out of tolerance. Decreasing the damping of the poles of the observer also improved stability.

Since modes 20, 21, and 23 were unstable in the previous case, these modes were added to the design model along with mode 22. The design model contained a complex conjugate pair of non-minimum phase zeros in this case. Although poles were placed to cancel the zeros, the non-minimum phase zeros were canceled in magnitude only. (Since the non-minimum phase zeros are well-damped, the two poles used to cancel these zeros could be placed to meet some other design or performance objective, such as ramp input following.) The step response was identical to Figure B.2.3-1. Unmodeled modes from Table B.2.1-1 were then included in the plant model, and the resulting system was unstable. This is not surprising since many of these modes were within the bandwidth of the observer. Provided that unmodeled modes can be stabilized, this controller is a candidate for a two-time scale implementation since modes 4 and 20 are more than one decade apart. Modes 1, 3, and 4 can be included in a slow-state controller and modes 20, 21, 22, and 23 can be included in a fast-state controller. These can be implemented as eighth and sixth order analog or digital filters, respectively, which are simpler and easier to implement than a single fourteenth order filter that incorporates all seven modes.

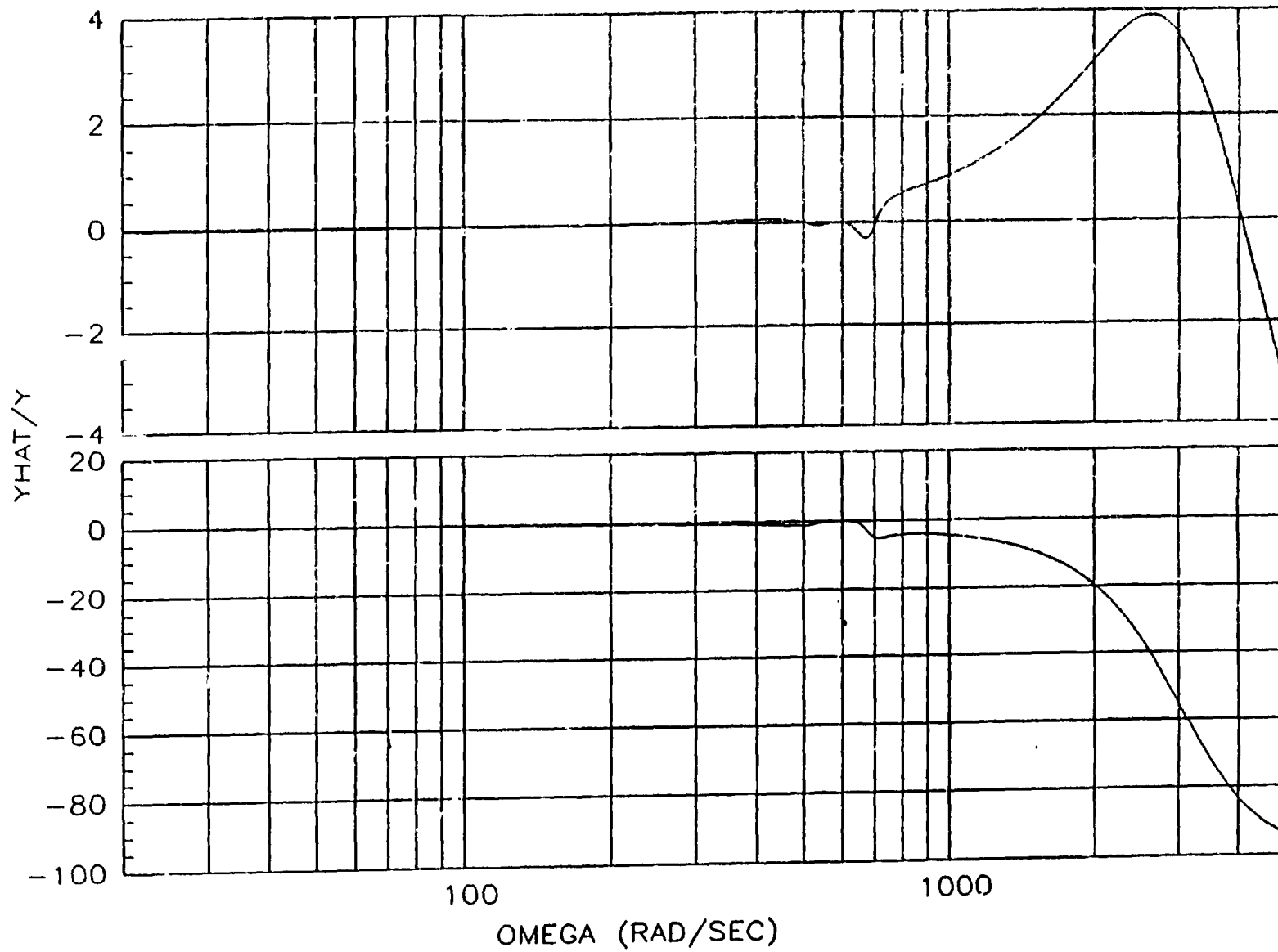


Figure B.2.3-21. D_πO. Frequency Response of the Estimated Shaft Angle (with measured shaft angle as input) for Controller Designed with Modes 1,3,4

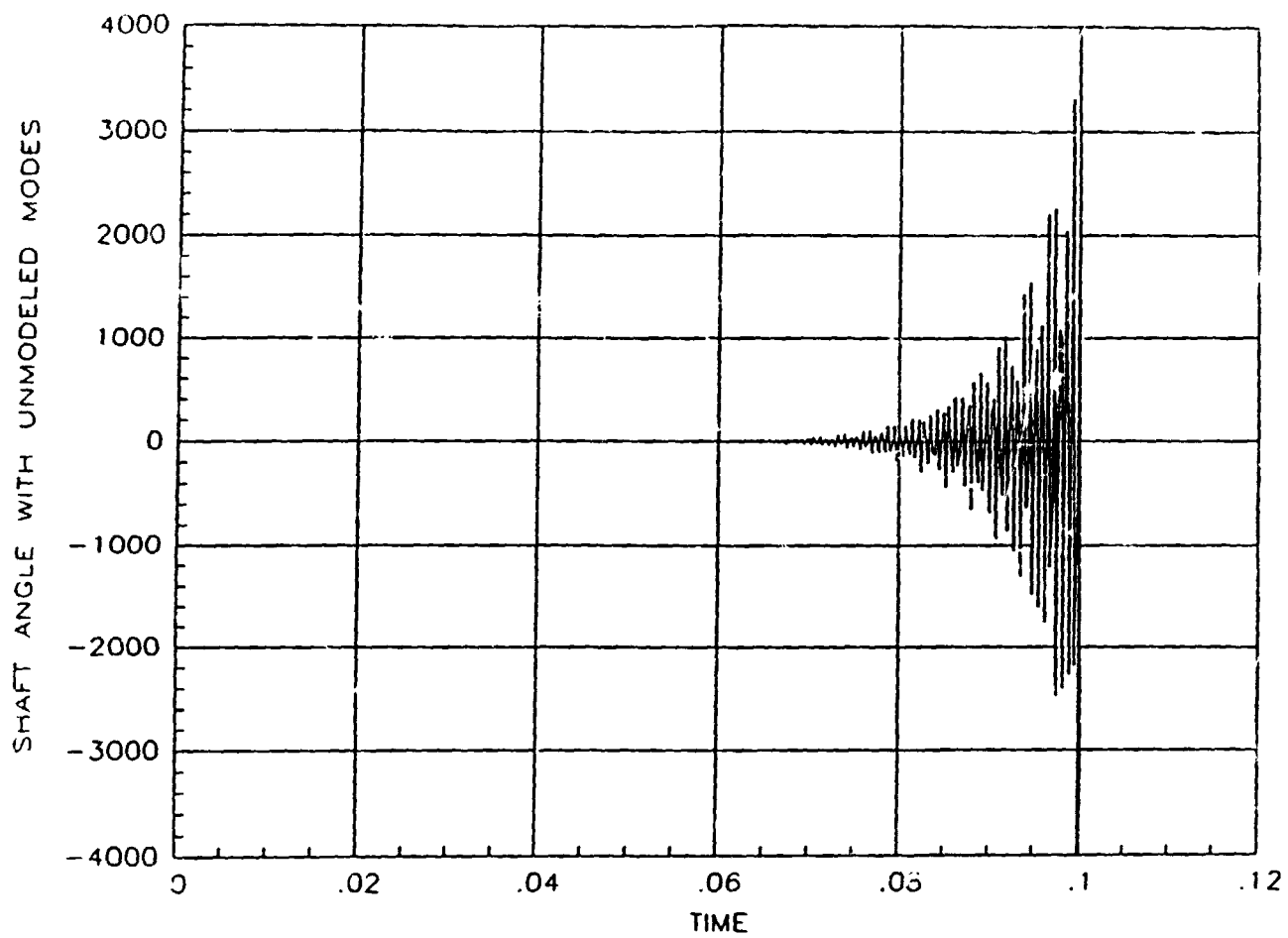


Figure B.2.3-22. Step Response for Plant with Modes 1,3,4,5,20,21,23 and Controller Designed with Modes 1,3,4. Modes 20,21, and 23 are Destabilized.

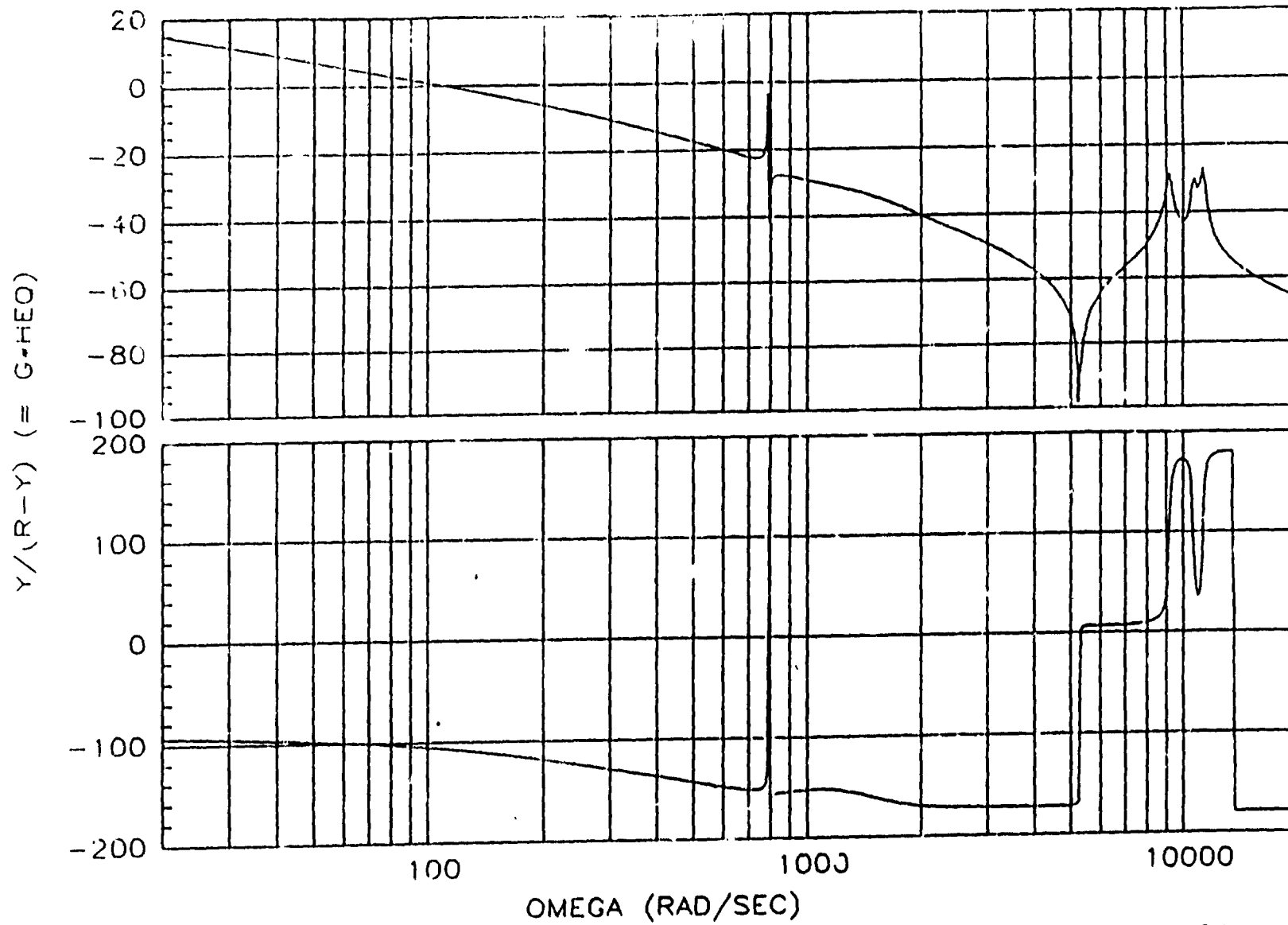


Figure B.2.3-23. Frequency Response for Plant with Modes 1,3,4,5,20,21,23 and Controller Designed with Modes 1,3,4. Modes 20,21,and 23 are Destabilized.

B.2.4 Conclusion

Although performance was excellent in the case of matched plant model and design model, where two significant flexible-body modes were modeled in one case and six in another case, instability resulted when unmodeled modes were included in the plant model. This indicates that any design presented as a candidate for GOES must be analyzed with at least some significant low-frequency modes and some significant high-frequency modes, otherwise the results may be meaningless.

Observer-based control provides a systematic way to design a dynamic compensator. Results show that overall performance requirements (time response, accuracy, and robustness) can be met with this approach, provided that modes for the design model are properly selected and that unmodeled modes are not de-stabilized by feedback. Contrary to what textbooks preach, the observer should be made as slow as possible and it should be underdamped so that the cutoff rate is as fast as possible. Techniques to avoid de-stabilization of the unmodeled high-frequency modes need to be investigated. One such technique is low-authority feedback discussed in [10].

B.2.4.1 Further study

This work has brought several considerations to attention: mode selection and reduced-order modeling, feedback (or parallel) versus cascade compensation, and robustness to unmodeled and uncertain dynamics. Further investigation into mode selection is warranted, and the reduced GFRP mode set that is in use should be reviewed to be sure that all important modes are included. Subsequent investigation will take into account the perturbation of the zeros due to the feedthrough term in the reduced order model.

The procedure outlined in this report enables one to place poles anywhere in the complex plane. However, this placement is governed by experience and judgement. Pole placement can also be achieved by model following, in which the feedback gain is determined by minimizing the quadratic performance index

$$T = \int_0^{\infty} \{ [y(t) - y_m(t)]^T Q(t) [y(t) - y_m(t)] + U^T(t) R(t) u(t) \} dt$$

where $Q(t)$ and $R(t)$ are weighting matrices, $y(t)$ is the plant output, and $y_m(t)$ is the output of an ideal plant model that has the same input $u(t)$ as the plant being controlled. The weighting matrices can be chosen to reduce or eliminate oscillatory control torques or to meet some other control objective. Model following may be useful in future developments, particularly with multi-input or multi-output systems.

The quadratic performance index can be transformed into a function of frequency using Parseval's theorem. Then Q can be made large at frequencies where minimal output disturbance is wanted and R can be made large at frequencies where minimal control effort is wanted. This is discussed in [10] and [11] and has application in the GOES control problem.

Placement of the shaft position sensor at the motor side of the shaft was considered in earlier GOES-N studies. It was found that the accuracy of the system was degraded severely by this placement because of the large shaft mode between the motor and the mirror. Position measurements at both ends of the shaft could be most useful in the observer-based controller design, since this would isolate the controlled object (the mirror) and result in improved state estimates and increased robustness. Although the mirror position is not measured directly (since there are shaft dynamics between the mirror and the position sensors), an auxiliary output equation giving the mirror position could prove useful in controller design and analysis.

Singular perturbation analysis is useful in obtaining a reduced-order model, determining regions of stability with regard to unmodeled high-frequency dynamics, and in the development of a two-time scale observer. This technique was applied in this study to obtain a reduced-order model, and its application to stability analysis was mentioned. For further investigation, singular perturbation analysis may be used to determine regions of stability with respect to unmodeled high-frequency dynamics and a two-time scale observer may be derived and tested.

The application of observer-based control can be applied to the imager control system, where a ramp input, turnaround command, and Image Motion Compensation (IMC) signal have to be taken into account. Pre-compensation of the plant with proportional-integral compensators can be used to increase the system type and can enhance the benefits of observer-based control.

3.2.5 References

1. Leavy, D., GOES-N Phase-A Study final Report on Passive Filtering, Sept. 1990.
2. D'Azzo, J. J. and C. H. Houpis, *Linear Control System Analysis and Design - conventional and Modern*, McGraw-Hill, 1975.
3. Moore, B. C., "Principal Component Analysis in Linear Systems: Controllability, Observability, and Model Reduction," *IEEE Trans. Auto. Control*, Vol. AC-26, pp. 17-32, Feb. 1981.
4. Pernico, L. and L. M. Silverman, "Model Reduction via Balanced State Space Realizations," *IEEE Trans. Auto. Control*, Vol. AC-27, p. 382-387, April 1987.
5. Brogan, W. L., *Modern Control Theory*, Quantum Publishers, Inc., 1974.
6. Porter, B., "Singular Perturbation Methods in the Design of Observers and Stabilizing Feedback Controllers for Multivariable Linear Systems," *Electron. Lett.*, vol. 10, pp. 494-495, Nov. 1974.
7. Sakseno, V. R., J. O'Reilly, P. V. Kokotovic, "Singular perturbation: and Time-Scale Methods in Control Theory: Survey 1976-1983," IEEE Press.

8. O'Reilly, J., "Dynamical Feedback Control for a Class of Singularly Perturbed Linear Dynamical Systems Using a Full-Order Observer," *Int. J. Control*, vol. 31, pp. 1-10, Jan 1980.
9. Javid, S. H., "Stabilization of Time-Varying Singularly Perturbed Systems by Observer-Based Slow-State Feedback," *IEEE Trans. Auto. Control*, vol. AC-27, pp. 702-704, June 1982.
10. Gupta, N. K., M. G. Lyons, J. N. Aubran, G. Marguiles, "Modeling, Control, and System Identification Methods for Flexible Structures," Paper No. 12, AGARD-AG-260: *Spacecraft Pointing and Position Control*, Nov. 1981.
11. Stein, G. and M. Athans, "The LQG/LTR Procedure for Multivariable Feedback Synthesis," *IEEE Trans. Auto. Control*, vol. AC-32, pp. 105-114, Feb. 1987.

B.3 TIME DOMAIN TWO AXIS SIMULATION OF IMAGER EAST/WEST AND NORTH/SOUTH SERVO "BASELINE" DESIGN

B.3.1 Introduction

B.3.1.1 Purpose

A two axis simulation of the GOES-N Imager East/West and North/South Servo design was created to investigate whether the structural coupling between the East/West and North/South axes is significant to the GOES-N+ budget specification.

B.3.1.2 Background

The ITT imager East/West and the North/South servos are both single input, single output controllers. (The shaft angle in East/West is measured by an inductosyn and is subtracted from the commanded signal to generate the error signal to the East/West controller; the same type of scheme is employed for the North/South axis.) However, the generated torque inputs to the East/West axis cause structural excitation of the North/South axis, and torque inputs to the North/South axis cause structural excitation of the East/West axis, i.e., the two axes are coupled through the structural modes.

B.3.2 Approach

B.3.2.1 ITT Imager East/West and North/South servo block diagrams

Shown in Figures B.3.2-1 and B.3.2-2 are the ITT East/West and North/South servo block diagrams. All of the transfer functions shown in the block diagrams (except for modifications to the plant model and to the friction model — more to be said about this later) were incorporated in the simulation model including non-linearities, such as limiters and sin functions, which can significantly affect performance. The DADS (Dynamic Analysis and Design System) computer software, which was used to generate the time domain simulations, contains a library of all the necessary linear and non-linear control elements. To better model the plant dynamics, the DADS general element was used containing two rigid body and 17 structural modal equations (more will be said about this later). Also, a Dahl friction model was included to model the friction on each of the shafts instead of the viscous friction used in the ITT design. A block diagram of the DADS simulation of the GOES Imager East/West and North/South servos is shown in Figures B.3.2-3 through B.3.2-8. Also, the commands for the East/West scan and turn around, the AEI on/off times, and the North/South stepping command is listed in Figure B.3.2-9.

B.3.2.2 Modal selection

A modal sorting procedure was used to select the significant modes (from the "correlated" baseline design) needed to model the dynamics of the GOES-N mirror in the simulation.

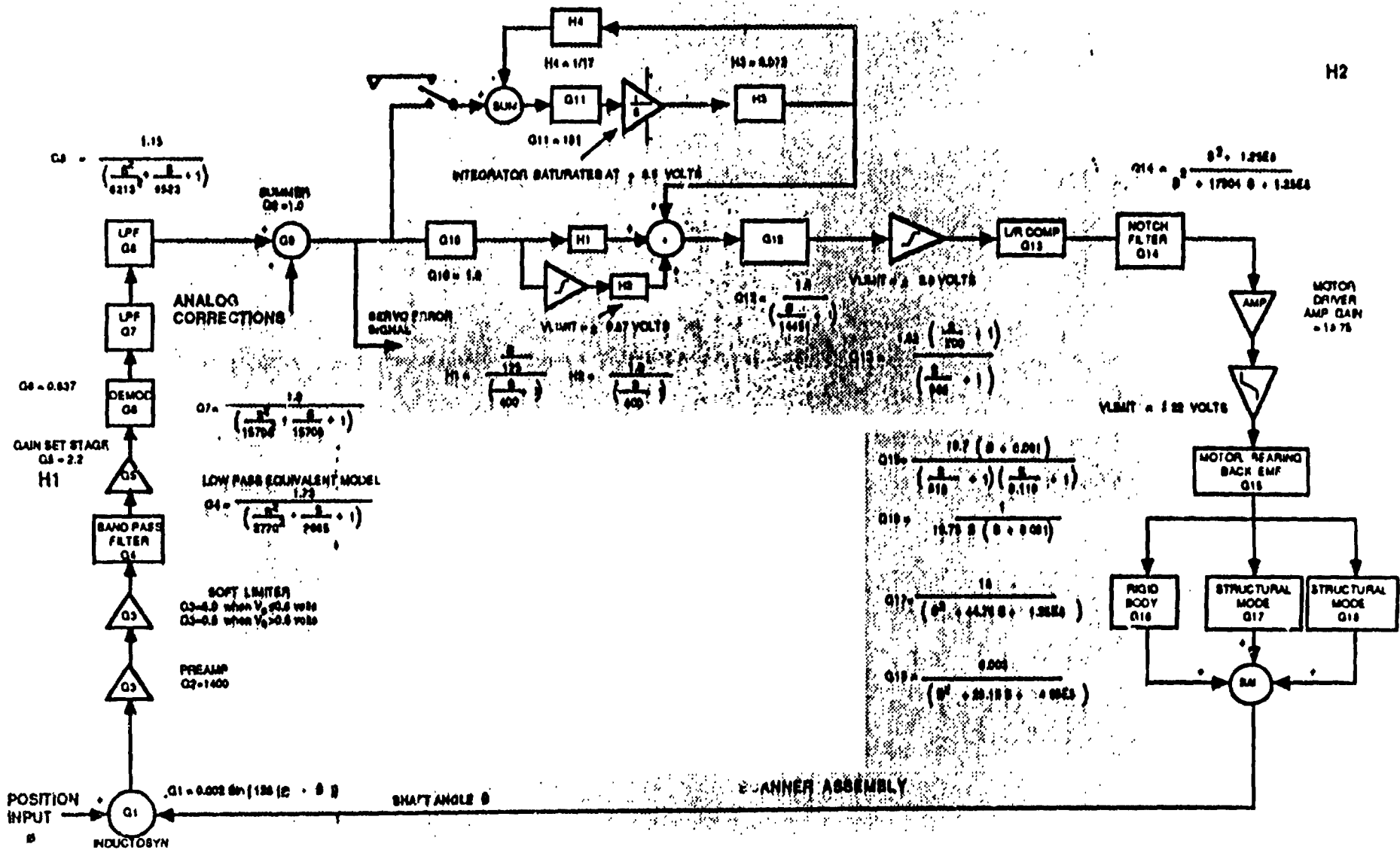


Figure B.3.2-2. Imager/Sounder North/South Servo Block Diagram

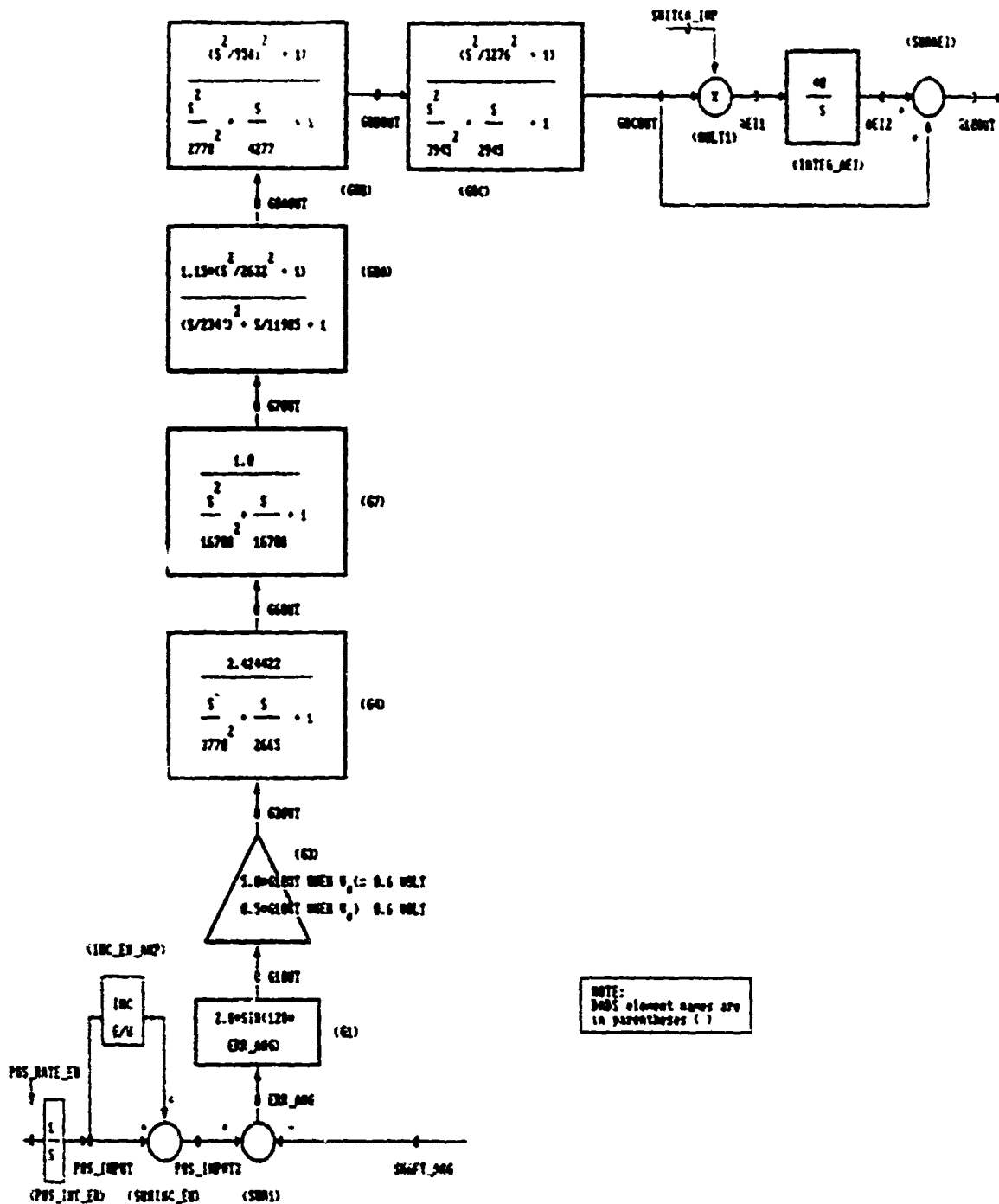


Figure B.3.2-3. GOES-N Imager East/West Servo

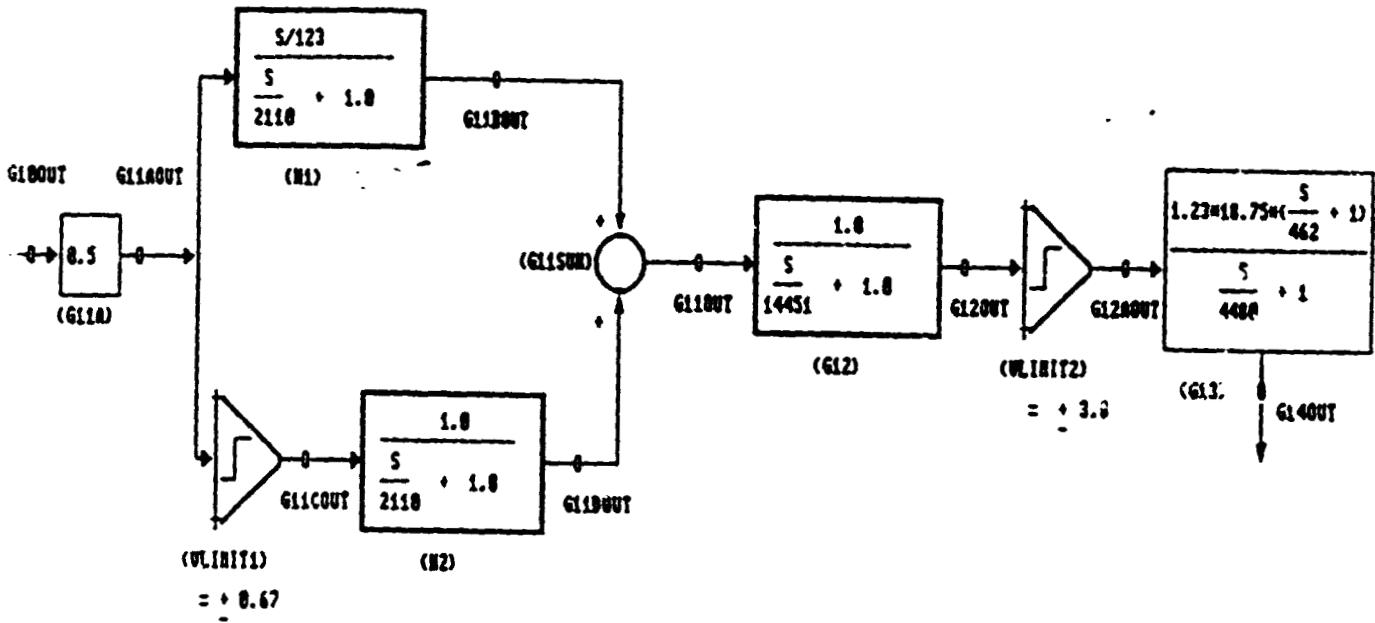


Figure B.3.2-4. GOES-N Imager East/West Servo

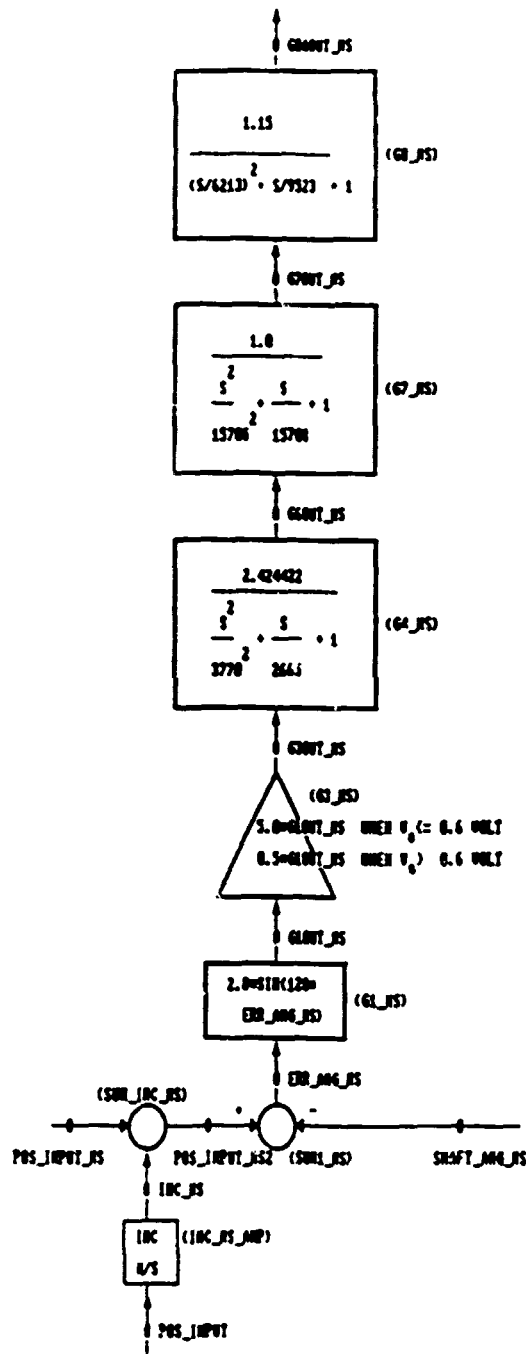


Figure B.3.2-6. GOES-N Imager North/South Servo

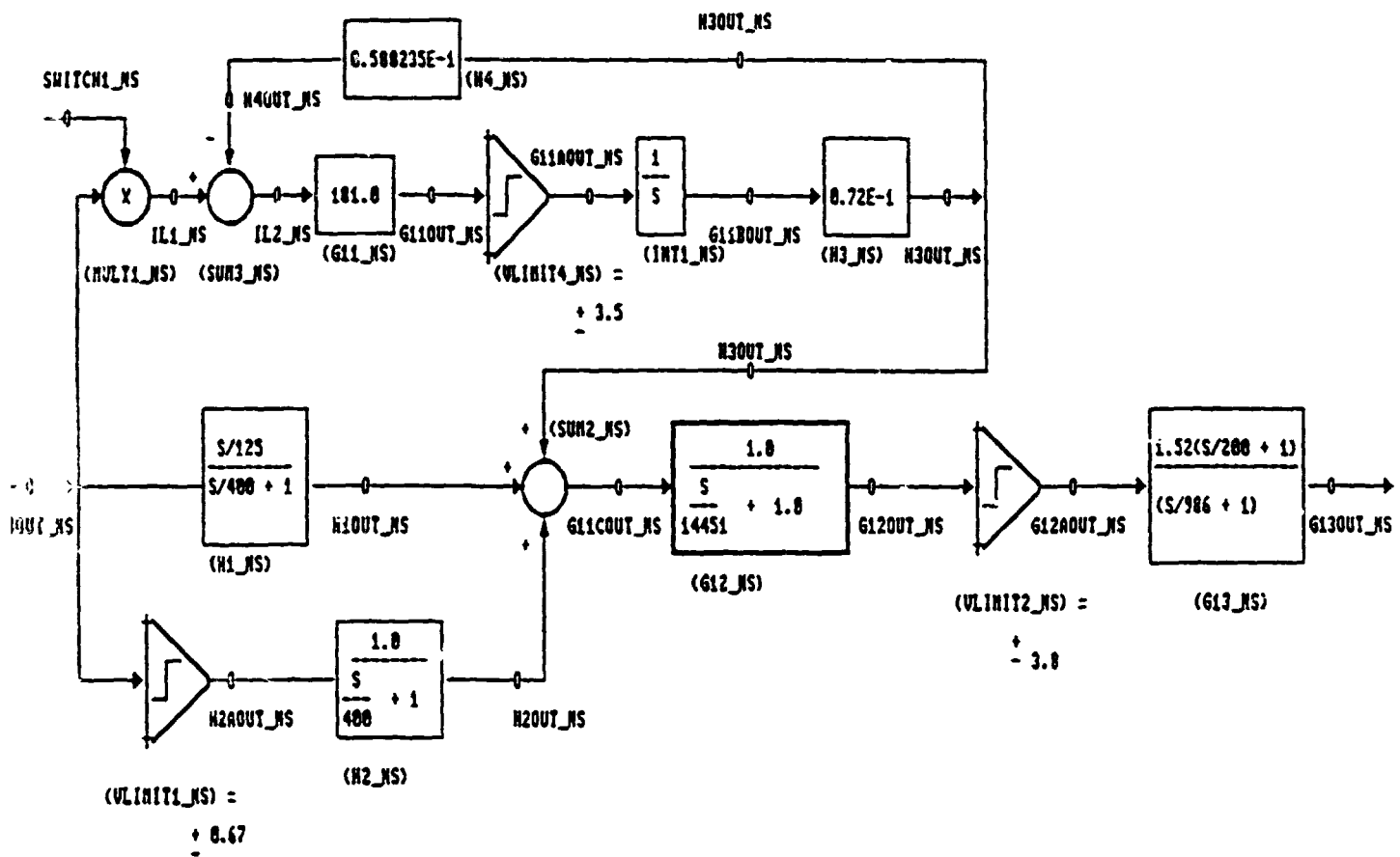


Figure B.3.2-7. GOES-N Imager North/South Servo

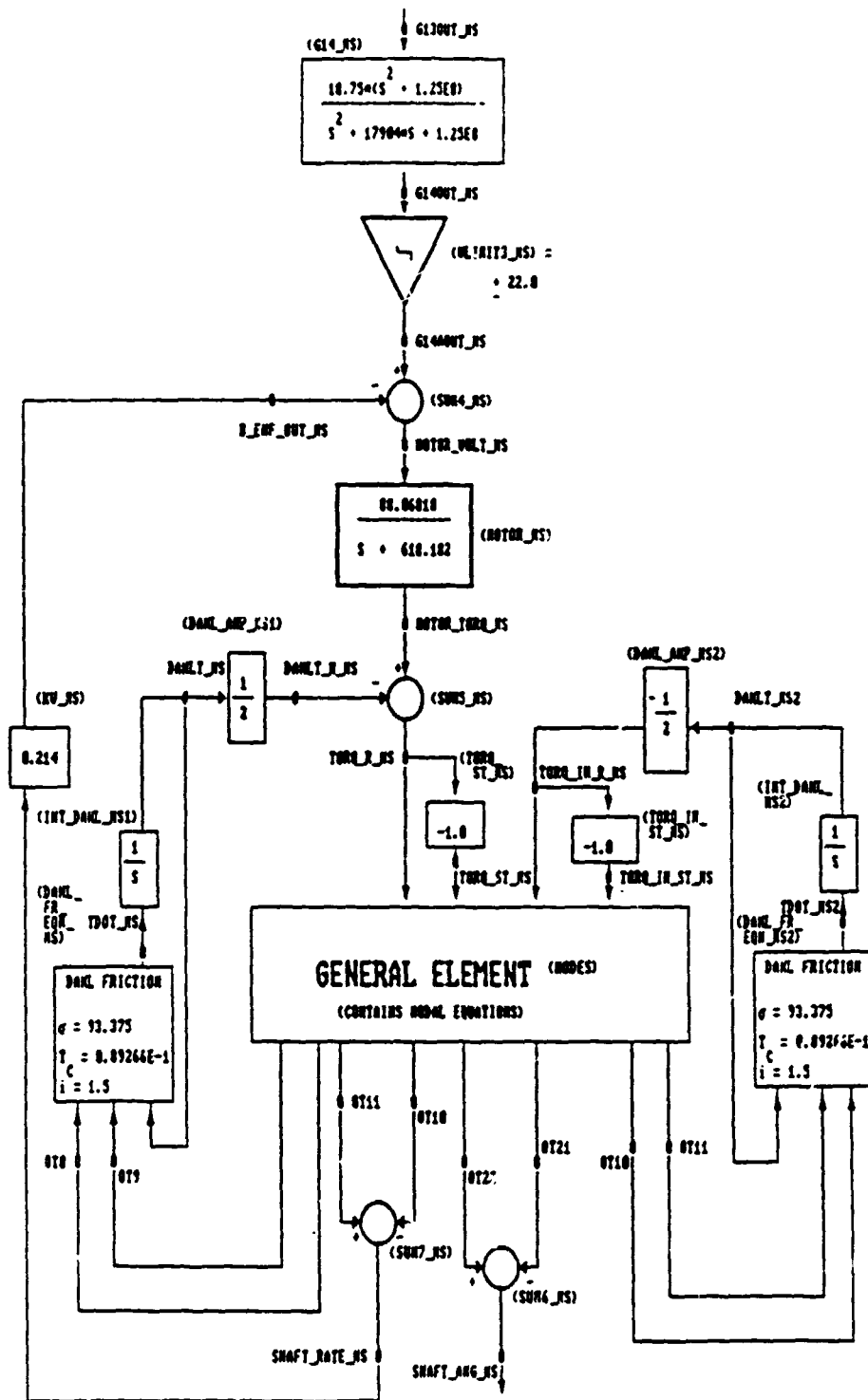
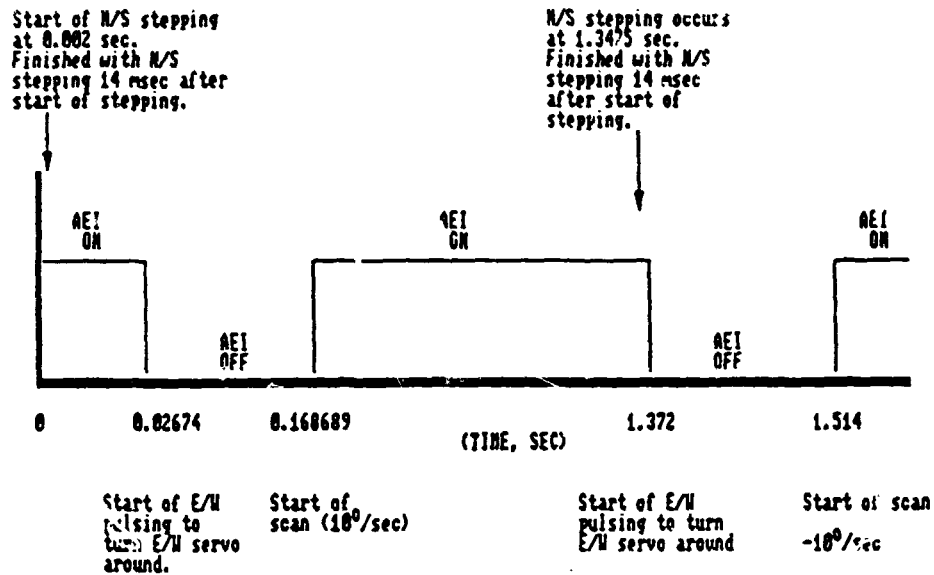


Figure B.3.2-8. GOES-N Imager North/South Servo

- a) E/W scan and turn around
- b) AEI on/off times
- c) N/S stepping command



NOTE:

N/S stepping command consists of
28 steps of 8 μrad each; 0.5 msec between each step

E/W turn around is a series of pulses that changes the
velocity of the mirror in E/W.

Both N/S and E/W commands are programmed into a FORTRAN
subroutine called USRING3B.FOR which is linked to the DADS code.

Figure B.3.2-9. Sequence of Events

1. The NASTRAN output 4 file containing the eigenvalues and eigenvectors for the "correlated" baseline case with the East/West and North/South axes unconstrained is located on the S&AI microvax at SAI08:[NICK.GOES.TWOAXIS]BL3B_FIXED.PHG. More specifically, this file contains eigenvalues up to 3000 Hz and the eigenvector matrix — 11 rows (dof's) x 226 columns (modes shapes). The 11 degrees of freedom included in the mode shapes are listed below.

- 1) Motor stator (East/West)
- 2) Motor rotor (East/West)
- 3) Inductosyn stator (East/West)
- 4) Inductosyn rotor (East/West)
- 5) Mirror Rx (East/West)
- 6) Mirror Ry
- 7) Mirror Rz
- 8) Motor stator (North/South)
- 9) Motor rotor (North/South)
- 10) Inductosyn stator (North/South)
- 11) Inductosyn rotor (North/South)

2. A FLAME (Flight Loads and Matrix Executive) input file (BL3B_FIXED.INP) was used to obtain an eigenvalue and an eigenvector file (OMEGSQ.DAT and PHISTM.DAT).

3. Three SISO methods (Modal Gain, Peak Amplitude, and a SISO version of Gregory's method) and MIMO version of Gregory's method were used to find the significant modes. The inputs needed for the significance methods were as follows:

- a) number of rigid body modes and their location in the $[\phi]$ matrix
- b) the damping used for the modes (0.001 in this case)
- c) the two input dof's which are differences to provide the relative input coordinates (for example dof's 2 - 1 represent the motor rotor - motor stator) (for Gregory's MIMO, the dof's for all inputs would be entered)
- d) the two output dof's which are differences to provide the relative output coordinates (for example dof's 4 - 3 represent the inductosyn rotor - inductosyn stator) (for Gregory's MIMO, the dof's for all outputs would be entered)
- e) maximum frequency cutoff (3000 Hz in this case)
- f) minimum normalized gain in % (0.1% - used for peak amplitude and gregarious; 1% - used for Modal Gain;)

Based on the locations of the controller's inputs and outputs in the structure, the methods calculate a significance factor for each mode in a set. The results are normalized so that the mode with the highest significance is assigned a value of 100%, and all of the others are expressed as a percentage of the highest value.

After applying each of the sorting methods, the modes to be used in the analysis were selected by examining the level of agreement between the various methods. Modes showing a normalized significance of at least one percent in more than one method were selected first. Next, the remaining modes were examined on a case by case basis to decide if they should be selected, keeping in mind the controller design bandwidth. As a last check of the sorting process, frequency response plots of the structure were made by first using the reduced mode set and then using the entire mode set. The plots were compared to ensure that the reduced mode set captured all of the important frequency domain characteristics of the full mode set.

B.3.2.3 Modeling the modal equations

The "correlated" baseline design included two rigid body and 17 significant structural modes. The frequencies of these modes are listed below.

MODE #	FREQUENCY (Hz)	MODE #	FREQUENCY (Hz)
1	0.0	11	7.691647E+02
2	0.0	12	1.007499E+03
3	4.954955E+01	13	1.696981E+03
4	9.228214E+01	14	1.765170E+03
5	9.446323E+01	15	1.779975E+03
6	3.341265E+02	16	1.786606E+03
7	3.591047E+02	17	1.811134E+03
8	4.944610E+02	18	2.476821E+03
9	7.273182E+02	19	2.476821E+03
10	7.553759E+02		

The "175 Hz mode" occurring in the modal survey test was not included. This mode did not occur in the frequency response test, and therefore its existence was suspect. The structural damping used for each mode was 0.3%.

The DADS general control element can be used to model the modal equations which can be formed into a state space representation, e.g.,

$$\dot{X}(t) = [A] \cdot X(t) + [B] \cdot U(t)$$

$$Y(t) = [C] \cdot X(t)$$

The contents of the [A], [B], and [C] matrices are shown in Figure B.3.2-10. The x 's in Figure B.3.2-10 (the X 's above) represent the modal displacements; the u 's are the torque inputs; and the y 's are the output displacements. A FLAME (software created at Swares and Associates) was

used to create the [A], [B], and [C] matrices from a NASTRAN output4 file and is included as Figure B.3.2-11a-c. The torque inputs (the u vector in the state space equations) are listed below.

- | | | |
|-----|---------------|---|
| 1) | TORQ_ST | - torque on stator side of motor (East/West) |
| 2) | TORQ_R | - torque on rotor side of motor (East/West) |
| 3) | TORQ_IN_ST | - torque on stator side of inductosyn (East/West) |
| 4) | TORQ_IN_R | - torque on rotor side of inductosyn (East/West) |
| 5) | 0 | - no applied torques directly to mirror dofs |
| 6) | 0 | |
| 7) | 0 | |
| 8) | TORQ_ST_NS | - torque on stator side of motor (North/South) |
| 9) | TORQ_R_NS | - torque on rotor side of motor (North/South) |
| 10) | TORQ_IN_ST_NS | - torque on stator side of inductosyn (North/South) |
| 11) | TORQ_IN_R_NS | - torque on rotor side of inductosyn (North/South) |

The output of the DADS general element was the shaft angle and rate measured by the inductosyn. This value is the feedback to the control system which is subtracted from the commanded input to generate the error signal. The other DADS control elements (amplifiers, summers, integrators, limiters, etc.) were used to model the GOES-N control system and produce the motor and friction torques. The motor and friction torques are the torque inputs listed above. Figures B.3.2-12 and B.3.2-13 show geometry.

B.3.2.4 Dahl friction

The ITT Goes Scanner Performance Review, November 15-17 1989, includes block diagrams of the motor/load rigid body model for the scanner assuming viscous friction and spring stiction bearing models (Figures B.3.2-14 through B.3.2-16). Figure B.3.2-17 shows IMC program parameters. Also included in the report was experimental data for the spring stiction model which, for this analysis, was used to obtain the parameters for the Dahl friction model to be used in the DADS simulation. Below are shown the curves for the Typical Solid Friction Force Function, the Friction Slope Functions, and the Solid (Dahl) Friction Simulator.

F_c = coulomb friction force (torque in this case) which can also be thought of as a "yield force" or as "running friction force," for example as found in bearing friction
 = 0.0892662 in*lbs (for this case)

θ_c critical angle ($F_c/\sigma = 956 \times 10^{-6}$ radians for this case)

σ "rest slope" 1494 in*oz/radian (for this case)

i exponent, ($i = 1, 2$ ductile type of friction, $i = 0, 1/4, 1/2$ brittle type of friction)
 = 1.5 (for this case)

```

* NUMBER OF NODES
PARM, PARNID=19
PARM, PARDNID=PARNID*2
PARM, PARNPID=PARNID-1
...

* LOAD DESIRED MODE NUMBERS
* THE MODE NUMBERS CORRESPOND TO COLUMNS IN EIGENVEC
ILOAD, DMOD, PARNID, 1
1, 2, 3, 8, 9, 26, 28, 40, 55, 57, 58, 76, 133, 139, 140, 141, 144, 151, 152

* LOAD TOTAL NUMBER OF DOF'S AND DEGREE OF FREEDOM LIST
* THE DOF LIST CORRESPONDS TO ROWS IN EIGENVECTOR MATRIX
PARM, PARNIP=11
ILOAD, INPHAP, PARNIP, 1
531, 477, 1053, 507, 429, 430, 421

* PARNOUT CONTAINS THE NUMBER OF DOF'S
PARM, PARNOUT=11
PARM, PARDOUT=PARNOUT*2
ILOAD, OUTMAP, PARNOUT, 1
531, 477, 1053, 507, 429, 430, 421

* THE FE DATA FOR THE GOES SPACECRAFT IS CONTAINED IN DATA 20
* USE THE LOADMAST COMMAND TO LOAD THE EXTENSILES AND EXTENSIT
OPEN, N1, N2, N3, N4
N1 = UNIT 20, N2 = 2=UNFORMATTED, N3 = 1=OLD, N4 = 1
OPEN, 20, 2, 1, 1
SAIOB (NICK, GOES) 8L36_FIXED.PHS
LOADMAST, TOTLAMB, N1, N2
N1 = 20 UNIT NO ; N2 = 0 TOTLAMB IS SINGLE PRECIS
LOADMAST, TOTPHI, 20, 0
LOADMAST, TOTLAMB, 20, 0
CLOSE, 20

* LAMB WILL CONTAIN THE RIGID BODY AND DESIRED FLEXIBLE STIFFNES
ZERO, NI, N1, N2, N3, N4
N1 - MATRIX NAME RBEVAL N1XN2 - SIZE OF RBEVAL
N3 - DIAGONAL TERMS OF RBEVAL = N2
N4 - OFF DIAGONAL TERMS OF RBEVAL = N4
- SAVCOL, N1, N2, N1
N2 IS CREATED FROM THE N1 COLUMNS OF MATRIX N1. N2 WILL
THE SAME ROW SIZE AS N1 BUT ONLY N3 COLUMNS. THE COLUMN
SPECIFIED (IN THIS CASE) ON NEXT LINE
- SAVROW, N1, N2, N3
N2 IS CREATED FROM THE N3 ROWS OF MATRIX N1
STOSH, NI, N2, N1, N2
STORES SUBMATRIX OF N2 STARTING AT ROW N1, COLUMN N2
IN MATRIX NI
ZERO, RBEVAL, 2, 1
SAVCOL, TOTLAMB, LAMB1, 1
1
SAVROW, LAMB2, LAMB, DMOD
STOSH, LAMB, RBEVAL, 1, 1

* PHI WILL CONTAIN THE RIGID BODY MODES AND DESIRED FLEXIBLE
SAVCOL, TOTPHI, PHI, DMOD
SAVROW, PHI, PHI, DMOD

```

Figure B.3.2-11a. FLAME Run for DADS State Space Model of Modal Equation

```

- ZERO, N1, N1, N2, N3, N4
  N1 - MATRIX NAME ZETA      N1XN2 - SIZE OF ZETA
  N2 - DIAGONAL TERMS OF RBEVAL = N3
  N4 - OFF DIAGONAL TERMS OF RBEVAL = N3
ZERO, ZETA, PARNM, 1, 1, 1
-----
' INPUT 2 TIMES DAMPING RATIO
' ZETA = T * A * T * T MATRIX
' SCALE, M1, M2
' REPLACES EACH TERM OF M1 WITH THE TERM MULTIPLIED BY
  THE TERM M2(1, 1) OF MATRIX M2
LOAD, ZETA, I, T
-0.006
SCALE, ZETA, ZETA
-----
' ZERO RIGID BODY MODE DAMPING FACTORS
' ZERO, N1, N1, N2, N3, N4
  N1 - MATRIX NAME M1      N1XN2 - SIZE OF M1
  N3 - DIAGONAL TERMS OF RBEVAL = N3
  N4 - OFF DIAGONAL TERMS OF RBEVAL = N4
ZERO, ZIPO, 2, 1
-----
' STORE, M1, M2, N1, N2
' STORES SUBMATRIX OF M2 STARTING AT ROW N1
  IN MATRIX M1
STORE, ZETA, ZIPO, 1, 1
-----
' CREATE OMEGA VECTOR
-----
' DUPLICATE LAMB AND PUT INTO OMEGA VECTOR
DUP, LAMB, OMEG
' SOREL, M1 REPLACES EACH TERM IN THE MATRIX NAMED M1
  THE SQUARE ROOT OF THE TERM
SOREL, OMEG
' MULTIPLY DAMPING FACTORS BY OMEGAS
' MPEL, M1, M2
' THIS OPERATION MULTIPLIES CORRESPONDING ELEMENTS OF MATRIX
  M1 AND M2 AND STORES THE RESULT IN M1
MPEL, ZETA, OMEG
' NEGATE EIGENVALUE VECTOR
LOAD, NEG, I, T
-1 0
SCALE, LAMB, NEG
-----
' CREATE SUBMATRICES FOR A MATRIX
ZERO, ZETA, PARNM, PARNM, 0, 0
-----
' STORE, M1, M2
' THIS OPERATION STORES A ROW OR COLUMN MATRIX NAMED M2
  AT THE DIAGONAL LOCATIONS OF MATRIX M1
STORE, ZETA, ZETA
ZERO, LAMB, PARNM, PARNM, 0, 0
STORE, LAMB, LAMB
-----
' ZERO, N1, N1, N2, N3, N4
  N1 - MATRIX NAME M1      N1XN2 - SIZE OF M1
  N3 - DIAGONAL TERMS OF RBEVAL = N3
  N4 - OFF DIAGONAL TERMS OF RBEVAL = N4
ZERO, IDENT, PARNM, PARNM, 0, 0
' COMBINE THE FOLLOWING SUBMATRICES TO FORM A MATRIX
  1. ZETA - LAMBAL - THE MODAL DAMPING TERMS ALONG DIAGONAL
  2. ZETA - LAMBAL - THE MODAL DAMPING TERMS ALONG DIAGONAL
  3. ZETA - LAMBAL - THE MODAL DAMPING TERMS ALONG DIAGONAL

```

Figure B.3.2-11b. Create Modal Damping Vector

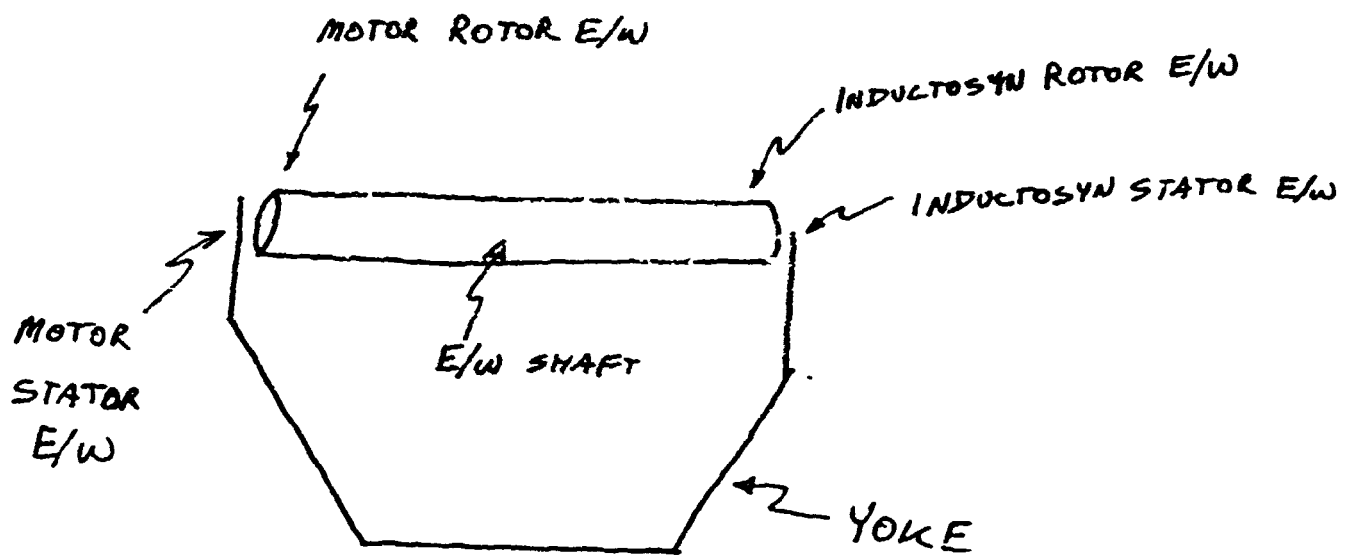
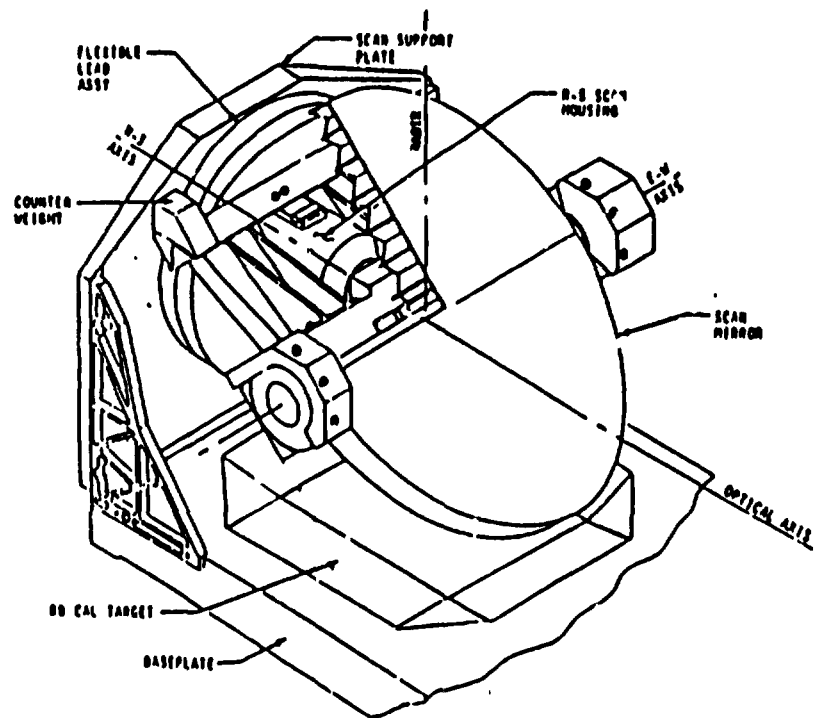


Figure B.3.2-12. Yoke Configuration



AEROSPACE/OPTICAL DIVISION **ITT**

Figure B.3.2-13. GOES Scan Assembly

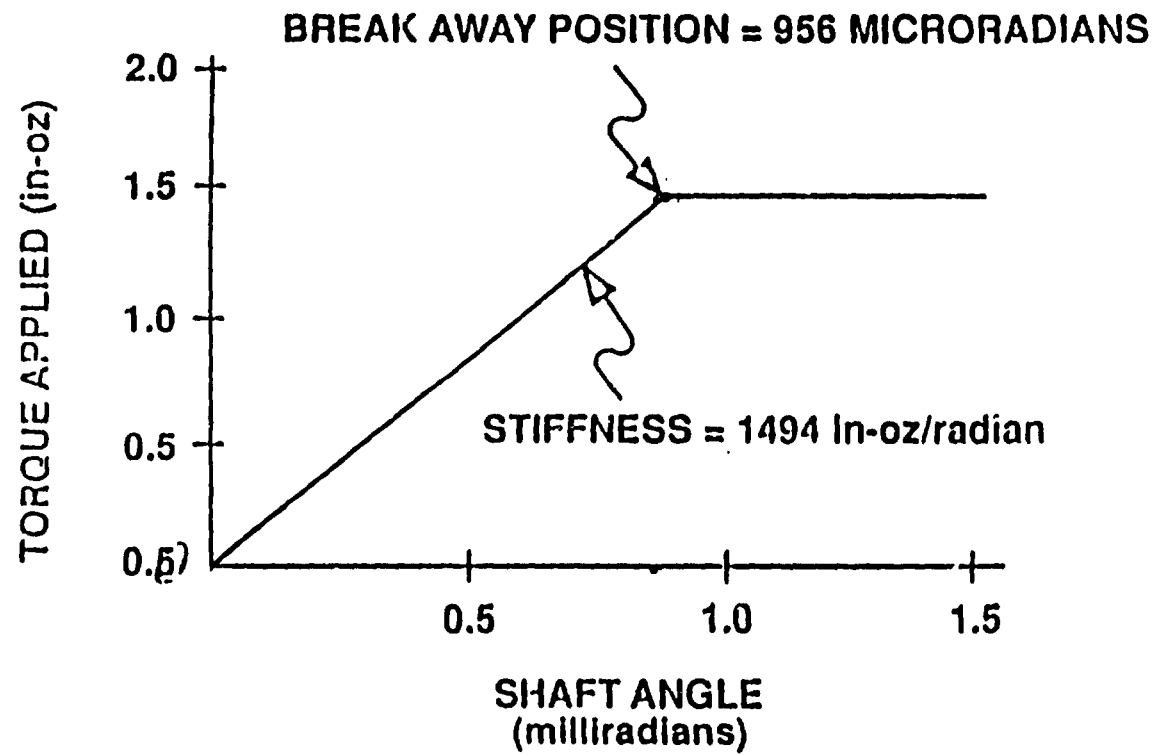
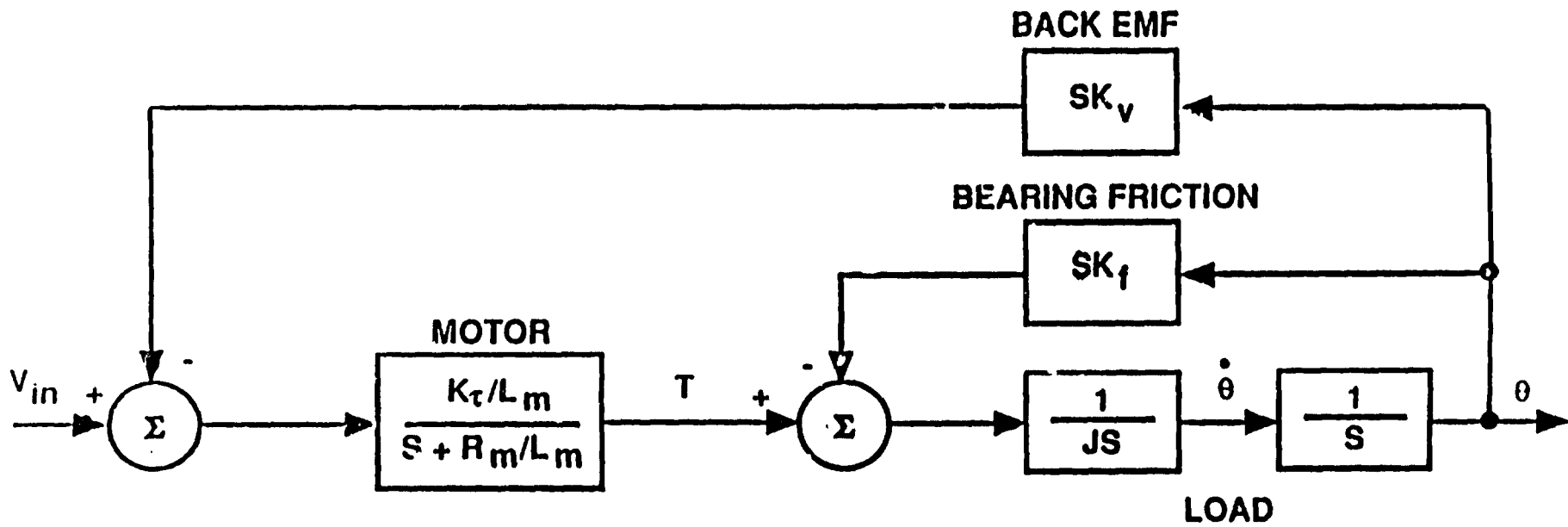


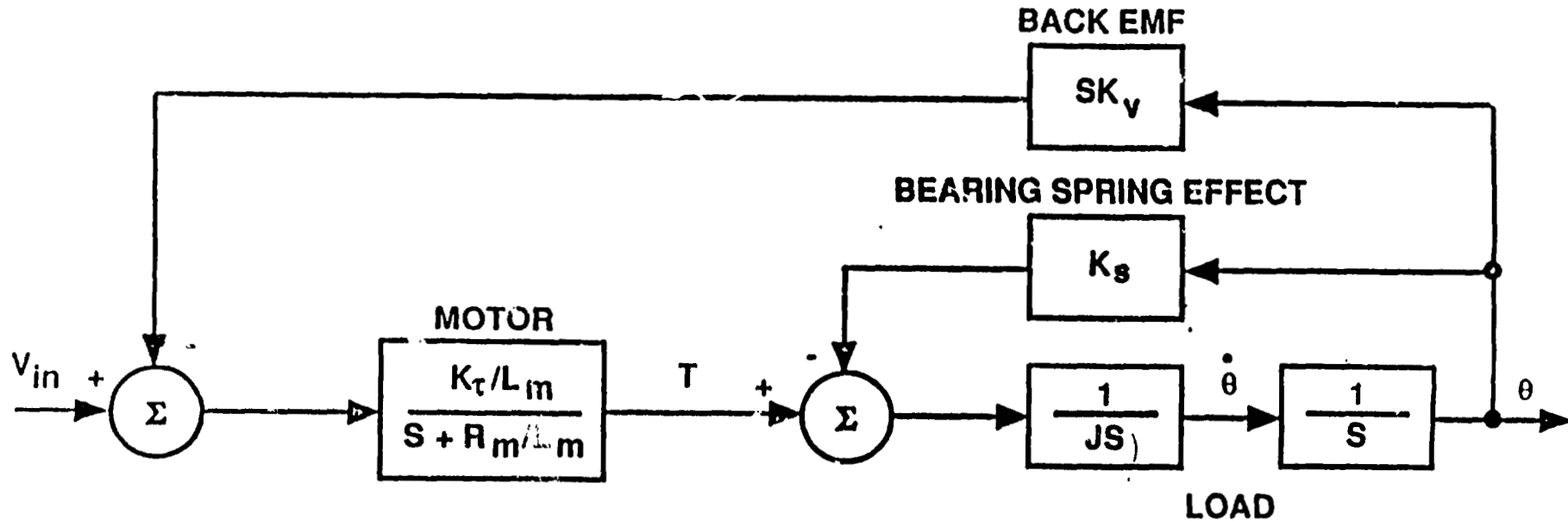
Figure B.3.2-14. Bearing Stiffness for Small Angular Motion (Experimental)



WHERE

- J = Total rigid body inertia = 4.85 in-oz-sec²**
- K_f = Linearized viscous friction constant of bearing = 1.8 in-oz/rad/sec.
@ .174 rad/sec**
- K_v = Back EMF constant = .214 V/rad/sec**
- K_τ = Motor torque constant = 31 in-oz/amp**
- L_m = Motor winding inductance = 22 mH**
- R_m = Motor winding resistance = 13.6Ω**

Figure B.3.2-15. Motor/Load Rigid Body Model for Scanner Assuming Viscous Friction Bearing Model



WHERE

J = Total rigid body inertia = 4.85 in-oz·sec²

K_s = Bearing stiction spring constant = 1494 in-oz/rad

K_v = Back EMF constant = .214 V/rad/sec

K_τ = Motor torque constant = 31 in-oz/amp

L_m = Motor winding inductance = 22 mH

R_m = Motor winding resistance = 13.6Ω

Figure B.3.2-16. Motor/Load Rigid Body Model for Scanner Assuming Spring Stiction Bearing Model

PROGRAM NAME	PARAMETER NAME	PROGRAM INPUT VALUE	COMMENTS
ORI	IN-TRACK	0	NO E/W ERROR
ORC	X-TRACK	357.9713	$42167 \cdot \sin(\pi/180 \cdot 0^\circ I)$ km
DRH	ALT	0	
ROLL	ROLL	0.5	INCLINATION
PITCH	PITCH	0	
YAW	YAW	0	
NS GIMBAL	NS GIMBAL	0	SEE NOTES

NOTES:

MC PROGRAM EXPECTED TO HAVE THE WORST CASE W/ NS GIMBAL ANGLE = 0.0 DEGREES (NADIR OR EQUATORIAL SCAN).

Figure B.3.2-17. IMC Program Parameters

In the DADS simulation model, shown in Figures B.3.2-5 and B.3.2-8, the friction was modeled on both sides of the East/West and North/South shafts. The friction torques were obtained by the following procedure applied to both inductosyn and motor side of the East/West and North/South shafts. The stator rate was differences from the rotor rate (both rates are outputs from the DADS general element) to obtain the angular rate of the shaft (on the side of interest) relative to the stator. This value for the rate was used as input to the Dahl friction element along with the dahl friction torque. The output of the Dahl friction element is then integrated and multiplied by 0.5 to obtain the Dahl friction torque. This torque is applied to the rotor side of the shaft and the reaction torque of this quantity (the negative) is applied to the stator side.

B.3.2.5 IMC (Image Motion Compensation) signal

If the spacecraft orbit inclination is inclined from geosynchronous, a compensation must be made for the apparent distortion of the earth image. This compensation is the IMC signal which is a correction signal based on the value of the East/West commanded angle. The IMC signal is an input to the East/West and North/South control systems which could induce the structural coupling which is being investigated in this section of the report. For the purposes of this simulation the IMC signal was added to the commanded input signal, and this quantity is differences with the inductosyn measured shaft angle to generate the error signal (Figures B.3.2-3 through B.3.2-8 are where the IMC signal occurs in the simulation block diagram). Plots of the East/West and North/South IMC signals for an orbit inclination of 0.5 deg (which results in the largest IMC correction signal possible) are shown in Figures B.3.2-18 and B.3.2-19.

B.3.3 Results

Shown in Figures B.3.3-1 and B.3.3-2 are plots of the East/West shaft angle error (at the inductosyn side of the shaft) versus time for the two axis simulation and the single axis simulation (in the two axis simulation both East/West and North/South control servos were modeled and were coupled through the structural modes; whereas, in the single axis simulation only the East/West control servo was modeled). During the East/West scan, oscillations of the shaft about its nominal motion occurred. For the two axis simulation, the magnitude of these oscillations are about 1.5 μ radians peak to peak; the single axis simulation oscillations are about 10% of two axis oscillations. These oscillations indicate that there is structural coupling between the East/West and North/South axes during the scan, even for this "benign" case — no 175 Hz mode and 0.3% structural damping.

It should be noted that when the IMC signal is turned off during the East/West scan, the East/West shaft error increased to about 4 μ r before settling out at about 1.5 μ r. (The actual IMC signals will differ slightly from those used in the simulation; detailed modeling of the IMC signal was beyond the scope of this effort.) The response due to the discontinuity in the IMC signal does indicate that disturbances to the system can induce a large shaft error which does not decay immediately due to the structural coupling.

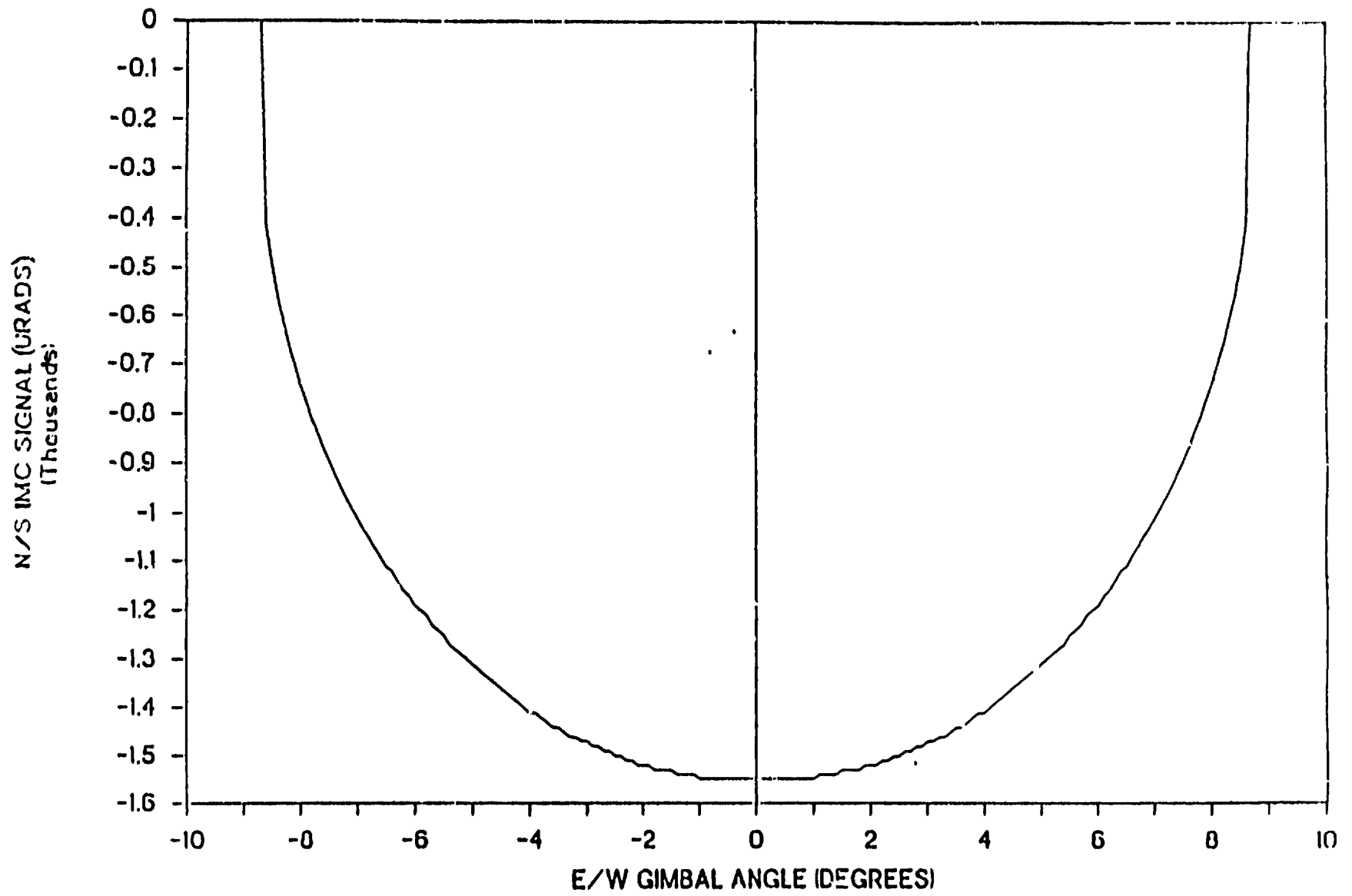


Figure B.3.2-18. IMC Signal - 0.5 deg - Inclination 0.0 - NS GIMBAL

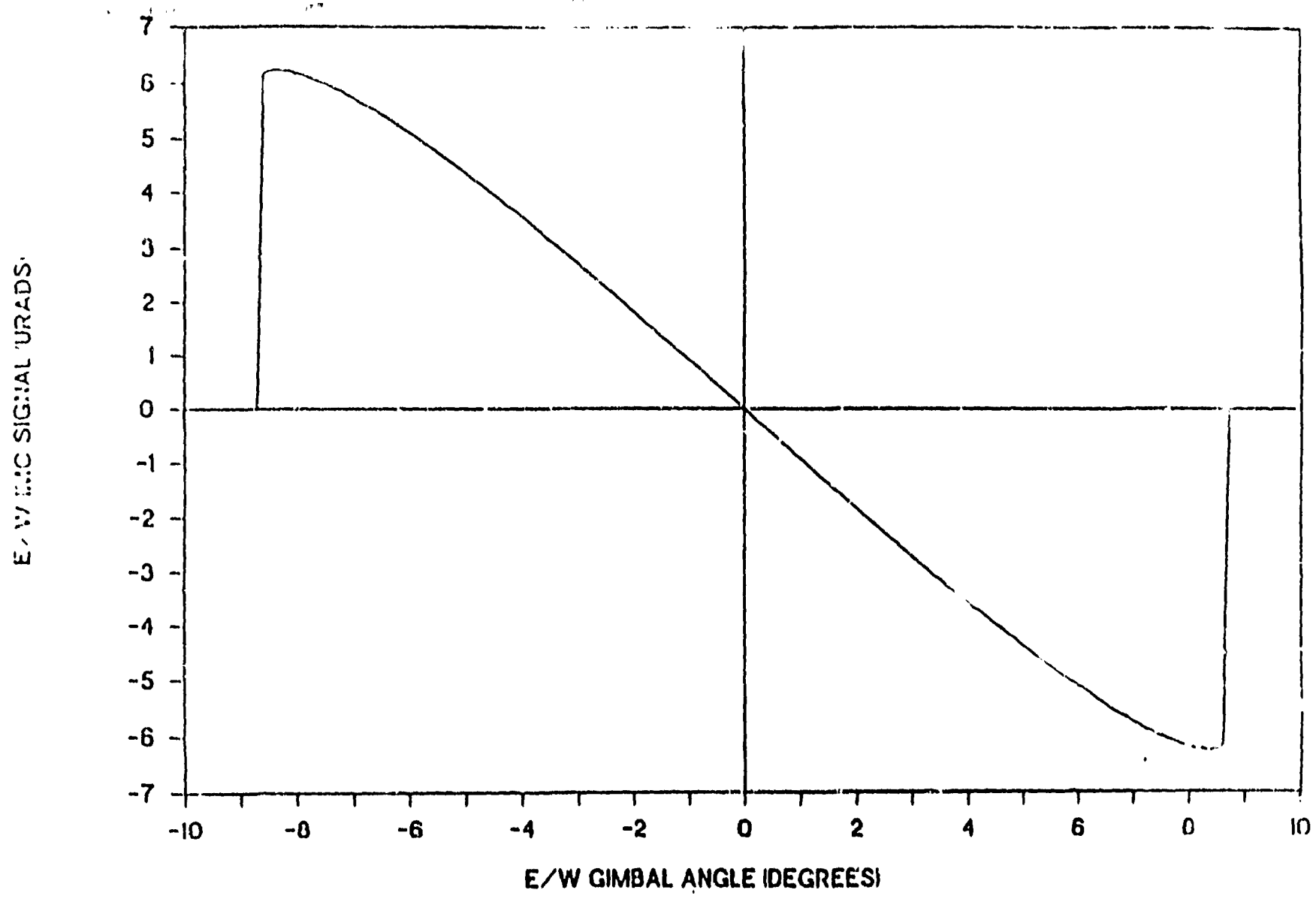


Figure B.3.2-19. IMC Signal - 0.5 deg - Inclination 0.0 - NS GIMBAL

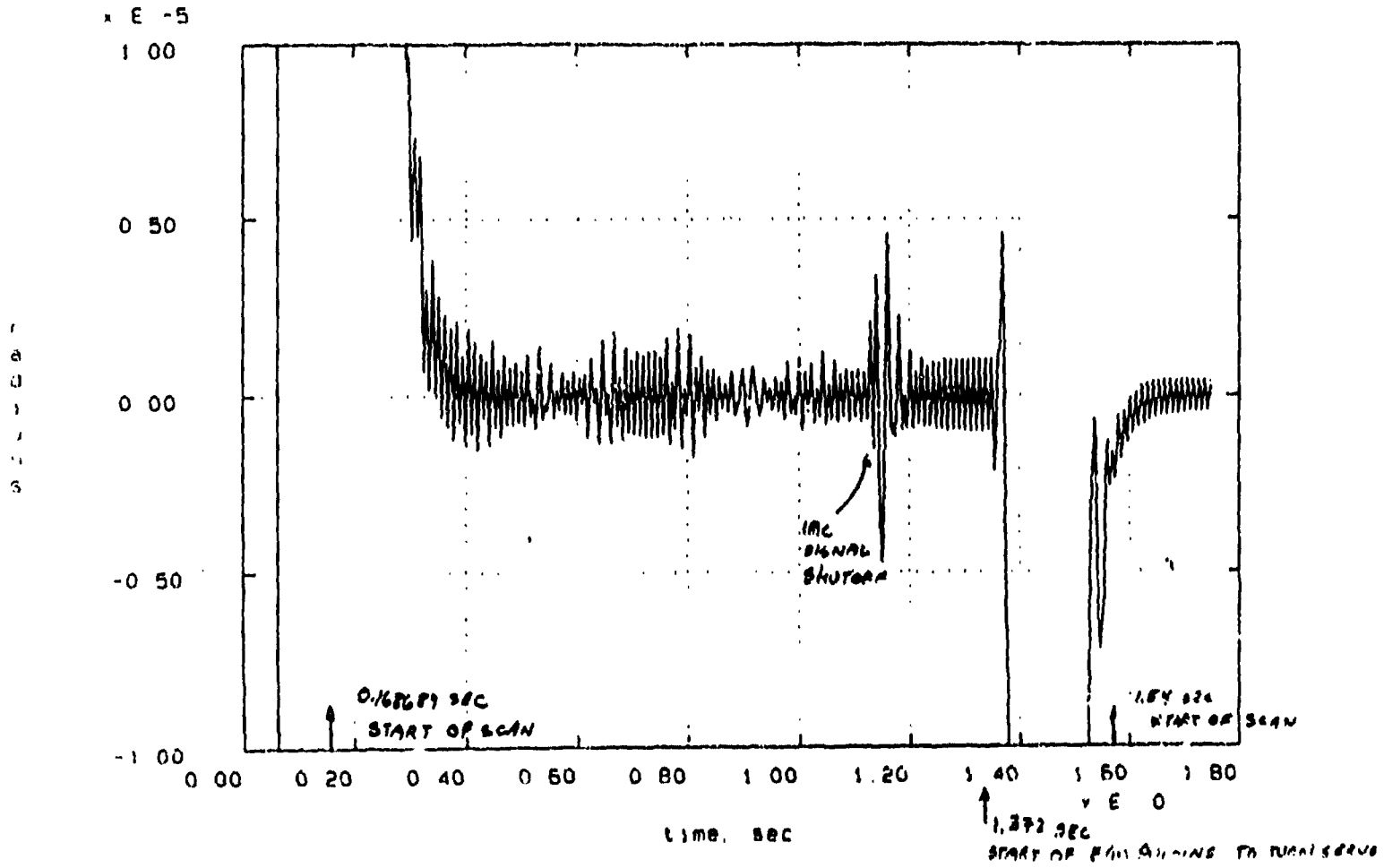


Figure B.3.3-1. E/W Shaft Error Angle vs Time (Two Axis Simulation)

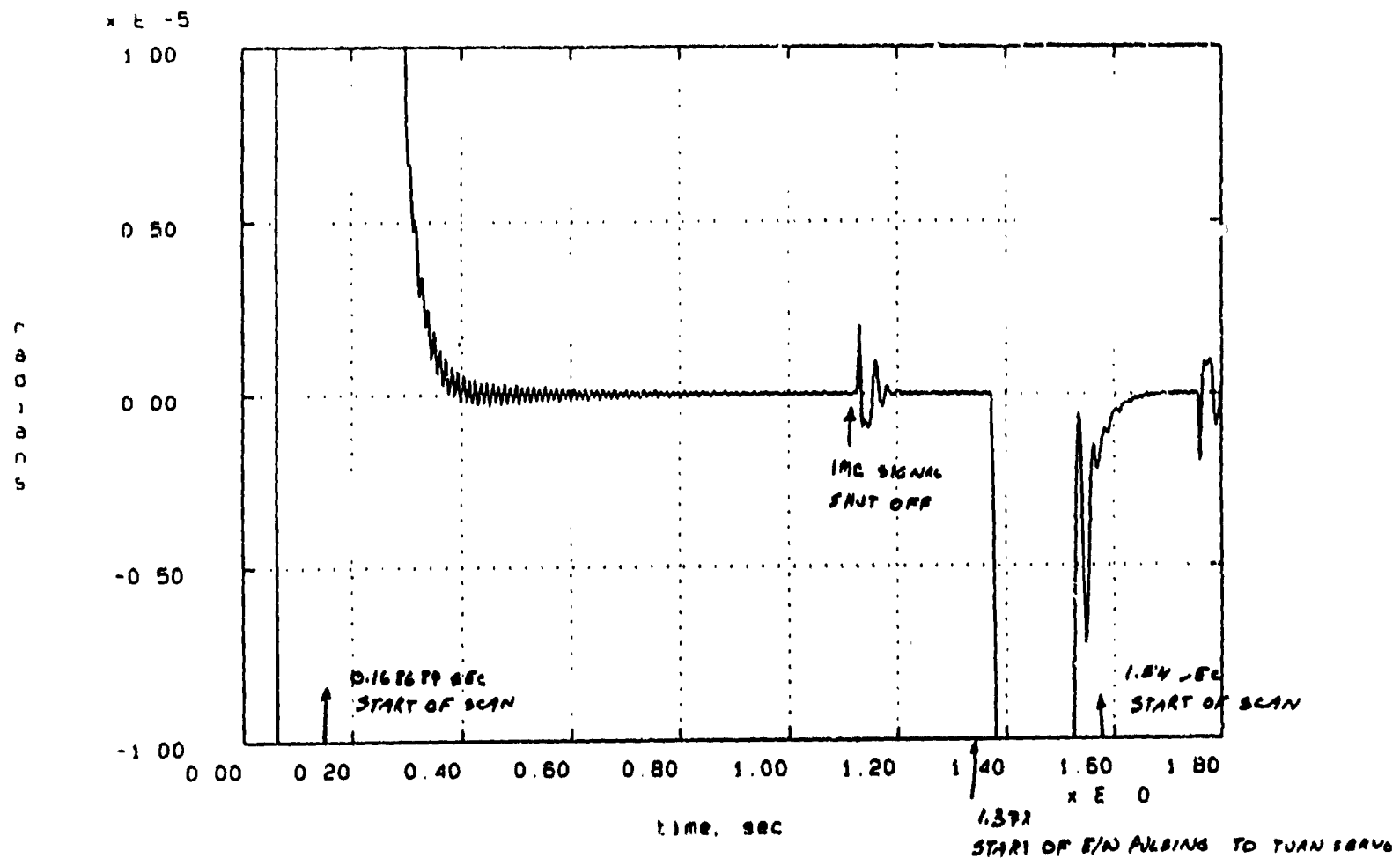


Figure B.3.3-2. E/W Shaft Error Angle vs Time (Single Axis Simulation)

B.3.4 Conclusions

Based on the shaft error response during an East/West scan and when the IMC signal is shut off, structural coupling could affect the desired performance of the GOES mirror instruments, especially in light of the more stringent pointing budget for GOES-N. By using the DALS code and by implementing the approach listed in Section B.2 above, the capability to simulate and investigate structural coupling in the GOES-N imager is available.

B.4 FEEDFORWARD COMPENSATION AS APPLIED TO GOES-I SOUNDER

B.4.1 Background

The problem of pointing an instrument to a desired location relative to its base is simpler than tracking a non-cooperative target. In the pointing problem, the desired pointing trajectory is known, and the command signal may be processed without affecting the closed loop dynamics. The GOES imager and sounder are pointing instruments. The scheme investigated here is one which takes advantage of open-loop processing, or feedforward compensation, of the command signal to improve the step response of a closed-loop system such as the GOES-I sounder East/West servo. The development presented here is quite general, and it would apply equally well to the GOES-N sounder or any other pointing instrument.

The feedforward compensation takes the plant dynamics into account and cancels them to some degree. On one hand, the performance of an existing servo can be improved by incorporating feedforward compensation. On the other hand, if the benefits of using feedforward compensation are taken into account from the start, a servo with otherwise inadequate performance can be designed, with the overall system yielding acceptable performance. Such a servo could have a lower bandwidth and simpler compensation than would be otherwise possible. In general, a lower bandwidth control loop tend to lessen the stability implications of flexible body dynamics.

The GOES-I sounder step and settle error budget is $5.25 \mu\text{r}$ after 28 milliseconds. Figure B.4.1-1 shows that the instrument meets this requirement, marginally. The high bandwidth of the servo has made stabilization of the flexible body modes a difficult task. The compensation for the sounder is fairly complex, and it must be fine-tuned in order to achieve the desired performance. Figure B.4.1-2 shows a block diagram of the GOES-I sounder.

One attempt at improving the step response of the GOES-I sounder was to sum an appropriately timed and scaled retropulse into the motor driver. This concept is based on the fact that the impulse response of a second order system is a scaled and time-shifted version of the step response error of that system. By applying an impulse at a zero crossing of the error, it is theoretically possible to completely cancel the error from that time on.

The retropulse scheme had very little success on the GOES-I sounder. A major problem is that the step response is dominated by low frequency structural modes. These modes cannot be canceled by a retropulse, and in fact, they are excited by the pulse.

Another problem is that the sounder is not a simple second order system, even if we ignore the structural modes. In general, the impulse response of higher order systems cannot cancel the step error, regardless of scaling and time shifting. The impulse and step responses are shaped differently, unlike those of a second order system, where both are exponentially damped sinusoids of equal frequency and equal damping ratio.

Also, the physical retropulse has non-zero width and finite height, whereas a mathematical impulse has zero width, infinite height, and finite area.

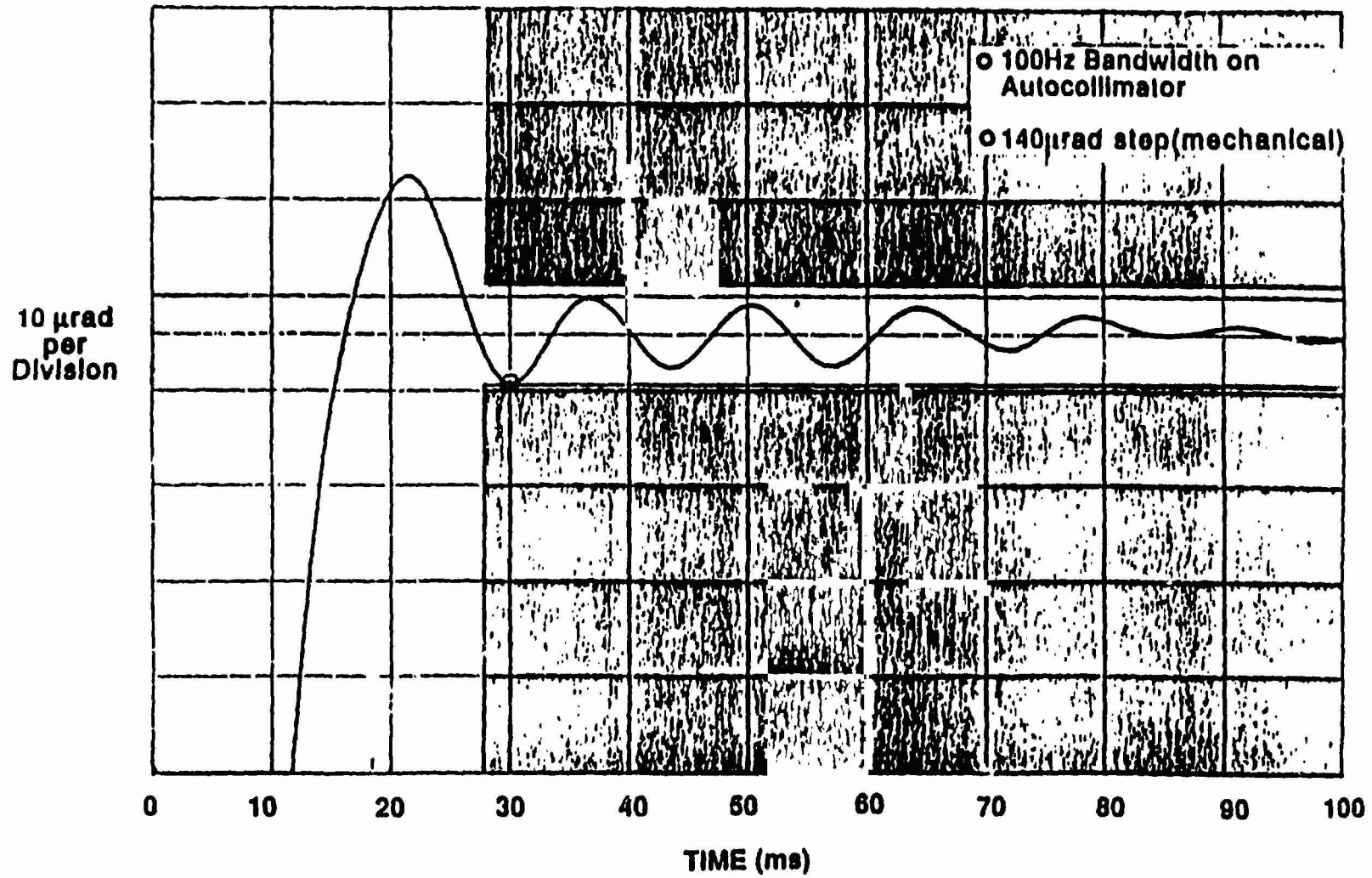
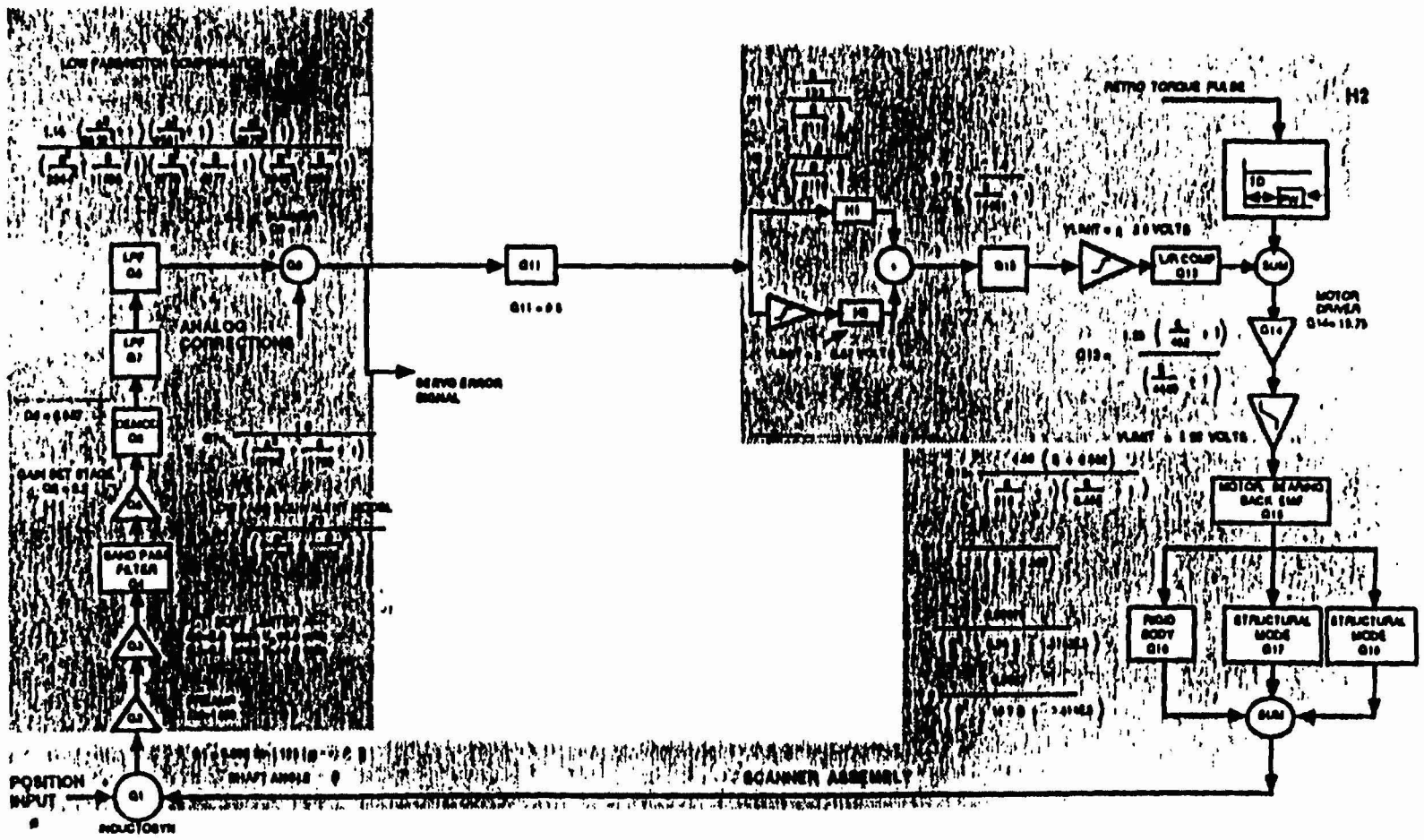


Figure B.4.1-1. GOES-I Sounder East/West Step and Settle Response
295



Reproduced from best available copy.

Figure B.4.1-2. GOES-1 Sounder East/West Servo Block Diagram
296

B.4.2 System concept

The basic concept of feedforward is to give the servo as much information as possible to help it perform as desired. In this case, we use our knowledge of the plant dynamics and desired angle profile to generate a torque command. The desired angle profile is then fed into the servo input, and the torque command is fed forward into the torque input of the plant.

If the plant were linear and we had perfect knowledge of its dynamics, we could mathematically invert the plant to generate the torque command. By feeding this torque command into the physical plant, we could achieve arbitrarily good performance without even closing a loop around the plant. In reality, of course, we need a closed loop to compensate for unmodeled plant dynamics, nonlinearities, and disturbances. (Figure B.4.2-1.) It is important to note that we do not depend on the closed loop to obtain good performance; this is obtained primarily through the use of feedforward compensation, which generates the torque command. The closed loop only has to compensate for the residual error due to disturbances and imperfect plant modeling in the feedforward compensation.

Generating a torque command from an angle command requires differentiation of the angle command, which is nominally a step function. We can reduce the impulses and discontinuities in the torque command by using a smooth angle command profile. A typical profile is one which has a constant acceleration followed by a constant deceleration. However, a command profile with sinusoidal acceleration is smoother and has less high frequency content. The high frequency components of the angle command are important because they can excite structural modes in the system, resulting in an undesirable response. The frequency content of the command profile is approximately limited to $2/T$ Hz, where T is the length of the profile. The angle, rate, and acceleration profiles used in this study are shown in Figure B.4.2-2.

Plant inversion is accomplished by driving a simulated high-bandwidth servo with the desired angle command, and then taking the torque signal from the plant model. (Figure B.4.2-3.) This technique avoids direct differentiation and also allows us to include nonlinearities and known coherent disturbances in the inverted plant.

Another noteworthy feature of the feedforward compensation scheme is that notch filters are used outside of the closed loop to attenuate frequency components of the command signal which would otherwise excite troublesome structural modes in the plant. Since the filters are outside of the loop, the phase lag in these filters do not affect system stability. However, the phase lag does increase the rise time of the servo command signal, and consequently, the overall response of the system is somewhat slower due to the open loop notch filtering. (Figure B.4.2-4.)

Figure B.4.2-5 shows the overall block diagram of the system concept, including open loop notch filters, feedforward compensation, and closed-loop compensation.

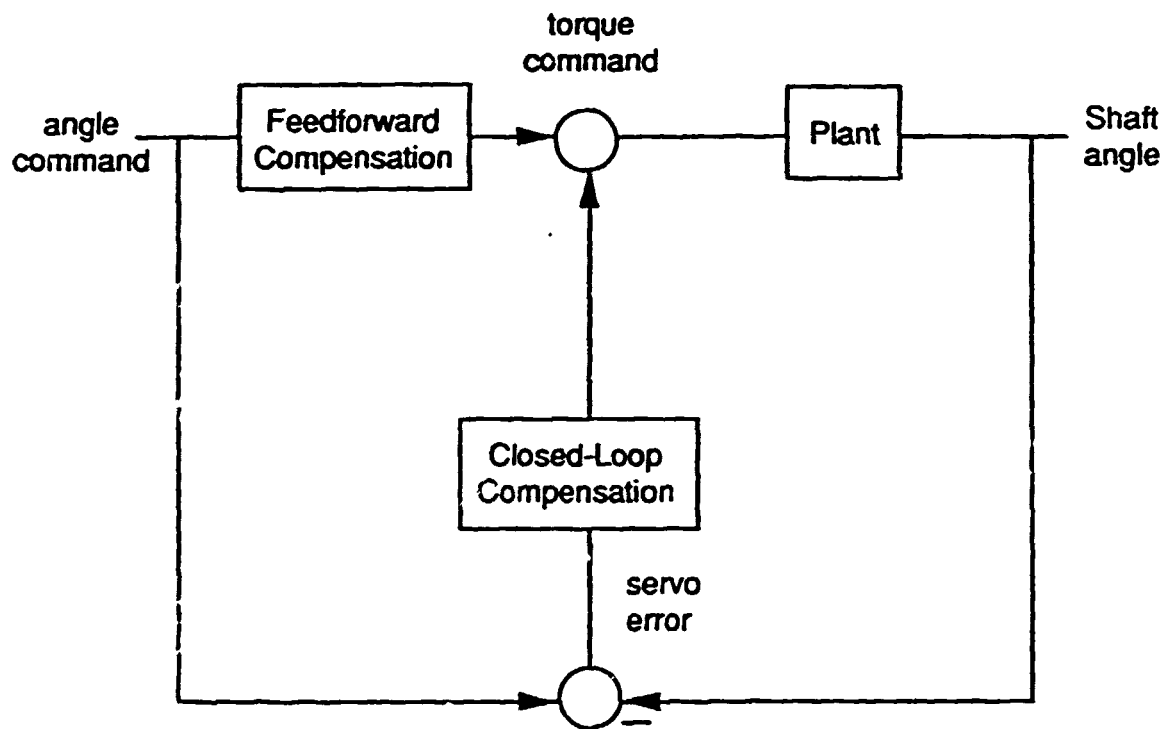


Figure B.4.2-1. Basic Concept

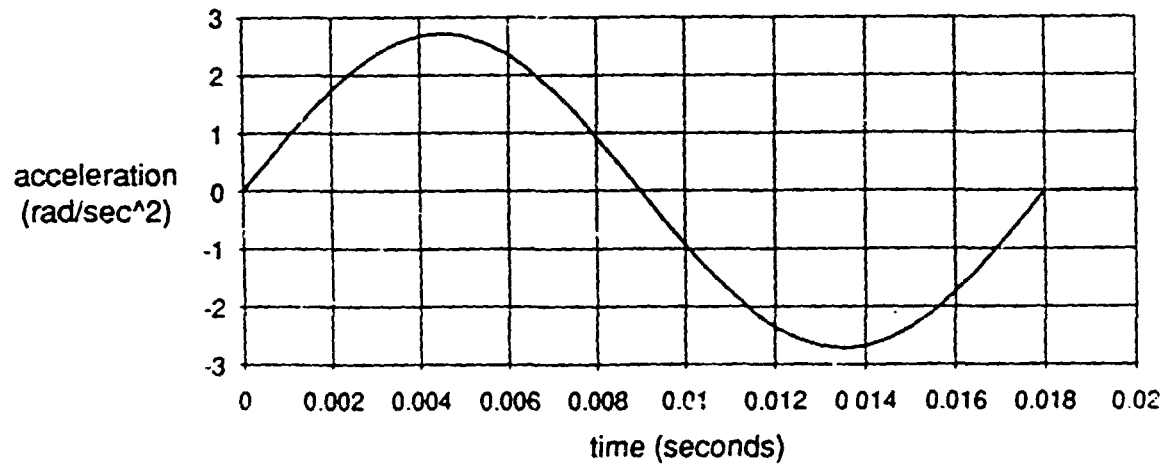
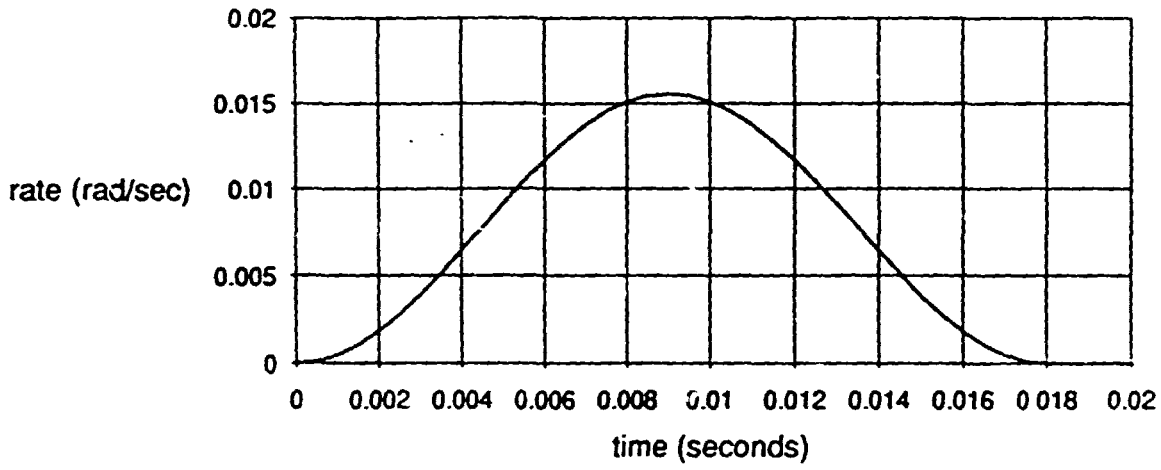
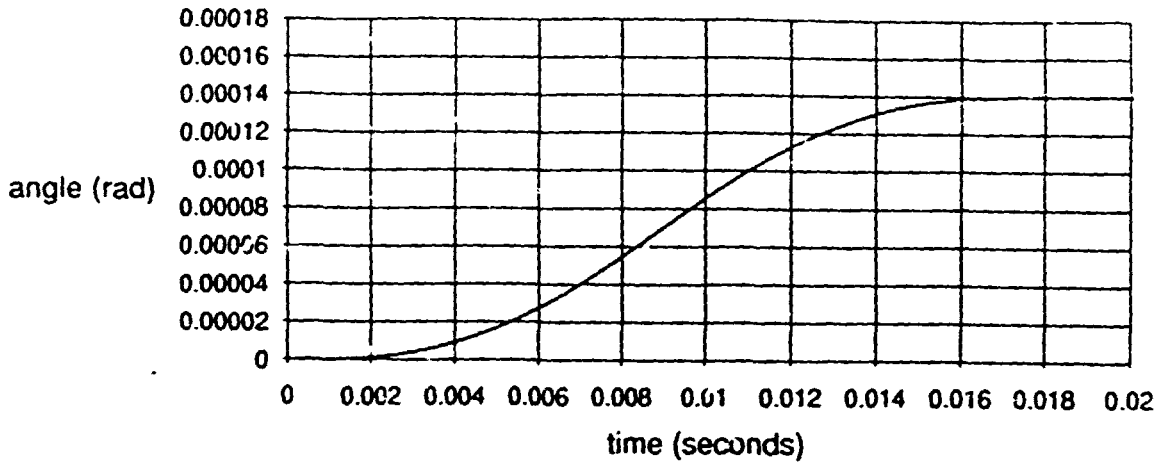


Figure B.4.2-2. Angle, Rate and Acceleration Profiles

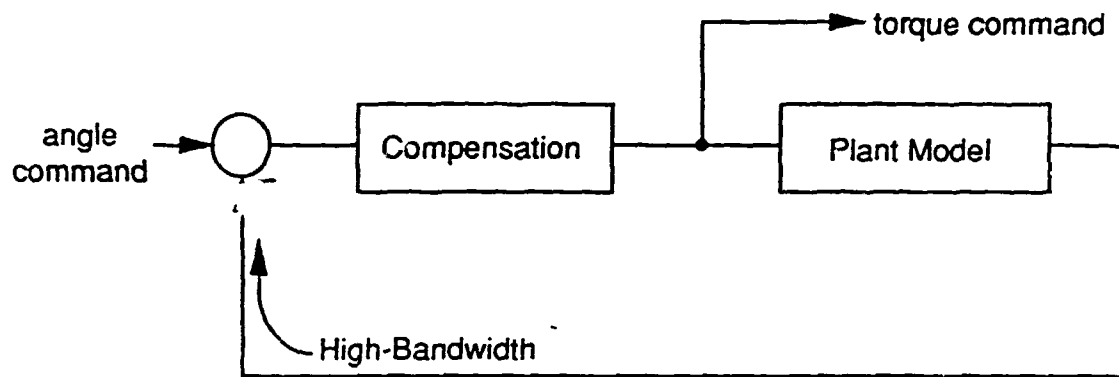


Figure B.4.2-3. Plant Inversion

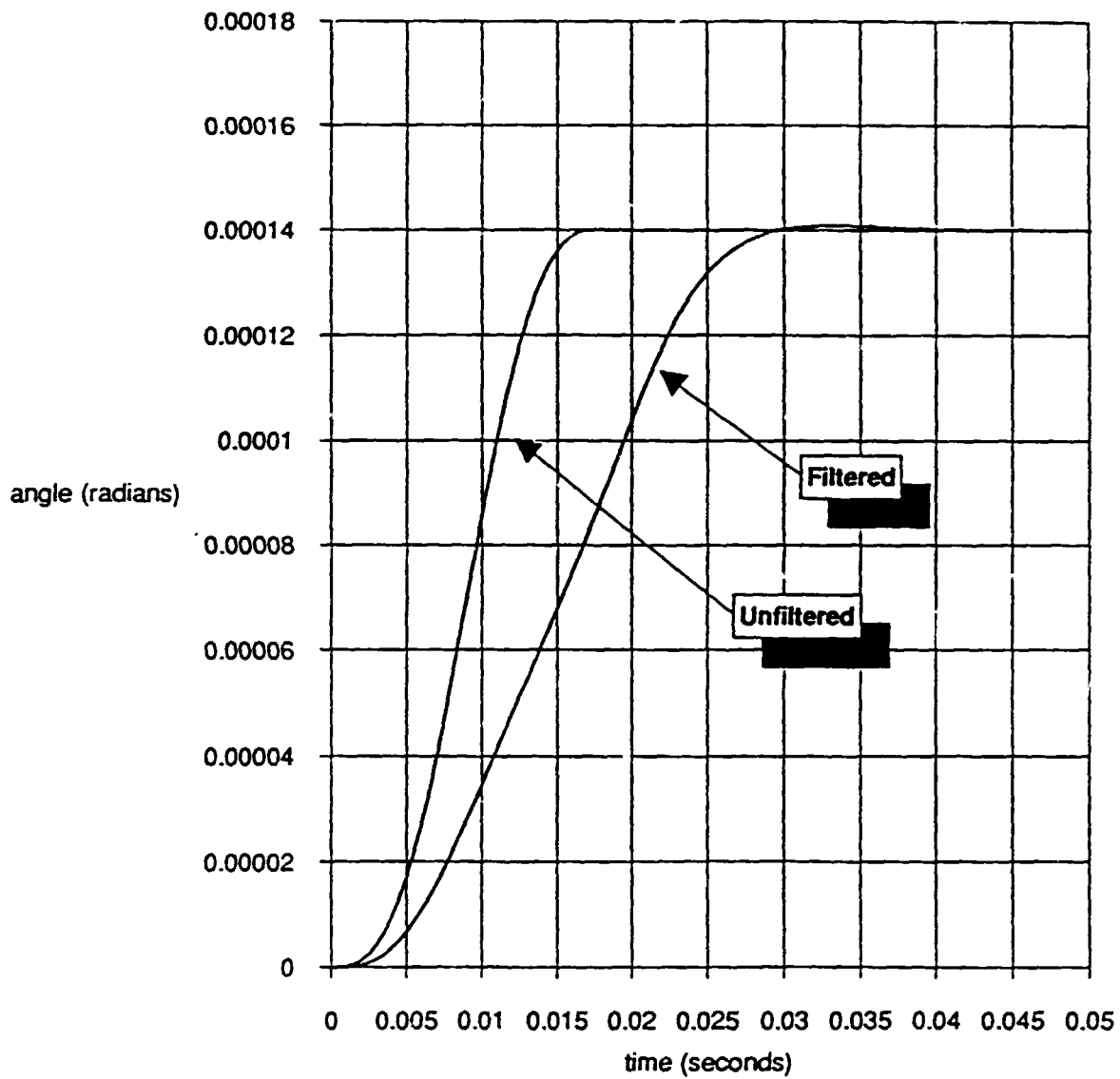


Figure B.4.2-4. Angle Command, Before and After Notch Filter

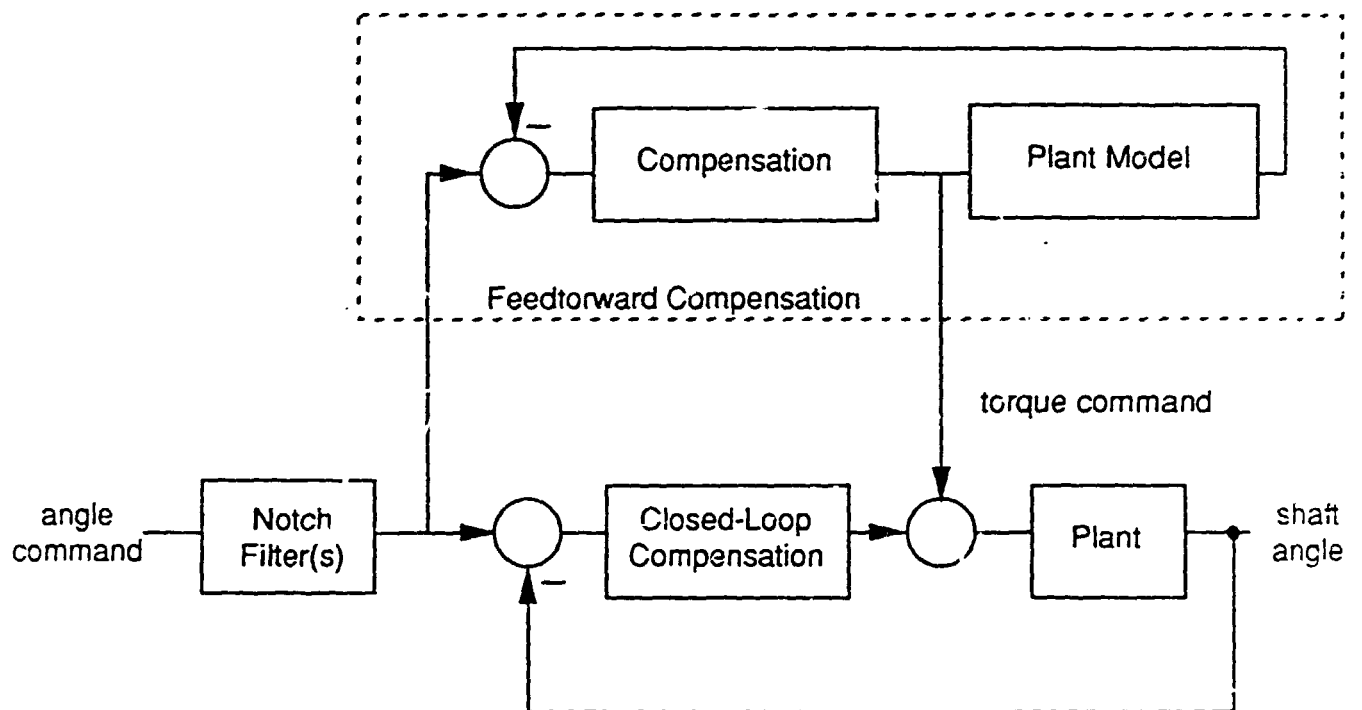


Figure B.4.2-5. Overall System Concept

B.4.3 Servo bandwidth considerations

Without feedforward compensation, a system depends on high closed-loop bandwidth to obtain good command-following and disturbance rejection. However, increasing the bandwidth of a system generally reduces its stability, demands more precise knowledge of structural modes, and results in more complex and critically-tuned compensation.

As the bandwidth is lowered, the adverse effects of high bandwidth diminish, but performance also diminishes. Feedforward can improve command-following, and if known coherent disturbances are included in the inverse plant model, cancellation of these disturbances can be quite good. As the bandwidth is lowered, the system's dependence on the feedforward signal increases, and therefore, the system becomes more sensitive to errors in this signal. Since the feedforward compensation is not perfect, the system requires high enough bandwidth so that the residual errors are acceptable.

Servo bandwidth should be made as low as possible, to avoid the problems associated with high bandwidth, and the lower bound on servo bandwidth is driven by our knowledge of the plant, its nonlinearities, and disturbances.

B.4.4 Performance expectations

Using the open-loop notch filter and torque feedforward concept, a servo with low bandwidth (20 Hz) and simple closed-loop compensation performs significantly better than the baseline GOES-I sounder servo, which has high bandwidth (over 40 Hz) and more complex compensation. The feedforward compensation concept improves the time response of a low-bandwidth servo in three areas: rise time, settling time, and structural mode excitation. With complete plant knowledge, simulations of the system show that the step response settles to within $2 \mu\text{r}$ (1.4%) in 28 ms.

We assume that the motor is driven by an ideal current feedback amplifier. Practical current drivers perform well enough to justify this assumption. Using a current driver eliminates the dynamics due to the motor inductance and resistance and therefore renders the system insensitive to uncertainty and drift in these parameters.

We assume that a 20 Hz closed-loop servo bandwidth is low enough so that the flexible body modes do not cause stability problems. A partial set of structural modes provided by a member of the GOES-N study team was used in this feedforward study. This set includes modes at 49 Hz, 93 Hz, 756 Hz, and 1787 Hz. The two high frequency modes are not very important, while the low frequency structural modes significantly affect the time response of the system.

The closed-loop compensation is a simple lead network with parameters chosen to yield a closed loop bandwidth of about 20 Hz and a damping ratio of about 0.7.

Figure B.4.4-1 shows a block diagram of the simulation used in the study.

Figure B.4.4-2 shows the response of the 20 Hz servo with no notch filter and no feedforward compensation. Notice the large overshoot and the 49 Hz ringing. The response begins to settle at about 40 ms, and at 65 ms the error is about 7 μ .

Figure B.4.4-3 shows the response of the servo with a 49 Hz notch filter on the command signal. There is no feedforward in the system. The 49 Hz structural mode is attenuated significantly, but the large overshoot and generally sluggish response of the 20 Hz servo is still present.

Figure B.4.4-4 shows the response with open-loop notch filtering and torque feedforward. The feedforward overcomes the slow response of the low bandwidth servo. In fact, the response would be virtually unchanged even if the loop were open because the plant model in the feedforward compensation is perfect. Figure B.4.4-5 shows a close-up of the response. The error is less than 2 μ from about 28 ms. The small overshoot is not due to the servo; it is due to the dynamics of the notch filter.

B.4.5 Robustness analysis

System performance does not depend on fine tuning the closed-loop compensation to the plant. Closed-loop compensation can be relatively simple, and its fine-grain details are unimportant to overall system performance. The performance of the system depends primarily on the fidelity of the plant and disturbance models in the feedforward compensation. The closed loop determines the sensitivity to modeling errors and shapes the system's response to these errors.

Modeling errors arise from parameter estimation error, incorrect model structure, and unmodeled phenomena. Regardless of source, modeling errors result in errors in the feedforward torque command. The difference between the ideal torque command and the actual torque command can be considered to be a torque disturbance. The robustness of the torque feedforward concept depends on our ability to minimize this disturbance torque and on the ability of the closed-loop servo to reject the disturbance.

The 20 Hz servo under consideration has a steady-state sensitivity to disturbance torques of about 13 μ /oz-in. Errors in the estimation of parameters in the dahl friction model result in bias errors in the torque command. For a steady-state error of less than 2.5 μ , the torque command can have a bias error of no more than 0.19 oz-in. Transient errors are more difficult to treat analytically, so simulation studies were required.

Table B.4.5-1 shows the allowable ranges for several parameters in order to meet the criterion of 2.5 μ maximum error after 28 ms, which may be the GOES-N sounder step and settle requirement. The estimates are those used in the plant model in the feedforward compensation. The ranges are for actual plant parameter values.

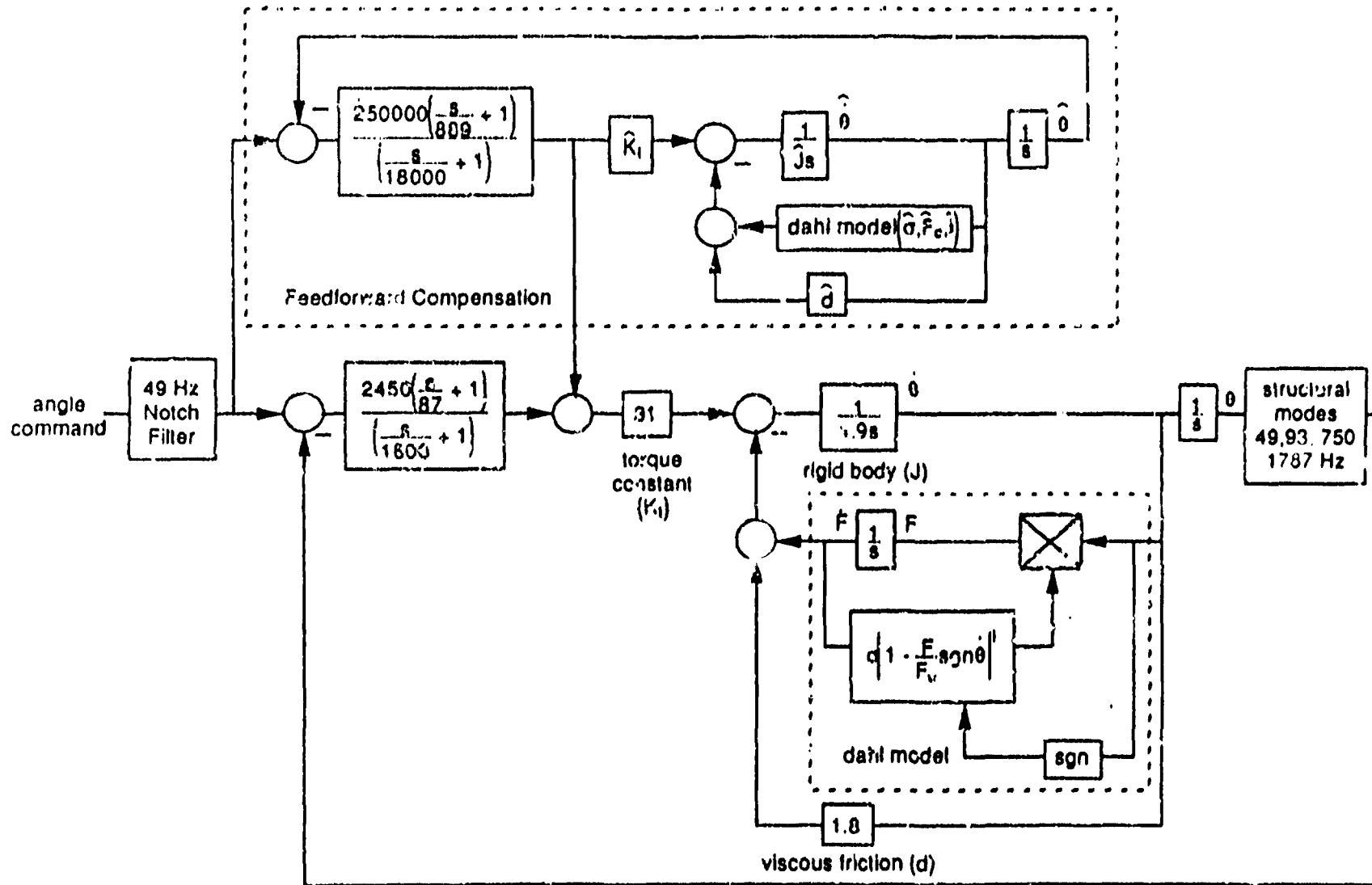


Figure B.4.4-1. Simulation Block Diagram

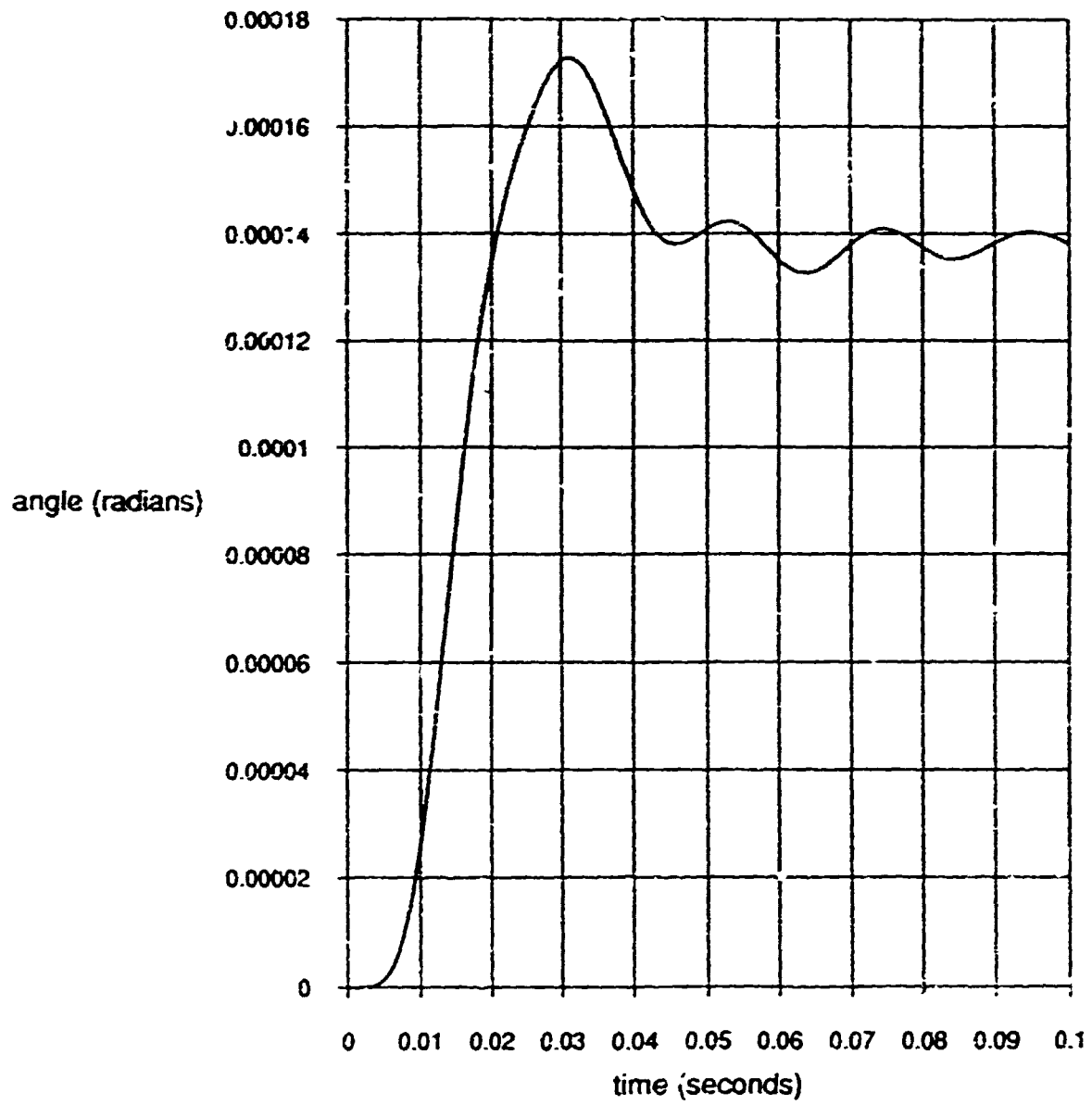


Figure B.4.4-2. Unaided Response

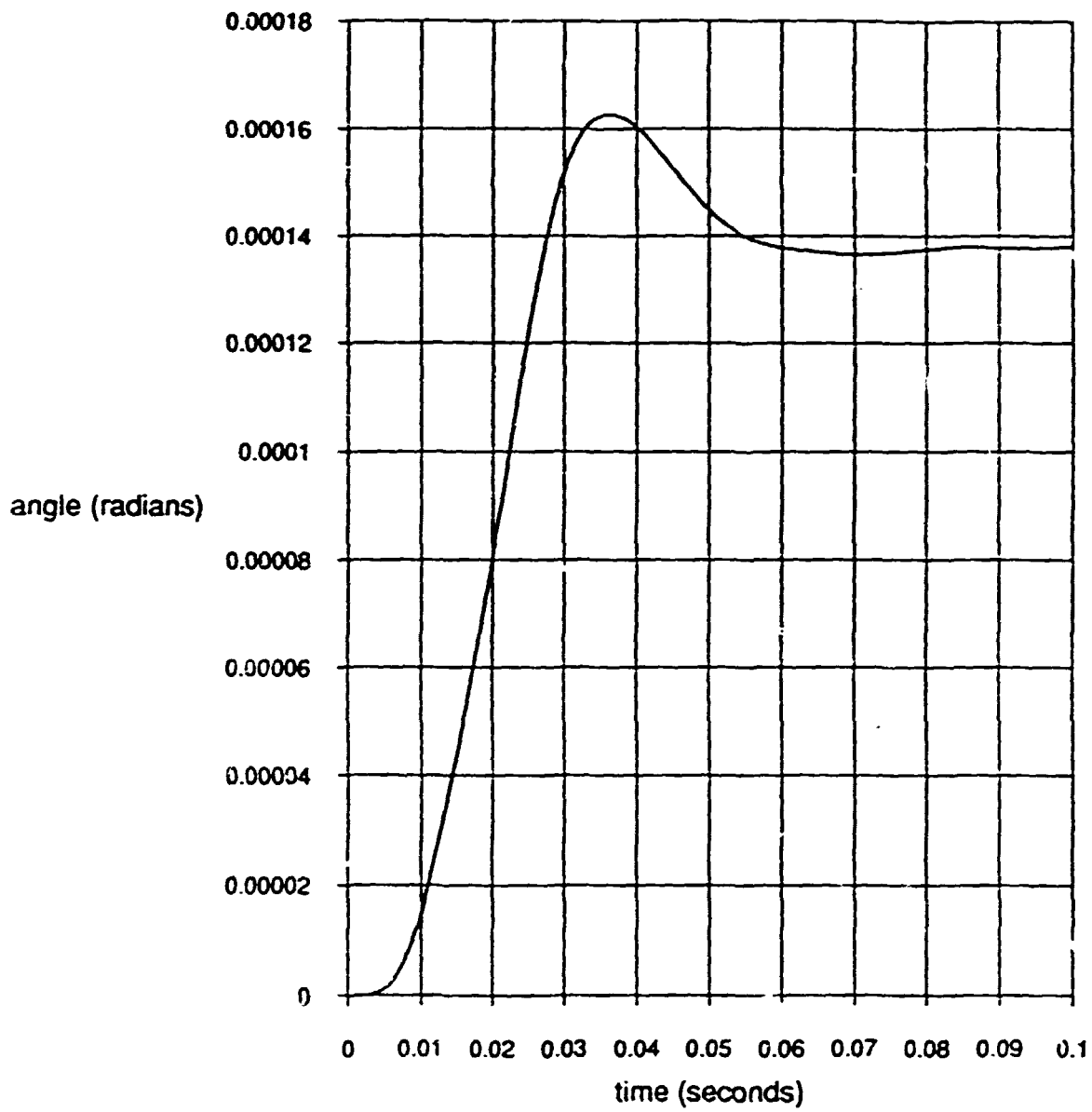


Figure B.4.4-3. Response with Notch Filter

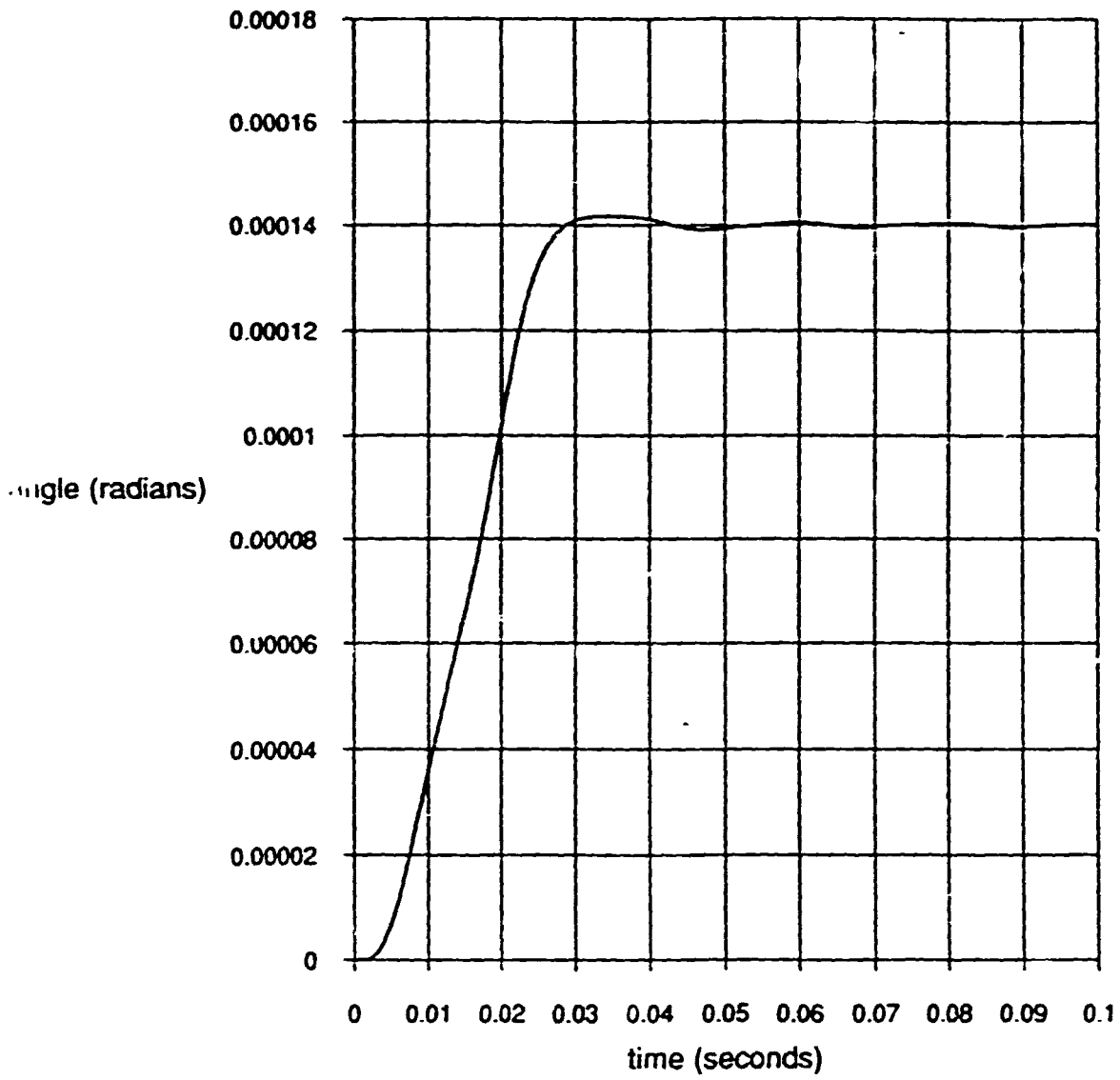


Figure B.4.4-4. Response with Notch Filter and Torque Feedforward

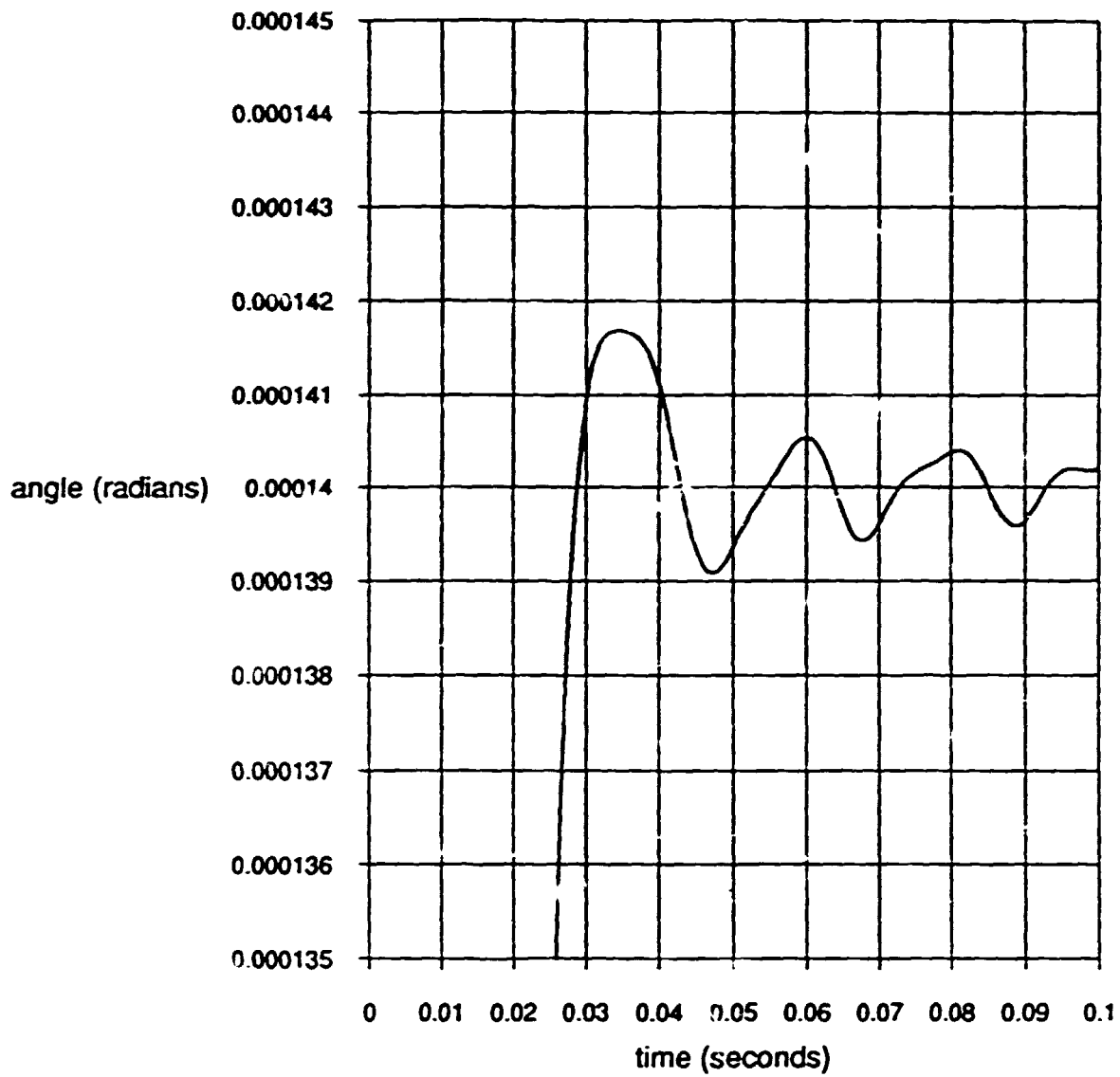


Figure B.4.4-5. Response with Notch Filter and Torque Feedforward Detail

TABLE B.4.5-1. Analysis Input Parameter

PARAMETER	ESTIMATE	RANGE
INERTIA	4.9	4.4 - 5
VISCOUS FRICTION	1.8	0 - 35
TORQUE CONSTANT	31	30 - 36
COULOMB FRICTION	1.4	1.21 - 1.59
REST STIFFNESS	1494	1100 - 2000
DAHL EXPONENT	2	1.3 - 3

The upper value for rigid body inertia and the lower bound for motor torque constant are close to the estimated values because the overshoot in the notch-filtered angle command causes the response to approach the 2.5μ boundary even for the perfect estimation case. It should be possible to adjust the angle profile and notch filter characteristics to minimize the overshoot. Minimizing the overshoot would increase the robustness of the system with respect to transient errors. The feedforward concept is insensitive to viscous friction estimation errors because the viscous friction in the plant is insignificant, and the torque command error due to this parameter estimation error is proportional to the commanded rate, which is small and quickly diminishes to zero.

The sensitivity of the system to estimation errors or changes in the low-frequency structural mode frequencies depends on the notch filter parameters. In selecting these parameters, there are tradeoffs involving the attenuation, phase lag, overshoot, and bandwidth of the filters. However, the selection is simplified by the fact that the filters do not affect the closed-loop characteristics of the servo. The sensitivity to notch filter parameters has not been covered in detail in this study. Low frequency modes are readily observable, and the notch filters can be adjusted as needed (see "Hardware Requirements" section).

B.4.6 Hardware requirements

Implementation of the torque feedforward concept will definitely require a digital computer. The feedforward compensation, which generates the torque command signal, consists of a simulated high-bandwidth, non-linear servo loop including rigid body dynamics and all known coherent disturbances. This simulation is best accomplished with a digital computer, which allows easy modification to the plant and disturbance models.

The feedforward computation does not have to be performed in real-time; it could even be performed on the ground with the resulting notch-filtered angle and torque command profiles being uploaded and stored into the instrument. Performing the computations off-line on the ground minimizes the hardware impact to the instrument and maximizes flexibility in upgrading the plant model and notch filters as required.

B.4.7 Conclusions

The advantage of the torque feedforward concept is that it improves the performance of a servo and allows a lower bandwidth and simpler closed-loop compensation than would be otherwise possible. The importance, complexity, and bandwidth of the closed-loop compensation vary inversely with our confidence the models of the plant and disturbances.

The disadvantage of the concept is that uncertainty in our models reduces the performance improvement and returns the burden of high performance to the closed loop.

Further work for the torque feedforward and open-loop notch filtering concept should be in the area of system identification. It should be possible to characterize and model the plant and coherent disturbances based on observable signals such as angle, rate, motor current, etc. The plant model can be updated as required and new angle and torque profiles can be generated, either in flight or on the ground.

Another approach that is similar to the feedforward concept would be to use a Coherent Error Integrator (CEI) or CEI-like scheme to improve sounder step and settle response. The CEI is essentially a real-time, adaptive, open-loop, feedforward device which could offer the same advantages as the concept presented here. However, the CEI is currently unstable (on the GOES-I imager) and requires further research and development.

B.5 INDUCTOSYN VS. OPTICAL ENCODER TRADE STUDY

B.5.1 Background

B.5.1.2 Summary

This trade study examines the relative merits of using the inductosyn versus an optical encoder for the GOES-N sounder and imager. The conclusion is that an absolute optical encoder will yield better performance and reliability than an inductosyn and at a lower overall cost.

B.5.1.2 Functional overview

Before comparing the two devices in detail, let us briefly review the fundamental principles of operation of each device.

The inductosyn functions like a resolver with one or many electrical cycles per mechanical revolution. The inductosyn can operate in two basic modes: stator excitation or rotor excitation. In the first mode, the sine and cosine windings of the stator are excited by carrier signals whose amplitudes are proportional to the sine and cosine of the desired angle. The resulting rotor signal is proportional to the difference between the desired angle and the actual shaft angle. In this mode, the inductosyn is an error detector.

In the second mode of operation, the rotor is excited with a constant amplitude carrier signal, and the resulting stator winding signals are proportional to the sine and cosine of the shaft angle. These signals can be converted to a shaft position by a tracking convertor, or they can yield an error signal by appropriately processing them with the sine and cosine of the desired angle.

In any case, the error signal or shaft position is relative to an electrical cycle of the inductosyn, typically 1 to 3 degrees of mechanical rotation (for 360- or 128-cycle inductosyns).

An optical encoder consists of a disk and one or more read stations. The read stations typically have a light source on one side of the disk and a light detector on the other side. As the disk, which is attached to the shaft, turns, it modulates the light detected by the read station. There are two basic types of optical encoders: incremental and absolute.

A basic incremental encoder has a disk with one track containing equally spaced pulses and another track with a single index pulse. The incremental pulses are counted relative to the index pulse to determine position. The number of pulses, or cycles, per revolution determines the resolution of the encoder. To obtain more bits, the disk and read station optics are designed so the output signals are not square pulses, but sine and cosine signals. These signals can be processed to yield additional bits that indicate the position within an encoder cycle. This process is called interpolation, because it allows us to measure angles smaller than the angular increment of the encoder disk.

An absolute encoder disk has a uniquely coded track for each bit so that the read stations can always read the absolute position of the disk, without having to count cycles relative to a reference. Similar to the incremental encoder, sine and cosine tracks are included on the disk and processed electronically to extend the resolution of the absolute encoder.

B.5.1.3 GOES-I inductosyn

The GOES-I instruments use 128-cycle inductosyns in the stator-excited, error detector mode. (The systems also include single-cycle inductosyn windings to measure absolute position.) After trimming and fixed error calibration in which corrections are stored in PROMS, the inductosyn and associated electronics contributes about 6.2μ (3-sigma, mechanical) of error to the system, at end of life.

B.5.2 Inductosyn limitations

It is difficult, but possible, to obtain resolution and accuracy on the order of microradians from an inductosyn system. To achieve high performance as is required in GOES instruments, the inductosyn requires complex, critically aligned electronics. Also, the system is highly sensitive to drift in the electronics after initial alignment and calibration.

As an example of inductosyn electronics requirements, some of the GOES-I requirements are listed below:

Signal/Noise:	78dB
Isolation:	126dB
Crosstalk:	-78dB
Balance:	0.1% (over life)

As another example, consider a 360-cycle inductosyn, in which each electrical cycle corresponds to one degree of mechanical rotation. For 0.4μ of resolution, for example, the inductosyn and its electronics must be able to divide the electrical cycles into more than 40000 parts! To accomplish this with good accuracy, the electronics must meet stringent requirements.

Another limitation of the inductosyn is that it is incremental. That is, it gives an error or angle measurement relative to its electrical cycle, not based on absolute position. Knowledge of absolute position requires either an additional, one-cycle inductosyn and its associated electronics or a mechanical reference position (a "stop") from which inductosyn cycles are counted.

Although the GOES-I instruments include a single-cycle (x1) inductosyn winding, the serious problems with this system led to the use of a mechanical stop as an absolute position reference. A major problem was that the carrier signal for the single-cycle system bled through to the 128-cycle inductosyn system causing intolerable errors.

B.5.3 Proposed optical encoder baseline

Model:	equivalent to BEI L690x
Type:	Absolute
Resolution:	0.375 μ r (24 bits)
Accuracy:	1.5 μ r, rms
Fine Track:	16384 cycles/rev (14 bits)
Interpolation:	10 bits
Max Rate:	3.75 rpm
Disk:	glass
	5 inch o.d.
	2 inch i.d.
	1/8 inch thick
	0.186 lb
Read Stations:	2 fine, 1 coarse
	1 LED /station
	0.75 W /station, typical
	0.13 lb /station

B.5.4 Trade study details

B.5.4.1 Assumptions

This trade study compares several aspects of an inductosyn and an optical encoder. The study compares the two different technologies, or classes of angular encoder, rather than examining two specific units. Where the usage is unambiguous, the word "encoder" implies "optical encoder," even though the inductosyn is also considered to be an encoder.

We assume that both devices would be mounted on the system's bearings. Therefore, we do not need to consider bearing friction and shaft coupling errors.

We assume that the disk diameters are comparable: seven inches for the inductosyn and between five to seven inches for the encoder. The inductosyn with seven inch plates was selected over the 3-1/2 inch inductosyn used on GOES-I in order to make the comparison as fair as possible, since the larger model offers better performance than the smaller one.

We assume that the inductosyn has 360-cycles, which is the highest cycle count for high performance applications recommended by Farrand Controls, the original manufacturer of the inductosyn, although higher cycle counts are available. We assume the encoder has 16384-cycle sine and cosine tracks (14 bits). This is conservative since some encoders have fine tracks with as many as 36000 sine and cosine cycles. (Canon laser encoders have up to 225000 cycles. See "Recommendations and Conclusions" section of this trade study.) For a six inch diameter disk, 16384 cycles corresponds to a linear spacing of approximately 1.15 mils.

B.5.4.2 Resolution

Let us define measurement resolution as the total range of uncertainty due to signal representation and noise. Inductosyn resolution depends on the signal to noise ratio of the inductosyn and associated electronics. Encoder resolution depends on the number of bits per revolution. We could theoretically interpolate an arbitrary number of bits from the encoder sine and cosine tracks, but for all bits to be meaningful, the noise level must be smaller than the angular equivalent of 1/2 of the least significant bit. Since a given resolution is a much smaller portion of an inductosyn cycle compared to an encoder fine track cycle, the inductosyn requires a much higher signal to noise ratio to achieve the same resolution as an encoder.

INDUCTOSYN:	0.4 μ r, 83 dB S/N required
ENCODER:	0.4 μ r, 10 bit interpolation 50 dB S/N required for < 0.5 LSB NEA

B.5.4.3 Accuracy

Encoders and inductosyns have similar sources of error, but the sensitivity to these sources of error is quite different.

Although the encoder is more accurate than the inductosyn, initial performance for either system is limited by the accuracy of the equipment used for initial calibration. For GOES-I, preflight calibration is performed with a theodolite, and IAT estimates total calibration accuracy to be 4.3 μ r (3-sigma, mechanical).

Since initial accuracy of both devices is equalized by calibration, drift over the life of the system is the most important consideration. The encoder has a big advantage over the inductosyn because it has many more cycles per mechanical revolution compared to the inductosyn. All errors which are relative to the electrical or fine cycle of the device are divided by the number of cycles per revolution. For the devices under consideration, the encoder has about 45 times more cycles than the inductosyn. (For a more ambitious encoder, this advantage could be a factor of more than 100.)

The following list contains a brief description of various error sources and the magnitude of these errors for the inductosyn and encoder. Where possible, both initial (uncalibrated) error and drift (over life) estimates are given. All errors are expressed in microradians, unless noted otherwise.

1) Pattern Error:

This is due to the accuracy of the printed circuit windings on the inductosyn and the accuracy of the optical pattern on the encoder disks. Farrand Controls quotes inductosyn repeatability as 10% of the initial accuracy; we assume that encoders have comparable stability.

	Initial	Drift
INDUCTOSYN:	10	1
ENCODER:	5	0.5

2) Centering and Eccentricity Error:

These errors result from imperfect centering of the pattern on the disk and of the disk on the shaft, and from pattern eccentricity. Multiple read stations on the encoder help reject these errors, as does the 360-degree averaging effect of the inductosyn. The following errors correspond to a decentering of 0.4 mils, and no eccentricity.

INDUCTOSYN:	7	
ENCODER:	0	(>1 read station)
	67	(1 read station)

3) Plate/Disk Spacing:

The inductosyn is more sensitive to plate spacing than the encoder. BEI Motion Systems Company, a manufacturer of precision optical encoders, claims that a deviation of +/- 10 mils causes no degradation in accuracy, since their read stations use collimated light. Disk to read station spacing is 12 to 25 mils. Farrand Controls indicates that the voltage transformation ratio (VTR) of the inductosyn changes 15% per 1 mil change in plate spacing. This affects the signal to noise ratio and possibly the linearity of the inductosyn system. Inductosyn plate spacing is nominally 5 mils.

Effect of 1 mil change in spacing:

INDUCTOSYN:	15% change in VTR
ENCODER:	no effect

3) Electronics errors:

The major electronics errors include amplitude and phase imbalance between the sine and cosine signals, crosstalk between these signals, harmonic distortion, and carrier feedthrough. All of these errors are cyclic; that is, these errors repeat for every electrical cycle. Therefore, these errors are divided by the number of cycles per revolution. The following inductosyn estimates were extrapolated from the performance of the GOES-I 128-cycle inductosyn system. The encoder estimates were derived by assuming the encoder optics and electronics contribute TEN TIMES the error per electrical cycle compared to corresponding inductosyn error sources.

	<u>Initial</u>	<u>Drift</u>
INDUCTOSYN:	10	1.5
ENCODER:	2.3	0.3

4) Wire Torques:

This error source does not reflect on the accuracy of the angular encoder, per se, but it is a disturbance torque introduced into the servo system by the encoding device. On GOES-I, the effect of this torque is five times greater for the East/West axis than for the North/South axis due to the folding effect of the scanner mirror and lower East/West servo loop gain.

The encoder has no wires connecting the disk (rotor) to the read stations, since all light sources and detectors are located in the stationary read stations. Typical wire counts for a 24-bit absolute encoder with remote electronics is 12.

The inductosyn has two wires and a shield per winding. An inductosyn has at least one rotor winding and two stator windings. The rotor wires mechanically connect the rotor to the stator, resulting in a disturbance torque. Single-cycle windings included for absolute position reference and redundant inductosyn plates would increase the total number of tracks with a corresponding increase in wire torque. Inductosyns with transformer-coupled rotor windings are available and would eliminate the wire torque, but the performance may be adversely affected. Transformer-coupled inductosyns were not considered in this trade study.

The following summary lists the number of wires which contribute disturbance torques for each scanner axis, assuming no redundancy and no single-cycle inductosyn windings.

	<u>East/West</u>	<u>North/South</u>
INDUCTOSYN:	3 (E/W rotor)	12 (3 N/S rotor + 9 E/W rotor and stator)
ENCODER:	0	12 (E/W encoder)

5) Slew Rates:

The slew rates of high resolution encoders and inductosyns are limited by the electronics used to process the sine and cosine signals. The maximum slew rates for the inductosyn and encoder are comparable, and typical values for 24 bit resolution are listed below.

INDUCTOSYN:	2.7 rpm
ENCODER:	3.75 rpm

1.5.4.4 Complexity

Exclusive of electronics, the encoder has more hardware than the inductosyn. The inductosyn consists of two plates containing printed circuit windings. The encoder has one optical disk and several read stations.

Both the inductosyn and encoder require sine and cosine signals to be electronically processed to obtain very high resolution. Functionally, the electronics for the two devices are similar, but due to the much higher spatial frequency of the encoder's sine and cosine signals, the requirements of the encoder electronics are much less stringent. The tighter requirements of the inductosyn electronics translate to a more complex design.

Compared to an absolute encoder, the inductosyn needs either additional hardware or increased operational complexity to establish and maintain an absolute position.

For an absolute encoder, it may be desirable to include a serial data interface in order to minimize the number of wires. This increases complexity slightly and decreases typical readout rates from 500kHz to 35kHz.

B.5.4.5 Reliability

The encoder is more reliable than the inductosyn in several respects. The encoder is much less dependent on finely-tuned electronics to maintain its accuracy than the inductosyn. The balance, isolation, drift, etc. in encoder electronics can be an order of magnitude worse than inductosyn electronics, and the encoder will still maintain better accuracy.

An absolute encoder is much more robust to power outages and glitches which can cause an inductosyn-based system to lose its place.

Encoders are less sensitive to mechanical misalignments than inductosyns. Since the spacing between the encoder disk and read stations is greater than the inductosyn plate spacing, the encoder may be more robust to mechanical shock and moment loading. The inductosyn plates are more rugged than the encoder read stations. The inductosyn is much less sensitive to contamination.

Inductosyns have no life-limited components. The LED light sources widely used in encoders today are more reliable than the incandescent lamps used in older encoders. Life expectancy for encoder LEDs is 100000 hours, and a life 40000 hours or more has been proven.

Encoders have more space experience than inductosyns.

B.5.4.6 Power, weight, size

The power, weight and size of an inductosyn and encoder are comparable, assuming that single-cycle windings are not included in the inductosyn system. The estimates given below include the inductosyn plates, encoder optical disk, and read stations, but not the electronics. The power, weight and size of the electronics should be either comparable or slightly favoring the encoder due to its less complex design.

	<u>Power</u>	<u>Weight</u>	<u>Size</u>
INDUCTOSYN:	2 W	2 lb	7" x 5/8"
ENCODER:	2.3 W	1 lb	6" x 2-1/2"

B.5.4.7 Cost

For high performance applications such as the GOES instruments, an encoder is much more cost effective than an inductosyn. This is because high performance is readily achievable with an encoder, whereas it is very difficult to achieve comparable performance with an inductosyn.

The cost of the inductosyn plates is less than the encoder disk and read stations, but this is offset by the more complex and highly precise electronics required by the inductosyn.

In addition to parts, we must consider the cost of electronics development, testing and calibration. These activities will be less expensive for encoder electronics because the requirements are far less demanding.

Installation of the inductosyn is simpler than the encoder because it is mechanically a less complex device. However, the mechanical alignment of the inductosyn plates (centering, spacing, and parallelism) is more critical than the encoder disk alignment. The difficulty in aligning the inductosyn would increase its total cost.

B.5.5 Volume, weight, power, and cost impacts

The volume, weight and power of the encoder and inductosyn are comparable, assuming that single-cycle windings are not included in the inductosyn system.

The volume of the encoder hardware to be mounted on and around the scanner shaft is somewhat more than that of the inductosyn. The encoder electronics are the same size or smaller than inductosyn electronics.

The encoder and its electronics weigh slightly less than the inductosyn and its electronics.

Both systems consume approximately the same amount of power.

The encoder has a much smaller overall cost, including parts, development, installation, alignment, testing, and calibration, compared to the inductosyn.

B.5.6 Recommendations and conclusions

The absolute optical encoder is superior to the inductosyn in almost every respect: performance, reliability, resource consumption, and cost. Therefore, we recommend that the GOES-N sounder and imager instruments should include absolute optical encoders as the baseline shaft encoding devices.

As a future possibility, laser optical encoders should be considered. These devices can have more than 200000 cycles per revolution (before interpolation) on a 4 inch diameter disk, with accuracy, power and weight comparable to standard high-performance optical encoder. This is relatively new technology which has not been used for space applications yet, but in time, this may become the encoder technology of choice.

B.6 Digital Image and Spacecraft Motion Compensation (IMC/SMC) Interface for Imager and Sounder

B.6.1 Introduction to the GOES I-M IMC system

In the GOES-I system, the IMC corrections to the sensor's line of sight compensates for three major sources of pointing error. The largest component is correcting the East/West and North/South line of sight for the distortion caused by the fact that the spacecraft is not precisely over the equator at the proper longitude. These compensations are a function of the orbital location of the satellite and the E-W and N-S line of sight of the instrument and vary rapidly along the scan line. The second largest component is to correct thermal distortions affecting the line of sight of the instruments. These vary during the day. The third component is to correct for the disturbances in the spacecraft pointing due to the mirror motions of the sensors, especially the black body calibrations used to calibrate the Infrared channels of the instruments. This Mirror Motion Compensation (MMC) is a damped nutation in roll and yaw and has about a 3 minute period with amplitudes of up to 150 μ r. In the GOES-I system all of these compensation are computed in real time in the AOCE computer on the spacecraft using information uploaded from the ground system and sent to the instruments as an analog signal. The errors introduced by this approach are within the GOES-I allocations but are too large if the GOES-N is to meet its pointing requirements.

B.6.1.1 Description of the GOES-I IMC interface approach

In the GOES-I design, the AOCE computer generates an IMC signal consisting of a set of starting points and slopes, with a set of 8 pair of values sent to an interface box every 128 milliseconds. The slope sets the frequency of an oscillator that steps a counter that is preset to the starting point every 16 Milliseconds, etc. The value of the counter has a least significant bit value of 4 μ r. The value of this counter is converted to an analogue voltage and sent to the instrument as a signal with a maximum level of plus or minus 10 volts. For a more complete description of this system see the document GOES-I,J,K/L,M IMAGE NAVIGATION AND REGISTRATION, DRL 300-06, January 15, 1987, starting on page 3-27. In the instrument this is received in a differential amplifier, switched through the proper gain setup resistors and converted into a digital portion which goes to the inductosyn drivers and to a $\pm 8 \mu$ r analogue portion which is summed into the servo error (Figure B.6.1-1, GOES-I E-W Servo Block Diagram).

This process introduces errors in the IMC response of the instrument which are estimated to be about 5 μ r in the GOES-I system. Going to an all digital interface can significantly reduce these errors.

B.6.2 Digital IMC and SMC approaches

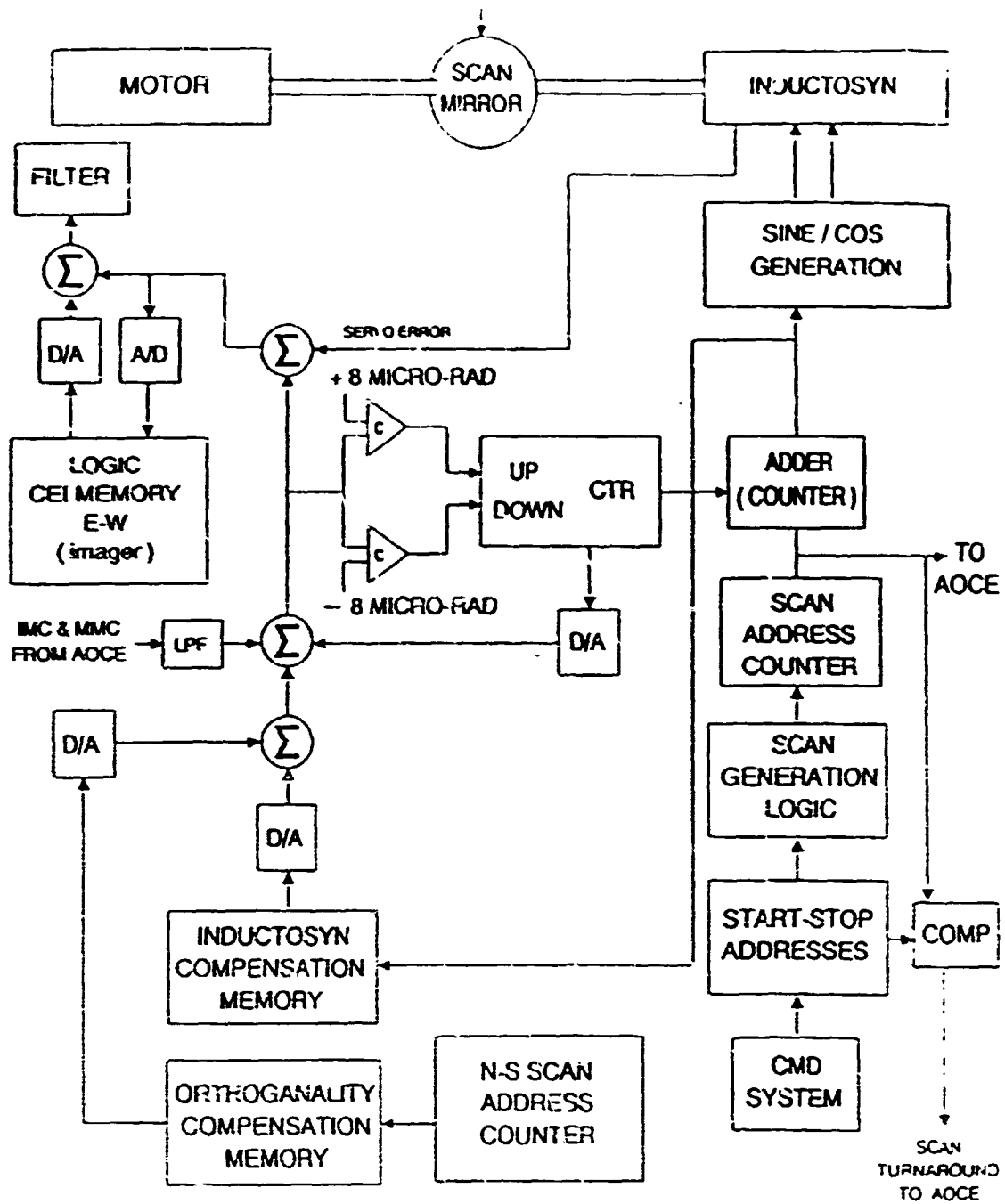


Figure B.6.1-1. GOES-I Servo Block Diagram

B.6.2.1 Approach 1

The change that provides the best total performance would be to move the IMC/SMC computation to a computer in the Imager or Sounder with the AOCE computer providing orbital location and MMC or Spacecraft Motion Compensation information in real time and the OATS ground computer providing the thermal distortion prediction data to the instrument computer once a day. This would eliminate the need for the AOCE computer to get the imager "present scan address" information and could allow generating a smoother IMC signal with smaller (or no) slope and step discontinuities as well as allowing some "look ahead" shaping of the servo driving signal to minimize errors in the servo response to the IMC. This design would significantly simplify the interface between the instruments and the control system and eliminate the interface errors of the GOES-I system (Figure B.6.2-1, GOES-N E-W Servo Block Diagram). This is the preferred approach for the New Imager and High Spectral Resolution Sounder. If the imager on the Option I or II system goes to an optical encoder then this approach is also preferred for these instruments.

This approach has a moderate to low technical risk because of the simplified interface between the spacecraft and the instrument. The weight impact should be less than 1kg. There will be a modest recurring cost impact because the instrument will have its own computer. There will be a significant non recurring cost in developing the software and hardware required.

B.6.2.2 Approach 2

If the Option I imager retains the present inductosyn encoders, then a simpler modification to provide a digital IMC interface may be adequate. This would be to send the "point-slope" values from the AOCE computer to the instrument, rather than to an AOCE interface box. New hardware would be required to send this data to the instrument and to expand this point-slope information in the Imager digitally and sum it with the address counters and generate an analogue residual of $\pm 8 \mu$ which would be combined with the servo error and other instrument compensations.

This approach has a low technical risk with a weight impact of less than 1kg and modest non-recurring and recurring costs.

B.6.2.3 Approach 3

The point-slope approach used degrades the servo performance because of the small (about 2μ) discontinuities that occur at the end of every straight line slope and the slope changes which occur every 16 milliseconds. An improvement would be to use a small computer in the Imager to take the point-slope data and generate a smooth curve by interpolating between the end points using a higher order fit to the data. This could reduce the interface error to about 1 microradian.

This approach has slightly higher risks, weight and costs than B.6.2.2.

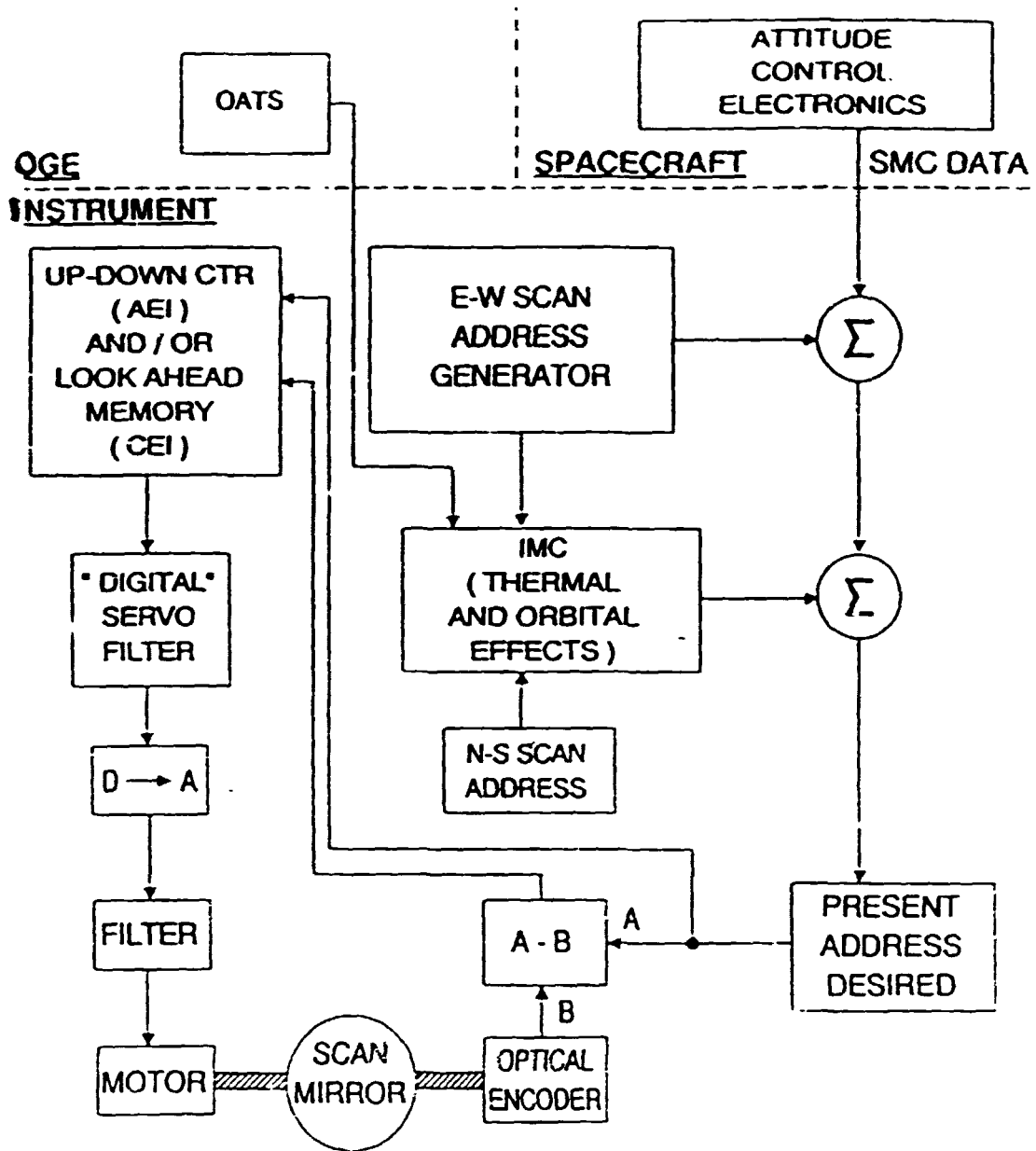


Figure B.6 2-1. GOES-N: East/West Servo Block Diagram

B.7 EAST/WEST FLEX PIVOT DESIGN STUDY

B.7.1 Introduction

B.7.1.1 Task objective

This task investigated the feasibility of using flex pivots and magnetic actuation to implement the E/W imager scan motion.

B.7.1.2 Rationale

The goal of this design approach is to eliminate the potential failure mode associated with lubricant degradation and wear debris generation resulting from the limited rotation and boundary film conditions of the E/W fast scan bearings. In addition to the enhanced lifetime and reliability, flexures eliminate all possibility of contamination due to lubricant outgassing. Additionally, they provide very linear and repeatable torque characteristics which completely eliminate concerns about bearing torque noise which may limit scan accuracy.

The proposed implementation of the E/W scan assumes closed loop position servo control using feedback from a high density optical encoder. The drive motor is a limited angle D.C. torque motor with a rare earth permanent magnet rotor.

The flex pivot approach has the potential for superior smoothness, accuracy, and life compared to previous ball bearing based scanners.

B.7.2 Design considerations

B.7.2.1 Known flex-pivot characteristics

Based upon the successful Landsat thematic mapper application, cross flexure pivots (formerly available from Bendix, now from Lucas Aerospace) can meet the ruggedness and life requirements of the GOES scanner.

The thematic mapper mirror is roughly the same size and weight as the GOES, therefore, the previous qualification for flight loads is valid. It is recommended that close fitting sleeves be utilized to limit transverse deflection as was done for the thematic mapper and COBE mirror transport mechanism.

Similarly, the demonstrated cycle life of the thematic mapper flexures exceeds that of a 10 year GOES mission by a factor of five. Additionally, deflection amplitude is slightly less for the GOES case.

Spring characteristics of the flexures are easily measured and are stable over life. Thus, the spring torque can be readily compensated for in the servo design by means of an offsetting current which is a function of position.

Flex pivots have a center shift characteristic as a function of rotation angle. (Figure B.7.2.2-1). If the two pivots are aligned such that the Y direction is normal to the mirror surface, the theoretical center shift for a 5 degree rotation is only 10 microinches. Since the pivots move together even this small translation theoretically cancels out. Practically, due to variations in blade thickness and alignment, center shifts of the order of .0001 inch can be expected in the Y direction. Assuming a 12" separation of pivots this would amount to $\pm 16 \mu$ cross axis error. Careful measurement and matching of pivots can reduce this by a factor of three or more.

B.7.2.2 Drive assembly

A conceptual arrangement for the flex pivot drive assembly is shown in Figure B.7.2.2-2. Identical drive units could be mounted at each side of the scan mirror for redundancy. One of the drive housings should be mounted on a two blades flexure mount which will allow motion along the rotation axis to prevent thermal gradients between the mirror and support structure causing axial over-stressing of the flex pivots.

B.7.2.3 Outstanding questions

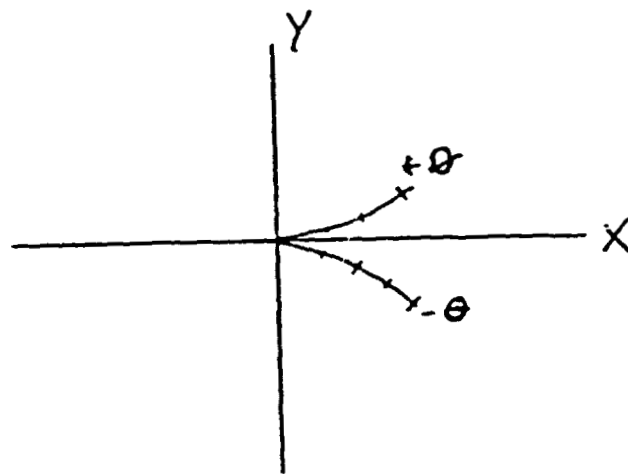
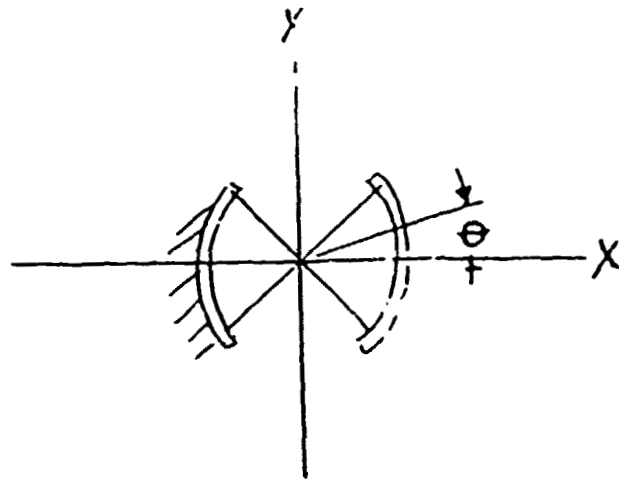
The principal question relative to the flex pivot scanner is the tolerance of the high density encoder to the large decentering motion in the X transverse direction. As tabulated in Table B.7.2.2-1, this is of the order of .00034 inches, a factor of three greater than recommended by encoder suppliers.

Table B.7.2.2-1

Mounting Accuracy Requirements For High Accuracy Optical Encoders (Typical 14000 Line/Revolution Encoder)

	MAX RUNOUTS	
TYPICAL ENCODE SPECIFICATION	RADIAL	.001 INCH
	FACE	.005 INCH
EXPECTED FOR 5/8" FLEX PIVOT (MATCHED PAIR)	RADIAL	.00034 INCH
	FACE	.0001

The readout error caused by the center-shift can be approximated (Figure B.7.2.2-3). Assume two encoder read stations located at 180 deg apart. The encoder output is the average of the two read stations. With no center shift the encoder output is $S+S/2 = S$. Assuming (conservatively) a .0005" center shift and precisely 5 deg actual rotation, the encoder output is $S+\Delta S$ where ΔS is $.0005 \times \sin 5 \text{ deg}$ (very nearly).



$$X = 2.15 \times 10^{-5} \theta^{0.5} D \cos \theta/2$$

$$Y = 2.15 \times 10^{-5} \theta^{0.5} D \sin \theta/2$$

For 5/8" Flex Pivot 5 deg Rotation

$$X = .00034"$$

$$Y = .00001"$$

Figure B 7 2.2-1 Flex Pivot Center Shift

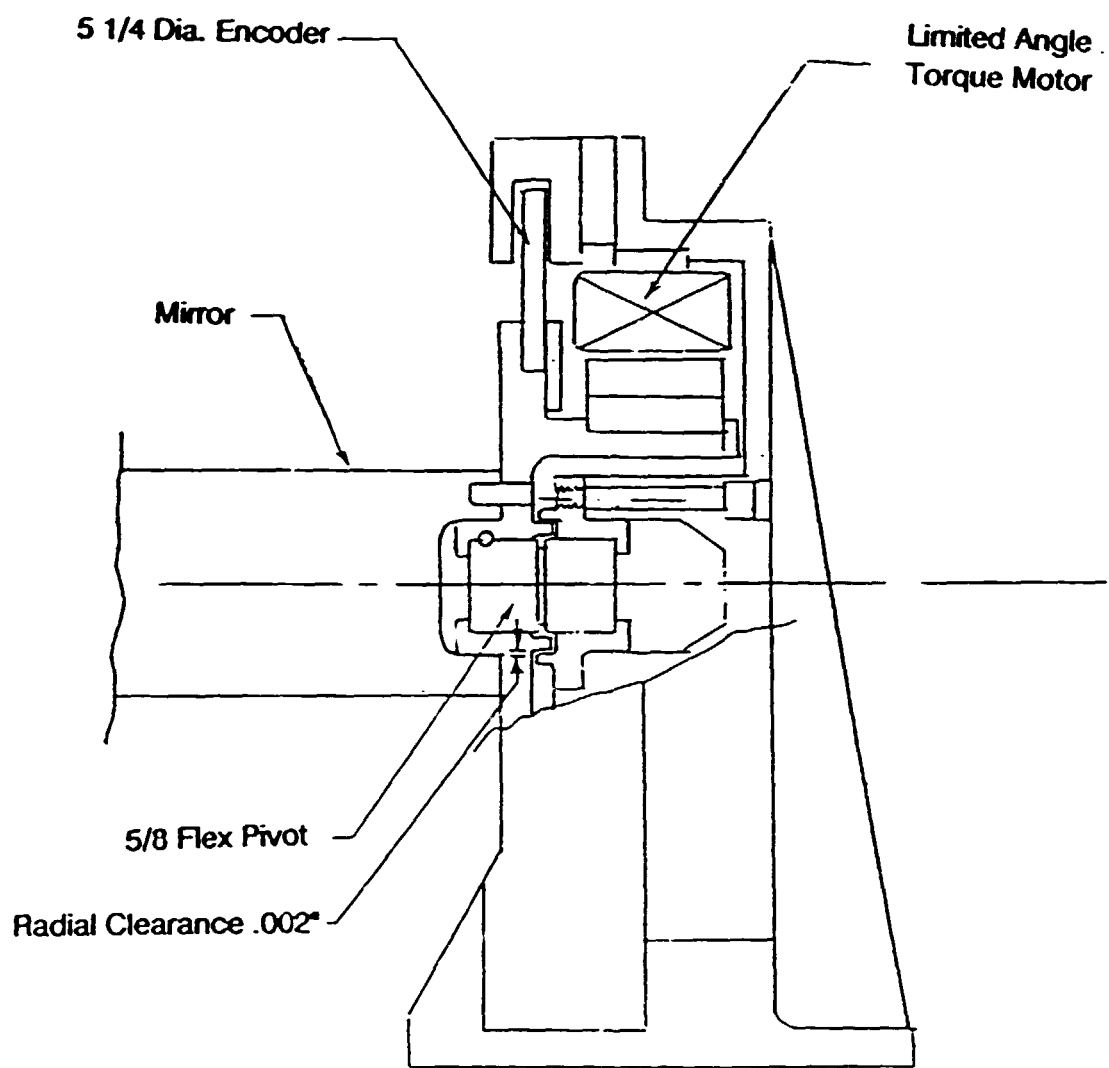


Figure B.7.2.2-2. Flex Pivot Drive Assembly

A. Typical Encode Specification

Max Runouts

Radial .0001 Inch

Face .0005 Inch

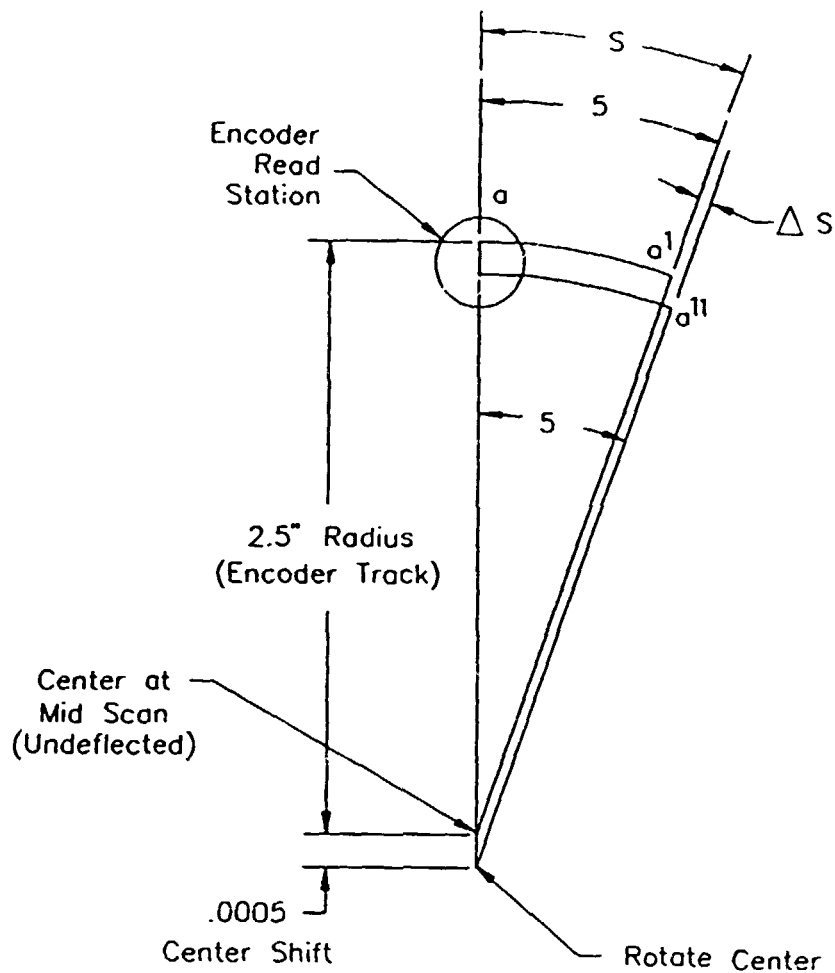
B. Expected for 5/8" Flex Pivot (Matched Pair)

Max Runouts

Radial .00034 Inch

Face .0001

Figure B.7.2.2-3. Mounting Accuracy Requirements for High Accuracy Optical Encoders



$$\text{ERROR } \theta \cong \frac{\Delta S}{R} \cong \frac{.0005 \sin 5^\circ}{2.5} = .000017 \text{ RADIANS}$$

ASSUMING FACTOR OF 10 COMPENSATION BY
READ STATION 180° FROM ONE SHOWN —

$$\theta \text{ ERROR } \cong .0000017 \text{ (2 } \mu\text{RAD)}$$

Figure B.7.2.2-4 Readout Error Caused by Flex Pivot Center-Shift

The encoder output from the single station would be in error by $\pm \Delta S$ or .000017 radians. Since a station at 180 deg would output $S - \Delta S$ the average of the two readouts would be exactly S and the error is canceled.

B.7.3 Conclusions

It is concluded that a flex pivot suspended scan system is feasible. In view of the life uncertainties associated with intermittent limited angle rotation of ball bearings it appears relatively attractive. Further investigation and (desirably) experimental verification of the achievable accuracy of a high density optical encoder suspended on flex pivots is indicated before a commitment is possible.

APPENDIX C

C.1 DISCUSSION OF ALLOCATION OF NAVIGATION, INFRAME REGISTRATION, AND IMAGE-TO-IMAGE ERROR BUDGET OVERVIEW

C.1.1 Purpose

The purpose of a system performance allocation is to distribute (allocate) errors and help identify the key areas in each design concept that will limit or prevent the system from meeting NOAA's requirements; these areas are then studied to determine if techniques are available to improve the performance or if there are other design approaches that do not have the same limitations. The system performance allocation also is a significant aid in identifying those requirements which will be difficult to achieve (i.e., high risk, cost and/or schedule impacts to one or more subsystems).

C.1.2 Background

The GOES I-M and Option I system performance allocations parallel the allocation developed by Dr. K.P. Bhat of FAC for the GOES-I system. This allocation is for pixel(s) at 60 deg Earth Central Angle (ECA) and an inclination of 0.1 deg. The Option II and III performance allocations are also based on the GOES-I allocation, but have been modified to better represent a star tracker/gyro control system. However, many of the performance values have been extrapolated or used as is from the GOES-I allocation for the GOES-N performance. This provides a measure of confidence in the GOES-N allocations, since almost all of the GOES-I allocations are based on analysis or test.

C.1.3 Organization of material

The material in the following sections is organized as follows:

- Section C.2 describes the individual error sources and discusses how the individual error sources are combined to provide the navigation, within frame registration, and the image to image registration allocations.
- Section C.3 presents the three conceptual GOES-N systems with increasing performance capabilities. The rationale for the improvements in the respective error sources changed in each of the conceptual GOES-N systems is provided.
- Section C.4 presents the results of the four system performance analyses. Note that the results of the analyses are discussed in Section 10 in the main body of the Report.

C.2 DESCRIPTION OF SYSTEM PERFORMANCE ALLOCATION ERROR SOURCES

C.2.1 Option I and GOES I-M

C.2.1.1 General

The GOES I-M and Option I systems are identical except for the performance of the Earth Sensor. In the Option I system the Earth Sensor performance is better by the square root of two; this performance improvement is considered conservative, and is based on implementing only 1 of the 3 recommendations for improving the GOES-I performance (Refer to Appendix A.2.1). Since the two systems are identical except for the Earth Sensor performance, the following discussion applies to both the GOES-I and Option I systems.

The GOES-I (Option I) allocation is divided into short and long term effects, which affect the instrument pointing at each pixel location. In all cases, the various errors are combined on a root sum square (RSS) basis. The overall results of root sum squaring agree reasonably well with the performances determined from the simulation programs developed by FAC and NASA for the GOES I-M system.

The differentiation between the short and long term budget in the GOES-I allocations groups effects that have time durations of less than or about the same amount as the nutation period (about 180 seconds), and greater than the nutation period.

It is important to note in the allocations that mispointing affects both the image being taken and the determination of star and landmark locations. The star and landmark locations are used to predict the pointing positions for compensating orbit and thermal effects for the following day. The following paragraphs summarize the various error term contributions.

C.2.1.2 Short term errors

C.2.1.2.1 Attitude stability (Line 9⁵)

The spacecraft attitude stability is comprised of (1) tachometer noise and the response to noise by the Earth Sensor and (2) the effects of dynamic interaction. Dynamic interaction includes effects from rigid body motion (e.g., solar array stepping and instrument mirror motion), momentum wheel imbalance, and nonrigid body motions due to the flexibility of the appendages.

C.2.1.2.2 Mirror Motion Compensation (MMC) errors (Line 19)

MMC error is the difference or residual error remaining after correcting for the effects on the spacecraft due to the movement of either instrument mirror (e.g., the difference between the applied compensation for a black body calibration and the actual movement).

⁵ Refers to Lines in Tables C.2.1-1, C.2.1-2 and C.2.1-3.

1	Spec - GOES-M Req't	112 uR
2	File Name NAV-REV	GOES I-M
3	Imager Navigation	
4		
5	COMBINED SHORT&LONG TERM	43.1
6		
7	SHORT TERM	28.9
8		
9	ATT. STAB.	22.0
10	ES/IRU NOISE	20.0
11	DYN. INTER.	9.1
12	RIGID BODY	6.4
13	SA STEPPING	4.0
14	MIRR.MOTION	5.0
15	OTHER	0.0
16	MW IMBALANCE	5.0
17	NONRIGD.BODY	4.0
18		
19	IMC COMP.ERR	7.0
20	IMC COMP.ERR	5.0
21		
22	INGR.POINT	15.9
23	IMC SERVO ERROR	4.0
24	IMC PRGC.ERR	7.0
25	INTER.TORQ	2.1
26	CNT.DRIFT	0.4
27	QUAD.ERRORS	0.0
28	LINEARITY	3.5
29	LINEARITY BIAS	12.0
30	NOISE/JITTER	2.0
31	STEP/SETTLE	1.0
32	DET.ROTATION	4.2
33	VIDEO DELAY	2.0
34	AOCE INTERFC	4.9
35	LINE NOISE	4.0
36	LPFILTER LAG	2.0
37	DAC ERROR	2.0
38		
39	LONG TERM ORBIT/ATTITUDE	32.0
40		
41	PERFECT O/A DETERMIN	26.0
42	(From INR Simulator)	
43		
44	NONRPTL. & O/A MOD. W/	18.7
45	ORBIT/ATTITUDE MODEL	30.0
46	THERM(IM&SC)	30.0
47	MODEL PARAMTR	0.0
48	NONRPTBL.ERR	81.9
49	CLOUD/RADGRD	70.0
50	HEATER OPS.	30.0
51	S/C YAW	30.0

Table C.2.1-1. GOES i-M (Option I) Navigation Error Allocation Budget
Pixel Location Accuracy

1	Spec - GOES-N Req't	42 μ R
2	File Name INFR-REV	GOES I-M
3	Imager Navigation	
4		
5	COMBINED SHORT&LONG TERM	49.7
6		
7	SHORT TERM	40.8
8		
9	ATT. STAB.*1.41	31.0
10	ES/IRU NOISE	20.0
11	DYN. INTER.	9.1
12	RIGID BODY	6.4
13	SA STEPPING	4.0
14	MIRR.MOTION	5.0
15	OTHER	0.0
16	MW IMBALANCE	5.0
17	NONRIGD.BODY	4.0
18		
19	IMC COMP.ERR*1.41	9.9
20	IMC COMP.ERR*1.41	7.0
21		
22	INGR.POINT * 1.41	22.5
23	IMC XVO ERROR	4.0
24	IMC PROC.ERR	7.0
25	INTER.TORQ	2.1
26	CTT.DRIFT	0.4
27	QUAD.ERRORS	0.0
28	LINEARITY	3.5
29	LINEARITY BIAS	12.0
30	NOISE/JITTER	2.0
31	STEP/SETTLE	1.0
32	DET.ROTATION	4.2
33	VIDEO DELAY	2.0
34	AOCTE INTERFC*1.41	6.9
35	LINE NOISE	4.0
36	LPFILTER LAG	2.0
37	DAC ERROR	2.0
38		
39	LONG TERM ORBIT/ATTITUDE	28.5
40		
41	PERFECT O/A DETERMIN	26.0
42	(From INR Simulator)	
43		
44	NONRPTL.& O/A MOD. W/	11.6
45	ORBIT/ATTITUDE MODEL	8.0
46	THERM(IM&SC)	8.0
47	MODEL PARAMTR	0.0
48	NONRPTBL.ERR	14.1
49	CLOUD/RADGRD	6.0
50	HEATER OPS.	8.0
51	S/C YAW	10.0

Table C.2.1-2. GOES I-M (Option I) Within Frame Relative Pixel-to-Pixel Location Error Allocation Budget.

1	Spec - GOES-N Req't	84/105 uR
2	File Name REG-RCV	GOES I-M
3	Imager Navigation	
4		
5	COMBINED SHORT&LONG TERM	45.9
6		
7	SHORT TERM	35.6
8		
9	ATT. STAB.*1.41	31.0
10	ES/IRU NOISE	20.0
11	DYN. INTER.	9.1
12	RIGID BODY	6.4
13	SA STEPPING	4.0
14	MIRR.MOTION	5.0
15	OTHER	0.0
16	MW IMBALANCE	5.0
17	NONRIGD.BODY	4.0
18		
19	IMC COMP.ERR*1.41	9.9
20	IHC COMP.ERR*1.41	7.0
21		
22	IMGR.POINT	10.5
23	IMC SERVO ERROR	4.0
24	IMC PROC.ERR	7.0
25	UNTER.TORQ	2.1
26	CKT.DRIFT	0.6
27	QUAD.ERRORS	0.0
28	LINEARITY	4.9
29	LINEARITY BIAS	0.0
30	NOISE/JITTER	2.8
31	STEP/SETTLE	0.0
32	DET.ROTATION	0.0
33	VIDEO DELAY	2.8
34	AOCE INTERFC*1.41	6.9
35	LINE NOISE	4.0
36	LPFILTER LAG	2.0
37	LAC ERROR	2.0
38		
39	LONG TERM ORBIT/ATTITUDE	28.9
40		
41	PERFECT O/A DETERMIN	26.0
42	(From INR Simulator)	
43		
44	NONRPTL. & O/A MOD. W/	12.6
45	ORBIT/ATTITUDE MODEL	12.0
46	THERM(IM&SC)	12.0
47	MODEL PARAMTR	0.0
48	NONRPTBL.ERR	22.6
49	CLOUD/RADGRD	14.0
50	HEATER OFS.	10.0
51	S/C YAW	15.0

Table C.2.1-3. GOES I-M (Option 1) Relative Image-to-Image Registration Error Allocation Budget

C.2.1.2.3 Image Motion Compensation (IMC) errors (Line 20)

The IMC error sources in this category are due to numerical approximations in the IMC calculations in the on board computer (e.g., the approximation of the required IMC correction needed along each scan line) and timing mismatch between the application of the compensating signal and when the correction should have been applied. Most of the error is due to implementation/choice of computer and does not appear in the GOES-N allocation.

C.2.1.2.4 Instrument pointing errors (Line 22)

Instrument pointing errors are related to the design of the instrument pointing control (See the ITT prepared "GOES CDR - Scanner," 5/5/88, for a discussion of these errors). These errors are used in the Option II and III allocations for the two GOES-N proposed implementations. They include:

- Servo response to IMC signal
- IMC processing errors and turn around discontinuity
- Internal torque disturbances
- Short term circuit drift
- Quadrature errors
- Linearity errors due to random and bias sources
- Noise and jitter errors
- Step and settle errors
- Detector rotation errors
- Video delay errors

C.2.1.2.5 Attitude/Orbit Control Electronics (AOCE) interface errors (Line 34)

The AOCE interface errors include line noise effects, low pass filter lag effects, and digital-to-analog converter errors. These errors are also primarily due to the current implementation, and will be significantly smaller in the GOES-N design.

C.2.1.3 Long Term Errors

C.2.1.3.1 Orb: Attitude Determination with Perfect Attitude Model (Line 41)

The long term error source accounts for the error between the true orbit and attitude (O/A) and the O/A determined by periodic measurements of stars, landmarks, and range. A perfect attitude model is assumed; the following Section C.2.1.3.2 accounts for the non-perfect attitude, where "perfect attitude" refers to having all the required terms in the model necessary to perfectly represent the time distortion. The measurements of stars and landmarks are corrupted by noise, systematic errors (e.g., incorrect landmark locations in the data base) and non-repeatable errors resulting from cloud, radiance gradient and/or heater induced thermal effects which are not related to a 24 hour cycle. These measurements then result in an incorrect estimate of the orbit and attitude for the next 24 hour period.

The complexity of the interrelationship between the measurements of stars, landmarks, and range throughout a 24 hour period and the determination of the O/A from these measurements precludes the use of a RSS technique for determining the mean and variance of the O/A error. As a result, this long term error source has been determined for a number of cases from both a NASA and FAC simulation. The simulations exhibit excellent agreement.

C.2.1.3.2 Non-repeatable and O/A modeling errors with short span attitude adjustment (SSAA) (Line 44)

The combined error resulting from O/A Modeling Errors and Non Repeatable Errors (Sections C.2.1.3.3 and C.2.1.3.4) are monitored during normal operations and, if the combined error exceeds 10 μ r for (say) a 2 hour period, biases are introduced to correct the pointing to be within 20 μ r (c.f., Section C.2.1.4.1 for additional explanation of this technique). This periodic SSAA correction has been shown to be capable of keeping the O/A Modeling and Non Repeatable Errors to within an allowable tolerance.

C.2.1.3.3 Modeling errors (Line 45)

This error source accounts for the deviation from the model for the perfect attitude assumed in the previous subsection. Specifically, the attitude model determined from the previous days measurements of stars, landmarks and range will be in error during the day because the combination of the Fourier Series and other terms is not sufficient to exactly represent the derived attitude.

C.2.1.3.4 Non-repeatable errors (Line 48)

Similar to but of greater magnitude than the sources of the modeling errors above are (1) non repeatable errors from clouds and radiance gradients that affect the Earth Sensor, (2) spacecraft heater operations which occur at different times on different days and modify the alignment between the Earth Sensor and instrument, (3) non repeatable thermal distortions (e.g., effects on pointing caused by hysteresis in thermal heating and cooling), (4) spacecraft yaw offsets primarily due to variations in the magnetic field, and (5) seasonal variations.

C.2.1.4 Combining error sources for navigation, within frame registration and image-image registration (Option 1)

C.2.1.4.1 Navigation allocation budget

Navigation pertains to the determination of the location of each pixel (S-480-19A, GOES I-M Specification).

The navigation allocation budget is generated by adding the square of each error source and taking the square root (i.e., RSS). Refer to Table C.2.1-1.

The long term, non repeatable error due to clouds, radiance gradients, and spacecraft heater operations are not used directly in the RSS process. This error is first attenuated by a short span attitude adjustment (SSAA) correction. SSAA is based on an examination of residual errors from star and landmark locations, re: expected locations as predicted by the previously determined O&A set. When a bias greater than about 10 μ r is found in any 2 (or 3) hour period, it is assumed that this bias will continue for the next 2 (or 3) hours. This bias is then used to change the zero ordered terms in the Fourier series representation of the Image Motion Compensation (IMC), which constantly corrects the pointing of the instrument mirrors to account for orbit/attitude changes.

Based on simulations, SSAA is expected to keep the O/A Modeling and Non Repeatable error sources under 20 μ r, whenever the error exceeds 10 μ r. As a result, this error term has been approximated by using the total non repeatable error if it is less than or equal to 10 μ r, and using $(10 + 0.1 * \text{error})$ when the error exceeds 10 μ r.

C.2.1.4.2 Within frame registration

Within frame registration pertains to the geometric relationship between pixels in the same image (See S-480-19A, GOES I-M Specification).

The within frame registration allocation is comprised of all the short and long term error sources presented in Sections C.2.1.2 and C.2.1.3 combined as follows (Refer to Table C.2.1-2):

- The short term error sources (i.e., error sources with periods less than 180 seconds) are multiplied by the square root of 2 (i.e., RSS with themselves) to account for the independent movement of any two separated pixels.
- The long term errors cause pixels taken at a later time to move relative to earlier pixels; the maximum error within a 25 minute period (the longest duration of a single image) were determined from the INR simulations for the O/A Determination error source, and from the worst case changes in the thermal curves and yaw effects for the Modeling and Non Repeatable errors.

C.2.1.4.3 Image-Image registration

Image-Image registration is the location relationship between the same pixel in two different images of the same geographical area (S-480-19A, GOES I-M Specification).

Since image-image registration compares the same two pixels in two different images, the slowly changing or invariant errors associated with imager pointing tend to cancel; and, in the case of linearity bias, the error cancels just about completely. The remainder of the short term error sources are the same as for the navigation error budget allocation. Refer to Table C.2.1-3.

The long term errors are treated in the same way as for the Within Frame Registration. These error sources have somewhat larger values in Image-Image Registration because of the longer time period of 90 minutes as compared with 25 minutes for the Within Frame Registration.

C.2.2 Options II and III (GOES-N):(Refer to Tables C.2.2-1 through C.2.2-6)

C.2.2.1 General

The GOES-N allocation for Options II and III divides the error into two main categories; one for errors related to satellite attitude stability and a second for errors related to instrument mispointing. The error from the two categories are combined on a RSS basis to give a system total, as for GOES-I/Option I.

C.2.2.2 Satellite attitude stability errors

The satellite attitude stability category characterizes error due to the spacecraft attitude controller and structural effects, both rigid body and flexible. Because the Option II and III systems use the same spacecraft bus and IRU/star tracker system, the budget entries for Options II and III are identical in this category. Sections C.2.2.2.1 through C.2.2.2.3 detail the major sources of error which fall into this category.

C.2.2.2.1 Attitude control (Line 8)

The attitude control error specifies errors resulting from imperfections in the attitude control process. Attitude control error is attributed to four sources: star catalog locations, attitude estimation, control law execution, and reaction wheel tachometer operation. The errors from these four sources are combined using an RSS process to give a final total for attitude control.

The first source, star catalog location error, causes star tracker readings to be referenced incorrectly. The commanded attitude is therefore in error, and the controller aligns the spacecraft to an orientation which is not inertially correct, even in the absence of other errors.

The second source describes errors from the attitude estimation process. Attitude estimation is imperfect because of gyro noise and drift, errors in star measurements, misalignment of the sensors, and ephemeris uncertainty. The ephemeris uncertainty ($9.9 \mu\text{r}$) is based on an RSS of the error associated with GPS hybrid ranging ($9.7 \mu\text{r}$) and a worst case estimate for error caused by thruster firings which eliminate the torque bias caused by solar pressure on the solar array ($2.0 \mu\text{r}$).

The third source represents error from quantization effects and computation delay in the execution of the control law. The final source is error resulting from reaction wheel tachometer quantization and noise.

C.2.2.2.2 Dynamic interaction - rigid body (Line 22)

Error due to rigid body dynamic interaction arises from two sources. First, motion of the Imager and Sounder mirrors causes spacecraft motion, thus producing attitude errors. Because there are two instruments producing uncorrelated residual motion, this error component has been multiplied by the square root of two to represent the RSS of the equal variance from each instrument.

1 REVISED GOES 4 BUDGET. IRU/STAR TRACKER
2 FILE NAME: IRU_NAV2.W01
3
4
5
6
7
8
9
10
11
12
13
14
15
16
17
18
19
20
21
22
23
24
25
26
27
28
29
30
31
32
33
34
35
36
37
38
39
40
41
42
43
44
45
46
47
48
49
50
51
52
53
54
55
56
57
58
59
60

	4TH LEVEL	3RD LEVEL	2ND LEVEL	1ST LEVEL
TOTAL - 1ST LEVEL W/ 50% MARGIN				34.0
TOTAL - 1ST LEVEL				22.6
SAT. ATTITUDE STABILITY				14.4
ATTITUDE CONTROL			12.2	
STAR CATALOG LOCATION ERROR		4.0		
ATTITUDE ESTIMATION		11.1		
GYRO NOISE (#)	0.7			
GYRO DRIFT	0.0			
STAR HSNMT. ERROR	0.0			
EPHEMERIS UNCERTAINTY	9.9			
RESIDUAL MISALIGNMENT	4.9			
CONTROL LAW		1.7		
QUANTIZATION	1.4			
COMPUTATIONAL DELAY	1.0			
REACTION MNL./TACH. PERFORMANCE		2.8		
TACH. QUANTIZATION	2.0			
TACH. NOISE	2.6			
DYNAMIC INTERACTION - RIGID BODY			4.3	
INCL/SIDR UNCOMP. HIROR MOTION*1.41		6.0		
RESIDUAL HIROR MOTION	4.2			
RESIDUAL MODELING ERROR	0.0			
RV IMBALANCE/FRICTION		2.0		
SOLAR ARRAY STEPPING		0.0		
DYNAMIC INTERACTION - NON RIGID BODY			4.1	
HIROR MOTION		1.0		
THERMAL SHAPPING		4.0		
OTHER		0.0		
MOTION COMPENSATION - INSTR.POINTING				17.5
INC (24 HOUR PERIODIC CORRECTIONS)			12.9	
S/C INTERFACE		2.0		
TIMING MISMATCH				
NUMERICAL APPROXIMATION				
PERFECT Q/A DETERMIN		2.0		
Q/A MODEL & NONOPTL. ERR (W/SSAA)		12.5		
ORBIT/ATTITUDE MODE.	25.0			
THERMAL (INSTR. & OPT. BENCH)	25.0			
MODEL PARAMETERS	0.0			
NONOPTL. ERR	5.0			
HEATER OPS.	5.0			
INC - BEAR REAL TIME COMPENSATION			4.5	
41 FREQ GYRO NOISE		1.4		
SAMPLING		1.4		
PARAMETER MISMATCH		4.0		
INSTRUMENT POINTING			11.0	
INC & SMC SERVO ERR. R = 1.41		2.8		
PROCESSING ERROR		2.0		
INTER.TORG		2.0		
JET.DRIFT		0.4		
QUAD.ERRORS		0.0		
LINEARITY		0.8		
LINEARITY BIAS		8.8		
NOISE/JITTER		2.0		
STEP/SETTLE		1.0		
JET.ROTATION		4.2		
VIDEO DELAY		2.0		

60 (#) INCLUDES EFFECTS OF GYRO DRIFT & STAR HSNMT. ERROR AFTER KALMAN FILTERING.

Table C.2.2-1. Option II Navigation Error Allocation Budget: Pixel Location Accuracy

1 REVISED GOCS = BUDGET. IRU/STAR TRACKER				
2 FILE NAME: IRU_REC2.WR1				
3				
	4TH LEVEL	3RD LEVEL	2ND LEVEL	1ST LEVEL
4				
5	TOTAL - 1ST LEVEL W/ 50% MARGIN			32.7
6	TOTAL - 1ST LEVEL			21.8
7	SAT. ATTITUDE STABILITY			13.1
8	ATTITUDE CONTROL		7.5	
9	STAR CATALOG LOCATION ERROR		5.0	
10	ATTITUDE ESTIMATION		5.1	
11	GYRO NOISE * 1.4142 (#)	1.0		
12	GYRO DRIFT	0.0		
13	STAR HSWMT. ERROR	0.0		
14	EPIHEMERIS UNCERTAINTY	5.0		
15	RESIDUAL MISALIGNMENT	0		
16	CONTROL LAW * 1.41		2.4	
17	QUANTIZATION	1.4		
18	COMPUTATIONAL DELAY	1.0		
19	REACTION WML./TACH. PERFORMANCE*1.41		4.0	
20	TACH. QUANTIZATION	2.0		
21	TACH. NOISE	2.0		
22	DYNAMIC INTERACTION - RIGID BODY*1.41			8.9
23	INCR/SWDR UNCOMP. ERROR MOTION*1.41		6.0	
24	RESIDUAL RIBBON MOTION	4.2		
25	RESIDUAL MODULING ERROR	0.3		
26	RU IMBALANCE/FRICTION		2.0	
27	SOLAR ARRAY STEPPING		0.0	
28	DYNAMIC INTERACTION-NON RIGID BODY*1.41			5.8
29	RIBBON MOTION		1.0	
30	THERMAL SHAPPING		4.0	
31	OTHER		0.0	
32	MOTION COMPENSATION - INSTR.POINTING			17.5
33	INC (24 HOUR PERIODIC CORRECTIONS)			15.2
34	S/C INTERFACE		2.0	
35	TIMING MISMATCH			
36	NUMERICAL APPROXIMATION			
37	PERFECT Q/A DETERMIN		10.0	
38	Q/A MODEL & NONOPTL. ERR (W/SSAA)		11.3	
39	ORBIT/ATTITUDE MODEL	12.0		
40	THERMAL (INSTR. & OPT. BENCH)	12.0		
41	MODEL PARAMETERS	0.0		
42	NONOPTL.ERR	5.0		
43	HEATER OPS.	5.0		
44	SHC - NEAR REAL TIME COMPENSATION*1.41			6.3
45	HI FREQ GYRO NOISE		1.4	
46	SAMPLING		1.4	
47	PARAMETER MISMATCH		4.0	
48	INSTRUMENT POINTING			5.8
49	INC & SHC SERVO ERROR * 1.41		2.8	
50	PROCESSING ERROR		2.0	
51	INTER.TORG		2.0	
52	CXT.DRIFT * 1.41		0.6	
53	QUAD.ERRORS		0.0	
54	LINEARITY * 1.41		1.1	
55	LINEARITY BIAS		0.0	
56	NOISE/JITTER * 1.41		2.8	
57	STEP/SETTLE		0.0	
58	DET.ROTATION		0.0	
59	VIDEO DELAY * 1.41		2.8	
60	#) INCLUDES EFFECTS OF GYRO DRIFT & STAR HSWMT. ERROR AFTER KALMAN FILTERING			

Table C.2.2-2. Option II Within Frame Relative Pixel-to-Pixel Location Error Allocation Budget

1 REVISED GOES 4 BUDGET: IRU/STAR TRACKER
2 FILE NAME: IRU_NAV3.W01
3
4
5
6
7
8
9
10
11
12
13
14
15
16
17
18
19
20
21
22
23
24
25
26
27
28
29
30
31
32
33
34
35
36
37
38
39
40
41
42
43
44
45
46
47
48
49
50
51
52
53
54
55
56
57
58
59
60 (#) INCLUDES EFFECTS OF GYRO DRIFT & STAR MSMT. ERROR AFTER KALMAN FILTERING

	4TH LEVEL	3RD LEVEL	2ND LEVEL	1ST LEVEL
TOTAL - 1ST LEVEL W/ 50% MARGIN				32.6
TOTAL - 1ST LEVEL				21.8
SAT. ATTITUDE STABILITY				14.4
ATTITUDE CONTROL			12.2	
STAR CATALOG LOCATION ERROR		4.0		
ATTITUDE ESTIMATION		11.1		
GYRO NOISE (#)	0.7			
GYRO DRIFT	0.0			
STAR MSMT. ERROR	0.0			
EPHEMERIS UNCERTAINTY	9.9			
RESIDUAL MISALIGNMENT	4.9			
CONTROL LAW		1.7		
QUANTIZATION	1.4			
COMPUTATIONAL DELAY	1.0			
REACTION MNL./TACH. PERFORMANCE		2.8		
TACH. QUANTIZATION	2.0			
TACH. NOISE	2.0			
DYNAMIC INTERACTION - RIGID BODY			6.3	
INCL/SIDR UNCOMP. MIRROR MOTION * 1.41		6.0		
RESIDUAL MIRROR MOTION	4.2			
RESIDUAL MODELING ERROR	0.0			
RV IMBALANCE/FRICTION		2.0		
SOLAR ARRAY STEPPING		0.0		
DYNAMIC INTERACTION - NON RIGID BODY			4.1	
MIRROR MOTION		1.0		
THERMAL SHAPPING		4.0		
OTHER		0.0		
MOTION COMPENSATION - INSTR. POINTING				16.3
INC (24 HOUR PERIODIC CORRECTIONS)			11.4	
S/C INTERFACE		2.0		
TIMING MISMATCH				
NUMERICAL APPROXIMATION				
PERFECT Q/A DETERMIN (INR SIMULATR)		2.0		
Q/A MODEL & NONOPTL. ERR (U/SSAA)		11.0		
ORBIT/ATTITUDE MODEL	10.0			
THERMAL (INSTR. & S/C)	10.0			
MODEL PARAMETERS	0.0			
NONOPTL.ERR	2.0			
HEATER OPS.	2.0			
SHC - NEAR REAL TIME COMPENSATION			4.5	
HI FREQ GYRO NOISE		1.4		
SAMPLING		1.4		
PARAMETER MISMATCH		4.0		
INSTRUMENT POINTING			10.8	
INC & SHC SERVO ERROR * 1.41		2.8		
PROCESSING ERROR		2.0		
INTER. GYRO		2.0		
CYT.DRIFT		0.4		
QUAD.ERRORS		0.0		
LINEARITY		0.4		
LINEARITY BIAS		8.8		
NOISE/JITTER		1.0		
STEP/SETTLE		1.0		
DET.ROTATION		4.2		
VIDEO DELAY		2.0		

Table C.2.2-3. Option II Relative Image to Image Registration Error Allocation Budget

1 REVISED GOES II BUDGET: 1 W/STAR TRACKER				
2 FILE NAME: IRU_INF3.W01				
3				
4				
	4TH LEVEL	3RD LEVEL	2ND LEVEL	1ST LEVEL
5				
6	TOTAL - 1ST LEVEL W/ 50% MARGIN			33.3
7	TOTAL - 1ST LEVEL			22.2
8	SAT. ATTITUDE STABILITY			12.0
9	ATTITUDE CONTROL		5.5	
10	STAR CATALOG LOCATION ERROR	2.0		
11	ATTITUDE ESTIMATION	2.2		
12	GYRO NOISE * 1.4142 (#)	1.0		
13	GYRO DRIFT	0.0		
14	STAR MSMT. ERROR	0.0		
15	EPHEMERIS UNCERTAINTY	2.0		
16	RESIDUAL MISALIGNMENT	0		
17	CONTROL LAW * 1.41		2.4	
18	QUANTIZATION	1.4		
19	COMPUTATIONAL DELAY	1.0		
20	REACTION LIM./TACH. PERFORMANCE*1.41		4.0	
21	TACH. QUANTIZATION	2.0		
22	TACH. NOISE	2.0		
23	DYNAMIC INTERACTION - RIGID BODY * 1.41			8.9
24	INGR/SMDR UNCOMP. MIRROR MOTION*1.41		6.0	
25	RESIDUAL MIRROR MOTION	4.2		
26	RESIDUAL MODELING ERROR	0.0		
27	RV IMBALANCE/FRICTION		2.0	
28	SOLAR ARRAY STEPPING		0.0	
29	DYNAMIC INTERACTION-NON RIGID BODY*1.41			5.8
30	MIRROR MOTION		1.0	
31	THERMAL SHAPPING		4.0	
32	OTHER		0.0	
33	MOTION COMPENSATION - INSTR.POINTING			18.7
34	IMC (24 HOUR PERIODIC CORRECTIONS)			8.7
35	S/C INTERFACE		2.0	
36	TIMING MISMATCH			
37	NUMERICAL APPROXIMATION			
38	PERFECT Q/A DETERMIN (INR SIMULATR)		2.0	
39	Q/A MODEL & NONRPTL. ERR (W/SSAA)		8.7	
40	ORBIT/ATTITUDE MODEL	8.0		
41	THERMAL (INSTR. & S/C)	8.0		
42	MODEL PARAMETERS	0.0		
43	NONRPTL.ERR	2.0		
44	HEATER OPS.	2.0		
45	SMC - NEAR REALTIME COMPENSATION * 1.41			6.3
46	HI FREQ GYRO NOISE		1.4	
47	SAMPLING		1.4	
48	PARAMETER MISMATCH		4.0	
49	INSTRUMENT POINTING			15.3
50	IMC & SMC SERVO ERROR * 2.0		4.0	
51	PROCESSING ERROR * 1.41		2.8	
52	INTER.TORQ * 1.41		2.8	
53	CKT.DRIFT * 1.41		0.6	
54	QUAD.ERRORS		0.0	
55	LINEARITY * 1.41		0.5	
56	LINEARITY BIAS * 1.41		12.4	
57	NOISE/JITTER * 1.41		1.4	
58	STEP/SETTLE * 1.41		1.4	
59	DET.ROTATION * 1.41		5.9	
60	VIDEO DELAY * 1.41		2.8	

60 (#) INCLUDES EFFECTS OF GYRO DRIFT & STAR MSMT. ERROR AFTER KALMAN FILTERING

Table C.2.2-4. Option III Navigation Error Allocation Budget: Pixel Location Accuracy

1 REVISED GOCS N BUDGET: IRU/STAR TRACKER				
2 FILE NAME: IRU_BCG3.M01				
3				
4				
	4TH LEVEL	3RD LEVEL	2ND LEVEL	1ST LEVEL
5	TOTAL - 1ST LEVEL W/ 50% MARGIN			28.7
6	- 1ST LEVEL			19.1
7	1. ATTITUDE STABILITY			13.1
8	ATTITUDE CONTROL		7.5	
9	STAR CATALOG LOCATION ERROR		3.0	
10	ATTITUDE ESTIMATION		5.1	
11	GYRO NOISE * 1.4142 (#)	1.0		
12	GYRO DRIFT	0.0		
13	STAR POSMT. ERROR	0.0		
14	EPHEMERIS UNCERTAINTY	5.0		
15	RESIDUAL MISALIGNMENT	0		
16	CONTROL LAM * 1.41		2.4	
17	QUANTIZATION	1.4		
18	COMPUTATIONAL DELAY	1.0		
19	REACTION LML./TACH. PERFORMANCE *1.41		4.0	
20	TACH. QUANTIZATION	2.0		
21	TACH. NOISE	2.0		
22	DYNAMIC INTERACTION - RIGID BODY * 1.41			8.9
23	(INCL/SHDR INCOMP. MIRROR MOTION)*1.41		6.0	
24	RESIDUAL MIRROR MOTION	3.0		
25	RESIDUAL MODELING ERROR	3.0		
26	RW IMBALANCE/FRICTION		2.0	
27	SOLAR ARRAY STEPPING		0.0	
28	DYNAMIC INTERACTION-NON RIGID BODY*1.41			5.8
29	MIRROR MOTION		1.0	
30	THERMAL SHAPPING		4.0	
31	OTHER		0.0	
32	MOTION COMPENSATION - INSTR. POINTING			14.0
33	1MC (24 HOUR PERIODIC CORRECTIONS)			11.4
34	S/C INTERFACE		2.0	
35	TIMING MISMATCH			
36	NUMERICAL APPROXIMATION			
37	PERFECT Q/A DETERMIN (INR SIMULATR)		2.0	
38	Q/A MODEL & NONRPTL. ERR (W/SSAA)		11.0	
39	ORBIT/ATTITUDE MODEL	10.0		
40	THERMAL (INSTR. & S/C)	10.0		
41	MODEL PARAMETERS	0.0		
42	NONRPTL. ERR	2.0		
43	WEAR OF S.	2.0		
44	SMC -WEAR REAL TIME COMPENSATION * 1.41			6.3
45	HI FREQ GYRO NOISE		1.4	
46	SAMPLING		1.4	
47	PARAMETER MISMATCH		4.0	
48	INSTRUMENT POINTING			5.1
49	1MC & SMC SERVO ERROR * 1.41		2.8	
50	PROCESSING ERROR		2.0	
51	INTER.TORG		2.0	
52	CKT.DRIFT * 1.41		0.6	
53	QUAD.ERRORS		0.0	
54	LINEARITY * 1.41		0.5	
55	LINEARITY BIAS		0.0	
56	NOISE/JITTER * 1.41		1.4	
57	STEP/SETTLE		0.0	
58	DET.ROTATION		0.0	
59	VIDEO DELAY * 1.41		2.0	
60	(#) INCLUDES EFFECTS OF GYRO DRIFT & STAR POSMT. ERROR AFTER KALMAN FILTERING			

Table C.2.2-5. Option III Within Frame Relative Pixel to Pixel Location Error Allocation Budget

1 REVISED GOES II BUDGET: IRU/STAR TRACKER		MOQA REQ'T: 14.4R			
2 FILE NAME: IRU_BEGC.M01		4TH LEVEL	3RD LEVEL	2ND LEVEL	1ST LEVEL
4					
5	TOTAL - 1ST LEVEL W/ 50% MARGIN				28.7
6	TOTAL - 1ST LEVEL				19.1
7	SAT. ATTITUDE STABILITY				13.1
8	ATTITUDE CONTROL			7.5	
9	STAR CATALOG LOCATION ERROR		3.0		
10	ATTITUDE ESTIMATION		5.1		
11	CYRO NOISE * 1.4142 (#)	1.0			
12	CYRO BIAS	0.0			
13	STAR MSHMT. ERROR	0.0			
14	EPHEMERIS UNCERTAINTY	5.0			
15	RESIDUAL MISALIGNMENT	0			
16	CONTROL LAG * 1.41		2.4		
17	QUANTIZATION	1.4			
18	COMPUTATIONAL DELAY	1.0			
19	REACTION TIME /TACH. PERFORMANCE * 1.41		4.0		
20	TACH. QUANTIZATION	2.0			
21	TACH. NOISE	2.0			
22	DYNAMIC INTERACTION - RIGID BODY * 1.41			8.9	
23	INSTR/SNR UNCOMP. RIGID MOTION * 1.41		6.0		
24	RESIDUAL RIGID MOTION	3.0			
25	RESIDUAL MODELING ERROR	3.0			
26	IM BALANCE/FRICTION		2.0		
27	SOLAR ARRAY STEPPING		0.0		
28	DYNAMIC INTERACTION-NON RIGID BODY * 1.41			5.8	
29	RIGID MOTION		1.0		
30	THERMAL SHAPPING		4.0		
31	OTHER		0.0		
32	MOTION COMPENSATION - INSTR.POINTING				14.0
33	INC (24 HOUR PERIODIC CORRECTIONS)			11.4	
34	S/C INTERFACE		2.0		
35	TIRING MISMATCH				
36	NUMERICAL APPROXIMATION				
37	PERFECT Q/A DETERMIN (1MR SIMULATR)		2.0		
38	Q/A MODEL & NONOPT. ERR (W/SSAA)		11.0		
39	ORBIT/ATTITUDE MODEL	10.0			
40	THERMAL (INSTR. & S/C)	10.0			
41	MODEL PARAMETERS	0.0			
42	NONOPT. ERR	2.0			
43	HEATER OPS.	2.0			
44	SMC -NEAR REAL TIME COMPENSATION * 1.41			6.3	
45	HI FREQ CYRO NOISE		1.4		
46	SAMPLING		1.4		
47	PARAMETER MISMATCH		4.0		
48	INSTRUMENT POINTING			5.1	
49	INC & SMC SERVO ERROR * 1.41		2.8		
50	PROCESSING ERROR		2.0		
51	INTER-TORG		2.0		
52	CXT.DRIFT * 1.41		0.6		
53	QUAD.ERRORS		0.0		
54	LINEARITY * 1.41		0.5		
55	LINEARITY BIAS		0.0		
56	NOISE/JITTER * 1.41		1.4		
57	STEP/SETTLE		0.0		
58	DET.ROTATION		0.0		
59	VIDEO DELAY * 1.41		2.8		
60	(#) INCLUDES EFFECTS OF CYRO DRIFT & STAR MSHMT. ERROR AFTER KALMAN FILTERING				

Table C.2.2-6 Option III Relative Image to Image Registration Error Allocation Budget

The second component of this category is imbalance and friction in the reaction wheels, which introduces disturbance torques which in turn produce attitude errors.

Error due to stepping of the solar array has been set to zero for Options II and III, because a continuous slew of the arrays is anticipated which will produce a momentum bias that will be compensated for in the control system.

C.2.2.2.3 Dynamic interaction – non-rigid body (Line 28)

Error due to non-rigid body dynamic interaction is broken down into two components; one due to flexibility of the instrument mirror and support structure, and a second to reflect thermal snapping of the structure as it experiences thermal cycling.

C.2.2.3 Motion compensation – instrument pointing

The motion compensation and instrument pointing category characterizes the error in the IMC and SMC signals and errors due to the imperfect performance of the servo controller. Options II and III exhibit differences in their respective budget entries in these categories, because the differences between the two Options are primarily contained in the instruments. Sections C.2.2.3.1 through C.2.2.3.3 detail the error contribution of the major sources in this category.

C.2.2.3.1 Image Motion Compensation (IMC) (Line 33)

The IMC signal is used to correct for the curvature of the earth so that scan lines will follow lines of constant latitude and hence correspond to horizontal lines in the image. The IMC signal is also used to correct for bias and slowly varying errors such as misalignments and periodic thermal effects. Errors in the IMC signal arise from three sources: (1) imperfect processing in generating the signal, (2) ephemeris uncertainty causing the system to apply the wrong correction for the actual spacecraft location, and (3) thermal effects which are either modeled incorrectly or not at all.

IMC processing error (line 34) results from round-off error and other numerical approximations made in the calculation of the signal. Also, the cycle time of the ACS computer precludes the application of the IMC signal at precisely the right time, and hence an error is produced. Options II and III exhibit less error from this source than in Option I due to improvements to the IMC circuitry.

Ephemeris uncertainty (line 37) causes the actual spacecraft location to differ from the nominal location. Therefore, the IMC signal that is calculated based on the nominal position will be slightly incorrect for the actual spacecraft location, resulting in a pointing error, even if the attitude were perfect. The magnitude of this error was taken as the worst case ephemeris uncertainty error divided by the ratio of the spacecraft orbit to the radius of the earth. The result was then rounded upward.

During any given day, thermal effects on instrument pointing are observed throughout the orbit. The IMC signal for the following day is then modified to contain a correction (which is based on the previous day's observations) for thermal effects. Error results from this process because the correction based on yesterday's data will not be entirely correct for today (line 40), and because the correction signal may not be implemented perfectly (line 41). Heater cycling on-board the spacecraft also causes uncompensated thermal transients which lead to errors (line 43). The error resulting from these sources is not combined in a simple RSS fashion as in the previous cases: as described in C.2.1.4.1, the short span attitude adjustment is a process wherein the error is monitored in real time and pointing corrections made when the error exceeds a preset value.

C.2.2.3.2 Spacecraft Motion Compensation (SMC) (Line 44)

The SMC is used to compensate for spacecraft attitude errors which vary too rapidly for the spacecraft attitude controller to correct. The Option II and III budgets contain three error sources associated with the SMC signal. First, the gyro introduces noise in sensing the high frequency attitude error (line 45). Second, limitations in sensor sample rate prevent a perfect characterization of the attitude error (line 46). Finally, the algorithm which generates the SMC signal will not be able to produce a signal which exactly cancels the attitude error (line 47).

C.2.2.3.3 Instrument pointing (Line 48)

Instrument pointing errors are related to the design of the instrument servo controller, as in Option I. Options II and III, however, exhibit reduced error in several of the categories because of improvements to the design. Specifically, the areas where performance is improved are as follows:

- Servo response to IMC and SMC signals: By limiting the commanded acceleration during turnaround, both Options II and III halve the Option I error in this case. The improvement is partly offset by the presence of both the IMC and SMC signals (instead of just IMC as in Option I), which multiplies the error by the square root of two.
- IMC and SMC processing errors: Options II and III employ an improved interface and a decreased computation interval to significantly reduce this error from Option I levels.
- Linearity errors due to random and bias sources: Linearity errors are reduced in Options II and III by replacing the inductosyns with optical encoders. Option II employs a 3 inch diameter optical disk, while Option III uses a 5 inch disk. As a result, random linearity errors are reduced in Option III over Option II levels. Linearity bias error is largely limited by calibration accuracy, which is independent of disk diameter, so Options II and III have identical bias error entries.
- Noise and jitter errors: Improvements in the IMC circuit design reduce this error in Option III.

C.2.2.4 Combining error sources for navigation, within frame registration and image-image registration (Options II & III)

The navigation error totals are computed by combining the various error sources on an RSS basis. The one exception is the IMC error from the orbit/attitude model (line 39) and non-repeatable effects (line 42), which are RSSed together, and then the result is adjusted for the short span attitude adjustment correction as described in section C.2.1.4.1. The result (line 38) is then RSSed with the other components in the budget.

Within frame registration considers the error in the relative position of two pixels in the same image. Slowly varying errors and errors which have an identical effect on different pixels in the same image are therefore reduced or eliminated in this category. In contrast, errors which have random effect on different pixels or vary significantly during the 25 minute image interval are more significant in this category, and are therefore multiplied by the square root of two in this budget (RSSed with themselves).

Frame to frame registration refers to the position of the same pixel over the ninety minute interval between frames. Errors are combined in the same manner as for within frame registration, except that the magnitude of the slowly varying errors is increased in this budget because the time period is longer (90 versus 25 minutes), which allows a larger errors to develop.

C.3 DESCRIPTION OF PROPOSED GOES-N SYSTEMS

C.3.1 GOES I-M/Option I system description

The proposed GOES-I and Option I systems are identical, except that Option I is defined to have an improved Earth Sensor with lower noise. The Earth Sensor noise performance improvement results in less noisy determinations of star and landmark locations, which in turn results in a small improvement in the estimate of the orbit and attitude for the next 24 hour period.

C.3.2 Option II system description

The proposed Option II system replaces the improved Earth Sensor in Option I with a long life, high performance Inertial Reference Unit (IRU) consisting of flight proven gyroscopes and star trackers. This results in a significant reduction in the noise (jitter) in the spacecraft attitude and orbit control system (AOCS). The control system design employs RWs in lieu of momentum wheels (MW) resulting in an improvement in the effect of wheel imbalance. The proposed zero momentum bias system has 4 RWs arranged in a tetrahedral configuration.

In addition to reducing the noise in the control system, the IRU/star tracker system has the following advantages with respect to Option I:

- High precision attitude control with the pitch axis maintained parallel with the Earth's N-S axis.
- No effect on the attitude from clouds/radiance gradients.

- SMC which provides continuous control loop monitoring of any spacecraft dynamic interactions, e.g., from mirror motions, as compared with the Option I open loop model for mirror motions only. The SMC signal from the control system is used to correct the mirror pointing.
- Continued use of IMC (24 hour predict ahead) to compensate for: thermal variations between the control system sensors and the instruments, and instrument perspective changes resulting from spacecraft inclination. The compensation for perspective permits the use of a fixed grid for all images.
- Continuous yaw axis monitoring, which reduces the observed image navigation and registration errors and provides for rapid recovery following a stationkeeping maneuver.

The overall implementation of the Option II system also assumes structural improvements to the spacecraft. The structural changes, along with the previously mentioned near real time correction of rigid body dynamic interactions using SMC, results in the overall reduction to the dynamic interaction error allocation.

The Option II design also assumes a common optical bench for the control system and the instruments. This will result in a mitigation of the thermal errors associated with the Option I system (GOES-I) diurnal variations between the instruments and the control system sensor (Earth Sensor).

C.3.3 Option III system description

All of the error source reductions in the Option II control system are maintained in the Option III system. In addition, the Option III system replaces the modified Imager on the Option I and II systems with a new (redesigned) instrument. This redesigned Imager will have an improved structure and use material with a low thermal expansion coefficient. As a result of the improved structure the servo performance will be improved; the better thermal properties of a material such as GFRP (graphite fiber reinforced plastic) will result in a significant reduction in the thermal errors introduced by the current Imager design.

C.4 SYSTEM PERFORMANCE ASSESSMENTS

Tables C.4-1 to C.4-3 provide a comparison of the GOES I-M, Options I, II and III system performances for Navigation, Within Frame Registration, and Image to Image Registration, respectively. The results presented in the tables are shown graphically in Figures C.4-1 to C.4-3. These performance results are for either the East/West (pitch) or North/South (roll) axis. This conforms with NOAA's statements for the navigation and registration requirements, and the current GOES I-M INR specifications which are for one axis.

The tables and figures reflect the bottom - up analyses performed to estimate the individual errors associated with each option. The individual errors are all 3 σ values. These estimates are combined on a Root Sum Square (RSS) basis to determine the overall 3 σ error. Since the individual errors in many cases are estimates of the best performance that could be achieved

through careful design, and ground and/or in-flight calibration an additional 50% margin has been added. This margin is to account for the usual performance shortfalls that occur, and are often too expensive to fix.

Detailed performance assessments are provided in Section 10 of the main body of the Report for each of the options.

	GOES 1-M (OPTION 1)		
	NAV	IN_FRAME	REG_90M
ATT. STAB.	22.0	31.0	31.0
MNC COMP.ERR	7.0	9.9	9.9
INC COMP.ERR	5.0	7.0	7.0
INCR.POINT	15.9	22.5	10.5
AOC: INTERFC	4.9	6.9	6.9
PERFECT O/A DETERM.	26.0	26.0	26.0
MONRPTL.ERR W/ SSAA	18.7	11.6	12.6
COMBINED ERROR	43.1	49.7	45.9
COMBINED ERROR W/ 50% MARGIN	64.7	74.6	68.8
% ATT. STAB.	15.0	26.0	28.2
% MNC COMP.ERR	1.5	2.6	2.9
% INC COMP.ERR	0.8	1.3	1.4
% INCR.PNT.W/O BIAS	7.8	13.6	3.2
% AOC: INTERFC	0.7	1.3	1.4
% PERFCT O/A DETERM	21.0	18.2	19.7
%MONRPTL.ERR W/SSAA	10.9	3.6	4.6
SPEC./REQD	112	112	112
ERROR RATIO:			
COMB.ERR./SPEC.	57.7	66.6	61.4
CHECK	57.7	66.6	61.4

Table C 4-1. GOES 1-M (Option 1) Comparison of 3 σ Performance for Navigation, Within Frame Registration, and Image-to-Image Registration

GOES OPTION 2			
	NAV	IN_FRAME	REG_90M
COMBINED ERROR W/ 50% MARGIN	34.0	37.3	32.7
COMBINED ERROR	22.6	24.8	21.8
ATT. CONTROL	12.2	5.5	7.5
DYN. INTER. RIGID BODY	6.3	8.9	8.9
DYN. INTER. NONRIGID BODY	4.1	5.8	5.8
IMC DIURNAL COMPENSATION	12.9	13.9	15.2
SMC NEAR RT COMPENSATION	4.5	6.3	6.3
INSTRUMENT POINTING	11.0	15.5	5.8
% ATT. CONTROL	30.0	13.3	28.0
% DYN. INTER. RIGID BODY	8.0	34.3	39.3
% DYN. INTER. NONRIGID BODY	3.4	14.6	16.7
% IMC DIURNAL COMPENSATION	33.2	83.2	113.8
% SMC NEAR RT COMPENSATION	4.0	17.1	19.6
% INSTRUMENT POINTING	24.2	103.8	10.3
NOAA REQ	33.0	14.0	14.0

Table C.4-2. Option II Comparison of 3σ Performance for Navigation, Within Frame Registration, and Image-to-Image Registration

GOES OPTION 3			
	NAV	IN_FRAME	REG_90M
COMBINED ERROR W/ 50% MARGIN	32.6	33.3	28.7
COMBINED ERROR	21.8	22.2	19.1
ATT. CONTROL	12.2	5.5	7.5
DYN. INTER. RIGID BODY	6.3	8.9	8.9
DYN. INTER. NONRIGID BODY	4.1	5.8	5.8
IMC DIURNAL COMPENSATION	11.4	8.7	11.4
SMC NEAR RT COMPENSATION	4.5	6.3	6.3
INSTRUMENT POINTING	10.8	15.3	5.1
% ATT. CONTROL	31.3	14.9	31.9
% DYN. INTER. RIGID BODY	8.4	38.3	44.8
% DYN. INTER. NONRIGID BODY	3.6	10.3	19.0
% IMC DIURNAL COMPENSATION	27.0	36.7	72.4
% SMC NEAR RT COMPENSATION	4.2	19.1	22.3
% INSTRUMENT POINTING	24.5	112.7	14.7
NOAA REQ	33.0	14.0	14.0

Table C.4-3 Option III Comparison of 3σ Performance for Navigation, Within Frame Registration, and Image-to-Image Registration

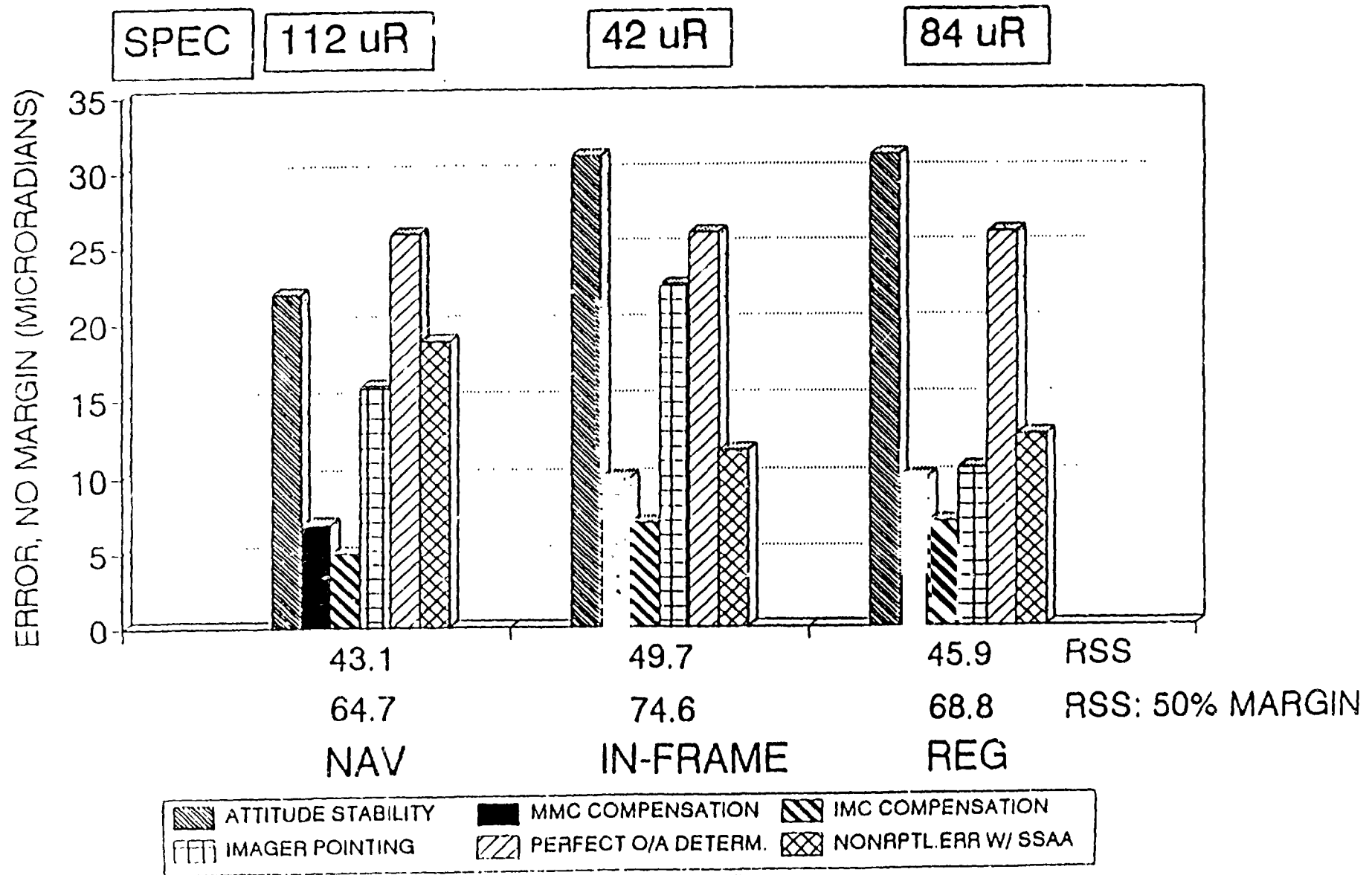


Figure C.4-1. GOES I-M (Option I) 3 σ Performance Assessment

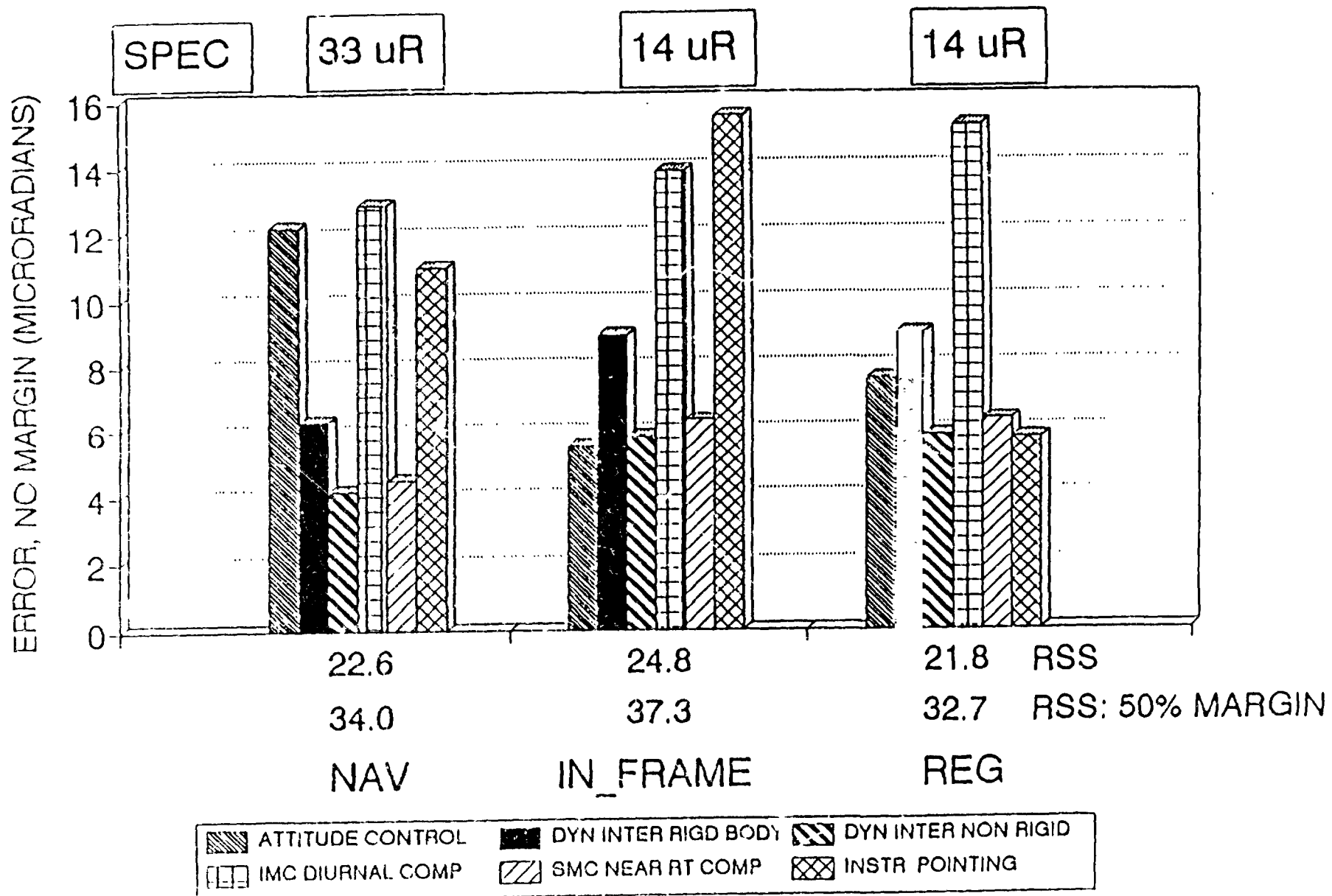


Figure C.4-2. Option II 3σ Performance Assessment

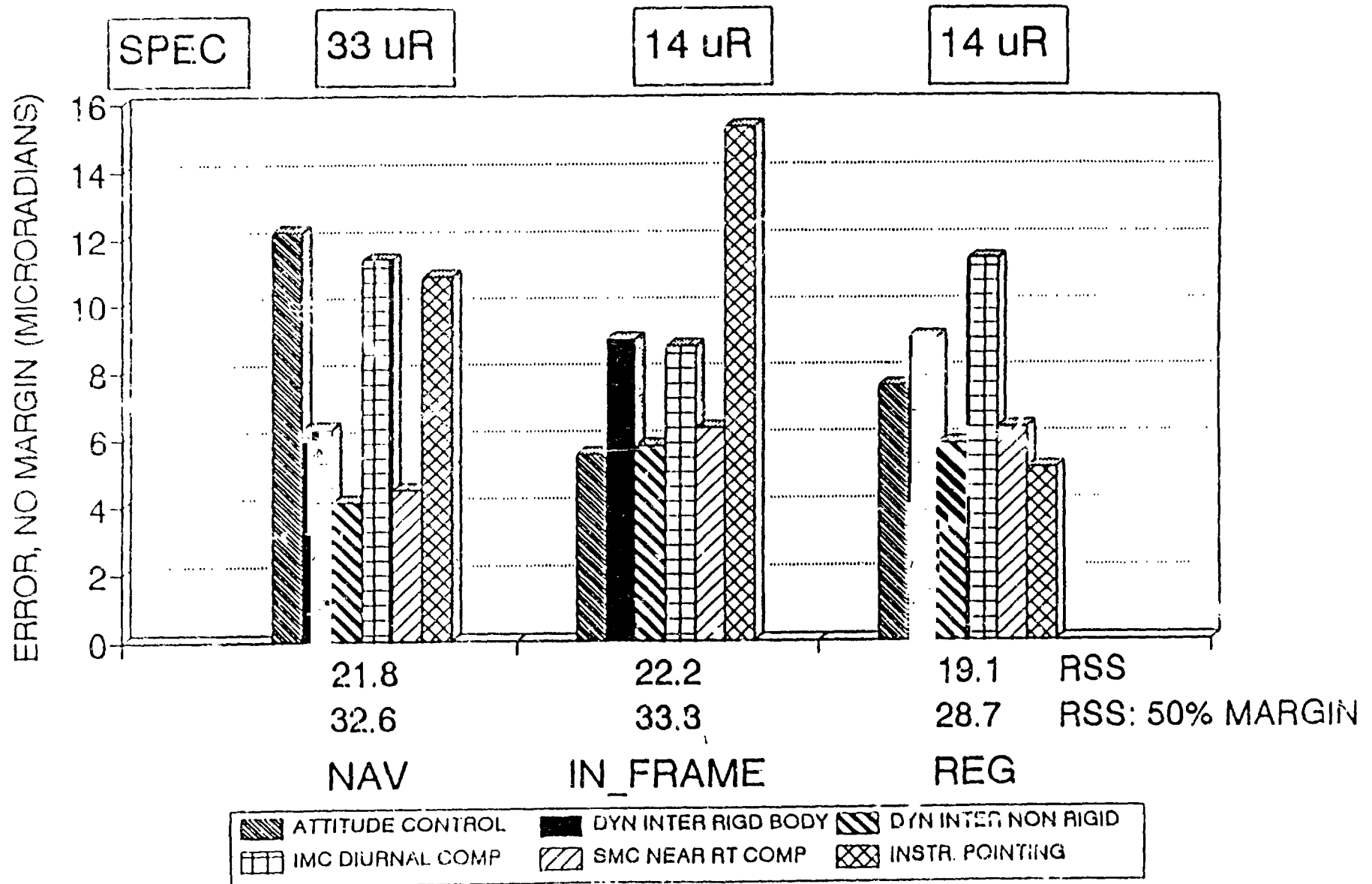


Figure C.4-3. Option III 3 σ Performance Assessment

APPENDIX D

D.1 SPATIAL RESPONSE AND CLOUD SMEARING STUDY

D.1.1 Overview

For the GOES imager, it is of concern to know the response of the system when scanning over the edge of a cloud. In particular, when alternately scanning from East to West then West to East, signal delays induced by the system can cause straight vertical lines to appear jagged after image reconstruction.

From an analytical viewpoint, the cloud edge response is analogous to the system "step" response. The objective of this study is to determine the response times for each of the imager channels. By convention, response time will be defined as the amount of time required for the system to reach 98% of its final value when subjected to a step input.

Ideally, when a step function is applied to the input of a system, we would like the output to be a step that closely matches the input; however, three factors will tend to delay, as well as distort the output response. The three factors are: optical aberrations and diffraction, finite detector width, and electronic filtering (for this analysis, a noiseless system is assumed). Both the individual and the combined effects of the three error factors are considered.

One of the variables in the analysis is the electronic filtering. The Thompson-Butterworth filters in the current ITT design are used in the analysis. For comparison, response times are computed for each channel with no filtering, and for a filter with a different cut-off frequency.

In addition to the step responses, rectangular pulse responses are computed and plotted. The pulse responses show the response of the system when scanning across a bright target of finite width (i.e., a cloud).

D.1.2 Theory

A block diagram of a single channel of the GOES imager is shown in Figure D.1.2-1(a). The input to the system, $U(s)$, is an impulse function. Optically, it is analogous to a bright, infinitely thin vertical line. Integrating the impulse function produces the desired system input (a step function, or in optical terms, a knife edge).

$H_1(s)$ is the transfer function of the optical system. It is the result of optical aberrations and diffraction, and is also referred to as the Line Spread Function (LSF).

$H_2(s)$ is the transfer function of the detector and is included because the detector has a finite width.

The electronic filter is represented by $H_3(s)$. For this analysis, the filter transfer function was set to either unity (no filtering) or to a Thompson-Butterworth filter with an appropriate cut-off frequency.

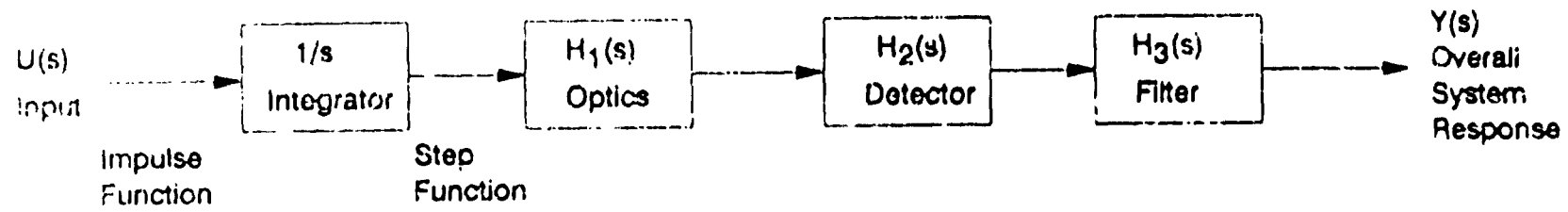


Figure D.1.2-1(a) System Block Diagram

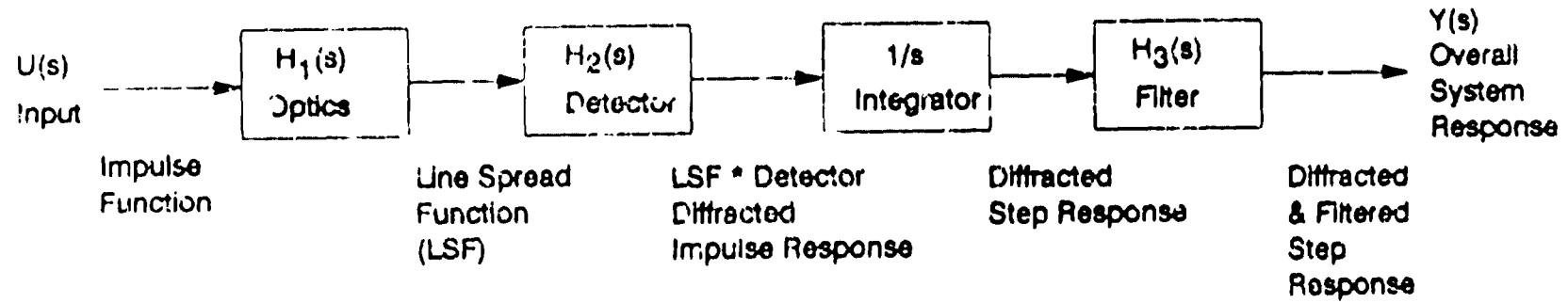


Figure D.1.2-1(b) Equivalent Block Diagram

The system response, $Y(s)$, is the product of the input with the individual transfer functions:

$$Y(s) = U(s) \cdot (1/s) \cdot H_1(s) \cdot H_2(s) \cdot H_3(s)$$

Assuming that linear system theory applies, the integrator can be moved behind the detector without affecting the overall response of the system. The resulting block diagram is shown in Figure D.1.2-1(b).

D.1.3 Implementation

GENII software was used to perform an optical ray trace on each of the 5 imager channels. The optical prescriptions were taken from the proposed ITT design.

GENII has utilities for generating the LSF, and convolving it with a rectangular (or square) detector to obtain the intermediate result $U(s) \cdot H_1(s) \cdot H_2(s)$. Outputs from GENII are in spatial units (μm), and must be converted to temporal units (μsec) before being integrated and applied to the filter.

Conversion of units is readily accomplished using knowledge of the resolution and scan rate of each channel. Table D.1.3-1 summarizes the important parameters for each channel. A sample calculation for channel 1 follows.

Table D.1.3-1. IMAGER Channel Specifications

Channel	Wave-length (μm)	Ground Resolution (km)	IFOV (μr)	IFOV (mm)	IFOV (μsec)
1	0.65	1	28	.107	80
2	3.90	4	112	.058	320
3	6.75	8	224	.113	640
4	10.70	4	112	.058	320
5	12.00	4	112	.058	320

Calculations for Channel 1:

$$IFOV(\mu\text{rad}) = \frac{1 \text{ Km}}{35600 \text{ Km}} = 28\mu\text{rad} \quad (41)$$

$$IFOV(\text{mm}) = .107 \text{ mm (in Focal plane, from GENII)} \quad (42)$$

$$SCAN\ RATE = \frac{20^\circ}{sec} = \left(\frac{20^\circ}{sec} \right) \left(\frac{\pi\ rad}{180^\circ} \right) = \frac{\pi\ rad}{9\ sec} \quad (43)$$

$$IFOV\ (\mu sec) = (28\ \mu rad) \left(\frac{9\ sec}{\pi\ rad} \right) = 80\ \mu sec \quad (44)$$

The intermediate result $[U(s) \cdot H_1(s) \cdot H_2(s)]$ computed by GENII was saved to an ASCII text file and imported into a LOTUS 123 spreadsheet. Within the spreadsheet, spatial units were scaled into temporal units, and the result was integrated to obtain the system step response with no filtering.

The final step in the analysis incorporates the effects of the electronic filter. The filter proposed in the current ITT design, a 4-pole low pass Thompson-Butterworth filter, was modeled. The transfer function is given by:

$$H_3(s) = \frac{5.158}{s^4 + 4.762s^3 + 10.212s^2 + 10.816s + 5.158} \quad (45)$$

This transfer function is normalized to give a 3 dB cutoff frequency $W_c = 1$ rad/sec. The following equation can be used to compute the desired cutoff frequency for each imager channel:

$$cutoff\ freq = f_c = \frac{1}{2 T_{IFOV}} \quad Hz \quad (46)$$

This cutoff frequency yields the maximum signal to noise ratio for a rectangular input pulse with a duration of 1 IFOV. Since the filters must be implemented with readily available resistor and capacitor values, the actual cutoff frequencies differ slightly from the values computed using equation 46.

A software package called "CC" was used to scale the normalized Thompson-Butterworth transfer function to yield the 3 dB cutoff frequencies listed in Table D.1.3-2.

Table D.1.3-2. Filter Bandwidths

	Fc, Cutoff Freq (Hz)	Wc, Cutoff Freq (rad/sec)
Channel 1	6575	41312
Channel 2	1644	10330
Channel 3	822	5165
Channel 4	1644	10330
Channel 5	1644	10330

The filter function was implemented using a 4th order Runge-Kutta¹⁰ algorithm with Gill's modification for increased precision. The program was written in C, using Microsoft's Quick C compiler. The unfiltered step response computed previously in the LOTUS spreadsheet was saved to an ASCII disk file and used as the input to the filter program. The filtered output was saved to a disk file for post analysis, and plotting.

A rectangular pulse can be viewed as the sum of two step functions, a positive step at time zero, and a negative step (with the same amplitude) at some time greater than zero. The width of the pulse is determined by the timing of the second step function. This strategy was used to generate pulse responses for the imager optics. The unfiltered step responses from the previous analysis were shifted in time and subtracted from the original step response to obtain optical pulse responses. The pulse responses were then saved to a disk file and applied to the filter program.

D.1.4 Results

Numerous plots of intermediate and end results can be found at the end of this appendix. All plots are normalized to unity amplitude, and the horizontal axes are scaled to give units in IFOV's. Discussions are presented in the following paragraphs.

Figures D.1.4-1a through 1e show the LSF's of the imager channels. The LSF's indicate the amount of spreading that occurs in the focal plane as a result of optical aberrations and diffraction. As expected, spreading in the longer wavelength channels is more pronounced due to diffraction effects.

The detector response is modeled as a rectangular pulse with an amplitude of 1, and a width of 1 IFOV. It is shown in Figure D.1.4-2.

The combined effect of the optics and the detector (i.e., the convolution of the LSF with the detector response) is computed by GENIE and plotted in Figures D.1.4-3a through 3e. These plots show how each imager channel would respond if scanned across a bright, infinitely thin vertical line; electronic filter effects are not included.

The time origins in Figures D.1.4-3a through 3e have been shifted so that the central maxima of each plot occurs at time 0.5 IFOV. This selection ensures that the leading edge of the detector coincides with the impulse input at time 0.

The impulse responses in Figures D.1.4-3a through 3e were integrated to obtain step responses, and applied to the filter simulation program. The filter cutoff frequencies (F_c) that were used in the simulation are listed in Table D.1.3-2. For comparison, filters were also simulated which had

¹⁰ - Runge-Kutta is a numerical method which provides a means of computing the output time response of a system given the input (as a function of time) and the transfer function of the system.

cutoff frequencies that were 2.2 times the values listed in Table D.1.3-2; this effectively causes the MTF of each filter to increase from 0.707 to 0.95 at F_c . The unfiltered and filtered step responses are plotted in Figures D.1.4-4a through 4c.

In Figures D.1.4-4a through 4c, the input step occurs at time 0. It is worth mentioning that the step responses (particularly the longer wavelengths) have attained values that are greater than 0 at time zero. This is possible because the optical system blurs the step function so that it is partially visible to the detector before time 0.

Table D.1.4-1 summarizes the rise times (in IFOV) for the system output to reach 98% of its final value when subjected to a step input (i.e., when scanning over a cloud, or knife edge). The filter "Cutoff Freq" is repeated from Table D.1.3-2 for the convenience of the reader.

The values in Table D.1.4-1 assume that the time origin ($t=0$) occurs when the leading edge of the detector meets the cloud edge. In order to match successive E/W and W/E scans, system and filter delays must be compensated for. A reasonable choice for a delay value is the amount of time required for the system output to reach 50% of its final value. This choice will ensure that in the reconstructed image, alternate left and right scans over a cloud edge will match up at the 50% intensity points.

Table D.1.4-1. 98% Rise Times (No Delay Compensation)

	Fc Cutoff Freq (Hz)	Rise Time (No Filter) (IFOV)	Rise Time Filter 3dB= 2.2 * Fc (IFOV)	Rise Time Filter 3dB=Fc (IFOV)
Channel 1	6575	1.01	1.35	1.85
Channel 2	1644	1.01	1.35	1.84
Channel 3	822	1.11	1.47	1.88
Channel 4	1644	1.37	1.59	1.98
Channel 5	1644	1.43	1.61	1.99

50% delay times are listed in Table D.1.4-2. The values were obtained by interpolating results from the previous analyses.

Table D.1.4-2. Delay Times to Reach 50% Intensity

	F_c Cutoff Freq (Hz)	Delay Time (No Filter) (IFOV)	Delay Time Filter 3dB= 2.2*F_c (IFOV)	Delay Time Filter 3dB=F_c (IFOV)
Channel 1	6575	0.49	0.76	1.12
Channel 2	1644	0.47	0.74	1.09
Channel 3	822	0.48	0.74	1.10
Channel 4	1644	0.44	0.63	1.00
Channel 5	1644	0.42	0.59	0.98

The delay adjusted rise time (the time required for the system output to advance from 50% to 98%) can be obtained by subtracting the values in Table D.1.4-2 from those in Table D.1.4-1. The results are tabulated below.

Table D.1.4-3. 98% Rise Time (Delay Compensated)

	F_c Cutoff Freq (Hz)	Rise Time (No Filter) (IFOV)	Rise Time Filter 3dB= 2.2*F_c (IFOV)	Rise Time Filter 3dB=F_c (IFOV)
Channel 1	6575	0.52	0.59	0.73
Channel 2	1644	0.54	0.61	0.75
Channel 3	822	0.63	0.73	0.78
Channel 4	1644	0.93	0.96	0.98
Channel 5	1644	1.01	1.02	1.01

Figures D.1.4-5a through 5e show the system pulse responses for channels 1 through 5 respectively. The top two plots in each figure show the system responses with filter cutoff frequencies of $2.2 F_c$ and F_c . Beneath each plot, the same information is plotted on an expanded scale.

Table D.1.4-4 lists the amount of time that the derived radiance of each channel will be within 2% of the actual value when scanning over clouds of various widths.

Table D.1.4-4. Duration Periods for 2% Absolute Radiometric Accuracy

	1 IFOV	2 IFOV	3 IFOV	4 IFOV	5 IFOV
Channel 1 - 2.2 Fc	0.00	0.85	1.85	2.85	3.85
Fc	0.00	0.60	1.55	2.50	3.45
Channel 2 - 2.2 Fc	0.00	0.80	1.80	2.82	3.85
Fc	0.00	0.56	1.56	2.61	3.64
Channel 3 - 2.2 Fc	0.00	0.63	1.63	2.63	3.63
Fc	0.00	0.52	1.47	2.42	3.42
Channel 4 - 2.2 Fc	0.00	0.00	1.11	2.11	3.14
Fc	0.00	0.00	1.02	2.03	3.04
Channel 5 - 2.2 Fc	0.00	0.00	1.09	2.04	2.99
Fc	0.00	0.00	0.98	1.96	2.91

D.1.5 Conclusions

It is evident from Table D.1.4-1 that optical effects and filtering play an important role in the response times of the imager channels. As expected, diffraction effects are most pronounced in the longer wavelength channels.

The current specification states that the output of the system, when subjected to a step input, must reach 98% of its final value within a distance of 1.00 IFOV. Tables D.1.4-1, -2 and -3 suggest that "rise time" is only meaningful if a convention is established for the time origin.

If the time origin is defined as the time at which the leading edge of the detector meets the cloud edge, then Table D.1.4-1 suggests that it is not possible to meet the rise time requirement (except in the idealized case of no diffraction and infinite bandwidth). Decreasing the detector size will cause a proportionate decrease in the IFOV, and is of no benefit in meeting the requirement as stated.

A more realizable statement of the requirement could be in terms of ground distance. For example, the output should reach 98% of its final value within a scan distance of x kilometers. In this way, an appropriate combination of detector size, optics and filtering could be chosen to satisfy the requirement.

The effects of increased bandwidth are illustrated in the last two columns of Tables D.1.4-1 and -3. With no delay compensation (Table D.1.4-1), all channels exhibit faster rise times with wider bandwidths. With the delay compensation included (Table D.1.4-3), only the shortest wavelength channels benefit from wider bandwidth filters. This is because the overriding bandwidth limitation for the longer wavelength channels is imposed by the optics rather than the electronic filters.

In channels 4 and 5, the electronic filter introduces a fixed delay which is readily corrected (Table D.1.4-3). One could argue that in these channels, it may be worthwhile to use tighter filters (narrower bandwidths). The improvement in system noise could be worth the penalty in system response time.

The computation of noise is a fairly complex subject that will not be covered in detail in this report; however, some general considerations are presented in the following paragraphs.

For channels 1 and 2, photo-voltaic (PV) detectors will be used in conjunction with transimpedance preamplifiers. For these channels, the preamplifier exhibits a "treble boost" characteristic which causes the noise density to increase with the third power of the frequency. The total noise will increase in proportion to the bandwidth raised to the 3/2 power; hence, a 2.2 times increase in the signal bandwidth will cause the total noise to increase by a factor of $(2.2)^{3/2} = 3.26$.

Channels 3-5 utilize photo-conductive (PC) detectors, and should exhibit flat noise spectra. The relative noise increase should be proportional to the square root of the bandwidth; so a 2.2 times increase in signal bandwidth will result in the total noise increasing by a factor of $(2.2)^{1/2} = 1.48$.

In all 5 channels, the S/N ratio should decrease in direct proportion to the increase in the total noise. Also, the figures of merit, NEAD for the visible band, and NEAT for the IR bands, will be degraded by the same factors.

Figures D.1.4-5a through 5e and Table D.1.4-4 give an indication of the system behavior when scanning over clouds of various widths. If it is of interest to make absolute radiance measurements, the output must not only attain the steady state value (to within 2%), but it must maintain that value long enough to ensure that at least one sample point falls within the interval. From Table D.1.4-4, we can conclude that clouds must be at least 2-3 IFOV's wide to have confidence in absolute radiance measurements.

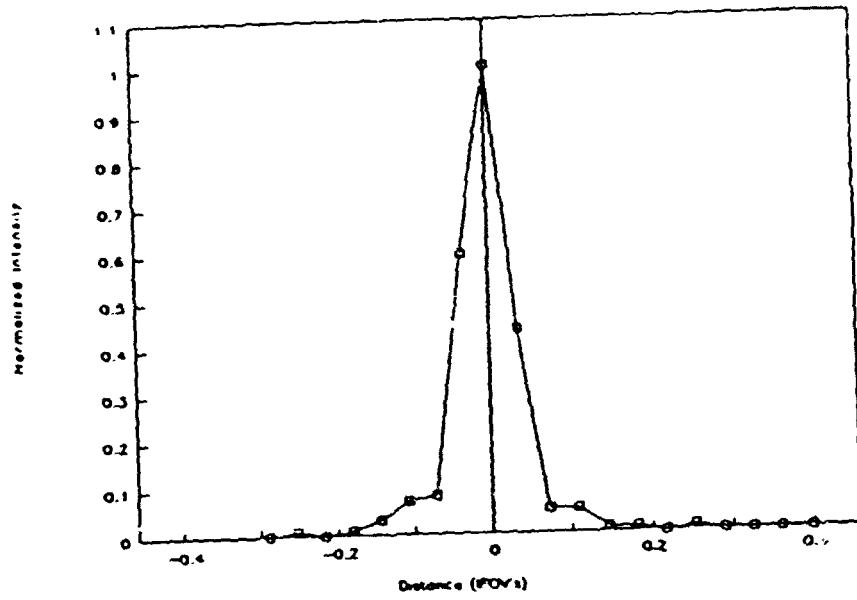


Figure D.1.4-1(a). Channel 1 Line Spread Function

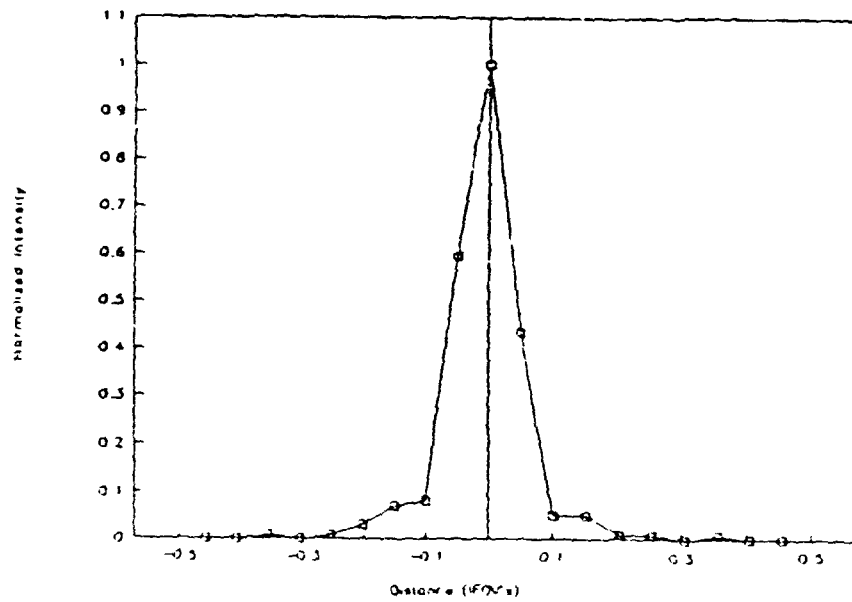


Figure D.1.4-1(b) Channel 2 Line Spread Function

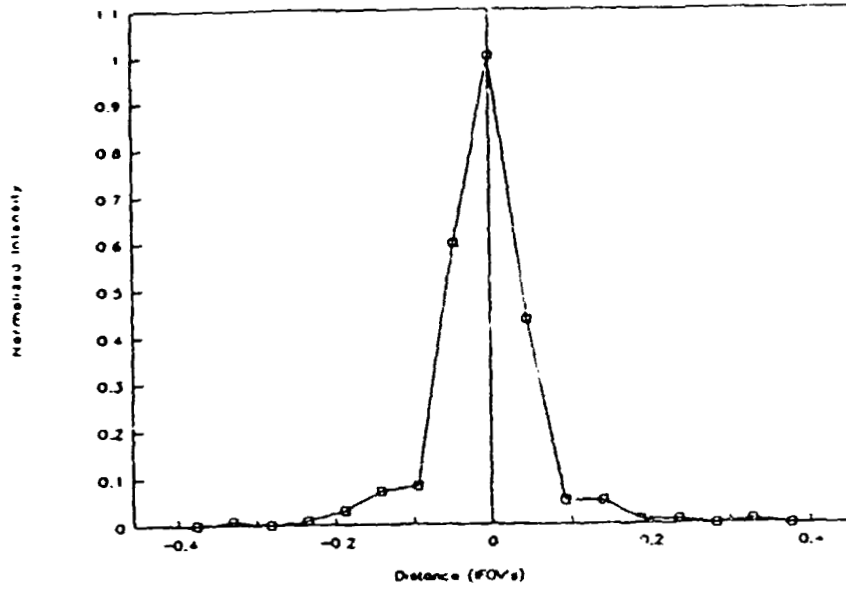


Figure D.1.4-1(c). Channel 3 Line Spread Function

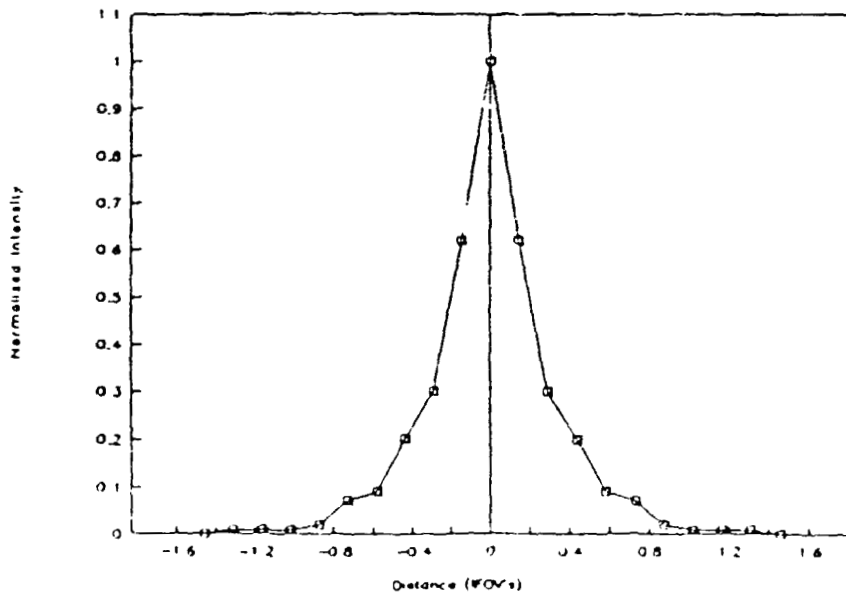


Figure D.1.4-1(d). Channel 4 Line Spread Function

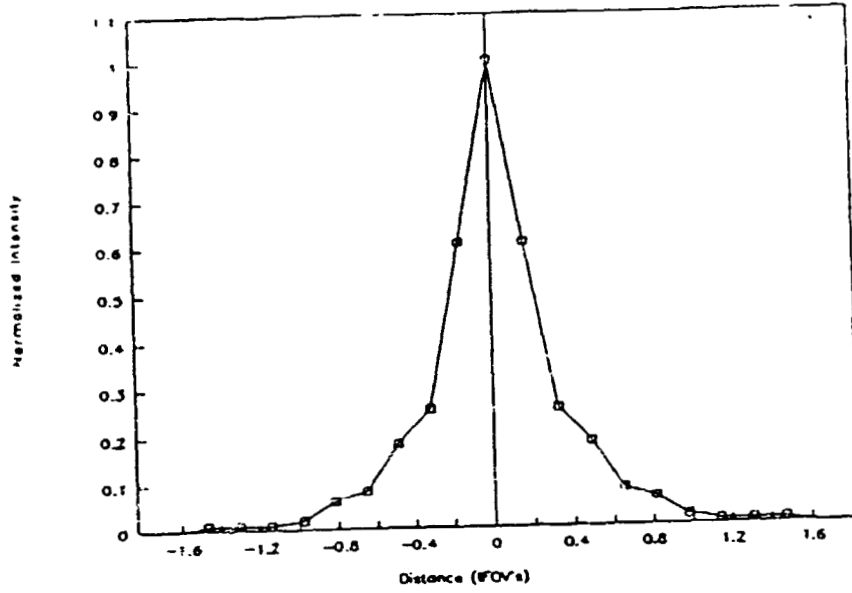


Figure D.1.4-1(c). Channel 5 Line Spread Function

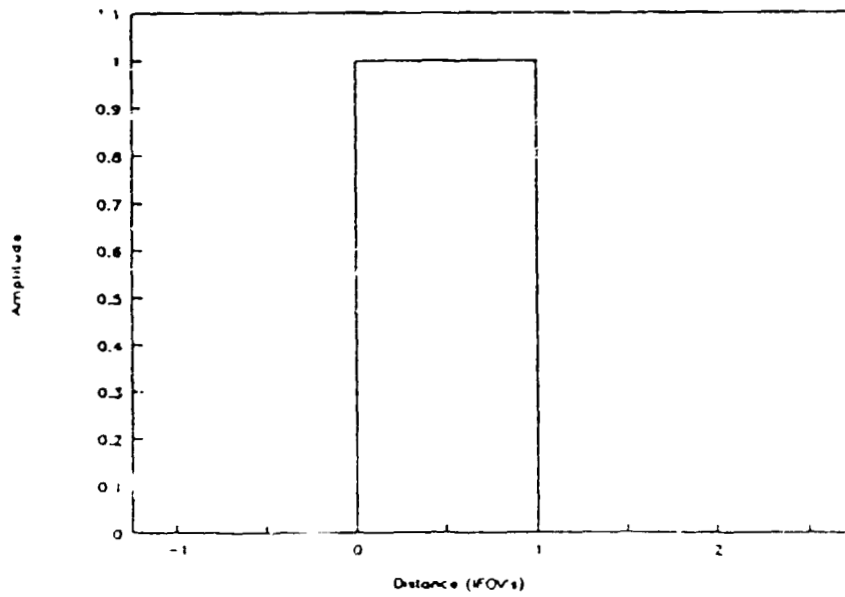


Figure D.1.4-2. Detector Model

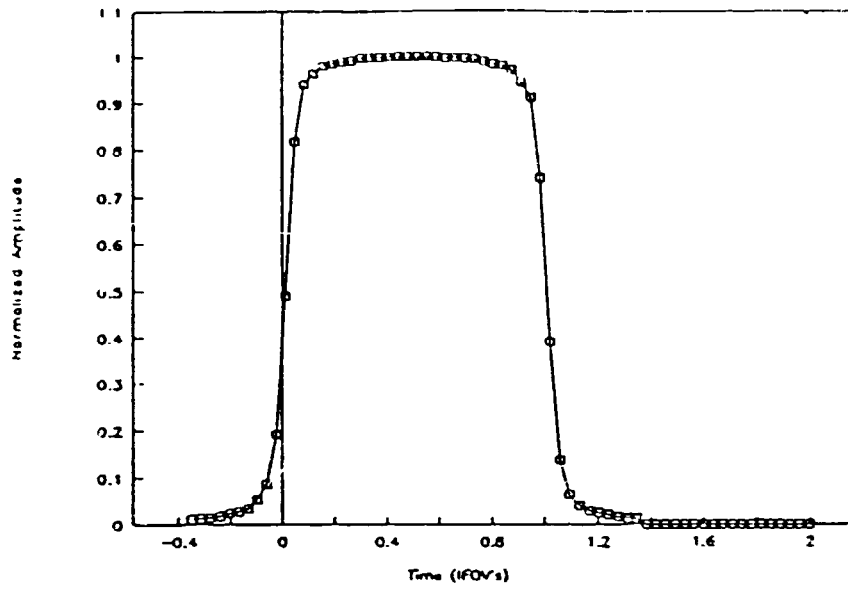


Figure D.1.4-3(a). Channel 1 LSF * Detector

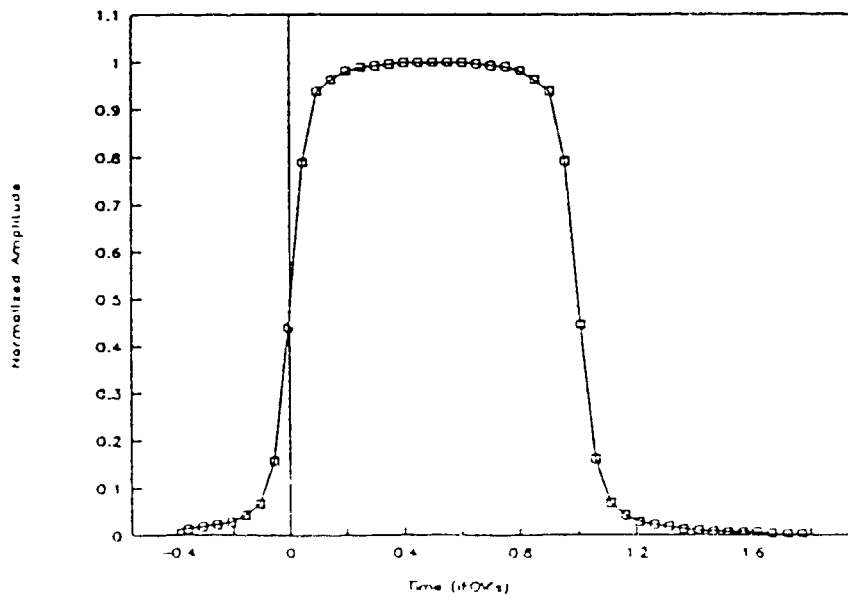


Figure D.1.4-3(b) Channel 2 LSF * Detector

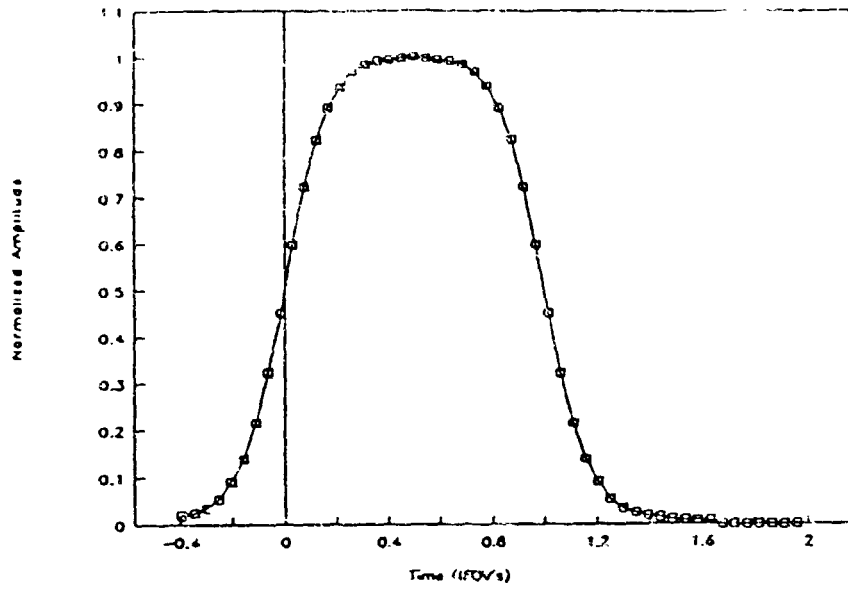


Figure D.1.4-3(c). Channel 3 LSF * Detector

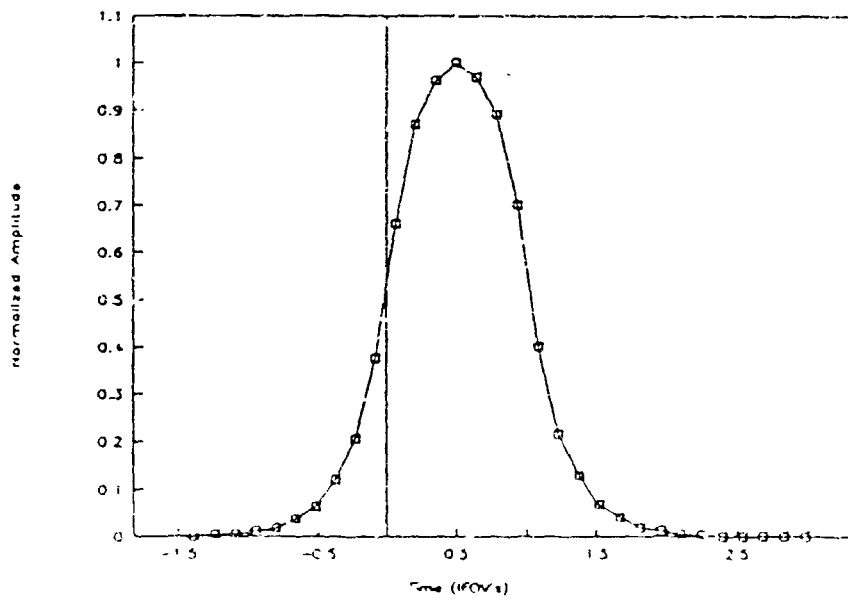


Figure D.1.4-3(d). Channel 4 LSF * Detector
370

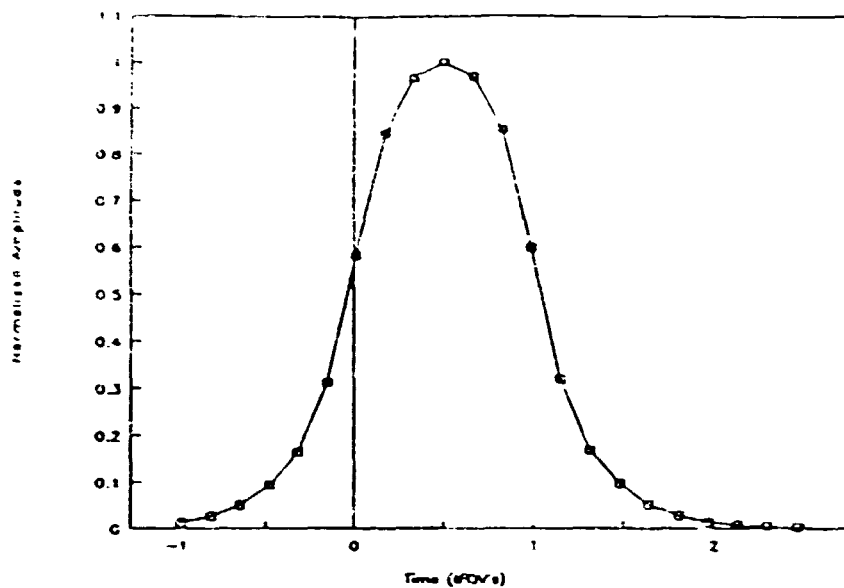


Figure D.1.4-3(e). Channel 5 LSF * Detector

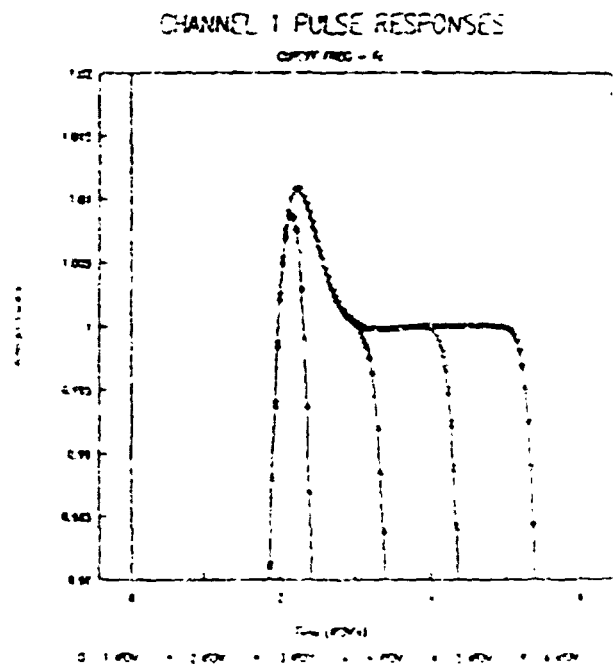
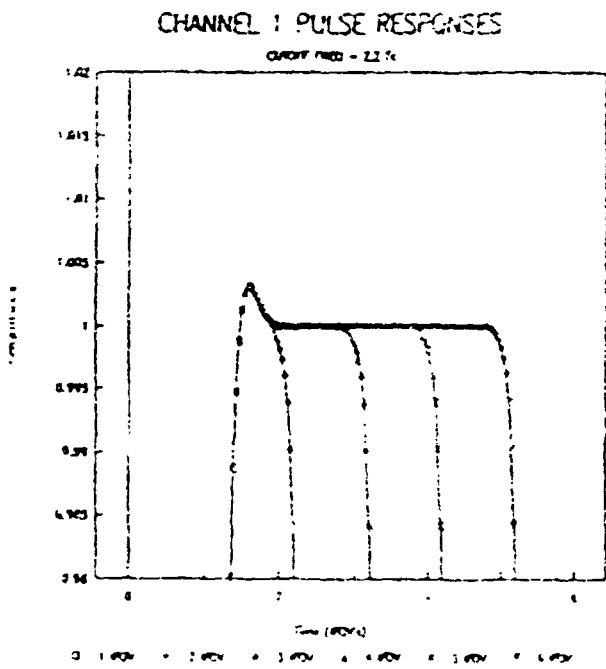
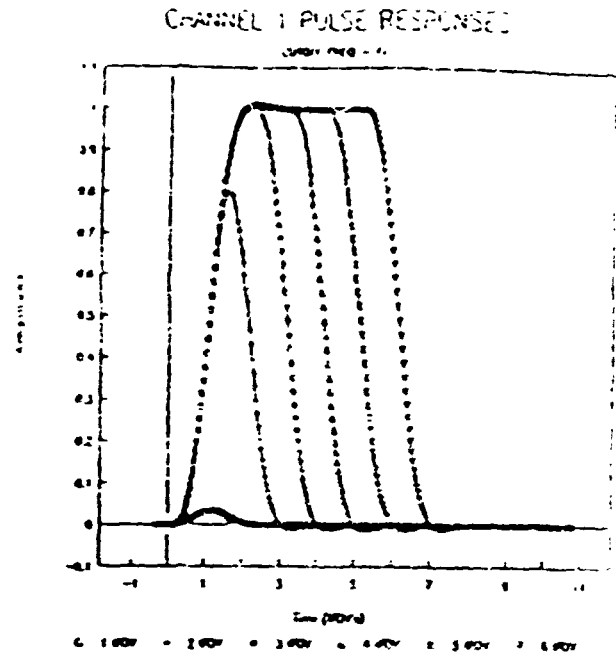
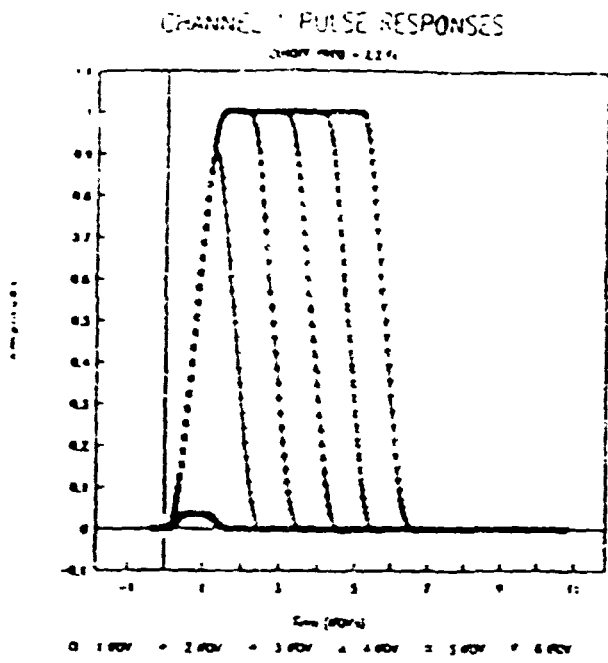
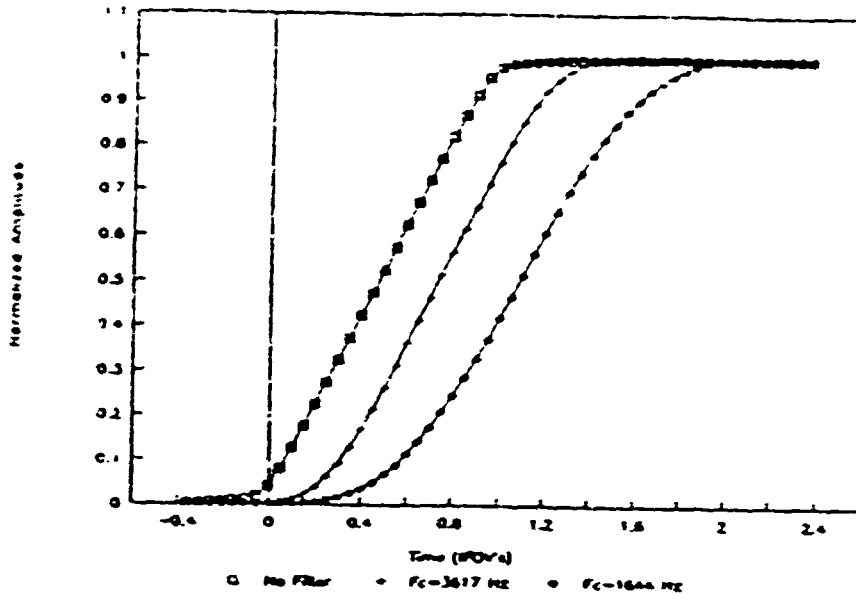


Figure D 1 4 - 4(a) Channel 1 Step Responses
372

CHANNEL 2 STEP RESPONSES



CHANNEL 2 STEP RESPONSES

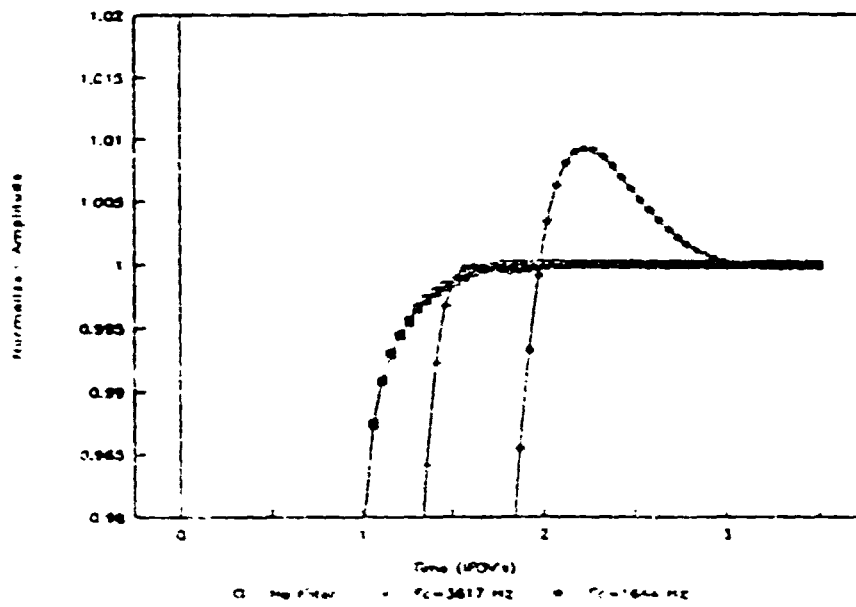
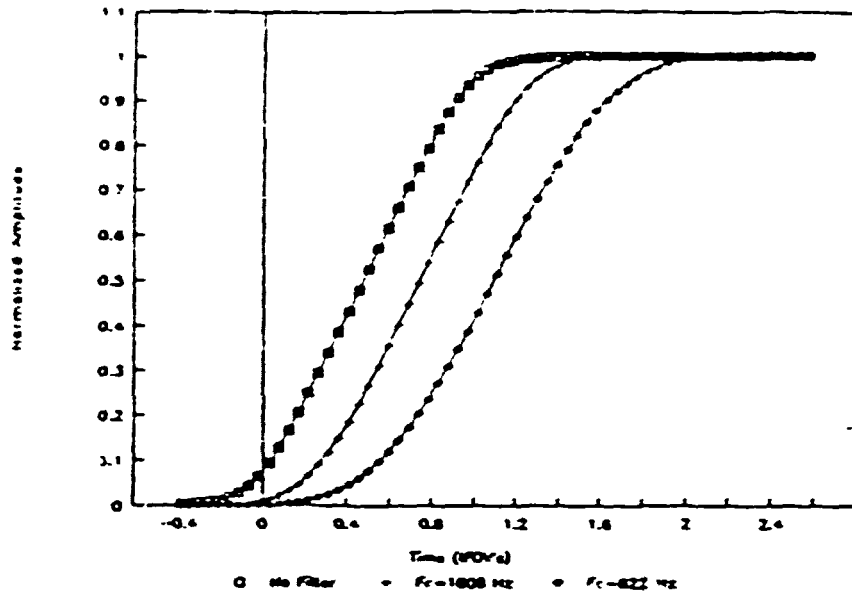


Figure D 1 4-4(b) Channel 2 Step Responses
573

CHANNEL 3 STEP RESPONSES



CHANNEL 3 STEP RESPONSES

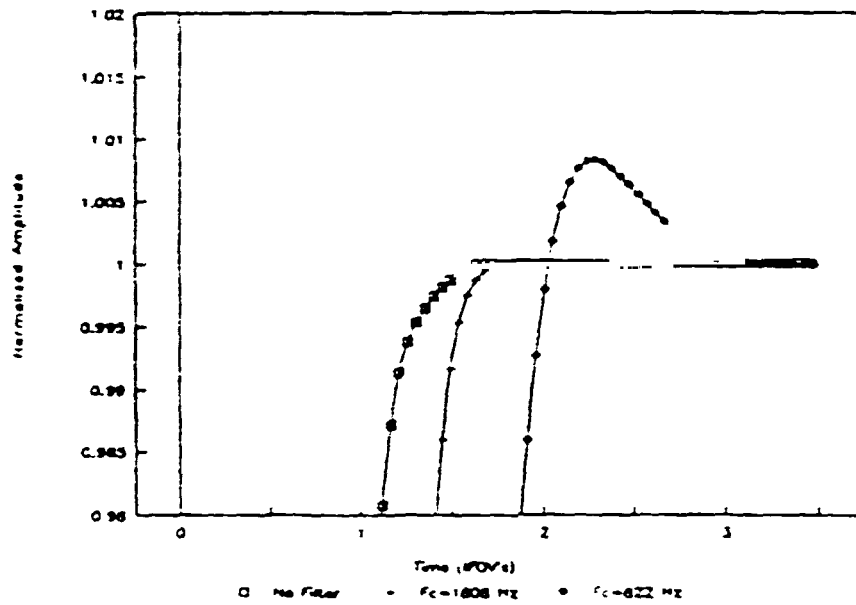
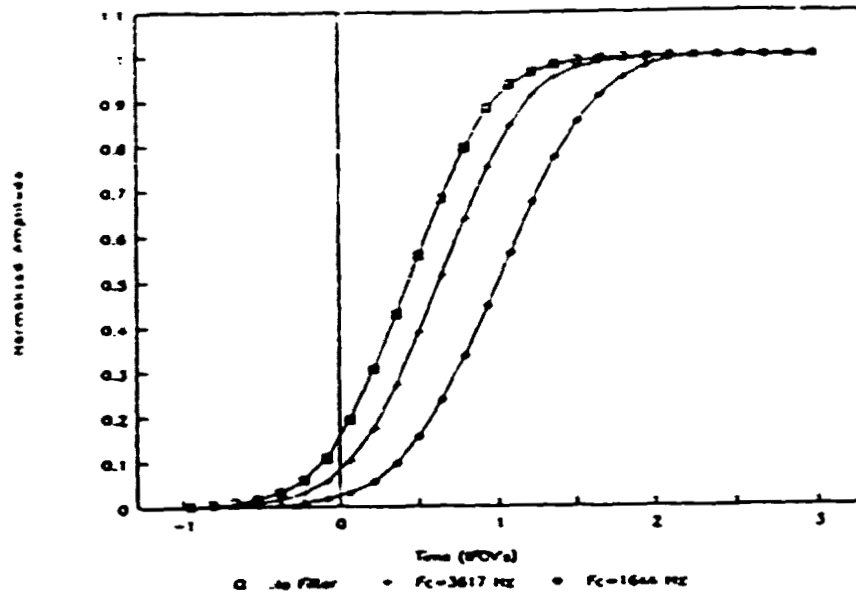


Figure D.1.4-4(c). Channel 3 Step Responses
374

CHANNEL 4 STEP RESPONSES



CHANNEL 4 STEP RESPONSES

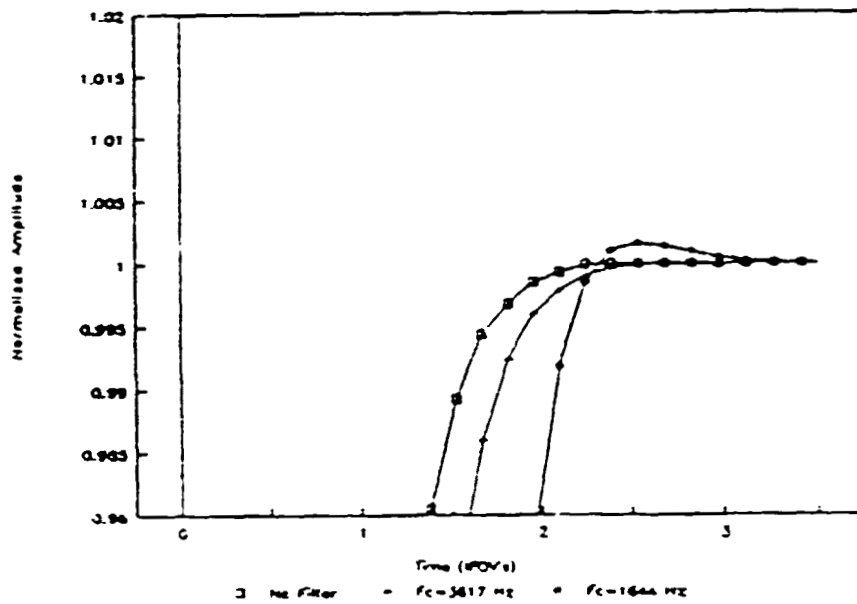
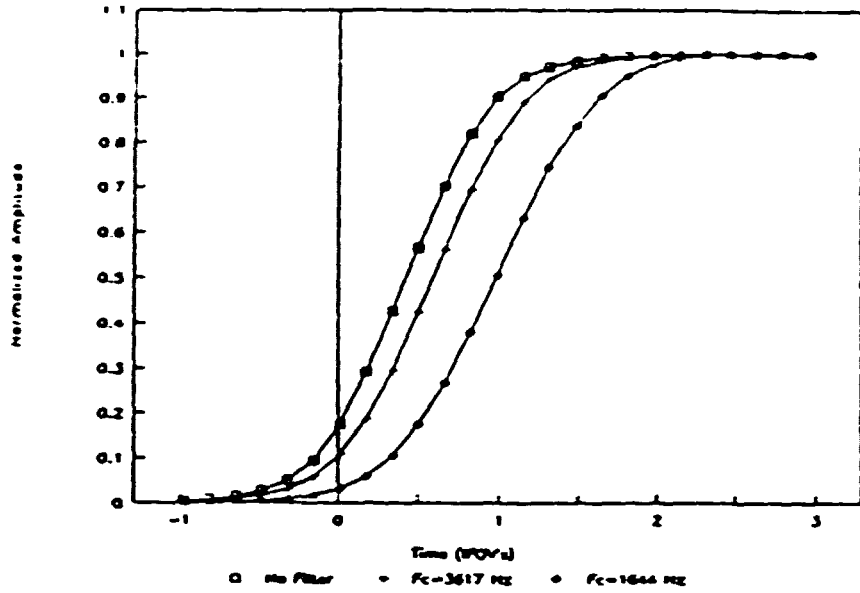


Figure D.1.4-4(d) Channel 4 Step Responses
375

CHANNEL 5 STEP RESPONSES



CHANNEL 5 STEP RESPONSES

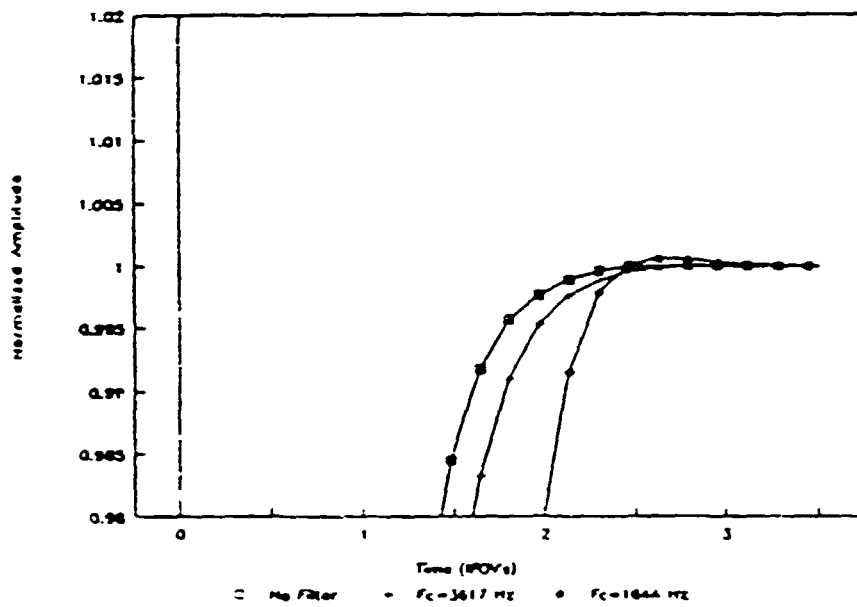
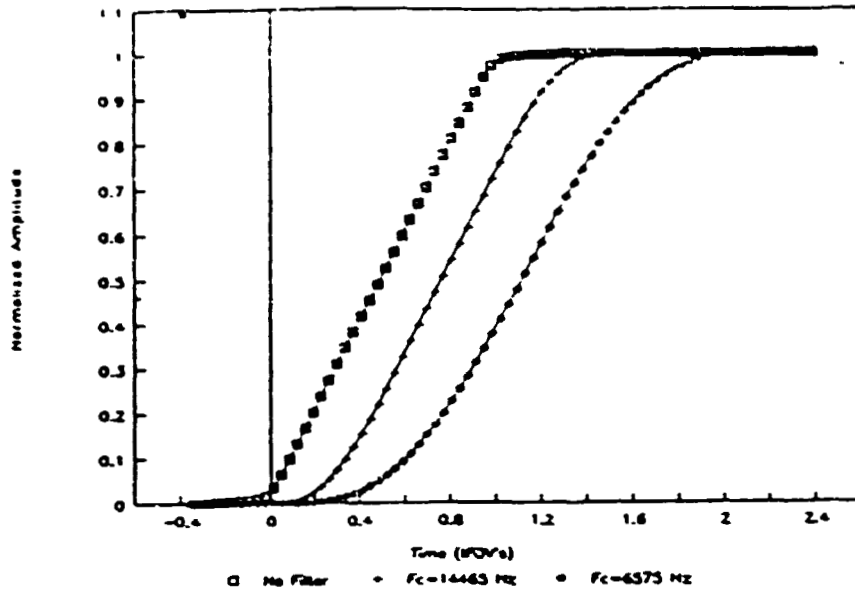


Figure D.1.4-4(c). Channel 5 Step Responses
376

CHANNEL 1 STEP RESPONSES



CHANNEL 1 STEP RESPONSES

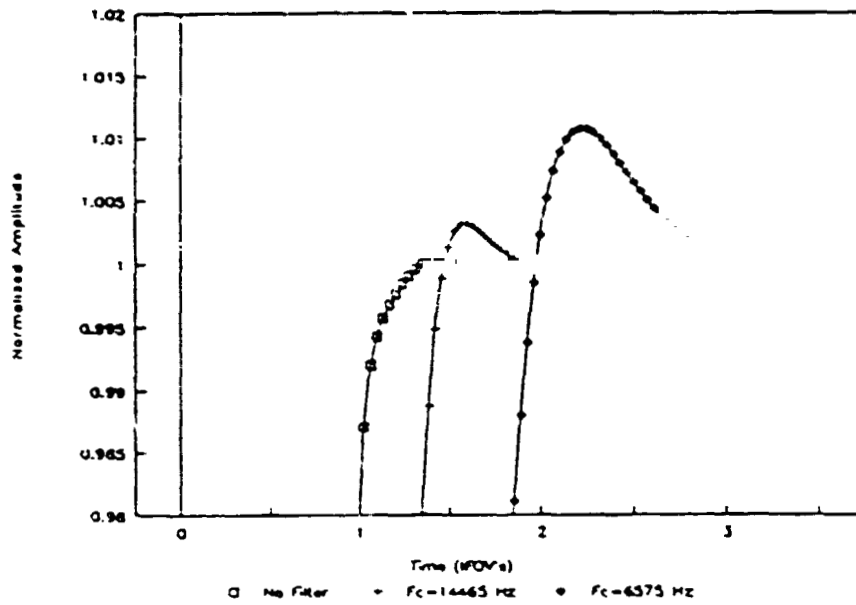
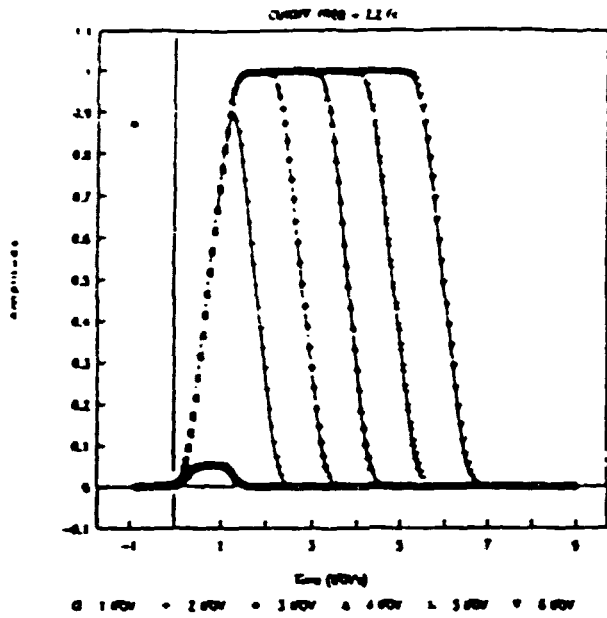
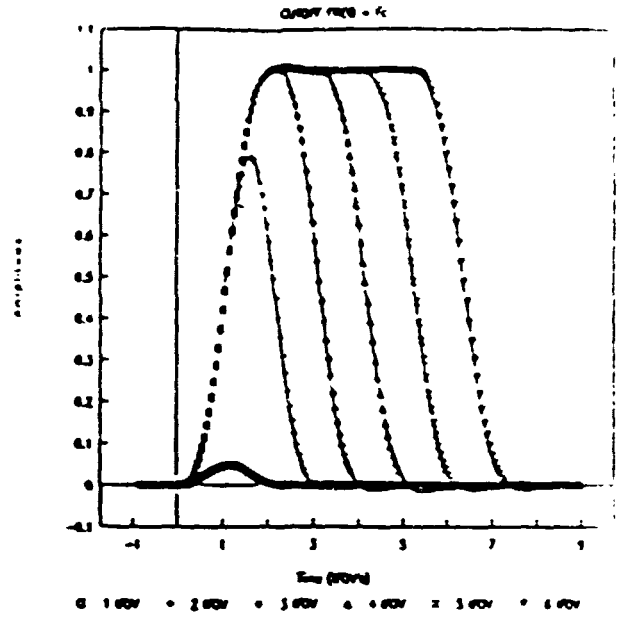


Figure D.1.4-5(a) - Channel 1 Pulse Responses
377

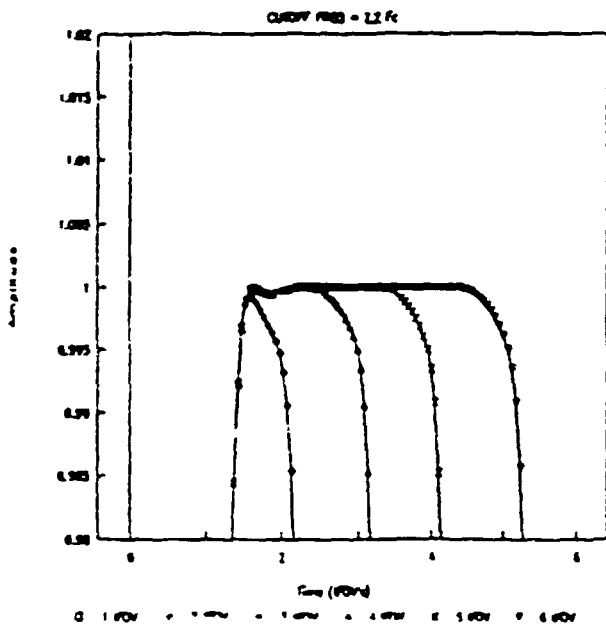
CHANNEL 2 PULSE RESPONSES



CHANNEL 2 PULSE RESPONSES



CHANNEL 2 PULSE RESPONSES



CHANNEL 2 PULSE RESPONSES

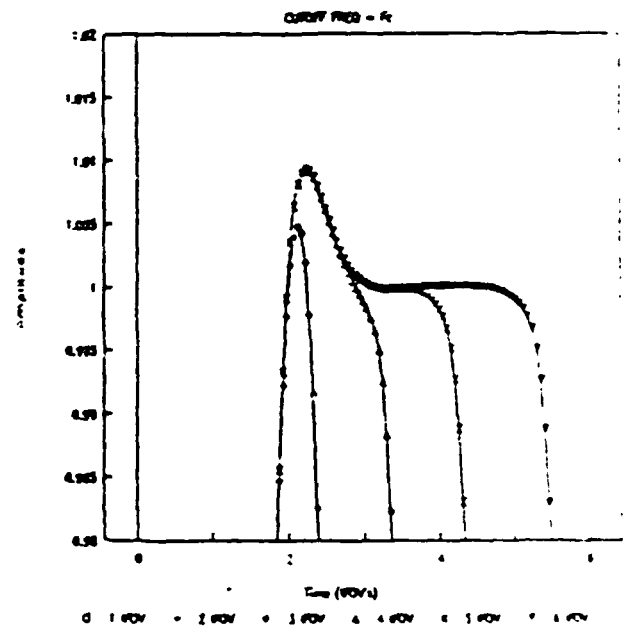


Figure D.1.4-5(b) - Channel 2 Pulse Responses
378

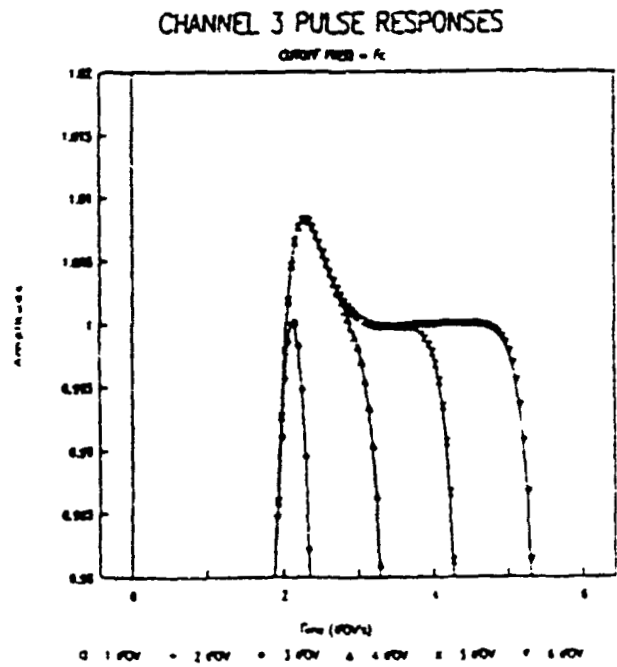
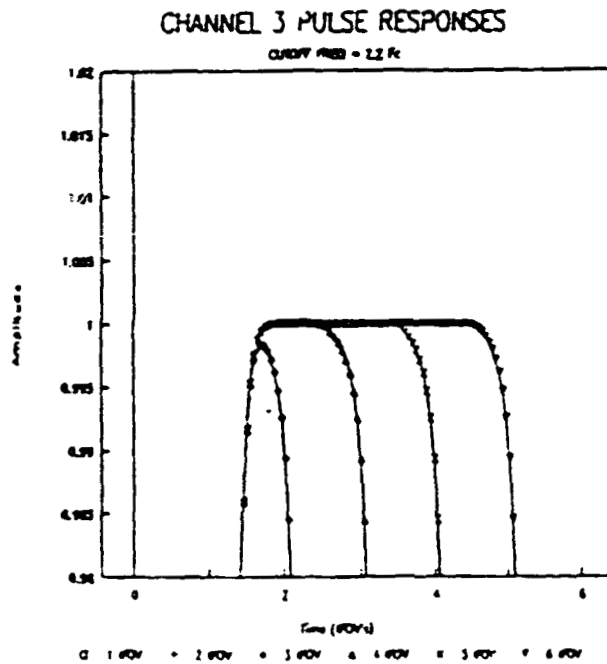
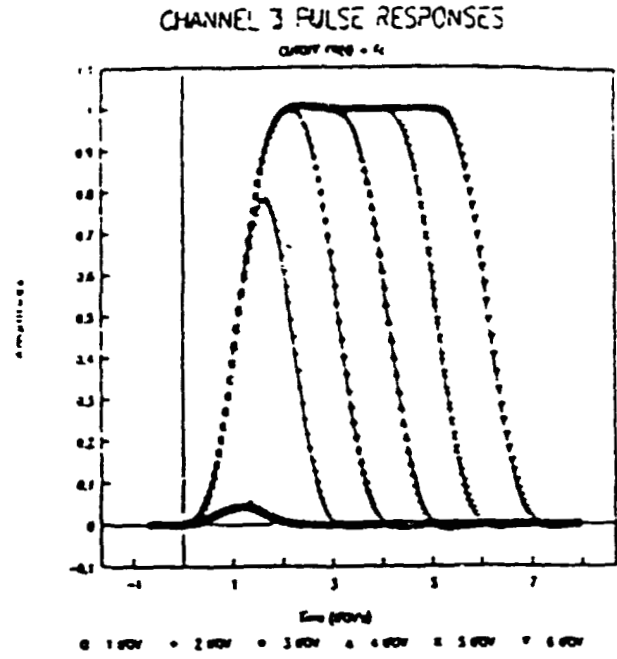
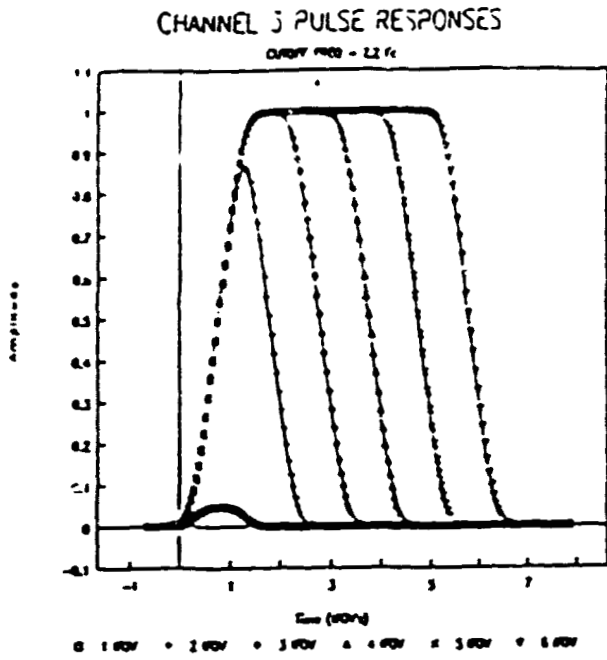
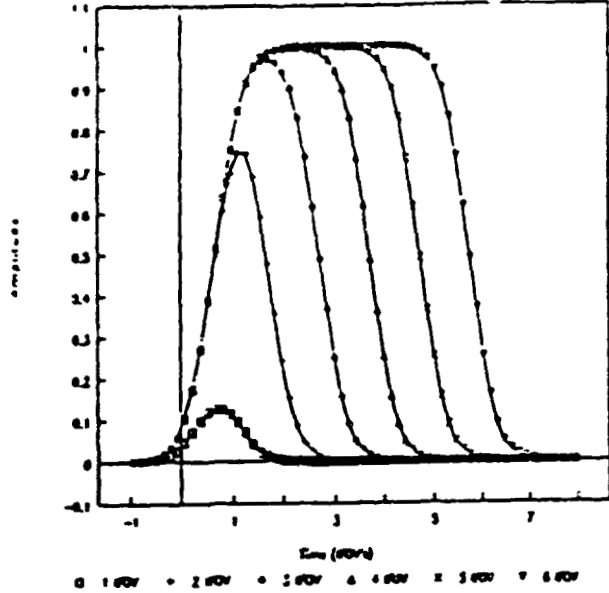


Figure D.1.4-5(c) - Channel 3 Pulse Responses
379

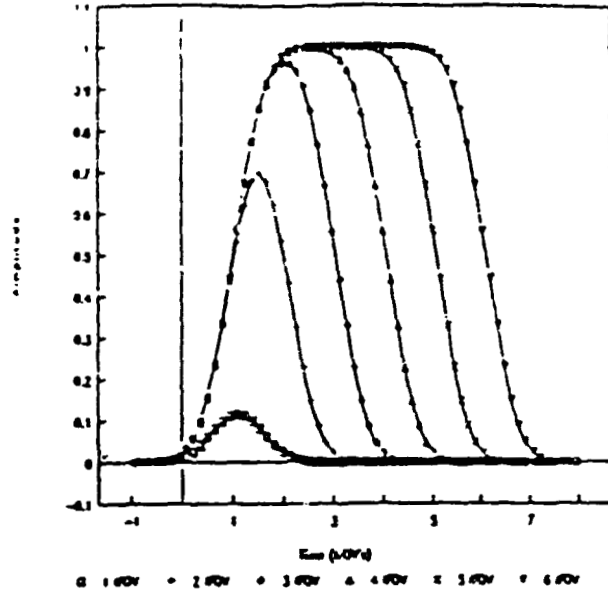
CHANNEL 4 PULSE RESPONSES

CUTOFF FREQ = 2.2 Kc



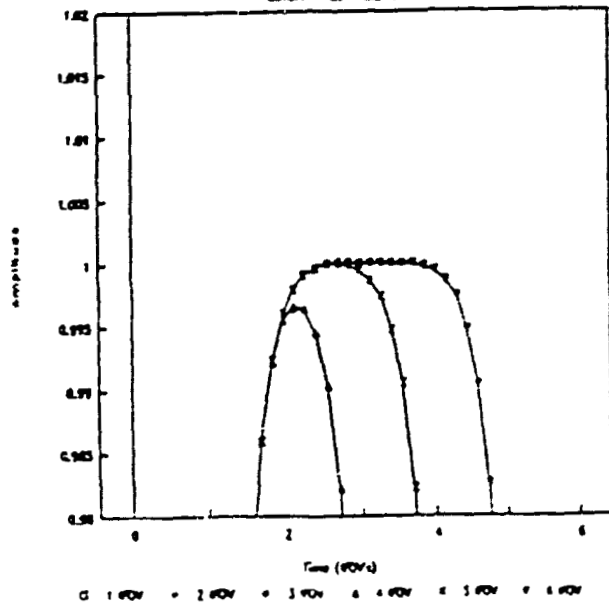
CHANNEL 4 PULSE RESPONSES

CUTOFF FREQ = Kc



CHANNEL 4 PULSE RESPONSES

CUTOFF FREQ = 2.2 Kc



CHANNEL 4 PULSE RESPONSES

CUTOFF FREQ = Kc

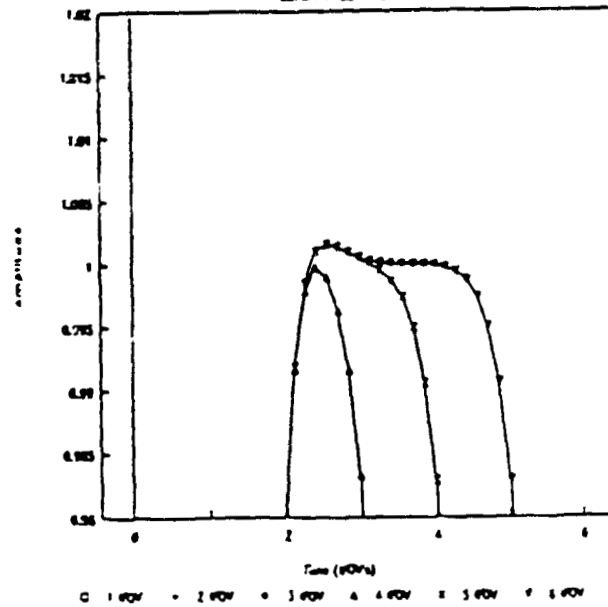


Figure D.1.4-5(d) - Channel 4 Pulse Responses
380

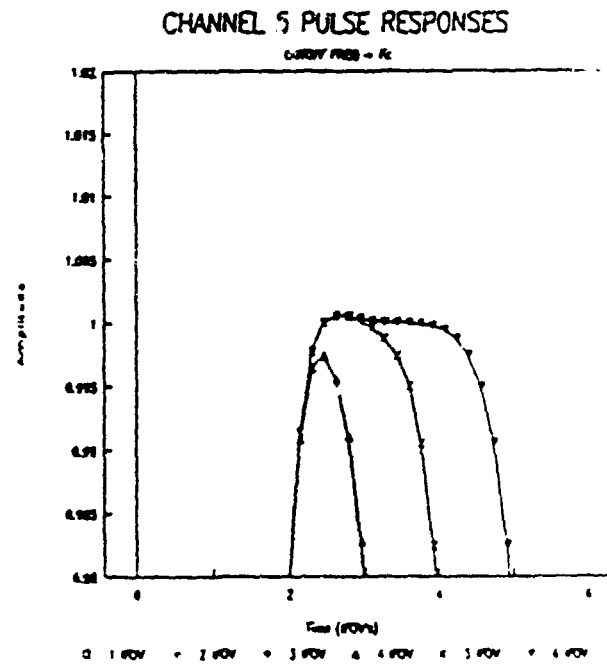
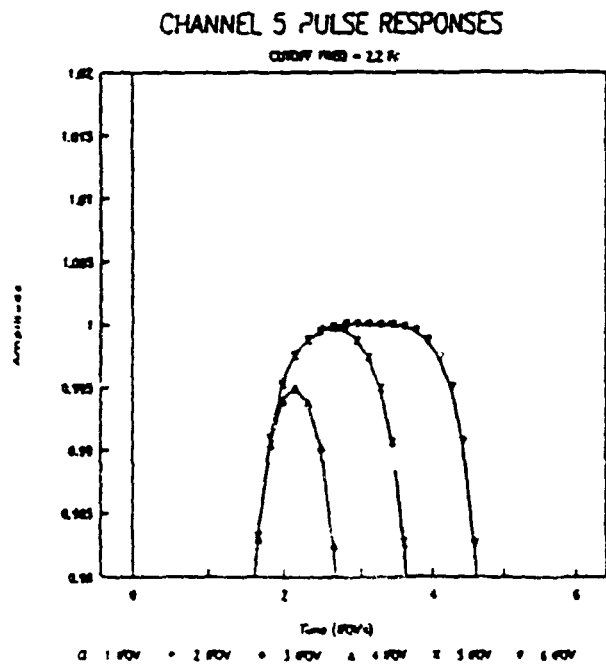
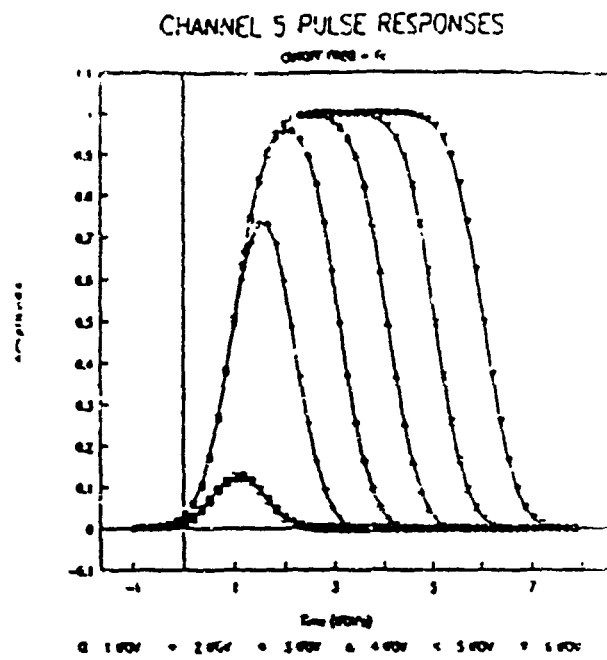
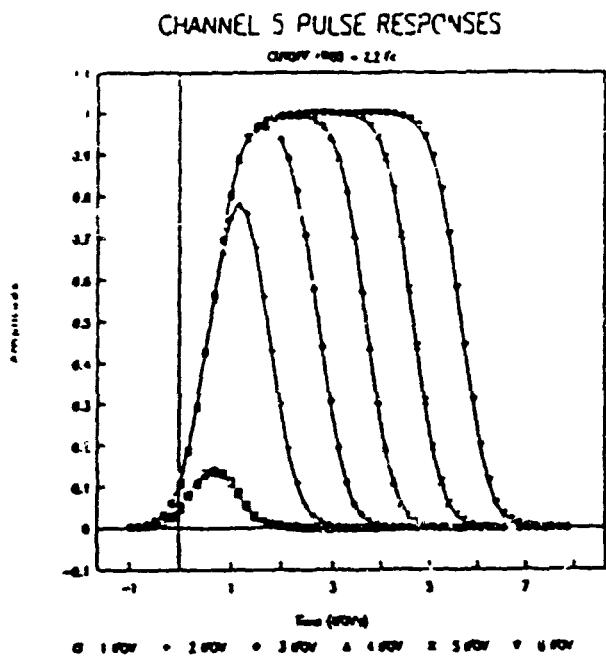


Figure D.1.4-5(c) - Channel 5 Pulse Responses
381

D.2 NOTES ON THE IMPACT OF IMC ON LARGE FOCAL PLANE ARRAYS FOR THE GOES-N IMAGER

Assuming that the instrument will acquire the data so that resampling is not required to meet the image to image registration specification, the required IMC signal in a well designed system will be dominated by orbital effects. For further information see pages 3-16 thru 2-22 FAC report "GOES-I,J,K/L,M IMAGE NAVIGATION AND REGISTRATION DRL 300-06" dated January 15, 1987 which describes the effect and provides some numbers for the dynamic ranges required as a function of Inclination, eccentricity and East/West station keeping error.

The imager in the GOES-I has a compact focal plane so that the accelerations required were not considered, except as they impact the pointing system design. The specified performance for GOES-I apply out to 60 deg ECA which corresponds to a scan angle of about 8 deg when scanning the equator. During some meetings various users have expressed a desire to operate nearer to the limb, but the accelerations grow rapidly beyond 60 deg ECA.

These effects are nearly linear with inclination over small inclination angles and magnitude. are shown in Figures D.2-1, D.2-2 and D.2-3, rate and acceleration of the IMC signal for an inclination of 3.5 deg with the North/South gimbal angle of 0.0 deg, i.e., scanning the equator, which is claimed to be the worst case for these effects. Note that the North/South IMC rate is about 2,500 $\mu\text{r}/\text{degree}$ of EW gimbal angle scan at 8 deg (60 deg ECA). These are 17,453 μr per degree which leads to a slope of 0.143 $\mu\text{r}/\mu\text{r}$ at an inclination of 3.5 deg, or 0.02 $\mu\text{r}/\mu\text{r}$ at $I = 0.5$ deg, or 0.004 $\mu\text{r}/\mu\text{r}$ at $I = 0.1$ deg.

The GOES-N band to band ∞ -registration specification is 14 μr . Allocating 5 μr of this error to effects due to IMC rates says that the maximum East/West separation of detectors in the focal plane would be 2,500 μr for an inclination less than 0.05 deg, 1,250 μr for a maximum inclination of 1.0 deg and 250 μr for an inclination of 0.5 deg.

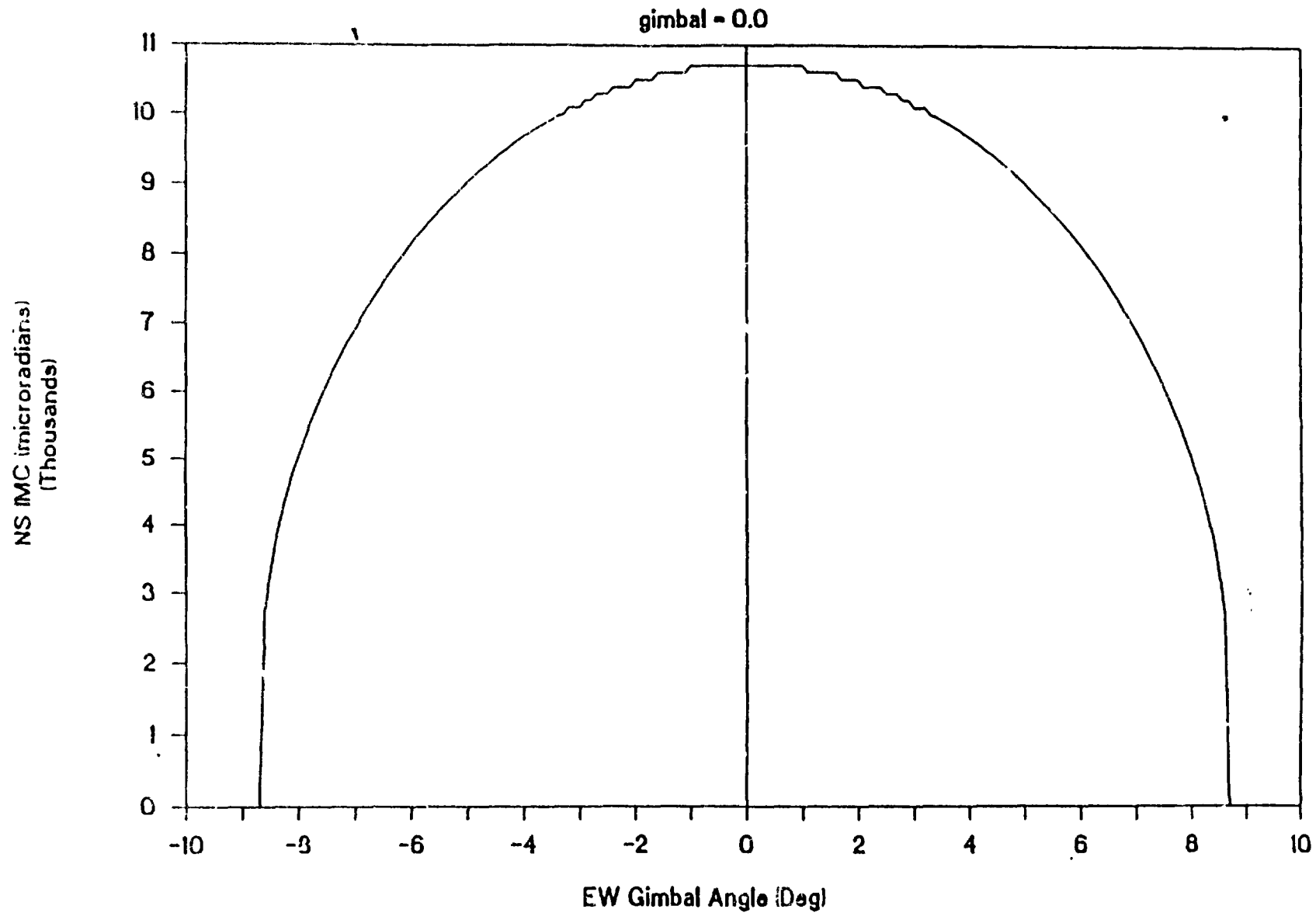


Figure D.2-1. IMC for -3.5 deg. Inclination

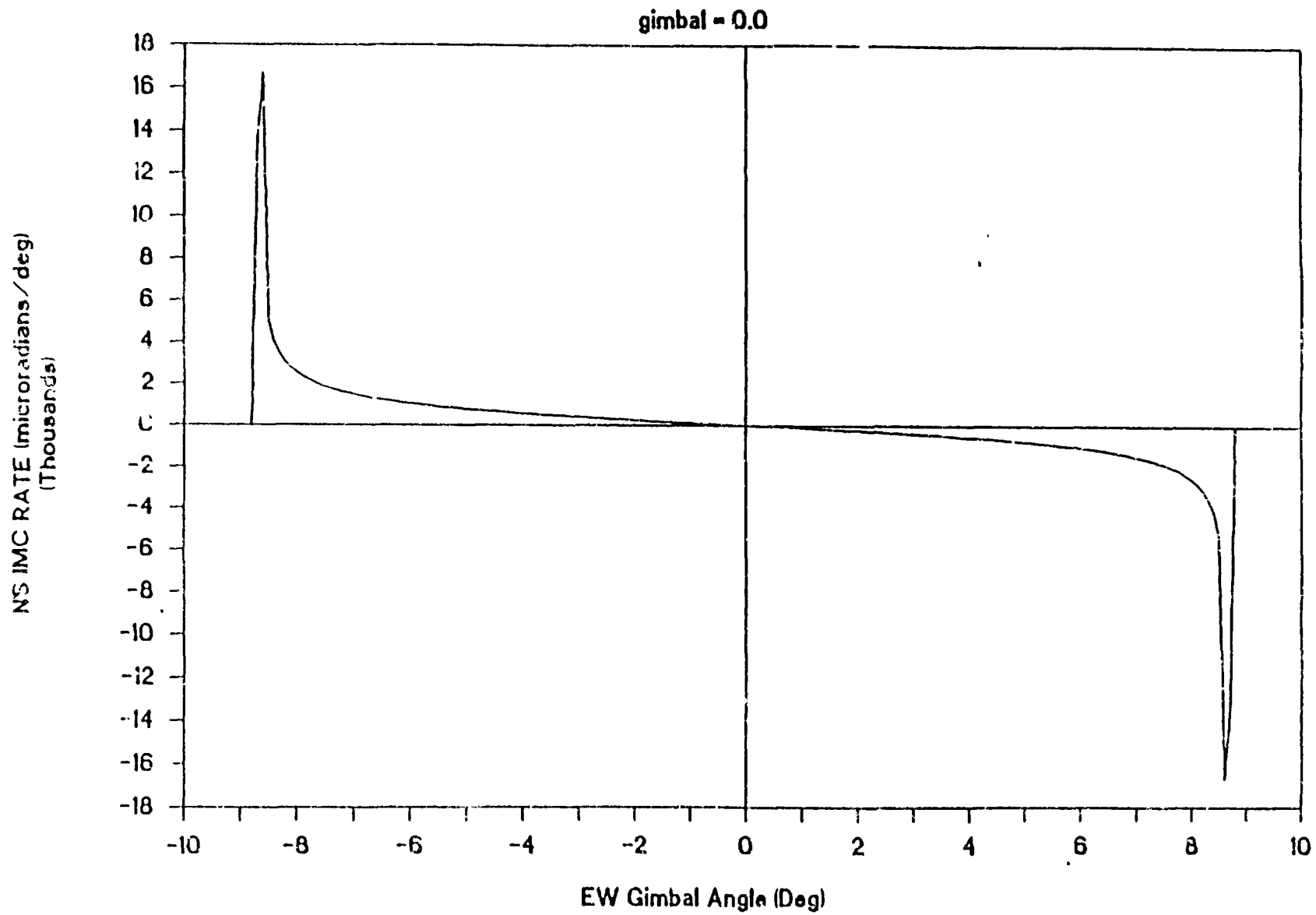


Figure D.2-2. IMC for -3.5 deg. Inclination

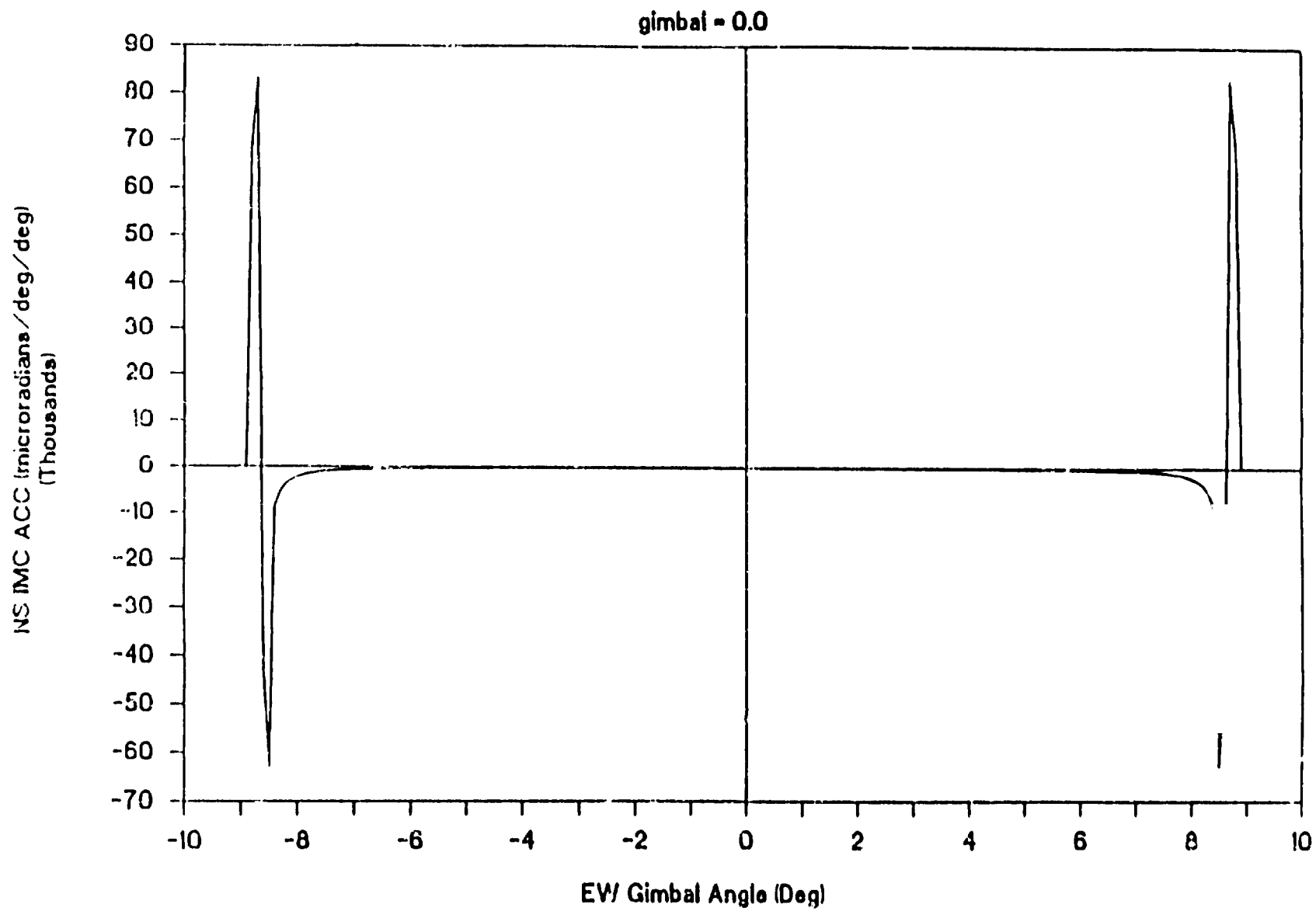


Figure D.2-3. IMC for -3.5 deg. Inclination

D.3 SUN SHADE GEOMETRY

D.3.1 Overview

For the GOES satellite, the angle of incidence of solar radiation depends not only upon the position of the satellite in its orbit around the earth, but the position of the earth in its orbit around the sun. As the solar incidence angle changes, thermal gradients are created within the satellite. These gradients result in unwanted aberrations in the optics of the imager. The aberrations are especially pronounced near local midnight, when sunlight impinges directly on the imager entrance optics.

A sun shade (or visor) placed in front of the entrance optics should decrease the severity of the aberrations by improving the thermal stability of the optical elements. The purpose of this study is to determine the effective shade length required to mask out direct solar radiation for various orbit positions and times of year.

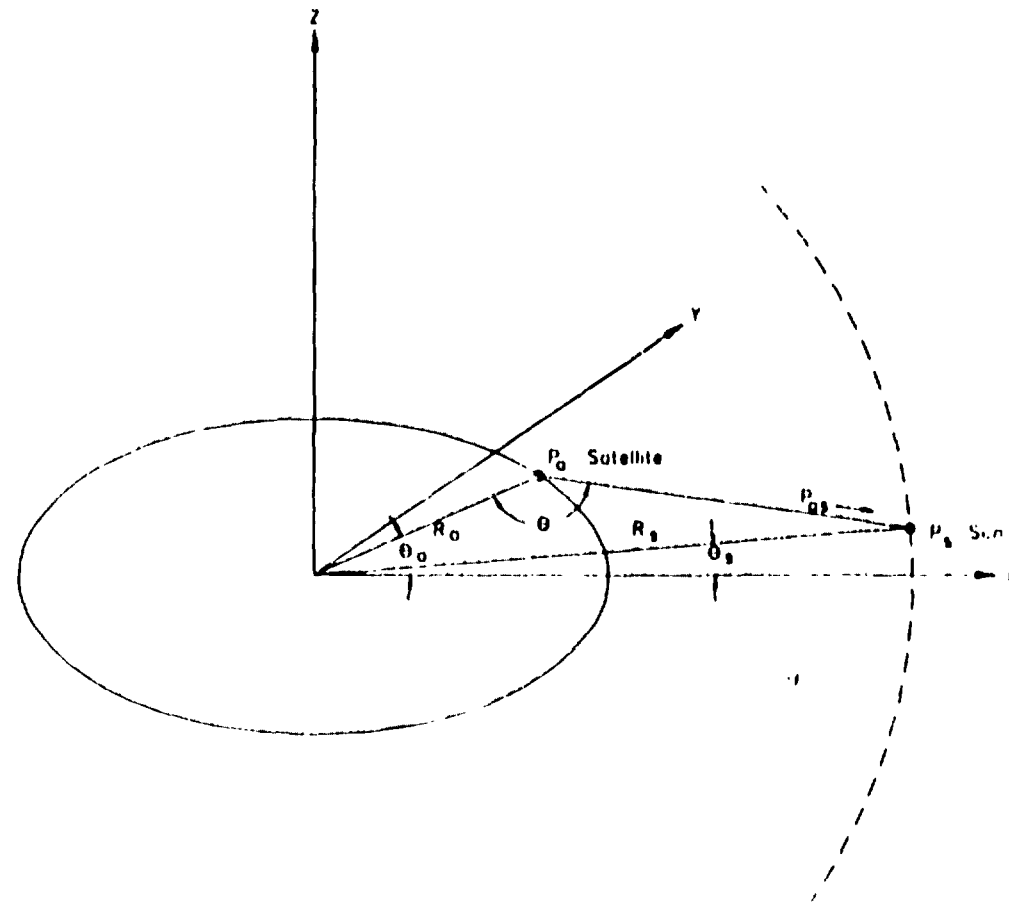
D.3.1.1 Theory

The analysis is divided into two parts. In the first part, the sun angle relative to the satellite is computed for various seasons and local satellite times. The second part utilizes the results of part 1 and computes the required shade length to keep sunlight from impinging on the optics.

The analysis is simplified with the choice of an appropriate coordinate system. For this analysis, a coordinate system is defined such that the origin is at the center of the earth, and the X-Y plane contains the path of the satellite. Additionally, the coordinate system is rotated so that the sun always has a Y coordinate of 0. The geometry is illustrated in the Figure D.3.1-1. In this figure R_a is the radius of the satellite orbit, R_s is the distance from the earth to the sun, θ_a is the satellite orbit position, and θ_s is the inclination of the sun relative to equatorial plane.

The angle between nadir and the sun vector, as viewed from the spacecraft, is θ . We are interested in computing the angle θ for various values of θ_a and θ_s . It is assumed that R_a and R_s are constants (i.e., that both the satellite's orbit around the earth and the earth's orbit around the sun are circular). θ_a corresponds to the satellite local time (at noon, $\theta_a=0$; at midnight, $\theta_a=180$ degrees). As the seasons change, the sun will appear to move up and down, tracing out an arc as shown by the dotted lines. At equinox, the sun will be on the X-Y plane ($\theta_s=0$). At the summer and winter solstices, the sun will be at the top and bottom of the arc respectively.

For the purposes of this analysis it will suffice to restrict the computations to one quarter of an earth year — since the other quarters are symmetric. As the satellite orbits the earth, it traces out a circle in the X-Y plane. The coordinates of the satellite can be written:



gsm\deford

Figure D.3.1-1. Geometry for Sun Shade Analysis

$$\text{Satellite Position: } \vec{P}_s = (R_s \cos \theta_s, R_s \sin \theta_s, 0)$$

The arrow above P_s denotes that it is a vector. The position of the sun is:

$$\text{Sun Position: } \vec{P}_s = (R_s \cos \theta_s, R_s \sin \theta_s, 0)$$

The vector extending from the satellite to the sun is computed by subtracting the coordinates of the satellite from the coordinates of the sun:

$$\vec{P}_{ss} = \vec{P}_s - \vec{P}_s = (R_s \cos \theta_s - R_s \cos \theta_s, -R_s \sin \theta_s, R_s \sin \theta_s)$$

From the dot product we can write:

$$-\vec{P}_s \cdot \vec{P}_{ss} = |\vec{P}_s| \cdot |\vec{P}_{ss}| \cdot \cos(\theta)$$

$|\vec{P}_s|$ and $|\vec{P}_{ss}|$ denote the magnitudes of P_s and P_{ss} respectively. Rearranging and solving for θ yields:

$$\theta = \cos^{-1} \left[\frac{-\vec{P}_s \cdot \vec{P}_{ss}}{|\vec{P}_s| \cdot |\vec{P}_{ss}|} \right] \quad (47)$$

The right hand side of (47) can be solved if R_s , R_s , θ_s , and θ_s are known. As mentioned previously, R_s and R_s are known constants and θ_s is a variable corresponding to the satellite local time. A separate computation must be performed to determine θ_s for various times of year.

To simplify the computation of θ_s , a new coordinate system is defined. The origin is still at the center of the earth, but the X axis is chosen to pass through the middle of the sun and the earth's axis of rotation is tilted at an angle of 23.45 degrees relative to the Z axis. The geometry is depicted in Figure D.3.1-2. In this figure D_s is the projection of the satellite - sun vector in the equatorial plane, θ_s is the tilt of the earth's axis, θ_s is the season of the year ($\theta_s = 0$: summer solstice, $\theta_s = 90$: autumnal equinox, $\theta_s = 180$: winter solstice, $\theta_s = 270$: vernal equinox) and θ_s is the sun angle relative to equatorial plane (same as θ_s in Figure D.3.1-1).

In Figure D.3.1-2, (a, b, c) are the coordinates of a unit vector along the direction of the earth's axis. The equatorial plane is perpendicular to (a, b, c) and is the plane containing the earth's equator (and the satellite's orbit). As the earth revolves around the sun, θ_s varies from 0 to 360 degrees and the unit vector (a, b, c) will precess

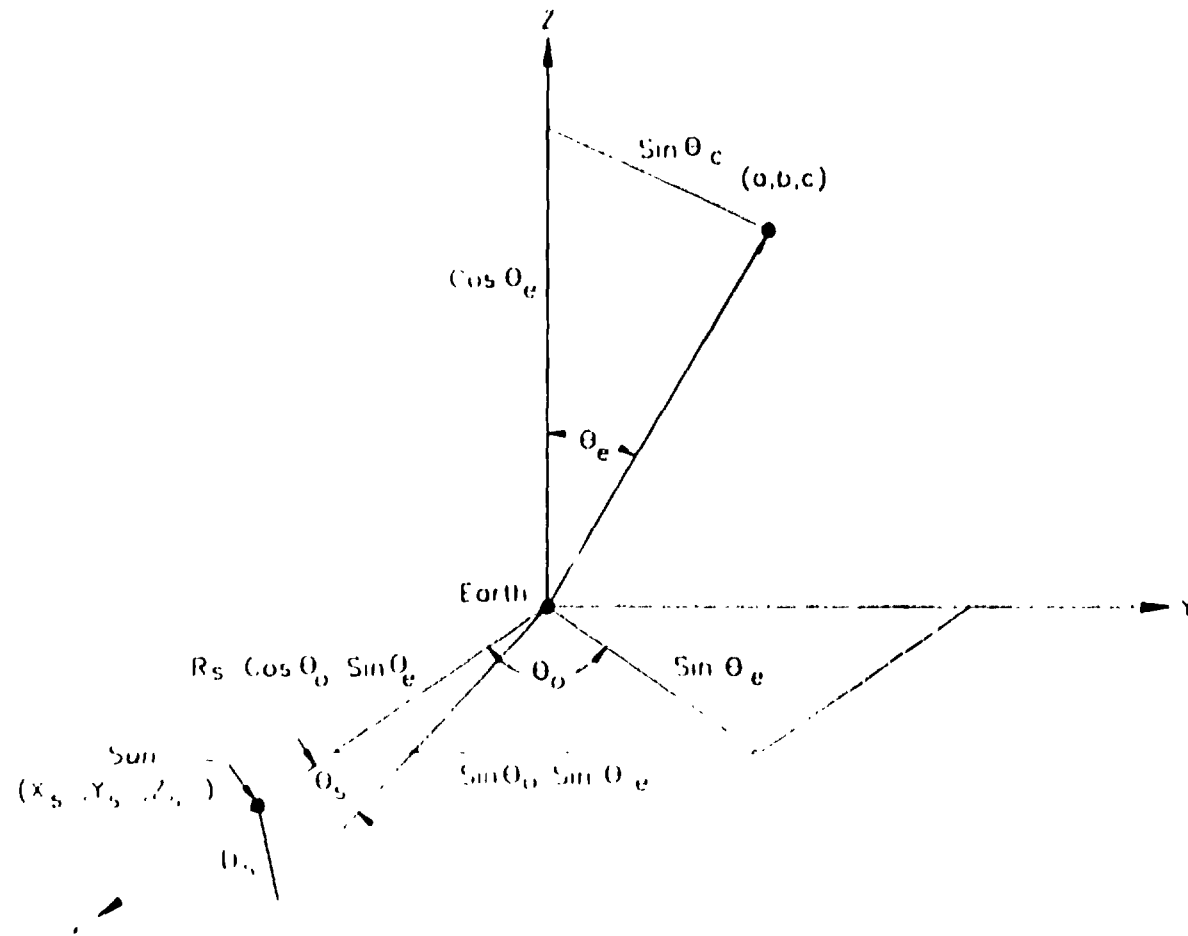


Figure D.3 1-2. Geometry for Computing Phases

around the Z axis, always maintaining the same tilt angle. Using simple trigonometry:

$$(a, b, c) = (\cos\theta_o \sin\theta_s, \sin\theta_o \sin\theta_s, \cos\theta_s)$$

The equatorial plane is defined by setting the dot product of the normal vector (a, b, c) and (x, y, z) to zero:

$$\text{Equatorial plane: } ax + by + cz = 0$$

D_s , the distance from the sun to the equatorial plane, can be computed from the following formula (a derivation can be found in most calculus textbooks):

$$D_s = \frac{ax_s + by_s + cz_s}{\sqrt{a^2 + b^2 + c^2}} \quad (48)$$

where (x_s, y_s, z_s) are the coordinates of the sun. (a, b, c) is a unit vector, so the denominator of (48) is unity. The sun is on the X axis and has coordinates:

$$(x_s, y_s, z_s) = (R_s, 0, 0)$$

Substituting into (48) yields

$$D_s = \cos\theta_o \sin\theta_s R_s$$

The angle of interest, θ_s , is given by:

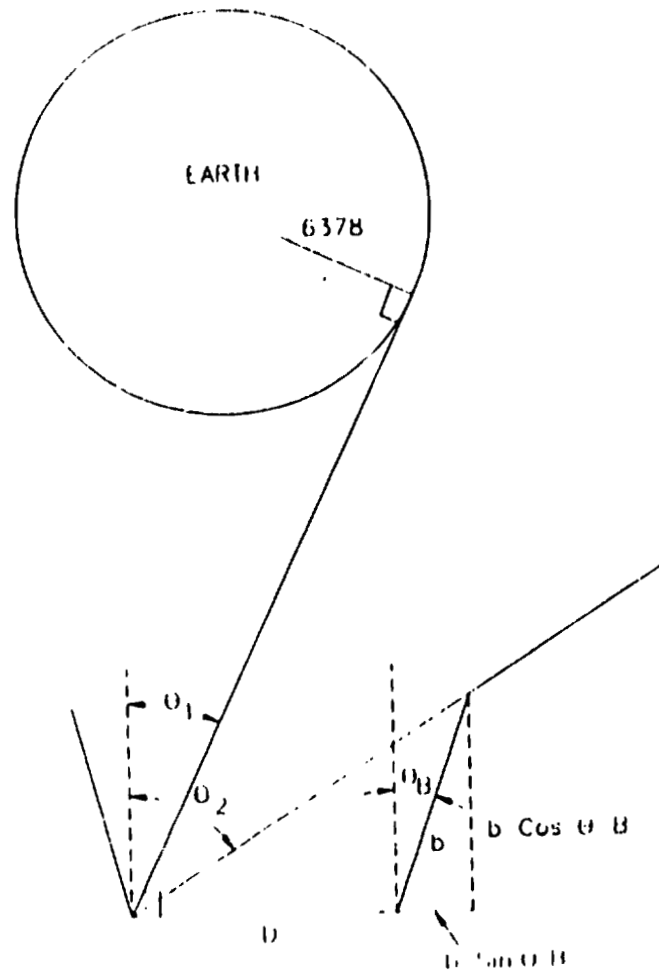
$$\theta_s = \sin^{-1} \left[\frac{D_s}{R_s} \right]$$

Substituting D_s into this expression yields:

$$\theta_s = \sin^{-1} [\cos\theta_o \sin\theta_s] \quad (48)$$

This expression yields the inclination of the sun relative to the equatorial plane for any time of year. The value computed from Equation (48) can be substituted into Equation (47) to compute the solar incidence angle θ .

The next step in the analysis is to compute the required sun shade length given the solar incidence angle computed from Equation (47). The geometry is illustrated in Figure D.3.1-3. In this figure b is the length of the shade, θ_s is the inclination of the shade, D is the diameter of entrance optics, θ_1 is the angle of earth tangent vector, and θ_2 is the limiting angle of the shade.



gpc/vic/df/012

Figure D.3.1-3. Sun Shade Geometry

It is assumed that the satellite is pointed directly at the earth. The sun shade is a conic section with a half cone angle of θ_b . All rays at angles greater than θ_2 will be blocked by the shade. θ_2 is given by the expression:

$$\tan\theta_2 = \frac{D + b \sin\theta_b}{b \cos\theta_b} \quad .$$

Rearranging and solving for b yields:

$$b = \frac{D}{\cos\theta_b \tan\theta_2 - \sin\theta_b} \quad (50)$$

Equation (50) can be used to compute the required shade length given the desired limiting angle, the inclination of the shade, and the diameter of the entrance optics.

Referring again to Figure D.3.1-3, θ_1 defines the eclipse angle of the earth (i.e., when the solar incidence angle is less than θ_1 , the sun will be eclipsed by the earth). θ_1 can be computed by knowing the radius of the earth, and the altitude of the satellite's orbit:

$$\theta_1 = \sin^{-1} \left[\frac{6378}{6378 + 35900} \right] = 8.677^\circ \quad (51)$$

D.3.1.2 Implementation

Equations (47), (49) and (50) were incorporated into a LOTUS 123 spreadsheet. Results were saved as ASCII files for inclusion in this report.

D.3.2.3 Results

Values from Equation (49) are listed in Table D.3.1-1. The table shows the angle between the sun and the equatorial plane of the earth for various times of year. Since there are approximately the same number of degrees in one revolution as the number of days in a year, the left hand column of Table D.3.1-1 is approximately equal to the number of days past the summer solstice.

Equations (47) and (50) were used to compute the length requirement of the sun shade. The results are summarized in Table D.3.1-2. The table shows the sun shade length (in inches) that will completely mask out the sun from the entrance optics.

Table D.3.1-2 covers the period from the spring equinox to the summer solstice. Each column is equally spaced in time and corresponds to 10 degrees in the earth's orbit around the sun (approximately 10 days).

TABLE D.3.1-1. SUN ANGLE RELATIVE TO EQUATORIAL PLANE

Earth Orbit Position θ_e (deg)	Sun Angle θ_s (deg)	
0	23.5	Summer Solstice
10	23.1	
20	22.0	
30	20.2	
40	17.7	
50	14.8	
60	11.5	
70	7.8	
80	4.0	
90	0.0	Fall Equinox
100	-4.0	
110	-7.8	
120	-11.5	
130	-14.8	
140	-17.7	
150	-20.2	
160	-22.0	
170	-23.1	
180	-23.5	Winter Solstice
190	-23.1	
200	-22.0	
210	-20.2	
220	-17.7	
230	-14.8	
240	-11.5	
250	-7.8	
260	-4.0	
270	0.0	Spring Equinox
280	4.0	
290	7.8	
300	11.5	
310	14.8	
320	17.7	
330	20.2	
340	22.0	
350	23.1	
360	23.5	Summer Solstice

TABLE D.3.1-2. SUN SHADE LENGTH REQUIREMENT

SATELLITE ORBIT POS (deg)	SATELLITE LOCAL TIME (24 hr)	SUN ANGLE RELATIVE TO EQUATORIAL PLANE (deg)									
		SPRING EQUINOX								SUMMER SOLSTICE	
		0.0	4.0	7.8	11.5	14.8	17.7	20.2	22.0	23.1	23.4
120.0	20.0	9	9	9	8	8	8	8	8	8	8
122.0	20.1	9	9	9	9	9	9	9	8	8	8
124.0	20.3	10	10	10	10	10	10	9	9	9	9
126.0	20.4	11	11	11	11	11	10	10	10	10	10
128.0	20.5	12	12	12	12	11	11	11	11	11	10
130.0	20.7	13	13	13	13	12	12	12	11	11	11
132.0	20.8	14	14	14	14	13	13	13	12	12	12
134.0	20.9	16	16	15	15	15	14	14	13	13	13
136.0	21.1	17	17	17	16	16	15	15	14	14	14
138.0	21.2	19	19	18	18	17	16	16	15	15	15
140.0	21.3	21	20	20	19	19	18	17	17	16	16
142.0	21.5	23	22	22	21	20	19	18	18	17	17
144.0	21.6	25	25	24	23	22	21	20	19	19	19
146.0	21.7	28	28	27	25	24	23	22	21	20	20
148.0	21.9	31	31	30	28	27	25	23	22	22	22
150.0	22.0	35	35	33	31	29	27	26	24	24	23
152.0	22.1	41	40	38	35	32	30	28	26	25	25
154.0	22.3	47	46	44	40	36	33	30	29	28	27
156.0	22.4	56	55	51	46	41	37	33	31	30	29
158.0	22.5	69	67	60	53	46	41	37	34	32	32
160.0	22.7	89	84	74	62	53	46	40	37	35	34
162.0	22.8	124	114	95	76	61	51	44	40	38	37
164.0	22.9	200	174	130	94	72	58	49	44	41	40
166.0	23.1	506	357	200	123	86	66	54	48	44	44
168.0	23.2	N/A	N/A	417	170	104	75	60	52	48	47
170.0	23.3	N/A	N/A	N/A	264	129	86	66	56	51	50
172.0	23.5	0	N/A	N/A	515	161	98	72	60	54	53
174.0	23.6	0	0	N/A	2466	203	110	78	64	57	56
176.0	23.7	0	0	N/A	N/A	252	121	82	67	60	58
178.0	23.9	0	0	0	N/A	296	128	85	69	61	59
180.0	0.0	0	0	0	N/A	314	131	87	69	62	60

ASSUMPTIONS:

Diameter of entrance optics = 12 (inches)
 Shade angle relative to normal = 12.677 (deg)

NOTES:

A required shade length of 0 indicates that the sun is eclipsed by the earth

An entry of "N/A" indicates that, given the assumed shade angle and the solar incidence angle, it is not possible to block out the sun, regardless of the length of the shade.

Each row of Table D.3.1-2 corresponds to a position of the satellite in its orbit around the earth. The table covers the period of time from 8 PM to midnight local satellite time.

D.3.1.4 Conclusions

From Table D.3.1-2 we can see that regardless of the length of the sun shade, there will be times when solar radiation will impinge directly on the optical system. Even for a large shade (say 48 inches), there will be a period of 1 to 2 hours each day when direct sunlight will fall on the optical system.

In order to get shading to within 4 hours of local midnight (no more than 8 hours of direct sunlight each day), the sun shade would have to be 9 inches in length.

D.4 LONG-TERM STABILITY CALIBRATION OF GOES-N VISIBLE CHANNEL

D.4.1 Requirements

One secondary, but nevertheless important, goal of the GOES-N satellite program is to collect data in support of global climatic change research. The specific role of the GOES-Next sensors will be to monitor long range changes in the earth's albedo. Accomplishment of this objective requires that the throughput of the reflective channels (visible and near IR) be known to a precision of about 1-2% over the mission lifetime.

The GOES-N visible channel has a central wavelength of 650 nm and a full-width, half-maximum (FWHM) of 200 nm. It also has a near-IR channel with a central wavelength of 860 nm. The raw throughput of these channels is expected to decrease with time due to effects such as degradation of optical surfaces and radiation damage to detectors. Calibration is essential, therefore, to determine and compensate for this decrease in throughput. In the design of the calibration system, the performance at 650 nm is to be optimized.

It is highly desirable to perform a full aperture, end-to-end calibration of the system using a known, stable source. The end-to-end requirement is driven by the fact that the forward-most elements in the optical train, i.e., the scan mirror(s) and the primary, are the elements most highly exposed to contamination and to solar vacuum ultraviolet (VUV) radiation. The full-aperture requirement stems from the fact that contaminants or other degradations may not be uniformly distributed on the surface of a mirror.

Calibration lamps may be used to perform periodic measurements of short-term stability, but they lack the power for a practical full-aperture calibration and are not stable enough to provide a reliable reference over the life of the mission. The preferred approach is to use indirect solar flux for the full aperture, end-to-end calibration.

The moon is one potential calibration target which provides indirect solar radiation. Alternative approaches involve attenuating direct sunlight to a radiance level within the dynamic range of the sensor. This may be accomplished either by diffuse reflection or by transmission through a blockage.

A blockage technique which uses full sunlight over a small sub-aperture is undesirable because the reflectivity of a degraded mirror may not be uniform over its surface, and the calibration path covers only a small portion of that surface. An alternative technique uses a perforated plate to illuminate the mirrors with approximately uniform, greatly attenuated sunlight. Most of the problems in this technique are due to diffraction effect.

D.4.2 Lunar Calibration

The moon is a far-field source of reflected sunlight with a radiance which lies within the dynamic range of an earth viewing visible/near-IR sensor. The moon's radiance is approximately 2×10^{-6} that of direct sunlight, while the radiance of an ideal Lambertian radiator, illuminated by sunlight at normal incidence, is 2.12×10^{-5} that of direct sunlight. Typical lunar albedo values are 0.07-

0.13; extreme values range from 0.05 to 0.18.[1] Consequently, the radiance of lunar radiation is well-suited for calibrating the response of the sensor to low-albedo targets. The sharp circular edge of the lunar image also provides a target against which the edge response of the sensor can be evaluated for MTF verification.

Because of these beneficial features, lunar calibration should definitely play a role in the characterization of GOES-N long term stability. Some limitations will result, however, if the moon is the only source for full-aperture calibration. In the first place, the moon is not intense enough to simulate a high albedo target, so data taken at the lunar flux level must be extrapolated to calibrate the detectors at the high end of the dynamic range. In addition, the reflected sunlight from the moon is more difficult to characterize than direct solar radiation.

Characterization of the lunar input requires mapping the lunar albedo with spectral resolution at least as great as that of the GOES-N sensor and with spatial resolution several times greater. (The higher spatial resolution is required because the spatial data must be re-sampled to match the sensor's IFOV.)

Mapping of the lunar albedo may be done from ground-based observations, in which stars of known magnitude and color are compared to IFOV on the lunar surface. When these lunar albedo maps are utilized, it is necessary to use a complex algorithm which corrects the lunar albedo data for sun/moon distance, solar incidence angle, and angle of observation. Due to the rough lunar surface, this process may not be straightforward. The reflected lunar radiation may also be slightly polarized, particularly when the phase of the moon is less than full. For example, a quarter moon exhibits a polarization of about 0.066-0.088.[2] Accounting for this polarization further complicates the sensor characterization problem.

Lunar calibration can also be used to make a crude determination of the bi-directional reflectance distribution function (BRDF) of the scan mirror or mirrors. This measurement can be accomplished by observing the pixels lying immediately outside of the lunar image.

Since it would be cumbersome to tilt the spacecraft for the purpose of viewing the moon, it is necessary to determine how often the moon will be within ± 10 degrees declination of the equator. Preliminary analysis, summarized in attachment A, indicates that the moon will have a window of potential availability approximately three days long at intervals of about 10 days. Some of these windows may not be useful, due to a new moon or phasing problems between the satellite and lunar orbits. Nevertheless, this availability is more than adequate to assess the long-term stability of a sensor.

D.4.3 Full aperture calibration with indirect sunlight

To calibrate an earth-viewing optical sensor in the top of its dynamic range, it is convenient to use sunlight which has been attenuated to a level of about $1.5-2 \times 10^{-5}$ the radiance of direct solar radiation. The most common approach is to use a diffuser plate which approximates an ideal Lambertian radiator. Attenuation is accomplished by diffuse scattering of the solar flux from a

nearly-collimated input which subtends a solid angle of 66 microsteradians into a Lambertian output with an effective solid angle of 3.14 steradians. The radiance is attenuated by the ratio of these two solid angles (2.12×10^{-5}) multiplied by the cosine of the solar incidence angle and the reflectivity of the plate.

When an ideal Lambertian radiator overfills the aperture of a sensor, then the flux observed by that sensor is independent of the normal angle of the radiator. It should be noted, however, that no surface is perfectly Lambertian. Characterization of and compensation for the non-ideal BRDF of the surface is necessary.

The main problem with a diffuser plate is the tendency of its diffusely reflective surface to degrade in time. Contaminants, either particulates or molecular films, can accumulate on the surface. In addition, many materials are unstable when exposed to VUV radiation. Some hydrocarbon contaminants are transparent in the visible and the near IR under normal conditions, but become strong absorbers after they react in the presence of VUV radiation.[3,4] Contaminants which exhibit in-band luminescence when exposed to UV radiation are another potential problem.

In order to monitor the degradation of a diffuser plate, it may be necessary to fix a ratioing radiometer, i.e., a radiometer which is specially designed to determine the ratio between direct and diffused sunlight. Ratioing radiometers generally use pupil imaging to convert this ratio from the natural value of about 2×10^{-5} to a value within the dynamic range of a detector. In typical designs, the image of the diffuser plate covers the field lens, but the image of the sun is much smaller. Because of this feature, the ratioing radiometer approach is susceptible to position-dependent variations in the throughput of the field lens. There is also some uncertainty in characterizing the FOV of the ratioing radiometer, which is critical when viewing the diffuser (The diffuser over-fills the ratioing radiometer's FOV.)

A diffuser plate must usually be deployed on a boom; so sun glints reflected off this boom can potentially corrupt the calibration. It is also difficult to characterize indirect illumination of the diffuser or of the ratioing radiometer by sun glints reflected off the spacecraft.

An integrating sphere may be used to closely approximate a Lambertian distribution of radiation. Its output radiance level may also be varied easily by changing the dimensions of the input aperture. In an integrating sphere, however, the surface degradation problems become even more critical than they are for a diffuser plate. This extreme sensitivity to surface degradation is due to the fact that the average ray undergoes several diffuse reflections in the sphere. The sphere's throughput is the effectively the reflectance of its surface raised to the Nth power, where N is the average number of reflections in the sphere, the surface degradation problem is compounded. Furthermore, the diameter of the integrating sphere must be significantly larger than the aperture of the telescope it is used to calibrate. Because of these problems, we did not give further consideration to an integrating sphere.

D.4.4 Perforated plate requirement

A perforated plate is a promising alternative to a diffuser plate. The design of a perforated plate solar calibration system involves trades among several conflicting requirements:

1. The need to achieve uniform illumination of the first mirror in the optical train tends to drive the design toward small holes in a uniform array. It also makes a large spacing between the plate and the first mirror desirable.
2. A uniform array of holes tends to act like a diffraction grating. To avoid grating effects, it is desirable to randomize the spacing of the holes so that they do not have long range order.
3. The diffraction of light by a hole increases as a function of the ratio of the wavelength of the light to the diameter of the hole. Thus, the solar image will appear "blue" in its center and "red" around its circumference when viewed through a plate containing small holes. It is desirable to minimize this effect by maximizing the size of the holes.
4. It is highly desirable to integrate the perforated plate and its deployment mechanism into the sunshade of the sensor. This approach not only minimizes the size and weight of the plate and its deployment mechanism, but also minimizes the exposure of the plate to stray light. This constraint tends to minimize the separation between the plate and the first mirror.
5. In order to minimize the cross-section of the plate, it is desirable to minimize the separation between the plate and the first scan mirror.
6. To avoid time-dependent degradation, the holes must be much larger than any molecular films or particulates which are likely to accumulate upon them during the lifetime of the mission. The holes must also have good geometric integrity, i.e., any burrs or kerf must have negligible effect upon the cross sections of the holes.

Since the perforated plate is used in transmission, its utility is restricted to windows of availability during which the sun lies within the FOV of the sensor. If we assume that the spacecraft cannot be tilted, then there are two windows of availability per year: the solar calibration is essentially restricted to the seasons of eclipses, i.e., a period of about one month centered about each equinox. Although this availability is less than optimal, it is sufficient to address the long-term changes in the throughput of an optical sensor which occur over the lifetime of a mission. Solar calibration should be augmented by lunar calibration and by short-term stability measurements to fully characterize the sensor.

D.4.5 Preliminary perforated plate parameters (P⁴)

If the plate is configured in a hexagonal grid, then the hexagons will contain holes in a pseudo-random pattern. Each of the hexagonal elements will contain a hole but the hole will be located at a random point within the hexagon. (A hexagonal grid is slightly preferable to a rectangular grid for this application.) This pattern will exhibit some interference maxima, but the modulation of intensity will be much lower than that produced by an array of uniformly spaced points. (Attachment B)

if S is the spacing between the centers of adjacent hexagons, then the area of each hexagon is $0.866 S^2$. The area of a hole of diameter D is $0.785 D^2$, so the fraction of the plate which is open is $0.907 (D/S)^2$.

The maximum value of S is dictated by the need for uniform, or at least nearly uniform, illumination of the first mirror. By considering adjacent holes as "pinhole cameras", we may require that the geometric solar image projected on the first mirror have a radius no smaller than λ . Since the solar disk subtends 9.2 milliradians, the maximum value of S becomes $0.0046 L$, where L is the separation between the perforated plate and the first mirror.

It would be convenient to locate the perforated plate (or foil) within the sunshade, which would not only minimize its size and weight, but would also avoid the stray light problems inherent in an external boom. A value of $L = 0.6$ m is an arbitrary, but reasonable assumption, leading to $S = 2.8$ mm.

In the absence of diffraction, the D/S ratio should be approximately 0.0045 to achieve the proper radiance level, resulting in a hole diameter, D , of 12.6 microns. Holes 48 microns in diameter in a hexagonal array with 2.8 mm spacing allow a total of 2.67×10^{-4} the direct solar exitance to penetrate the plate. If the solid angle were unaltered, the radiance would be more than an order of magnitude too large. When viewed through the perforated plate, however, the solar image is blurred by diffraction, so its radiance may be expected to lie within the high albedo range. (Refer to the following analysis.)

At 650 nm, the first ring of the Airy disk of a point source imaged through a 48 micron hole will have a diameter of $2.44 \lambda/D$, or 33.0 milliradians, which is large in comparison to the 9.2 milliradian solar disk. To obtain an order of magnitude estimate of the intensity at the center of the blurred solar image, we assume that the solar exitance is uniformly distributed over a disk 34.3 milliradians in diameter (the RSS of these two values). These assumptions result in a calculated equal to 1.92×10^{-5} that of direct sunlight (an effective albedo of 91%). Further analysis is required to obtain refined values of the above parameters.

D.4.6 Ordered array vs random array trade-off

We recommend a pseudo-random array of holes to minimize both the interference effects inherent in a perfectly ordered array and the fluctuations in illumination inherent in a perfectly random array. Although neither a regular array nor a random array of holes will be used, it is instructive to determine the diffraction pattern which would result from a regular array of holes and the fluctuations in illumination which would result from a random array.

When illuminated by monochromatic light, a regular hexagonal array with an inter-hole spacing of S produces a two-dimensional diffraction pattern which also has hexagonal symmetry. The spacing between adjacent lines of holes is $0.866 S$, so the angular separation between adjacent maxima of the diffraction pattern is simply the wavelength divided by the line spacing, or 268μ for $\lambda = 650$ nm. and $S = 2.8$ mm. The intensity of the maxima is determined by the diffraction pattern of the circular aperture.

If a plate with a regular array of holes were illuminated by a point source, these maxima would be evident when observed in a narrow spectral band. The sun is an extended source, however, with a diameter of 9.2 milliradians, or 34 diffraction orders. Diffraction by the small diameter of the holes causes the solar image to have a diameter several times greater than its geometric value, so that the diameter of the blurred solar image subtends a very large number of orders.

The visible band to be calibrated has an effective FWHM of 550–750 nm. Because of this moderately large passband, diffraction-induced modulation of the integrated intensity is restricted to the first few diffraction orders. At higher orders, the diffraction pattern is wiped out by interference among overlapping orders. For example, the 3rd order path difference at 750 nm is 2250 nm, which exceeds the 4th order path difference at 550 nm is 2200 nm, producing overlap between the 3rd and 4th orders. As the orders increase, the overlap becomes more pronounced: orders 6 through 8 have regions of mutual overlap, as do orders 9 through 12, orders 12 through 16, etc.

To obtain a more quantitative estimate of the angular extent of structure in the diffraction pattern, we may approximate the spectral dependence of the channel's throughput by a Gaussian function with the same FWHM. A Gaussian function with a FWHM of 200 nm has a standard deviation, σ , of 85 nm.

As stated above, the angular separation between adjacent diffraction orders is $\lambda/0.866 S$. The standard deviation of the angular width of an Nth order diffraction maximum is $N\sigma/0.866 S$. Two Gaussian functions which are separated by less than 2σ merge into a smoothed curve with a single maximum. Taking the ratio of the angular width of an Nth order maximum to its angular separation, we find that the overlap of adjacent orders will wipe out structure in the diffraction pattern whenever, N, the order of the diffraction maximum, satisfies the following inequality:

$$N > \lambda/2\sigma$$

When $\lambda = 650$ nm and $\sigma = 85$ nm, this inequality is satisfied by the fourth and higher order maxima. Since the angular separation between maxima is $268 \mu\text{r}$, any structure produced by the sharp change in intensity at the circumference of the solar disk will not extend more than four orders, or 1.07 milliradians, from the geometric edge of the solar disk.

It is clear from the above analysis that the structure in the diffraction pattern will be insignificant when convolved with the central portion of the image of the solar disk. The circular region 7 milliradians in diameter at the center of the solar image should have a very uniform intensity in which diffraction-induced structure is completely negligible.

Due to the variable angle of incident sunlight and to any non-uniformities in the deployment mechanism of the perforated plate, the portion of the plate's cross-section which lies in front of the aperture will probably vary. Since the holes on the plate are not perfectly ordered, there will be some fluctuation in the total number of holes through which the sun is viewed. The following analysis quantified the error induced by this fluctuation.

The sensor has an aperture diameter of 300 mm, so its area is $7.07 \times 10^4 \text{ mm}^2$, while each hole occupies a hexagon of area 6.79 mm^2 . The average number of holes in this area is 1.04×10^4 . Because each hole is situated in a random position within its hexagonal cell, the number of holes in front of the aperture will not remain fixed if the plate is translated. The presence or absence of a hole in a cell along the circumference of the aperture may be treated as a random event. If there are N hexagonal cells along the circumference and if one-half of them contain holes, then the average of holes is $N/2$ and the standard deviation in the number of holes is $(N^{1/2})/2$. An aperture 300 mm in diameter has a circumference of $1.89 \times 10^3 \text{ mm}^2$. Since the grid spacing is 2.8 mm, approximately 675 hexagonal cells will lie on the circumference. Therefore, the average number of holes on the circumference is 338 and the standard deviation is 13, or 0.13% of the total number of holes. An error of three standard deviations, or 0.39%, is used in the error analysis of the perforated plate system.

The preceding analysis shows that the strawman parameters are reasonable and will yield a solar image whose radiance is appropriate for the calibration of the sensor with respect to high-albedo targets. A more detailed investigation must be performed to optimize the parameters of the perforated plate.

D.4.7 Implementation of the perforated plate

Holes 48 microns in diameter are well within the state-of-the-art. The holes in the perforated plate should be tapered, with their small, aperture-defining diameters on the sunward side of the plate. This geometry will avoid multiple reflections in the holes, and will prevent shadowing when the solar incidence angle is near normal. The sensor-facing side of the plate should be blackened to prevent stray light from being reflected into the sensor.

Since the perforated plate introduces diffraction into the solar image, the vignetting constraint is slightly more severe for the calibration mode than it is for the normal, data-gathering mode. To avoid this problem, calibration data should not be collected at angles within one Airy disk diameter (33 mrad) of the angle at which the undiffracted image becomes vignetted.

The effective area of each hole varies as the cosine of the solar incidence angle. Diffraction also increases along the direction in which the holes are foreshortened, so the peak irradiance in the solar image is approximately proportional to the square of the cosine of the solar incidence angle. Assuming a quadratic relationship, we find the change in the normalized radiance, dL , as a function of the change in the incidence angle, $d\theta_i$:

$$dL = -[2 \tan(\theta_i) / \cos(\theta_i)] d\theta_i$$

where $d\theta_i$ is expressed in radians.

When the plane is illuminated at within a few degrees of normal incidence, then the variation in throughput is very insensitive to solar incidence angle. In the actual implementation, the plate will be integrated into the sunshade at a fixed angle. Its normal will point toward nadir, so the solar incidence angle will typically be $\theta_i = 10$ – 12 degrees during calibration measurements (since the earth blocks the direct sun viewing angle).

At an incidence angle of 12 degrees with an uncertainty of 0.5 degree, the normalized radiance is 0.9568 with a normalized uncertainty of 0.38% which is within the error budget for visible/near IR calibration. The lax tolerance on uncertainty is significant because it implies that a perforated foil would be acceptable.

The perforated plate or foil will tend to heat and expand when it is illuminated by sunlight. Uniform expansion will preserve the D/S ratio, so the total exitance of the plate will remain unchanged. The increase in diameter of the holes will tend to sharpen the image, however, increasing its radiance over a smaller solid angle. Once again, this effect is well within the error budget.

To quantify the above effect, consider an aluminum plate. Aluminum has a relatively high coefficient of thermal expansion of $25 \times 10^{-6}/\text{C}$. Even if the plate undergoes a thermal excursion of 40 C during calibration, the value of D will change by only 0.1%, so the irradiance at the center of the solar image will change by no more than 0.2%.

The single most important advantage of a perforated plate over a diffuser plate is the perforated plate's relative insensitivity to surface degradations. For example, a monolayer of hydrocarbon contaminant film can have a significant impact on the reflectivity of a surface, particularly if it is chemically altered by VUV radiation. On the other hand, a monolayer ($<10^{-3}$ μm in thickness) will have a completely negligible effect upon a hole 48 μm in diameter. Likewise, VUV radiation, atomic oxygen, and charged particle bombardment may effect the reflectivity of a surface, but will not change the area of a hole. A micrometeoroid bombardment will degrade a perforated plate only if perforates the plate or causes significant warpage.

It is necessary, of course, to use reasonable care in avoiding contamination of the plate. Particulate contaminants may decrease the throughput if they obstruct the holes. The plate should be handled in a clean room environment on the ground, and should be stowed when not in use in space.

The calibration system could make use of a perforated metallic foil, rolled up like a window shade in a mechanism attached to the sunshade. It could then be unrolled to cover the full aperture in its deployed position. A back-up mechanism would be required to provide a redundant means of removing the perforated foil from its deployed position.

The signal to noise ratio (SNR) of the sensor is specified at 150/1 for a full-albedo target. When a detector which subtends 28 μr is scanned at one sample per dwell over the central 7 milliradians of the solar disk, it collects 250 individual samples. Averaging these measurements improves the SNR by a factor of the square root of 250, or 15.8. The resultant error, i.e., the reciprocal of 2,370, is 0.042%, which yields a 3σ error of 0.13%.

D.4.8 Earthshine

The earth subtends about 300 milliradians when viewed from geostationary altitude. If the earth/satellite line is offset 12 degrees (209 milliradians) from the earth/sun line, then the tangent altitude of the line of sight from the sun to the satellite will be about 2500 km., so there will be

no atmospheric extinction. The satellite will see a crescent-shaped "new earth" which subtends 300 milliradians in height and $300[1 - \cos(12^\circ)]$ milliradians in width. Multiplying these two dimensions by a factor of 0.7854 to account for the crescent shape, we obtain an illuminated solid angle of 1.54 milliradians.

The irradiance level on the ground is greatly reduced due to the twilight conditions in this area. To obtain an order of magnitude estimate of the earthshine, we may neglect atmospheric extinction and assume that the flux on the earth's surface is equal to the direct solar flux multiplied by $\sin(6^\circ)$, or 0.105.

If the entire illuminated area acts as a perfect Lambertian radiator, then its ratio of incident to reflected radiance is 2.12×10^{-5} . Since the sun subtends 66 microsteradians, the ratio of earthshine to sunshine for a 12-degree crescent Lambertian earth is $(0.00154)(0.105)(2.12 \times 10^{-5}) / (66 \times 10^{-6}) = 5.2 \times 10^{-5}$. It is clear that Lambertian earthshine is negligible.

Another potential contribution to earthshine is the specular reflection of solar radiation of the ocean's surface. At grazing incidence, 84 degrees off-normal, the reflectivity of the water can be high. If the earth acts as a specular sphere, then the area of the bright spot (viewed from the satellite) will be a circle of diameter 0.0046 multiplied by the earth's radius, i.e., 29.3 km in diameter.

Since the bright spot is at the limb, and not at nadir, the distance from the satellite to the bright spot is 43×10^3 km. When viewed from this distance at an angle of 84 degrees, the spot appears elliptical with a major axis of 681 μ r and a minor axis of 71 μ r. Therefore, it subtends 38 nanosteradians. Even if we assume that the ocean is a perfect specular reflector, then the ratio of the earthshine to sunshine for a specular earth is only $(38 \times 10^{-9})(0.105) / (66 \times 10^{-6}) = 6.0 \times 10^{-5}$.

We can assume a worst case in which there is a specular reflection at the appropriate angle and Lambertian reflection elsewhere, so that the two preceding terms must be added. Even in this case, the earthshine is only 0.011% of the direct sunshine which reaches the sensor, and is negligible.

It should be noted that this analysis applies to reflected solar radiation which reaches a geosynchronous satellite when the angle between the earthline and the sunline is 12 degrees. Under other conditions, earthshine may be significant.

D.4.9 Strawman radiometric error budget

The following error budget provides an estimate of the precision to which the throughput of the perforated plate can be characterized. The error estimate is the root-sum-square of the pessimistic error estimates (worst-case or 3σ) which result from individual sources of error, so it represents a pessimistic assessment of the performance of a perforated plate calibration system.

Even with these highly pessimistic assumptions, the predicted worst-case error is only 0.73%. This radiometric precision is well within the scientific requirements for long term stability monitoring and represents a significant improvement over the performance of other candidate calibration techniques.

SOURCE OF ERROR	ESTIMATED MAGNITUDE
VARIANCE IN VIS/NIR SOLAR FLUX	0.3%
Earthshine	0.01%
Uncertainty in solar incidence angle at $12 \pm 0.5^\circ$	0.38%
Fluctuation in number of holes in front of aperture	0.39%
Diffraction due to thermal expansion	0.2%
Sensor SNR	0.13%
Misc. characterization errors	0.3%
ROOT SUM SQUARE	0.73%

D.4.10 Conclusions

Long term changes in the throughput of GOES-N visible channels should be monitored by full aperture, end-to-end calibration. Lunar calibration should play a role in this process, due to its minimal requirement for spaceborne hardware, minimal impact on spacecraft operations, and frequent windows of availability. Characterization of the lunar albedo, polarization of the lunar radiation, and the low level of the lunar albedo are all factors which restrict the precision of lunar calibration, however.

A high intensity source of indirect sunlight should also be used. There are two potential techniques for reducing the radiance of the sun to an appropriate level: a reflective diffuser plate or a transmissive perforated plate.

The perforated plate technique has several significant advantages over the diffuse plate technique and should be studied further. The most obvious advantage is that the transmissivity of a perforated plate depends upon geometry only, and is independent of surface conditions, while the reflectivity of a diffuser plate is subject to degrade when exposed to the space environment. The primary problem of the perforated plate is diffraction.

When viewed through a perforated plate, the solar image will be blurred by diffraction and will be biased toward short wavelengths in its center and toward long wavelengths around its circumference. The wavelength-dependent blurring of the solar image should be

straightforward to characterize, however. Of greater concern is the diffraction pattern produced by the small holes of the perforated plate. Excessive structure in this pattern would make the plate too difficult to characterize. The following factors will tend to wipe out structure in the diffraction pattern:

1. Suppression of the peaks of the diffraction pattern (other than the central, zero-order peak) due to randomization of the hole locations within the hexagonal grid.
2. Overlap of higher-order diffraction peaks due to the broad bandwidth of the sensor.
3. Convolution of the diffraction pattern over the 9.2 milliradian diameter solar disk.

The calibration of the sensor will be restricted to two windows of availability per year, around the equinoxes. These solar calibration measurements, used in conjunction with the other, more frequent calibration measurements, should improve the precision to which the sensor's throughput can be characterized over the lifetime of the mission. The perforated plate approach has the potential to achieve a precision of better than 1% between beginning and end of life, which is better than any alternative approach can achieve.

The feasibility of the perforated plate approach has been established by the preliminary analyses and simulations presented in this report. Further analysis is required to optimize the parameters of the plate and to address fabrication and deployment issues.

D.4.11 References

- 1 Minnaert, M., "Chapter 6, Photometry of the Moon", in *Planets and Satellites*, edited by G. P. Kuiper and B. M. Middlehurst, University of Chicago Press, Chicago, pp. 213-247.
- 2 Dollfus, A., "Chapter 9, Polarization Studies of the Planets", *op. cit.*, pp. 367-371.
- 3 Hass, G., W. R. Hunter, "Laboratory Experiments to Study Surface Contamination and Degradation of Optical Coatings and Materials in Simulated Space Environments," *Applied Optics*, Vol. 9, No. 9, pp. 2101-10, (1970).
- 4 Heaney, J. B., H. Herzig, and J. F. Ozantowski, "Auger Spectroscopic Examination of MgF₂-Coated Al Mirrors Before and After UV Irradiation," *Applied Optics*, Vol. 16, No. 7, pp. 1886-9, (1977).

Attachment A

LUNAR AVAILABILITY

The attached letter and table were sent to W. Bryant by J. Carr., 1989.

SWALES & ASSOCIATES, INC.

5050 Powder Mill Rd.
Beltsville, MD 20705
(301) 595-5500

10 March 1989

To: Bill Bryant/GSFC
From: J. Carr
Re: Lunar Availability for On-Orbit Testing

This memo makes a preliminary assessment of the moon's availability to support post-launch testing. The public domain program "PLANETS" has been used to tabulate dates for which the moon is $\pm 10^\circ$ declination of the equator and an approximate phase. This table is given on the next page for the period of one year after the nominal launch date of 31 July 1990. Dates and phases are only approximate and must be verified with a more accurate tool. (PLANETS accurately shows the lunar eclipse of 8/6/90 but it is several weeks in error in predicting the solar eclipse of 7/11/91.)

In general, windows for lunar availability open about once every 10 days, each of which is open for a period of 3 to 4 days. This means that under a nominal scenario one would have wait no more than 7 days for a 3 day window for lunar observation. Each window opens with the moon either at the extreme northern or the extreme southern boundary of the FOV and closes with the opposite extreme. Windows alternate between the moon entering at the northern or southern boundaries. Since the earth occults a significant fraction of the sensor's FOV, the moon is most useful when it is near the window opening or closing. Then it may appear in an image corner when the satellite's diurnal motion brings the moon into the FOV; however, there are no guarantees that this configuration will occur because of the phasing between the lunar and the satellite orbits. The moon like any other celestial object will be within the FOV for up to about 90 minutes but may spend the majority of this time occulted by the earth. The moon phases during successive windows tend to be approximately 180° apart and there are only two windows tabulated where a new moon exists.

Table of Lunar Availability

<u>Entry Date</u>	<u>Exit Date</u>	<u>Phase</u>
8/8/90	8/11/90	Full
8/20/90	8/23/90	New
9/4/90	9/7/90	Full
9/16/90	9/20/90	1/4
10/1/90	10/4/90	3/4
10/14/90	10/17/90	1/4
10/28/90	11/1/90	1/2
11/10/90	11/13/90	1/2
11/25/90	11/28/90	1/2
12/7/90	12/11/90	1/2
12/22/90	12/26/90	1/2
1/3/91	1/7/91	3/4
1/18/91	1/22/91	1/4
1/31/91	2/3/91	3/4
2/15/91	2/18/91	1/4
2/27/91	3/3/91	Full
3/14/91	3/17/91	New
3/27/91	3/30/91	3/4
4/10/91	4/14/91	1/4
4/22/91	4/26/91	3/4
5/8/91	5/11/91	1/2
5/20/91	5/23/91	1/4
6/4/91	6/7/91	1/2
6/16/91	6/20/91	1/4
7/1/91	7/5/91	1/2
7/14/91	7/17/91	1/4
7/28/91	8/1/91	3/4

• Lunar eclipse 8/6/90

•• Solar eclipse 7/11/91

Attachment B

COMPUTER SIMULATION OF PSEUDO-RANDOM HEXAGONAL PERFORATED PLATE

This Appendix quantifies the effect of the pseudo-random array in suppressing interference effects. The analysis treats a circular cross-section of an hexagonal array of 10450 cells, illuminated by coherent, monochromatic light. Each point acts as an omni-directional radiator.

If the array is perfectly ordered, then each diffraction order produces a maximum which is as intense as the main, zero-order peak. To understand the effects of pseudo-random ordering, we give each point a random coordinate in the direction perpendicular to the rows of the array. Each point is given a random displacement of up to $\pm 0.346S$ from the center of its hexagonal cell. Since the distance between adjacent rows of the array is $0.866S$, this displacement corresponds to a "disorder parameter" of $2 \times 0.346S / 0.866S = 0.8$.

Maxima occur when the phase angle between adjacent rows of the array is an integral multiple 2π , i.e., when $1.155 \lambda/S$ is an integer. Table B-1 corresponds to one half of the central peak. As expected, all wavefronts add coherently at an angle of zero degrees, so the intensity is $10,450^2$. The full-width, half maximum (FWHM) of this peak is about three degrees.

Tables B-2 and B-3 correspond to the first-order and second-order maxima, respectively. The maximum intensity in the first diffraction order was approximately 3.6% that of the central peak; the maximum intensity in the second diffraction order was approximately 0.5% that of the central peak. The FWHM of each peak was approximately three degrees. Due to the randomization, the maximum intensity was usually displaced from the nominal center of the peak by a few tenths of a degree in phase difference.

Table B-4 corresponds to the first-order peak of a perfectly-aligned hexagonal array of holes. Notice that its peak intensity and FWHM are virtually identical to those parameters of the zero-order peak. Even the sidelobe structures of the two peaks are virtually identical.

This simulation confirms the importance of pseudo-randomization, i.e., selection of a random location for each hole within its hexagonal cell. The structure of the diffraction pattern is not totally eliminated, but it is suppressed to a great extent. When the residual diffraction pattern is convolved over the spectral passband of the sensor and the extended solar image, any residual diffraction effects should be negligible.

Tables B-5, B-6, and B-7 tabulate the diffraction pattern from the pseudo-random hexagonal array in coarser, 2.5 degree increments, from 0-125 deg, 135-250 deg, and 270-395 deg, respectively. No spurious diffraction peaks are observable. Note that the first peak appears as a maximum at 90 deg in Table B-7.

Table B-1

HEXGRATE
 DISORDER PARAMETER .8
 PHASE ANGLE BETWEEN LINES .2
 ORDER OF DIFFRACTION PATTERN 0

ANGLE	INTENSITY
0	1.092025E+08
.2	1.079339E+08
.4	1.041997E+08
.6	9.821532E+07
.8	9.032152E+07
1	8.094515E+07
1.2	7.06012E+07
1.4	5.978328E+07
1.6	4.901933E+07
1.8	3.878566E+07
2	2.944161E+07
2.2	2.128561E+07
2.4	1.449833E+07
2.6	9133911
2.8	5168266
3	2473650
3.2	874746.7
3.4	133486.7
3.6	16415.53
3.8	294181.5
4	755108.5
4.2	1244414
4.4	1638956
4.6	1868114
4.8	1914291
5	1796898
5.2	1535341
5.4	1207579
5.6	853973.5
5.8	531368.2
6	268108.6
6.2	90952.79
6.4	9419.278
6.6	10288.74
6.8	73695.12
7	171186.4
7.200001	278943.4
7.4	371161
7.6	431789.2
7.8	448883.7
8	430164
8.2	375165.7
8.399999	254206.7
8.600001	205314.4
8.8	120337.6
9	57036.59
9.2	14328.24
9.399999	51.87173
9.600001	10450.13
9.8	36513.34
10	76935.86

Table B-2

HEXGRATE
 DISORDER PARAMETER .6
 PHASE ANGLE BETWEEN LINES .2
 ORDER OF DIFFRACTION PATTERN 1

ANGLE	INTENSITY
0	3733400
.2	3830482
.4	3880275
.6	3746169
.8	3353139
1	2958566
1.2	2915707
1.4	1950079
1.6	1698353
1.8	1212926
2	858953.6
2.2	795302.5
2.4	737988.1
2.6	211645.6
2.8	157609
3	53857.46
3.2	4612.285
3.4	18019.04
3.6	5929.909
3.8	28346.99
4	36901.66
4.2	73464.96
4.4	37742.11
4.6	68852.03
4.8	72917.22
5	68505.96
5.2	74058.23
5.4	62003.17
5.6	32049.02
5.8	1366.82
6	30628.88
6.2	1717.338
6.4	6100.42
6.6	906.8962
6.8	.4497242
7	2238.364
7.200001	4570.239
7.4	4.890286
7.6	9311.754
7.8	49908.9
8	57599.43
8.2	19082.8
8.399999	1736.791
8.600001	.6914312
8.8	1810.394
9	3118.308
9.2	2812.959
9.399999	1928.77
9.600001	992.6442
9.8	3318.219
10	6587.783

Table B-3

HEXGRATE
DISORDER PARAMETER .8
PHASE ANGLE BETWEEN LINES .2
ORDER OF DIFFRACTION PATTERN 2

ANGLE	INTENSITY
0	395159.3
.2	445290.5
.4	299256.7
.6	501485
.8	459482.7
1	164299.3
1.2	215905.3
1.4	305418
1.6	279101.3
1.8	194389.2
2	50124.97
2.2	62069.05
2.4	53127.82
2.6	31231.98
2.8	44347.36
3	186.8179
3.2	8839.558
3.4	70.97608
3.6	1261.41
3.8	5415.202
4	7722.594
4.2	1741.637
4.4	40202.24
4.6	1004.422
4.8	19044.68
5	371.4111
5.2	14334.68
5.4	2242.271
5.6	4452.532
5.8	14556.9
6	2391.263
6.2	256.9744
6.4	28218.74
6.6	8211.299
6.8	16.78576
7	1124.416
7.200001	23896.22
7.4	2.522431
7.6	12873.42
7.8	5.621914
8	19181.48
8.2	5969.091
8.399999	10987.49
8.600001	2794.095
8.8	12966.27
9	13278.27
9.2	6866.104
9.399999	1616.809
9.600001	44.40731
9.8	5064.265
10	12370.48

Table D-4

HEXGRATE
DISORDER PARAMETER 0
PHASE ANGLE BETWEEN LINES .2
ORDER OF DIFFRACTION PATTERN 1

ANGLE	INTENSITY
0	1.092025E+08
.2	1.079229E+08
.4	1.041836E+08
.6	9.81876E+07
.8	9.028786E+07
1	8.091071E+07
1.2	7.05539E+07
1.4	5.974397E+07
1.6	4.898846E+07
1.8	3.875414E+07
2	2.941574E+07
2.2	2.12638E+07
2.4	1.447689E+07
2.6	9118924
2.8	5157208
3	2468601
3.2	868486.2
3.4	131287.8
3.6	17121.16
3.8	294589.4
4	759206.5
4.2	1246784
4.4	1640652
4.6	1873149
4.8	1921347
5	1798138
5.2	1543057
5.4	1209370
5.6	853450.6
5.8	525752.3
6	264140.9
6.2	90092.78
6.4	0609.781
6.6	10020.06
6.8	73864.3
7	173733.1
7.200001	282285.8
7.4	375637.9
7.6	436595.6
7.8	455984.5
8	433547.5
8.2	376115.5
8.399999	295614.3
8.600001	206504.6
8.8	122938
9	56555.73
9.2	14755.98
9.399999	47.78529
9.600001	10198.72
9.8	39176.23
10	78530.4

Table B-5

HEXGRATE
DISORDER PARAMETER .8
PHASE ANGLE BETWEEN LINES 2.5
ORDER OF DIFFRACTION PATTERN 0

ANGLE	INTENSITY
0	1.092025E+08
2.5	1.163651E+07
5	1795940
7.5	411347
10	77069.66
12.5	4576.416
15	3931.695
17.5	17751.08
20	21659.83
22.5	22094.93
25	12553.79
27.5	4243.805
30	202.2862
32.5	694.904
35	1052.413
37.5	6193.647
40	3422.932
42.5	3160.707
45	1092.137
47.5	97.94318
50	2.374525
52.5	123.7917
55	2266.307
57.5	820.3658
60	933.4332
62.5	98.64516
65	186.5655
67.5	506.7109
70	266.3852
72.5	3.043545
75	537.1636
77.5	28.88046
80	1412.39
82.5	5.729965
85	2331.417
87.5	299.4916
90	125.7957
92.5	42.58031
95	721.4469
97.5	46.02089
100	209.4185
102.5	197.653
105	757.6813
107.5	319.3422
110	1145.845
112.5	55.60936
115	1622.917
117.5	355.3612
120	2.424636
122.5	13.7658
125	209.4035

Table B-6

HEXGRATE
DISORDER PARAMETER .8
PHASE ANGLE BETWEEN LINES 2.5
ORDER OF DIFFRACTION PATTERN .375

ANGLE	INTENSITY
0	255.3088
2.5	11687.41
5	289.2334
7.5	1327.069
10	464.759
12.5	10.82072
15	2555.095
17.5	5541.46
20	610.1597
22.5	55.69729
25	6.533535
27.5	2020.439
30	.1342761
32.5	972.3725
35	87.09179
37.5	669.4276
40	171.426
42.5	43.99057
45	386.6928
47.5	3406.375
50	3066.201
52.5	1157.859
55	1228.423
57.5	3104.637
60	4235.351
62.5	13.57518
65	4817.106
67.5	4093.784
70	670.0438
72.5	405.051
75	800.3826
77.5	52.83431
80	26.09213
82.5	1679.85
85	2164.816
87.5	10853.57
90	515.1577
92.5	6974.419
95	7.013032
97.5	5000.043
100	592.08
102.5	6086.13
105	1653.516
107.5	2519.014
110	695.3199
112.5	1466.508
115	1480.406
117.5	864.1603
120	9175.346
122.5	747.0915
125	560.1855

Table B-7

HEXGRATE
 DISORDER PARAMETER .8
 PHASE ANGLE BETWEEN LINES 2.5
 ORDER OF DIFFRACTION PATTERN .75

ANGLE	INTENSITY
0	2199.165
2.5	3402.047
5	102.7816
7.5	66.225
10	61.28015
12.5	11799.38
15	1074.937
17.5	1601.736
20	2173.618
22.5	46.66492
25	1491.36
27.5	6444.015
30	8515.354
32.5	397.4418
35	94.00262
37.5	192.696
40	198.3214
42.5	1042.185
45	5045.588
47.5	11533.28
50	4370.922
52.5	1406.247
55	.8119998
57.5	3858.959
60	279.9333
62.5	203.9864
65	223.1267
67.5	3589.017
70	1013.341
72.5	1178.836
75	1630.32
77.5	3750.718
80	145.9179
82.5	15084.52
85	60825.47
87.5	260507.1
90	3929895
92.5	476346.7
95	122986.1
97.5	20991.39
100	1437.168
102.5	14.03609
105	2816.369
107.5	4253.685
110	1268.75
112.5	8934.926
115	10293.15
117.5	9733.894
120	4662.526
122.5	9.960901
125	4469.059

D.5 ABERRATIONS OF REFLECTING TELESCOPES

This analysis compares the aberrations of several reflecting telescope design forms. Equations are presented for computing the aberrations of the two most popular designs, the Cassegrain and the Ritchey-Chretien (RC) telescopes. The RC design is essentially the same as the Cassegrain, except that the primary mirror is an ellipsoid rather than a parabola. Both designs are free of spherical aberration, but only the RC design is free of coma. The packaging envelope of these two designs is approximately the same, and is strongly dependent upon the f-number of the primary mirror. Aberrations are computed at the largest anticipated field angles of the imager and the sounder (1.25 and 2.5 mrad respectively).

Two off-axis designs are also considered. These design forms are unobscured and provide greater field coverage than the Cassegrain or the RC. Though the aberrations are not explicitly computed for these designs, a table is presented showing the aberrations that are present. These aberrations can be improved by optimization. Schematic representations of the different telescope designs are shown in Figure D.5-1.

D.5.1 Cassegrain and Ritchey-Chretien (RC) aberrations

The following equations were used to compute the aberrations of the Cassegrain and the RC telescopes. Expressions for mirror curvatures, aspheric deformations, and aberrations were taken directly from *The Infrared Handbook*, except that aberration expressions were multiplied by a factor of 2 to convert radius into diameter. In the analysis, nominal values were chosen for Y (primary mirror semi-aperture), and β (the ratio of the back focal distance to the primary-secondary mirror spacing).

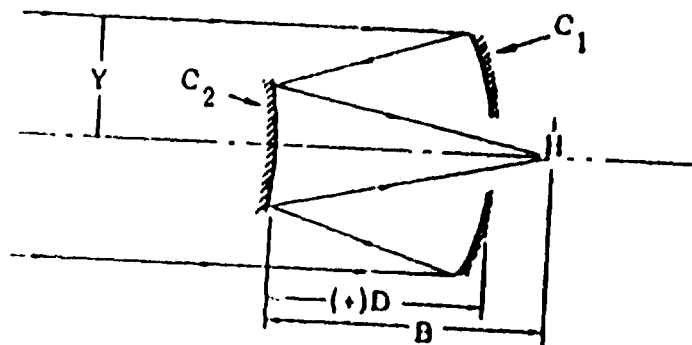
ASSUMPTIONS:

Symbol	Value	Description
Y	152.4	Primary Semi-Aperture (mm), (12" diam.)
β	1.2	Ratio of BFL to D (nd) ¹¹

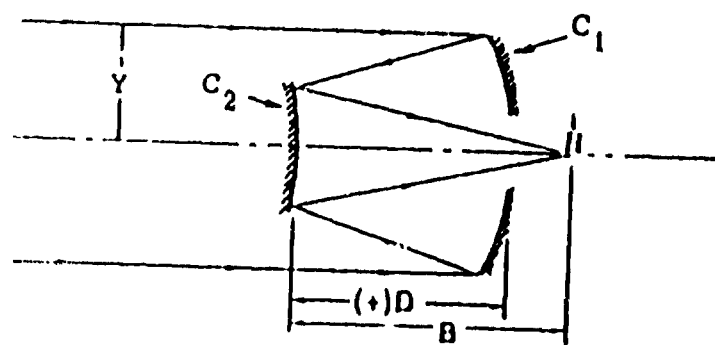
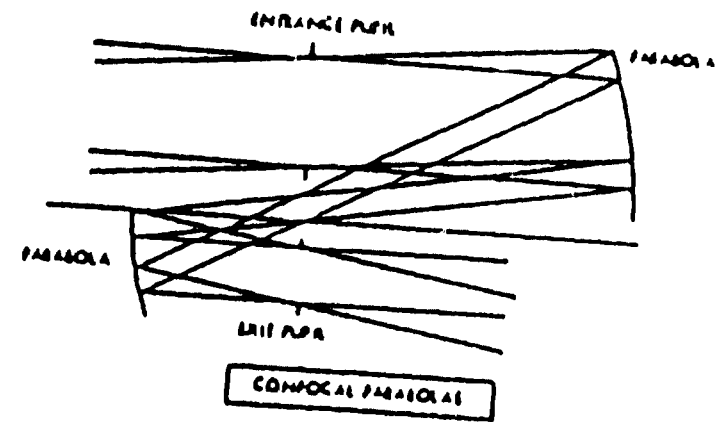
MISCELLANEOUS PARAMETERS:

Symbol	Description
f_N	System f-number (nd) ¹¹
f_{N_1}	f-number of primary mirror (nd) ¹¹
θ	Field angle (rad)

¹¹ nd - "non-dimensional"



Cassegrain Design
 • Paraboloidal Primary
 • Hyperboloidal Secondary



Ritchey-Chretien Design
 • Elliptical Primary
 • Hyperboloidal Secondary

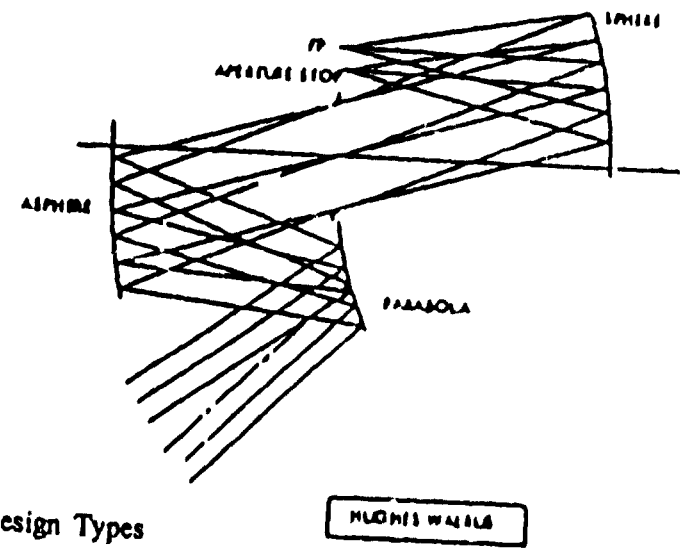


Figure D.5-1. Reflective Telescope Design Types

PRIMARY/SECONDARY MIRROR SPACING:¹²

$$R_1 = 2 F_1 = 2 (-2 Y f_{M1}) = -4 Y f_{M1} \quad (\text{mm}) \quad \text{Radius of Primary}$$

$$D = \frac{R_1 F}{\beta R_1 - 2F} \quad (\text{mm}) \quad \text{Primary/Secondary Spacing}$$

BASIC OPTICAL CALCULATIONS:

$F = 2 Y f_n$	Effective Focal Length (mm)
$B = \beta D$	Back Focal Length (mm)
$H = F \theta$	Image Height (mm)

MIRROR CURVATURES:

$$C_1 = \frac{(B - F)}{2DF} \quad (\text{mm}^{-1}) \quad \text{Curvature of primary}$$

$$C_2 = \frac{(B + D - F)}{2DB} \quad (\text{mm}^{-1}) \quad \text{Curvature of secondary}$$

CASSEGRAIN TELESCOPE:

$$K_1 = \frac{(F-B)^3}{64 D^3 F^3} \quad (\text{mm}^{-3}) \quad \text{Primary aspheric deformation}$$

$$K_2 = \frac{(F-D-B)(F+D-B)^2}{64 B^3 D^3} \quad (\text{mm}^{-3}) \quad \text{Secondary aspheric deformation}$$

$$S.A. = 0.0 \quad (\text{mm}) \quad \text{Spherical aberration}$$

$$COMA = \frac{H Y^2}{2 F^2} \quad (\text{mm})$$

$$ASTIG = \frac{H^2 Y (D-F)}{B F^2} \quad (\text{mm})$$

$$P-CURV = \frac{H^2 Y [DF - (B-F)^2]}{B D F^2} \quad (\text{mm}) \quad \text{Petzval curvature}$$

¹² The equation for D is obtained by setting $B = \beta D$ in the expression for C_1 (curvature of the primary) and letting $C_1 = 1/R_1$.

RC TELESCOPE:

$$K_1 = \frac{2BD^2 - (B-F)^3}{64D^3F^3} \quad (\text{mm}^{-3}) \quad \text{Primary aspheric deformation}$$

$$K_2 = \frac{2F(B-F)^2 + (F-D-B)(F+D-B)(D-F-B)}{64B^3D^3} \quad (\text{mm}^{-3}) \quad \text{Secondary aspheric deformation}$$

$$S.A. = 0.0 \quad (\text{mm}) \quad \text{Spherical aberration}$$

$$COMA = 0.0 \quad (\text{mm})$$

$$ASTIG = \frac{H^2 Y (D-2F)}{2BF^2} \quad (\text{mm})$$

$$P-CURV = \frac{H^2 Y [DF - (B-F)^2]}{BDF^2} \quad (\text{mm}) \quad \text{Petzval Curvature}$$

TOTAL ABERRATION:

$$TOTAL ABERRATION = \frac{|S.A.| + |COMA| + |ASTIG| + |P-CURV|}{F} \quad (\text{rad})$$

Both the Cassegrain and RC designs have curved focal surfaces. The Petzval curvature is an off-axis aberration that results when using a flat focal plane positioned at the paraxial focus.

When multiple aberrations are present in an optical system, the resultant total aberration can be quite complex and is not easily computed. Summing the absolute values of the aberrations, as in the above expression for "TOTAL ABERRATION," provides a simple way of estimating the worst case (or upper bound) on the total aberration.

The relative magnitudes of the Cassegrain and RC aberrations are strongly dependent upon the f-number of the primary mirror (f_{N1}), and the f-number of the overall optical system (f_N).¹³ These two parameters also determine the packaging envelope of the telescope. Several representative cases are listed in Table D.5-1. From the table, it is clear that the packaging envelope can be minimized by choosing small values for both f_N and f_{N1} .

Aberrations for the cases in Table D.5-1 were computed and plotted in Figures D.5-2,3,4,5. Each figure shows the aberrations at a given system f-number. Cassegrain aberrations are shown on the left, and RC aberrations are shown on the right. The top two plots in each figure are at a field angle of 1.25 mrad, and the bottom two are at a field angle of 2.5 mrad.

Diffraction limiting wavelengths are listed on the right margin of each figure. The values represent the wavelength of light that would produce an Airy disk diameter equal to the aberration blur diameter. Since diffraction effects are proportional to wavelength, all wavelengths larger than a value listed on the right margin will produce a diffraction blur diameter larger than the corresponding numbers on the left axis scale.

¹³ - "f-number of the overall system" refers to the f-number of the fore optics only, and does not include the effects of relay optics.

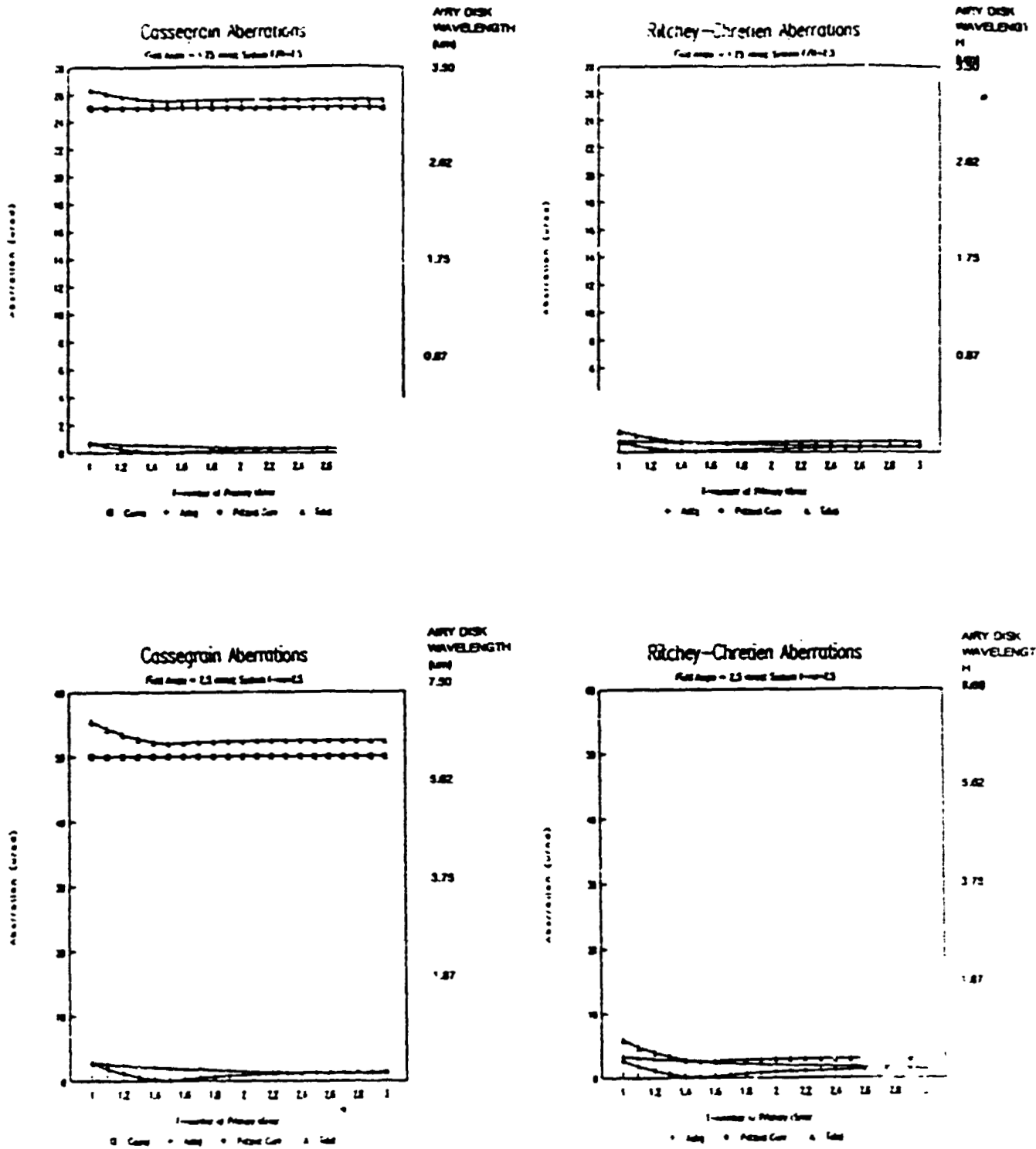


FIGURE D.5-2
 CASSEGRAIN AND RITCHEY-CHRETIEN ABERRATIONS AT F/2.5

Reproduced from
 best available copy.

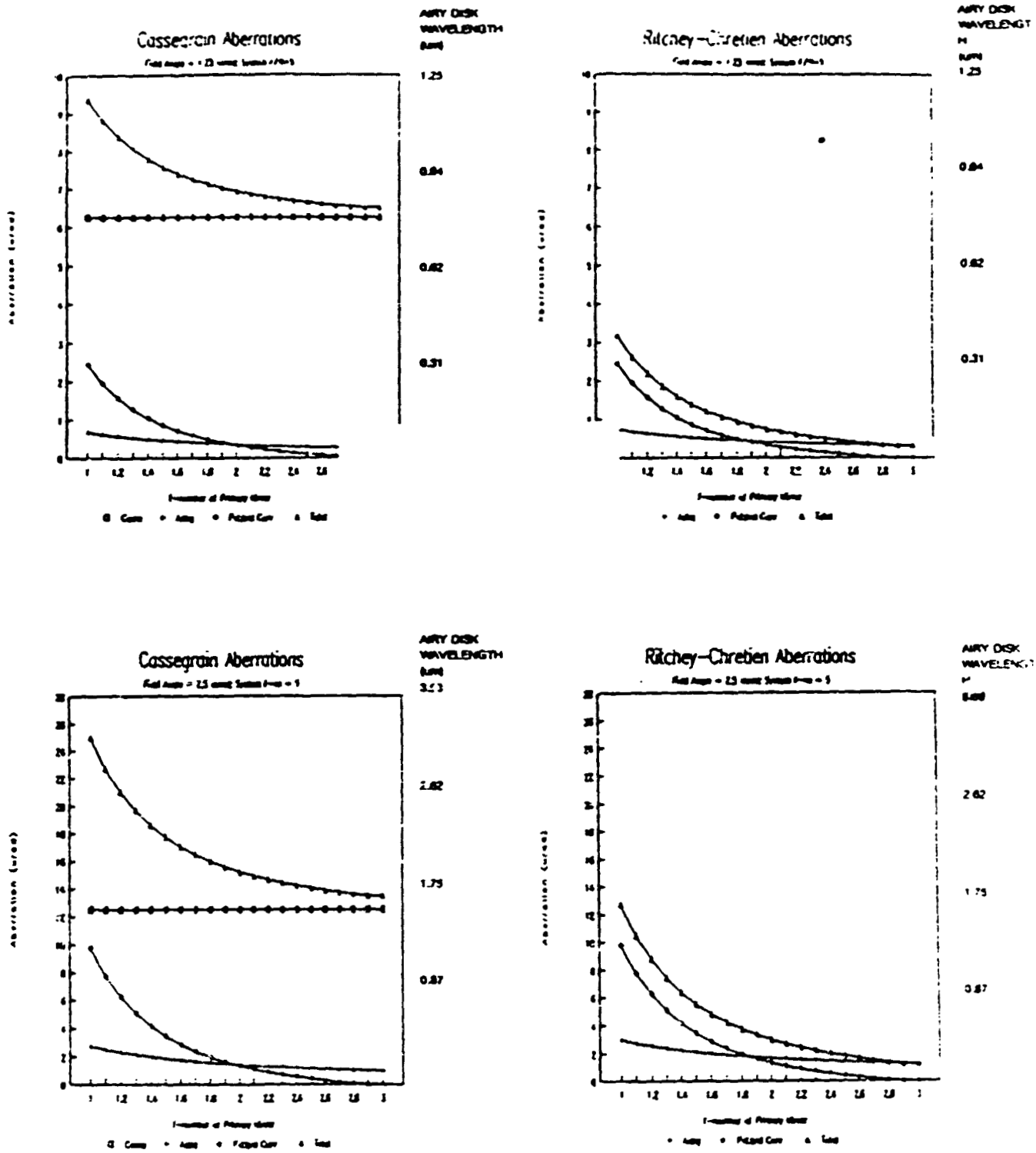


FIGURE D.5-3
CASSEGRAIN AND RITCHEY-CHRETIEN ABERRATIONS AT F/5.0

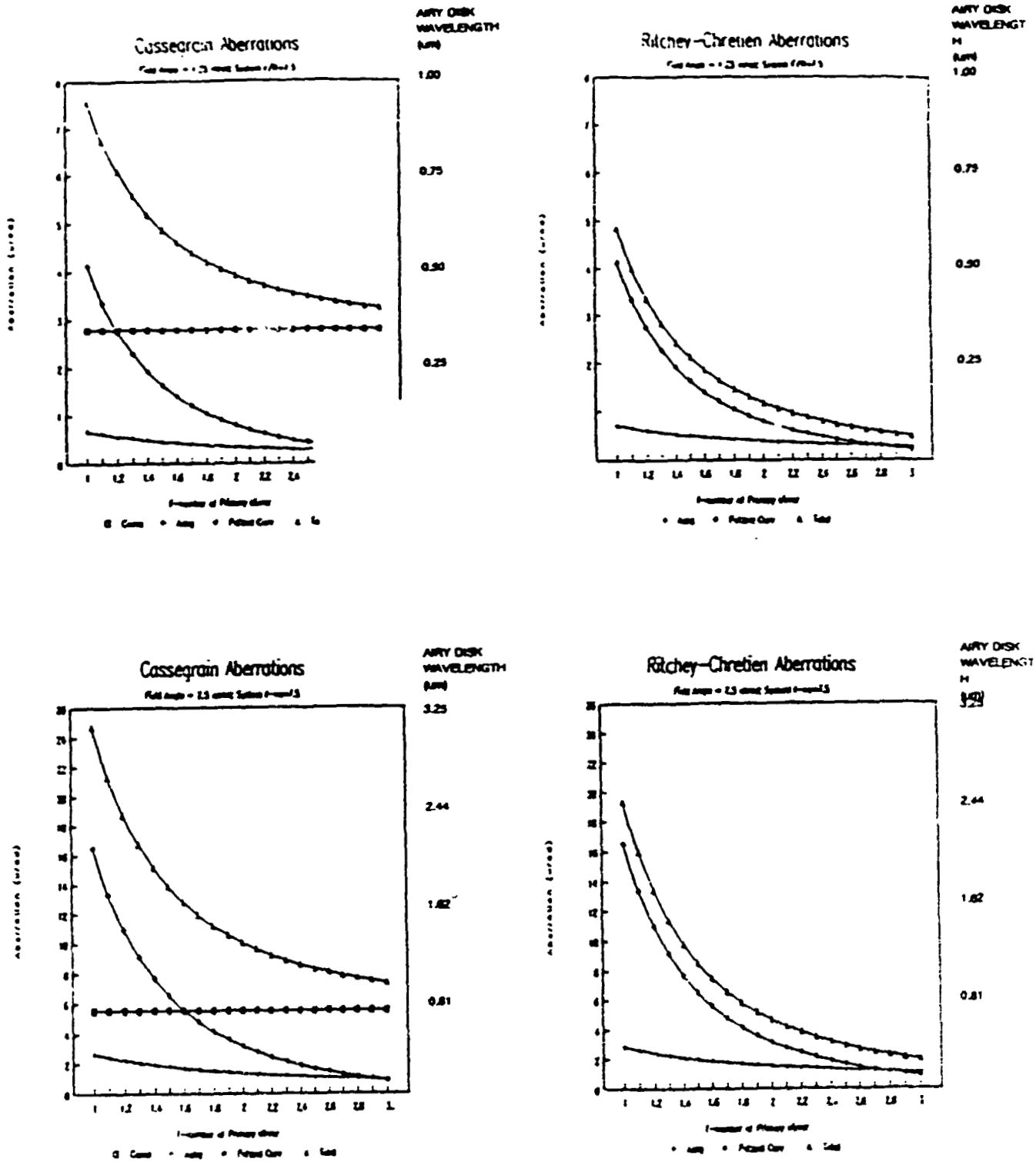


FIGURE D.5-4
 CASSEGRAIN AND RITCHEY-CHRETIEN ABERRATIONS AT F/7.5

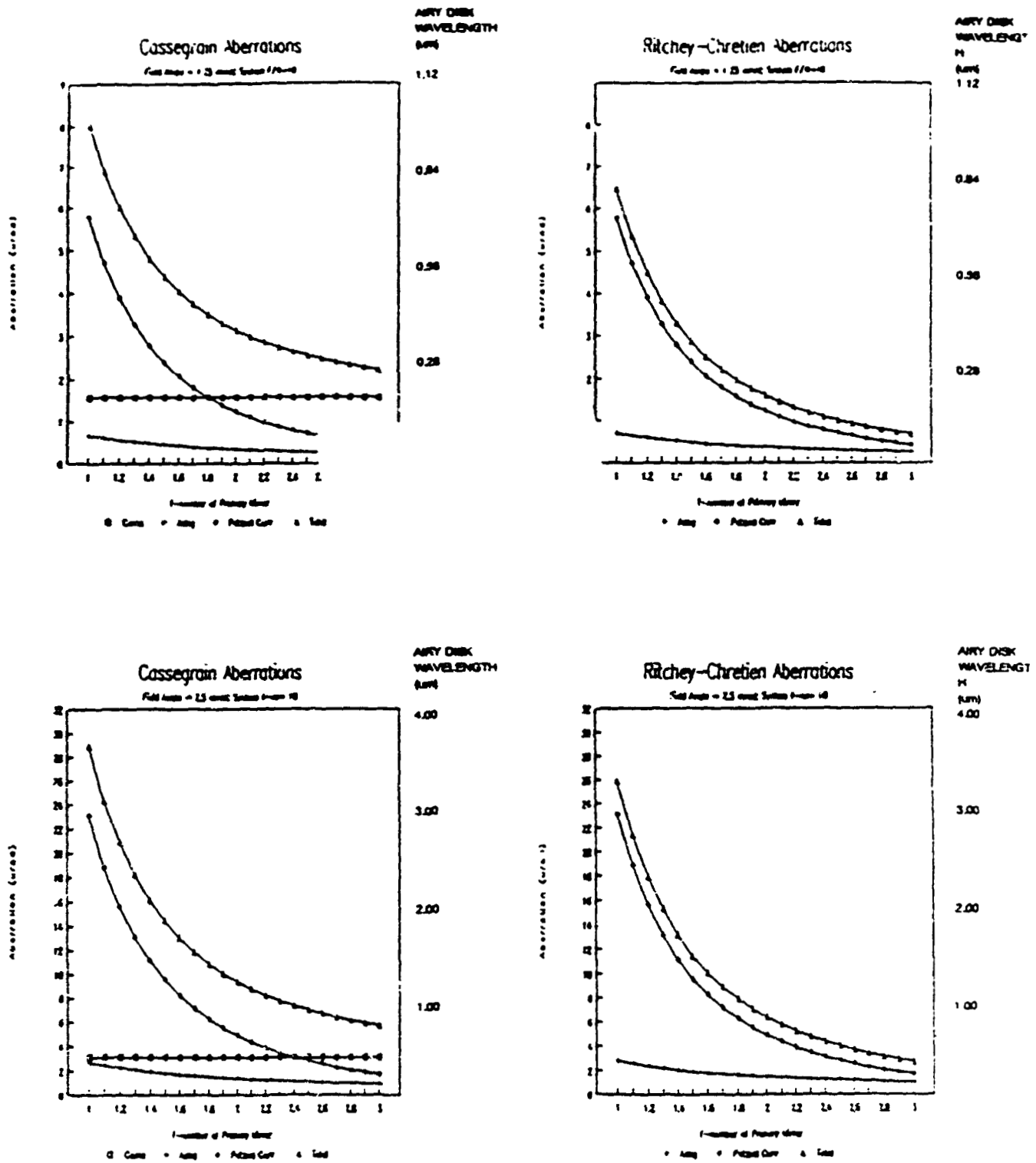


FIGURE D.5-5
 CASSEGRAIN AND RITCHEY-CHRETIEN ABERRATIONS AT F/10.0

TABLE D.5-1
DESIGN CASE STUDIES

f_n System f-number	f_n Primary Mirror f-number	F System Effective Focal Length (mm)	D Prim./Sec. Mirror Spacing (mm)
2.5	1.0	762	205.9
2.5	2.0	762	311.0
2.5	3.0	762	374.8
5.0	1.0	1524	245.8
5.0	2.0	1524	411.9
5.0	3.0	1524	531.6
7.5	1.0	2286	262.8
7.5	2.0	2286	461.8
7.5	3.0	2286	617.8
10.0	1.0	3048	272.1
10.0	2.0	3048	491.6
10.0	3.0	3048	672.3

D.5.2 Aberration vs. aperture and field size

Table D.5-2¹⁴ shows the relationships between several important aberrations and the semi-aperture y (in column one) and the image height h (in column two). While the table does not provide the absolute magnitudes of the aberrations, it can be used to estimate the change in the aberrations as a function of aperture and field size. For example, if the magnitude of the coma is known at a particular aperture size, then increasing the aperture by 20% will cause the coma to increase by a factor of $1.2^2 = 1.44$.

Table D.5-3¹⁵ lists the important aberrations in each of the four telescope designs. An entry of 'X' indicates that the aberration is present and uncorrected. A blank indicates that the aberration is either corrected or non-existent.

¹⁴ Table D.5-2 was obtained from reference [2].

¹⁵ Information in Table D.5-3 for the Confocal Parabola Telescope and the Hughes WALRUS was obtained from [3].

TABLE D.5-2

ABERRATION vs. APERTURE AND FIELD SIZE

Aberration	vs Aperture	vs Field Size
Spherical (longitudinal)	y^2	—
Spherical (transverse)	y^3	—
Coma	y^2	h
Petzval curvature	—	h^2
Astigmatism	—	h^2
Length of astigmatic lines	y	h^2
Distortion (linear)	—	h^3
Distortion (percentage)	—	h^2
Axial chromatic (longitudinal)	—	—
Lateral chromatic	—	h

TABLE D.5-3

OPTICAL ABERRATIONS OF VARIOUS TELESCOPE DESIGN FORMS

Aberration	Cassegrain	Ritchey- Chretien	Confocal Parabolas	Hughes WALRUS
3rd order spherical				
3rd order coma	X			
3rd order astigmatism	X	X		
3rd order petzval curv.	X	X	X	X
5th order spherical				
5th order coma	X			X
5th order astigmatism	X	X	X	X
Tangential oblique spherical aberration				X
Elliptical coma			X	X

D.5.3 Conclusions

From the figures, it is possible to make the following conclusions:

1. Longer telescopes (large system f -numbers and primary mirror f -numbers) produce lower aberrations.
2. Astigmatism is present in both design forms, but is small in comparison to the coma and the Petzval curvature.
3. Coma is independent of the f -number of the primary, and is largest for low system f -numbers.
4. Petzval curvature is the same for the Cassegrain and the RC designs. It is largest for high system f -numbers, and increases as the f -number of the primary is decreased.

For low system f -numbers (7.5 or less), the Cassegrain design is dominated by coma, and the RC produces substantially better performance. When the system f -number is large (10 or greater), Petzval curvature becomes the dominant aberration (especially when the f -number of the primary is small), and the RC design is not much better than the Cassegrain.

With the Cassegrain design, in order to achieve near diffraction limited performance in the visible spectrum at a field angle of 1.25 mrad, a long telescope must be used (i.e., system f -number of 7.5 or greater, and primary mirror f -number of 2.0 or greater). Note that all aberrations are zero on-axis; hence, if the visible detectors are kept close to the optical axis, longer telescopes could be used and still produce diffraction limited performance. At very long wavelengths (5.0 μm and greater), diffraction becomes the limiting factor in optical performance.

D.5.4 References

- 1 Wolfe, William L. and Zissis, George J., *The Infrared Handbook*, Office of Naval Research, Department of the Navy, 1978, pp 9-20,21,22,23.
- 2 Smith, Warren J., *Modern Optical Engineering*, McGraw-Hill Book Company, 1966.
- 3 Abel, Irving R. and Hatch, Marcus R., "The pursuit of symmetry in wide-angle reflective optical designs," *Proceedings of the SPIE*, Vol 237, 1980, pp 271-280

D.6 SOUNDER PERFORMANCE PREDICTION

D.6.1 Overview

This report presents the radiometric performance analysis of the GOES-N Advanced Sounder. The baseline requirements for the sounder are as follows:

BASIC REQUIREMENTS

Frame area: 3000 X 3000Km
Frame time: 30 minutes
IGFOV: 8Km
NEΔT: 0.2°K

SPECTRAL BANDS			RESOLUTION
SHORTWAVE	2150 – 2721cm ⁻¹	(3.7 – 4.7 μm)	2.5 cm ⁻¹
MIDWAVE	1210 – 1740 cm ⁻¹	(5.8 – 8.3 μm)	1.0 cm ⁻¹
LONGWAVE	620 1150 cm ⁻¹	(8.7 – 16.1 μm)	0.5 cm ⁻¹

Three technologies are being considered for the application: Fourier Transform Spectrometer (FTS), grating spectrometer, and Fabry-Perot interferometer. Rather than develop separate models specific to each approach, an existing LOTUS 123 spreadsheet was modified and used to do a generic analysis. The highlights of each approach are presented in Attachment D.

The radiometric equations used in the spreadsheet are documented in [1]. With the exception of a few changes, which are listed in Attachment A, the equations presented in [1] have been used without modification.

D.6.2 Assumptions

The following assumptions have been made in the analysis; where exact specifications are not known, conservative estimates have been used:

SCENE CONDITIONS

Atmospheric temperature: 260°K
Atmospheric emissivity: 1.0 (0% transmission)
Saturation radiance to scene radiance ratio: 1.0 (shortwave), 4.0 (midwave) ; 2.0 (longwave)

OPTICAL CHARACTERISTICS

	SHORTWAVE	MIDWAVE	LONGWAVE
OPTICS F-NUMBER	1.0		
OPTICS DIAMETER	12 INCHES		
COLD FILTER			
TRANSMISSION:	0.85		
BANDPASS (COLD FILTER)	3.68 - 4.65 μ m	5.75 - 8.26 μ m	8.75 - 16.13 μ m
OPTICAL THROUGHPUT TRANSMISSION:	0.12	0.11	0.14

BACKGROUND CONDITIONS

AFT OPTICS TEMPERATURE	160°K (WITH 65°K FOCAL PLANE) 220°K (WITH 85°K FOCAL PLANE)
AFT OPTICS EMISSIVITY	0.30
FORE OPTICS TEMPERATURE	295°K
FORE OPTICS EMISSIVITY	0.30

DETECTOR CHARACTERISTICS

	SHORTWAVE	MIDWAVE	LONG WAVE
FOCAL PLANE TEMPERATURE:	95°K (PASSIVE COOLER) 65°K (ACTIVE COOLER)		
D* @ 85°K	8.0 X 10 ¹¹	1.6 X 10 ¹¹	2.0 X 10 ¹⁰
D* @ 65°K	3.0 X 10 ¹²	6.4 X 10 ¹¹	1.0 X 10 ¹¹
QUANTUM EFFICIENCY	0.70	0.65	0.60

MISCELLANEOUS

Electrical Bandwidth ¹⁶ :	$1.5/(2 \times \zeta T_{\text{FOV}})\text{Hz}$ $1.5/(2 \times T_{\text{FOV}})$
AD RESOLUTION	13 BITS
SCAN MIRROR STEP & SETTLE TIME	25 MS

The spreadsheet model does not attempt to simulate the effects of complex atmospheric profiles. Instead, it is assumed that the atmosphere is a black body ($\epsilon=1$) with a constant temperature.

D.6.2 Noise Sources

In order to compare the various noise sources directly, they must be computed in the same units. For the sounder analysis, all noise sources were computed in electrons. The following subsections describe the noise sources that were included in the analysis, and those that were not. Where applicable, mathematical formulas are given.

It is assumed that the individual noise sources are independent (i.e., have random phase relationships with one another). Hence, they can be summed in an RSS sense; that is, the total noise is the square root of the sum of the squares of the individual noises:

$$N_T = (N_1^2 + N_2^2 + \dots + N_n^2)^{1/2}$$

D.6.3.1 Detector noise

Detector noise, also referred to as D^* noise in the spreadsheet, is computed from D^* and is due to the generation and recombination of charge carriers in the detector substrate. Equations for computing detector noise from D^* are presented in the appendix.

The detector noise computation may be somewhat pessimistic for Near-BLIP detectors since some of the noise measured by the manufacturer while ascertaining D^* is due to the background and not the detector itself. To compute the detector noise alone, the background contribution should be subtracted. Unfortunately, detector manufacturers rarely supply detailed information about background conditions during the measurement of D^* . Hence, for the GOES-N advanced sounder model, it is assumed that all of the noise that was measured by the manufacturer in determining D^* is from the detector, and will still be present when the detector is in the spacecraft.

¹⁶ - T_{FOV} is the integration time for each instantaneous field-of-view.

D.6.3.2 Shot noise

The shot noise, or quantum noise, can be expressed as the square root of the number of electrons produced in a detector element by incident photons during an integration period. The total number of electrons can be computed by summing the effects of three independent sources:

- The earth's atmosphere
- Sensor fore optics
- Sensor aft optics

It is assumed that the earth's atmosphere has an emissivity of 1 (i.e., is opaque). Hence photons that are emitted by the earth's surface are absorbed by the atmosphere and do not reach the sensor.

D.6.3.3 Quantizer noise

Quantizer noise is caused by the resolution limit imposed by the A/D converter. In order to compute quantizer noise, one must know the relative magnitude of the signal being measured to the full scale reading of the A/D converter.

Under normal operating conditions, the amplified and filtered detector signal should have a reasonable margin of error before saturating the A/D converter. Amplification of the detector signal should be such that only the largest signals will be close to the ceiling of the A/D converter.

The "Saturation radiance to scene radiance ratio," specifies the factor by which the scene radiance would have to increase in order to produce a full scale A/D reading. The listed values were taken from empirical data from the HIS instrument. As an example, a "Saturation radiance to scene radiance ratio" of 10.0 in the shortwave band indicates that the A/D converter will be operating at roughly 1/10 of full scale.

The saturation signal is the signal level in electrons that produces a full scale A/D reading and is denoted by E_{SAT} . It is computed by multiplying the electrons produced by the scene by the "Saturation radiance to scene radiance ratio." The quantizer noise is computed using the following formula:

$$N_Q = \frac{E_{SAT}}{\sqrt{12} \cdot 2^n} \quad [electrons] \quad (6)$$

where n is the number of bits of the A/D converter.

D.6.3.4 Omitted noise sources

Two known noise sources have been omitted from the analysis:

- Electronic noise (pre-amp, filters, etc.)
- Detector 1/f noise

Electronic noise typically ranges from 1 to 3 nV/Hz^{1/2}. It can be neglected if high responsivity detectors are used (i.e., those with voltage noise densities much larger than 3 nV/Hz^{1/2}).

Detector 1/f noise can be neglected if chopping techniques are used; however, a chopping degradation factor¹⁷ must be incorporated into the analysis.

To compensate for the exclusion of these two noise sources, the noise bandwidth of the system was set to 1.5 times the information bandwidth (i.e., 1.5 times the Nyquist frequency¹⁸).

D.6.4 Results

Results of the analysis are presented in Figures D.6-1 through D.6-8. For comparison, two sets of operating conditions are considered. For the purposes of discussion, the two operating conditions are referred to as "baseline" and "extended" conditions, and are summarized in the following table.

	FRAME TIME (min)	GROUND RESOLUTION (km)	FOCAL PLANE ARRAY
BASELINE CONDITIONS	30	8	2x2
EXTENDED CONDITIONS	60	10	4x4

In the "Baseline" conditions, all baseline requirements with the exception of NEDT are satisfied. The "Extended" conditions were chosen to produce favorable NEDT values (values at or below 0.2 °K) for an actively cooled focal plane.

D.6.5 Conclusions

It is evident from the figures at the end of this document that the overriding limitation on NEAT performance is detector noise. Even when the focal plane is actively cooled, noise generated by the detector is by far the largest noise source. Whether passive or active cooling is used, additional sacrifices must be made in order to meet the NEAT requirement of 0.2 °K. Such sacrifices could include:

- Larger IGFOV
- Smaller frame size
- Increased frame time

¹⁷ - The chopping degradation factor is $\pi^{1/2}$ for a square wave chopper, and $\pi/2^{1/2}$ for a triangular chopper. It is the amount of degradation that results in both S/N ratio and NEDT when chopping techniques are used.

¹⁸ - The Nyquist frequency is defined as $1/2T_{\text{IFOV}}$.

- Wider spectral bandwidths
- Larger optics (or lower f-number)
- Larger focal plane array

Because of the large amount of detector noise, the following courses of action will **not** substantially improve the GOES sounder performance:

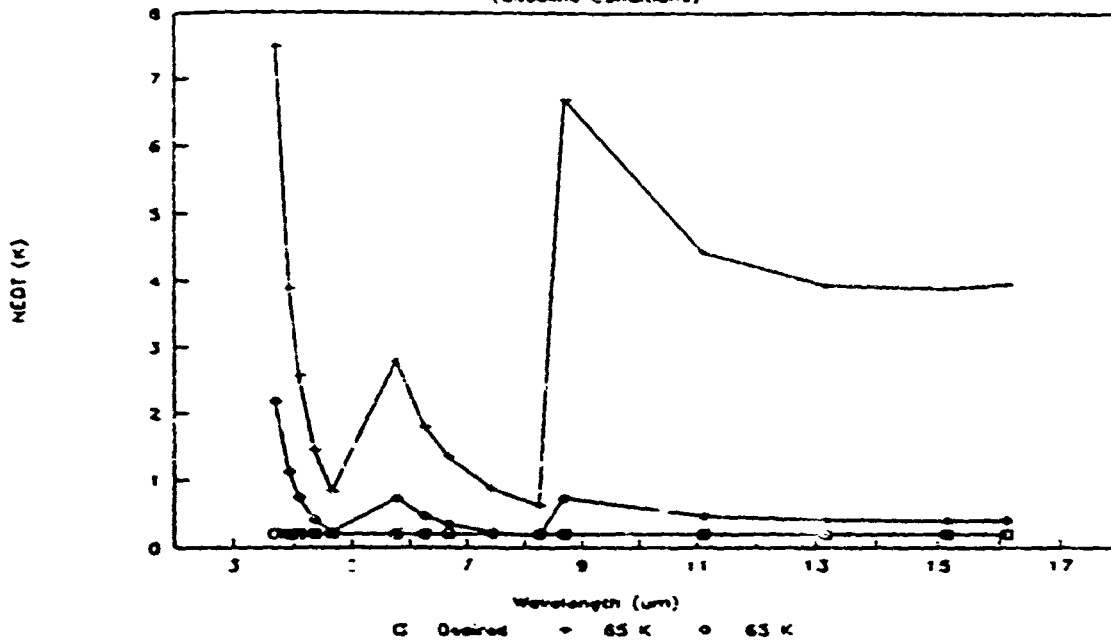
- Cooler fore optics
- Cooler aft optics
- Increased A/D resolution

D.6.6 Bibliography

- 1 Montgomery, H.E., et al., "Sensor Performance Analysis," *NASA Reference Publication 1241*, July 1990.

85 K vs 65 K FOCAL PLANE

(Baseline Conditions)



85 K vs 65 K FOCAL PLANE

(Extended Conditions)

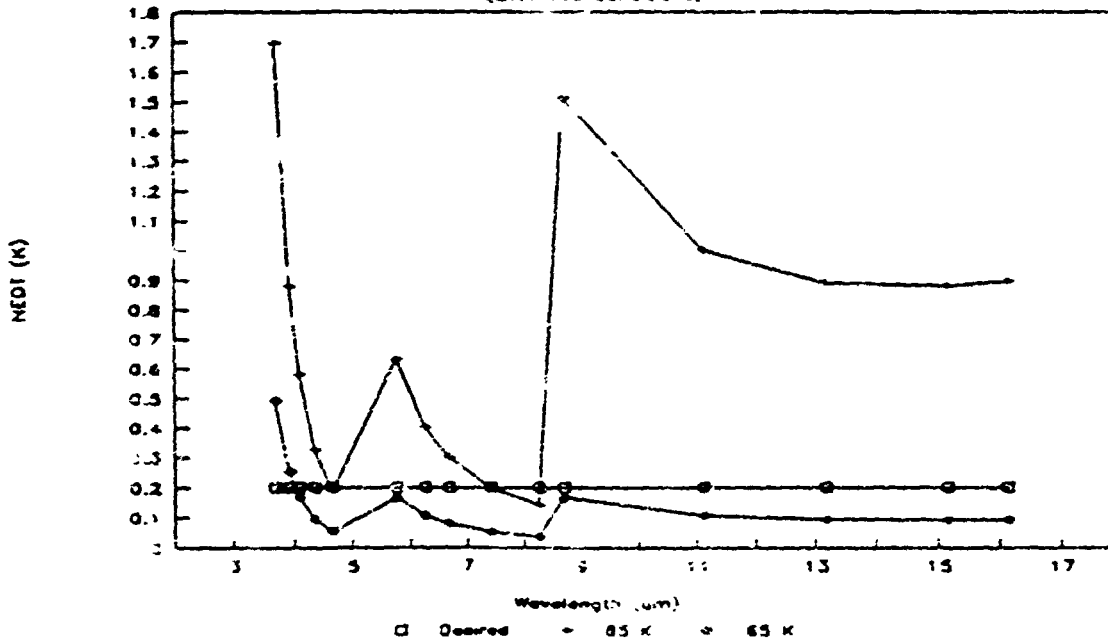


Figure D.6-1 - NEΔT vs Focal Plane Temperature
(Note: vertical scales are different)

Shows the effect of active cooling of the focal plane (i.e., reducing detector noise). "Baseline" conditions are shown in the upper graph, and "Extended" conditions are shown in the lower.

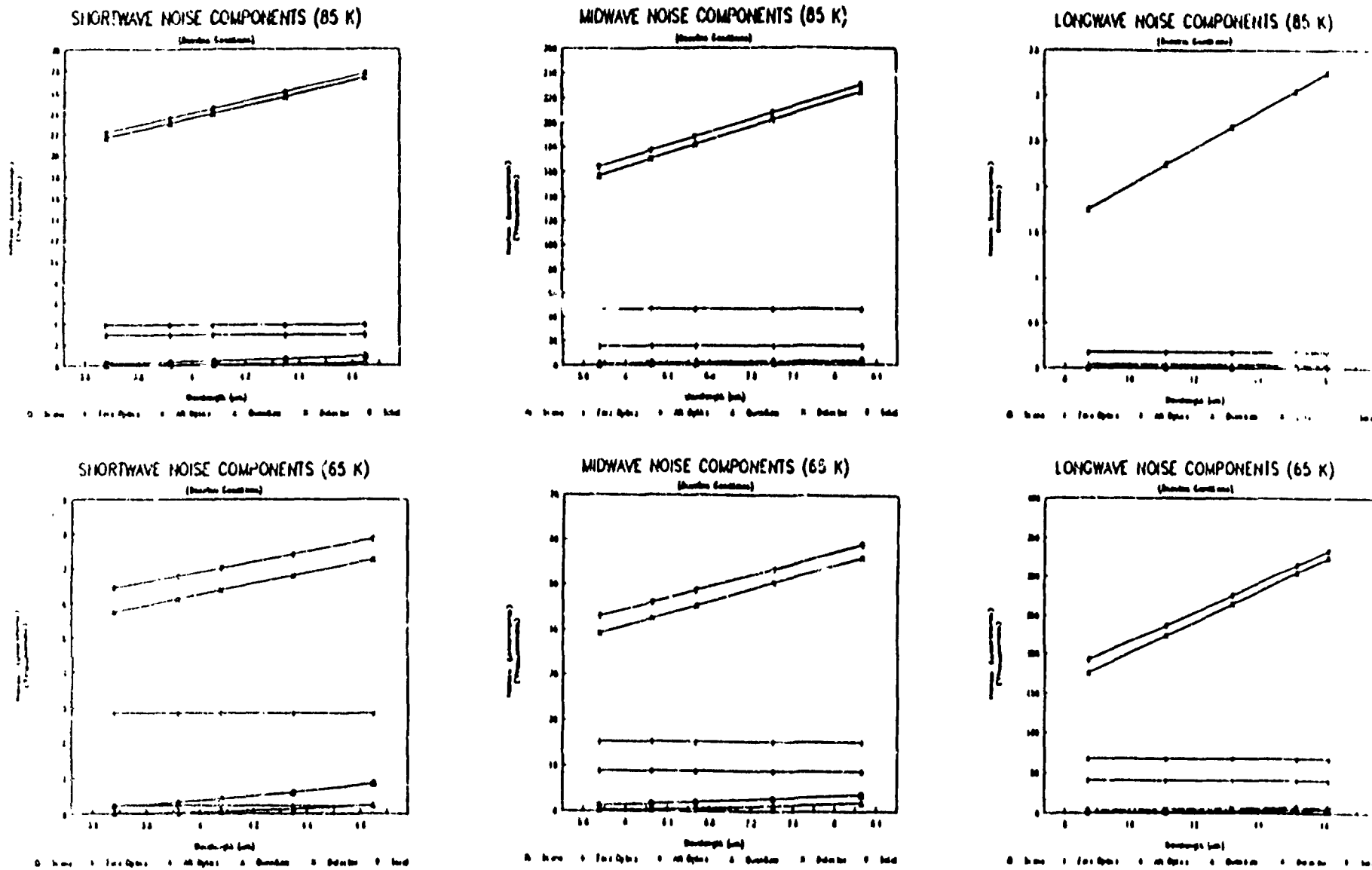


Figure D.6-2 - Noise Elements (Baseline conditions)
 (Note: vertical scales are different)

Shows the individual noise elements for the "Baseline" conditions at 85 K and at 65 K.

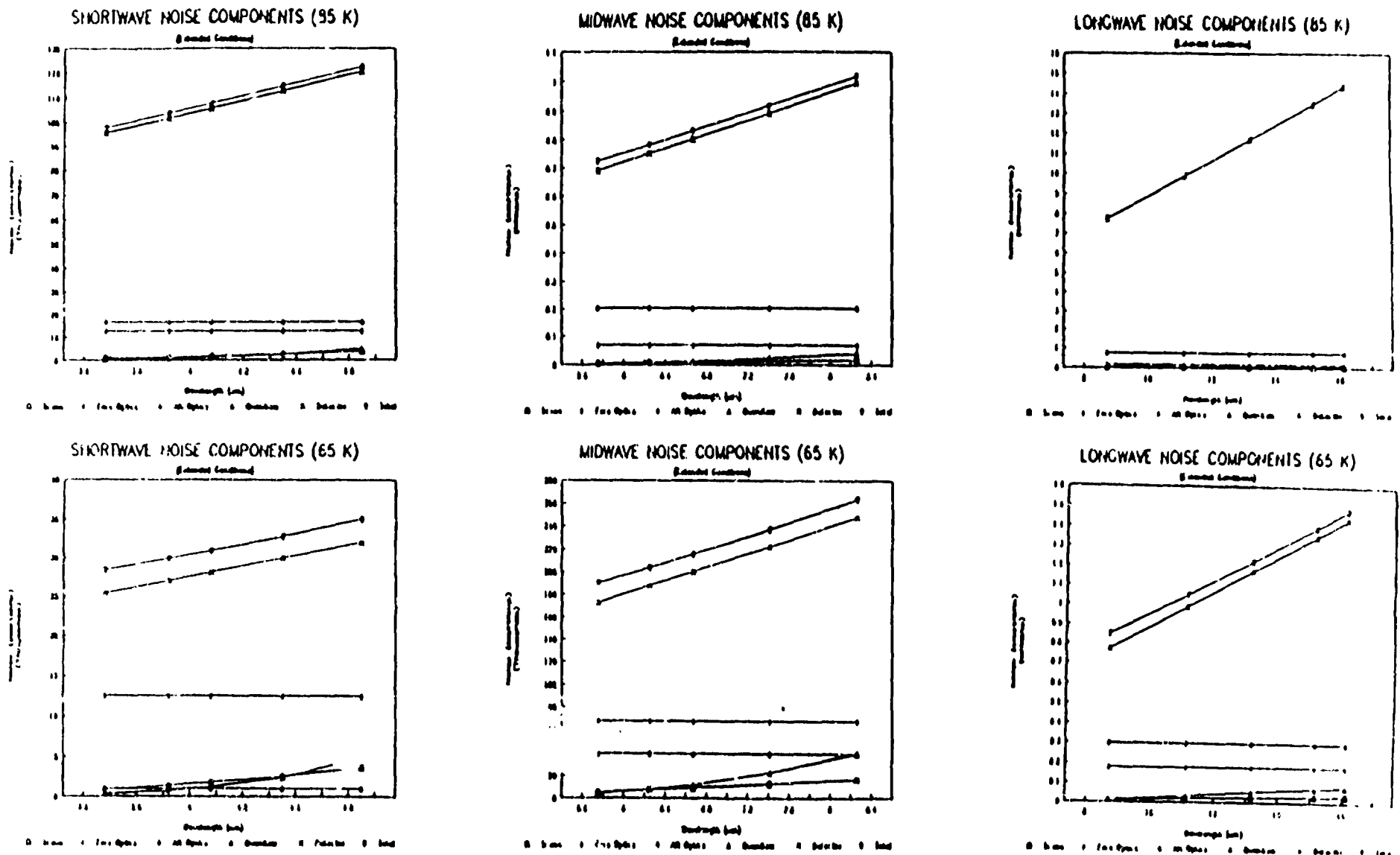


Figure D.6-3 - Noise Elements (Extended conditions)
 (Note: vertical scales are different)

Shows the individual noise elements for the "Extended" conditions at 85 K and at 65 K.

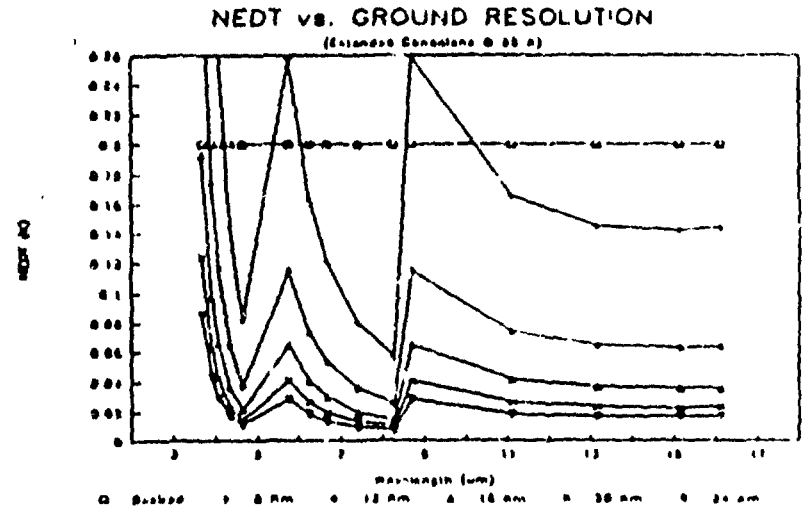
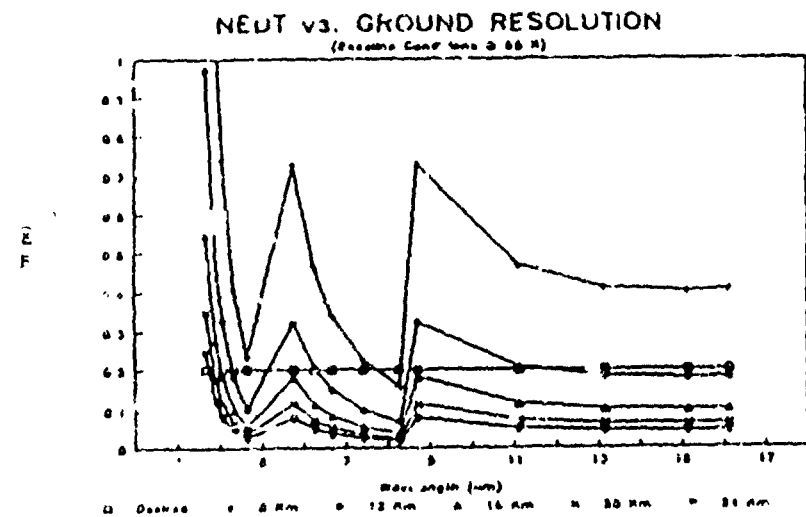
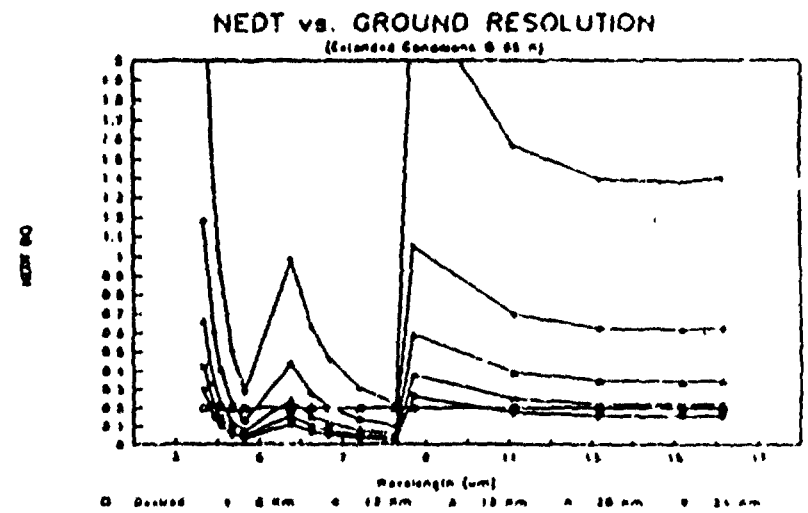
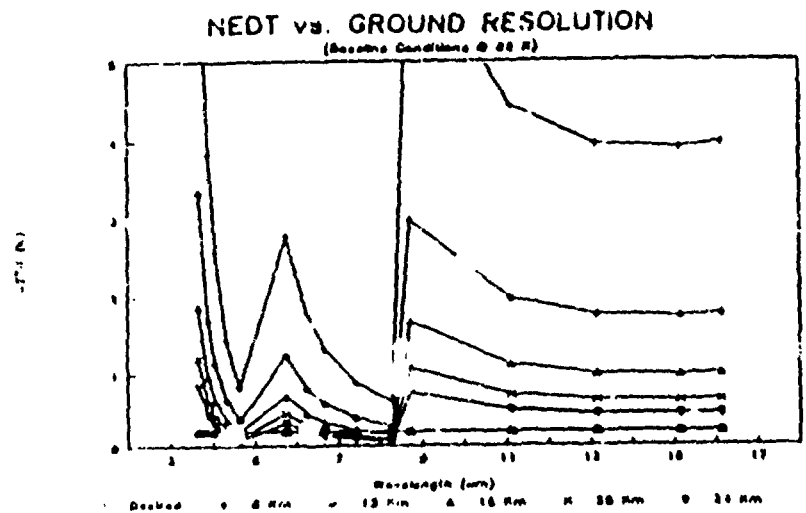


Figure D.6-4 - Comparison of Different Ground Resolutions
(Note: vertical scales are different)

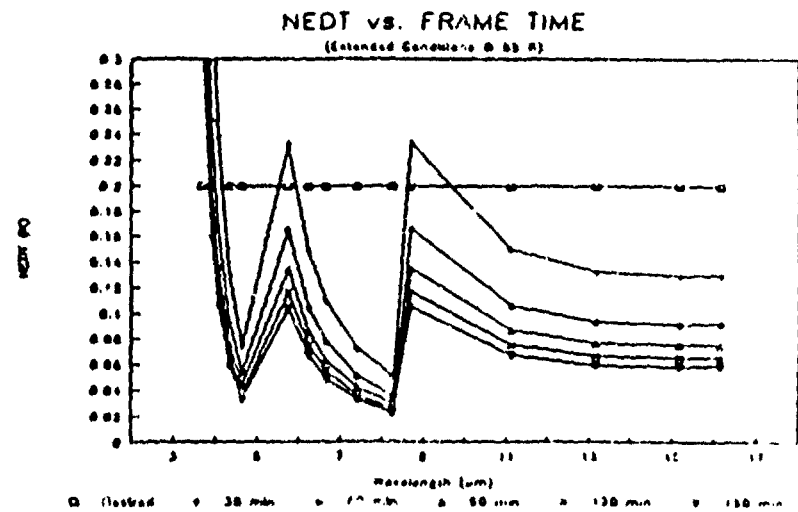
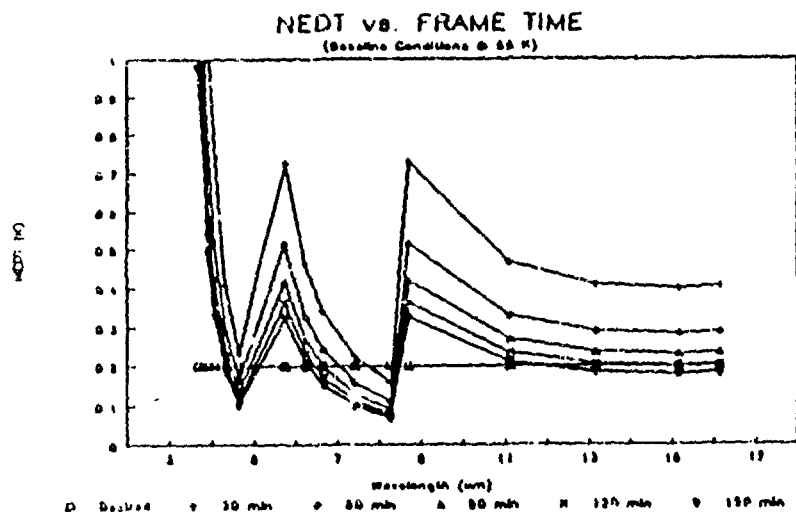
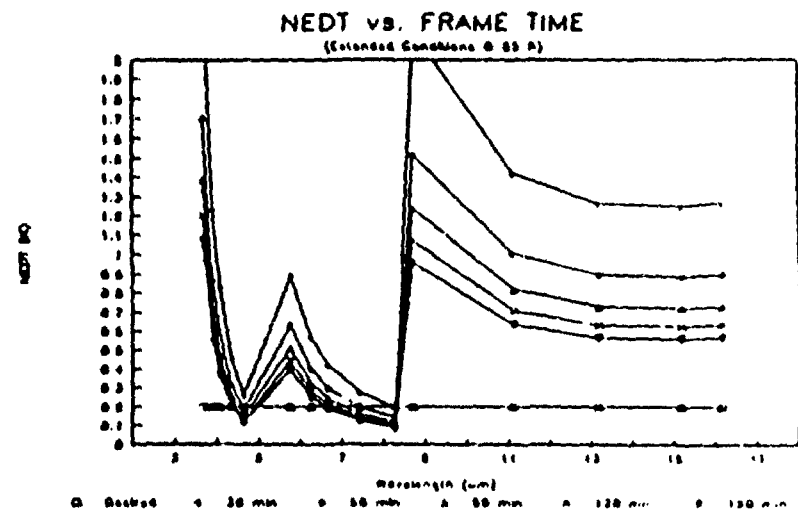
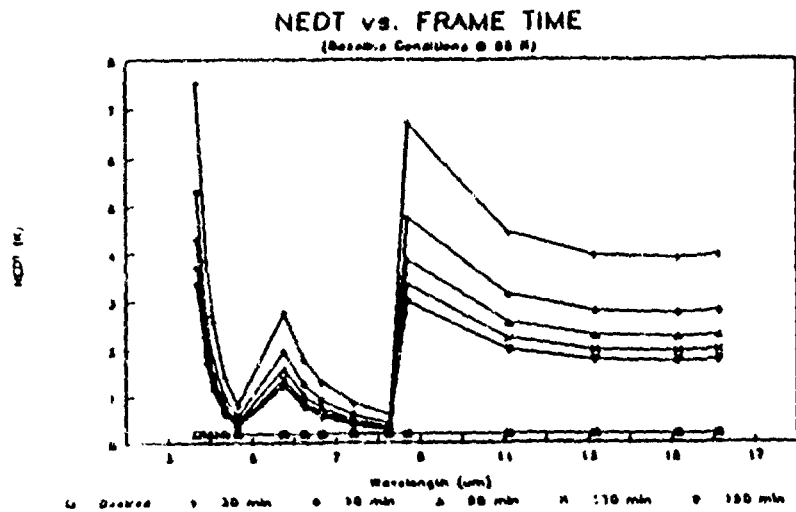


Figure D.6-5 - Comparison of Different Frame Times
(Note: vertical scales are different)

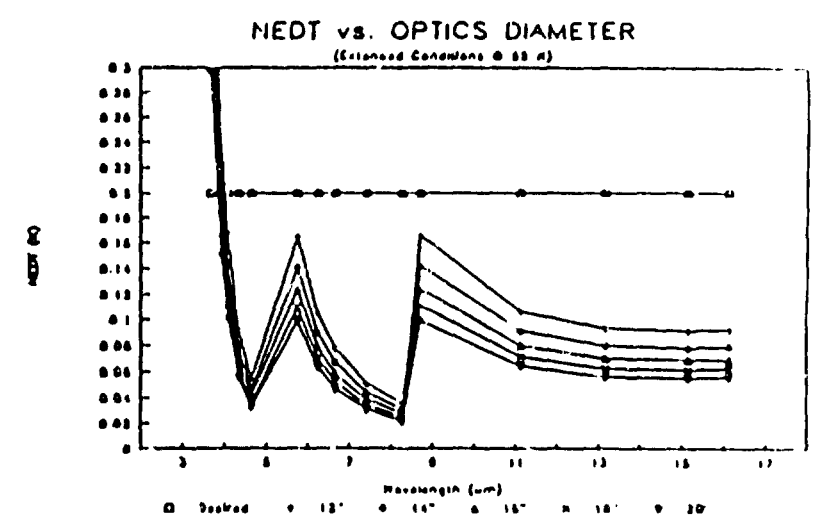
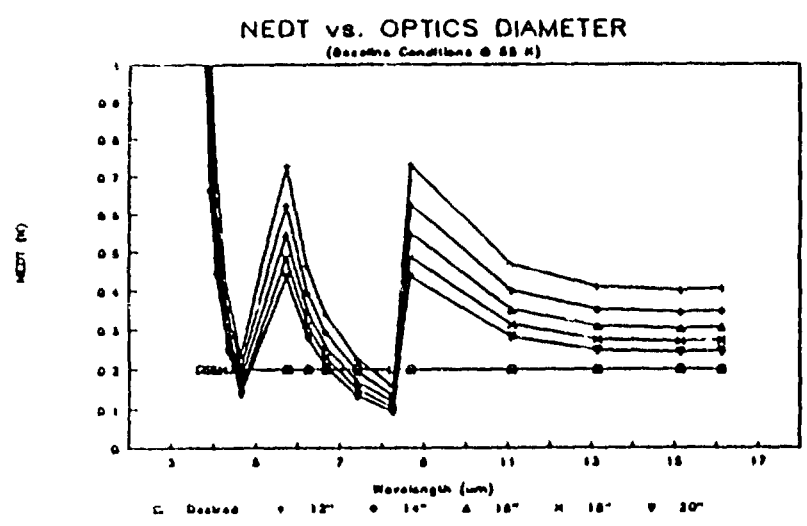
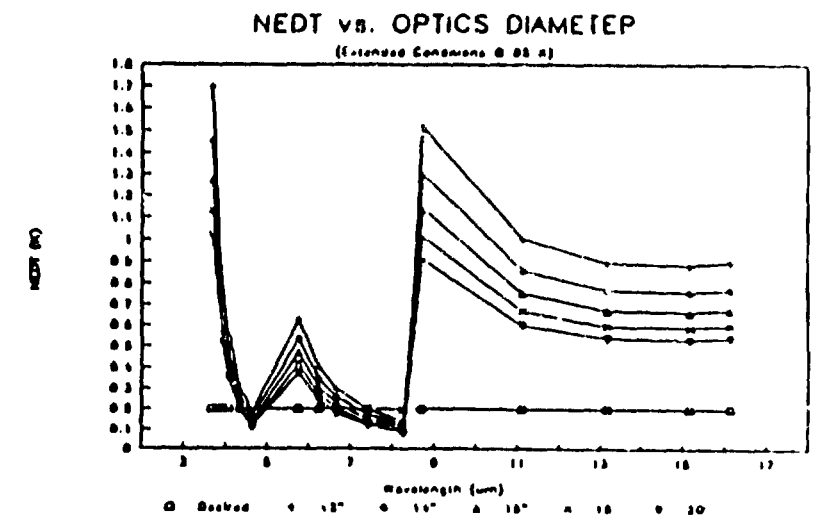
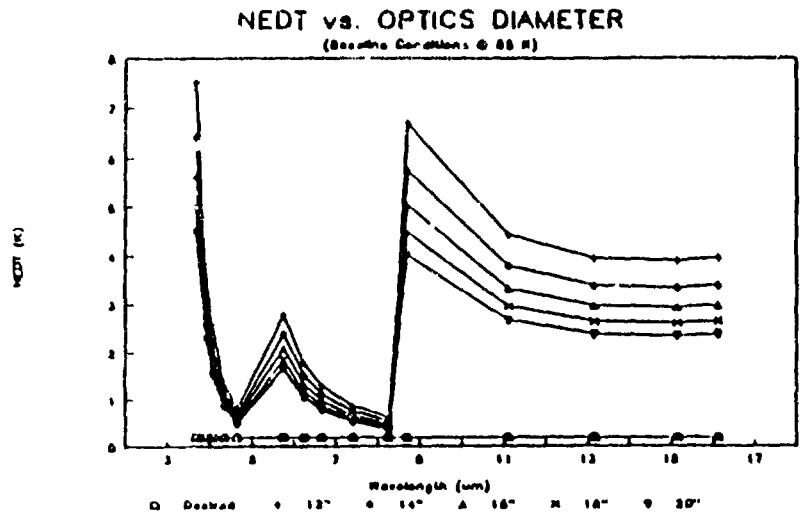


Figure D.6-6 - Comparison of Different Optics Diameters
(Note: vertical scales are different)

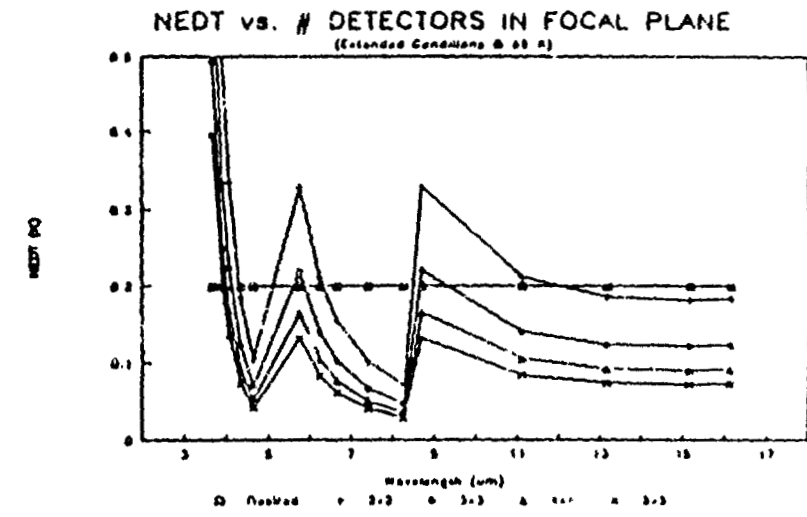
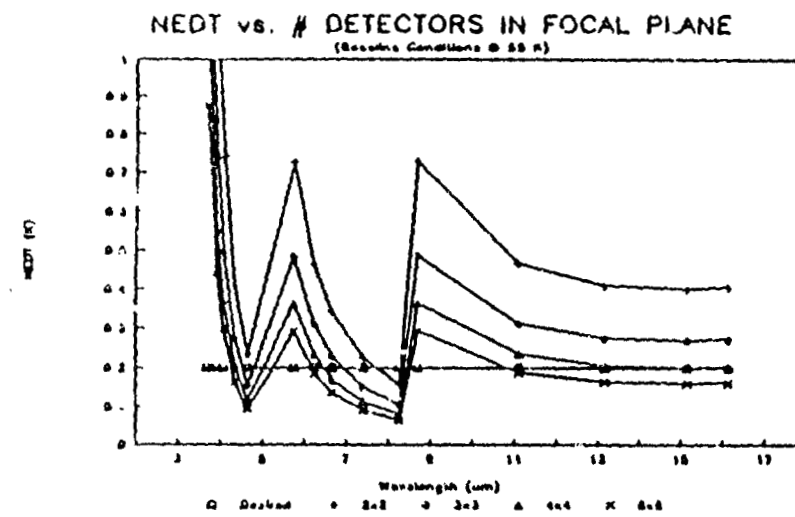
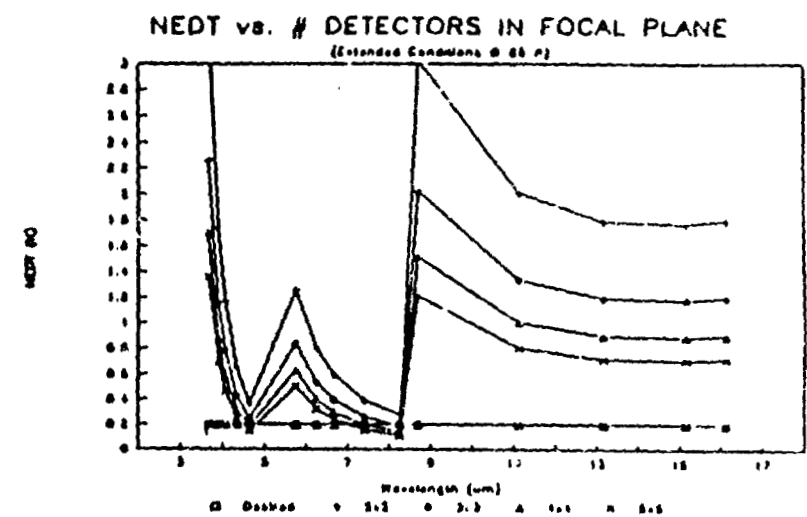
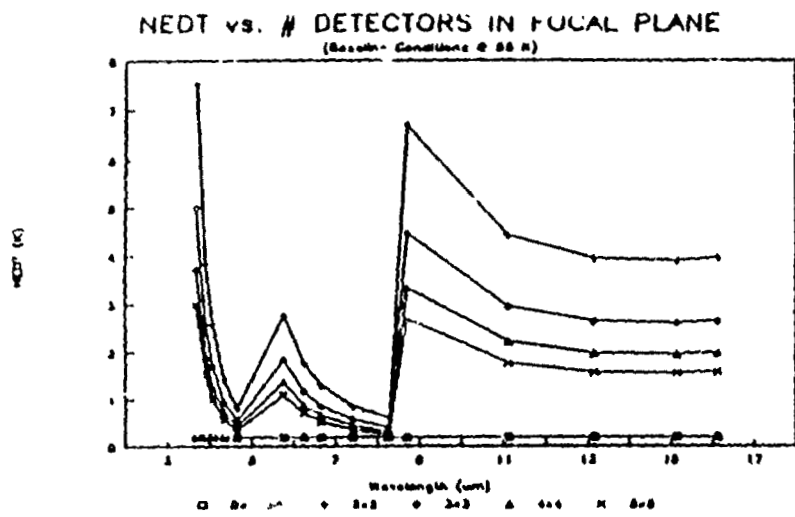


Figure D.6-7 - Comparison of Different Focal Plane Arrays
(Note: vertical scales are different)

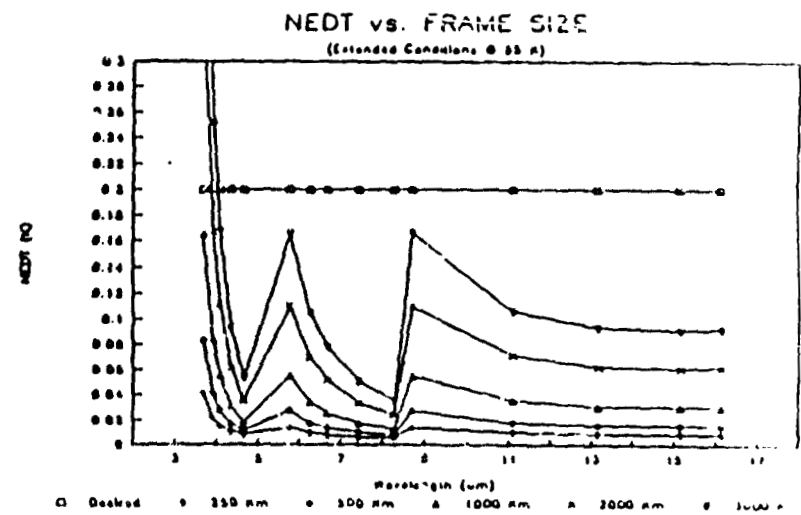
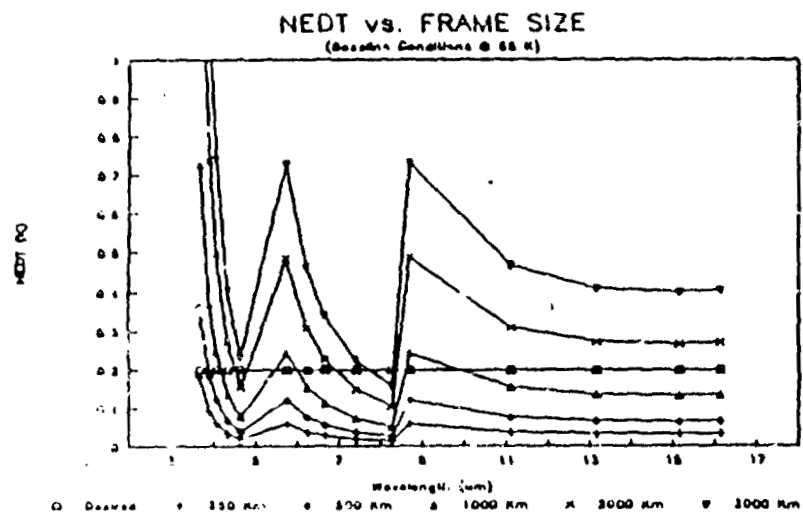
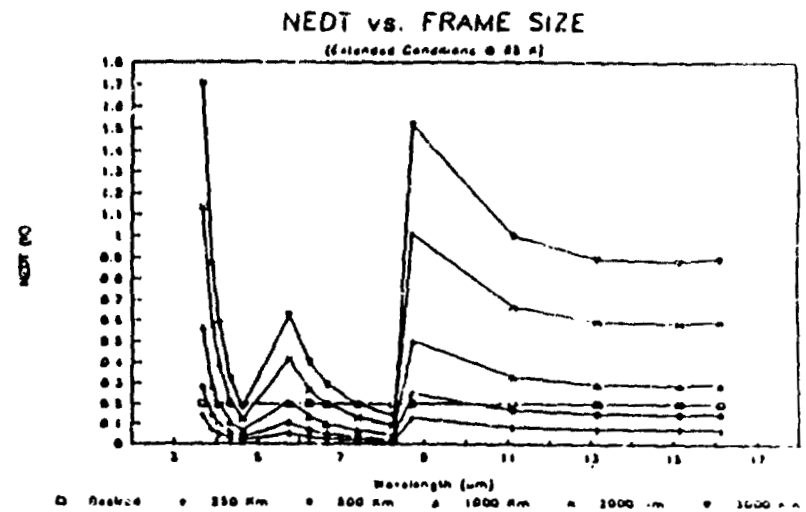
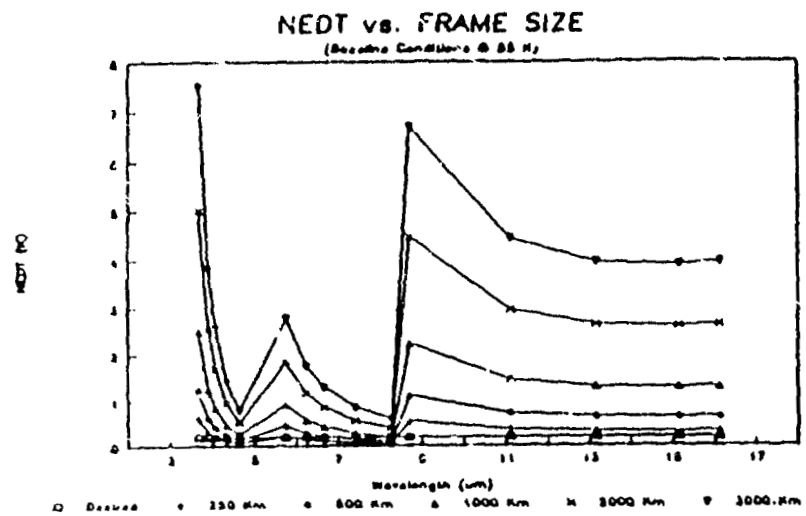


Figure D.6-8 - Comparison of Different Frame Sizes
(Note: vertical scales are different)

ATTACHMENT A -- SPREADSHEET CHANGES

This attachment presents the changes that were made to the spreadsheet in tailoring it to this study. Aside from these changes, all other formulas and calculations are as presented in [1].

Computation of Detector Noise

The detector noise computation is detailed in Attachment E. The computation does not subtract out background shot noise as in the original spreadsheet.

Sensor Background

The "sensor background" is composed of photon radiation which emanates from optical elements within the spacecraft. The original spreadsheet treated the optics as a single grey body radiator with a fixed temperature. Revisions have been made so that two grey bodies can be included, one for the fore optic, and one for the aft optics. Each have their own temperature and emissivity.

NEAT Computation

For the GOES-N application, scientists are looking at the earth's atmosphere, rather than the surface. The computation of NEAT has been revised so that NEAT is the noise equivalent change in the atmospheric temperature.

Integration Time

Integration time was originally computed for a "whisk broom" type polar orbiting satellite. The computation was modified for geosynchronous orbit. The equations are presented in Attachment C.

ATTACHMENT B - DETECTOR NOISE COMPUTATION

By definition:

$$D^* = \frac{(A\Delta f)^{1/2}}{NEP} \left[\frac{\text{cm}\sqrt{\text{Hz}}}{\text{W}} \right]$$

where,

- A - Detector Area (cm²)
- Δf - Electrical Bandwidth (Hz)
- NEP - Noise equivalent power (W)

The expression for D^* can be rearranged to obtain an expression for noise equivalent power:

$$NEP = \frac{(A\Delta f)^{1/2}}{D^*} \text{ [W]}$$

The noise in electrons can be derived from NEP as follows:

$$NEE = NEP \frac{\mathfrak{R} T_i}{q} \text{ [e]}$$

Where,

$$\mathfrak{R} \equiv \text{Detector Responsivity} \left[\frac{\text{A}}{\text{W}} \right]$$

$$q = 1.602 \times 10^{-19} = \text{electron charge} \text{ [coul]}$$

$$T_i = \text{Integration Time} \text{ [sec]}$$

Substituting for NEP yields the detector noise in electrons:

$$NEE = \frac{(A\Delta f)^{1/2}}{D} \frac{\mathfrak{R} T_i}{q} \text{ [e]}$$

ATTACHMENT C – INTEGRATION TIME COMPUTATION

The integration time is defined as the amount of time that the sensor will spend staring at each pixel location. If there are N_D detectors in the focal plane, and each detector is mapped to a ground distance equal to the Ground Resolution (GR), the instantaneous area of coverage is given by:

$$\text{Instantaneous Area} = N_D \cdot GR^2$$

The area of the Field of View (FOV), or a single frame, is given by FOV^2 . The number of scan mirror positions required to cover the entire frame without overlap is given by the ratio of the frame area to the instantaneous area of coverage.

$$\text{No. of Mirror Positions} = \frac{\text{Frame Area}}{\text{Instantaneous Area}} = \frac{FOV^2}{N_D GR^2}$$

Given a frame time of T_f seconds, the time that can be allotted to each scan mirror position will be given by:

$$\text{Pixel Time} = \frac{\text{Frame Time}}{\text{No. of Mirror Positions}} = \frac{T_f N_D GR^2}{FOV^2} \quad (\text{sec})$$

This "Pixel Time" includes both the integration time and the time required to move the mirror from one pixel to the next. The integration time is computed by subtracting the mirror step and settle time from the pixel time.

$$\text{Integration Time} = \text{Pixel Time} - T_{MS} = \frac{T_f N_D GR^2}{FOV^2} - T_{MS} \quad (\text{sec})$$

where,

- T_{MS} = Time required to move the scan mirror (sec)
- T_f = Frame time (sec)
- FOV = Total field of view (frame dimension, km)
- N_D = Number of detectors in the focal plane (dimensionless)
- GR = Ground resolution (km)

ATTACHMENT D - COMPARISON OF TECHNOLOGIES

The main considerations for each of the three sounder technologies are presented below.

GRATING SPECTROMETER

- Requires thousands of detectors in the focal plane
- A "normal" passive radiator is not feasible
- AIRS optics is not suited for geosynchronous orbit

Note: This approach is not recommended at this time

FABRY-PEROT INTERFEROMETER

- Excellent spectral resolution over a small free spectral range (10 to 20cm⁻¹)
- Meets the sensitivity requirements, but may need cryo-refrigeration
- Straightforward calibration
- Uses complex aft optics in order to cover NOAA spectral range requirement with contiguous high spectral resolution

Note: NOAA spectral coverage requirements discourage the use of Fabry Perot

FOURIER TRANSFORM INTERFEROMETER (MICHELSON)

- Meets NOAA spectral coverage requirement
- Optical complexity similar to a filter wheel spectrometer
- Does not meet core temporal coverage requirement with passive radiator due to limits on size and temperature of focal plane
- Use of cryo-refrigerator will sound 3000x3000km in 60 minutes at high spectral resolution with 10km IGFOV
- Must use very linear detector technology; may not be able to use highest sensitivity detectors
- Ground and space based signal processing are more complex than other approaches

Note: This approach offers lower complexity compared to other approaches.

D.7 SOUNDER DIFFRACTION STUDY

The purpose of this task is to compare the diffraction effects in the short-, mid- and longwave Infrared (IR) channels of the GOES sounder. The analysis is identical to cloud smearing analysis of the imager, except that the detector is circular, and there are no electronic filters.

D.7.1 Channel specifications

The sounder is composed of 3 IR Bands. Out of the three bands: short-, mid- and longwave, the longest longwave channel (channel 1), the middle midwave channel (channel 10) and the shortest shortwave channel (channel 18) were selected for the analysis and thus cover the full IR band of the sounder. These channels and their specifications are listed in Table D.7-1. Note that the size of the field stop is constant in all 3 channels.

Table D.7-1. Sounder Channel Specifications

BAND	CHANNEL	WAVELENGTH (UM)	FIELD STOP RADIUS (MM)
LW	1	14.706	1.57
MW	10	7.435	1.57
SW	18	3.744	1.57

D.7.2 Implementation

GENII software was used to compute the convolution of the telescope Line Spread Function (LSF) with the detector Instantaneous Field of View (FOV). Since the sounder is a staring, rather than scanning instrument, the Spatial Weighting Function (SWF) is a slice through the center of the resulting two dimensional convolution. For the ideal circular symmetry of the optic system and field stop, the SWF represents the relative weight given scene radiance as a function of distance from the center of the Field of View. GENII processing introduces an artificial offset of the IFOV in these plots.

D.7.3 Results

The SWF of the three channels under investigation are plotted in Figures D.7-1 through D.7-3. As expected, longer wavelengths exhibit the most spreading due to diffraction.

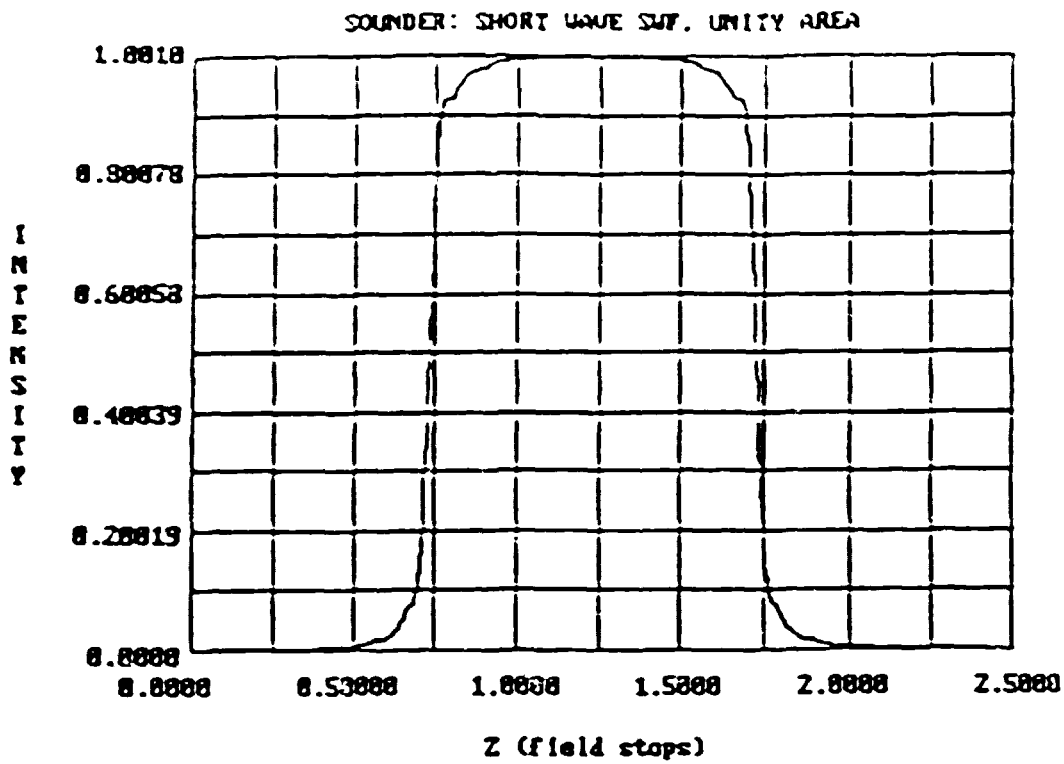


Figure D.7-1

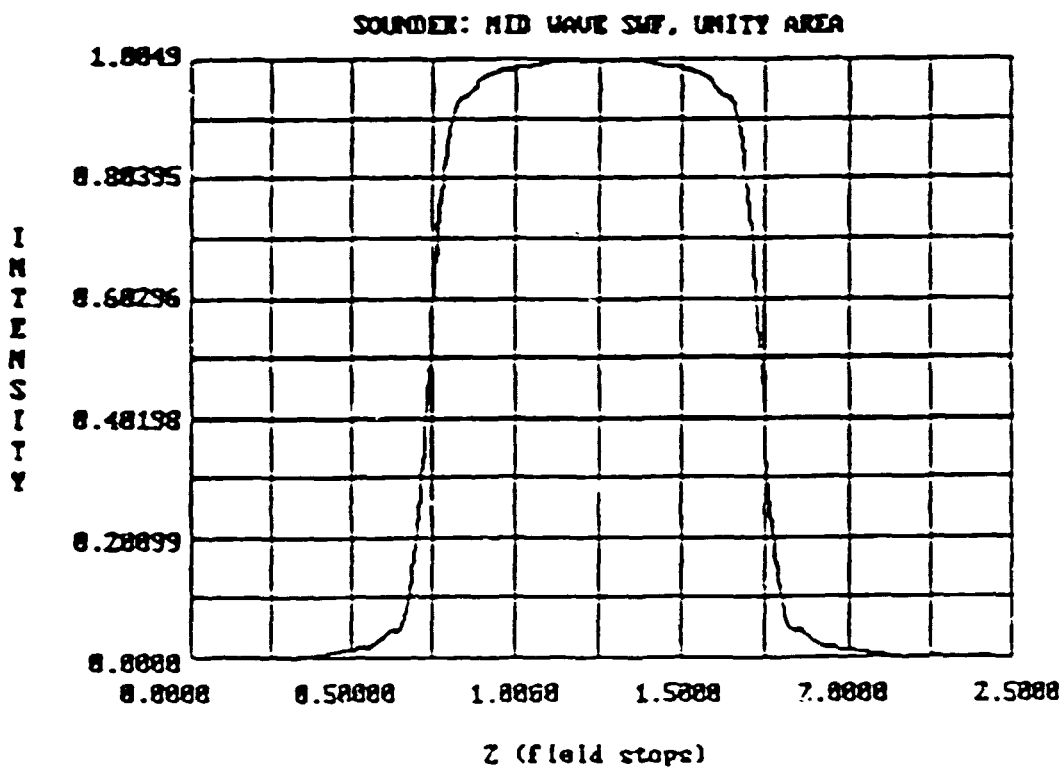


Figure D 7-2

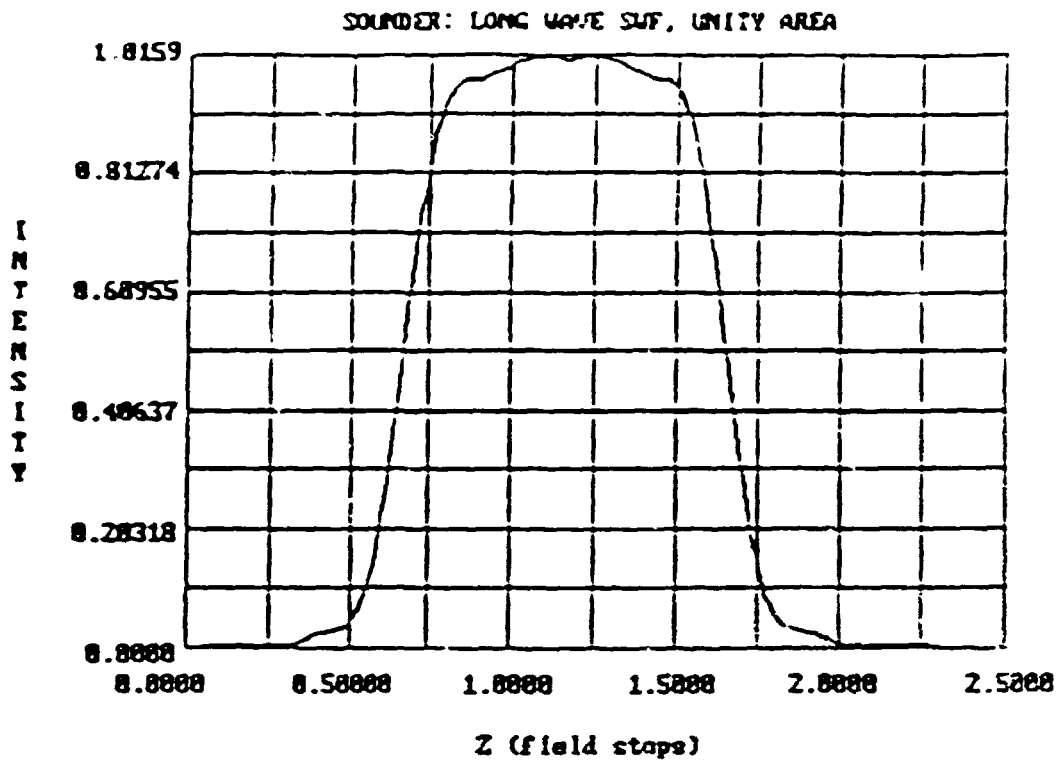


Figure D.7-3

APPENDIX E SOUNDER DIFFRACTION STUDY

E.1 TASK DESCRIPTION

The purpose of this task is to compare the diffraction effects in the short-, mid-, and longwave Infrared (IR) channels of the GOES sounder. The analysis is identical to cloud smearing analysis of the imager, except that the detector is circular, and there are no electronic filters.

E.2 Channel Specifications

The sounder is composed of 3 IR Bands. Out of the three bands: short-, mid-, and longwave, the longest longwave channel (channel 1), the middle midwave channel (channel 10) and the shortest shortwave channel (channel 18) were selected for the analysis and thus cover the full IR band of the sounder. These channels and their specifications are listed in Table E.2-1. Note that the size of the field stop is constant in all 3 channels.

Table E.2-1. Sounder Channel Specifications

BAND	CHANNEL	WAVELENGTH (UM)	FIELD STOP RADIUS (MM)
LW	1	14.706	1.57
MW	10	7.435	1.57
SW	18	3.744	1.57

E.3 Implementation

GENII software was used to compute the convolution of the telescope Line Spread Function (LSF) with the detector Instantaneous Field of View (FOV). Since the sounder is a staring, rather than scanning instrument, the Spatial Weighting Function (SWF) is a slice through the center of the resulting two dimensional convolution. For the ideal circular symmetry of the optic system and field stop, the SWF represents the relative weight given scene radiance as a function of distance from the center of the FOV. GENII processing introduces an artificial offset of the IFOV in these plots.

E.4 Results

The SWF of the three channels under investigation are plotted in Figures E.4-1 through E.4-3 expected, longer wavelengths exhibit the most spreading due to diffraction.

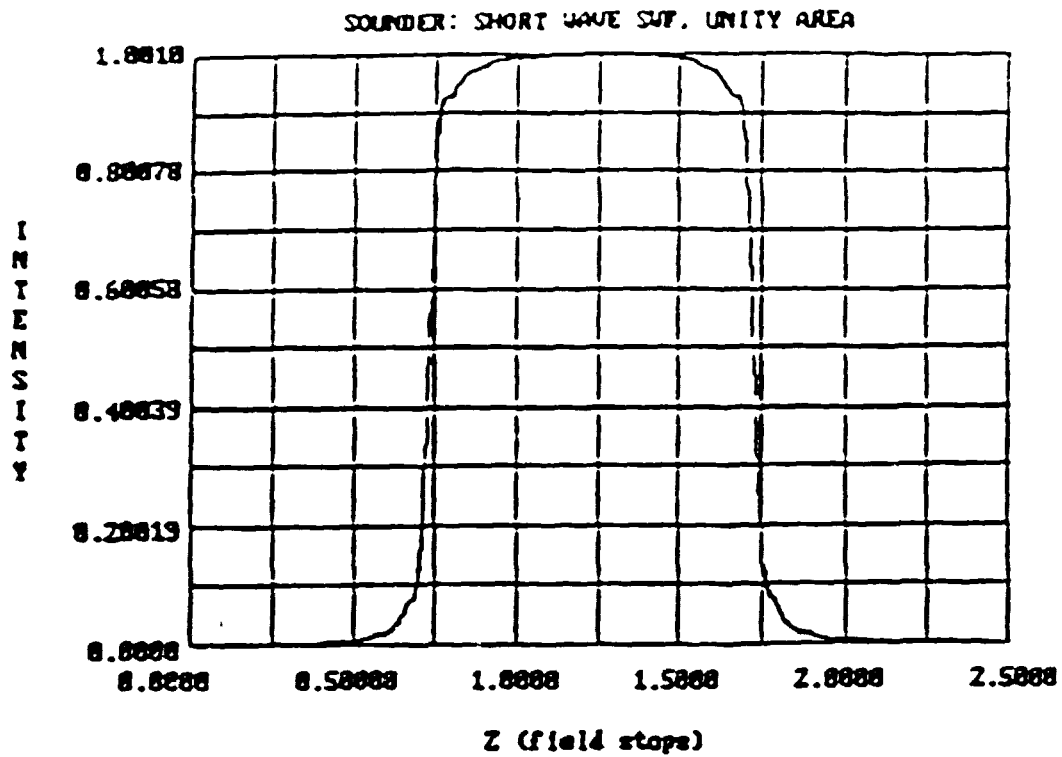


Figure E.4-1

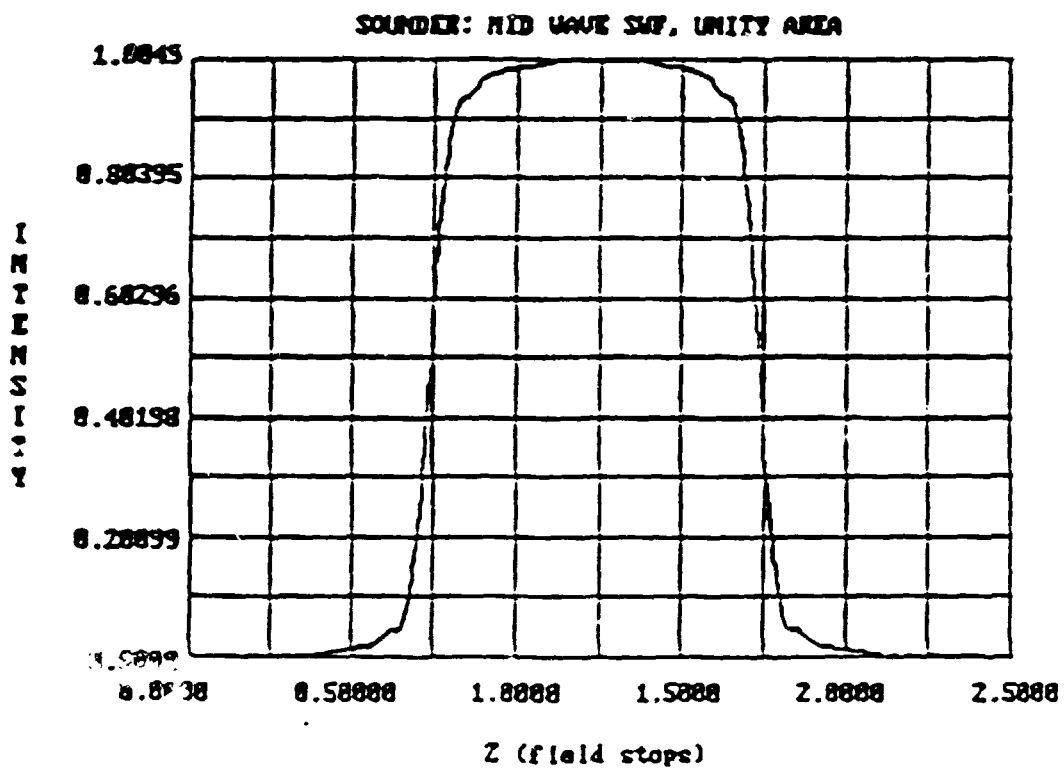


Figure E.4-2

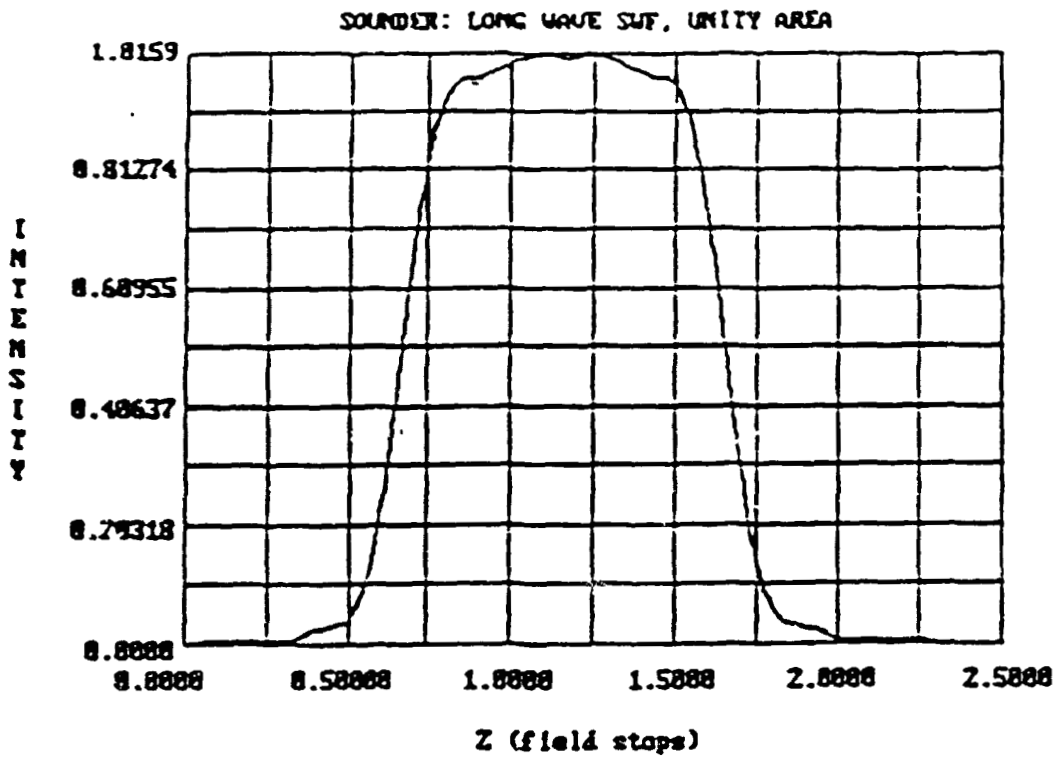


Figure E.4-3